ADVANCES IN HEAT TRANSFER

Volume 8

James P. Hartnett &
Thomas F. Irvine, Jr.

ADVANCES IN HEAT TRANSFER

Volume 8

Contributors to Volume 8

R. D. CESS
I. J. KUMAR
SIMON OSTRACH
S. N. TIWARI
Z. ZARIĆ
A. ŽUKAUSKAS

Advances in

HEAT TRANSFER

Edited by

James P. Hartnett

Department of Energy Engineering
University of Illinois
at Chicago
Chicago, Illinois

Thomas F. Irvine, Jr.

State University of New York
at Stony Brook
Stony Brook, Long Island
New York

Volume 8

1972

ACADEMIC PRESS · New York · London

ACADEMIC PRESS, INC.
111 Fifth Avenue, New York, New York 10003

United Kingdom Edition published by
ACADEMIC PRESS, INC. (LONDON) LTD.
24/28 Oval Road, London NW1

LIBRARY OF CONGRESS CATALOG CARD NUMBER: 63-22329

PRINTED IN THE UNITED STATES OF AMERICA

CONTENTS

List of Contributors vii
Preface ix
Contents of Previous Volumes xi

Recent Mathematical Methods in Heat Transfer

I. J. KUMAR

I. Introduction 2
II. Perturbation Methods 3
III. Asymptotic Methods 14
IV. Variational Methods 22
V. Methods Related to the Solution of Integral Equations . . . 34
VI. Methods Based on the Use of the Complex Variable 42
VII. Special Methods for the Solution of Partial Differential Equations 53
VIII. Application of Matrices 62
IX. Eigenfunction Expansions 66
X. Miscellaneous Methods 70
XI. Conclusion 78
Nomenclature 79
References 84

Heat Transfer from Tubes in Crossflow

A. ŽUKAUSKAS

I. Introduction 93
II. Flow Past a Single Tube 95
III. Flow Past a Tube in a Bank 105
IV. Influence of Fluid Properties on Heat Transfer 112
V. Heat Transfer of a Single Tube 116
VI. Heat Transfer of a Tube in a Bank 133
VII. Hydraulic Resistance of Banks 150
VIII. Calculation of Banks of Tubes in Crossflow 155
Nomenclature 158
References 158

Natural Convection in Enclosures

SIMON OSTRACH

I. Introduction 161
II. Rectangular Cavities 174
III. Horizontal Circular Cylinder 196
IV. Concluding Remarks 224
Nomenclature 225
References 226

Infrared Radiative Energy Transfer in Gases

R. D. CESS AND S. N. TIWARI

I. Introduction 229
II. Band Absorptance Models 230
III. Basic Equations 246
IV. Radiative Transfer Analyses 254
V. Concluding Remarks 280
Nomenclature 281
References 282

Wall Turbulence Studies

Z. ZARIĆ

I. Introduction 285
II. Turbulence Problem 287
III. Current Experimental Methods 292
IV. Survey of Illustrative Experimental Results 299
V. Hot Wire–Cold Wire Experimental Method 309
VI. Experimental Results 318
VII. Statistical Analysis 335
VIII. Concluding Remarks 345
Symbols 348
References 348

Author Index 351
Subject Index 359

LIST OF CONTRIBUTORS

R. D. CESS, *College of Engineering, State University of New York, Stony Brook, New York*

I. J. KUMAR, *Defense Science Laboratory, Delhi-6, India*

SIMON OSTRACH, *Division of Fluid, Thermal, and Aerospace Sciences, Case Western Reserve University, Cleveland, Ohio*

S. N. TIWARI,* *College of Engineering, State University of New York, Stony Brook, New York*

Z. ZARIĆ, *Boris Kidrič Institute, University of Beograd, Beograd, Yugoslavia*

A. ŽUKAUSKAS, *Academy of Sciences of the Lithuanian SSR, Vilnius, USSR*

* Present address: Department of Thermal Engineering, College of Engineering, Old Dominion University, Norfolk, Virginia 23508.

This Page Intentionally Left Blank

PREFACE

The serial publication "Advances in Heat Transfer" is designed to fill the information gap between the regularly scheduled journals and university level textbooks. The general purpose of this series is to present review articles or monographs on special topics of current interest. Each article starts from widely understood principles and in a logical fashion brings the reader up to the forefront of the topic. The favorable response to the volumes published to date by the international scientific and engineering community is an indication of how successful our authors have been in fulfilling this purpose.

The editors are pleased to announce the publication of Volume 8 and wish to express their appreciation to the current authors who have so effectively maintained the spirit of the series.

This Page Intentionally Left Blank

CONTENTS OF PREVIOUS VOLUMES

Volume 1

The Interaction of Thermal Radiation with Conduction and Convection Heat Transfer
R. D. CESS
Application of Integral Methods to Transient Nonlinear Heat Transfer
THEODORE R. GOODMAN
Heat and Mass Transfer in Capillary-Porous Bodies
A. V. LUIKOV
Boiling
G. LEPPERT and C. C. PITTS
The Influence of Electric and Magnetic Fields on Heat Transfer to Electrically Conducting Fluids
MARY F. ROMIG
Fluid Mechanics and Heat Transfer of Two-Phase Annular-Dispersed Flow
MARIO SILVESTRI

AUTHOR INDEX—SUBJECT INDEX

Volume 2

Turbulent Boundary-Layer Heat Transfer from Rapidly Accelerating Flow of Rocket Combustion Gases and of Heated Air
D. R. BARTZ
Chemically Reacting Nonequilibrium Boundary Layers
PAUL M. CHUNG
Low Density Heat Transfer
F. M. DEVIENNE
Heat Transfer in Non-Newtonian Fluids
A. B. METZNER
Radiation Heat Transfer between Surfaces
E. M. SPARROW

AUTHOR INDEX—SUBJECT INDEX

Volume 3

The Effect of Free-Stream Turbulence on Heat Transfer Rates
J. KESTIN
Heat and Mass Transfer in Turbulent Boundary Layers
A. I. LEONT'EV
Liquid Metal Heat Transfer
RALPH P. STEIN
Radiation Transfer and Interaction of Convection with Radiation Heat Transfer
R. VISKANTA
A Critical Survey of the Major Methods for Measuring and Calculating Dilute Gas Transport Properties
A. A. WESTENBERG

AUTHOR INDEX—SUBJECT INDEX

Volume 4

Advances in Free Convection
A. J. EDE
Heat Transfer in Biotechnology
ALICE M. STOLL
Effects of Reduced Gravity on Heat Transfer
ROBERT SIEGEL
Advances in Plasma Heat Transfer
E. R. G. ECKERT and E. PFENDER
Exact Similar Solution of the Laminar Boundary-Layer Equations
C. FORBES DEWEY, JR., and JOSEPH F. GROSS

AUTHOR INDEX—SUBJECT INDEX

Volume 5

Application of Monte Carlo to Heat Transfer Problems
JOHN R. HOWELL
Film and Transition Boiling
DUANE P. JORDAN
Convection Heat Transfer in Rotating Systems
FRANK KREITH
Thermal Radiation Properties of Gases
C. L. TIEN
Cryogenic Heat Transfer
JOHN A. CLARK

AUTHOR INDEX—SUBJECT INDEX

Volume 6

Supersonic Flows with Imbedded Separated Regions
A. F. CHARWAT
Optical Methods in Heat Transfer
W. HAUF and U. GRIGULL
Unsteady Convective Heat Transfer and Hydrodynamics in Channels
E. K. KALININ and G. A. DREITSER
Heat Transfer and Friction in Turbulent Pipe Flow with Variable Physical Properties
B. S. PETUKHOV

AUTHOR INDEX—SUBJECT INDEX

Volume 7

Heat Transfer near the Critical Point
W. B. HALL
The Electrochemical Method in Transport Phenomena
T. MIZUSHINA
Heat Transfer in Rarefied Gases
GEORGE S. SPRINGER
The Heat Pipe
E. R. F. WINTER and W. O. BARSCH
Film Cooling
RICHARD J. GOLDSTEIN

AUTHOR INDEX—SUBJECT INDEX

This Page Intentionally Left Blank

Recent Mathematical Methods in Heat Transfer

I. J. KUMAR

Defense Science Laboratory, Delhi-6, India

I. Introduction 2
II. Perturbation Methods 3
A. PLK Method 3
B. Method of Matched Asymptotic Expansions 7
C. Method of Multiple Scales and Other Singular Perturbation Methods 12
D. Method of Series Truncation in Elliptic Flow Problems . . 13
III. Asymptotic Methods 14
A. Meksyn's Method 14
B. WKBJ Approximation 19
IV. Variational Methods 22
A. Biot's Variational Principle 23
B. Variational Principles Based on Local Potentials 26
C. Other Variational Formulations and Their Application . . . 32
V. Methods Related to the Solution of Integral Equations 34
A. Integral Equations in Radiative Heat Transfer 34
B. Reduction of Other Heat Transfer Problems to Integral Equations 34
C. Lighthill–Volterra Approach 35
D. Perelman's Asymptotic Method 37
E. A New Method Based on the Mellin Transform 40
VI. Methods Based on the Use of the Complex Variable 42
A. Solution of Harmonic and Biharmonic Equations 42
B. Schwarz–Christoffel Transformation 45
C. Wiener–Hopf Method 49
VII. Special Methods for the Solution of Partial Differential Equations 53
A. Method of Characteristics 53
B. A Method of Analytic Iteration 56
VIII. Application of Matrices 62
A. An Application to Simultaneous Diffusion of Two Entities 62
B. Further Applications 65

IX. Eigenfunction Expansions 66
A. Eigenvalues of the Heat Conduction Equation 66
B. Application to Perturbation Solutions of Momentum and Energy Equations 67
C. Further Applications 70
X. Miscellaneous Methods 70
A. Rosenweig's Matching Technique 70
B. Dorfman's Method for Nonsimilar Boundary Layers . . . 74
C. Surkov's Method for Problems Involving Change of Phase 75
D. Duhamel's Principle 78
XI. Conclusion 78
Nomenclature 79
References 84

I. Introduction

With the recent advancements in the fields of atomic energy, aeronautics, and astronautics, an engineer is faced with more and more complex problems in heat transfer. While sophisticated instrumentation has greatly helped him to achieve accuracy and reliability in experimental measurements, the computer has immensely increased his capacity to theoretically study more realistic models. These advancements, however, are no substitute for the power and ingenuity of the mathematical methods which are, and would remain as, the main tool in the hands of engineers for the solution of practical problems. In the present review some of the most important methods employed in recent heat transfer literature will be reviewed, with a special stress on those still under development, and examples from the literature cited, to demonstrate the power of a method and indicate the branches of heat transfer where one may look upon a particular method as a potential tool for obtaining the solution. While reviewing a particular method, examples will be presented from the recent literature irrespective of the location of the problem in the hierarchy of heat transfer literature. Thus, it will be attempted to synthesize the recent developments in heat transfer from the point of view of mathematical methods. From a physical point of view, these developments have already been brought to light in a systematic and cohesive manner in the recently published monographs [1–7]. No claim to completeness of the review is made in view of the limitations of space and the availability of other literature, especially of Soviet literature.

No reference will be made in this review to the method of weighted residuals or integral methods. A review of these methods by Finlayson and Scriven [8] and an account of their application to unsteady heat conduction [9] have recently appeared. Similarly, the classical method of operational

calculus used extensively by Carslaw and Jaeger [10] and Luikov [11] in the theory of heat conduction and by Luikov and Mikhaylov [12] in the theory of combined heat and mass diffusion will not be touched upon.

It would not be out of place here to mention a few words about nomenclature. Although highly desirable, it is very difficult to achieve uniform nomenclature in a review article of this nature, where various branches of heat transfer and many mathematical methods used therein are being reviewed. Therefore, for ease of reference, a comprehensive nomenclature has been provided separately for each section at the end of the review. The symbols which have the same meaning throughout the review have been listed under the section where they were used for the first time.

II. Perturbation Methods

The perturbation method consists essentially of expanding the dependent variable in a series of powers of a quantity known to be small. When this small quantity is a parameter the method is known as parameter perturbation and where it is a coordinate the method is termed a coordinate perturbation. Taking this small quantity to be ϵ, the solution of the differential equation for ϵ is the zeroth-order solution or the solution of the unperturbed problem. When the expansion is substituted in the differential equation and the like powers of ϵ equated, we get a system of differential equations for the subsequent order solutions. The assumed series is convergent in the asymptotic sense [13] and if the above scheme succeeds, we speak of it as a regular perturbation. This method has been used in a number of problems and has produced very useful results.

In many problems, however, the ratio of successive terms in the solution ceases to be small and the regular perturbation scheme therefore fails in some region of the flow field. Thus it is not possible to obtain a uniformly valid solution throughout the region of interest by a regular perturbation scheme. Such problems are known as singular perturbation problems. We propose to discuss some of the methods of dealing with such problems in the context of heat transfer.

A. PLK Method

Sometimes the regular perturbation fails because of the presence of a singularity in the zeroth-order solution at a point or on a line in the region of investigation. This singularity becomes progressively more and more severe as the order of the solution increases. A technique for solving such problems

by a perturbation method was presented by Lighthill [14], in which the dependent variable v and the independent variable x are both expanded in powers of the small quantity ϵ. The method consists of expanding v and x thus:

$$v = v_0(\chi) + \epsilon v_1(\chi) + \epsilon^2 v_2(\chi) + \cdots, \tag{1}$$

$$x = \chi + \epsilon x_1(\chi) + \epsilon^2 x_2(\chi) + \cdots, \tag{2}$$

where χ takes the place of the original independent variable x, $v_0(\chi)$ is simply the zeroth-order solution of the regular perturbation method with χ replacing x, and $x_n(\chi)$, $n = 1, 2, 3, \ldots$ are so chosen that the higher approximations shall be no more singular than the first. This remark will become clear in the example discussed below. This method with various applications is presented by Tsien [15] who called it the Poincaré–Lighthill–Kuo or, in short, the PLK method because of the contribution of Poincaré [16] and Lighthill [14] to this method and its extensive application by Kuo [17]. The method has also been referred to as the method of strained coordinates (see Van Dyke [18], Chapter 6), where many examples of the applications of this method in aerodynamics are also presented. Lighthill [19] has applied the method to conical shock waves in steady supersonic flows and Legras [20, 21] to supersonic air foils.

The PLK method is also applicable to cases where the nonuniformity of the solution arises in higher than the zeroth-order regular perturbation solution. While studying the nonlinear problem of temperature distribution in a melting slab with the melting face subject to a constant heat flux, the farther end of the slab being insulated, Goodman and Shea [22], by an integral method, derived the system of nonlinear coupled differential equations

$$\frac{ds}{d\theta} + \mu \frac{dw}{d\theta} + \mu \frac{dv}{d\theta} = 2\mu\alpha_1, \tag{3}$$

$$\frac{s^2}{3} \frac{dw}{d\theta} = \alpha_1 s^2 - vw, \tag{4}$$

$$(1 - s)^2 \frac{dv}{d\theta} = -3v, \tag{5}$$

to be solved with the initial conditions

$$s(0) = 0, \qquad w(0) = 0, \qquad v(0) = -2\alpha_1/3, \tag{6}$$

where s, w, v represent the nondimensional parameters related to the position of the melting interface and the temperature in the melted and unmelted parts of the slab, respectively, and α_1 is a parameter with natural restriction $0 < \alpha_1 < 1$. If a regular perturbation scheme is adopted for the solution of

the above system of equations, namely, if we assume an expansion of the following type

$$f(\alpha_1, \mu, v, \theta) = f_0(\mu, v, \theta) + \alpha_1 f_1(\mu, v, \theta) + \alpha_1^2 f_2(\mu, v, \theta) \cdots \tag{7}$$

for each of the dependent variables s, w, v, it is found that the second-order solution $v_2(\theta)$ contains terms of the type $\theta \exp(-3\theta)$ and $\theta^2 \exp(-3\theta)$. Thus the value of v obtained by this method for large θ achieves positive values and for moderately large θ these terms create humps in the solution. Since it follows from Eq. (5) and the last of the initial conditions in Eq. (6) that v has to be negative, the entire solution obtained by the regular perturbation scheme is invalidated.

To obtain a uniformly valid solution, we make recourse to the PLK method. Thus we define a new independent variable ζ and expand s, v, w and the independent variable θ in terms of the new independent variable ζ in powers of the small parameter α. Thus we assume

$$\theta(\alpha_1, \mu, v, \zeta) = \zeta + \alpha_1 \theta_1(\mu, v, \zeta) + \alpha_1^2 \theta_2(\mu, v, \zeta) + \cdots \tag{8}$$

and expansions similar to Eq. (7) with θ replaced by the new independent variable ζ for s, w, v. Thus the problem posed by Eqs. (3)–(6) can be restated as

$$\frac{ds}{d\zeta} + \mu \frac{dw}{d\zeta} + \mu \frac{dv}{d\zeta} = 2\mu\alpha_1 \frac{d\theta}{d\zeta}, \tag{9}$$

$$\frac{s^2}{3} \frac{dw}{d\zeta} = (\alpha_1 s^2 - vw) \frac{d\theta}{d\zeta}, \tag{10}$$

$$\frac{(1-s)^2}{3} \frac{dv}{d\zeta} = -v \frac{d\theta}{d\zeta} \tag{11}$$

with initial conditions

$$s(\zeta = 0) = 0, \qquad w(\zeta = 0) = 0, \qquad v(\zeta = 0) = -2\alpha_1/3, \tag{12}$$

provided $\theta_i(\zeta)$ in Eq. (8) are so chosen that $\theta_i(\zeta = 0) = 0$, $i \geqslant 1$.

Introducing the expansion in Eq. (8) and similar expansions for s, w, v in the system of equations (9)–(12), the zeroth-order solution is given as

$$s_0(\zeta) = w_0(\zeta) = v_0(\zeta) = 0, \tag{13}$$

and the first-order solution as

$$s_1(\zeta) = 2\mu\zeta + (2\mu/3)[\exp(-3\zeta) - 1], \tag{14}$$

$$w_1(\zeta) = 0, \tag{15}$$

$$v_1(\zeta) = -\tfrac{2}{3} \exp(-3\zeta). \tag{16}$$

The equations for the second-order approximation become

$$\frac{ds_2}{d\zeta} + \mu \frac{dw_2}{d\zeta} + \mu \frac{dv_2}{d\zeta} = 2\mu \frac{d\theta_1}{d\zeta}, \tag{17}$$

$$w_2 = 0, \tag{18}$$

$$\frac{dv_2}{d\zeta} + 3v_2 = 2s_1 \frac{dv_1}{d\zeta} - 3v_1 \frac{d\theta_1}{d\zeta}$$

$$= 2 \exp(-3\zeta) \left\{ 4\mu[\zeta - \tfrac{1}{3} + \tfrac{1}{3} \exp(-3\zeta)] + \frac{d\theta_1}{d\zeta} \right\}. \tag{19}$$

It is clear from the above that if the right-hand side of Eq. (19) is free from terms of the type $\exp(-3\zeta)$ and $\zeta \exp(-3\zeta)$; v_2 would no longer contain the undesired terms $\zeta \exp(-3\zeta)$ and $\zeta^2 \exp(-3\zeta)$. Thus θ_1 should be chosen such that

$$\frac{d\theta_1}{d\zeta} + 4\mu(\zeta - \tfrac{1}{3}) = 0,$$

or

$$\theta_1 = -2\mu(\zeta^2 - \tfrac{2}{3}\zeta). \tag{20}$$

With this choice of θ_1 we get

$$s_2 = -4\mu^2(\zeta^2 - \tfrac{2}{3}\zeta) - \tfrac{8}{9}\mu^2[\exp(-3\zeta) - \exp(-6\zeta)], \tag{21}$$

$$v_2 = \tfrac{8}{9}\mu[\exp(-3\zeta) - \exp(-6\zeta)]. \tag{22}$$

The corresponding third-order approximation is given by

$$v_3 = \tfrac{4}{27}\mu^2[-9 \exp(-3\zeta) + 20 \exp(-6\zeta) - 11 \exp(-9\zeta)], \tag{23}$$

$$s_3 = 2\mu\theta_2 - (\mu/\nu){s_1}^2 - \mu v_3, \tag{24}$$

$$w_3 = {s_1}^2/\nu, \tag{25}$$

where the choice of θ_2 as dictated by this method is

$$\theta_2 = 4\mu^2\{(\zeta - \tfrac{1}{3})^3 + \tfrac{2}{9}(\zeta + \tfrac{1}{3})[\exp(-3\zeta) - 1] + \tfrac{1}{27}\}. \tag{26}$$

In this manner we have been able to obtain a uniformly valid solution for all ζ.

Ahuja and Kumar [23] have applied the same technique for rendering uniformly valid the solution of the problem of the temperature distribution in a melting cylindrical tube, while the method has been used by Morris [24] to obtain a uniformly valid solution of the laminar convective flow in a heated vertical tube rotating about a parallel axis. Olstad [25] considered the

problem of radiating flow near a stagnation point as a perturbation of the case without radiation. It was found that near the wall the regular perturbation procedure failed and therefore the PLK method was used for obtaining a uniformly valid solution.

B. METHOD OF MATCHED ASYMPTOTIC EXPANSIONS

Where the highest derivative in a differential equation is multiplied by the small parameter the PLK method fails. The basic difficulty in such problems arises from the fact that when the order of the equation is reduced certain boundary conditions cannot be satisfied. For such problems the works of Lagerstrom and Cole [26], Lagerstrom [27], and Kaplun [28, 29] developed the method of matched asymptotic expansions.

Let $v(x, \epsilon)$ be the solution of the singular perturbation problem. The usual asymptotic expansion in powers of ϵ, $\epsilon \to 0$ is called the outer expansion for $x > 0$ fixed. This expansion is valid in the interval $\gamma \leqslant x \leqslant 1$ with γ independent of ϵ. The expansion may also hold for $\gamma \leqslant x \leqslant 1$ even if γ depends on ϵ and approaches zero as $\epsilon \to 0$, provided $\gamma/\epsilon \to \infty$. Let the outer expansion be denoted by v°. To obtain the inner expansion a stretching transformation $x = Z\epsilon$ is introduced [30]. The asymptotic expansion $v(Z\epsilon, \epsilon)$, for $\epsilon \to 0$ while $Z \geqslant 0$ is fixed, is called the inner expansion denoted by v^{i}. This expansion is valid for $0 \leqslant (Z = x/\epsilon) \leqslant \delta$. The inner and outer expansions thus have a common region of validity and in this region we can write the inner expansion of the outer expansion $(v^{\mathrm{o}})^{\mathrm{i}}$ and the outer expansion of the inner expansion $(v^{\mathrm{i}})^{\mathrm{o}}$. The asymptotic matching principle (Van Dyke [18], p. 64) states that:

$$\text{The } m\text{-term inner expansion (of the } n\text{-term outer expansion)} = \text{the } n\text{-term outer expansion (of the } m\text{-term inner expansion)}, \tag{27}$$

where m and n are any two integers. In practice m is usually chosen either equal to n or $n + 1$. The unknown constants in v^{o} and v^{i} are determined by matching the two in the common region of validity with the help of the above stated matching principle. Sometimes a composite expansion v^{c} is formed to obtain a solution uniformly valid throughout the interval $0 \leqslant x \leqslant 1$. v^{c} can be formed either according to the additive law

$$v^{\mathrm{c}} = v^{\mathrm{o}} + v^{\mathrm{i}} - (v^{\mathrm{o}})^{\mathrm{i}} \tag{28a}$$

or the multiplicative law as detailed in [18, p. 94]:

$$v^{\mathrm{c}} = v^{\mathrm{o}} v^{\mathrm{i}} / (v^{\mathrm{o}})^{\mathrm{i}}. \tag{28b}$$

A very instructive application of the method of matched asymptotic expansions has been made by Inger [31] in the analysis of near-equilibrium

dissociating boundary layers. We describe briefly part of this work to illustrate the method.

1. *An Example*

Consider the near equilibrium dissociating boundary layer flow of a diatomic gas along an impervious, axisymmetric or two-dimensional body which is either adiabatic or has a uniform surface temperature. Introducing the variables

$$\eta = \rho_e u_e r_B^j (2\xi)^{-\frac{1}{2}} \int_0^y (\rho/\rho_e)\, dy, \tag{29}$$

$$\xi = C \int_0^x \rho_e \mu_e u_e r_B^{2j}\, dx, \tag{30}$$

$$u = u_e\, df/d\eta = u_e f', \tag{31}$$

and assuming the Prandtl number and the Lewis number to be unity and $\rho\mu = \text{const.}$, we can write down the equations of momentum, atom concentration, and energy in the form

$$ff'' + f''' = 0, \tag{32}$$

$$f\frac{\partial \alpha}{\partial \eta} + \frac{\partial^2 \alpha}{\partial \eta^2} - 2\xi f' \frac{\partial \alpha}{\partial \xi} = \bar{\Gamma}\xi^R(\alpha - C_1 - C_2 t), \tag{33}$$

$$f\frac{\partial H}{\partial \eta} + \frac{\partial^2 H}{\partial \eta^2} - 2\xi f' \frac{\partial H}{\partial \xi} = 0. \tag{34}$$

The total enthalpy H is related to the static temperature t and atom mass fraction α by

$$H = c_p t + \alpha h_D + \tfrac{1}{2} u_e^2 (f')^2. \tag{35}$$

It may be noted that $\bar{\Gamma} \to 0$ for chemically frozen flow and $\bar{\Gamma} \to \infty$ for complete equilibrium. The boundary conditions are

$$\begin{gathered} f'(\infty) = 1, \qquad \alpha(\xi,\infty) = \alpha_e = C_1 + C_2 t_e, \qquad t(\xi,\infty) = t_e \\ H(\xi,\infty) = H_e = c_p t_e + \alpha_e h_D + \tfrac{1}{2} u_e^2. \end{gathered} \tag{36}$$

At the surface

$$f(0) = f'(0) = 0, \tag{37}$$

$$t(\xi,0) = t_w = \text{const.} \quad \text{or} \quad \partial H(\xi,0)/\partial \eta = 0, \tag{38}$$

$$H(\xi,0) = c_p t_w + h_D \alpha(\xi,0). \tag{39}$$

For a perfectly catalytic wall we also have

$$\alpha(\xi,0) = \alpha_{EQ,w} = C_1 + C_2 t_w. \tag{40}$$

Thus in Eq. (33) for $\bar{\Gamma} \to \infty (1/\bar{\Gamma} \to 0)$, all derivatives including the highest order vanish and the problem is therefore a singular perturbation problem. We may write Eqs. (33) and (34) in terms of the new dependent variables $\bar{\alpha}$, G and the new parameter Γ as

$$f\frac{\partial \bar{\alpha}}{\partial \eta} + \frac{\partial^2 \bar{\alpha}}{\partial \eta^2} + 2\xi f' \frac{\partial \bar{\alpha}}{\partial \xi} = \Gamma \xi^R \left(\bar{\alpha} - \frac{DG}{1+D} \right) - (f\alpha'_{EQ} + \alpha''_{EQ}), \tag{41}$$

$$f\frac{\partial G}{\partial \eta} + \frac{\partial^2 G}{\partial \eta^2} - 2\xi f' \frac{\partial G}{\partial \xi} = 0, \tag{42}$$

subject to the following boundary conditions for the catalytic wall:

$$\bar{\alpha}(\xi,\infty) = 0 = G(\xi,0), \tag{43}$$

$$\bar{\alpha}(\xi,0) = 0 = G(\xi,0). \tag{44}$$

Noting that the temperature profile can be written as

$$t(\xi,\eta) = t_{EQ}(\eta) + c_p^{-1} G h_D - h_D c_p^{-1} \bar{\alpha}, \tag{45}$$

it follows from Eq. (42) that

$$G(\xi,\eta) = 0. \tag{46}$$

a. Outer Expansion. Consider Eq. (41) for near-equilibrium flow where Γ is very large. The outer expansion can therefore be assumed for $\bar{\alpha} - D(1+D)^{-1}G$ in the form

$$\bar{\alpha} - D(1+D)^{-1}G = \sum_{N=1}^{\infty} \bar{\alpha}_N^o(\eta)(\Gamma \xi^R)^{-N}. \tag{47}$$

Substituting from Eq. (47) in Eq. (41), using Eq. (42) and collecting terms in like powers of Γ, we determine the following equations governing the perturbation functions:

$$\bar{\alpha}_1^o(\eta) = f\alpha'_{EQ} + \alpha''_{EQ} = \alpha''_{EQ}(0)[f''(\eta)/A]^2, \tag{48}$$

$$\bar{\alpha}_2^o(\eta) = f(\bar{\alpha}_1^o)' + (\bar{\alpha}_1^o)'' + 2Rf'\bar{\alpha}_1^o \tag{49}$$

$$\bar{\alpha}_N^o(\eta) = f(\bar{\alpha}_{N-1}^o)' + (\bar{\alpha}_{N-1}^o)'' + 2R(N-1)f'\bar{\alpha}_{N-1}^o, \tag{50}$$

where Eq. (45) has been used to simplify the right-hand side of Eq. (48). Although the expansion in Eq. (47) satisfies the outer boundary condition Eq. (43) it cannot satisfy the inner boundary condition Eq. (44). We therefore try to obtain the solution near the wall in a contracted variable Q.

b. Inner Expansion. From Eq. (41) it follows that the coefficient of the highest order derivative on the left-hand side would not vanish for $\Gamma \to \infty$ if we use a new independent variable $Q = \Gamma^{1/2}\eta$. To obtain the inner

solution in terms of the new independent variable we first rewrite Eq. (41) in terms of this variable. Thus we get

$$\frac{\partial^2\bar{\alpha}}{\partial Q^2} + \frac{AQ^2}{2\Gamma^{3/2}}\left(1 - \frac{2BQ^3}{A\Gamma^{3/2}}\right)\frac{\partial\bar{\alpha}}{\partial Q} - \frac{2\xi AQ}{\Gamma^{3/2}}\left(1 - \frac{5BQ^3}{A\Gamma^{3/2}}\right)\frac{\partial\bar{\alpha}}{\partial\xi}$$

$$= \xi^R\left[\bar{\alpha} - \frac{DG(\xi,0)}{1+D} - \frac{DQ}{1+D}\,\Gamma^{-1/2}\,\frac{\partial G(\xi,0)}{\partial\eta}\right] - \alpha''_{EQ}(0)/\Gamma \qquad (51)$$

subject to the wall boundary condition Eq. (44). Equation (51) is to be solved subject to Eq. (44). Let us assume that

$$\bar{\alpha} = \sum_{N=1}^{\infty} \alpha^i_N(\xi,Q)\Gamma^{-N/2} \,. \qquad (52)$$

Substitution of the series Eq. (52) in Eq. (51) yields a sequence of linear second-order differential equations governing the inner perturbation functions. Solving these equations we get

$$\bar{\alpha}^i_1(\xi,Q) = E_1 \sinh(\xi^{R/2}\,Q)\,, \qquad (53)$$

$$\bar{\alpha}^i_2(\xi,Q) = E_2 \sinh(\xi^{R/2}\,Q) - \xi^{-R}\alpha''_{EQ}(0)[1 - \exp(-\xi^{R/2}\,Q)]\,, \qquad (54)$$

$$\bar{\alpha}^i_3(\xi,Q) = E_3 \sinh(\xi^{R/2}Q)\,, \qquad (55)$$

where $E_1, E_2, \ldots, E_n$ are arbitrary constants to be determined by matching the outer and the inner solutions.

c. Matching. From Eqs. (46)–(50) we have the outer solution for the atom concentration

$$\bar{\alpha}^o(\eta,\xi) = [\alpha''_{EQ}(0)/(\Gamma\xi^R)][f''(0)/A]^2 + O(\Gamma^{-2}\xi^{-2R})\,. \qquad (56)$$

Rewriting in terms of the inner variable Q, expanding for large Γ, and using the fact that $f'''(0) = 0$, Eq. (56) becomes

$$\bar{\alpha}^o(Q,\xi) = \alpha''_{EQ}(0)(\Gamma\xi^R)^{-1} + O(\Gamma^{-2}\xi^{-2R}) \qquad (57)$$

From Eqs. (52)–(55) the inner solution is

$$\bar{\alpha}^i(Q,\xi) = E_1\Gamma^{-1/2}\sinh(\xi^{R/2}Q) + E_2\Gamma^{-1}\sinh(\xi^{R/2}Q)$$

$$+ \alpha''_{EQ}(0)[1 - \exp(-\xi^{R/2}\,Q)]\,\Gamma^{-1}\xi^{-R}$$

$$+ E_3\Gamma^{-3/2}\sinh(\xi^{R/2}Q) + O(\Gamma^{-2})\,, \qquad (58)$$

which, in terms of the outer variable for large Γ, is

$$\bar{\alpha}^{i}(\eta,\xi) = \sinh(\eta\xi^{1/2}\Gamma^{1/2}) \sum_{N} E_N \Gamma^{-N/2} \qquad E_N \neq 0,$$

$$= (\Gamma\xi^{R})^{-1}\alpha''_{EQ}(0)[1 - \exp(-\xi^{R/2}Q)] \qquad E_N = 0. \tag{59}$$

Neglecting the exponentially small terms, Eqs. (57) and (59) will match if $E_1 = E_2 = E_3 = 0$. Thus the final inner solution for the catalytic wall is

$$\bar{\alpha}^{i}_{1}(Q,\xi) = 0, \tag{60}$$

$$\bar{\alpha}^{i}_{2}(Q,\xi) = \alpha''_{EQ}(0)\xi^{-R}[1 - \exp(-\xi^{R/2}Q)], \tag{61}$$

$$\bar{\alpha}^{i}_{3}(Q,\xi) = 0. \tag{62}$$

Thus we have determined the uniformly valid solution consisting of Eqs. (48)–(50) and Eqs. (60)–(62) in terms of the velocity variable f.

2. *Other Applications*

Lam [32] has discussed the inner and outer expansions of the solution of the boundary layer on the walls of a hypersonic nozzle with special reference to the interaction of heat transfer and the boundary layer with a highly favorable pressure gradient. The method has been used in [33] to obtain a uniformly valid solution of the laminar flow in a uniformly porous channel with large injection. Varma and Murgai [34] have used the method of stretching the inner coordinate for obtaining the solution to the problem of natural convection above fires. Mueller and Malmuth [35] have discussed the temperature distribution in a radiating heat shield with arbitrary aerodynamic heat source and longitudinal heat conduction. While the problem for low radiation led to a regular perturbation problem, the problem for low conduction poses a singular perturbation problem for which the above method has been used. Cess [36] pointed out that the solution of the non-dimensionalized boundary layer equations describing the free convection of a radiating, absorbing, and emitting gas presented a singular perturbation problem. Burgraff [37] has considered the viscous flow of a transparent radiating gas in the stagnation region by taking the boundary layer equations as an approximate model of the shock layer. In the case of constant density he obtained an exact solution and clarified the interaction between the viscous and inviscid regions by considering the asymptotic expansion of the above solution in terms of the Reynolds number. He then proceeded to construct the solution of the general case by the method of matched asymptotic expansions.

Ellinwood [38] has used a pair of matched asymptotic expansions to

obtain the solution for hypersonic flow across the shock layers around blunted slender cones and wedges. Drake and Rhodes [39] used the same technique to study the problem of heat transfer from a warm sphere held at rest in a fluctuating stream. The solution of the boundary layer equations for large values of the pressure gradient parameter provides another example of a singular perturbation problem. This was pointed out by Coles [40] and later by Beckwith and Cohen [41]; it has been briefly discussed by Lagerstrom [42] and in detail by Dewey and Gross [43].

Novotny and Yang [44] have analyzed the flow of a gas in a two-dimensional laminar boundary layer with radiation, assuming a small temperature difference within the flow field. While examining the optically thick approximation they encountered a problem of singular perturbation of the energy equation. The problem was then analyzed by matched asymptotic expansions with a parameter characterizing the optical thickness of the gas. Fendell [45] has used the same method in the solution of laminar natural convection about an isothermally heated sphere at small Grashoff numbers. The problem of similar compressible boundary layers with large injection and favorable pressure gradient has been treated in [46] where matched asymptotic expansions have been obtained for each of the two layers: (a) an inner layer adjacent to the surface where viscosity is unimportant and (b) an outer boundary layer where transition takes place from the inner layer to the outer flow.

Based on the method developed earlier [35] Mueller and Malmuth [47] have discussed the asymptotic solution for heat conduction in radiating shells subject to discontinuous solar flux. Kuiken [48] has applied the method to the free convective boundary layer for the case of Prandtl number approaching zero.

The method of matched asymptotic expansions has recently been critically examined by Frankel [49] who has rigorously established the sufficient conditions under which the asymptotic matching principle of Van Dyke [18, p. 64] is correct. He has applied the method to an ordinary differential equation with a turning point and has shown that a restricted matching principle is valid even when it is applied to truncated inner and outer expansions which do not overlap, to the order of terms being matched.

C. Method of Multiple Scales and Other Singular Perturbation Methods

Cochran [50] and Mahony [51] have developed the method of multiple scales to deal with singular perturbation problems. In their solution, the sensitive coordinate is replaced by a pair of coordinates, namely, the unstretched coordinate x and the stretched coordinate $Z = x/\epsilon$. One can then

assume a conventional asymptotic expansion uniformly valid throughout the region. Thus we assume an asymptotic expansion of the form

$$f(x,\epsilon) = f_1(x,Z) + \epsilon f_2(x,Z) + \epsilon^2 f_3(x,Z) + \cdots . \tag{63}$$

This expansion holds uniformly for $0 \leqslant x \leqslant 1$ and also for $0 \leqslant Z \leqslant \infty$, and the necessity of matching has been obviated. The above expansion is substituted in the differential equation and $f_2, f_3, \ldots$ are determined in a manner parallel to the PLK method with the requirement that the higher order solutions are no more singular than the first. A similar idea has been advanced by Cole and Kevorkian [52], and the method has recently been elaborated by Fowkes [53].

Vasileva [54] has set out a method of finding a uniformly valid solution of a system of differential equations containing a small parameter multiplied to the highest order derivative. Using this technique Varma and Murgai [55] have obtained an analytical solution to the problem of natural convection above fires, the medium being assumed to contain solid particles. A comprehensive list of contributions of Soviet mathematicians to the mathematical theory of perturbation methods appear in Vasileva [54].

Another related method of dealing with singular perturbation problems, called the method of intermediate limits, has been described by Kaplun [29] and in the collection of papers of Kaplun recently published [56].

Some of the very recent contributions to the basic aspects of the singular perturbation method are presented in O'Melley and Keller [57–59], Murray [60], Erdelyi [61, 62], Vasileva [63], Visik and Lyusternik [64, 65], Friedman [66], Fife [67], and Mackie [68].

D. METHOD OF SERIES TRUNCATION IN ELLIPTIC FLOW PROBLEMS

Perturbation methods are only partially successful in problems governed by elliptic partial differential equations. In the case of such problems, when a power series expansion is substituted in the differential equation, it so happens that the nth-order equation involves $(n + 1)$th-order terms. This is in contrast to the parabolic equations where the nth order equations involve terms of the order up to n only as, for example, in the case of Blasius expansion in the boundary layer theory. It therefore becomes essential to somehow truncate such terms of a particular order to match the number of unknowns to the number of equations. This method is sometimes termed the method of series truncation [69]. Swigart [70] and Bazzin and Gladkov [71] first applied the method of series truncation to treat the inverse problem of inviscid two- and three-dimensional, axisymmetric nonradiating flows over blunt bodies. In this approach the dependent variables, namely, the stream

function and density ρ, are first expanded in a power series in the longitudinal curvilinear coordinate ξ or in the trigonometric functions of the angular distance. Substitution of this series in the governing partial differential equations and collection of terms of like powers of ξ yield differential equations with the normal coordinate η as the independent variable. By truncating the series of a definite order, a closed set of equations is obtained which are solved numerically. Kao [72] and Conti [73] have applied the method to viscous flows and nonequilibrium reacting flows, respectively. Conti [73] found that if the pressure rather than the density is expanded in a power series, the accuracy at each truncation is greatly improved. Van Dyke [74] has been able to achieve much higher accuracy with a second-order truncation by using pressure as the primary variable and also (a) by the use of $\xi/(\xi^2 + 1)$ as the expansion variable instead of ξ and (b) by interchanging the roles of η and χ. Closely following Van Dyke's scheme, Cheng and Vincenti [75] extended the method to the problem of radiating inviscid flows over a blunt body.

In all the above cases, however, the higher order terms were truncated arbitrarily only to reduce the number of variables. The magnitude of the terms dropped in the truncation is usually as large as the magnitude of the terms retained. Kao [69] has shown that if the momentum equation is replaced by Bernoulli's equation, the higher order terms in each truncation become the velocity components normal to the body or the shockwave. Since such terms are actually very small in the case of hypersonic flows, an order of magnitude analysis could therefore be applied. It has been shown [69] that if the other terms of the order of truncated terms are also dropped, analytic solutions could be obtained in some cases even up to third order.

III. Asymptotic Methods

A. MEKSYN'S METHOD

Meksyn [76] has developed a very effective asymptotic method based on the method of steepest descent [77, p. 437] and series inversion [78, p. 184] to find solutions to the velocity and thermal boundary layers. The method has since been used by many authors in various fields of heat transfer. It essentially consists of expanding the solution in powers of η with all but one coefficient in the series determined. This unknown coefficient is asymptotically determined so as to satisfy the condition at infinity. To start with the series is substituted in the differential equation for all derivatives except the two highest order ones. The differential equation is now treated as a linear one for the next lower derivative. An integration with respect to η gives the

integral from which the yet unknown coefficient is to be determined. This is done by evaluating the integral asymptotically by the method of steepest descent, the integrand having a stationary point at $\eta = 0$.

1. *Example*

We illustrate the technique by describing the solution of the problem of natural convection in two-dimensional plane flow due to a source singularity of heat. Following Kotorynski [79] it can be shown that the system of partial differential equations governing the problem can be reduced with boundary layer approximations to the system of the following ordinary differential equations

$$f''' + ff'' - \tfrac{1}{3}f'^2 + h = 0, \tag{64}$$

$$h' + \sigma f h = 0, \tag{65}$$

with the boundary conditions

$$\int_{-\infty}^{\infty} f'h\,d\eta = 9/25, \tag{66}$$

$$f' \to 0, \qquad \eta \to \pm\,\infty, \tag{67}$$

$$f(0) = f''(0) = 0, \tag{68}$$

where f and h are respectively the nondimensional velocity and temperature functions, and the primes denote the order of differentiation with respect to the similarity variable. Equations (64) and (65) are together equivalent to the fourth-order equation

$$f^{(\mathrm{iv})} + (1 + \sigma)f''' + \tfrac{1}{3}f'f'' + \sigma^2 f^2 f'' - \frac{\sigma}{3}ff'^2 = 0. \tag{69}$$

The essential steps in determining f and h by Meksyn's method can be listed as:

(i) Expanding $f(\eta)$ in a power series in η satisfying the boundary conditions at $\eta = 0$.

(ii) Assuming that the expansion for f, f' is known, Eq. (64) is formally solved as a linear inhomogeneous first order equation in f''. Integrating with respect to η gives $f'(\eta)$ from which $f'(0)$ can be determined.

(iii) Another condition for determining the unknown parameters is provided by the integral condition Eq. (66).

(iv) By a transformation of the independent variable η, the integrals are expressed as asymptotic expansions involving gamma functions, thus reducing the above two conditions to algebraic equations. Euler's transformation [76, p. 58] is used if necessary to make the series convergent.

From Eq. (65) we obtain $h(\eta)$ in terms of $f(\eta)$ by integrating it as a linear differential equation. Thus

$$h(\eta) = h(0) \exp [-\sigma F(\eta)], \tag{70}$$

where

$$F(\eta) = \int_0^\eta f(u)\, du.$$

Writing Eq. (64) in the form

$$f''' + ff'' = \tfrac{1}{3}f'^2 - h(0) \exp [-\sigma F(\eta)]. \tag{71}$$

it is easily shown that

$$\begin{aligned} f''(\eta) &= \exp[-F(\eta)]\phi_1(\eta) \\ &= \exp[-F(\eta)]\left\{C + \frac{1}{3}\int_0^\eta f'^2(u) \exp[F(u)]\, du - h(0)\right. \\ &\quad \left.\int_0^\eta \exp [(1 - \sigma)F(u)]\, du\right\} \qquad \sigma \geqslant 1, \end{aligned} \tag{72}$$

The condition Eq. (68) on $f''(0)$ requires that $C = 0$. Also

$$\begin{aligned} f''(\eta) &= \exp [-F(\eta)]\phi_2(\eta) \\ &= \exp [-F(\eta)]\left\{\frac{1}{3}\int_0^\eta f'^2(u) \exp [\sigma F(\eta) - F(\eta) + F(u)]\, du - h(0)\right. \\ &\quad \left.\int_0^\eta \exp \{(\sigma - 1)[F(\eta) - F(u)]\}\, du\right\} \qquad \sigma \leqslant 1, \end{aligned} \tag{73}$$

and therefore by one further integration with respect to η and letting $\eta \to \infty$, we can write

$$\int_0^\infty \exp [-F(\eta)]\phi_1(\eta)\, d\eta = -f'(0) \qquad \sigma \geqslant 1, \tag{74}$$

$$\int_0^\infty \exp [-F(\eta)]\phi_2(\eta)\, d\eta = -f'(0) \qquad \sigma \geqslant 1. \tag{75}$$

Also the integral boundary condition Eq. (66) is transformed to

$$h(0) \int_0^\infty \exp [-(1 + \sigma)F(\eta)]\chi_1(\eta)\, d\eta = 9/50 \qquad \sigma \geqslant 1, \tag{76}$$

$$h(0) \int_0^\infty \exp [-(2\sigma)F(\eta)]\chi_2(\eta)\, d\eta = 9/50 \qquad \sigma \leqslant 1. \tag{77}$$

Assuming

$$f(\eta) = \sum_{1}^{\infty} \frac{a_n \eta^n}{\eta!} \qquad a_2 = 0, \tag{78}$$

and substituting the above expansion in Eq. (69) we obtain the difference equation

$$a_{n+4} + (1+\sigma)\sum_{k=0}^{n}\binom{n}{k} a_{n+3-k}a_k + \frac{1}{3}\sum_{k=0}^{n}\binom{n}{k} a_{n+2-k}a_{k+1}$$
$$+ \sigma \sum_{\substack{k=0 \\ j\le k}}^{n}\binom{n}{k}\binom{k}{j} a_{n+2-k}a_{k-j}a_j - \frac{\sigma}{3}\sum_{\substack{k=0 \\ j\le k}}^{n}\binom{n}{k} a_{n-k}a_{k+1-j}a_{j+1} = 0 \tag{79}$$

for the coefficients a_n. It may be noted that $f(\eta)$ is an odd function and therefore $a_{2n} = 0$ for all n. Let

$$F(\eta) = \eta^2 \sum_{0}^{\infty} c_n \eta^n = \tau \tag{80}$$

and

$$\phi_1(\eta) = \sum_{0}^{\infty} b_n \eta^n, \tag{81}$$

where

$$c_n = \frac{a_{n+1}}{(n+2)!} \tag{82}$$

$$b_n = \frac{\phi_1^{(n)}(0)}{n!} = \frac{1}{n!}\frac{d^n}{d\eta^n}\left[\exp F(\eta) f^{(n)}(\eta)\right]_{\eta=0} \tag{83}$$

$$b_{2m} = 0 \qquad m = 1, 2, \cdots .$$

We now perform the inversion of variables η and τ in Eq. (80). If $|\tau|$ is small we may write [78, p. 184]

$$\eta = \sum \frac{A_n}{n+1} \tau^{(n+1)/2} \tag{84}$$

where

$$A_n = \int_{\gamma'} \frac{d\eta}{d\tau} \frac{d\tau}{\tau^{(n+1)/2}} = \int_{\gamma} [F(\eta)]^{-(\eta+1)/2} d\eta, \tag{85}$$

where γ, γ' are the circles about the origin described in a positive sense. Since the transformation in Eq. (84) is double-valued, a single closed circuit around the origin in the η-plane corresponds to a double circuit in the τ-plane. It follows from Eq. (85) that A_n is the coefficient of η^n in the expression

$$[c_0 + c_1\eta + c_2\eta^2 + \cdots]^{-(n+1)/2}.$$

Having thus determined A_n, we now transform η in the integral on the left-hand side of Eq. (74) to τ and write the integral as

$$\int_0^\infty \exp(-\tau\epsilon^{-2})\phi_1[F^{-1}(\tau)]\frac{d[F^{-1}(\tau)]}{d\tau}\,d\tau,$$

where ϵ is an arbitrary small parameter, the power of ϵ being so chosen so as to make the final expression an expansion in integral powers of ϵ. The expansion would be convergent for small ϵ and we may use if necessary the Euler expansion for $\epsilon = 1$. Assuming

$$\phi_1[F^{-1}(\tau)]\frac{d[F^{-1}(\tau)]}{d\tau} = \tau^{1/2}\sum d_n\tau^{n/2}, \tag{86}$$

Eq. (74) can be written as

$$-f'(0) = \sum_0^\infty d_n\Gamma\left(\frac{n+1}{2}\right)\epsilon^{n+1}. \tag{87}$$

In view of the relations (80) and (81), it can be shown in a fashion exactly similar to how A_n was determined in Eq. (85) that d_n is one half of the coefficient of η^n in the expression

$$(b_0 + b_1\eta + b_2\eta^2 + \cdots)(c_0 + c_1\eta + c_2\eta^2 + \cdots)^{-(n+1)/2}$$

The coefficients b_n and c_n being already known, we may then determine d_n. In a similar fashion, if we assume that $\chi_1(\eta)$ in Eq. (76) may be given as

$$\chi_1(\eta) = \Sigma\, e_n\eta^n, \tag{88}$$

we can determine e_n. Similarly the coefficients in the expansion of ϕ_2 in Eq. (73) and X_2 in Eq. (77) can be determined. Having determined these coefficients we get from Eq. (76) the condition

$$9/50 \sim h(0)\sum f_n(1+\sigma)^{-(n+1)/2}\Gamma[(n+1)/2]\,\epsilon^{n+1}, \tag{89}$$

where

$$f_n = \frac{1}{4\pi i}\int_\gamma \chi_1(\eta)F^{-(n+1)/2}(\eta)d\eta,$$

and similarly for $\sigma \leqslant 1$ the condition

$$9/50 \sim h(0)\sum l_n(2\sigma)^{-(n+1)/2}\Gamma[(n+1)/2]\epsilon^{n+1}, \tag{90}$$

where the coefficients l_n are given by

$$l_n = \frac{1}{4\pi i}\int_\gamma \chi_2(\eta)F^{-(n+1)/2}(\eta)\,d\eta.$$

Having thus determined $f''(0)$ and $h(0)$ we have found the complete solution of the boundary layer problem. Kotorynski [79] has compared the results so obtained with the known exact solution of the problem [80] and found excellent agreement between the two solutions.

2. *Applications*

Sovershenny and Tirski [81] used Meksyn's technique to analyze the sublimation of a solid near a critical point in flat and axisymmetric gas flows. Brindley [82] applied the technique to problems of free laminar convective flow and combined forced and free convection at a vertical heated plate. Li and Kirk [83] similarly analyzed the binary boundary layer equations in the presence of an external flow field pressure gradient with the Mach number being not necessarily small. Chao and Jeng [84] have applied a method based on Laplace transforms and Meksyn's technique to the analysis of unsteady laminar forced convection heat transfer at a two-dimensional and axisymmetrical front stagnation point, with an arbitrary prescribed wall temperature and heat flux variation. Jeng [85] has suggested a solution to the problem of radiative heat transfer in an absorbing boundary layer based on the same method. More recently Li and Kirk [86] have used the method in the problem of a dissociated boundary layer over a flat plate with the first-order atom recombination rate distributed in an arbitrary continuous manner. Hayday and Bowles [87] have applied the method to heat transfer near the stagnation point in three-dimensional flows. The method has also been applied in [88] to a laminar boundary layer flow of a dissociated gas past a catalytic surface. Lock and Gunn [89] have used the method in the analysis of the laminar free convection from a downward projecting fin. In [90], the method has been applied to obtain the higher approximations of the boundary layer. Cooper [91] has analyzed by the same method the nonlinear conductive heat transfer in a semi-infinite slab of variable conductivity under continuous surface heating.

A very useful application of Meksyn's technique is to determine the effect of nonsimilarity on a boundary layer. Assuming that the boundary layer is approximately described by some similar solution, the effect of nonsimilarity terms may be calculated by expanding the solution of the full boundary layer equations in terms of the small parameter characterizing the departure from similarity. Merk [92] and Bush [93], following Meksyn's approach, have analyzed the effect of nonsimilarity on a boundary layer.

B. WKBJ APPROXIMATION

Another asymptotic method, namely the WKBJ approximation, initially developed in quantum mechanics [94–96], has recently been used by various

authors for tackling problems in different modes of heat transfer. The method concerns itself with the asymptotic solution of a differential equation with respect to a large parameter occuring in the equation. If the coefficient of the large parameter in the equation vanishes at some point, this point is termed a transition or a turning point and it becomes necessary to determine the transformation of the solution through this point. The method of achieving this transformation was discovered by Wentzel, Kramers, and Brillouin and independently by Jefferys and is therefore named the WKBJ method.

1. *Asymptotic Solution of Liouville's Differential Equation*

Consider Liouville's differential equation

$$\frac{d^2y}{dx^2} + [\lambda^2 p(x) + r(x)]y = 0 \tag{91}$$

where x is real and Eq. (91) holds for $a \leqslant x \leqslant b$. $p(x)$ is a real and twice continuously differentiable function and $r(x)$ is continuous for $a \leqslant x \leqslant b$. Let $p(x)$ have a zero at $x = c$ in the interval $a < x < b$. It is shown in many texts, for example, Erdelyi [96, p. 91], that Eq. (91) has an asymptotic solution of the form

$$y = C_1[p(x)]^{-1/4} \cos\{\lambda \int [p(x)]^{1/2}\, dx\} + C_2[p(x)]^{-1/4} \times \sin\{\lambda \int [p(x)]^{1/2}\, dx\}, \tag{92a}$$

valid in $c + \epsilon \leqslant x \leqslant b$, $\epsilon > 0$ while in the interval $a < x \leqslant c - \epsilon$ where $p(x)$ is negative Eq. (91) has the solution of the form

$$y = C_3[-p(x)]^{-1/4} \exp\{\lambda \int [-p(x)]^{1/2} dx + C_4[-p(x)]^{-1/4} \exp\{-\lambda \int [-p(x)]^{1/2}\, dx\}. \tag{92b}$$

The above two solutions are valid only where the function

$$\rho(p) = \frac{1}{4}\frac{p''}{p^2} - \frac{5}{16}\frac{p'^2}{p^3} - \frac{r}{p} \tag{93}$$

is positive and finite [96, p. 79]. Obviously at $x = c$ both the above solutions are invalidated. The WKBJ method deals firstly with finding the relation between the constants C_1 and C_2 in Eq. (92a) on the one hand, and C_3 and C_4 in Eq. (92b) on the other, and secondly with finding the solution in the interval $c - \epsilon < x < c + \epsilon$. Sufficiently near the point $x = c$ we can write

$$p(x) = (x - c)p'(c). \tag{94}$$

Neglecting $r(x)$ in Eq. (91) and substituting for $p(x)$ from Eq. (94), it can be solved in terms of the Bessel functions of order 1/3. By using the asymptotic expressions for Bessel functions and comparing the solution with those given by Eqs. (92a) and (92b) we obtain the connection between C_1, C_2 and C_3, C_4. To determine the solution which is valid in the interval $c - \epsilon < x < c + \epsilon$, Eq. (91) is reduced to the form

$$\frac{d^2\eta_1}{d\xi_1^2} + \lambda^2\xi_1\eta_1 = \rho(\xi_1)\eta_1 \tag{95}$$

by what is known as Langer's transformation [96, p. 94]. The solution of Eq. (95) with the right-hand side equated to zero is well known and provides the first approximation to the solution of Eq. (91) near $x = c$.

2. *Application to Boundary Layer Heat Transfer*

Imai [97] has developed the WKBJ procedure for the second-order linear differential equation

$$\frac{d^2\phi}{dx^2} + a^2P(x)\phi = 0, \tag{96}$$

where a is a parameter and

$$P(x) = a_1x(1 + b_1x + b_2x^2 + \cdots) \qquad a_1 \neq 0, \tag{97}$$

and applied it to solve the nondimensionalized energy equation

$$T'' + \sigma fT' - \sigma n(2 - \beta)f'T = 0 \tag{98}$$

in the boundary layer, with temperature varying as the nth power of the distance and the velocity in the outer flow varying as the mth power of distance along the boundary layer. Through the transformation

$$T = \exp\left[-\tfrac{1}{2}\sigma\int_0^\eta f d\eta\right]\Theta, \tag{99}$$

the energy equation (98) is reduced to the form

$$\Theta'' - P(\eta)\Theta = 0, \tag{100}$$

where

$$P(\eta) = \tfrac{1}{4}\sigma^2f^2 + \sigma[\tfrac{1}{2} + n(2 - \beta)]f' \tag{101}$$

and

$$f = \tfrac{1}{2}\alpha\eta^2 - \tfrac{1}{6}\beta\eta^3, \tag{102}$$

where $\beta = 2m/(m + 1)$ and $\alpha = f''(0)$, which has been tabulated by Hartree [98] for several values of β. The function $P(\eta)$ in Eq. (100) is zero at $\eta = 0$

as f and f' vanish at the wall. The form of Eq. (100) therefore suggests the WKBJ method for its solution. It is shown by Imai [97] that for large n the flux at the wall is given by

$$\left.\frac{\partial\theta}{\partial\eta}\right|_{\eta=0} = \left.\frac{\partial\Theta}{\partial\eta}\right|_{\eta=0} = \frac{\beta}{10\alpha} - \left(\frac{1}{3}\right)^{2/3} \frac{\Gamma(2/3)A^{1/3}}{\Gamma(4/3)} + O(A^{-1/3}), \tag{103}$$

where

$$A = \alpha\sigma[\tfrac{1}{2} + n(2 - \beta)].$$

The results of Imai for $\beta = 0$ and $\sigma = 0.72$ have been compared [97] with those of Chapman and Rubesin [99], Levy [100], and Lighthill [101] and are found to be in very good agreement.

3. *Further Applications*

Sellars *et al.* [102] have used the WKBJ approximation for analysis of forced convection heat transfer in a fluid with constant density which is in steady laminar motion in a circular tube. The velocity profile is assumed to be fully developed when it enters the tube whose wall is kept at a constant temperature or a flux applied to it. The solution of the analogous problem with turbulent flow has been obtained in [103]. Cess and Sparrow [104] have used the technique in conjunction with Laplace transforms to determine the temperature–time history of a rotating disk which is initially at the fluid temperature and is then subjected to a step change in surface temperature. More recently Nayfeh [105] has used the method to obtain asymptotic expressions for large eigenvalues of the eigenfunctions of a differential equation with two turning points. It has been shown that the higher eigenvalues of the Graetz problem obtained in [102] follow as a particular case of the solution [105].

IV. Variational Methods

The variational formulation of a problem whenever possible utilizes the powerful tool of the direct methods of the calculus of variations [106] and [107] for obtaining an approximate solution to the problem. It is well known that the problems governed by linear self-adjoint equations can be formulated as variational problems. For the class of nonlinear and nonself-adjoint equations to which the non-steady conservation equations of mass, momentum, and energy with variable coefficients belong, a variational formulation in the classical sense is not possible, and recourse has therefore been made to looser or extended variational formulations based on functionals having some physical content. We will describe two such attempts on the variational

formulation in continuous systems, namely, those of Biot and of Glansdorff and Prigogine.

A. BIOT'S VARIATIONAL PRINCIPLE

1. *Variational Formulation of the Heat Conduction Equation and Its Applications*

Beginning with the establishment of a generalized theorem of Minimum Entropy Production [108] in an irreversible process, Biot [109] has developed the formulation of Lagrangian thermodynamics, similar to the Lagrangian equations in mechanical systems. The principle is developed through the use of a heat flow vector $\mathbf{H}$ whose time rate of change $\dot{\mathbf{H}}$ is the heat flux across an area normal to it. The variational formulation then has the form in the case of isotropic, one-dimensional heat conduction:

$$\delta V + \delta D = -t\delta\mathbf{H}, \tag{104}$$

where V is the thermal potential defined as

$$V = \int_x \int_t (Ct)\, dt\, dx \tag{105}$$

and D is the volume-dissipation function

$$D = \int_x \frac{1}{2K} (\dot{\mathbf{H}})^2\, dx. \tag{106}$$

If the heat flow field $\mathbf{H}$ is defined in terms of time dependent generalized coordinates $q_i(t)$ as

$$\mathbf{H} = \mathbf{H}(q_i, x, \tau), \tag{107}$$

it is shown [109] that the nonlinear heat conduction equation with temperature dependent thermal conductivity and specific heat $C = c_v\rho$, namely,

$$C\frac{\partial t}{\partial \tau} = \frac{\partial}{\partial x}\left(K\frac{\partial t}{\partial x}\right) \tag{108}$$

is equivalent to the Lagrangian equation

$$\frac{\partial V}{\partial q_i} + \frac{\partial D}{\partial \dot{q}_i} = Q_i, \tag{109}$$

where $Q_i = [t(\partial\mathbf{H}/\partial q_i)]_{x=0}$ and is named the thermal force. The method for using the above variational formalism in practice consists of assuming a temperature profile usually of the form

$$t = q_1[1 - (x/q_2)]^p, \tag{110}$$

where p is any integer greater than two. In the case of a finite slab with a prescribed temperature at the surface, q_1 is the known temperature at $x = 0$ and q_2 is the "penetration depth," a concept analogous to the thermal boundary layer. After the "penetration time," that is, the time when q_2 becomes equal to the slab thickness, the second generalized coordinate becomes the prescribed temperature at the other surface. In the case of a prescribed flux condition, an additional condition of overall energy balance at the surface, namely,

$$\dot{\mathbf{H}}_n = F \tag{111}$$

is also satisfied. This is the approach followed by Lardner [110] who has presented various applications of the Biot's formulation. The values of V and D for the assumed profile are calculated and substituted in Eq. (109), reducing the nonlinear partial differential equation of the second order to one or more first-order ordinary differential equations which can usually be solved in closed form for the constant properties, and reducing to simple quadrature in the case of temperature dependent thermal properties.

The above method has been used by Biot and Daughaday [111], Biot and Agrawal [112], and Lardner [113] in problems involving change of phase. Bukhvotsov and Frankel [114] applied Biot's method to obtain temperature distributions in round disks and rectangular plates cooled by a fourth power law at the flat surfaces with the edges being kept at a constant temperature. Muchnik and Polykov [115] have demonstrated the validity of Biot's formulation in the case of time dependent boundary conditions. Richardson [116] has analyzed the unsteady heat conduction in a semi-infinite solid with the boundary condition of the flux varying as the nth power of the surface temperature. Ahuja [117] has used the same method in the analysis of nonlinear heat conduction in a solid in contact with a well-stirred fluid of variable properties. Chu [118] and Lardner [119] have described the method of obtaining the solution to nonlinear heat conduction in a slab with convective boundary condition. Weiss [120] has reviewed the method in comparison to the weighted residual method of the heat balance integral [9] and the Galerkin method and the collocation methods [8]. He applied Biot's method to evaluate the temperature distribution in a composite plate made of various materials heated under aerodynamic conditions. Rafalski and Zyszkowski [121], using the approach of [110], have developed Biot's formulation for the boundary condition $B_\nu(s, t, \tau) = 0$, $\nu = 1, 2, \ldots, p$, where B_ν is a function of temperature with coefficients dependent on time and is prescribed on each surface s_ν of the body where $\Sigma_{\nu=1}^{p} s_\nu = s$, and applied it to the semi-infinite body with the boundary condition

$$B(s, t, \tau) = K\mathbf{n}\cdot\text{grad}\, t + h(t^m - t_0^m)$$

on the surface. Nazarov [122] has modified the variational principle of Biot with the thin plate approximation and applied the new variational principle to a composite layer of $2n$ thin plates with fourth power radiation boundary condition.

2. *Variational Formulation of Unsteady Heat Transfer in a Moving Fluid*

In further papers Biot [123–125] has generalized his method to heat transfer problems in an incompressible, laminar and turbulent fluid flow, although it has been recognized [125] that in systems involving fluid motion the basis of the formulation of the Lagrangian thermodynamics, namely, the validity of Onsager's reciprocity relations, is violated. Thus the transient energy equation

$$C\frac{\partial t}{\partial \tau} + C\boldsymbol{u}\cdot\nabla t - \nabla\cdot(k\nabla t) = 0 \quad \text{in} \quad V_1, \qquad \tau > 0 \tag{112}$$

and the boundary condition

$$K\boldsymbol{n}\cdot\nabla t + h_w(t - t_w) = 0 \quad \text{on} \quad S, \qquad \tau > 0 \tag{113}$$

with the initial condition

$$t = \psi(x) \quad \text{in} \quad V_1, \qquad \tau \leqslant 0 \tag{114}$$

are shown to be equivalent to the Lagrangian equation [126]

$$\frac{\partial V}{\partial q_i} + \frac{\partial(D + D_s)}{\partial \dot{q}_i} + Q_i, \tag{115}$$

where

$$V = \int_{V_1}\int_t t\, dh\, dV_1, \tag{116}$$

$$D = \frac{1}{2}\int_{V_1}\frac{1}{K}\left(\frac{\partial \mathbf{H}}{\partial \tau} - h\boldsymbol{u}\right)^2 dV_1, \tag{117}$$

$$Q_i = -\int_S t_w\boldsymbol{n}\cdot\mathbf{H}_n\, dS, \tag{118}$$

$$D_s = \frac{1}{2}\int_S \frac{1}{h_w}\left(\boldsymbol{n}\cdot\frac{\partial \mathbf{H}}{\partial \tau}\right)^2 dS, \tag{119}$$

$$h = \int C\, dt = -\nabla\cdot\mathbf{H}, \tag{120}$$

and the initial condition Eq. (114) is taken into account on integrating the first-order equation (115). In [125] Biot introduced a new concept of a "trailing function" to replace the usual heat transfer coefficient. The trailing

function $r(P, P')$ is defined as the temperature increase at a point P in the fluid when a unit quantity of heat is injected at P'. Then using the conduction analogy, namely, the similarity between the equation of transient heat conduction and steady-state boundary layer heat transfer, he finds the value of the trailing function by his variational method. He has shown [127] how the concept of the trailing function can be used to find quite accurate solutions to laminar and turbulent boundary layer heat transfer. Biot has further clarified [128] the notions of the thermal potential and the dissipation function and has demonstrated the relation of his formulation to irreversible thermodynamics. It may be noted that the Lagrangian equations are applicable to a mixed system composed of a solid matrix and a fluid moving through it. Such problems are encountered in sweat cooling and drying of porous bodies. Chu and Seader [129] have applied Biot's method to the problem of sweat cooling. Based on Biot's formulation, Nigam and Agrawal [130] produced a variational formulation for the convective heat transfer from a constant property fluid. Gupta [131] presented a formulation very much like that of Biot for the fully developed laminar heat transfer in uniform channels and another variational principle [132] for the convection of heat in anisotropic media.

B. Variational Principles Based on Local Potentials

1. *Generalized Evolution Criterion*

The basis of the formulation of variational principles for continuous systems is the search for a potential which, in some sense at least, could play the role parallel to that of a Lagrangian in the mechanical systems. For linear problems governed by steady-state balance equations, the answer was provided by the Theorem of Minimum Entropy Production [133]. For systems in which (i) the phenomenological coefficients are constant, (ii) the Onsager relations are satisfied, and (iii) convective terms are negligible, the stationary state of the system is a state of minimum entropy production [134, 135]. The restrictions stated above made use of the variational formulation of the problem in continuous systems unnecessary since they could be successfully treated by classical methods. Recently Glansdorff and Prigogine [136, 137] have presented a generalized evolution criterion based on the concept of local potential, valid for systems not subject to the restrictions of the type stated above. From the evolution criterion, the systems of equations of balance follow as Euler–Lagrange equations, the latter term being used in a more extended sense than the classical one. This can be understood from the fact that the variational formulation of the conservation equations is of a special nature involving two types of variables, namely, the assumed

macroscopic variables not subject to variation and also the same variables which are to be evaluated and are subject to variation [138–140].

The conservation equations of mass, momentum, and energy for a system of n components in which r reactions take place are

$$\frac{\partial \rho_\gamma}{\partial \tau} = -\frac{\partial \rho_\gamma v_{\gamma j}}{\partial x_j} + v_{\gamma p} M_\gamma u_p, \qquad \gamma = 1, 2, \cdots, n \quad p = 1, 2, \cdots, r \tag{121}$$

$$\rho \frac{\partial v_i}{\partial \tau} = -\rho v_j \frac{\partial v_i}{\partial x_j} + \rho X_i - \frac{\partial P_{ij}}{\partial x_j}, \qquad i = j = x, y, z \tag{122}$$

$$\frac{\partial \rho e}{\partial \tau} = -\frac{\partial}{\partial x_j}(W_j + \rho e v_j) - P_{ij}\frac{\partial v_i}{\partial x_j} + \rho_\gamma \Delta_{\gamma j} X_{\gamma j}, \tag{123}$$

where summations over the dummy suffixes are everywhere implied. It is shown in Prigogine and Glansdorff [140] that the above conservation equations (121)–(123) follow as the extended Euler–Lagrange equations of the functional F, called the unsteady local potential. Thus

$$F = \int dV L(t, t^*, \mu_\gamma, \mu_\gamma^*, v_i, v_i^*), \tag{124}$$

where

$$L = \Lambda - \frac{\partial}{\partial \tau} \rho^* e^* t^{-1} + \mu_\gamma t^{-1} \frac{\partial \rho_\gamma^*}{\partial \tau} + \frac{\partial v_i^*}{\partial \tau} \frac{\rho^*}{t^*} v_i \tag{125}$$

and Λ is defined in terms of the local potential Φ for the stationary state as

$$\Phi = \int dV \Lambda(t, t^*, \mu_\gamma, \mu_\gamma^*, v_i, v_i^*) \tag{126}$$

so that

$$\delta F = \int dV \left[J_\alpha \, \delta X_\alpha - \frac{\partial \rho^* e^*}{\partial \tau} \delta t^{-1} + \frac{\partial \rho_\gamma^*}{\partial \tau} \delta(\mu_\gamma t^{-1}) + \frac{\partial v_i^*}{\partial \tau} \frac{\rho^*}{t^*} \delta v_i \right], \tag{127}$$

where J_α and the corresponding X_α are listed in Table I. The J_α and the corresponding X_α which have been listed below have been called the

TABLE I

J_α	X_α
1. $W_j + \rho v_j e + P_{ij} v_j + \rho v_j (v^2/2)$	1. $(\partial/\partial x_j)(t^*)^{-1}$
2. $-\rho v_{\gamma j}$	2. $(\partial/\partial x_j)(\mu_\gamma {t^*}^{-1}) - t^{*-1} X_{\gamma j}$
3. $-(P_{ij} + \rho v_i v_j)$	3. $(\partial/\partial x_j)(v_i^*/T^*)$
4. $-\rho X_j$	4. $v_j^* t^{-1}$
5. $-P_\gamma v_{\gamma j} t^{-1}$	5. $X_{\gamma j}$
6. u_p	6. A_p/t^*

components of Generalized Entropy Production. The Euler–Lagrange equations are

$$\left[\frac{\delta L}{\delta(\mu_\gamma t^{-1})}\right]_{t^*,\mu_\gamma{}^*,v_i{}^*} = 0, \qquad \left[\frac{\delta L}{\delta v_i}\right]_{t^*,\mu_\gamma{}^*,v_i{}^*} = 0, \qquad \left[\frac{\delta L}{\delta t^{-1}}\right]_{t^*,\mu_\gamma{}^*,v_i{}^*} = 0, \quad (128)$$

with subsidiary conditions

$$t = t^*, \qquad \mu_\gamma = \mu_\gamma^*, \qquad v_i = v_i^*. \quad (129)$$

It may be noted that L is a function dependent on both the assumed macroscopic variables t^*, μ_γ^*, v_i^* and also on t, μ_γ, and v, which are to be determined. While taking the variation of F with respect to the variables $\mu_\gamma t^{-1}$, v_i, and t^{-1} the corresponding starred quantities are kept constant, and after taking the variation the subsidiary conditions Eq. (129) are imposed. The Euler–Lagrange equations (128) are therefore not the classical conditions known as such and have been referred to as the extended Euler–Lagrange equations. It is through these equations that the complete conservation equations (121)–(123) are recovered in the variational formulation based on local potentials.

2. *Mathematical Methods Used with Local Potential Formulation*

a. An Iteration Scheme. For simplicity let us assume that we are interested in determining the temperature t in a system under given boundary and initial conditions. Firstly the Lagrangian, Eq. (125), and the corresponding functional F, Eq. (124), would be constructed for the appropriate energy equation governing the temperature. We now assume a plausible function for t satisfying the initial and boundary conditions, and a first approximate value for t^* is calculated by the minimization of F as in the Ritz method [106]. This value of t^* is taken as the new approximation for t and a second approximation for t^* is calculated. This iteration scheme has been shown to converge by Kruskal [141].

b. Self-Consistent Approach. In the same problem of determining the temperature the self-consistent approach envisages the assumption

$$t = t(\alpha_i), \qquad t^* = t^*(\alpha_i^*), \quad (130)$$

where t and t^* are assumed to be plausible functions satisfying the boundary and initial conditions and α_i, α_i^* are two sets of arbitrary parameters. Using the values of t and t^* from Eq. (130) the corresponding functional F, Eq. (124), is evaluated, and using the Ritz method [106] for the minimization of F we obtain the equations

$$\partial F/\partial \alpha_i = 0 \qquad i = 1, 2, 3, \ldots, m. \quad (131)$$

The subsidiary condition Eq. (129) is now affected by setting $\alpha_i = \alpha_i^*$. The algebraic equations (131) are then solved for the coefficients. Convergence properties of this scheme have been discussed in [142].

3. *Applications*

Hays [143, 144] has applied the above formulation to the analysis of a slow viscous motion of an incompressible fluid with temperature dependent viscosity in Couette and Poiseuille flows. The formulation has also been applied by Hays [145] and by Hays and Curd [146] to various nonlinear problems of heat conduction. Butler and Rackley [147] have applied the same method to the problem of heat transfer in a slow moving incompressible fluid between parallel plates or in a circular tube with the assumptions of temperature dependent viscosity and conductivity. Very recently Weihs and Gal-Or [148] have applied the local potential formulation to the fluid flow in the boundary layer including viscous effects, coupled heat and multicomponent mass transfer, and chemical reactions. A distinguishing feature of this work is the breaking up of the local potential in parts by application of the Curie principle [134, p. 57] resulting in a great simplification. Recently, Kumar [149] has formulated the local potential for the nonlinear coupled heat and mass transfer in a porous medium involving phase changes. These equations are in a nondimensional form

$$\frac{\partial T}{\partial \theta} = \frac{\partial}{\partial X_i}\left[F_1(T,\Theta)\frac{\partial T}{\partial X_i}\right] - \mathrm{Ko}^* F_2(T,\Theta)\frac{\partial \Theta}{\partial \theta}, \tag{132}$$

$$\frac{\partial \Theta}{\partial \theta} = \mathrm{Lu}_0 \frac{\partial}{\partial X_i}\left[F_3(T,\Theta)\frac{\partial \Theta}{\partial X_i}\right] - \mathrm{Lu}_0\,\mathrm{Pn}_0 \frac{\partial}{\partial X_i}\left[F_3 F_4(T,\Theta)\frac{\partial T}{\partial X_i}\right], \tag{133}$$

where $F_n(T, \Theta)$, $n = 1, 2, 3, 4$, are the functions describing the effect of temperature and moisture transfer potential on the various thermophysical characteristics of the porous medium. It has been shown that the Euler–Lagrange equations

$$\left(\frac{\delta J}{\delta T}\right)_{T^*,\Theta^*,F_n^*} = 0, \qquad \left(\frac{\delta J}{\delta \Theta}\right)_{T^*,\Theta^*,F_n^*} = 0, \tag{134}$$

with the subsidiary conditions

$$T = T^*, \qquad \Theta = \Theta^*, \qquad F_n = F_n^*, \tag{135}$$

yield Eqs. (132) and (133) where

$$J = \int_{V_1}\int_{\theta}\left[T\frac{\partial T^*}{\partial \theta} + \mathrm{Ko}^* F_2^* \frac{\partial \Theta}{\partial \theta} T + \frac{1}{2} F_1^*\left(\frac{\partial T}{\partial X_i}\right)^2 + \frac{1}{2}\mathrm{Lu}_0 F_3^*\left(\frac{\partial \Theta}{\partial X_i}\right)^2 + \Theta\frac{\partial \Theta^*}{\partial \theta} - \mathrm{Lu}_0\,\mathrm{Pn}_0 F_3^* F_4^* \frac{\partial T^*}{\partial X_i}\frac{\partial \Theta}{\partial X_i}\right] dV_1 d\theta. \tag{136}$$

The formulation has been applied to the problem of heat and mass transfer in an infinite plate of finite thickness with thermal and mass diffusivity assumed to be linearly dependent on temperature and moisture transfer potential, respectively, under boundary conditions of the first kind (constant temperature).

Recently Kumar and Gupta [150] have pointed out that a boundary layer approach in the local potential formulation, using the concept of penetration depth, can greatly simplify the arduous calculations involved in the determination of coefficients of the assumed profile. This simplification is achieved by assuming one-parameter polynomial profiles in terms of the penetration depth. The approach can be used for one-dimensional heat flow problems in semi-infinite media for all times and for finite slabs for the initial time. This new approach has been applied by them to problems of heat conduction, complex solid–fluid systems, and to concentration dependent diffusion.

a. A Problem of Melting. Consider a solid $x > 0$ of melting temperature t_m and maintained at a uniform zero temperature initially. Let the position of the melting face be at $x = a(\tau)$ at time τ. Assuming that a constant flux R is supplied at this face which is initially at $x = 0$, the solid would start melting when the face temperature becomes t_m. Let $q(\tau)$ be the penetration depth for the temperature beyond the melting front so that $t = 0$ at $x = a(\tau) + q(\tau)$. Following the approach of [150], we write the local potential for the volume of the solid contained between the surfaces $x = a(\tau)$ and $x = a(\tau) + q(\tau)$, with constant thermal properties, in the form

$$J = \int_a^{a+q(\tau)} \left[(k/2)(\partial t/\partial x)^2 + t(\partial t^*/\partial \tau) \right] dx, \tag{137}$$

where t^* is the assumed temperature distribution not subject to variation and t is the temperature we wish to determine. Assuming cubic profiles for t and t^* satisfying the conditions at $x = a(\tau)$ and $x = a(\tau) + q(\tau)$,

$$t = t_m \left(1 - \frac{x - a}{q} \right)^3, \qquad t^* = t_m \left(1 - \frac{x - a}{q^*} \right)^3. \tag{138}$$

The parameter $q(\tau)$ is determined as a function of τ by following the self-consistent approach. Thus the condition $(\partial J/\partial q)_{q^*} = 0$ followed by $q = q^*$ gives

$$2q\dot{q} + 7q\dot{a} = 21k. \tag{139}$$

Equation (139) involves two unknowns q and a and we therefore require another condition to determine both of them. This second condition is provided by the energy balance equation

$$R = (l + Ct_m)\,\dot{a} + \frac{d}{dt} \int_a^{a+q} Ct\, dx. \tag{140}$$

Using the profile for t, Eq. (138), in the integral on the right-hand side of Eq. (140), we get

$$R = (l + Ct_m)\dot{a} + \tfrac{1}{4}Ct_m\dot{q}. \tag{141}$$

Solving Eqs. (139) and (141) as simultaneous equations we get the nondimensional rate of melting

$$\frac{l\dot{a}}{R} = \frac{m}{m+4\sqrt{\pi}}\left(\frac{4\sqrt{\pi}}{m} - \frac{21}{mq}\right), \tag{142}$$

where

$$m = (\sqrt{\pi}/2l)Ct_m. \tag{143}$$

If we define the nondimensional melting time as

$$\tau_m = (\pi kC/4)(t_m/k)^2, \tag{144}$$

and if $q_1 = q/\sqrt{k\tau_m}$ we get $q_1(\tau)$ from the equation

$$-\frac{m+4\sqrt{\pi}}{14\sqrt{\pi}m}\,q_1 - \frac{3(\sqrt{\pi}+2m)(m+4\sqrt{\pi})}{14m^2\pi}\log\left[1 - \frac{mq_1}{3(1+2m/\sqrt{\pi})}\right]$$

$$= 0.392 + \left(\frac{\tau}{\tau_m} - 1\right) \tag{145}$$

Having thus determined $q_1(\tau)$, and therefore $q(\tau)$, the temperature distribution in the melting solid is given by Eq. (138).

TABLE II

COMPARISON OF NONDIMENSIONAL RATES OF MELTING FOR VARIOUS VALUES OF NONDIMENSIONAL TIME AND FOR $m = 0$ AND $m = 0.2$

	$m=0$			$l\dot{a}/R$ $m=0.2$		
$(\tau/\tau_m) - 1$	[a]	[b]	[c]	[a]	[b]	[c]
0.01	0.011	0.012	0.063	0.013	0.014	0.060
0.1	0.101	0.106	0.204	0.099	0.102	0.187
0.2	0.177	0.184	0.270	0.169	0.168	0.254
0.3	0.237	0.244	0.319	0.231	0.225	0.300
1	0.457	0.466	0.500	0.426	0.423	0.457
2	0.584	0.592	0.607	0.541	0.534	0.542
3	0.650	0.657	0.666	0.600	0.591	0.600
10	0.799	0.810	0.804	0.728	0.716	0.720
20	0.857	0.860	0.850	0.773	0.761	0.770

[a] Results obtained by the variational method based on local potential using the boundary layer approach [150].

[b] Results obtained by Biot's variational formulation [111].

[c] Exact solution of Landau [151].

A comparison of the nondimensional melting rate obtained by the present method with the exact results of Landau [151] and the variational solution obtained by Biot and Doughaday [111] is presented in Table II. It is seen that the results obtained by the local potential formulation using the boundary layer approach are quite accurate and are closer to the exact solution than the corresponding results of [111], except for the case of $m = 0$ which is of very little practical importance.

Gupta [152] has extended the above analysis to the case of heat conduction in an ablating solid with variable thermal properties, using a very general law of dependence of thermal conductivity on temperature as applicable to glassy materials, and has shown that as a particular case of this law, his results are quite comparable to those of Biot and Agrawal [112]. The boundary layer approach, in conjunction with the local potential formulation, has been used by Schechter [153, p. 205] for the analysis of transient temperature distribution in the entrance length of channels. In another application of the same method Gupta [154] has analyzed the problem of transient temperature distribution in a transpiration cooled half-space with variable conductivity and specific heat.

4. *Relation to the Method of Weighted Residuals and Classical Variational Calculus*

Finlayson and Scriven [126] have critically examined the mathematical formulation of the variational principles of Biot [108] and [109] and that of Glansdorff and Prigogine [137–139]. They have shown that the above variational principles are outside the scope of classical variational calculus and are closely related to the method of weighted residuals. These authors have therefore recommended [8, 126, 155] the direct use of the method of weighted residuals in the nonlinear problems of nonequilibrium processes. While it is agreed that the variational methods of Biot and of Glansdorff and Prigogine have a close relation to the method of weighted residuals, it is felt by the present author that the physical content of these variational methods is a definite advantage over the method of weighted residuals. Further, such a formulation has led to the extension of classical variational calculus to enable it to bring dissipative systems into its fold. The direct methods of the classical calculus of variations and the method of weighted residuals can be understood within the more general framework of the self-consistent scheme presented by Glansdorff and Prigogine [137].

C. OTHER VARIATIONAL FORMULATIONS AND THEIR APPLICATION

A problem in heat transfer which suggests the use of classical variational calculus is that of finding the fin geometry for maximum dissipation of heat

in a fin of given weight. It may be appreciated that the problem stated above is a maximization problem in contrast to the problems of continuous non-equilibrium systems where the recourse to variational calculus was taken only to make available the direct method of the calculus of variations for their solution. The problem of fin geometry with maximum dissipation has been dealt with in [156–158].

As in other branches of physics, classical variational calculus has been used in heat transfer for the approximation of eigenvalues. Using the Ritz method, Sparrow and Siegel [159] have determined the lower eigenvalues of the eigenfunctions associated with convective laminar heat transfer in the thermal entry region of ducts. In the case of circular and parallel plate channels, the problem of convective heat transfer can be reduced to the solution of a Sturm–Liouville type of ordinary differential equation. Pnueli [160] has used the variational method for the analysis of forced convection heat transfer in ducts of arbitrary cross section. Tsoi [161] has used the variational method in conjuction with the integral transforms to the problem of unsteady convective heat transfer in tubes of arbitrary cross section, and considered the cases of circular and plane parallel channels in detail.

Morse and Feshbach [77] have presented a scheme of formulating adjoint variational principles for dissipative systems governed by linear nonself-adjoint equations. The scheme envisages the introduction of functions governed by the equations and initial and boundary conditions adjoint to ones governing the original functions. Physically the adjoint to a given system means a system with negative dissipation equal to the dissipation in the original system. If the two systems are considered together the entire system is a conservative system. Thus the formulation [77] is equivalent to artificially reducing a dissipative system to a conservative one for which a potential can be formulated. Based on this idea, Nichols and Bankoff [162] have formulated the adjoint variational principle for nonstationary convective diffusion.

A general discussion of variational principles for approximate solution of the boundary value problems is given by Stallybrass [163] along with a bibliography of similar works.

Gurtin [164] has formulated variational principles for linear initial value problems of wave and heat conduction equation by first reducing these problems to equivalent boundary value problems through an integro-differential equation containing the initial condition implicitly and then deriving the variational principle for these boundary value problems. The variational principle of Gurtin [164] has been developed and applied in heat conduction problems by Ainola [165] and generalized for very general types of boundary conditions by Rafalski and Zyszkowski [166].

V. Methods Related to the Solution of Integral Equations

A. Integral Equations in Radiative Heat Transfer

The most frequent use of the methods of solution of integral equations has been made in the theory of radiative heat transfer. This is so as the transfer equation for radiative flux, by its very nature, is formulated as an integro-differential equation, which in some special cases is reducible to an integral equation. Excellent surveys in radiative heat transfer have recently appeared [167] and [168], listing the recent contributions to the field as well as the mathematical methods which can be used in the solution of the integral equations governing the problems in this field. A detailed account of these methods is given by Chandrashekhar [169], Kourganoff [170], and Busbridge [171] along with some very sophisticated mathematical techniques for obtaining exact solutions to radiative transfer equations in some special cases. In the case of radiant interchange between grey surfaces and in grey diffuse enclosures with isothermal surfaces and nonuniformly distributed radiant flux, the problem of determining the temperature distribution reduces to solving a Fredholm type integral equation. Various methods of solutions in this case are discussed in the review by Sparrow [172] and by Howell and Siegel [173]. The methods of solution include numerical integration, the use of approximate separable kernels, approximate solutions by variational methods, and solution by the Taylor series expansion. Detailed information on these methods can be obtained in [174–178]. Carrier [179] has discussed two approximate methods, namely, the Substitute Kernel Method and that of Integral Equation Boundary Layers which are specially suited for the integral equations in radiative transfer.

In view of the available literature cited above for the solution of integral equations of radiative heat transfer we will not endeavor to discuss any further the radiation problems as they concern this section on methods relating to the solution of integral equations. We would, however, present some examples from other fields of heat transfer where the partial differential equations have been converted to integral equations, with the purpose of using the methods available for the solution of such equations.

B. Reduction of Other Heat Transfer Problems to Integral Equations

Boley [180] transformed the partial differential equation of heat conduction in a melting or a solidifying region to an integro-differential equation which was solved in series. Koh and Hartnett [181] reduced the equations of

momentum and energy of laminar flow over a permeable wedge with suction to ordinary integral equations which were solved numerically by iteration procedures. The same approach has been used in [182, 183] for a two-component compressible boundary layer over a surface with temperature dependent physical properties. Tolubinskiy [184, 185] has given a very general integral equation approach to transfer processes assuming finite velocity of diffusion. Provided the solution of the problem for an infinite space is known, the corresponding solution for any region can be constructed by this method. Grinchenkov and Ulitko [186] reduced the problem of the steady temperature distribution in a semi-infinite medium, with its surface maintained at zero temperature and with the disk $0 < r < a$ or the ring $r_1 < r < r_2$ kept at a constant temperature to a Fredholm integral equation of the second kind. Vasilevski [187] reduced the nonlinear parabolic equations of simultaneous heat and mass diffusion under unsteady conditions to a set of two ordinary integro-differential equations by using Boltzman's similarity transformation, and obtained approximate analytic solutions to these equations. Patankar [188], using a two-parameter profile for the temperature, has reduced the analysis of heat transfer across turbulent boundary layers with step change in temperature at the wall to two integral equations for determining the parameters in the profile. These integral equations have been solved for the laminar velocity profile, the seventh power law velocity profile, and for the universal law of the wall due to Spalding [189]. Savino and Siegel [190] derived an integral equation for the temperature distribution in the solidified layer formed in a moving warm liquid on to an isothermal cold surface.

C. LIGHTHILL–VOLTERRA APPROACH

Lighthill [101], in a contribution to the theory of heat transfer in a boundary layer over a surface with variable temperature along its extent in the direction of flow, introduced a new approach based on the solution of singular integral equations of the Volterra type. This approach has since been used in many other applications and may therefore be rightly termed the Lighthill–Volterra approach. Using the linear approximation to the velocity near the surface in the laminar boundary layer,

$$u = \tau_w(x)y/\mu, \tag{146}$$

Lighthill has shown that the value of the local heat transfer to the wall is

$$Q_w(x) = -K_f\left(\frac{\sigma\rho}{9\mu^2}\right)^{1/3} \frac{[\tau_w(x)]^{1/2}}{\Gamma(4/3)} \int_0^x \left(\int_{x_1}^x [\tau_w(z)]^{1/2}\, dz \right) d(t_\varepsilon(x_1)), \tag{147}$$

where $t_e(x) = t_w(x) - t_\infty$ and the integral in the above equation is a Stieltjes Integral used in the sense

$$\int_0^x f(t,x)\,dg(t) = f(0,x)g(0) + \int_0^x f(t,x)g'(t)\,dt. \tag{148}$$

The above formula Eq. (147) for heat transfer is in the nature of a high Prandtl number approximation. With increasing σ the thermal boundary layer gets thinner in comparison to the velocity boundary layer and therefore the linear velocity approximation Eq. (146) becomes more and more exact. Lighthill [101] has pointed out that in the above formula μ and ρ only appear as the product. If this product is constant, the above low-speed solution holds for all Mach numbers. Thus for a flat plate where

$$\tau_w(x) = 0.332(\mu\rho U_\infty/x)^{1/2}, \tag{149}$$

the above formula finally simplifies to

$$Q_w(x) = 0.339(K_f/\mu)\sigma^{1/3}(\mu\rho U_\infty)^{1/2}x^{-1/4} \int_0^x (x^{3/4} - x_1^{3/4})^{-1/3} t_w(x_1)\,dx_1. \tag{150}$$

Tifford [191] has given a method for the application of Lighthill's method to boundary layers with a pressure gradient by replacing the value of $\tau_w(x)$ in Eq. (147) by the value which takes into account the pressure gradient. Important contributions have been made by Spalding [192], Liepmann [193], and Davies and Bourne [194] to improve the accuracy of Lighthill's method and to extend it to boundary layers with pressure gradients. Illingworth [195] and Lilley [196] have extended the method to compressible boundary layers with pressure gradients and heat transfer. A concise account of these methods is given in [197].

The application of Lighthill's integral relation to chemically active boundary layers with surface reactions has been made in [198–202]. Frank-Kamenetskii [200] has given the results of numerical integration of an equation quite similar to Eq. (150). These equations determine the concentration of a component in a boundary layer with reactions of orders $\frac{1}{2}$ and 2. Chambre [203] and Mann and Wolf [204] have reduced the solution of the problem of heat conduction in a semi-infinite solid with nonlinear boundary conditions to an exactly similar type of integral equation. The inverse problem of heat transfer has been reduced in [205] and [206] to the solution of a singular integral equation of the Volterra type. A similar integral equation which arose in the discussion of the effect of a discontinuity of surface catalycity on the boundary layer flow of a dissociating gas has been treated by a series method and also numerically in [207]. Perelman [208] has shown that the

solution of the conjugate problem of heat transfer, namely, the problem where the energy equation of the fluid and the heat conduction equation within the solid wall are solved simultaneously with matching of temperature and flux at the interface, can be reduced to the solution of such equations.

It may be pointed out that the series solutions to the above type of equations have small radii of convergence and are useful only for very small values of the argument. The basic difficulty in obtaining the analytic solution of the above type of equation for large or moderately large argument is the fact that the asymptotic form of the solution cannot be directly substituted, as it is necessary to consider the contribution of the integral near the lower limit. It is thus evident that in such equations the asymptotic solution for $x \to \infty$ depends upon the behavior of the solution near $x \to 0$. These equations are therefore usually solved by numerical techniques. In view of the very wide application of these integral equations in heat transfer it is, however, essential to find methods to obtain their analytical solutions for large arguments. In the following we propose to discuss two methods of doing so.

D. PERELMAN'S ASYMPTOTIC METHOD

Perelman's [208, 209] method is based on the Mellin transform for finding asymptotic solutions to the linear singular integral equations of the type

$$a(x)\phi(x) = g(x) + \int_0^\infty k(x/y)x^\alpha y^\beta \phi(y)\, dy, \tag{151}$$

where $a(x)$ is a finite sum

$$a(x) = \sum_{l=1}^{\infty} a_l x^{\gamma_l} \tag{152}$$

or a linear differential operator of the form

$$a(x) = \sum_l a_l x^{\gamma_l} d^{n_l}/dx^{n_l}, \tag{153}$$

in which case the above integral equation (151) would become an integro-differential equation. Defining the Mellin transform of $f(x)$ as

$$F(S) = \int_0^\infty f(x)x^{S-1}\, dx, \tag{154}$$

and applying this transform to both sides of Eq. (151) with the expression on the right-hand side of Eq. (152) for $a(x)$, we obtain the difference equation

$$\sum_l a_l \Phi(S + \gamma_l) = G(S) + K(S + \alpha)\Phi(S + \alpha + \beta + 1) \tag{155}$$

valid in some region of the S-plane. Without loss of generality we may assume that the above relation holds in some strip $0 < \operatorname{Re} S < h$, where h is some positive number.

The crucial step in the method of Perelman [208, 209] is the introduction of a new function $\Psi(S)$ such that

$$\Phi(S + \delta) = \Omega(S)\Psi(S) \qquad \operatorname{Re} S > 0, \tag{156}$$

where δ is the least of the numbers γ_l and $\alpha + \beta + 1$. In terms of the new function $\Psi(S)$ defined in Eq. (156), Eq. (155) can be rewritten as

$$\sum_l a_l \Omega(S + \gamma_l - \delta)\Psi(S + \gamma_l - \delta) = G(S) + K(S + \alpha)\Omega(S + \alpha + \beta + 1 - \delta)\Psi(S + \alpha + \beta + 1 - \delta). \tag{157}$$

The function $\Omega(S)$ in Eq. (156) is chosen such that the inverse Mellin transforms of all the functions and $\Omega(S + \alpha + \beta - \delta + 1)$ exist and vanish exponentially. For this, the necessary condition is that the above function not possess any singularity in the half-plane $\operatorname{Re} S > 0$. Whether this condition would be sufficient also depends on the choice of $\Omega(S)$. If we now search for the function $\psi(x)$, the inverse Mellin transform of $\Psi(S)$ in the form

$$\psi(x) \sim \sum_{n=0}^{\infty} (C_n / x^{an+b}), \tag{158}$$

the coefficients C_n are obtained from Eq. (157) as recurrence relations and the required function $\phi(x)$ can be determined by applying the inverse Mellin transform to Eq. (156).

To bring out further the salient points of the method we propose to find the asymptotic solution of the Volterra type integral equation

$$\phi(x) = 1 - \int_0^x \frac{\phi(y)}{(x - y)^{1/2}}\, dy. \tag{159}$$

This equation, except for a constant in the second term on the right-hand side, is the one to which the partial differential equation of one-dimensional heat conduction with a Newton type radiation condition on its surface can be reduced [203]. The exact solution of the above equation is well known and can be obtained by application of the Laplace transform. This solution is

$$\phi(x) = \exp(\pi x) \operatorname{erfc}(\pi x)^{1/2}, \tag{160}$$

where

$$\operatorname{erfc}(x) = (2/\sqrt{\pi}) \int_x^{\infty} \exp(-t^2)\, dt. \tag{161}$$

Taking the Mellin transform of the above equation, where unity on the right-hand side is represented as $1 = \lim_{\varepsilon \to 0} \exp(-\varepsilon\sqrt{x})$, we obtain

$$\lim_{\epsilon \to 0} 2\epsilon^{-2S}\Gamma(2S) - \Phi(S) = \sqrt{\pi}\,\frac{\Gamma(\frac{1}{2} - S)}{\Gamma(1 - S)}\Phi(S + \tfrac{1}{2}). \tag{162}$$

Equation (162) is valid in the strip $0 < \operatorname{Re} S < \frac{1}{2}$ of the S-plane. A new function $\Psi(S)$ is now introduced as

$$\Phi(S) = \frac{\Gamma(2S)\Gamma(S)}{\Gamma(1 - S)}\Psi(S) \tag{163}$$

or

$$\Phi(S + \tfrac{1}{2}) = \frac{\Gamma(2S + 1)\Gamma(S + \frac{1}{2})}{\Gamma(\frac{1}{2} - S)}\Psi(S + \tfrac{1}{2}). \tag{164}$$

It may be noted here that the function $\Psi(S)$ is not unique. Basically it has been introduced to remove the singularity of the right-hand side of Eq. (162) at $S = \frac{1}{2}$. This explains the factor in the denominator on the right-hand side of Eq. (163). Other factors are such that in the equation obtained after substituting for $\Phi(S + \frac{1}{2})$ from Eq. (164) in the Eq. (162), each term has an inverse Mellin transform. It is here that the nonuniqueness is being introduced. The particular choice of the factors in Eq. (163) appears to have been made so as to lead to the desired expansion. Thus in terms of $\Psi(S)$ Eq. (162) can be written as

$$-\lim_{\varepsilon \to 0} 2\epsilon^{-2S}\Gamma(-S) - \frac{\Gamma(S)}{S}\Psi(S) = 2\sqrt{\pi}\,\Gamma(S + \tfrac{1}{2})\Psi(S + \tfrac{1}{2}). \tag{165}$$

Introducing an expansion of the type Eq. (158) for $\psi(x)$ and substituting the Mellin transform of Eq. (166) in Eq. (165) it can be seen that the difference equation (165) would hold if

$$a = \tfrac{1}{2}, \tag{166}$$

$$b = \tfrac{1}{2}, \tag{167}$$

and also the recurrence relations

$$C_0 = \frac{1}{\sqrt{\pi}}, \qquad C_n = \frac{1}{n\sqrt{\pi}}\,\frac{\Gamma(n/2)}{\Gamma(n + \frac{1}{2})}\,C_{n-1} \qquad n = 1, 2, \cdots, \tag{168}$$

from which we obtain, in view of Eq. (163),

$$\phi(x) = \sum_{n=0}^{\infty} \frac{C_{2n}}{x^{n+1/2}}\,\frac{\Gamma(2n + 1)\Gamma(n + \frac{1}{2})}{\Gamma(\frac{1}{2} - n)}, \tag{169}$$

which is the expansion of the exact solution given in Eq. (160) for $x \to \infty$.

The above method has been used by Perelman [208] for the solution of a number of problems where the solution of the energy equation in the boundary layer has been solved in conjunction with the heat conduction equation within the solid in contact with the fluid. Kumar [210] has used this method in the solution of the conjugate problem of heat transfer in a laminar boundary layer with injection from the surface of a solid body of semi-infinite extent over which the boundary layer exists.

E. A New Method Based on the Mellin Transform

Recently Kumar and Bartman [211] suggested a new method for the asymptotic solution of such equations both near the origin and also for large x. This method has now been developed by Kumar [212] and applied to the solution of various problems in nonlinear heat conduction and surface chemical reactions in compressible boundary layers. The method is illustrated below by the solution of Lighthill's problem [101] of finding the radiation–convection equilibrium temperature distribution in a strip. Neglecting the conduction in the strip, we are interested in determining the temperature distribution such that the energy radiated out from the strip, according to the Stefan–Boltzmann law, is just compensated for by the convective flux received by it. Using Lighthill's integral relation [101] the problem is reduced to the solution of the equation

$$[F(Z)]^4 = -\frac{1}{2Z^{1/2}} \int_0^Z \frac{F'(Z_1)\, dZ_1}{(Z^{3/2} - Z_1^{3/2})^{1/3}}; \qquad F'(Z) = \frac{dF}{dZ}, \tag{170}$$

where

$$F(Z) = T(Z)/T_r. \tag{171}$$

The above equation is to be solved for the boundary conditions

$$F(0) = 1, \tag{172}$$

$$F(\infty) \to 0. \tag{173}$$

Applying Abel's transformation formula [174, p. 158] and integrating once using Eq. (172) we can write

$$\Phi(Z) = 1 - F(Z) = \frac{3\sqrt{3}}{2\pi} \int_0^Z \frac{ZF^4(Z_1)\, dZ_1}{(Z^{3/2} - Z_1^{3/2})^{2/3}}. \tag{174}$$

Formally, the Mellin transform of Eq. (174) can be written as

$$\mathbf{M}(\Phi) = (\sqrt{3}/\pi)\beta(\tfrac{2}{3} - \tfrac{2}{3}S, \tfrac{1}{3})\mathbf{M}(F^4 Z^{-1}) \tag{175}$$

where the operator $\mathbf{M}(F)$ stands for the Mellin transform $\int_0^\infty F(Z)Z^{s-1}\,dZ$ of $F(Z)$. Further we would use $\mathbf{M}_-(F)$ and $\mathbf{M}_+(F)$ to denote the functions $\int_0^1 F(Z)Z^{s-1}\,dZ$ and $\int_1^\infty F(Z)Z^{s-1}\,dZ$, respectively. Thus Eq. (175) can be written as

$$\mathbf{M}_-(\Phi) + \mathbf{M}_+(\Phi) = (\sqrt{3}/\pi)\beta(\tfrac{2}{3} - \tfrac{2}{3}S, \tfrac{1}{3})[\mathbf{M}_-(F^4Z^{-1}) + \mathbf{M}_+(F^4Z^{-1})]. \quad (176)$$

If we assume

$$\Phi(Z) \sim \sum_{n=1}^{\infty} A_n Z^{an} \qquad Z \to 0, \quad (177)$$

then in the half-plane Re $S < -a$ we write

$$\mathbf{M}_-(\Phi) = (\sqrt{3}/\pi)\beta(\tfrac{2}{3} - \tfrac{2}{3}S, \tfrac{1}{3})\mathbf{M}_-(F^4Z^{-1}). \quad (178)$$

For this functional equation to be valid the poles and residues of the two sides of Eq. (178) must coincide [213]. Taking the Mellin transform of Eq. (177) and substituting it in the left-hand side of Eq. (178), we get by equating at the first pole of the two sides of Eq. (178), $a = 1$, and equating the residues the successive poles $S = -a, -2a, \ldots$, the following recurrence relation for A_n

$$A_1 = \frac{2\Gamma(\frac{4}{3})}{\Gamma(\frac{2}{3})\Gamma(\frac{5}{3})} = 1.461,$$

$$A_2 = -\frac{2\Gamma(2)}{\Gamma(\frac{2}{3})\Gamma(3)}\,4A_1 = -7.252,$$

$$A_3 = -\frac{(4A_2 - 6A_1^2)2\Gamma(\frac{10}{3})}{\Gamma(3)\Gamma(\frac{2}{3})} = 46.46,$$

so that for $Z \to 0$ we have

$$F(Z) = 1 - 1.461Z + 7.252Z^2 - 46.46Z^3 + \cdots. \quad (179)$$

To obtain the solution for large Z we can write

$$\mathbf{M}_+(\Phi) = (\sqrt{3}/\pi)\beta(\tfrac{2}{3} - \tfrac{2}{3}S, \tfrac{1}{3})\mathbf{M}_+(F^4Z^{-1}). \quad (180)$$

Assuming

$$F(Z) \sim \sum_{n=1}^{\infty} B_n Z^{-nb}, \quad (181)$$

and proceeding exactly as above, we get $b = \frac{1}{4}$ and

$$B_1^4 = \tfrac{1}{2},$$

$$4B_1^3B_2 = \tfrac{1}{2}[\Gamma(\tfrac{2}{3})\Gamma(\tfrac{5}{6})/\Gamma(\tfrac{1}{2})],$$

$$4B_1^3B_3 + 6B_2^2B_1^2 = \tfrac{1}{2}[\Gamma(\tfrac{2}{3})\Gamma(\tfrac{2}{3})/\Gamma(\tfrac{1}{3})]B_2,$$

$$4B_4B_1^3 + 12B_3B_2B_1^2 + 4B_2^3B_1 = \tfrac{1}{2}[\Gamma(\tfrac{2}{3})\Gamma(\tfrac{1}{2})/\Gamma(\tfrac{1}{6})]B_3,$$

giving for $Z \to \infty$

$$F(Z) \sim 0.8409Z^{-1/4} - 0.1524Z^{-1/2} - 0.0195Z^{-3/4} - 0.0038Z^{-1}. \quad (182)$$

The solutions in Eqs. (179) and (182) are exactly the same as obtained by Lighthill [101] by a rather complicated order-of-magnitude analysis of the integrals. It should be noted that the application of Abel's transformation formula to Eq. (170) and an integration thereafter to include the boundary condition at Eq. (172) within the new integral equation (174) is an important step in the present technique which takes into account the dependence of the solution for large Z on the solution for $Z \to 0$. In contrast to this, Perelman's method [208, 209] for finding the asymptotic solution for $Z \to \infty$ cannot take into account the boundary condition at $Z \to 0$. It has been shown [212] that the method can be applied to a large number of problems of conductive and convective heat transfer and also to boundary layers with chemical reactions, with useful analytical results obtained for problems where up until now only numerical solutions were available. Kumar and Trivedi [214] have further applied the technique to the boundary layer flow of a dissociating gas with discontinuous catalycity of the wall and obtained analytic solutions showing excellent agreement with the numerical results of [207].

VI. Methods Based on the Use of the Complex Variable

A. Solution of Harmonic and Biharmonic Equations

Methods based on the use of the complex variable were developed by Muskhelishvili [215] for the solution of the boundary value problems in the theory of elasticity, and have been extensively used since then by other authors. Recently these methods have been applied to obtain the solution to the problem of forced convection heat transfer of a fluid through a channel of arbitrary cross section. This method essentially involves the solution of a harmonic or a biharmonic equation with complex independent variable.

Tao [216–218] was the first to use the above method in the analysis of forced convection heat transfer in channels of various shapes with fully

developed laminar flow, in the presence of heat sources with a constant temperature gradient along the axis of the channel. Consider a steady fully developed laminar flow in the channel of cross section D bounded by a closed curve Γ. Let the axis of the channel be in the Z direction. The momentum and energy equations for a constant property dissipating fluid can be written as

$$\nabla^2 u = \frac{1}{\mu}\frac{dp}{dZ} = C_1, \tag{183}$$

$$\nabla^2 t = \left(\frac{\rho c_p}{K}\frac{dt}{dZ}\right)u - \frac{Q}{K} - \frac{\mu}{K}\left[\left(\frac{\partial u}{\partial x}\right)^2 + \left(\frac{\partial u}{\partial y}\right)^2\right],$$

$$= C_2 u - M - \frac{\mu}{K}\left[\left(\frac{\partial u}{\partial x}\right)^2 + \left(\frac{\partial \mu}{\partial y}\right)^2\right], \tag{184}$$

with the boundary conditions

$$u = 0, \quad t = t_w \quad \text{on } \Gamma, \tag{185}$$

where the second and the third terms on the right-hand side of Eq. (184) represent respectively the source function and the dissipation function. It has been shown by Tao [216, 217] that the solution of the above problem, neglecting the third term on the right-hand side of Eq. (184), reduces to the solution of the biharmonic equation

$$\frac{\partial^4 \theta_1}{\partial z^2\, d\bar{z}^2} = 0 \tag{186}$$

and the harmonic equation

$$\frac{\partial^2 \theta_2}{\partial z\, \partial \bar{z}} = 0, \tag{187}$$

with the respective boundary conditions

$$\left.\begin{aligned} \theta_1 &= -\frac{C_1 C_2}{64}(z\bar{z})^2 \\ \frac{\partial^2 \theta_1}{\partial z\, \partial \bar{z}} &= -\frac{C_1 C_2}{16}(z\bar{z}) \end{aligned}\right\} \text{On} \quad \Gamma \tag{188}$$

and

$$\theta_2 = \frac{1}{4}\iint M\, dz\, d\bar{z} \quad \text{On} \quad \Gamma, \tag{189}$$

where

$$\theta_1 = T_1 - \frac{C_1 C_2}{64}(z\bar{z})^2, \tag{190}$$

$$\theta_2 = T_2 + \frac{1}{4}\iint M(z, \bar{z})\, dz\, d\bar{z}, \tag{191}$$

and T_1 and T_2 are the two components of $T = t - t_w$ such that T_1 is independent of the heat source function M and T_2 is independent of the velocity field u. The general solution of Eqs. (186) and (187) can be written as

$$\theta_1 = \bar{z}\phi(z) + z\bar{\phi}(z) + \psi(z) + \bar{\psi}(z), \tag{192}$$

$$\theta_2 = \lambda(z) + \bar{\lambda}(z), \tag{193}$$

where the bar denotes the complex conjugate, $\phi(z)$ and $\psi(z)$ in Eq. (192) are two holomorphic functions in D satisfying the boundary condition Eq. (188), and $\lambda(z)$ is another holomorphic function satisfying the boundary condition Eq. (189). It has been shown [216] that the method outlined above can be used in conjunction with conformal mapping for the channel bounded by an arbitrary noncircular closed contour. This was illustrated in the case of channels with elliptic and triangular cross sections. At [217] it has been shown that the commonly used technique of equivalent circular duct leads to unreliable results. Shastry [219], using the methods described in [216–218], obtained the mean values of the Nusselt number, the mean velocity, and the mean mixed temperature in the case of cardoid and ovaloid (circular profile with two opposite flat sides) forms of channels.

Tyagi [220, 221] has generalized all earlier works and found solutions for channels of various shapes with flowing fluid having heat sources and dissipating energy due to internal friction, and therefore considered the problem represented by the complete equations (183) and (184). For the case of gases flowing through the channel [220] yet another term representing the compressional work was introduced on the right-hand side of Eq. (184). Thus in [220] the solution has been obtained for the problem described by the momentum equation (183), the energy equation

$$\nabla^2 t = C_2 u - M - \frac{\mu}{K}\left[\left(\frac{\partial u}{\partial x}\right)^2 + \left(\frac{\partial u}{\partial y}\right)^2\right] + u\frac{dp}{dz}, \tag{194}$$

and the boundary conditions Eq. (185). The case of temperature dependent viscosity has been considered in [222] and the Newton type radiation boundary condition in [223].

B. SCHWARZ–CHRISTOFFEL TRANSFORMATION

1. *The Transformation Formula*

For studying steady-state heat conduction problems in two-dimensional regions with nonclassical boundaries, the method of transforming such regions in one complex plane into the upper half of another complex plane offers a very powerful tool. A very general method of transforming an n-angled polygon in the z-plane with exterior angles $\phi_1, \phi_2, \ldots, \phi_n$ on to the upper half of the w-plane is the Schwarz–Christoffel transformation formula [77, p. 445]

$$dz/dw = A(w - b_1)^{-\phi_1/\pi}(w - b_2)^{-\phi_2/\pi} \cdots. \tag{195}$$

Integrating both sides of Eq. (195), we get

$$z = z_0 + A\int (w - b_1)^{-\phi_1/\pi}(w - b_2)^{-\phi_2/\pi} \cdots dw, \tag{196}$$

where z_0, $|A|$, and $\mathrm{Arg}(A)$ are chosen to fix the origin, scale, and orientation of the polygon and $b_1, b_2, \ldots$ are the points in the w-plane which correspond to the corner points of the polygon. If one of the corners is placed in the w-plane at infinity, the corresponding factor in the expression on the right-hand side of Eq. (195) is neglected.

Having found the appropriate transformation to transform the region of interest in the z-plane to the upper half of the w-plane the solution of the steady-state two-dimensional heat conduction equation

$$\nabla^2 t = 0 \qquad \nabla^2 = \frac{\partial^2}{\partial u^2} + \frac{\partial^2}{\partial v^2}; \qquad w = u + iv \tag{197}$$

can be found by the application of Poisson's integral [77, p. 371]. Thus the solution of Eq. (197) in the upper half-plane with the boundary condition

$$t = f(u) \qquad v = 0 \tag{198}$$

at the point u_1, v_1 is given by

$$t = \frac{v_1}{\pi}\int_{-\infty}^{\infty} \frac{f(u)\,du}{(u - u_1)^2 + v_1^2} \tag{199}$$

2. *An Illustration*

While studying a problem suggested by the probe method of determining the conductivity of rocks and soils, Kumar [224] has used the Schwarz–Christoffel transformation to find the steady-state temperature distribution

in a doubly infinite strip of finite width with a rectangular cut at one of its edges, assuming a constant temperature over the boundary of the cut and zero temperature on the rest of the boundary. The region of investigation assumed to be in the z-plane and the corresponding upper half of the w-plane, to which the above region has been transformed, are illustrated in Fig. 1.

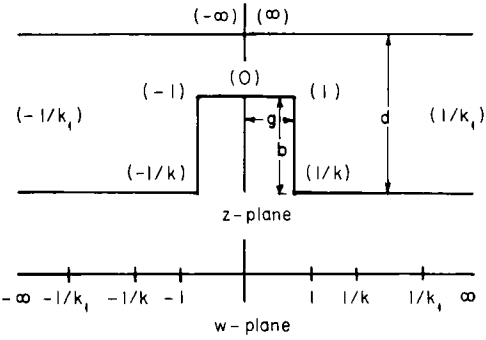

FIG. 1. Transformation of a doubly infinite strip in the z-plane with a symmetric rectangular cut to the upper half-plane. (Reproduced from Kumar [224].)

Let the points 0, g, g-ib, and ∞ in the z-plane correspond to the points 0, 1, $1/k$, and $1/k_1$ in the w-plane, and therefore from symmetry the points $-g$, $-g$-ib, $-\infty$ correspond to -1, $-1/k$, and $-1/k_1$ respectively. From the Schwarz–Christoffel transformation formula Eq. (195) we obtain

$$\frac{dz}{dw} = C\left(w - \frac{1}{k_1}\right)^{-1}\left(w - \frac{1}{k}\right)^{-1/2}(w+1)^{1/2}\left(w + \frac{1}{k_1}\right)^{-1}\left(w + \frac{1}{k}\right)^{-1/2}$$

$$(w-1)^{1/2} \qquad 1/k_1 > 1/k > 1. \tag{200}$$

Integrating both sides of Eq. (200) with respect to w, we get

$$z = C' \int_0^w \frac{(1-w^2)^{1/2}\, dw}{(1-k_1{}^2w^2)(1-k^2w^2)^{1/2}} + D \tag{201}$$

where

$$C' = C/(k_1{}^2k). \tag{202}$$

since the origins in the two planes correspond, we get in Eq. (201), $D = 0$. The integral on the right-hand side of Eq. (201) can be evaluated in terms of elliptic integrals and functions. Further, C' can be determined by noting that as we pass in the w-plane through the point $1/k_1$, there is an abrupt jump in the value of z by an amount id. Thus

$$id = \frac{C'}{2}\left[\frac{k_1^2 - 1}{k_1^2 - k^2}\right]^{1/2} \int_{\substack{\varepsilon \to 0}}^{(1/k_1)+\varepsilon} \frac{dw}{1 - k_1 w} = \frac{iC'\pi}{2k_1}\left[\frac{1 - k_1^2}{k^2 - k_1^2}\right]^{1/2}, \quad (203)$$

and we get, on substituting the value of C' from Eq. (203) in Eq. (201),

$$z = \frac{2d}{\pi}\left[\frac{k^2 cn\ \alpha\ sn\ \alpha}{dn\ \alpha}\zeta - \Pi_1(\zeta, \alpha)\right] \quad (204)$$

where α is defined by the relation

$$\alpha = sn^{-1}(k_1/k) = \int_0^{k_1/k} dw/(1 - w^2)^{1/2}(1 - k^2 w^2)^{1/2}, \quad (205)$$

$$\zeta = sn^{-1} w,$$

and

$$cn\ \alpha = (1 - sn^2\ \alpha)^{1/2}, \quad (206)$$

$$dn\ \alpha = (1 - k^2 sn^2\ \alpha)^{1/2}, \quad (207)$$

and

$$\Pi_1(\zeta, \alpha) = k^2 sn\ \alpha\ cn\ \alpha\ dn\ \alpha \int_0^{\xi} \frac{sn^2\ \zeta\ d\zeta}{1 - k^2 sn^2\ \alpha\ sn^2\ \zeta} \quad (208)$$

is the Jacobi elliptic integral of the third kind [225]. There are now two unknowns left, namely, k, α which can be determined by connecting them with the known length ratios g/d and b/d. Using some properties of elliptic functions [225] we get

$$g/d = \frac{2K}{\pi}\left[\frac{k^2 cn\ \alpha\ sn\ \alpha}{dn\ \alpha} - Z(\alpha)\right], \quad (209)$$

$$b/d = \frac{2K'}{\pi}\left[Z(\alpha) - \frac{k^2 cn\ \alpha\ sn\ \alpha}{dn\ \alpha}\right] + \frac{\alpha}{K}. \quad (210)$$

where K and K' are the complete integrals of the first kind with moduli k and k', respectively. Thus

$$K = \int_0^1 dw/(1 - w^2)^{1/2}(1 - k^2 w^2)^{1/2} \quad (211)$$

$$K' = \int_0^1 dw/(1 - w^2)^{1/2}(1 - k'^2 w^2)^{1/2} \quad (212)$$

In a particular problem, one has to choose k and α such that these correspond to the given values of g/d and b/d.

To determine the temperature along the axis of symmetry we find various points on the v-axis corresponding to various values of y in the z-plane. For this, writing iv for w we get

$$\zeta = i\beta = F(iv, k) = iF(v/(1 + v^2), k'), \tag{213}$$

and the corresponding value of z is given from Eq. (204) as

$$z = \frac{2d}{\pi}\left[\frac{k^2 cn\,\alpha\; sn\,\alpha}{dn\,\alpha} i\beta - \Pi_1(i\beta, \alpha)\right]. \tag{214}$$

Equating the imaginary parts of the two sides of Eq. (204) we get

$$\frac{y}{d} = \frac{2}{\pi}\left\{\left[\frac{k^2 cn\,\alpha\; sn\,\alpha}{dn\,\alpha} - Z(\alpha)\right]\beta + \tan^{-1}\frac{-2\sum^{m}(-1)^m q^{m^2} \sin(\pi m\alpha/K) \sinh(\pi m\beta/K)}{1 + \sum^{m}(-1)^m q^{m^2} \cos(\pi m\alpha/K) \cosh(\pi m\beta/K)}\right\} \tag{215}$$

where

$$q = \exp(-\pi K'/K).$$

The solution of the steady-state two-dimensional heat conduction equation (197) in the w-plane, with the real axis between the points $-1/k$ and $1/k$ maintained at a given temperature t_0 and with the rest of the boundary kept at zero temperature, is given from Eq. (199) for $u = 0$

$$(t/t_0) = (2/\pi) \tan^{-1}(1/kv). \tag{216}$$

For a specific case in which $b/d = 0.5533$ and $g/d = 0.0122$, corresponding to the values $k = \sin 20°$, and $\alpha = 0.972$, the temperature distribution along the axis of symmetry in the w-plane is tabulated in Table III.

TABLE III

TEMPERATURE DISTRIBUTION ALONG THE AXIS OF SYMMETRY OF THE REGION SHOWN IN z-PLANE IN FIG. 1 (from Kumar [224])

y/d	v	t/t_0	y/d	v	t/t_0
0.0032	0.0963	0.9791	0.0491	1.1917	0.7533
0.0065	0.1763	0.9616	0.0607	1.4281	0.7111
0.0099	0.2679	0.9418	0.0759	1.7320	0.6595
0.0136	0.3660	0.9211	0.0971	2.1445	0.5970
0.0176	0.4663	0.8993	0.1276	2.7475	0.5197
0.0221	0.5773	0.8760	0.1724	3.7320	0.4229
0.0270	0.7002	0.8501	0.2389	5.6713	0.3028
0.0331	0.8391	0.8219	0.3322	11.4301	0.1595
0.0402	1.0000	0.7900	0.4470	∞	0

3. *Further Applications*

Balcerzok and Rayner [226] used conformal mapping to obtain the steady-state temperature distribution and heat flow in three cases of prismatic bars: (i) n-sided regular polygon with a small circular hole in the center, (ii) variable aspect-ratio rectangle with small circular hole, and (iii) elliptic cross section with confocal elliptic hole. Sholokhov [227] has used the Schwarz–Christoffel transformation for solving temperature field problems for complicated regions bounded by straight lines. Varshavski *et al.* [228] obtained the steady-state heat flow and the temperature distribution in a two-dimensional rectangular configuration with mixed boundary conditions. Siegel [229] has used the same method to determine the shape of a two-dimensional solidified layer formed on a cold surface immersed in a warm flowing liquid. The liquid is assumed to supply heat by convection to the frozen interface and the shape of the frozen layer adjusts itself such that this energy is conducted through the layer to the cold surface. Laura and Chi [230] have described an approximate method based on the complex variable and the collocation method to generate a solution to the unsteady heat conduction equation in a region whose cross section can be conformally mapped on to a circle. Transformation formulas for transforming many nonclassical regions of practical interest on to a unit circle or the upper half-plane are given in [231, 232].

C. WIENER–HOPF METHOD

In many practical problems of heat transfer one is required to solve the unsteady heat conduction equation with mixed boundary conditions. For example, the temperature may be assigned over a part of the boundary, while the rest of the boundary is subjected to a prescribed flux. Application of the Fourier transform or a combination of Laplace and Fourier transforms, taking into account the mixed boundary conditions, would usually lead us to the following mathematical problem.

Find the unknown functions $\phi_+(p)$ and $\psi_-(p)$ satisfying the functional equation

$$A(p)\phi_+(p) + B(p)\psi_-(p) + C(p) = 0, \tag{217}$$

where this equation holds in the strip $\beta_- < \beta < \beta_+$, $-\infty < \alpha < \infty$ of the complex p-plane ($p = \alpha + i\beta$) where the function $\phi_+(p)$ is regular in the half-plane $\beta > \beta_-$ and the function $\psi_-(p)$ is regular in $\beta < \beta_+$. The functions $A(p)$, $B(p)$, and $C(p)$ are given functions of p, regular in the strip $\beta_- < \beta < \beta_+$.

The above problem is solved by what is known as the Wiener-Hopf method [233].

The most important step in the Wiener-Hopf method is to find a function $K_+(p)$, regular and nonzero in $\beta > \beta_-$, and $K_-(p)$, regular and nonzero in $\beta < \beta_+$, such that

$$A(p)/B(p) = K_+(p)/K_-(p). \tag{218}$$

$K_+(p)$, $K_-(p)$ can be determined by inspection or in many cases with the help of certain theorems [233, p. 13]. Substituting for $A(p)$ from Eq. (218) in Eq. (217) we get

$$K_+(p)\phi_+(p) + K_-(p)\psi_-(p) + K_-(p)C(p)/B(p) = 0. \tag{219}$$

If we can put

$$K_-(p)C(p)/B(p) = C_-(p) + C_+(p), \tag{220}$$

we would be able to arrange Eq. (219) to define a new function $J(p)$ such that

$$J(p) = K_+(p)\phi_+(p) + C_+(p) = -K_-(p)\psi_-(p) - C_-(p), \tag{221}$$

where $C_+(p)$ is regular in $\beta > \beta_-$ and $C_-(p)$ is regular in $\beta < \beta_+$. The newly defined function $J(p)$ is valid in the strip $\beta_- < \beta < \beta_+$ and it can be analytically continued throughout the p-plane. Thus $J(p)$ is some polynomial and Eq. (221) gives $\phi_+(p)$ and $\psi_-(p)$.

Let us see how the above problem appears in the context of transient heat conduction in the half-space $-\infty < x < \infty$, $y \geqslant 0$ with mixed boundary conditions at the boundary $y = 0$. The problem is stated as

$$\frac{\partial t}{\partial \tau} = \frac{\partial^2 t}{\partial x^2} + \frac{\partial^2 t}{\partial y^2} \qquad \tau > 0, \qquad -\infty < x < \infty, \qquad y \geqslant 0, \tag{222}$$

with initial condition

$$t(x, y, 0) = 0 \tag{223}$$

and the boundary condition

$$t(x, 0, \tau) = \exp(-x) f(\tau) \qquad x > 0, \tag{224}$$

$$\partial t(x, 0, \tau)/\partial y = 0 \qquad x < 0.$$

This problem has recently been studied by Rutner and Skryabina [234] and the treatment given in the following closely follows this work. Defining the Laplace transform $\bar{t}$ of t with respect to τ as

$$\bar{t}(x, y) = \int_0^\infty t(x, y, \tau) \exp(-s\tau)\, d\tau \qquad \operatorname{Re} s > \sigma_0, \tag{225}$$

and the Fourier transform $U(y)$ of $\bar{t}$ with respect to the variable x

$$U(y) = \frac{1}{\sqrt{2\pi}} \int_{-\infty}^{\infty} \bar{t}(x, y) \exp(ipx)\, dx \qquad -1 < \beta < 1 \tag{226}$$

and applying in succession these transforms to Eq. (222) and taking into account the conditions Eqs. (223) and (224) we get

$$\left(\frac{d^2}{dy^2} - \gamma^2\right) U(y) = 0 \qquad -1 < \beta < 1 \tag{227}$$

and

$$U_+(0) = F(k^2)/\sqrt{2\pi}(1 - ip) \qquad \beta > 1, \quad k^2 = s, \quad k = k_1 + ik_2, \tag{228}$$

$$U'_-(0) = 0 = (dU/dy)\,|_{y=0}, \tag{229}$$

where

$$\gamma^2 = k^2 + p^2 \qquad \text{Re}\,\gamma > 0, \tag{230}$$

$$F(s) = \int_0^\infty f(\tau) \exp(-s\tau)\, d\tau \qquad \text{Re}\, s > \sigma_0, \tag{231}$$

$$U_+(y) = (1/\sqrt{2\pi}) \int_0^\infty \bar{\imath}(x, y) \exp(ipx)\, dx \qquad \beta > -1, \tag{232}$$

$$U_-(y) = (1/\sqrt{2\pi}) \int_{-\infty}^0 \bar{\imath}(x, y) \exp(ipx)\, dx \qquad \beta < 1. \tag{233}$$

Taking into account the fact that the solution remains finite, we have the solution of Eq. (227):

$$U(y) = A(p) \exp(-\gamma y), \tag{234}$$

and thus

$$U_+(0) + U_-(0) = A(p), \tag{235}$$

$$U'_+(0) + U_-'(0) = -\gamma A(p), \tag{236}$$

whence

$$U'_+(0) + U'_-(0) = -\gamma[U_+(0) + U_-(0)]. \tag{237}$$

Substituting in Eq. (237) the values of $U_+(0)$ and $U_-'(0)$ from Eqs. (228) and (229), we obtain the functional equation

$$U'_+(0) + (p^2 + k^2)^{1/2} U_-(0) = (p^2 + k^2)^{1/2} F(k^2)/\sqrt{2\pi}(ip - 1). \tag{238}$$

This equation must be solved for $U_+'(0)$ and $U_-(0)$. Thus we are faced with a problem exactly parallel to that of determining the functions $\phi_+(p)$ and $\psi_-(p)$ from Eq. (217). Equation (238) should be valid in the strip $-m < \beta < m$ of the complex plane p, where $m = \min[1, k]$, $U'_+(0)$ being regular in $\beta > -m$ and $U_-(0)$ in the half-plane $\beta < m$. Since we can write

$$\gamma = (p + ik)^{1/2}(p - ik)^{1/2}, \tag{239}$$

where $(p + ik)^{1/2}$ is regular and has no zeros in $\beta > -k_1$ and $(p - ik)^{1/2}$ is regular and has no zeros in half-plane $\beta < k_1$, we can write Eq. (238) in the form

$$\frac{U'_+(0)}{(p + ik)^{1/2}} + (p - ik)^{1/2}U(0) = \frac{(p - ik)^{1/2}}{(ip - 1)} \frac{F(k^2)}{\sqrt{2\pi}}, \tag{240}$$

where the first member on the left-hand side of Eq. (240) is regular in $\beta > -m$ and the second member is regular in the half-plane $\beta < m$, while on the right-hand side

$$\phi(p) = \frac{(p - ik)^{1/2}F(k^2)}{(ip - 1)\sqrt{2\pi}} \tag{241}$$

is regular in the strip $-m < \beta < m$. The function $\phi(p)$ defined in Eq. (241) can now be easily divided into two parts $\phi_+(p)$ and $\phi_-(p)$ such that $\phi_+(p)$ is regular in $\beta > -m$ and $\phi_-(p)$ is regular in $\beta > m$. This can be achieved by application of the theorem given in Noble [233, p. 13]. Thus

$$\phi_+(p) = \frac{F(k^2)(-i - ik)^{1/2}}{\sqrt{2\pi}(ip - 1)}, \tag{242}$$

$$\phi_-(p) = \frac{(p - ik)^{1/2} - (-i - ik)^{1/2}}{(ip - 1)} \frac{F(k^2)}{\sqrt{2\pi}}. \tag{243}$$

We can thus define $J(p)$ regular in $-m < \beta < m$, which can be analytically continued in the entire p-plane. $J(p)$ is therefore a polynomial. From the condition $U'_+(0) = 0$ as $p \to \infty$, it follows that $J(p) \to 0$ as $p \to \infty$. This can happen only if $J(p) \equiv 0$ and thus we have

$$J(p) = \frac{U'_+(0)}{(p + ik)^{1/2}} - \frac{F(k^2)(-i - ik)^{1/2}}{\sqrt{2\pi}(ip - 1)},$$

$$= -(p - ik)^{1/2}U_-(0) - \frac{F(k^2)[(-i - ik)^{1/2} - (p - ik)^{1/2}]}{\sqrt{2\pi}(ip - 1)}$$

or

$$U'_+(0) = \frac{(-i - ik)^{1/2}F(k^2)(p + ik)^{1/2}}{\sqrt{2\pi}(ip - 1)} \tag{244}$$

and

$$U_-(0) = \frac{[(p - ik)^{1/2} - (-i - ik)^{1/2}]F(k^2)}{\sqrt{2\pi}(ip - 1)(p - ik)^{1/2}}. \tag{245}$$

Applying the inverse Fourier transform to Eq. (244) we get for $x > 0$, and for the special case of $f(\tau) = 1$ in Eq. (224).

$$-\frac{\partial \bar{t}(x,0)}{\partial y} = \frac{1}{\sqrt{\pi x}}\frac{1}{s}\exp(-x\sqrt{s})(1+\sqrt{s})^{-1/2} + \frac{1}{s}(s-1)^{1/2}\exp(-x)$$

$$-\operatorname{erfc}[(\sqrt{s}-1)x]^{1/2}\exp(-x)\frac{(s-1)^{1/2}}{s}. \tag{246}$$

The application of the inverse Laplace transform to Eq. (246) gives

$$-\frac{\partial t(x,0,\tau)}{\partial y} = H(x,\tau), \tag{247}$$

where $H(x, \tau)$ is the inverse Laplace transform of the right-hand side of Eq. (246). Thus the original problem stated in Eqs. (222)–(224) with mixed boundary conditions has been reduced to an ordinary heat conduction problem described by the differential equation (222), the initial condition Eq. (223), and the boundary condition

$$\begin{aligned} \partial t(x,0,\tau)/\partial y &= 0 \qquad && x < 0, \\ &= -H(x,\tau) && x > 0, \end{aligned} \tag{248}$$

and can therefore be solved, for example, by the method of Green's function [10, p. 353].

The Wiener–Hopf method has been used by Horvay [235] for finding the temperature distribution in a slab moving from a chamber at one temperature to another at a different temperature. The corresponding case of a solid circular cylinder has been treated in a similar fashion in [236]. Sih [237] has reduced the problem of the steady temperature distribution in an infinite region with lines of discontinuity (for example cracks) to the solution of the Hilbert problem [176] using complex variables, and has given closed form solutions to a number of problems of practical interest.

VII. Special Methods for the Solution of Partial Differential Equations

A. Method of Characteristics

The method of characteristics in the solution of hyperbolic partial differential equations is well known and has been applied to problems of supersonic flow [238]. Siegel [239] has shown that the unsteady free convection equations of momentum and energy, when placed in integral form (Karman-Polhausen integral method) with a parabolic profile for temperature and a cubic one for velocity, are hyperbolic in nature and he therefore applied the

method of characteristics to their solution. Two boundary conditions were considered for a vertical flat plate of infinite width and semi-infinite length, which is initially at ambient temperature. These conditions were those of step rise in temperature of the plate and that of start of constant heat flux from the plate.

A more interesting and a novel application of the method of characteristics was made by Siegel and his colleagues in a series of papers [240–242]. They have made use of the method of characteristics, as applicable to the linear and quasi-linear partial differential equations of the first order [243, p. 386], for various problems of unsteady forced convection in channels with the assumption of slug flow. The general method followed by them is illustrated below. We are interested in the solution of the unsteady equation

$$\frac{\partial t}{\partial \tau} + \bar{u}\frac{\partial t}{\partial x} = k\frac{\partial^2 t}{\partial y^2} \qquad x > 0, \qquad \tau > 0 \tag{249}$$

of heat flow in the moving fluid with the assumption of slug flow. Equation (249) can be nondimensionalized to the form

$$\frac{\partial T}{\partial \theta} + \frac{\bar{u}}{u_m}\frac{\partial T}{\partial X} = \frac{\partial^2 T}{\partial y^2} \qquad X > 0, \qquad -1 < Y < 1, \qquad \theta > 0, \tag{250}$$

which is to be solved with the nondimensional boundary conditions

$$T = 0 \qquad X = 0 \qquad \text{for all } \theta \text{ and } Y, \tag{251}$$

$$T = 1 \qquad Y = \pm 1 \qquad \text{for all } X \text{ and } \theta, \tag{252}$$

$$\partial T/\partial Y = 0 \qquad Y = 0 \qquad \text{for all } X \text{ and } \theta, \tag{253}$$

where $\bar{u}/u_m$ in Eq. (250) is given as a function $[1 + K(\theta)]$ of the nondimensional time θ from the solution of the transient equation of momentum

$$\frac{\partial u}{\partial \tau} = -\frac{1}{\rho}\frac{dp}{dx} + \nu\frac{\partial^2 u}{\partial y^2}, \tag{254}$$

with the assumption of slug flow ($\bar{u}$ being a function of time only).

The starting point of the solution is the requirement that in the steady state, the solution should reduce to the known steady-state temperature distribution with slug flow in the channel [244]

$$T = 1 - 2\sum_{n=0}^{\infty}\frac{(-1)^n}{E_n}\exp(-E_n^2 X)\cos(E_n Y), \tag{255}$$

where $E_n = (n + \frac{1}{2})\pi$. The solution of Eq. (250) is therefore assumed to be of the form

$$T = 1 - 2\sum_{n=0}^{\infty}\frac{(-1)^n}{E_n}G_n(X, \theta)\cos(E_n Y), \tag{256}$$

such that in the steady state $G_n = \exp(-E_n^2 X)$. When this solution is substituted in the energy equation (250), we get

$$\frac{\partial G_n}{\partial \theta} + (1 + K(\theta)] \frac{\partial G_n}{\partial X} = -E_n^2 G_n. \tag{257}$$

Applying now the method of characteristics we write three auxiliary differential equations which are equivalent to Eq. (257). These equations are

$$d\theta = \frac{dX}{1 + K(\theta)} = \frac{dG_n}{-E_n^2 G_n}. \tag{258}$$

The first two terms in Eq. (258) yield a set of characteristic curves on the X–θ plane. The curves of interest are those starting at $X = 0$ and at an arbitrary value of $\theta = \theta_0$. These characteristics are given by

$$\int_{\theta_0}^{\theta} [1 + K(\theta)] \, d\theta = \int_0^X dX$$

or

$$\theta - \theta_0 - S(\theta, \theta_0) = X, \tag{259}$$

where

$$S(\theta, \theta_0) = -\int_{\theta_0}^{\theta} K(\theta) \, d\theta. \tag{260}$$

Equating the first and third terms in Eq. (258) we get a relation for G_n as function of θ. Integrating we get

$$\theta - \theta_0 = -(1/E_n^2) \log G_n = H. \tag{261}$$

Eliminating θ_0 between Eqs. (259) and (261) we get a relation of the form

$$X = H - S_1(\theta, H), \tag{262}$$

where $S_1(\theta, H) \to 0$ as $X \to H$. Equation (262) is an implicit expression for H. From Eq. (261), G_n are given by

$$G_n = \exp(-E_n^2 H). \tag{263}$$

The final solution is

$$T = 1 - 2 \sum_{n=0}^{\infty} \frac{(-1)^n}{E_n} \exp(-E_n^2 H) \cos(E_n Y). \tag{264}$$

For $H \to X$, that is, for small values of $S_1(\theta, H)$, the solution in Eq. (264) converges to the correct solution (255) in the steady state.

Based on the method of characteristics and network analysis, Siegel [242] has analyzed forced convection in a channel with variable wall heating as a function of axial position and time, taking into account wall heat capacity.

He has applied the method to the problem including uniform wall heating that varies sinusoidally in time, and heating varying sinusoidally with axial distance and exponentially in time. The method of characteristics set out above has been applied by Lindauer and Hsu [245] to analyze the unsteady heat transfer in MHD forced convect in a parallel plate channel, the transient being caused by a step change in axial pressure gradient or magnetic field.

Jischke and Baron [246] have used parametric differentiation in nonlinear problems to introduce a real parameter characteristic along which one can integrate the parametrically differentiated equations. The method has been demonstrated in the case of a one-dimensional hypersonic radiating shock layer and in the solution of inviscid radiating gas flow in the stagnation region of a blunt body.

B. A METHOD OF ANALYTIC ITERATION

The solution of boundary value problems in regions where the entire boundary, or a part thereof, is not parallel to any of the coordinates in the specified coordinate system is not straightforward because of the difficulty in satisfying the given boundary condition on the boundary. The usual method of dealing with such regions is to transform them by a suitable transformation to the upper half-plane or to the inside of a unit circle, the field equations being transformed accordingly. The use of such transformations in some important problems in heat transfer has already been considered in Section VI,B. A method of analytic iteration called the method of Schwarz for the solution of Laplace's equation in such regions has been

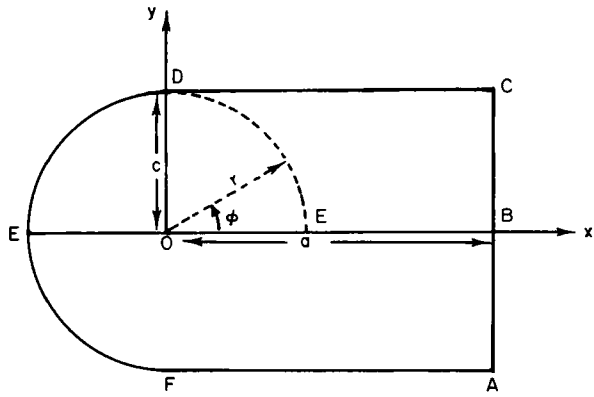

FIG. 2. Region ABCDEFA, a rectangle ended by a semicircle. (Kumar and Achari [247].)

described in detail in [106, p. 616]. The technique consists in first breaking up the region into subregions, where the boundary value problem can be solved, and then iterating the solution in each of the subregions and matching the same, step by step, in the sub-subregion common to the subregions.

Recently, Kumar and Achari [247] have extended the technique to parabolic equations and have proved the convergence of the process by showing that the iteration scheme is exactly similar to the iteration scheme for the solution of a system of integral equations in the "potential of double layers" of Mikhlin [175].

Consider unsteady heat conduction in the region ABCDEFA, Fig. 2, formed by the rectangle ACDF and the semicircle DEF. We are interested in the solution of the equation

$$\nabla^2 t = \frac{1}{k}\frac{\partial t}{\partial \tau} \qquad \tau > 0 \tag{265}$$

in the region ABCDEFA with the initial and boundary conditions

$$t = 0, \qquad \tau = 0, \tag{266}$$

$$t = t_0, \qquad \tau > 0 \text{ along DEF}, \tag{267}$$

$$t = 0, \qquad \tau > 0 \text{ along ABC}, \tag{268}$$

$$\partial t/\partial y = 0, \qquad \tau > 0 \text{ along FA and CD}. \tag{269}$$

Due to symmetry we need only consider the half region BCDEOB with

$$\partial t/\partial y = 0 \quad \text{along BE}. \tag{270}$$

With center 0 we complete the semicircle EDE'. If $t_1(r, \phi, \tau)$ is the temperature distribution in the region EDE'E and $t_2(x, y, \tau)$ is the temperature distribution in the rectangle BCDOB, which we seek to determine, the boundary value problem for the nth approximation $T_{1,n}$ of T_1 which in nondimensional form is described by

$$\frac{\partial^2 T_{1,n}}{\partial R^2} + \frac{1}{R}\frac{\partial T_{1,n}}{\partial R} + \frac{1}{R^2}\frac{\partial^2 T_{1,n}}{\partial \phi^2} = \frac{\partial T_{1,n}}{\partial \theta} \qquad \begin{matrix} \theta > 0 \\ 0 < R < C \\ 0 < \phi < \pi \end{matrix} \tag{271}$$

with initial conditions

$$T_{1,n} = 0 \qquad \theta = 0 \tag{272}$$

and boundary conditions

$$\frac{\partial T_{1,n}}{\partial \phi} = 0 \qquad \phi = 0, \qquad 0 < R < C, \qquad \theta > 0, \tag{273}$$

$$\frac{\partial T_{1,n}}{\partial \phi} = 0 \qquad \phi = \pi, \qquad 0 < R < C, \qquad \theta > 0, \tag{274}$$

$$T_{1,n} = \psi_n(\phi, \theta) \qquad R = C, \quad 0 < \phi < \pi, \quad \theta > 0, \tag{275}$$

where

$$\psi_n(\phi, \theta) = 1 \qquad n = 1 \tag{276}$$

and

$$\psi_n(\phi, \theta) = 1 \qquad \pi/2 < \phi < \pi, \quad n \geqslant 2, \tag{277}$$

$$= T_{2,n-1} \qquad 0 < \phi < \pi/2.$$

The boundary condition Eq. (275), along with Eqs. (276) and (277), express the fact that we assume the temperature along the arc DE′, in continuity with ED for the first approximation and for subsequent approximations $T_{1,n}$ is matched to $T_{2,n-1}$ where $T_{2,n}$ is given by

$$\frac{\partial^2 T_{2,n}}{\partial X^2} + \frac{\partial^2 T_{2,n}}{\partial Y^2} = \frac{\partial T_{2,n}}{\partial \theta} \qquad \theta > 0 \text{ in BCDO} \tag{278}$$

with initial condition

$$T_{2,n} = 0, \qquad \theta = 0 \tag{279}$$

and the boundary conditions

$$\partial T_{2,n}/\partial Y = 0, \qquad Y = 0, \quad 0 < X < 1, \quad \theta > 0, \tag{280}$$

$$\partial T_{2,n}/\partial Y = 0, \qquad Y = C, \quad 0 < X < 1, \quad \theta > 0, \tag{281}$$

$$T_{2,n} = 0, \qquad X = 1, \quad 0 < Y < C, \quad \theta > 0, \tag{282}$$

$$T_{2,n} = T_{1,n}|_{\phi=\pi/2} = f_n(Y, \theta), \qquad X = 0, \quad 0 < Y < C, \quad \theta > 0. \tag{283}$$

The solution $T_{1,n}$ of Eq. (271) with initial and boundary conditions Eqs. (272)–(275) can be written as

$$T_{1,n}(R, \phi, \theta) = \frac{2}{\pi C} \sum_{S_i} \frac{S_i J_0(S_i R)}{J_1(CS_i)} \int_0^\theta \alpha_o{}^n \exp\left[-S_i{}^2(\theta - \lambda)\right] d\lambda$$

$$+ \frac{4}{\pi C} \sum_{m=1}^{\infty} \sum_{S_i} \frac{S_i J_m(S_i R)}{J_{m+1}(S_i C)} \cos m\phi \int_0^\theta \alpha_m{}^n \exp\left[-S_i{}^2(\theta - \lambda)\right] d\lambda, \tag{284}$$

and the solution of Eq. (278), subject to conditions (279)–(283), is

$$T_{2,n}(X, Y, \theta) = \frac{2\pi}{C} \sum_{p=1}^{\infty} p \sin(p\pi X) \int_0^\theta \gamma_0{}^n \exp\left[-\mu_{p0}(\theta - \lambda)\right] d\lambda$$

$$+ \frac{4\pi}{C} \sum_{p=1}^{\infty} \sum_{q=1}^{\infty} p \sin(p\pi X) \cos \frac{q\pi Y}{C} \int_0^\theta \gamma_q{}^n \exp\left[-\mu_{pq}(\theta - \lambda)\right] d\lambda, \tag{285}$$

where J_m denotes the Bessel functions of order m, S_i are the roots of the equation

$$J_0(S_iC) = 0, \tag{286}$$

and

$$\mu_{pq} = \pi^2(p^2 + q^2/C^2). \tag{287}$$

Further,

$$\alpha_m^n(\lambda) = \int_0^\pi \psi_n(\phi, \lambda) \cos m\phi \, d\phi, \tag{288}$$

$$\gamma_q^n(\lambda) = \int_0^C f_n(Y, \lambda) \cos(q\pi Y/C) \, dY, \tag{289}$$

with the following recurrence relations between α_m^n and γ_q^n:

$$\alpha_m^n = \frac{2\pi}{C} \sum_{p=1}^{\infty} pI(m, p, 0) \int_0^\theta \gamma_0^{n-1} \exp[-\mu_{p0}(\theta - \lambda)] \, d\lambda + \frac{4\pi}{C} \sum_{p=1}^{\infty} \sum_{q=1}^{\infty} pI(m, p, q) \int_0^\theta \gamma_q^{n-1} \exp[-\mu_{pq}(\theta - \lambda)] \, d\lambda, \tag{290}$$

$$\gamma_q^n = \frac{2}{\pi C} \sum_{S_i} \frac{S_i}{J_1(CS_i)} \int_0^C J_0(S_iY) \cos \frac{q\pi Y}{C} \, dY + \frac{4}{\pi C} \sum_{m=2,4,6,\ldots,} \sum_{S_i} \frac{S_i \cos(m\pi/2)}{J_{m+1}(CS_i)} \int_0^C J_m(S_iY) \cos\left(\frac{q\pi y}{C}\right) dy \int_0^\theta \alpha_m^n \times \exp[-S_i^2(\theta - \lambda)] \, d\lambda, \tag{291}$$

where

$$I(m, p, q) = \int_0^{\pi/2} \sin(p\pi C \cos\phi) \cos(\pi \sin\phi) \cos(m\phi) \, d\phi. \tag{292}$$

Starting from some assumed value of $\psi_n(\phi, \theta)$ in Eq. (288) we can obtain the successive values of α_m^n and γ_q^n from Eqs. (289)–(291). In this way we can obtain $T_{1,n}$ and $T_{2,n}$ to any order of approximation. It is found however, in practice that the process is very rapidly convergent and even the second approximation is quite good for engineering purposes. To illustrate the convergence of the process, the values of the coefficients α_m^n and γ_q^n calculated up to the fourth order of approximation are tabulated in Table IV for two values of the nondimensional time, namely, $\theta = 0.005$ and $\theta = 0.1$, and for $c/a = 0.25$. It is apparent from Table IV that to find the solution with a given degree of accuracy one has to go to higher approximations for larger values of θ. The fourth order solutions obtained from the above analysis along the lines EB and OD (Fig. 2) are depicted in Figs. 3 and 4, respectively, for various values of θ.

TABLE IV

VALUES OF AND UP TO α_m^n AND γ_q^n UP TO THEIR FOURTH APPROXIMATION FOR $\theta = 0.0005$ AND $\theta = 0.1$

		α_m^n				γ_q^n			
	n	$m = 0$	$m = 1$	$m = 2$	$m = 3$	$q = 0$	$q = 1$	$q = 2$	$q = 3$
$\theta = 0.005$	1	3.1416	0	0	0	− 0.0864	0.0866	− 0.0233	0.0098
	2	1.7726	− 0.8026	0.2130	0.0712	− 0.0856	0.0847	− 0.0212	0.0092
	3	1.7715	− 0.8201	0.2125	0.0708	− 0.0850	0.0814	− 0.0209	0.0092
	4	1.7710	− 0.8200	0.2124	0.0708	− 0.0846	0.0813	− 0.0209	0.0092
$\theta = 0.1$	1	3.1416	0	0	0	0.0448	0.3168	− 0.0792	0.0352
	2	2.0316	0.0192	2.0720	−0.6859	0.0405	0.2988	− 0.0747	0.0321
	3	1.9761	0.0181	1.9802	− 0.6825	0.0397	0.2902	− 0.0715	0.0308
	4	1.9687	0.0178	1.9800	− 0.6811	0.0389	0.2815	− 0.0702	0.0301

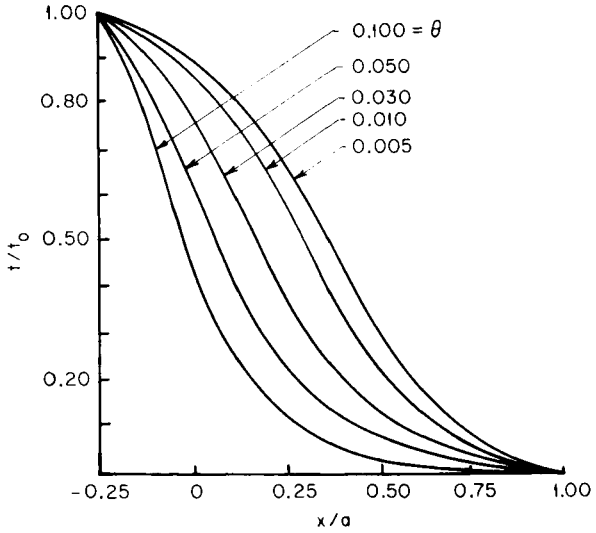

FIG. 3. Fourth-order approximated nondimensional temperature along OD (see Fig. 2) for various nondimensional values of time. (Kumar and Achari [247].)

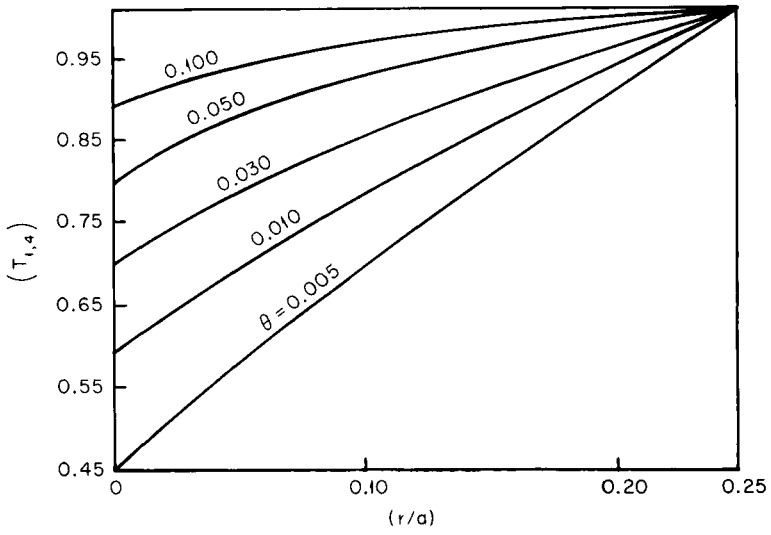

FIG. 4. Fourth-order approximated nondimensional temperature along EB (see Fig. 2) for various nondimensional values of time. (Kumar and Achari [247].)

VIII. Application of Matrices

The methods of matrix algebra are especially suitable for handling the problem of temperature distributions in composite media consisting of several layers of materials with different thermal characteristics. The governing differential equations and the matching conditions at each of the interfaces, namely, the continuity of temperature and flux can be elegantly handled in the form of a matrix differential equation. Matrix methods also offer the possibility of the application of discrete models for difficult engineering problems where it is impossible to get exact solutions, and as such have proved useful in the analysis of heat transfer in irregular domains. Yet another field where matrix methods are directly applicable is the analysis of coupled irreversible phenomena like the simultaneous flow of heat, multicomponent mass, and electricity in the presence of a magnetic field in a continuous system where one has to deal with a system of coupled partial differential equations.

A. An Application to Simultaneous Diffusion of Two Entities

Consider the mutually dependent transfer of two entities, for example, that of heat and mass in a three-dimensional semi-infinite space. Let the diffusion of the two entities U_J, $J = 1, 2$, be governed by the following system of parabolic equations

$$\frac{\partial U_J}{\partial \tau} = \sum_{K=1}^{2} (a_{JK}\nabla^2 U_K + b_{JK}U_K) \qquad J = 1,2$$

$$\nabla^2 = \frac{\partial^2}{\partial x^2} + \frac{\partial^2}{\partial y^2} + \frac{\partial^2}{\partial z^2} \qquad \begin{matrix} 0 \leqslant x < \infty \\ -\infty < y < \infty \\ -\infty < z < \infty, \end{matrix} \tag{293}$$

where U_J satisfy the following initial and boundary conditions

$$U_J(x, y, z, \tau)|_{\tau=0} = f_J(x, y, z), \tag{294}$$

$$(\partial U_J/\partial x)|_{x=0} = \phi_J(y, z, \tau). \tag{295}$$

Following Tsoi [248] we write the above system in the matrix form

$$\partial U/\partial \tau = A\nabla^2 U + BU, \tag{296}$$

with initial and boundary conditions

$$U(x, y, z, \tau)|_{\tau=0} = f(x, y, z), \tag{297}$$

$$(\partial U/\partial x)|_{x=0} = \phi(y, z, \tau), \tag{298}$$

where

$$U = \begin{Vmatrix} U_1 \\ U_2 \end{Vmatrix}, \qquad A = \begin{Vmatrix} a_{11} & a_{12} \\ a_{21} & a_{22} \end{Vmatrix}, \qquad B = \begin{Vmatrix} b_{11} & b_{12} \\ b_{21} & b_{22} \end{Vmatrix},$$

and

$$f = \begin{Vmatrix} f_1 \\ f_2 \end{Vmatrix}, \qquad \phi = \begin{Vmatrix} \phi_1 \\ \phi_2 \end{Vmatrix}.$$

With the help of the substitution

$$U(x, y, z, \tau) = \exp(B\tau)V(x, y, z, \tau), \tag{299}$$

Eqs. (296)–(298) can be written in the form

$$\partial V/\partial\tau = A\nabla^2 V, \tag{300}$$

$$V(x, y, z, \tau)|_{\tau=0} = f(x, y, z), \tag{301}$$

$$(\partial V/\partial x)|_{x=0} = \phi(y, z, \tau)\exp(-B\tau). \tag{302}$$

The solution of differential equation (300), subject to conditions (301) and (302), is well known and can be written in view of Eq. (299) as

$$\begin{aligned} U(x, y, z, \tau) = {} & \frac{1}{[2\sqrt{\pi\tau}]^3}\int_0^\infty\int_{-\infty}^{\infty}\int_{-\infty}^{\infty}\frac{1}{\sqrt{A^3}} \\ & \exp\left[-\frac{(x-\alpha)^2 + (y-\beta)^2 + (z-\gamma)^2}{4A\tau}\right] \\ & \left[1 + \exp\left(-\frac{x\alpha}{A\tau}\right)\right]\exp(B\tau)f(\alpha, \beta, \gamma)\, d\alpha\, d\beta\, d\gamma \\ & - \frac{1}{4\sqrt{\pi^3}}\int_0^\tau\int_{-\infty}^{\infty}\int_{-\infty}^{\infty}\frac{1}{(\tau-\lambda)^3}\frac{1}{\sqrt{A}} \\ & \exp\left[-\frac{x^2 + (y-\beta)^2 + (z-\gamma)^2}{4A(\tau-\lambda)}\right] \\ & \exp[B(\tau-\lambda)]\phi(\beta, \gamma, \tau)\, d\beta\, d\gamma\, d\tau. \end{aligned} \tag{303}$$

To completely determine the solution of our boundary value problem Eqs. (296)–(298), it is necessary to determine the elements of the single column matrices on the right-hand side of Eq. (303). Using the well known properties

of matrices [249], it is easy to show that any arbitrary function $F(A)$ of matrix A can be represented as

$$F(A) = \frac{1}{\nu_1 - \nu_2} \times \left[\begin{Vmatrix} a_{11} - \nu_2 & a_{12} \\ a_{21} & a_{22} - \nu_2 \end{Vmatrix} F(\nu_1) - \begin{Vmatrix} a_{11} - \nu_1 & a_{12} \\ a_{21} & a_{22} - \nu_1 \end{Vmatrix} F(\nu_2) \right] \tag{304}$$

where ν_1 and ν_2 are the real roots of the characteristic determinant

$$\left| A - \nu E \right| = 0 = \begin{vmatrix} a_{11} - \nu & a_{12} \\ a_{21} & a_{22} - \nu \end{vmatrix}. \tag{305}$$

Similarly, $F(B)$ can be represented as

$$F(B) = \frac{1}{\mu_1 - \mu_2} [\|B - \mu_1 E\| F(\mu_2) - \|B - \mu_2 E\| F(\mu_1)], \tag{306}$$

where μ_1 and μ_2 are the roots of $|B - \mu E| = 0$. Taking $F(B) = \exp[B(\tau - \lambda)]$ and calculating the product $F(B)\phi(\beta, \gamma, \lambda)$ we may write

$$\exp[B(\tau - \lambda)]\phi(\beta, \gamma, \lambda) = \exp[B(\tau - \lambda)] \begin{Vmatrix} \phi_1 \\ \phi_2 \end{Vmatrix} = \frac{1}{\mu_1 - \mu_2} \begin{Vmatrix} \phi_1^* \\ \phi_2^* \end{Vmatrix}, \tag{307}$$

where

$$\phi_1^* = \{(b_{11} - \mu_2)\exp[\mu_1(\tau - \lambda)] - (b_{11} - \mu_1)\exp[\mu_2(\tau - \lambda)]\}\phi_1 + \phi_2\{b_{12}\exp[\mu_2(\tau - \lambda)] - b_{12}\exp[\mu_1(\tau - \lambda)]\}, \tag{308}$$

$$\phi_2^* = \{(b_{22} - \mu_2)\exp[\mu_1(\tau - \lambda)] - (b_{22} - \mu_1)\exp[\mu_2(\tau - \lambda)]\}\phi_2 + \phi_1\{b_{21}\exp[\mu_1(\tau - \lambda)] - b_{21}\exp[\mu_2(\tau - \lambda)]\}, \tag{309}$$

and therefore

$$F(A)\frac{1}{\mu_1 - \mu_2} \begin{Vmatrix} \phi_1^* \\ \phi_2^* \end{Vmatrix} = \frac{1}{(\nu_1 - \nu_2)(\mu_1 - \mu_2)} \times \begin{Vmatrix} \sum_{K=1}^{2} \phi_{1K}^*(\beta, \gamma, \lambda) \frac{1}{\sqrt{\nu_K}} \exp\left[- \frac{x^2 + (y - \beta)^2 + (z - \gamma)^2}{4\nu_K(\tau - \lambda)} \right] \\ \sum_{K=1}^{2} \phi_{2K}^*(\beta, \gamma, \lambda) \frac{1}{\sqrt{\nu_K}} \exp\left[- \frac{x^2 + (y - \beta)^2 + (z - \gamma)^2}{4\nu_K(\tau - \lambda)} \right] \end{Vmatrix}, \tag{310}$$

where

$$F(A) = \frac{1}{\sqrt{A}} \exp\left[- \frac{x^2 + (y - \beta)^2 + (z - \gamma)^2}{4A(\tau - \lambda)} \right] \tag{311}$$

and

$$\phi_{11}^* = (a_{11} - v_2)\phi_1^* + a_{12}\phi_2^*, \qquad \phi_{12}^* = -[(a_{11} - v_1)\phi_1^* + a_{12}\phi_2^*],$$
$$\phi_{21}^* = (a_{22} - v_2)\phi_2^* + a_{21}\phi_1^*, \qquad \phi_{22}^* = -[a_{21}\phi_1^* + (a_{22} - v_1)\phi_2^*]. \tag{312}$$

Thus we have determined the elements in the integral matrices in the second term on the right-hand side of Eq. (303). The elements of the matrices in the first term can be similarly determined and we finally get

$$\begin{aligned} U_J(x, y, z, \tau) = {} & \frac{1}{(v_1 - v_2)(\mu_1 - \mu_2)\pi^{3/2}} \\ & \times \sum_{K=1}^{2} \left\{ \frac{1}{(2\sqrt{v_K}\tau)^3} \int_0^\infty \int_{-\infty}^\infty \int_{-\infty}^\infty f_{jk}^*(\alpha, \beta, \gamma) \right. \\ & \times \exp\left[\frac{(x - \alpha)^2 + (y - \beta)^2 + (z - \gamma)^2}{4v_K\tau} \right] \\ & \times \left[1 + \exp\left(\frac{\alpha x}{v_k \tau} \right) \right] d\alpha\, d\beta\, d\gamma \\ & - \frac{1}{4\sqrt{v_K}} \int_0^t \int_{-\infty}^\infty \int_{-\infty}^\infty \frac{\phi_{JK}^*(\beta, \gamma, \tau, \lambda)}{\sqrt{(\tau - \lambda)^3}} \\ & \left. \times \exp\left[- \frac{x^2 + (y - \beta)^2 + (z - \gamma)^2}{4\lambda_K(\tau - \lambda)} \right] d\alpha\, d\beta\, d\gamma \right\} \end{aligned} \tag{313}$$

where

$$f_{11}^* = (a_{11} - v_2)f_1^* + a_{12}f_2^*, \qquad f_{12}^* = -[(a_{11} - v_1)f_1^* + a_{12}f_2^*],$$
$$f_1^* = [(b_{11} - \mu_2)\exp(\mu_1\tau) - (b_{11} - \mu_1)\exp(\mu_2\tau)]f_1 + [b_{12}\exp(\mu_1\tau) - b_{12}\exp(\mu_2\tau)]f_2,$$
$$f_2^* = [b_{21}\exp(\mu_1\tau) - b_{21}\exp(\mu_2\tau)]f_1 + [(b_{22} - \mu_2)\exp(\mu_2\tau) - (b_{22} - \mu_1)\exp(\mu_2\tau)]f_2.$$

B. FURTHER APPLICATIONS

Vodicka [250] and Vanko [251] have applied the matrix method to steady-state temperature distributions in composite slabs. Negi and Singh [252],

while studying a problem in connection with the geophysical phenomenon of gradual settling down of sediments on the ocean floor and the migration of interstitial water upwards due to compaction by gravitational effects, have discussed the problem of the temperature distribution in a stratified infinite slab with convective heat removal. Jarmai [253] and Lorass-Nagy [254] have presented methods based on matrices for the calculation of temperature distributions in arbitrary irregular two-dimensional regions. Gamayunov [255] has used Green's matrices for the solution of a set of parabolic partial differential equations of second order in anisotropic, orthotropic, and isotropic multidimensional space for boundary conditions of various kinds. Hsia and Love [256] have applied matrix methods to the analysis of radiative heat transfer between parallel plates separated by a nonisothermal medium with anisotropic scattering.

IX. Eigenfunction Expansions

A. Eigenvalues of the Heat Conduction Equation

Consider the heat conduction equation

$$L(t) = \partial t/\partial \tau \tag{314}$$

in a volume G with surface Γ satisfying the homogeneous boundary condition

$$\frac{\partial t}{\partial n} + ht = 0 \tag{315}$$

on the surface Γ of the body, and the initial condition

$$t(x, y, z, 0) = \phi(x, y, z). \tag{316}$$

In Eq. (314) L is a linear second-order operator. Writing

$$t = v(x, y, z)g(\tau) \tag{317}$$

in Eq. (314) we get

$$L(v)/v = g'/g = -\lambda'. \tag{318}$$

The solution of Eq. (314) thus reduces to the eigenvalue problem for v.

$$L(v) + \lambda' v = 0 \quad \text{in} \quad G \tag{319}$$

and

$$\frac{\partial v}{\partial n} + hv = 0 \quad \text{on} \quad \Gamma. \tag{320}$$

The solution of the differential equation (314) has the form

$$t = av \exp(-\lambda'\tau) \tag{321}$$

for a given eigenvalue λ and its eigenfunction v. Using the eigenfunction expansion theorem [174, p. 312] the function $\phi(x, y, z)$ in Eq. (316), which is continuous in G, together with its derivatives of first and second order can be expanded in terms of the eigenfunctions v_n and the eigenvalues λ_n. The solution of Eq. (314) is given as

$$t(x, y, z, \tau) = \sum_{n=1}^{\infty} C_n v_n(x, y, z) \exp(-\lambda_n'\tau), \tag{322}$$

where

$$C_n = \iiint_G \phi v_n \, dx \, dy \, dz$$

and the eigenfunctions $v_1, v_2, \ldots$ and the associated eigenvalues form a complete set. The above fundamental result has been used extensively in the literature for obtaining solutions to very general and complicated problems of heat conduction.

In a series of papers Ölcer [257–261] has exploited the method of eigenfunction expansion to tackle general problems of heat conduction in a plane as well as in cylindrical and spherical geometries, with generalized boundary and initial conditions in the presence of space- and time-dependent heat sources. Charpakov [262] has described a method of eigenfunctions based on what the author calls the "Regular Regime" theory. In heat conduction this terminology means the possibility of writing the solution of the heat conduction equation in terms of products of eigenfunctions and exponentials containing the corresponding eigenvalues. In another paper [263] Charpakov has applied the method to unsteady heat and mass transfer and has given estimates of the time for the system to achieve regularization with a given percentage of error with respect to the first eigenvalue.

B. Application to Perturbation Solutions of Momentum and Energy Equations

In order to study the velocity fields which may be described by the perturbation of the Blasius solution, Fox and Libby [264] have introduced an approximate method based on linearization about the Blasius solution. A corresponding study of the energy equation for flows with velocity described by the Blasius solution, but with nonunity Prandtl number and a variable product $\rho\mu$, has been discussed in Fox and Libby [265]. Libby [266] has given a more accurate procedure for determining the eigenvalues in the

above problems. Kotorynski [267] has provided an analytical approximation, uniformly valid over the infinite range of the similarity variable, to evaluate the complete set of orthogonal functions satisfying an irregular Sturm–Liouville system arising in the investigations of Fox and Libby [264–265].

The energy and momentum equations of the laminar boundary layer in a uniform external stream, of Prandtl number σ, are considered in the form

$$(Cf_{\eta\eta})_\eta - ff_{\eta\eta} - 2\xi(f_\eta f_{\eta\xi} - f_\xi f_{\eta\eta}) = 0, \tag{324}$$

$$(Cg_\eta)_\eta + \sigma f g_\eta + 2m(\sigma - 1)(Cff_{\eta\eta})_\eta - 2\sigma\xi(f_\eta g_\xi - f_\xi g_\eta) = 0, \tag{325}$$

where η and ξ are defined in Eqs. (29) and (30) and the subscripts denote differentiation. If $f_0(\eta)$ is the solution of Blasius, it is given by the differential equation

$$f_0''' + f_0 f_0'' = 0, \tag{326}$$

with boundary conditions

$$f_0(0) = f_0'(0) = 0 \qquad f_0'(\infty) = 1. \tag{327}$$

The solutions of Eqs. (324) and (325) are attempted in the form

$$f(\xi, \eta) = f_0(\eta) + \sum_i f_i(\xi, \eta), \qquad g(\xi, \eta) = g_0(\xi, \eta) + \sum_i g_i(\xi, \eta), \tag{328}$$

where C and σ have been taken to be unity. The linearization procedure consists of substituting $f(\xi, \eta)$ and $g(\xi, \eta)$ from Eq. (328) into Eqs. (324) and (325) and neglecting the products of g_i and f_i and their derivatives. The equations for determining f_i and g_i (after dropping the subscripts) are then given by

$$f_{\eta\eta\eta} + f_0 f_{\eta\eta} + f_0'' f - 2\xi(f_0' f_{\xi\eta} - f_0'' f_\xi) = F_i(\xi, \eta), \tag{329}$$

$$g_{\eta\eta} + f_0 g_\eta - 2\xi f_0' g_\xi = G_i(\xi, \eta), \tag{330}$$

where the right-hand sides of these equations are known in terms of earlier known functions f_i and g_i. Assuming that the solutions of the homogeneous equations associated with Eqs. (329) and (330) are given by

$$f = \sum_0^\infty A_n \xi^{-\lambda_n/2} N_n(\eta), \qquad g = \sum_0^\infty B_n \xi^{-\mu_n/2} H_n(\eta), \tag{331}$$

N_n are solutions of the Sturm–Liouville system

$$N''' + f_0 N'' + \lambda f_0' N' + (1 - \lambda) f_0'' N = 0 \tag{332}$$

with conditions

$$N(0) = 0, \qquad N'(0) = 0, \qquad N'(\infty) = 0, \tag{333}$$

and H_n are the solutions of

$$H'' + f_0 H' + \mu f_0' H = 0 \tag{334}$$

with conditions

$$H(0) = 0, \qquad H(\infty) = 0, \tag{335}$$

where the functions N_n and H_n have been shown to form complete orthogonal sets [267] with respect to functions having exponential decay at infinity and the eigenvalues λ_n and μ_n are real and positive. To obtain an analytic estimate of these values, Kotorynski [267] has shown that Eq. (332) can be transformed to the form

$$\frac{d^2w_1}{dt^2} + [\bar{\lambda} - q(t)]w_1 = 0, \tag{336}$$

where

$$q = \frac{3}{4}\frac{f_0 f_0''}{f_0'^2} + \frac{7}{16}\frac{f_0''^2}{f_0'^3} + \frac{1}{4}\frac{f_0^2}{f_0'}, \tag{337}$$

and

$$\bar{\lambda} = \lambda - \tfrac{1}{2},$$

$$t = \int_0^{\eta} f_0'^{1/2}(\xi)\, d\xi. \tag{338}$$

From the known solutions of the Blasius equation for $\eta \to 0$ and $\eta \to \infty$ it can be deduced that $q \sim t^2/4$ for $t \to \infty$ and $q \sim (7/36t^2)$ as $t \to 0$. Thus, instead of Eq. (336), the equation

$$\frac{d^2w_1}{dt} + \left[\bar{\lambda} - \frac{t^2}{4} - \frac{7}{36t^2}\right]w_1 = 0 \tag{339}$$

has been analyzed, where $q(t)$ has been replaced by an expression which uniformly approximates $q(t)$ in the range zero to infinity. The solution of the above equation can be obtained in terms of Laguerre polynomials. Thus

$$w_{1,n} = \exp(-\tfrac{1}{4}t^2)t^{2(\alpha+1/4)}L_n^{(2\alpha)}(t^2) \tag{340}$$

for

$$\lambda_n = 2(n+1) + \tfrac{1}{6} \qquad n = 0, 1, 2, \ldots . \tag{341}$$

α is chosen such that $w_{1,n}$ has the correct asymptotic behavior for $\eta \to \infty$ and also for $\eta \to 0$. Now $\alpha = \frac{1}{3}$ provides the proper choice. Thus the solution given in Eq. (340) provides the analytic approximations to the eigenvalues of Eq. (336).

The eigenvalues of the problem presented by the energy equation can similarly be reduced to the form

$$\frac{d^2w_2}{dt^2} + \left[\bar{\mu} - \frac{t^2}{4} + \frac{5}{36t^2}\right]w_2 = 0, \tag{342}$$

and its solution is given in the form

$$w_{2,n} = \exp(-t^2/4)t^{2(\gamma+1/4)}L_n^{(2\gamma)}(t^2) \tag{343}$$

for the eigenvalue

$$\mu_n = 2(n+1) - \tfrac{1}{6} \qquad n = 0, 1, 2, \ldots , \tag{344}$$

and for the correct asymptotic behavior of $w_{2,n}$, $\gamma = \frac{1}{6}$. A comparison of the approximate eigenvalues λ_n of the momentum equation obtained above and the computed values has been made in [267] and good agreement between the two sets of values has been found.

C. FURTHER APPLICATIONS

As in the case of heat conduction, the problem of forced convection heat transfer under homogeneous boundary conditions can also be reduced to an eigenvalue problem. Thus Dennis *et al.* [268] have used the method of eigenfunction expansion for the forced steadystate heat convection in laminar flow through rectangular ducts with a Newton type convection boundary condition at the surface. Schenk and Han [269] have obtained the solution of laminar heat flow in ducts with elliptic cross section in the form of a double series of eigenfunctions. The method has also been extensively used in the problems of liquid-metal forced convection heat transfer. This subject has recently been revived by Stein [270] who has unified the various investigations on the subject through the mathematical technique of eigenfunction expansions.

Case [271] has given a method involving the construction of a complete set of eigenfunctions of the homogeneous transport equation in which any other solution can be expanded. Sources and boundary conditions are used to determine the coefficients. Based on Case's method [271], Simmons and Fersiger [272] constructed a complete set of eigenfunctions of the homogeneous radiative transfer equation for nongrey radiative heat transfer between parallel plates.

X. Miscellaneous Methods

A. ROSENWEIG'S MATCHING TECHNIQUE

In the solution of many problems of heat transfer one is faced with the problem of obtaining an approximate solution valid for all times, knowing the asymptotic solutions for small and large values of time. Rosenweig [273] has described one such technique. The technique essentially consists in assuming the form for the Laplace transform of the solution valid for all values of time with a certain number of unknown constants. The above form is guessed from the known asymptotic solutions of the problem for large and small values of time, and the number of unknown constants in it is governed by the total number of terms known in the asymptotic solutions.

The unknown constants are determined by matching an appropriate number of terms in the expansion of the assumed expression with the Laplace transform of the corresponding known terms in the asymptotic solutions. The technique has been used by Cess [274] in obtaining the transient temperature distribution in the semi-infinite mass of a moving incompressible fluid and the heat flux at its surface of contact with the solid at $y = 0$. We propose to follow this work in the following to explain Rosenweig's technique.

The energy equation for the fluid in terms of the nondimensional temperature $T = (t - t_\infty)/(t_w - t_\infty)$ is given by

$$\frac{\partial T}{\partial \tau} + u\frac{\partial T}{\partial x} + v\frac{\partial T}{\partial y} = k\frac{\partial^2 T}{\partial y^2}, \tag{345}$$

with the initial condition

$$T = 0, \qquad \tau = 0, \tag{346}$$

and the boundary conditions

$$T = 0, \qquad x = 0, \qquad y > 0, \qquad \tau > 0, \tag{347}$$

$$T = 1, \qquad y = 0, \qquad x > 0, \qquad \tau > 0, \tag{348}$$

$$T = 0, \qquad y \to \infty, \qquad x > 0, \qquad \tau > 0, \tag{349}$$

where u and v are the velocity components in Eq. (345) and are given as

$$u = U_\infty f', \tag{350}$$

$$v = \tfrac{1}{2}(vU_\infty/x)^{1/2}(\eta f' - f), \tag{351}$$

where $f(\eta)$ is the dimensionless Blasius stream function and $\eta = y\sqrt{U_\infty/vx}$. In terms of the new variables $\bar{\tau} = U_\infty \tau/x$ and $\bar{y} = y/\sqrt{v\tau}$, the energy equation (345) can be put in the form

$$(\bar{\tau} - f'\bar{\tau}^2)\frac{\partial T}{\partial \bar{\tau}} + \tfrac{1}{2}(f'\bar{y}\bar{\tau} - f\bar{\tau}^{1/2} - \bar{y})\frac{\partial T}{\partial \bar{y}} = \frac{1}{\sigma}\frac{\partial^2 T}{\partial \bar{y}^2}, \tag{352}$$

where

$$f(\eta) = (\beta/2)(\bar{y}\bar{\tau}^{1/2})^2 - \tfrac{1}{2}(\beta^2/5!)(\bar{y}\bar{\tau}^{1/2})^5 + \cdots \tag{353}$$

and $\beta = 0.3321$. A series solution of Eq. (352) is given in terms of powers of $\bar{\tau}$ in the form

$$T = \operatorname{erfc}\left(\frac{\sqrt{\sigma}\,\bar{y}}{2}\right) + \frac{\bar{\tau}^{3/2}\beta}{2\sqrt{\sigma}} \times \left[\frac{1}{6\sqrt{\pi}}(1 + \sigma\bar{y}^2)\exp\left(-\frac{\sigma\bar{y}^2}{4}\right) - i^3 \operatorname{erfc}\frac{\sqrt{\sigma}\,\bar{y}}{2}\right] + \cdots, \tag{354}$$

from which we can write

$$-(\partial T/\partial \eta)_{\eta=0} = (\sigma/\pi)^{1/2}\bar{\tau}^{1/2} - (\beta/16)\bar{\tau} + \cdots \tag{355}$$

since $\eta = \bar{y}\sqrt{\bar{\tau}}$ and $\partial T/\partial \eta = \tau^{-1/2}(\partial T/\partial \bar{y})$. For large values of time we use the independent variables $\bar{\tau}$ and η and the equation (345) is transformed to

$$\frac{\partial T}{\partial \bar{\tau}} - f'\bar{\tau}\frac{\partial T}{\partial \bar{\tau}} - \frac{1}{2}f\frac{\partial T}{\partial \eta} = \frac{1}{\sigma}\frac{\partial^2 T}{\partial \eta^2}. \tag{356}$$

Defining a new dependent variable

$$\phi(s, \eta) = s\int_0^\infty T(\bar{\tau}, \eta)\exp(-s\bar{\tau})\, d\bar{\tau} \tag{357}$$

where $\phi(s)/s$ represents the Laplace transform of T, it can be shown that Eq. (356) can be rewritten in terms of ϕ as

$$s\phi + sf'\frac{\partial \phi}{\partial s} - \tfrac{1}{2}f\frac{\partial \phi}{\partial \eta} = \frac{1}{\sigma}\frac{\partial^2 \phi}{\partial \eta^2} \tag{358}$$

which has the solution of the form

$$(\partial \phi/\partial \eta)_{\eta=0} = -\phi_0'(0) - \phi_1'(0)s - \phi_2'(0)s^2 + \cdots, \tag{359}$$

where the functions $\phi_0'(0)$, $\phi_1'(0)$, and $\phi_2'(0)$ have been tabulated in Cess [274]. Also, the solution for small $\bar{\tau}$ in Eq. (355) is transformed in terms of ϕ as

$$-(\partial \phi/\partial \eta)_{\eta=0} = \sigma^{1/2}s^{1/2} - (\beta/16)s^{-1} + \cdots. \tag{360}$$

Equations (359) and (360) represent the flux at $\eta = 0$ for large and small $\bar{\tau}$, respectively. To obtain an expression for $(\partial \phi/\partial \eta)_{\eta=0}$ uniformly valid for all $\bar{\tau}$ it is assumed, following Rosenweig [273], that

$$-\left(\frac{\partial \phi}{\partial \eta}\right)_{\eta=0} = a_1\frac{s + a_2}{(s + a_3)^{1/2}} + \frac{a_4 s}{(s + a_5)^2} \tag{361}$$

for all $\bar{\tau}$. The above expression may be written

$$-\left(\frac{\partial \phi}{\partial \eta}\right)_{\eta=0} = \frac{a_1 a_2}{a_3^{1/2}} + \left(\frac{a_1}{a_3^{1/2}} - \frac{a_1 a_2}{2a_3^{3/2}} + \frac{a^4}{a_5^2}\right)s \tag{362}$$

for small s, and for large s it can be represented as

$$-(\partial \phi/\partial \eta)_{\eta=0} = a_1 s^{1/2} + a_1(a_2 - \tfrac{1}{2}a_3)s^{-1/2} + a_4 s^{-1}. \tag{363}$$

The five unknown constants on the right-hand side of Eq. (361) are so evaluated that the first two terms in Eq. (362) agree with Eq. (359) and the first three terms in Eq. (363) agree with Eq. (360). Thus we get

$$a_1 = \sigma^{1/2}, \qquad a_2 = (2/\sigma)[\phi_0'(0)]^2,$$
$$a_3 = (4/\sigma)[\phi_0'(0)]^2, \qquad a_4 = -\beta/16,$$
$$a_5 = \left(\frac{\beta\phi_0'(0)}{16\phi_0'(0)\phi_1'(0) - 6\sigma}\right)^{1/2}.$$

It can be seen from Fig. 5, depicting both the asymptotic solutions in the Laplace transform coordinate and the corresponding uniformly valid solution obtained by the above technique, that the approximate solution

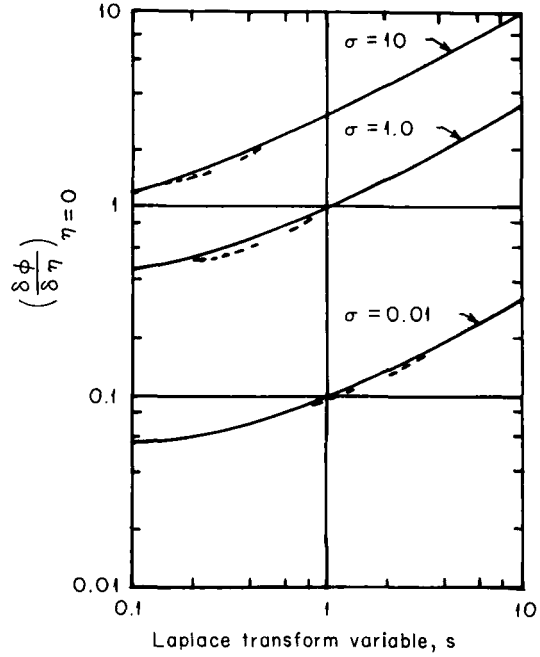

FIG. 5. Comparison of the limiting solutions of the Laplace transformed variable, for the temperature derivative at the surface, with the corresponding uniformly valid solution obtained by Rosenweig's matching technique. (Reproduced from Cess [274].) ——— Approximate solution; - - - - limiting solution.

correctly joins the limiting solutions and therefore provides a very useful approximation of the solution for those values of time for which it cannot be otherwise easily determined. The approximate solution for the heat flux at the surface valid for all values of time is

$$-(\partial T/\partial\eta)_{\eta=0} = 0.5642\sqrt{\sigma}/\bar{\tau}\exp(-a_3\bar{\tau}) - 0.02076\exp(-a_5\bar{\tau}) - \phi_1'(0)\operatorname{erf}(\sqrt{a_3}\bar{\tau}). \qquad (364)$$

It is noted that Cess and Sparrow [104] have used the same technique for obtaining the temperature–time history of a rotating disk subject to a step change in temperature.

B. DORFMAN'S METHOD FOR NONSIMILAR BOUNDARY LAYERS

An approximate analytical method for obtaining solutions to nonsimilar velocity and thermal boundary layers has been described by Dorfman [275, 276]. Dorfman's method consists of linearizing the momentum equation with the assumption of a one-parameter profile for the velocity distribution in the boundary layer, the unknown parameter in the profile being determined by the method of moments or the method of least squares. Let us consider the momentum and energy equations in the Von-Mises form [275]:

$$\frac{\partial Z}{\partial \phi} = \frac{u}{U}\frac{\partial^2 Z}{\partial \psi^2}, \tag{365}$$

$$\frac{\partial T}{\partial \phi} = \frac{1}{\sigma}\frac{\partial}{\partial \psi}\left(\frac{u}{U}\frac{\partial T}{\partial \psi}\right), \tag{366}$$

where

$$\phi = \int_0^x U\,dx, \qquad \psi = \int_0^y u\,dy, \qquad Z = U^2 - u^2, \qquad T = t - 1, \tag{366a}$$

with the boundary conditions

$$\phi = 0, \qquad Z = Z_0(\psi), \qquad T = T_0(\psi) \tag{367}$$

$$\phi > 0, \qquad \psi = 0, \qquad u = U^2(\phi), \qquad T = T_w(\phi), \tag{368}$$

$$\psi = \infty, \qquad u = T = 0. \tag{369}$$

To simplify the system, let us assume that the velocity profile is given as

$$u/U = \alpha(\psi, \beta), \tag{370}$$

where β is an unknown parameter. If we substitute the approximate form of the velocity distribution from Eq. (370) in Eqs. (365) and (366), the system stands simplified as the first of these equations now becomes linear. Thus we get

$$\frac{\partial Z}{\partial \phi} = \alpha(\psi, \beta)\frac{\partial^2 Z}{\partial \psi^2}, \tag{371}$$

$$\frac{\partial T}{\partial \phi} = \frac{1}{\sigma}\frac{\partial}{\partial \psi}\left[\alpha(\psi, \beta)\frac{\partial T}{\partial \psi}\right]. \tag{372}$$

The solutions of Eqs. (371) and (372) with boundary conditions (367)–(369) could be obtained in terms of a special function, and these solutions will be in terms of an unknown parameter which β can be determined from the condition

$$\int_0^\infty \left[\frac{\partial Z}{\partial \phi} - \frac{u}{U}\frac{\partial^2 Z}{\partial \psi^2}\right] d\psi = 0, \tag{373}$$

or

$$\int_0^\infty \left[\frac{u}{U} - \alpha(\psi, \beta)\right]\frac{\partial^2 Z}{\partial \psi^2}\, d\psi = 0. \tag{374}$$

Dorfman has further remarked [277] that $\alpha(\psi, \beta)$ contains ψ in powers of $\psi^{1/2}$. Also in contrast to the Polhausen profile the limits of the integral in Eqs. (373) and (374) vary from 0 to ∞. Therefore he suggests that α can assume, with some advantage, the form

$$\alpha = 1 - \exp(-\beta\psi^{1/2}), \tag{375}$$

or for still greater accuracy

$$\alpha = \sum^{n} C_n \eta^k; \qquad \eta = 1 - \exp(-\psi^{1/2}). \tag{376}$$

Dorfman [275, 276] has applied the above method to various problems in nonsimilar boundary layers. His solutions show remarkable coincidence with earlier known numerical and exact results.

C. SURKOV'S METHOD FOR PROBLEMS INVOLVING CHANGE OF PHASE

It is well known that problems involving changes of phase are nonlinear by nature [10, p. 284] and require special methods for their solution. The essential difficulty in such problems arises because of the motion of the melting front whose position is also to be determined along with the temperature distributions in the melted and unmelted parts of the original solid. Surkov [277] and Krylovich and Surkov [278] have presented a general method based on the finite Fourier transform or Hankel transform (depending upon the geometry of the region under consideration) and the breaking up of the time interval into various subintervals for obtaining approximate solutions to the above type of problems. We propose to illustrate the method by considering the melting of an infinite hollow cylindrical tube $R_1 < r < R_2$ with prescribed time-dependent temperature at the outer surface and with prescribed time-dependent flux at the inner surface. The problem of the temperature distribution in the tube in the initial heating period before the onset of melting can be described as

$$\frac{\partial t}{\partial \tau} = k\left(\frac{\partial^2 t}{\partial r^2} + \frac{1}{r}\frac{\partial t}{\partial r}\right) \qquad \tau > 0, \qquad R_1 < r < R_2, \tag{377}$$

$$t(r, \tau) = 0 \qquad \tau = 0, \tag{378}$$

$$[\partial t(r, \tau)/\partial r]_{r=R_1} = -q_1(\tau)/\mathrm{K}, \tag{379}$$

$$t(r, \tau)_{r=R_2} = \phi(\tau). \tag{380}$$

The solution of the problem stated by Eqs. (377)–(380) can easily be obtained by application of the finite Hankel transform [279, p. 82]. Thus

$$\begin{aligned} r, \tau) &= \frac{\pi^2}{2R_1^2} \sum_{n=1}^{\infty} \mu_n^2 J_0^2(k\mu_n) \exp\left[-\frac{k\mu_n^2\tau}{R_1^2}\right] W_0\left(\mu_n \frac{r}{R_1}\right) \int_0^{\tau} \left[\frac{kR_1 q_1(\tau)}{K\mu_n}\right. \\ &\quad \left. + \frac{k\mu_n R_2}{R_1}\phi(\tau) W_0'\left(\mu_n \frac{R_2}{R_1}\right)\right] \exp\left[\frac{k\mu_n^2\tau}{R_1^2}\right] d\tau \\ &= f(r, \tau), \end{aligned} \tag{381}$$

where μ_n are the roots of the transcendental equation

$$W_0(k'\mu_n) = Y_1(\mu_n)J_0(k'\mu_n) - J_1(\mu_n)Y_0(k'\mu_n) = 0 \quad k' = R_2/R_1, \tag{382}$$

and

$$W_0'[\mu_n(R_2/R_1)] = (d/dr)\{W_0[\mu_n(r/R_1)]\}_{r=R_2}. \tag{383}$$

From Eq. (381) we can determine the time τ_0 when the melting starts at the inner surface. This would happen when the temperature at the inner boundary rises to the melting temperature t_m. Thus τ_0 is to be determined from the relation

$$t(r,\tau_0)_{r=R_1} = t_m. \tag{384}$$

From this moment onward the inner boundary at $r = R_1$ starts receding and the boundary conditions at the moving front become

$$K\frac{\partial t}{\partial r} = -\frac{Q(\tau)}{2\pi r} + \rho l \frac{dS}{d\tau} \tag{385}$$

$$t = t_m, \tag{386}$$

where $S(\tau)$ is to be determined from the solution. Let τ_m be the time required to completely melt the tube. Thus $S(\tau)$ is to be determined for the time interval $\tau_0 < \tau < \tau_0 + \tau_m$. It has been suggested by Surkov [277] and Surkov and Krylovich [278] that the time interval τ_m be divided into n equal parts at points $\tau_1, \tau_2, \ldots, \tau_n$, such that $\tau_n = \tau_m$ and $\Delta\tau_i = \tau_{i+1} - \tau_i$. Thus the position of the melting front at time τ_i is assumed to be at the point 0_i along the r direction. It is assumed that 0_i moves in jumps at the end of the intervals and remains stationary during $\tau_i < \tau < \tau_{i+1}$. Thus Surkov's scheme provides an approximation consisting of a discontinuous curve in the graph

for $S(\tau)$ against the time τ. The heat flow problem for t_i in the interval of time $\Delta\tau_i$ is governed by Eq. (377), the initial condition $t_i = f_i(r, \tau_i)$ with the boundary condition Eq. (380) satisfied at $r = R_2$ and the boundary condition Eq. (384) being satisfied at $r = r_i$. The solution of the above boundary value problem for t_i is given as

$$t_i(r, \tau) = \frac{\pi^2}{2r_i^2} \sum_{\delta_{n_i}} \frac{\delta_{n_i}^2 J_0^2(k_i\delta_{n_i}) V_0(\delta_{n_i} r/r_i)}{J_0^2(\delta_{n_i}) - J_0^2(k_i\delta_{n_i})}$$
$$\times \left\{ k \exp\left[- \frac{k\delta_{n_i}^2 \tau}{r_i^2} \right] \int_{\tau_i}^{\tau} \left[\frac{\delta_{n_i} R_2 \phi(\tau)}{r_i} V_0'\left(\delta_{n_i} \frac{R_2}{r_i} \right) + t_m \right] \right.$$
$$\times \exp\left[\frac{k\delta_{n_i}^2 \tau}{r_i^2} \right] d\tau + \exp\left[- \frac{k\delta_{n_i}^2}{r_i^2} (\tau - \tau_i) \right]$$
$$\left. \times \int_{r_i}^{R_2} r f_i(r, \tau_i) V_0\left(\delta_{n_i} \frac{r}{r_i} \right) dr \right\} \qquad r \geq r_i, \tag{387}$$

where δ_{n_i} are the roots of the equation

$$V_0(k_i\delta_{n_i}) = Y_0(\delta_{n_i}) J_0\left(\delta_{n_i} \frac{r}{r_i} \right) - J_0(\delta_{n_i}) Y_0\left(\delta_{n_i} \frac{r}{r_i} \right) = 0 \qquad k_i = R_2/r_i. \tag{388}$$

Noting that $f_i(r, \tau_i) = t_{i-1}(r, \tau_i)$ we can use Eq. (387) to express t_{i-1} in terms of t_{i-2} which itself can be expressed in terms of t_{i-3}, and so on. Using Eq. (385) we can determine the unknown values $r_i = S(\tau_i)$ and thus the position of the moving front at any time. For $\tau_i < \tau < \tau_{i+1}$ we can write Eq. (385) in the form

$$\frac{dS}{d\tau} = \frac{Q(\tau)}{2\pi S_i \rho l} + \frac{K}{\rho l} \frac{\partial t_i}{\partial r}. \tag{389}$$

The right-hand side of Eq. (389) is a known function of τ which could be written in the form

$$\begin{aligned} S(\tau_i) - S(\tau_0) &= \sum_{i=0}^{p-1} [S(\tau_{i+1}) - S(\tau_i)], \\ &= \sum_{i=0}^{p-1} \int_{\tau_i}^{\tau_{i+1}} \left(\frac{Q(\tau)}{2\pi S_i \rho l} + \frac{K}{l\rho} \frac{\partial t_i}{\partial r} \right) d\tau \end{aligned} \tag{390}$$

for $i = 0, 1, 2, \ldots, p \leqslant n$, and knowing $S(\tau_i)$ we obtain $t_i(r, \tau_i)$ from Eq. (387).

A similar technique has been used by Jaworski [279] to obtain the solution to the heat conduction problem with an arbitrary time-dependent flux boundary condition. The methods developed in [277, 278, 279] provide an analytic alternative to the elaborate difference schemes used until now for the solution of such problems.

D. DUHAMEL'S PRINCIPLE

A method intimately connected with the Laplace transform, namely, Duhamel's Principle [10, p. 30], has proved to be most useful in breaking up the very general and complicated boundary value problems with time-dependent boundary conditions and space- and time-dependent sources into simpler steady-state and unsteady heat conduction problems with time-independent boundary conditions [280]. The above method has been applied [281–283] to the solution of heat flow problems in cylindrical regions with sinusoidal and other types of time-dependent boundary conditions.

Very recently, Matsumoto [284] has formulated Duhamel's principle for the stationary internal radiation field in a nonhomogeneous atmosphere of finite or semi-infinite optical thickness. Through this principle, the non-classical radiation field due to arbitrary incident radiation is expressed as an integral of the radiation field due to incident radiation in a specified direction. Duhamel's principle in the nonstationary radiation field has been developed in [285].

XI. Conclusion

In the foregoing we have reviewed some of the most important analytical methods used in the recent heat transfer literature. It emerges that the most powerful methods are the perturbation methods. Regular perturbation methods can be used in almost all branches of heat transfer involving non-linear equations. Boundary layer heat transfer problems and problems involving the interaction of radiation with other modes of heat transfer usually lead to problems of singular perturbations. It is hoped that further work in the basic theory of singular perturbations will establish the regions of validity for various methods of obtaining uniformly valid solutions, and will probably lead to a unified theory for these methods. The recently developed Lighthill–Volterra approach has been used in many problems of fluid flow and, with further work on the techniques of obtaining analytical solutions to the singular integral equations of the volterra type, this method may find many further applications. Although variational methods have until now been mostly used in heat conduction and diffusive mass transfer, they have a great potential for application, especially in their extended form, to problems involving fluid flow with variable properties and chemical reactions, as well as to problems involving many simultaneously coupled irreversible processes.

In the opinion of the author there is now a definite trend to use more and more analytical methods, which were hitherto used exclusively in other branches of applied mathematics, in various types of problems of heat transfer. The recent use of analytical function theory, the method of characteristics, and the WKBJ method applied to problems in heat transfer illustrated in the present review indicate a trend in this direction.

NOMENCLATURE

Perturbation Methods—Section II

ϵ	small parameter
$v(x, \epsilon)$	solution of some singular perturbation problem with an independent variable and ϵ as a small parameter
x, y, z	Cartesian coordinates
χ	new independent variable Eq. (2)
$v_n(x, \epsilon)$	nth-order perturbation solution
$s(a_1, \mu, \nu, \theta)$	nondimensional distance describing the position of the melting front
$w(a_1, \mu, \nu, \theta)$	nondimensional temperature in the melted region
$v(a_1, \mu, \nu, \theta)$	nondimensional temperature in the solid region
μ	nondimensional parameter inversely proportional to the latent heat of the solid
θ	nondimensional time
a_1	nondimensional parameter with natural restriction $0 < a_1 < 1$
ν	ratio of diffusivities of the melted and solid regions
ζ	stretched independent variable representing nondimensional time
γ	a number between zero and one
v_0	outer solution
$Z = x/\epsilon$	stretched inner variable
v^i	inner solution
δ	a number between γ and one
v^c	composite solution

Boundary Layer Flow—Section III

η	nondimensional coordinate normal to the body Eq. (29)
ξ	nondimensional coordinate along the body Eq. (30)
ρ	density
C	$= \rho\mu/\rho_e u_e$ Chapman-Rubes in constant Eq. (30)
u	velocity along the direction ξ
f	nondimensional stream function $= \frac{1}{2}A\eta^2 - B\eta^5$
r_B	radius of the axisymmetric body
j	index of r_B $j = 0$ for two-dimensional flow and $j = 1$ for axisymmetric flow
t	temperature
$a(\xi, \eta)$	atom concentration
H	total enthalpy Eq. (35)
c_P	specific heat at constant pressure
R	represents the streamwise variation of the reaction effect along the body. $R = 0$ for symmetrical bodies
$\bar{\Gamma}$	Damkohler number $= 2\xi^{R+1}K_R(u_e\, d\xi/dx)^{-1}$ describing the gross magnitude of chemical reaction
h_D	energy of dissociation per unit atom mass
G	$= h_D^{-1}H[(\xi, \eta) - H_{EQ}(\eta)]$
Γ	$= \bar{\Gamma}(1 + D)$
D	$= h_D(a_e - a_{EQ,w})/\{c_P(t_e - t_w)\}$

$\bar{a}$ $= a(\xi, \eta) - a_{EQ}(\eta)$
Q $= \Gamma^{1/2}\eta$
$O(x)$ order of magnitude of x
ψ stream function

SUPERSCRIPTS

o outer solution
i inner solution
c composite solution
$'$ differentiation with respect to η

SUBSCRIPTS

n number in the subscript refers to the order of perturbation
e values at the outer edge of the boundary layer
w value at the wall
EQ equilibrium value

Asymptotic Methods—Section III

h nondimensional temperature function Eq. (64)
σ Prandtl number
$\binom{n}{k}$ binomial coefficient
$= \dfrac{\Gamma(n+1)}{\Gamma(k+1)\Gamma(n-k+1)} \quad n > k$
τ inverted variable Eq. (80)
λ large parameter in Eq. (91)
$\Gamma(x)$ gamma function with argument x
T nondimensional temperature
Θ transformed temperature function Eq. (99)

Variational Methods—Section IV

δF variation of F
V thermal potential Eqs. (105) and (116)
D volument dissipation functions Eqs. (106) and (117)
$\mathbf{H}$ heat flux vector
τ time
C volume specific heat capacity $= \rho c_v$
c_v heat capacity at constant volume
$q_i(\tau)$ time dependent generalized coordinates
Q_i thermal force Eqs. (109) and (118)
$\mathbf{u}$ velocity vector
D_s surface dissipation function Eq. (119)
∇ gradient operator
h integrated heat capacity Eq. (120)
h_w surface heat transfer coefficient
K thermal conductivity
v_{rJ} velocity of component γ in the J direction Eq. (121)
$\nu_{\gamma p}$ stoichiometric coefficient for component γ for pth reaction
M_γ molecular mass of the component γ
u_p rate of pth reaction
X_γ external force on component γ
P_{iJ} component of pressure tensor
e energy per unit mass
W_J heat flow in J direction
$\Delta_{\gamma J}$ diffusion flow of γ component in J direction
A_p $= -\nu_{\gamma p} M_\gamma \mu_\gamma$
μ_γ chemical potential
X_α thermodynamic forces
J_α thermodynamic fluxes
F unsteady local potential
Φ local potential for stationary state
α_i parameters in the assumed solution, $i = 1, 2, \ldots, m$
k thermal diffusivity
Θ nondimensional mass transfer potential
θ nondimensional time
$F_n(\Theta, T)$ $n = 1, 2, 3, 4$ functions describing the effect of temperature and mass transfer potential on various thermophysical characteristics in a porous body

X_i	$i = 1, 2, 3$; nondimensional Cartesian coordinates
Lu_0	initial value of the Luikov number
Pn_0	initial value of Posnov number
$\mathrm{K}_0{}^*$	modified Kossovich number
V_1	volume of the porous body
$a(\tau)$	position of the melting front at time τ
$q(\tau)$	penetration depth for temperature
t_m	melting temperature
m	$= \sqrt{C}\, t_m/2l$, nondimensional number Eq. (143)
l	latent heat of melting
R	heat flux at $x = a(\tau)$
τ_m	nondimensional melting time Eq. (144)
$q_1 = q/\sqrt{k}\,\tau_m$	nondimensional penetration depth

SUPERSCRIPTS

$\cdot$	derivative with respect to time
$*$	assumed macroscopic variables not subject to variation

SUBSCRIPTS

n	normal to the surface
j	components in the j direction
γ	pertaining to component γ, $\gamma = 1, 2, \ldots, n$
p	pertaining to reaction p, $p = 1, 2, \ldots, r$

Methods Related to the Solution of Integral Equations—Section V

$\tau_w(x)$	$= \mu(\partial u/\partial v)_{y=0}$, skin friction at the wall
μ	coefficient of viscosity
$Q_w(x)$	heat flux at the wall
$a(x), k(x), g(x)$	known functions of x in the integral equation (151)
$\phi(x)$	unknown function in the integral equation (151)
γ_i	powers of x in the expansion of $a(x)$ Eq. (152)
S	parameter in the Mellin transform
$\Psi(S)$	analytic function in Re $S > 0$
Re S	real part of S
$F(S)$	$= \mathbf{M}(f) = \int_0^\infty f(x)x^{S-1}\,dx$, Mellin transform of $f(x)$
$\mathbf{M}_-(f)$	$\int_0^1 f(x)x^{S-1}\,dx$
$\mathbf{M}_+(f)$	$\int_1^\infty f(x)x^{S-1}\,dx$
a, b	powers of x, Z in Eqs. (158) (177), and (181)
C_n	coefficients in the series solution Eq. (158)
A_n	coefficients in the series solution Eq. (177)
B_n	coefficients in the series solution Eq. (181)
$F(Z)$	nondimensional temperature along the plate Eq. (170)
Z	independent variable describing the distance along the plate
$\mathrm{T}(Z)$	temperature along the plate
$\mathrm{T}_r(Z)$	recovery temperature

SUBSCRIPTS

f	relating to fluid
∞	relating to free stream

Methods Based on the Use of the Complex Variable—Section VI

D	cross section of the channel
Γ	contour of the channel
p	pressure
Z	coordinate along the axis of the channel
Q	strength of the heat source
C_1	$= (1/\mu)\,dp/dz =$ constant
C_2	$= (\rho c_p/K)\,dt/dZ$
z	complex variable

$\bar{z}$	conjugate complex variable
T_1, T_2	components of T explained after Eq. (191)
θ_1	temperature function related to T_1 Eq. (190), and solution of Eq. (186) with boundary conditions Eq. (188)
θ_2	temperature function related to T_2 and solution of Eq. (187) with boundary condition Eq. (189)
ϕ_n	$n = 1, 2, \ldots$, exterior angles of a polygon in z-plane
w	complex variable $w = u + iv$
u	real axis in the w-plane
v	imaginary axis in the w-plane
d	the width of the doubly infinite strip in the z-plane
g	half width of the cut in the strip in z-plane
b	height of the cut in the strip in z-plane
$sn\ \alpha, cn\ \alpha, dn\ \alpha$	elliptic functions defined in Eqs. (205)–(207)
$Z(\alpha)$	Jacobi's zeta function Eqs. (209) and (210)
$\Pi_1(\zeta, \alpha)$	elliptic integral of the third kind
K, K'	complete elliptic integrals of the first kind defined in Eqs. (211) and (212)
p	complex variable $(p = \alpha + i\beta)$
$\bar{t}(x, y)$	the Laplace transform of $t(x, y, \tau)$ with respect to τ Eq. (225)
$U(y)$	Fourier transform of $\bar{t}(x, y)$ with respect to x
γ	$= \sqrt{k^2 + p^2}$ $\quad \mathrm{Re}\,\gamma > 0$
k^2	$= s$
$H(x, \tau)$	inverse Laplace transform of the right-hand side of Eq. (246)

SUPERSCRIPT

$-$	denotes conjugate complex

Special Methods for the Solution of Partial Differential Equations—Section VII

$\bar{u}$	velocity averaged over the cross section of the channel
X	nondimensional x-coordinate
Y	nondimensional y-coordinate
u_m	velocity averaged over time and y
H	$= -(1/E_n^2) \log G_n$ Eq. (261)
$G_n(X, \theta)$	functions in the assumed solution Eq. (256)
r	radial coordinate in the semicircular region in Fig. 2
c	radius of the end circle Fig. 2
a	length of the rectangular region Fig. 2
R	$= r/a$
C	$= c/a$
μ_{pq}	$= \pi^2(p^2 + q^2/C^2)$; $p = 1, 2, \ldots, \infty$, $q = 1, 2, \ldots, \infty$
ϕ	angular coordinate in the circular region Fig. 2
S_i	roots of the transcendental equation (286)
$J_m(x)$	Bessel function of order m and argument x
$f_n(Y, \theta)$	function describing the nondimensional temperature along $X = 0$ Eq. (283)
$\psi_n(\phi, \theta)$	assumed temperature along $R = C$ Eqs. (275)–(277)
a_m^n, γ_q^n	coefficients defined in Eqs. (288)–(291)

SUBSCRIPTS

1	refers to circular part for $x < 0$ in Fig. 2
2	refers to rectangular part for $x > 0$ in Fig. 2
n	nth approximation

Application of Matrices—Section VIII

U_J	diffusing entities satisfying the partial differential equation (293) and boundary and initial conditions Eqs. (294)–(295), $J = 1, 2$
A, B	square matrices of the second order
U, f, ϕ	column matrices
ν_1, ν_2	eigenvalues of matrix A Eq. (305)
μ_1, μ_2	eigenvalues of matrix B Eq. (306)
E	unit square matrix

Eigenfunction Expansions—Section IX

λ_n'	eigenvalues of the heat conduction equation (314)
v_n	eigenfunctions of the heat conduction equation (314)
$N_n(\eta)$	solutions of the Sturm–Liouville system Eqs. (332)–(333) related to momentum equation (324)
$H_n(\eta)$	solutions of the Sturm–Liouville system Eqs. (334)–(335) related to energy equation (325)
$\mu_n\ \lambda_n$	eigenvalues of the homogeneous equation associated with Eq. (330) and Eq. (329), respectively
$L_n^m(x)$	$= d^m/dx^m \{\exp x\, d^n/dx^n \times [x^n \exp(x)]\}$, associated Laguerre polynomial

Miscellaneous Methods—Section X

T	$= (t - t_\infty)/(t_w - t_\infty)$
ν	coefficient of dynamic viscosity
$\bar{\tau}$	$= U\ \tau/x$
$\bar{y}$	$= y/\sqrt{\nu\tau}$
η_i	$= y\sqrt{U^\alpha}/\sqrt{\nu x}$
$\phi_n'(0)$	$n = 0, 1, 2$, coefficients in the series solution of Eq. (358)
a_n	$n = 1, 2, 3, 4, 5$, unknown constants in the assumed uniformly valid solution in Laplace transformed variable ϕ Eq. (361)
ϕ, ψ	independent variables in the momentum and energy equations in the Von-Mise's form Eqs. (365)–(366) defined in Eq. (366a)
$\alpha(\psi, \beta)$	assumed velocity profile in the nonsimilar boundary layer Eq. (370)
R_1	inner radius of the unmelted hollow cylindrical tube
R_2	outer radius of the hollow cylindrical tube
$q_1(\tau)$	time-dependent flux at the inner boundary of the hollow cylindrical tube
$\phi(\tau)$	time-dependent temperature at the outer surface of the tube
$Y_m(x)$	Bessel function of order m and argument x and of second kind
μ_n	roots of the transcendental equation (382)
t	melting temperature
$Q(\tau)$	time-dependent flux at the melting boundary depending on the inner radius of the melting tube
τ_m	time required for complete melting of the tube
$\Delta\tau_m$	$= \tau_{i+1} - \tau_i$
o_i	the position of the inner boundary during the time interval $\tau_i \leqslant \tau < \tau_{i+1}$
δ_{n_i}	roots of the transcendental equation (388)

REFERENCES

1. "Advances in Heat Transfer" (J. P. Hartnett and Thomas F. Irvine Jr., eds.), Vol. 1. Academic Press, New York and London, 1964.
2. "Advances in Heat Transfer" (J. P. Hartnett and Thomas F. Irvine Jr., eds.), Vol. 2. Academic Press, New York and London, 1965.
3. "Advances in Heat Transfer" (J. P. Hartnett and Thomas F. Irvine Jr., eds.), Vol. 3. Academic Press, New York and London, 1966.
4. "Advances in Heat Transfer" (J. P. Hartnett and Thomas F. Irvine Jr., eds.), Vol. 4. Academic Press, New York and London, 1967.
5. "Advances in Heat Transfer" (J. P. Hartnett and Thomas F. Irvine Jr., eds.), Vol. 5. Academic Press, New York and London, 1968.
6. "Advances in Heat Transfer" (J. P. Hartnett and Thomas F. Irvine Jr., eds.), Vol. 6. Academic Press, New York and London, 1969.
7. "Advances in Heat Transfer" (J. P. Hartnett and Thomas F. Irvine Jr., eds.), Vol. 7. Academic Press, New York and London, 1970.
8. B. A. Finlayson and L. E. Scriven, *Appl. Math. Rev.* **19,** 735 (1966).
9. T. R. Goodman, in reference (1), p. 52.
10. H. S. Carslaw and J. C. Jaeger, "Conduction of Heat in Solids," 2nd ed. Oxford Univ. Press, London and New York, 1959.
11. A. V. Luikov, "Analytical Heat Diffusion Theory." Academic Press, New York, 1968.
12. A. V. Lykov (A. V. Luikov) and Y. A. Mikhaylov, "Theory of Energy and Mass Transfer." Prentice-Hall, Englewood Cliffs, New Jersey, 1961.
13. G. Doetsch, "Guide to the Application of Laplace Transform," p. 209. Van Nostrand–Reinhold, New York, 1961.
14. M. J. Lighthill, *Phil. Mag.* **40,** 1179 (1949).
15. H. S. Tsien, *in* "Advances in Applied Mechanics," (H. L. Dryden and Th. Von. Karman, eds.) Vol. 4, p. 281. Academic Press, New York and London, 1956.
16. H. Poincaré, "Les methodes nouvelles de la mecanique celeste," Vol. 1. Dover, New York, 1892.
17. Y. H. Kuo, *J. Aeronaut. Sci.* **23,** 125 (1956).
18. M. Van Dyke, "Perturbation Methods in Fluid Mechanics." Academic Press, New York and London, 1964.
19. M. J. Lighthill, *Phil. Mag.* **40,** 1202 (1949).
20. J. Legras, *C.R. Acad. Sci. Paris* **233,** 1005 (1951).
21. J. Legras, O.N.E.R.A. Publ. No. 66. 1953 (Noted from Van Dyke (18), p. 218).
22. T. R. Goodman and J. J. Shea, *J. Appl. Mech.* **27,** 16 (1960).
23. K. L. Ahuja and I. J. Kumar, *Def. Sci. Jl. India* **16,** 203 (1966).
24. W. D. Morris, *J. Fluid. Mech.* **21,** 453 (1965).
25. W. G. Olstad, *Proc. Heat Transfer Fluid Mechanics Inst.* p. 138. Univ. of California Press, Berkeley, California (1965).
26. P. A. Lagerstrom and J. D. Cole, *Arch. Rat. Mech. Anal.* **4,** 817 (1955).
27. P. A. Lagerstrom, *J. Math. Mech.* **6,** 605 (1957).
28. S. Kaplun, *Z. Ang. Math. Phys.* **5,** 111 (1954).
29. S. Kaplun, *J. Math. Mech.* **6,** 595 (1957).
30. A. Erdelyi, *J. Soc. Ind. Appl. Math.* **11,** 105 (1963).
31. G. R. Inger, *J. Fluid Mech.* **26,** 793 (1966).
32. S. H. Lam, *Proc. Heat Transfer Fluid Mech. Inst.* p. 44. Univ. of California Press, Berkeley, California (1965).

33. R. M. Terrill and G. M. Shreshta, *Appl. Sci. Res.* **A15,** 440 (1965).
34. R. K. Varma and M. P. Murgai, *Quart. Appl. Math.* **22,** 345 (1965).
35. H. F. Mueller and N. D. Malmuth, *Int. J. Heat Mass Transfer* **8,** 915 (1965).
36. R. D. Cess, *Int. J. Heat Mass Transfer* **9,** 1269 (1966).
37. O. R. Burgraff, *AIAA J.* **4,** 1725 (1966).
38. J. W. E. Ellinwood, *J. Math. Phys.* **46,** 281 (1967).
39. D. G. Drake, and P. C. Rhodes, *Z. Angew. Math. Phys.* **3,** 342 (1967).
40. D. E. Coles, *Proc. Heat Transfer Fluid Mech. Inst.* p. 119. Stanford Univ. Press, Stanford, California (1957).
41. I. E. Beckwith and N. B. Cohen, NASA, TN-D-625 (1961).
42. P. A. Lagerstrom, *in* "High Speed Aerodynamics and Jet Propulsion" (F. K. Moore ed.) Vol. 4, p. 125. Princeton Univ. Press, Princeton, New Jersey (1964).
43. C. F. Dewey and J. F. Gross, in reference (4), p. 317 (1967).
44. J. L. Novotny and K. T. Yang, *J. Heat Transfer Trans. ASME,* **C89,** 309 (1967).
45. F. E. Fendell, *J. Fluid Mech.* **34,** 163 (1968).
46. T. Kubota and F. L. Fernandez, *AIAA J.* **6,** 22 (1968).
47. H. F. Mueller and N. D. Malmuth, *AIAA J.* **7,** 1631 (1969).
48. H. K. Kuiken, *J. Fluid Mech.* **37,** 785 (1969).
49. L. E. Frankel, *Proc. Cambridge Phil. Soc.* **65,** 209 (1969).
50. J. Cochran, A New Approach to Singular Perturbation Problems. Ph.D. Dissertation Stanford Univ., Stanford, California (1962).
51. J. J. Mahony, *J. Aust. Math. Soc.* **2,** 440 (1962).
52. J. D. Cole and J. Kevorkian, *in* "Non-linear Differential Equations and Non-linear Mechanics" (J. P. Laselle and S. Lefschetz, eds.) p. 113. Academic Press, New York, 1963).
53. N. D. Fowkes, *Quart. Appl. Math.* **26,** 57 (1968).
54. A. B. Vasileva, *USSR Computat. Math. & Math. Phys.* **3,** 823 (1963).
55. R. K. Varma and M. P. Murgai (to be published).
56. S. Kaplun, "Fluid Mechanics and Singular Perturbations. A Collection of papers by S. Kaplun" (P. A. Lagerstrom, L. N. Howard, and C. S. Liu, eds.). Academic Press, New York, 1967.
57. R. O'Melley and J. R. Keller, *Comm. Pure. Appl. Math.* **21,** 263 (1968).
58. R. O'Melley and J. R. Keller, *J. Math. Anal. Appl.* **19,** 291 (1967).
59. R. O'Melley and J. R. Keller, *J. Math. Mech.* **16,** 1143 (1967).
60. J. D. Murray, *J. Math. Phys.* **47,** 111 (1968).
61. A. Erdelyi, *J. Inst. Math. Appl.* **4,** 113 (1968).
62. A. Erdelyi, *Arch. Rat. Mech. Anal.* **29,** 1 (1968).
63. A. B. Vasileva, *Usp. Matemat. Nauk* (In Russian) **18,** 15 (1963).
64. M. I. Visik and L. A. Lyusternik, *Dokl. Akad. Nauk USSR* (In Russian) **121,** 778 (1958).
65. M. I. Visik and L. A. Lyusternik, *Usp. Matemat. Nauk* (In Russian) **12,** 3 (1957).
66. A. Friedman, *Arch. Rat. Mech. Anal.* **29,** 289 (1968).
67. P. C. Fife, *Arch. Rat. Mech. Anal.* **28,** 184 (1968).
68. J. W. Mackie, *Arch. Rat. Mech. Anal.* **24,** 219 (1967).
69. H. C. Kao, *J. Fluid Mech.* **27,** 789 (1967).
70. R. J. Swigart, *AIAA J.* **1,** 1034 (1963).
71. A. P. Bazzin and A. A. Gladkov, *Inz. Zh.* (In Russian) **3,** 517 (1963).
72. H. C. Kao, *AIAA J.* **2,** 1892 (1964).
73. R. J. Conti, *J. Fluid Mech.* **24,** 65 (1966).
74. M. Van Dyke, *J. Mecanique* **4,** 477 (1965).

75. P. Cheng and W. G. Vincenti, *J. Fluid Mech.* **27,** 625 (1967).
76. D. Meksyn, "New Methods in Laminar Boundary-Layer Theory." Pergamon Press, Oxford, 1961.
77. P. M. Morse and H. Feshbach, "Methods of Theoretical Physics," Vol. 1. McGraw–Hill, New York, 1953.
78. K. Knopp, "Theory and Application of Infinite Series." Blackie and Son, London, 1951.
79. W. P. Kotorynski, *J. Math. Phys.* **47,** 170 (1968).
80. C. S. Yih, *Trans. Amer. Geophys. Union* **33,** 669 (1952).
81. V. D. Sovershenny and G. A. Tirski, *Int. J. Heat Mass Transfer* **4,** 119 (1961).
82. J. Brindley, *Int. J. Heat Mass Transfer* **6,** 1035, (1963).
83. T. Y. Li and P. S. Kirk, *Int. J. Heat Mass Transfer* **8,** 1217 (1965).
84. B. T. Chao and D. R. Jeng, *J. Heat Transfer Trans. ASME* **C87,** 221 (1965).
85. D. R. Jeng, *J. Heat Transfer Trans. ASME* **C88,** 205 (1966). Discussion on paper by C. C. Oliver and P. W. Macfadden.
86. T. Y. Li and P. S. Kirk, *Int. J. Heat Mass Transfer* **10,** 257 (1967).
87. A. A. Hayday, and D. A. Bowlus, *Int. J. Heat Mass Transfer* **10,** 415 (1967).
88. A. A. Hayday and D. A. Bowlus, *Int. J. Heat Mass Transfer* **11,** 963 (1968).
89. G. S. H. Lock and J. C. Gunn, *J. Heat Transfer, Trans. ASME* **C90,** 63 (1968).
90. C. C. Hsu, *J. Math. Phys.* **47,** 185 (1968).
91. L. Y. Cooper, *Quart. Appl. Math.* **27,** 173 (1969).
92. H. J. Merk, *J. Fluid Mech.* **5,** 460 (1959).
93. W. B. Bush, *AIAA J.* **2,** 1857 (1964).
94. B. S. Jefferys, *in* "Quantum Theory" (D. R. Bates, ed.), Vol. 1, p. 229. Academic Press, New York and London, 1961.
95. N. Froman and P. O. Froman, "JWKB Approximation, Contributions to the Theory." North Holland Publ., Amsterdam, 1965.
96. A. Erdelyi, "Asymptotic Expansions." Dover, New York 1956.
97. I. Imai, *Quart. Appl. Math.* **16,** 33 (1958).
98. D. R. Hartree, *Proc. Cambridge Phil. Soc.* **33,** 223 (1937).
99. D. R. Chapman and M. W. Rubesin, *J. Aeronaut. Sci.* **16,** 547 (1949).
100. S. Levy, *J. Aeronaut. Sci.* **19,** 341 (1952).
101. M. J. Lighthill, *Proc. Roy. Soc. London* **A202,** 359 (1950).
102. J. R. Sellars, M. Tribus, and J. S. Klein, *Trans. ASME* **78,** 441 (1959).
103. C. W. Sterling and C. A. Sleicher, *J. Aerospace Sci.* **29,** 109 (1962).
104. R. D. Cess and E. M. Sparrow, *in* "International Developments in Heat Transfer, 1961–62," p. 468. Amer. Soc. Mech. Eng., New York, 1962.
105. A. H. Nayfeh, *J. Math. Phys.* **46,** 349 (1967).
106. L. V. Kantorovich and V. I. Krylov, "Approximate Methods of Higher Analysis." Noordhoff Ltd., Groningen, The Netherlands, 1958.
107. I. Akhiezer, "The Calculus of Variations," Chapter 4. Blaisdell Publ., New York and London, 1962.
108. M. A. Biot, *Phys. Rev.* **97,** 1463 (1955).
109. M. A. Biot, *J. Aerospace Sci.* **24,** 857 (1957).
110. T. J. Lardner, *AIAA J.* **1,** 196 (1963).
111. M. A. Biot and H. Daughaday, *J. Aerospace Sci.* **29,** 227 (1962).
112. M. A. Biot and H. C. Agrawal, *J. Heat Transfer Trans. ASME* **C86,** 437 (1964).
113. T. J. Lardner, *AIAA J.* **5,** 2079 (1967).
114. A. P. Bukhvotsov and W. V. Frankel, *Inzh. Fiz. Zh.* (In Russian) **5,** 78 (1962).

115. G. F. Muchnik and Yu. A. Polykov, *Teplofiz. Visokikh. Temp.* (In Russian) **2,** 424 (1964).
116. P. D. Richardson, *J. Heat Transfer Trans. ASME* **C86,** 298 (1964).
117. K. L. Ahuja, *ZAMM* **48,** 353 (1968).
118. H. N. Chu, *J. Spacecraft Rockets* **1,** 686 (1964).
119. T. J. Lardner, *J. Spacecraft Rockets* **2,** 479 (1965).
120. R. O. Weiss, Appl. Phys. Lab. Rep. No. BFR–68–02, Johns Hopkins Univ., Maryland (1968).
121. P. Rafalski and W. Zyszkowski, *AIAA J.* **6,** 1606 (1968).
122. N. I. Nazarov, *Proc. 3rd All Union Conf. Heat Mass Transfer* (In Russian) **8,** 302. Heat and Mass Transfer Inst. of BSSR, Adad. of Sciences, Minsk (1968).
123. M. A. Biot, *J. Aerospace Sci.* **26,** 367 (1959).
124. M. A. Biot, *J. Aerospace Sci.* **29,** 558 (1962).
125. M. A. Biot, *J. Aerospace Sci.* **29,** 568 (1962).
126. B. A. Finlayson and L. E. Scriven, *Int. J. Heat Mass Transfer* **10,** 799 (1967).
127. M. A. Biot, *Phys. Fluid* **10,** 1424 (1967).
128. M. A. Biot, *J. Math. Mech.* **15,** 177 (1966).
129. H. N. Chu and J. D. Seader, *J. Spacecraft Rockets* **2,** 984 (1965).
130. S. D. Nigam and H. C. Agrawal, *J. Math. Mech.* **9,** 869 (1960).
131. S. C. Gupta, *Appl. Sci. Res.* **A10,** 85 (1961).
132. S. C. Gupta, *Appl. Sci. Res.* **A10,** 279 (1961).
133. I. Prigogine, *Bull. Acad. Belg. Cl. Sci.* **31,** 600 (1945).
134. S. R. deGroot and P. Mazur, "Non-Equilibrium Thermodynamics." North-Holland Publ., Amsterdam, 1962.
135. R. J. Donnelly, R. Herman, and I. Prigogine, eds., "Non-Equilibrium Thermodynamics, Variational Techniques and Stability." Univ. of Chicago Press, Chicago, Illinois, 1966.
136. P. Glansdorff and I. Prigogine, *Physica* **20,** 773 (1954).
137. P. Glansdorff and I. Prigogine, *Physica* **30,** 351 (1964).
138. I. Prigogine, in Donnelly *et al.* (135), p.3.
139. P. Glansdorff in Donnelly *et al.* (135), p. 45.
140. I. Prigogine and P. Glansdorff, *Physica* **31,** 1242 (1965).
141. M. Kruskal, in Donnelly *et al.* (135), p. 287.
142. P. Glansdorff, *Physica* **32,** 1745 (1966).
143. D. F. Hays, *Bull. Aced. Roy. Belg. (Classe Sci.) Seance* **8,** 576 (1963).
144. D. F. Hays, *Int. J. Heat Mass Transfer* **9,** 165 (1966).
145. D. F. Hays, in Donnelly *et al.* (135), p. 17.
146. D. F. Hays and H. N. Curd, *Int. J. Heat Mass Transfer* **11,** 285 (1968).
147. H. W. Butler and R. L. Rackley, *Int. J. Heat Mass Transfer* **10,** 1255 (1967).
148. D. Weihs and B. Gal-Or, *Int. J. Eng. Sci.* **8,** 231 (1970).
149. I. J. Kumar, *Int. J. Heat Mass Transfer* **14,** 1759 (1971).
150. I. J. Kumar and L. N. Gupta, *Indian J. Pure Appl. Math.* **2,** 692 (1971).
151. H. G. Landau, *Quart. Appl. Math.* **8,** 81 (1950).
152. L. N. Gupta *Indian J. Pure Appl. Math.*, **3** (1972) (to be published).
153. R. S. Schechter, "The Variational Method in Engineering," McGraw-Hill, New York, 1967.
154. L. N. Gupta *Indian J. Pure Appl. Math.* (to be published).
155. B. A. Finlayson, *Brit. Chem. Eng.* **14,** 53 (1969).
156. R. J. Duffin, *J. Math. Mech.* **8,** 47 (1959).
157. C. Y. Liu, *J. Soc. Ind. Appl. Math.* **10,** 19 (1962).

158. J. E. Wilkins, *J. Soc. Ind. Appl. Math.* **10,** 62 (1962).
159. E. M. Sparrow and R. Siegel, *Int. J. Heat Mass Transfer* **1,** 161 (1960).
160. D. Pnueli, *Int. J. Heat Mass Transfer* **10,** 1743 (1967).
161. P. V. Tsoi, *Inzh. Fiz. Zh.* (In Russian) **14,** 520 (1968).
162. R. A. Nichols and S. G. Bankoff, *Int. J. Heat Mass Transfer* **8,** 329 (1965).
163. M. P. Stallybrass, *J. Math. Mech.* 1247 (1967).
164. M. E. Gurtin, *Quart. Appl. Math.* **22,** 252 (1964).
165. L. Y. Ainola, *Inzh. Fiz. Zh.* (In Russian) **12,** 465 (1967).
166. P. Rafalski and W. Zyszkowski, *AIAA J.* **7,** 606 (1969).
167. R. Viskanta and R. J. Grosh, *Appl. Mech. Rev.* **17,** 91 (1964).
168. R. Viskanta, in Hartnett and Thomas (3), p. 176.
169. S. Chandrashekhar, "Radiative Transfer." Dover, New York, 1960.
170. V. Kourganoff, "Basic Methods in Transfer Problems." Oxford Univ. Press (Clarendon), London and New York, 1952.
171. L. W. Busbridge, "The mathematics of Radiative Transfer." Cambridge Univ. Press, London and New York, 1960.
172. E. M. Sparrow, in Hartnett and Thomas (2), 399.
173. J. R. Howell and R. Siegel, Thermal Radiation Heat Transfer, Vol. 2. NASA, SP-164 (1969).
174. R. Courant and D. Hilbert, "Methods of Mathematical Physics," Vol. 1. Wiley (Interscience), New York, 1953.
175. S. G. Mikhlin, "Integral Equations," Pergamon Press, Oxford, 1957.
176. N. I. Muskhelishvili, "Singular Integral Equations." Noordhof Ltd., Groningen, The Netherlands, 1953.
177. F. G. Tricomi, "Integral Equations." Wiley (Interscience), New York, 1957.
178. M. L. Kasnov, A. I. Kiselev, and G. I. Makarenko, "Integralnie Uravnenia" (Integral Equations) (In Russian). Nauka, Moskva, 1968.
179. G. F. Carrier, *J. Soc. Ind. Appl. Math.* **13,** 68 (1965).
180. B. A. Boley, *J. Math. Phys.* **40,** 300 (1961).
181. J. C. Koh and J. P. Hartnett, *Int. J. Heat Mass Transfer* **2,** 185 (1961).
182. E. R. G. Eckert, A. A. Hayday, and W. J. Minkowycz, *Int. J. Heat Mass Transfer* **4,** 17 (1961).
183. E. R. G. Eckert, A. A. Hayday, and W. J. Minkowycz, in "Teplo-i-Massoperenos" (A. V. Luikov and B. M. Smolsky, eds.), Vol. 3, Obshie Voprosi Teploobmena (In Russian), p. 65. Moskva, Gosenergoisdat, 1963.
184. E. V. Tolubinskiy, *Dok. Akad. Nauk SSSR* (In Russian) **160,** 1289 (1965).
185. E. V. Tolubinskiy, *Int. J. Heat Mass Transfer* **9,** 1471 (1966).
186. V. T. Grinchenkov and A. F. Ulitko, *Inzh. Fiz. Zh.* (In Russian) **6,** 67 (1963).
187. K. K. Vasilevski, *Teplofiz. Visokikh Temp.* (In Russian) **2,** 260 (1964).
188. S. V. Patankar, *Int. J. Heat Mass Transfer* **9,** 829 (1966).
189. D. B. Spalding, *in* "International Development in Heat Transfer," Part II, p. 439. Amer. Soc. Mech. Eng., New York, 1963.
190. J. M. Savino and R. Siegel, *Int. J. Heat Mass Transfer* **12,** 803 (1969).
191. A. N. Tifford, *J. Aeronaut. Sci.* **18,** 283 (1951).
192. D. B. Spalding, *J. Fluid Mech.* **4,** 22 (1958).
193. H. W. Liepmann, *J. Fluid Mech.* **3,** 357 (1958).
194. D. R. Davies and D. E. Bourne, *Quart. J. Mech. Appl. Math.* **9,** 457 (1956).
195. C. R. Illingworth, *Quart. J. Mech. Appl. Math.* **7,** 8 (1954).
196. G. M. Lilley, College of Aeronautics Note No. 93 (1959).

197. N. Curle, "The Laminar Boundary Layer Equations." Oxford Univ. Press (Clarendon) London and New York, 1962.
198. P. L. Chambre and A. Acrivos, *J. Appl. Phys.* **27,** 1322 (1956).
199. D. E. Rosner, *J. Aerospace Sci.* **26,** 281 (1959).
200. D. A. Frank-Kamenetskii, "Diffuzia-i-Teploperedachaf Khimicheskoi Kinetike" (In Russian). Nauka, Moskva, 1967.
201. P. L. Chambre, *Appl. Sci. Res.* **A6,** 97 (1956).
202. A. Acrivos and P. L. Chambre, *Ind. Eng. Chem.* **49,** 1025 (1957).
203. P. L. Chambre, *J. Appl. Phys.* **30,** 1683 (1959).
204. W. R. Mann and F. Wolf, *Quart. Appl. Math.* **9,** 163 (1951).
205. J. R. Jones and B. Frank, *Comm. Pure Appl. Math.* **16,** 33 (1963).
206. G. T. Aldoshin, A. C. Golosov, and V. I. Zhuk, *Proc. All Union Conf. Heat Mass Transfer, 3rd* (A. V. Luikov and B. M. Smolsky, eds.), Vol. 8 (In Russian), p. 186. Heat and Mass Transfer Inst. of BSSR, Acad. of Sci., Minsk (1968).
207. P. M. Chung, S. W. Lieu, and H. Mirels, *Int. J. Heat Mass Transfer* **6,** 193 (1963).
208. T. L. Perelman, in "Teplo-i-Massoperenos" (A. V. Luikov and B. M. Somolsky eds.) p. 79. BSSR Academy of Sciences, Minsk, 1963.
209. T. L. Perelman, *Prik. Mat. Mekh (PMM)* (In Russian) **25,** (1961).
210. I. J. Kumar, *Inzh. Fiz. Zh.* (In Russian) **14,** 781 (1968).
211. I. J. Kumar and A. B. Bartman, *Proc. All Union Conf. Heat Mass Transfer, 3rd* (In Russian) (A. V. Luikov and B. M. Smolsky, eds.), Vol. 9, p. 481. Heat and Mass Transfer Inst. of the BSSR Acad. of Sci., Minsk (1968).
212. I. J. Kumar, *Proc. Roy. Soc. London* **A324,** 45 (1971).
213. M. A. Evgrafov, "Analiticheskie Funktsii" (In Russian) p. 314. Nauka, Moskva, 1968.
214. I. J. Kumar and V. K. Trivedi, Proc. First National Conf. on Heat Mass Transfer, IIT Madras, Dec. 6–8, 1971.
215. N. I. Muskhelishvili, "Some Basic Problems of Mathematical Theory of Elasticity." Noordhoff Ltd., Groningen, Holland, 1953.
216. L. N. Tao, *J. Heat Transfer Trans. ASME* **C83,** 467 (1961).
217. L. N. Tao, *in* "Development in Mechanics" (J. E. Lay and L. E. Malvern, eds.), *Proc. Midwestern Mech. Conf. 7th* p. 510. North-Holland Pub, Amsterdam, 1961.
218. L. N. Tao, *Proc. Int. Heat Transfer Conf. 2nd* p. 598 1961.
219. U. A. Shastry, *Appl. Sci. Res.* **A13,** 269 (1964).
220. V. P. Tyagi, *Int. J. Heat Mass Transfer* **9,** 1321 (1966).
221. V. P. Tyagi, *J. Heat Transfer Trans. ASME* **C88,** 161 (1966).
222. V. P. Tyagi, *Int. J. Heat Mass Transfer* **8,** 1481 (1965).
223. V. P. Tyagi, *Proc. Cambridge Phil. Soc.* **62,** 555 (1966).
224. I. J. Kumar, *Proc. Nat. Inst. Sci. India* **A30,** 625 (1964).
225. P. F. Byrd and M. D. Friedman, "Handbook of Elliptic Integrals for Engineers and Physicists." Springer-Verlag, 1954.
226. M. J. Balcerzok and S. Rayner, *Int. J. Heat Mass Transfer* **3,** 113 (1961).
227. A. A. Sholokhov, *Inzh. Fiz. Zh.* (In Russian) **6,** 76 (1963).
228. G. A. Varshavski, E. M. Gernier, and D. V. Feddosev, *Inzh. Fiz. Zh.* (In Russian) **8,** 754 (1965).
229. R. Siegel, NASA TND—4771 (1968).
230. P. A. Laura and M. Chi, *J. Heat Transfer Trans. ASME* **C86,** 466 (1964).
231. L. M. Milne- Thomson, "Theoretical Hydrodynamics," Macmillan, London (1955).
232. H. Kober, "Dictionary of Conformal Representations." Dover, New York, 1952.

233. B. Noble, "Methods Based on the Wiener-Hopf Technique for the solution of Partial Differential Equations." Pergamon Press, Oxford, 1958.
234. Ya. F. Rutner and L. P. Skryabina, "Differential Equations." Translation of Differentsial'nye Uravneniya by The Faraday Press. Vol. 2, p. 570 (1966).
235. G. Horvay, *J. Heat Transfer Trans. ASME* **C83,** 391 (1961).
236. G. Horvay and M. Dacosta, *J. Heat Transfer Trans. ASME* **C86,** 265 (1964).
237. G. C. Sih, *J. Heat Transfer Trans. ASME* **C87,** 293 (1965).
238. R. Courant and K. O. Friedrichs, "Supersonic Flow and Shock Waves," Vol. 1. Wiley (Interscience), New York, 1948.
239. R. Siegel, *Trans. ASME* **80,** 347 (1958).
240. M. Perlmutter and R. Siegel, *J. Heat Transfer Trans. ASME* **C83,** 432 (1961).
241. R. Siegel and M. Perlmutter, *J. Heat Transfer Trans. ASME* **C84,** 111 (1962).
242. R. Siegel, *Int. J. Heat Mass Transfer* **6,** 607 (1963).
243. F. B. Hildebrand, "Advanced Calculus for Engineers." Prentice-Hall, Englewood Cliffs, New Jersey, 1949.
244. R. Siegel, *J. Appl. Mech. Trans. ASME* **26,** 140 (1959).
245. G. C. Lindauer and C. J. Hsu, *AIAA J.* **6,** 1973 (1968).
246. M. C. Jischke and J. R. Baron, *AIAA J.* **7,** 1326 (1969).
247. I. J. Kumar and P. J. Achari, (To be published).
248. P. V. Tsoi, *Int. J. Heat Mass Transfer* **7,** 1217 (1964).
249. F. R. Gantmacher, "Applications of the Theory of Matrices" Wiley (Interscience), New York, 1959.
250. V. Vodicka, *Appl. Sci. Res.* **A9,** 190 (1960).
251. V. I. Vanko, *Prik. Mat. Tekh. Fiz.* (In Russian) **3,** 138 (1963).
252. J. G. Negi and R. N. Singh, *Earth Planetary Sci. Lett.* **2,** 335 (1967).
253. L. Jarmai, *Proc. Congr. Theoret. Appl. Mech. Delhi, Dec.* 1960, 6*th* p. 117, Indian Soc. Theoret. Appl. Mech., I.I.T. Kharagpur (1960).
254. V. Lorass-Nagy, *ZAMM* **42,** 110 (1962).
255. N. I. Gamayunov, *Proc. All Union Conf. Heat Mass Transfer,* 3*rd* (In Russian) (A. V. Luikov and B. M. Somolsky eds.), Vol. 8, p. 3. Heat and Mass Transfer Inst. of the BSSR Acad. of Sci., Minsk (1968).
256. H. M. Hsia and T. J. Love, *J. Heat Transfer Trans. ASME* **C89,** 197 (1967).
257. N. Y. Ölcer, *Int. J. Heat Mass Transfer* **7,** 307 (1964).
258. N. Y. Ölcer, *Int. J. Heat Mass Transfer* **8,** 529 (1965).
259. N. Y. Ölcer, *Quart. Appl. Math.* **24,** 380 (1967).
260. N. Y. Ölcer, *Nucl. Eng. Design* **7,** 97 (1968).
261. N. Y. Ölcer, *Quart. Appl. Math.* **26,** 355 (1968).
262. P. V. Charpakov, *Inzh. Fiz. Zh.* (In Russian) **6,** 61 (1963).
263. P. V. Charpakov, *Proc. All Union Conf. Heat Mass Transfer,* 3*rd* (In Russian) (A. V. Luikov and B. M. Somolsky eds.), Vol. 8, p. 135. Heat and Mass Transfer Inst. of the BSSR Acad. of Sci., Minsk (1968).
264. H. Fox, and P. A. Libby *J. Fluid Mech.* **17,** 433 (1963).
265. H. Fox and P. A. Libby *J. Fluid Mech.* **19,** 433 (1964).
266. P. A. Libby, *AIAA J.* **3,** 2164 (1965).
267. W. P. Kotorynski, *SIAM J. Appl. Math.* **16,** 1132 (1968).
268. S. C. R. Dennis, A. McD. Mercer, and G. Poots, *Quart. Appl. Math.* **17,** 285 (1959–60).
269. J. Schenk and B. S. Han, *Appl. Sci. Res.* **17,** 96 (1967).
270. R. P. Stein, in Hartnett and Irvine (3), p. 101.
271. K. M. Case, *Ann. Phys.* **9,** 1 (1960).
272. G. M. Simmons and J. H. Fersiger, *Int. J. Heat Mass Transfer* **11,** 1611 (1968).

273. M. L. Rosenweig, Ph.D. Thesis. Cornell Univ., Ithaca, New York (1959).
274. R. D. Cess, *J. Heat Transfer Trans. ASME* **C83,** 274 (1961).
275. A. Dorfman, *Proc. All Union Conf. Heat Mass Transfer, 3rd* (In Russian) (A. V. Luikov and B. M. Somolski eds.), Vol. 1, p. 181. Heat and Mass Transfer Inst. of the BSSR Acad. of Sci., Minsk (1968).
276. A. Dorfman, *Teplofiz. Visokikh Temp.* (In Russian) **5,** 858 (1967).
277. G. A. Surkov, *Inzh. Fiz. Zhur.* (In Russian) **8,** 473 (1965).
278. G. A. Surkov and V. I. Krylovich, *Inzh. Fiz. Zh.* (In Russian) **7,** 80 (1964).
279. W. Jaworski, *Astronaut. Acta* **12,** 127 (1966).
280. I. N. Sneddon, "Fourier Transforms," p. 162. McGraw–Hill, New York, 1951.
281. I. J. Kumar, *Proc. Nat. Inst. Sci. India* **26,** 414 (1960).
282. I. J. Kumar, *Proc. Nat. Inst. Sci. India* **28,** 325 (1962).
283. I. J. Kumar, and V. R. Thiruvenkatachar, *Indian J. Math.* **3,** 47 (1962).
284. M. Matsumoto, *Publ. Astronaut. Soc. Japan* **18,** 456 (1966).
285. M. Matsumoto, *J. Math. Anal. Appl.* **21,** 445 (1968).

This Page Intentionally Left Blank

Heat Transfer from Tubes in Crossflow

A. ŽUKAUSKAS

Academy of Sciences of the Lithuanian SSR, Vilnius, USSR

I. Introduction 93
II. Flow Past a Single Tube 95
A. Flow of an Ideal Fluid 95
B. Flow of a Real Fluid 96
C. Flow in a Restricted Channel 103
III. Flow Past a Tube in a Bank 105
A. General Flow Pattern 105
B. Velocity Distribution 107
C. Drag of a Tube in a Bank 111
IV. Influence of Fluid Properties on Heat Transfer 112
A. Influence of Prandtl Number 112
B. Choice of Reference Temperature 113
V. Heat Transfer of a Single Tube 116
A. Local Heat Transfer 116
B. Mean Heat Transfer 126
C. Heat Transfer of a Tube in a Restricted Channel 132
VI. Heat Transfer of a Tube in a Bank 133
A. Local Heat Transfer 133
B. Mean Heat Transfer 138
VII. Hydraulic Resistance of Banks 150
A. Resistance Calculation Methods 150
B. Mean Resistance of Banks 151
C. Proposals for Calculations of Hydraulic Resistance 154
VIII. Calculation of Banks of Tubes in Crossflow 155
Nomenclature 158
References 158

I. Introduction

The present article is devoted to the heat transfer and hydraulic resistance of single tubes and banks of tubes of various arrangement in flows of gases and viscous liquids. The process of heat transfer from tubes in crossflow

has been extensively studied. However, recent developments in the field of boiler equipment required more detailed information about the heat transfer of single tubes and banks of tubes in flows of gases than was available. Most of the previous experiments were carried out in flows of air, as its physical properties scarcely differ from those of smoke gases.

Earlier investigations were concerned with the heat transfer of a single tube [1, 2] as well as with the intensity of the heat transfer of a tube in the inner rows of a bank [3, 4]. These were followed by detailed investigations of the influence of the geometrical parameters of banks on heat transfer [5–7]. The results led to the conclusion that the intensity of the heat transfer of a tube in a bank is higher than that of a single tube, and depends on the arrangement of tubes in a bank.

At the same time the development of similarity theory improved the methods of generalization of test data. In the twenties and thirties the calculation formulas, including dimensionless groups, became commonly used. Similarity theory, as applied to the process of convective heat transfer, not only suggested the necessary direction of experiments, but also supplied a common basis for the generalization and analysis of the experimental data obtained by different authors, and yielded the relations suitable for practical calculations.

According to the results of numerous investigations and the wide generalizations of Antuf'yev and Kozachenko [8], Grimison [9] and other workers [10, 11], Kuznetsov [12] and other authors suggested even more general relations for the calculations of heat transfer and hydraulic resistance of banks of tubes in a crossflow of gas, which have been widely applied in the design of steam power boilers.

Further investigations of flow past a single tube and its heat transfer [13–16] facilitated the understanding of the physical phenomenon of heat transfer in banks of tubes in crossflow, the development of thermoanemometry, and the solution of other technical problems. Several books appeared, in which extensive information was presented and summarized. Those by Antuf'yev and Beletsky [17], Kays and London [18], and Gregorig [19] are the first to be mentioned.

The works mentioned above dealt only with heat transfer in flows of gases and only with in a moderate range of Reynolds numbers. Recent accelerated development of science and technology has revealed a number of new problems in the field of heat transfer of tubes in crossflow. A need for reliable formulas for the calculation of the heat transfer of tubes in flows of gases at high Reynolds numbers became apparent. The fast growth of chemical and power industries and the emergence of some new branches of engineering caused an increased interest in heat transfer in flows of viscous fluids at higher Prandtl and Reynolds numbers.

The shift to higher temperatures and forced heat fluxes requires more precise studies of local heat transfer and flow patterns, as well as the need to consider the influence of heat flux direction, temperature, and other factors on the intensity of heat transfer. More important became the choice of the reference temperature, to which physical properties, included in similarity criteria, are related.

In the last decade, the investigation of heat transfer and hydraulic resistance of tubes in flows of gases and viscous liquids at high Reynolds numbers has been extensively carried out at the Institute of Physico-Technical Problems of Energetics of the Academy of Sciences of Lithuanian SSR and in other research centers. In particular, the heat transfer of tubes in crossflow of gases at high Reynolds numbers has been investigated at the Institute für Reaktobauelemente Kernforschungsanlage (Julich, West Germany). Interesting methods of investigation have also been developed at the Boris Kidrič Institut (Belgrad, Yugoslavia). Results of these and other new investigations will be discussed below. Some of the problems are at least partially considered in the book by Žukauskas *et al.* [20] that has recently appeared.

In the present chapter we shall be concerned with important problems of heat transfer and the hydraulic resistance of tubes as mentioned above, and in particular with the heat transfer of single tubes, banks of tubes, and systems of tubes in crossflow. In connection with this, separate sections will be devoted to the influence of the physical properties of fluids on heat transfer. Extensive experimental data will be analyzed and will include investigations of banks of tubes of various arrangements and a single tube in crossflow in the range of Prandtl number from 0.7 to 500 and that of Reynolds number from 1 to 2×10^6.

Heat transfer is considerably influenced by the flow regime around the tube, while flow past banks of tubes is one of the most complicated problems of practical importance. Knowledge of these processes will enable us to carry out more extensive studies of heat transfer. Therefore, before discussing problems of heat transfer, we shall first consider descriptions of flow past a single tube and a tube in a bank.

II. Flow Past a Single Tube

A. Flow of an Ideal Fluid

The theory of an ideal fluid is based on assumptions of a possibility of slip between the fluid and the wall and of the absence of internal friction.

The velocity distribution in a flow of an ideal fluid past a tube is expressed by

$$u_x = u_0 \sin \phi[1 + (R_0/R)^2], \tag{1}$$

where R_0 and R are distances from the tube axis to its surface and to the point considered, respectively, and u_0 is the velocity of the main flow. It is obvious from Eq. (1) that the tangential velocity u_x decreases as the distance from the surface increases, e.g., at $R = 2R_0$ it constitutes 1.25 of u_0 and reaches its maximum value on the tube surface:

$$u_x = 2u_0 \sin \phi. \tag{2}$$

Equation (2) suggests that the fluid velocity is zero in the front and rear stagnation points and reaches its maximum at $\phi = 90°$. By use of Eq. (2) and Bernoulli's equation, the pressure distribution on the tube surface can be determined from

$$P = \frac{p_{x=\phi} - p_0}{\rho u_0^2/2} = 1 - 4 \sin^2 \phi, \tag{3}$$

where p_0 is the static pressure in the channel.

Pressure is inversely proportional to velocity, i.e., it is a maximum at stagnation points and a minimum in the main cross section. It follows from the symmetrical pressure distribution on the tube surface that the tube offers no resistance to the flow of an ideal fluid (d'Alembert paradox).

B. Flow of a Real Fluid

1. *General Flow Pattern*

Because of the viscosity of real fluids, on the front portion of the tube a laminar boundary layer is formed, the thickness of which increases downstream. According to the ratio of inertial and viscous forces in the flow, characterized by its Reynolds number, several types of flow regimes can be distinguished.

At $\mathrm{Re} < 1$ inertial forces are negligibly small as compared to frictional forces [21], and if the tube is streamlined, the laminar boundary layer separates from the surface at the rear stagnation point.

With increasing Reynolds number, the relative influence of inertial forces increases, and at $\mathrm{Re} > 5$ the laminar boundary layer separates the tube surface without reaching the rear stagnation point. Behind the tube there appears a symmetrical pair of stable vortices which form a circulation region confined by flow lines. With a further increase in Reynolds number the vortices become extended downstream, and at $\mathrm{Re} > 40$ the stability of

movement in the circulation region is lost, and the vortices are periodically shed from the rear of the tube.

The phenomenon of boundary layer separation is due to internal friction within the boundary layer, and is closely connected with the pressure and velocity distribution around the tube. As is known, a certain amount of energy is consumed in overcoming the internal friction in the boundary layer and thus dissipated. With a velocity decrease and pressure increase over the rear portion of the tube ($dp/dx > 0$) the remainder of the energy does not suffice to overcome the increased pressure. Fluid particles of the boundary layer that have low velocity because of friction become even slower, until they eventually stop and start moving in the opposite direction. Fluid sheets of opposite movement begin to curl, and give rise to vortices that shed from the tube. The boundary layer separation point is at approximately $\phi = 80°$. This flow pattern is observed up to the critical Reynolds number of 2×10^5.

With a further increase of Reynolds number, the boundary layer becomes turbulent and receives additional energy from the main flow through turbulent fluctuations. This results in the displacement of the turbulent boundary layer downstream. The separation point, according to measurements in air flow by Achenbach [22], is removed to $\phi = 140°$. At $\mathrm{Re} = 2 \times 10^6$ (Fig. 1) the separation point is moved up to $\phi = 115°$ and the supercritical flow regime is established.

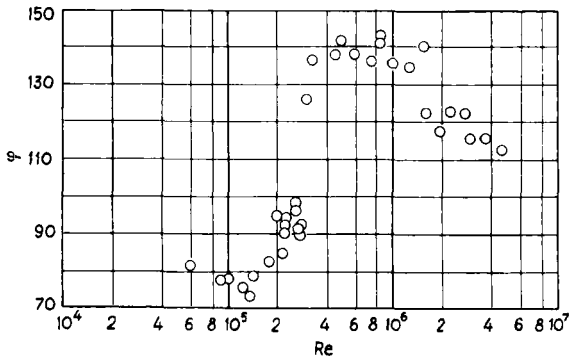

FIG. 1. Position of the separation point on a tube as a function of Re [22].

Transition from a laminar to a turbulent boundary layer is due to the loss of stability in the flow, which depends on the thickness of the laminar boundary layer and the shape of velocity profile that is directly determined by the pressure gradient. In [23] the points of loss of stability in flows past different bodies have been calculated. It is interesting to note that on a circular tube, the displacement of the point of transition with change of

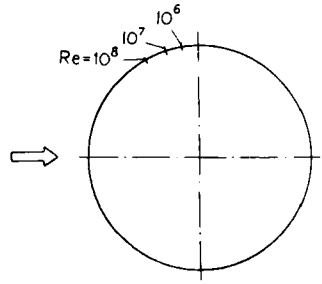

FIG. 2. Instability point in the boundary layer on a tube as a function of Re.

Reynolds number is not large (Fig. 2). At very high Reynolds numbers the point of loss of stability and subsequent transition to turbulent flow is at $\phi = 75°$.

2. *Flow in the Wake*

As noted above, at $Re > 40$ a vortex path is formed behind the tube. It appears as the result of a loss of stability in the circulation region, formed previously by a pair of vortices. With Reynolds number increasing further, a regular path of staggered vortices is observed in the wake. According to measurements of Roshko [24], velocity fluctuations in the wake have a distinct periodicity, noted even at a considerable distance behind the tube. Interaction between vortices and fluid in the wake does not disturb the flow in the range of Reynolds number up to 150. With a further increase in Reynolds number, irregular velocity fluctuations in the wake are observed. These give rise to small vortices which are formed at a certain distance from the tube, and are destroyed much earlier than the ones formed from the laminar layer.

At $Re > 300$, vortices formed behind the tube consume only a certain part of the energy of disturbances of the separated boundary layer. The rest of the energy dissipates in the wake in the form of small turbulent vortices. This flow pattern persists up to the critical regime. In the supercritical regime regular fluctuations are superimposed on the turbulent ones.

Thus in a flow with regular vortex shedding there is a constant and intensive exchange of substance and momentum between the circulation region and the undisturbed flow. At $Re < 40$ there is only molecular exchange as the vortices are not shed.

Periodicity of vortex shedding is characterized by the Strouhal number, which establishes the relation between vortex shedding frequency, cylinder diameter, and main flow velocity:

$$Sh = fD/u_0.$$

It is obvious from Fig. 3 that with increasing Reynolds number, the Strouhal number increases up to 0.2 but is practically constant in the range of Re from 10^3 to 2×10^5. In the critical regime, the Strouhal number increases greatly up to 0.46. In the supercritical regime it decreases to 0.25, as reported in Roshko [25].

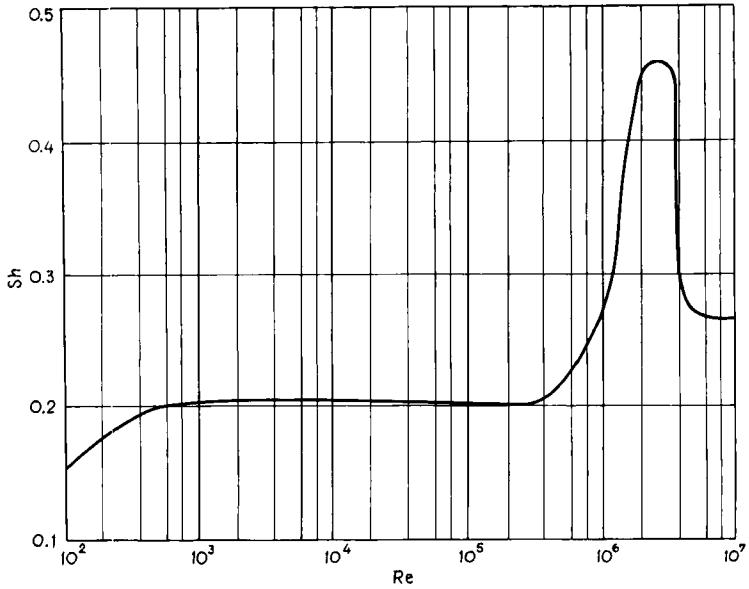

FIG. 3. Dependence of Sh for a tube on Re.

Flow analysis reveals that in the predominant range of Reynolds number vortices are shed intermittently from the two sides of the tube and symmetrically to the wake axis. Periodical and asymmetrical variations in pressure distribution on the surface give rise to forces of intermittent direction, which lead to crosswise vibration of the tube [26]. This has to be taken into account in the design of heat exchangers.

3. *Velocity Distribution Around the Tube*

The variations in the hydrodynamic conditions in the flow around the tube are illustrated by the distribution of pressure and local velocity.

Figure 4, compiled from experimental data of various authors, shows that up to $\phi = 50°$ the distribution of pressure as well as of local velocity around the tube outside the boundary layer does not depend on Reynolds number and correlates well with calculations according to Eq. (3). The influence of Reynolds number begins at $\phi > 50°$. The solid circles in the

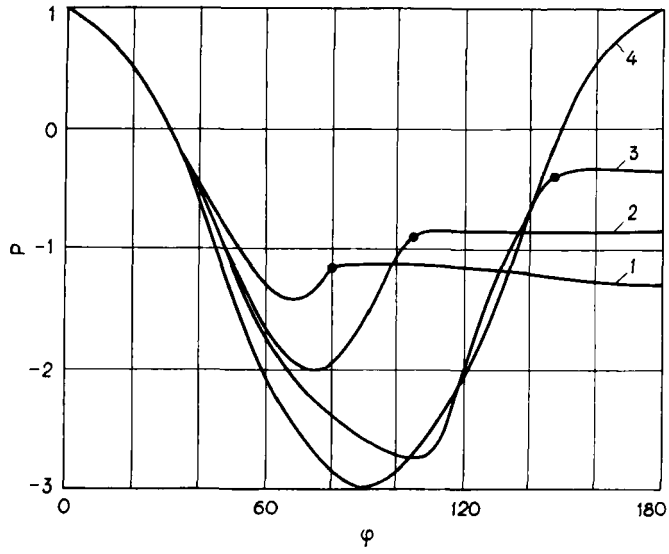

FIG. 4. Distribution of pressure coefficient $P = (p_{x=\phi} - p_0)/(\rho u_0^2/2)$ around a tube at various Re. Curve 1—Re = 1.1×10^5, after Fage and Folkner [27]; curve 2—8.4×10^6, after Roshko [25]; curve 3—8.5×10^5, after Achenbach [22]; curve 4—potential flow.

figure represent the points of boundary layer separation. The location of these points is characterized by the angle ϕ at which the pressure downstream is stable and constant.

From measurements of pressure on the surface and by the use of Bernoulli's equation, the velocity distributions on the outer edge of the boundary layer can be determined. The velocity distribution in a real fluid differs considerably from that in an ideal fluid because of the displacement of the main flow by the boundary layer and the complicated vortical flow in the wake.

A regular velocity distribution outside the boundary layer is characteristic only for the front portion of a tube and is expressed by

$$u_x/u_0 = 3.631(x/D) - 2.171(x/D)^3 - 1.514(x/D)^5. \quad (4)$$

4. *Drag of the Tube*

The total drag D_f of the tube is equal to the sum of the forces of friction and pressure. At very low Reynolds numbers the tube is streamlined. According to theoretical calculations [21] and measurements, frictional forces prevail in the drag.

With an increase in Reynolds number, the relative influence of inertial forces increases and that of frictional forces becomes negligibly small. In

the range of an intensive vortical flow past a tube, the frictional drag constitutes just a few percent of the total drag. Nevertheless, the flow pattern may be judged from the frictional distribution around the tube. Data of different authors (Fig. 5) for air flow suggest an increase of friction from

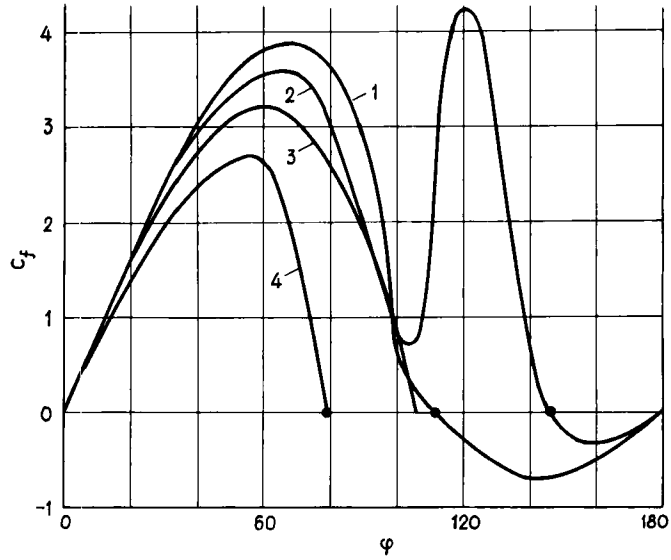

FIG. 5. Distribution of skin friction coefficient $c_f = (\tau/\rho u_0^2)\sqrt{\mathrm{Re}}$ around a tube at various Re. Curve 1—Re = 8.5×10^5 and curve 2—3.6×10^6, after Achenbach [22]; curve 3—the calculation curve; curve 4—1.1×10^5, after Fage and Folkner [27].

zero to a maximum at $\phi = 60°$ and a subsequent decrease to a minimum. The solid circles represent boundary layer separation points, where friction is equal to zero. The first minimum of the curve at Re = 8.5×10^5 corresponds to the boundary layer transition from laminar to turbulent flow.

Figure 6 shows the variation of frictional drag of a heated tube in air flow as measured by Žiugžda and Ruseckas [28]. A definite influence of heating on frictional drag can be noticed.

From the position of the separation points on the tube, the width of the circulation region and consequently the pressure drag may be determined. Pressure drag is caused mainly by boundary layer separation and depends on the width of the circulation region and the frequency of vortex shedding. The maximum width of the vortex region in the subcritical flow regime corresponds to the maximum pressure drag coefficient and minimum Strouhal number, and in the critical flow regime the minimum width of the vortex region corresponds to the minimum pressure drag coefficient and maximum Strouhal number.

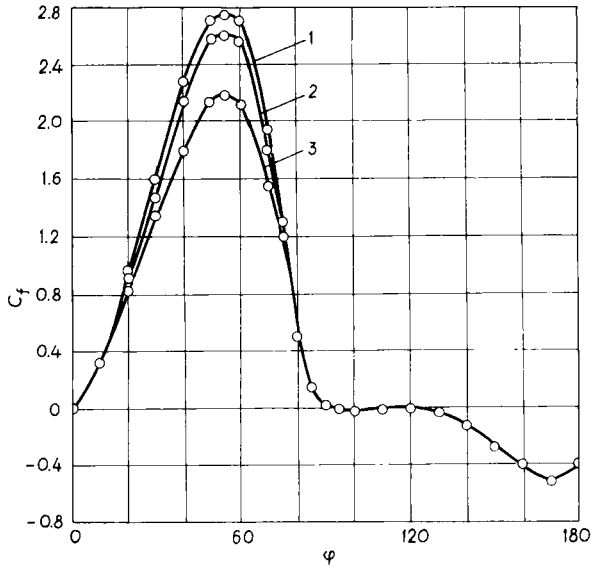

FIG. 6. Distribution of skin friction coefficient around a tube in the presence of heat transfer at Re = 5.2×10^4. Curve 1—$\Delta t = 50°C$; curve 2—$\Delta t \cong 30°C$; curve 3—$\Delta t \cong 0$.

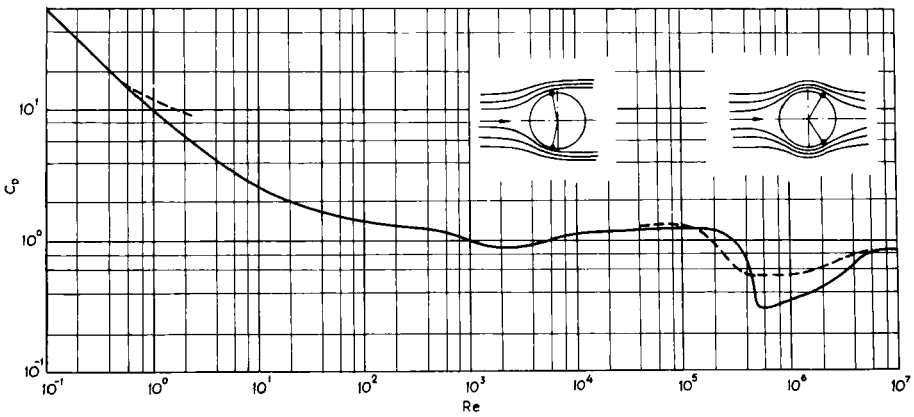

FIG. 7. Drag coefficient of a tube $C_D = D_f/(\rho u_0^2\, DL/2)$ as a function of Re.

The general flow pattern past a tube is reflected in the variation of drag coefficient C_D with Reynolds number. It is clear from Fig. 7 that the dependance of C_D on Re in the range of the subcritical regime is negligible and at $Re > 2 \times 10^5$ the drag coefficient decreases sharply. This is because the boundary layer separation point is moved downstream, as mentioned above, and with the convergence of the wake, the drag decreases considerably. The dotted line at low Reynolds numbers corresponds to calculations of potential flow past a tube [21].

Turbulence in the main flow exerts a certain influence on the flow pattern around immersed bodies. In the subcritical regime turbulence has no effect on the drag coefficient, but in the range of the critical regime the variation of drag coefficient, indicated by a dotted line in Fig. 7, depends on the turbulence. The origin of the critical flow regime is displaced to lower Reynolds numbers, with an increase of turbulence.

A rough surface of the immersed tube has a similar influence on the drag coefficient and flow pattern. As the relative roughness of the surface increases, the Reynolds number at which the critical flow regime is established decreases. On the other hand, the presence of roughness increases the drag coefficient C_D in the critical flow regime.

C. FLOW IN A RESTRICTED CHANNEL

In practice, circular tubes are usually placed in flows restricted by walls and with considerable blockage of the flow cross section (Fig. 8). In the case of a circular tube in a channel, blockage is expressed by the ratio D/H.

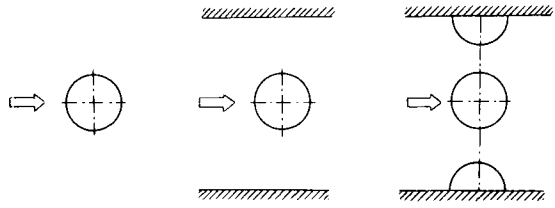

FIG. 8. Different conditions of flow past a tube.

As the blockage ratio increases, the velocity around the tube outside the boundary layer increases, and the pressure and velocity distribution are changed accordingly.

In Fig. 9 the velocity distribution for a distance of 4.2 mm over the tube surface is represented as measured by [29] at a main flow velocity of 20 m/sec and for blockage ratios of 0.39 and 0.63. In the separation region particles of fluid near the surface move in the opposite direction, as seen from Fig. 9.

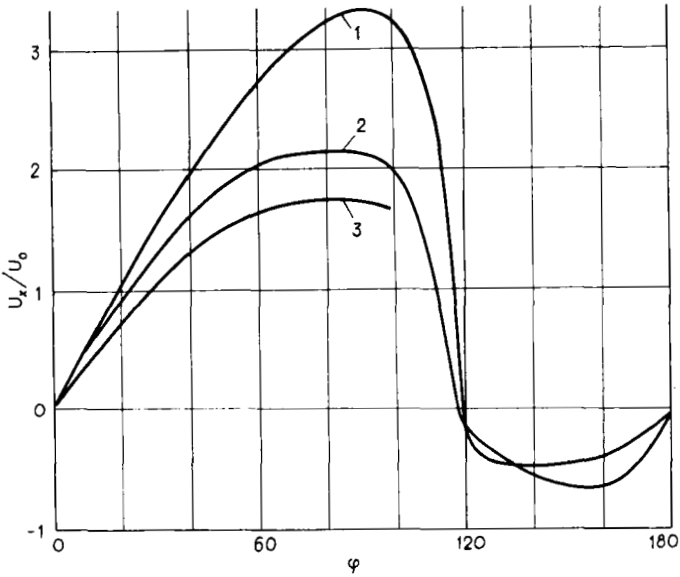

FIG. 9. Velocity distribution around a tube. Curve 1—$D/H = 0.63$, and curve 2—$D/H = 0.39$, after Akilba'yev *et al.* [29]; curve 3—$D/H = 0.16$, after Perkins and Leppert [30].

As was stated by the same author, the increasing blockage ratio from 0 to 0.8 causes the minimum pressure point to be displaced from $\phi = 70°$ to 90°, and the separation point moved downstream to $\phi = 100°$.

The change in blockage ratio alters flow patterns in the wake. Periodical vortex shedding in the rear is observed at low blockage ratios. At higher ratios exceeding 0.6 unperiodical vortex flow behind the tube [29] is established. As a consequence, the drag coefficient C_D increases sharply.

To take into account the blockage ratio, the mean velocity in the minimum free cross section of the channel is usually used as a reference in technical calculations of heat transfer and drag.

$$u = [1/(1 - D/H)]u_0, \tag{5a}$$

where u_0 is the velocity of an unrestricted flow.

This choice of reference velocity, however, allows no comparison between drag and heat transfer in systems of tubes in various arrangements since different velocity distributions on the surface are not taken into account. Calculated reference velocities may be the same on a tube in an unrestricted flow, a tube in a channel, and one in the first row of a bank, velocities in the front portion being different. For this reason, the introduction of an

average velocity seems reasonable, i.e., the average value of the velocity evaluated by integrating over the cylinder surface,

$$u = \frac{1}{l}\int_0^l u(x)\,dx \tag{5b}$$

or

$$u = u_0\left(1 - \frac{\pi}{4}\frac{D}{H}\right)^{-1}. \tag{5c}$$

At high blockage ratios, the flow pattern is basically changed, and the above mentioned reference velocities are no longer applicable in determining drag and heat transfer coefficients. Thus in the calculation of drag and heat transfer at $D/H > 0.8$ various semi-empirical equations [29, 30] are recommended for the evaluation of a reference velocity.

III. Flow Past a Tube in a Bank

A. General Flow Pattern

The flow pattern around a tube in a bank is influenced by the surrounding tubes. In a contraction between adjacent tubes of a transverse row, the pressure gradient changes even more. This causes a corresponding change of velocity distribution in the boundary layer and of the flow pattern in the rear.

The flow pattern around a tube in a bank is determined by the arrangement and geometrical parameters of the bank. Banks of in-line and a staggered arrangement of tubes are most common (Fig. 10), and they are usually defined by the relative transverse $a = s_1/D$ and longitudinal $b = s_2/D$

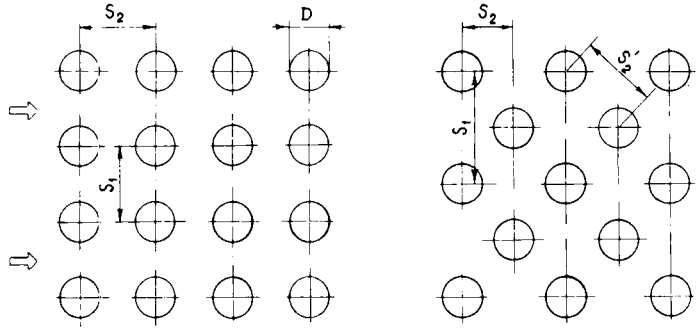

FIG. 10. Arrangement of tubes in a bank.

center-to-center distances, called transverse and longitudinal pitches, respectively. In banks of both arrangements, flow around a tube in the first row is similar to that around a single tube, but the flow pattern in subsequent rows is different.

In staggered banks, the flow is comparable with flow in a curved channel of periodically converging and diverging cross section. Thus the velocity distributions around tubes in different rows in a staggered bank have a similar character. Flow in an in-line bank is sometimes comparable with that in a straight channel. The velocity distribution in the minimum cross section of an inner row is mainly determined by the pitch ratio. Two extreme cases of the relative longitudinal pitch equal to unity and to infinity can be noted here. Flow in the first case is closely similar to a flow in a channel, and in the other case it is a flow through a single transverse row, with the velocity profile of the flow behind the preceding row being straightened. In intermediate cases, inner rows are located in the circulation regions of the preceding rows, and the flow preceding one of the inner rows is vortical with a nonuniform velocity distribution.

At low Reynolds numbers the flow in a bank is laminar with large scale vortices in the circulation regions, their effect on the boundary layer of the front portion of a subsequent tube being eliminated by viscous forces and a negative pressure gradient. The flow in the boundary layer is laminar. Such a flow pattern existing at $\mathrm{Re} < 10^3$ may be described as predominantly laminar.

With increasing Reynolds number, the flow pattern in a bank undergoes considerable variations. The flow between tubes becomes vortical with a higher degree of turbulence. Although the front portion of an inner tube is influenced by the vortical flow, a laminar boundary layer persists on it. The pattern of flow, with a laminar boundary layer on the tube being under the influence of a turbulent flow and with an intensive vortical flow in the rear, may be described as mixed.

The production of turbulence and its intensity in a bank depends on the bank arrangement and Reynolds number. In banks of large longitudinal pitches, the transition from laminar to turbulent flow in the bank is gradual and depends on the increase in Reynolds number. The flow in the bank consists initially of large scale vortices, the size of which decreases with increasing velocity. Thus in the range $10^3 < \mathrm{Re} < 10^4$ there may exist a flow pattern intermediate between the predominantly laminar and the mixed one.

In staggered banks with small longitudinal pitches at $\mathrm{Re} > 10^3$ small vortices appear suddenly and flow in the bank becomes turbulent instantly.

The mixed flow regime covers a wide range of Reynolds numbers and alters its character only at $\mathrm{Re} > 2 \times 10^5$. Then flow in the bank becomes

highly turbulent. The total drag of the bank varies like that of a single tube in the critical flow regime.

Thus we may distinguish three flow regimes in banks with respect to the Reynolds numbers: a predominantly laminar flow regime at $\mathrm{Re} < 10^3$, a mixed or subcritical flow regime at $5 \times 10^2 < \mathrm{Re} < 2 \times 10^5$, and a predominantly turbulent or critical flow regime at $\mathrm{Re} > 2 \times 10^5$.

B. VELOCITY DISTRIBUTION

Pressure and velocity distributions around a tube in a longitudinal row of a bank differ substantially from that around a single tube. Figure 11

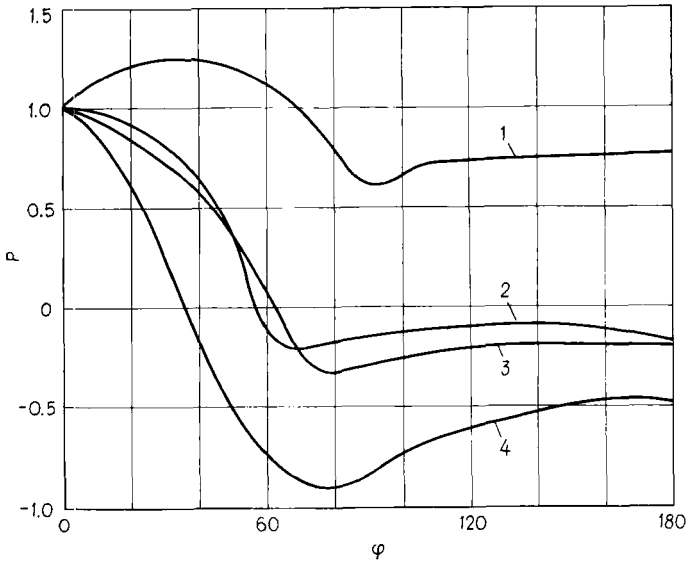

FIG. 11. Distribution of pressure coefficient $P = 1 - [(p_{\phi=0} - p_\phi)/(\rho u^2/2)]$ on a tube in a bank [31]. Curve 1—fourth, and curve 2—first rows of an in-line bank; curve 3—first, and curve 4—fourth rows of a staggered bank.

illustrates the variation of pressure coefficient around tubes in the first and the fourth rows of in-line and staggered banks for $a = 2.0$ and $b = 2.0$ at $\mathrm{Re} = 10{,}800$ [31]. The pressure coefficient for a tube in a bank is given by

$$P = 1 - [(p_{\phi=0} - p_\phi)/(\rho u^2/2)], \tag{6}$$

where u is the mean velocity in the minimum free cross section.

Equation (3) does not apply to the determination of pressure coefficient variation for a tube in a bank, because the static pressure varies considerably along a bank.

It is obvious that flow around tubes in the first row is similar to that around a single tube in the subcritical flow regime. But on any of the inner tubes of a staggered bank, the pressure in front of the separation point is higher than that on a single tube. In inner rows of an in-line bank, the maximum pressure point is at about $\phi = 40°$ where the impact of the main stream on the tube surface occurs. Thus there are two impact points and two maximum pressure points on any of the inner tubes of an in-line bank. It has been noticed by Bressler [31] that for in-line banks of small pitch the pressure at one of the points is higher. From the third row on, the reciprocal positions of the minor and major pressure points interchange from row to row.

For in-line banks, the position of the impact point is dependent on the longitudinal pitch and Reynolds number. An investigation [32] of the pattern in the wake behind the tube at Re = 13,000 is interesting in this respect. The distance between the two tubes was changed in the range $1.6 < L/D < 9$. Figure 12 shows a qualitative change of pressure distribution along the perimeter of the second tube for $L/D \leqslant 3$, substantially differing from that of a single tube in an infinite flow. For $L/D = 6$ the point of attack and impact point coincide at $\phi = 0$, and for $L/D = 1.6$ the

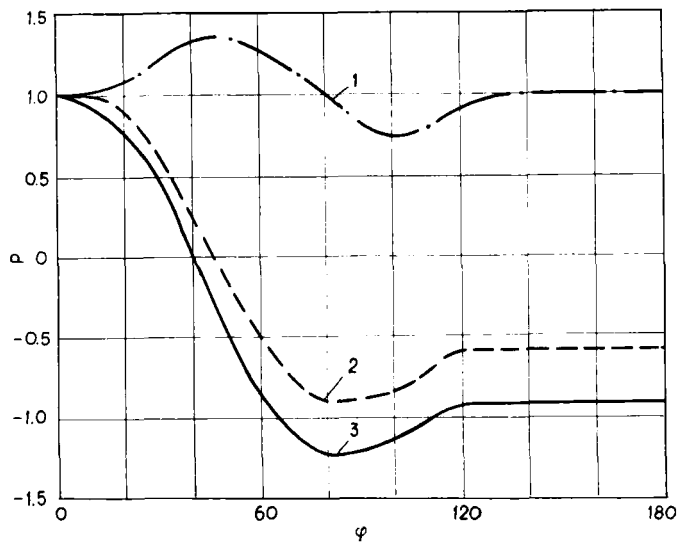

FIG. 12. Variation of pressure coefficient as a function of longitudinal pitch [32]. Curve 1—$L/D = 3$; curve 2—$L/D = 6$; curve 3—$L/D = 9$.

impact point is removed to $\phi = 75°$. The general flow pattern based on the results of [32] is illustrated in Fig. 13.

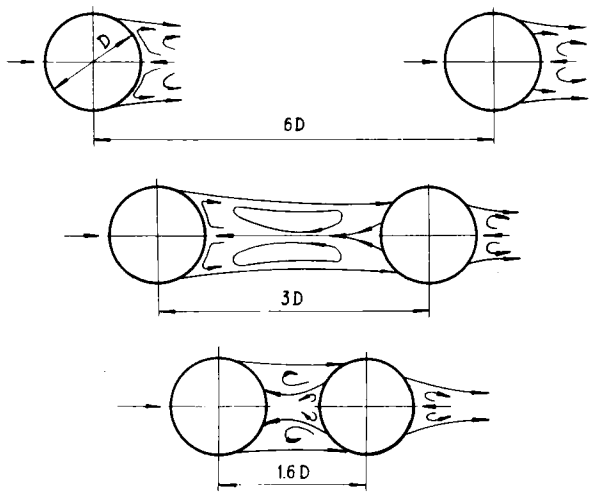

FIG. 13. Pattern of flow past a tube in a longitudinal row.

The position of the impact point is also influenced by Reynolds number. Investigation [20] of flow around a tube in the inner rows of the in-line bank, 2.0 × 1.3, suggests that for low Reynolds numbers the impact point is close to the front stagnation point, but with an increase of Re to 4000 it is removed to $\phi = 55°$, and later at Re > 4000 again to the front (Fig. 14). Figures 13 and 14 imply that for in-line banks, laminar boundary layers develop from the two impact points and separate from the tube at approximately $\phi = 145°$. Sometimes there is a laminar–turbulent transition in the boundary layer.

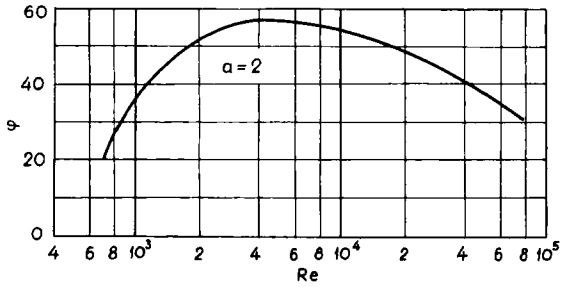

FIG. 14. Position of the impact point on a tube in a bank of in-line arrangement as a function of Re.

In the case of flow around a tube in staggered banks, as in the case of a single tube, the flow is divided at the front stagnation point and a laminar boundary layer develops on the front portion of an inner tube. Figure 15 suggests a certain influence of Reynolds number on pressure distribution of an inner tube in the staggered bank. The position of the boundary layer

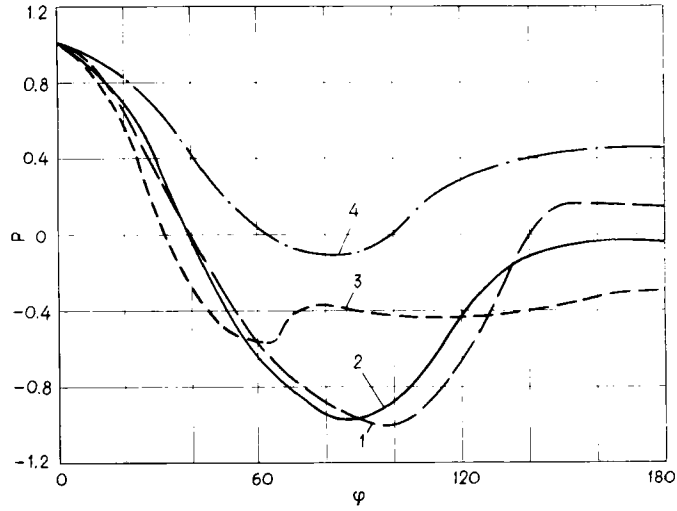

FIG. 15. Distribution of pressure coefficient in inner rows of staggered banks as a function of Re. Curve 1—second, and curve 2—fourth row of bank, 2.0 × 1.4, at Re = 1.5 × 10^6 [33]; curve 3—second, and curve 4—fourth row of bank, 2.2 × 1.5, at Re = 2.7 × 10^4 [34].

separation point in this case differs from that of a single tube because the transition from a laminar to a turbulent boundary layer moves this point to $\phi = 150°$. At high Reynolds numbers [33] the position of the separation point (Fig. 16) is somewhat different.

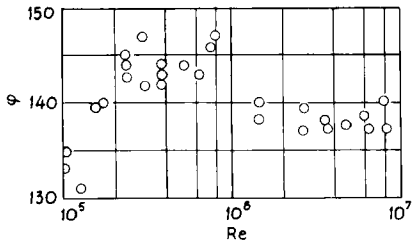

FIG. 16. Position of the separation point on a tube in a staggered bank as a function of Re [33].

In studies of the velocity distribution in banks, the influence of the transverse pitch should be mentioned. With a decrease of the transverse pitch, the velocity in the free cross section increases rapidly. The calculations of mean velocity in the minimum free cross section, as a function of the transverse pitch, may be based on the constant rate of volume

$$u = u_0[a/(a - 1)]. \tag{7}$$

The mean velocity in any free cross section is then calculated by

$$u_\phi = u_0[a/(a - \sin \phi)]. \tag{8}$$

Theoretical calculations of velocity distributions, as well as their determination by the method of electrical analogy for a potential flow through a row, yield velocity profiles in the minimum free cross section which have a more or less pronounced concave shape in the central part, their values depending on the transverse pitch.

In the flow of a real fluid through a row, under the influence of viscous forces, boundary layers are formed on the surface. The velocity near the surface decreases, the velocity profiles are straightened, and the concave shapes in the curves diminish accordingly. Plots of pressure distribution imply that velocity distributions around a tube in a longitudinal row differ substantially from that of a single tube. Changes of the longitudinal pitch cause considerable changes in velocity distributions on the front and rear portions of an inner tube.

C. DRAG OF A TUBE IN A BANK

Figure 17 shows the distribution of skin friction around a tube in a bank as a function of Reynolds number [33]. The effect of Reynolds number on

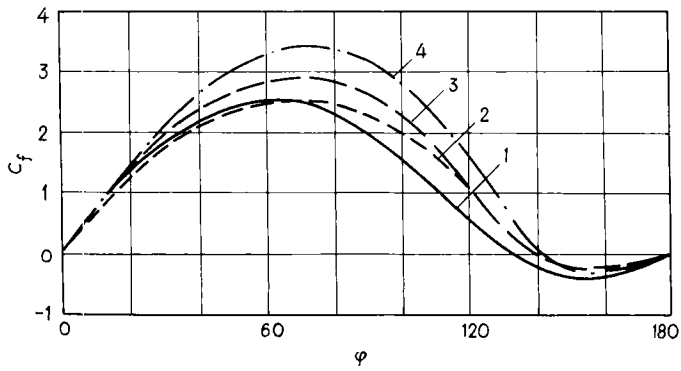

FIG. 17. Distribution of skin friction coefficient $c_f = (\tau/\rho u^2)\sqrt{\mathrm{Re}}$ on a tube in a staggered bank, 2.0 × 1.4, [33]. Curve 1—Re = 1.3×10^5; curve 2—Re = 8.0×10^6; curve 3—Re = 3.7×10^5; curve 4—Re = 1.4×10^6.

the friction is most evident in the region $60° < \phi < 75°$. The friction drag of a tube in a bank constitutes only about 5% of the total drag, and in the critical flow regime it decreases to about 0.5%. Surface roughness causes an increase of friction drag in the critical flow regime.

The pressure drag of a tube in a bank is determined mainly by the longitudinal pitch. In an in-line bank for $b < 3$ under the influence of the preceding tube, the pressure drag decreases suddenly. The hydraulic resistance of banks of tubes will be generally considered in Section VII.

IV. Influence of Fluid Properties on Heat Transfer

The heat transfer of a single tube and a tube in a bank is determined mainly by flow velocity, physical properties of the fluid, heat flux intensity, heat flux direction, and the arrangement of the tubes. The dimensionless relation is as follows

$$\mathrm{Nu} = f\left(\mathrm{Re}, \mathrm{Pr}, \frac{\mu_f}{\mu_w}, \frac{\lambda_f}{\lambda_w}, \frac{c_{pf}}{c_{pw}}, \frac{\rho_f}{\rho_w}, \frac{s_1}{D}, \frac{s_2}{D}\right). \tag{9}$$

For the generalization of experimental data the following power equation based on the functional relation (9) is commonly used

$$\mathrm{Nu} = c\mathrm{Re}^m\mathrm{Pr}^n. \tag{10}$$

For gases of equal atomicity, i.e., for which the Prandtl numbers are equal and constant, Eq. (10) becomes

$$\mathrm{Nu} = c\mathrm{Re}^m. \tag{11}$$

A. Influence of Prandtl Number

Most of the fluids commonly used in practice have Prandtl numbers ranging from 1 to 1000. This means that in calculations of heat transfer a wrong choice of power index of Prandtl number may lead to considerable errors. A power index of Prandtl number equal to 0.31–0.33 is still accepted by some authors. This value of n is suggested by theoretical investigations of heat transfer in a laminar boundary layer on a plate. However, later calculations and experimental measurements [35, 36] have revealed the dependence of the power index of the Prandtl number on the flow regime in the boundary layer. For a laminar boundary layer on a plate $n = 0.33$, but for a turbulent boundary layer it amounts to 0.43.

The above suggests that for mean heat transfer from a tube the value of n may be somewhere between 0.33 and 0.43.

Investigations of heat transfer in laminar and turbulent boundary layers suggest certain changes in the value of the power index with large variations of Prandtl number. Numerical solutions of heat transfer in the region of the front stagnation point, performed by V. Makarevičius and the author, gave $n = 0.37$ for $Pr < 10$ and $n = 0.35$ for $Pr > 10$.

Our detailed studies of mean heat transfer from a tube in cross flows of transformer oil, water, and air [37] at t_w = const. yielded an approximate value of the power index of the Prandtl number between 0.37 and 0.38. In later investigations of local heat transfer from a tube in flows of various fluids [38] at q_w = const. it was determined that n varies along the tube perimeter, reaching the value of 0.39 in the rear. The mean value of n is equal to 0.365. The mean value of n for a circular tube, 0.37, is acceptable for $Pr < 10$ and somewhat lower for $Pr > 10$.

Our investigations of heat transfer [20] in 27 banks of tubes of different arrangements in flow of various fluids in the range of Pr from 0.7 to 500 suggest (Fig. 18) that for the mean heat transfer of all sorts of banks the

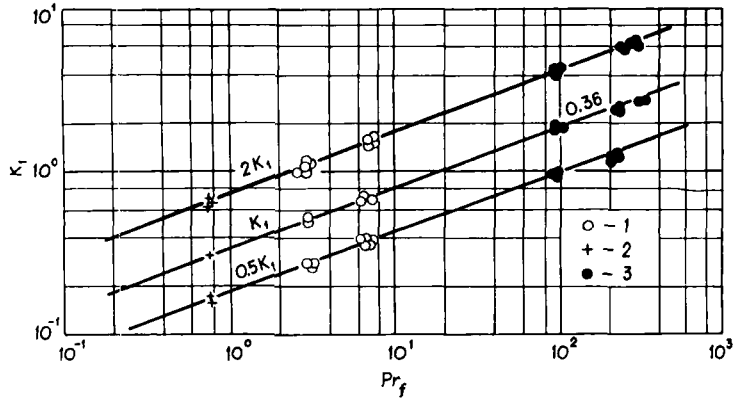

FIG. 18. Determination of the power index n for Pr in various staggered banks. 1—Water; 2—air; 3—transformer oil; $K_1 = Nu_f Re_f^{-0.60}(Pr_f/Pr_w)^{-0.25}$.

power index of the Prandtl number has the value 0.36. In practical calculations of the mean heat transfer of banks of tubes $n = 0.36$ is sufficiently accurate.

B. CHOICE OF REFERENCE TEMPERATURE

In the process of heat transfer, the fluid temperature varies, which causes variations of its physical properties. Thus evaluation of the influence of the

fluid physical properties on heat transfer is closely connected with accounting for the temperature variations in the boundary layer, in other words, with the choice of the so-called reference temperature, according to which the physical properties are evaluated.

The influence of the variations of physical properties may be established by two methods. By the first method the physical properties are referred to the main flow temperature and an additional parameter is introduced in Eq. (10) to account for the properties variation. The second method is to choose a certain value of temperature between that of the flow and the wall, which enables evaluation of the influence of the physical properties on heat transfer. In this case the relations for the heat transfer calculation remain the same as for constant physical properties.

Analysis of relations for heat transfer calculations in the flow of gases, proposed by different authors, shows that the main cause of discrepancies is due to different choices of the reference temperature.

Detailed experimental investigations of heat transfer from a single tube [15] and banks of tubes [39] in the crossflow of gases suggest that the physical properties should be evaluated at the main flow temperature t_f. This generalizes the results of heat transfer in gas flow with sufficient accuracy and no additional parameters for the evaluation of temperature difference are necessary. In investigations of heat transfer of banks of tubes in air at high Reynolds numbers [40] the properties are also referred to the main flow temperature t_f.

A certain mean temperature of the boundary layer has sometimes been proposed as the reference temperature by some authors [9]. We prefer to take the main flow temperature as the reference in the range of moderate temperatures. This method is simple in practice and sufficiently accurate for practical purposes.

In flows of viscous fluids the intensity of heat transfer depends markedly on physical property variation in the boundary layer with heat flux direction and temperature difference. Experimental results referred to the main flow temperature are higher for heating than for cooling, the discrepancy increasing with the increase of temperature difference.

Mikhe'yev [41] has proposed to account for the influence of sharp changes in the physical properties of fluids in the boundary layer near the surface by the ratio Pr_f/Pr_w to the power 0.25. The ratio μ_f/μ_w is often used also. It should be noted that for viscous fluids, like water and oil, it is mainly viscosity that changes with temperature, and therefore $Pr_f/Pr_w \approx \mu_f/\mu_w$. However, calculations of heat transfer in laminar boundary layers on a plate in flows of various fluids [42] lead to the conclusion that the influence of other physical properties constitutes up to 7% of the total influence.

Our investigations [37] confirm that variations of viscosity and other

properties in the boundary layer on a circular tube may well be accounted for by the ratio Pr_f/Pr_w, with a corresponding power index. In this case the results are referred to the main flow temperature.

Computer aided calculations [42] suggest that for a laminar boundary layer on a plate the power index of Pr_f/Pr_w is 0.25 for heating and 0.19 for cooling. It was also found to depend to a certain extent on the value of Pr_w, increasing slightly with high values of the latter. In Fig. 19 the curve and circles correspond to theoretical calculations and experimental measurements [35], respectively.

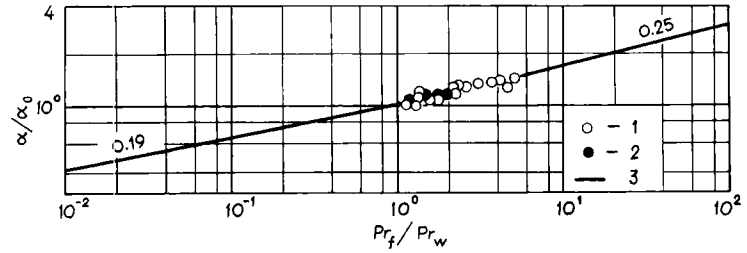

FIG. 19. Local heat transfer of a plate in laminar flow as a function of heat flux direction. 1, 2—heating of water and transformer oil, respectively, after Žukauskas and Žiugžda [35]; 3—calculated curve, after Švenčianas *et al.* [42]; α_0—heat transfer coefficient at constant physical properties.

Our investigations [43] of changes of the power index of Pr_f/Pr_w for the case of a turbulent boundary layer on a plate give $n = 0.25$ for heating and $n = 0.17$ for cooling (Fig. 20). Thus the power index of Pr_f/Pr_w is lower for cooling than for heating. In any case, for most practical purposes, $n = 0.25$ is sufficiently accurate for both cases.

Some other parameters have also been proposed to account for radical changes of physical properties [44]. However, we still prefer the ratio Pr_f/Pr_w as the most simple and convenient to use.

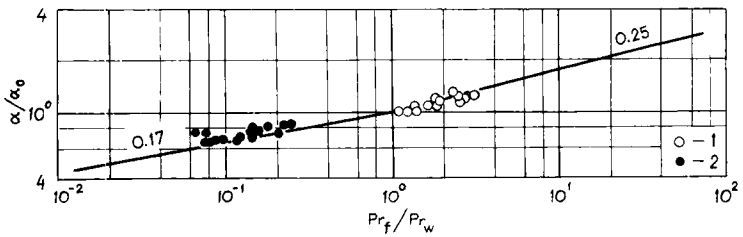

FIG. 20. Local heat transfer of a plate in turbulent flow as a function of heat flux direction. 1—Transformer oil; 2—glycerine.

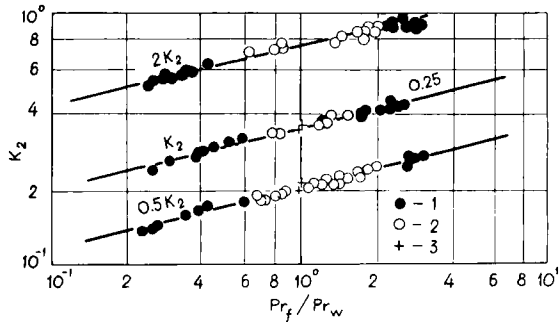

FIG. 21. Determination of the power index for Pr_f/Pr_w in different staggered banks. 1—Transformer oil; 2—water; 3—air; $K_2 = Nu_f\, Re_f^{-0.60}\, Pr_f^{-0.36}$.

In Fig. 21 the changes of intensity of heat transfer in staggered banks as a function of Pr_f/Pr_w are shown from our experiment [20]. When physical properties are referred to the main flow temperature the ratio $(Pr_f/Pr_w)^{0.25}$ accounts satisfactorily for changes of the physical properties both for heating and cooling. For gases with constant Prandtl number, $Pr_f/Pr_w = 1$.

Therefore for the calculation of heat transfer from a tube in the cross-flow of viscous fluids, the following relation will be be used

$$Nu_f = cRe_f^m Pr_f^n (Pr_f/Pr_w)^{0.25}. \tag{12}$$

V. Heat Transfer of a Single Tube

A. Local Heat Transfer

1. *Theoretical Calculations of the Local Heat Transfer*

The analysis presented in Section II suggests that flow past a single tube is a rather complicated process. The same applies to its heat transfer. At various Reynolds numbers the boundary layer on the front portion of a tube is laminar. Therefore theoretical methods for the calculation of heat transfer may be applied. The rear portion is in the region of a complicated vortical flow. Here the theoretical calculation of heat transfer is almost impossible, though some attempts have been made in recent years. Furthermore, the heat transfer in the front stagnation point and in the boundary layer separation region has some peculiar features.

First, the calculations of heat transfer on the front portion of a tube by means of an approximate integral method were performed by Kruzhilin [45]. This method has been used for the calculation of heat transfer from a plate

and in a modified form was applied to the evaluation of heat transfer from the front portion of a tube. The following relation for local heat transfer was obtained

$$\mathrm{Nu}_x = [2/F(\phi)]\mathrm{Re}^{0.5}\mathrm{Pr}^{0.33}, \tag{13}$$

where $F(\phi)$ is a hydrodynamical factor, accounting for the changes in the boundary layer around the tube and the velocity distribution outside the boundary layer. The relation applies only for $\mathrm{Pr} \geqslant 2.6$.

Other theoretical methods have been applied to the heat transfer calculations of wedge-shaped bodies, having a velocity variation outside the boundary layer which is expressed by the exponential relation

$$u_x = cx^{m_1}. \tag{14}$$

These methods can be used only for some definite portions of a circular tube. Thus for the region near the front stagnation point the value of m_1 in Eq. (14) is unity and for the separation region $m_1 = -0.0804$. In the first case, the velocity outside the boundary layer changes linearly along the perimeter.

Boundary layer equations can be applied to the heat transfer from wedge-shaped bodies:

$$\begin{aligned} \rho u \frac{\partial u}{\partial x} + \rho v \frac{\partial u}{\partial y} &= \mu \frac{\partial^2 u}{\partial y^2} - \frac{dp}{dx}, \\ \frac{\partial u}{\partial x} + \frac{\partial v}{\partial y} &= 0, \\ \rho c_p u \frac{\partial T}{\partial x} + \rho c_p v \frac{\partial T}{\partial y} &= \lambda \frac{\partial^2 T}{\partial y^2}, \end{aligned} \tag{15}$$

together with Eq. (14), and with boundary conditions:

$$\begin{aligned} &\text{for} \quad y = 0 \qquad u = v = 0, \qquad T = T_w, \\ &\text{for} \quad y = \infty \qquad u = u_x, \qquad\quad T = T_f. \end{aligned}$$

The flow function

$$\psi = f(\eta)\left(\frac{2}{m_1 + 1} uvx\right)^{1/2}$$

and the following new variables are also introduced

$$\theta = \frac{T - T_w}{T_f - T_w}, \qquad \eta = y\left(\frac{m_1 + 1}{2} \frac{u}{vx}\right)^{1/2}. \tag{16}$$

Equations (15) have been solved for the above conditions by a number of authors. Heat transfer coefficients calculated for different wedge profiles for the range of Prandtl number from 0.7 to 10 were presented by Eckert [46] in the form

$$\mathrm{Nu}_x\sqrt{\mathrm{Re}_x} = 0.56A/\sqrt{2-\beta}. \tag{17}$$

The generalization of calculated data [46] yields the following expression for A:

$$A = (\beta + 0.2)^{0.11}\,\mathrm{Pr}^{0.333+0.067\beta-0.026\beta^2}, \tag{18}$$

where

$$\beta = 2m_1/(m_1 + 1). \tag{19}$$

By substituting for β in Eq. (17), the local heat transfer can be calculated in regions near the front stagnation point and near the separation point assuming the above values of m_1.

For flow past curvilinear bodies, the power index in Eq. (14) may be determined from

$$m_1 = \frac{x}{u_x}\frac{du_x}{dx}, \tag{20}$$

where u_x is the local velocity outside the boundary layer.

For a circular tube in crossflow, the velocity distribution on the front portion is determined from Eq. (4) according to Hiemenz [46]. The power index determined from Eq. (20) accounts for the velocity distribution around the tube decreasing downstream from unity in the front stagnation point to zero and below zero.

For heat transfer at the front stagnation point, the following relation is derived from Eqs. (17) and (18) for $\mathrm{Pr} < 10$:

$$\mathrm{Nu}_x = 0.57\,\mathrm{Re}_x^{0.5}\,\mathrm{Pr}^{0.37}. \tag{21}$$

Equation (18) suggest that the power index of the Prandtl number decreases downstream along the perimeter, reaching the value of 0.3 in the separation region.

Merk [47] proposed a simplified method for heat transfer calculations from the front portion of a tube for $\mathrm{Pr} > 10$. He used only the first term in the polynomial of the influence of Pr and β, neglecting the rest as infinitesimally small at high Prandtl numbers. The relation for heat transfer calculation therefore at the front stagnation point is

$$\mathrm{Nu}_x = 0.569\,\mathrm{Re}_x^{0.5}\,\mathrm{Pr}^{0.33}. \tag{22}$$

A numerical solution similar to that of Eckert's [46], performed by Makarevičius and the author in the range of Pr from 10 to 100, yielded the

following relation for heat transfer in the region near the front stagnation point:

$$\mathrm{Nu}_x = 0.57\,\mathrm{Re}_x^{0.5}\,\mathrm{Pr}^{0.35}. \tag{23}$$

As a result of the exact solution of the boundary layer equations, Frössling [48] proposed an asymptotic relation for the calculation of local heat transfer from the front portion of a tube in air:

$$\mathrm{Nu}_x = [0.9450 - 0.7696(x/D)^2 - 0.3478(x/D)^4]\,\mathrm{Re}^{0.5}. \tag{24}$$

The relation was obtained by using a velocity distribution outside the boundary layer similar to that in Eq. (4).

The relations presented above refer only to the heat transfer of the front portion of a tube. Theoretical calculations by Krall and Eckert [49] apply to the whole perimeter of a tube at low Reynolds numbers. At first the lines of flow in the front and rear regions were calculated, and the heat transfer was determined from the temperature gradient at the tube surface, as a result of numerical solutions of the boundary layer equations in cylindrical coordinates by the method of finite differences. From 800 to 1000 iterations were performed. Solutions were obtained for the two boundary conditions on the wall, i.e., constant surface temperature and constant heat flux. Results of the calculations at two different values of Reynolds number are presented in Fig. 22. The point of minimum heat

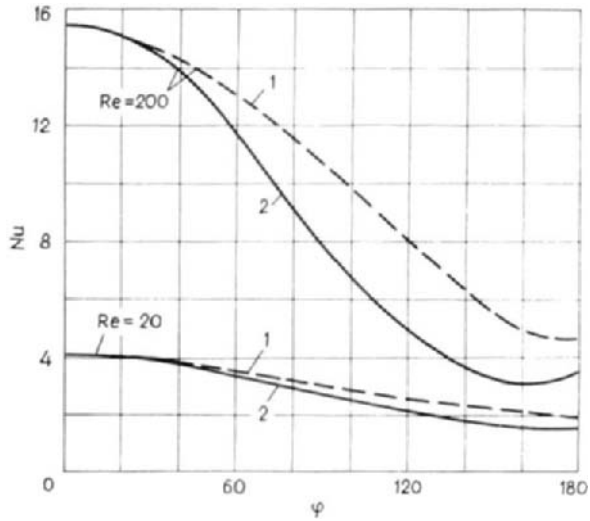

FIG. 22. Calculated local heat transfer distributions [49]. Curves 1—q_w = const. Curves 2—t_w = const.

transfer is clearly removed downstream and is located in the region between 125 and 145°, which is considered characteristic of low Reynolds number flow. The influence of boundary conditions on the heat transfer is also obvious. For a constant heat flux, the heat transfer is more intensive than for a constant surface temperature, the average difference of the mean heat transfer being in the range of 15 to 20% and depending on the Reynolds number. It is interesting to note that in the front portion up to $\phi = 30°$ the heat transfer is independent of the boundary conditions on the wall. Different theoretical calculations of the heat transfer of the front portion in air lead to similar results (Fig. 23).

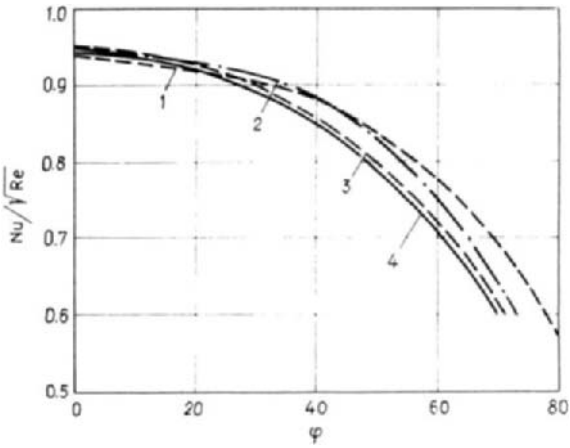

FIG. 23. Comparison of heat transfer calculations in the front portion of a tube. Curve 1—after Kruzhilin [45]; curve 2—after Merk [47]; curve 3—after Eckert [46]; curve 4—after Frössling [48].

Some recent publications have described attempts to calculate the heat transfer in the rear portion of a circular tube at higher values of Reynolds numbers. However, these approximate methods are based on simplified flow patterns and do not take into account the numerous factors of separation. Therefore experimental data are preferred in practice for this case.

2. *Heat Transfer in Gas Flow*

At low Reynolds number, as long as the vortical path is formed, theoretical results of local heat transfer [49] correlate well with experimental data [50] (Fig. 24). The heat transfer in the rear portion is at a minimum.

For higher values of Reynolds number, the heat transfer is a minimum at the separation point and increases downstream. Nevertheless, the variation

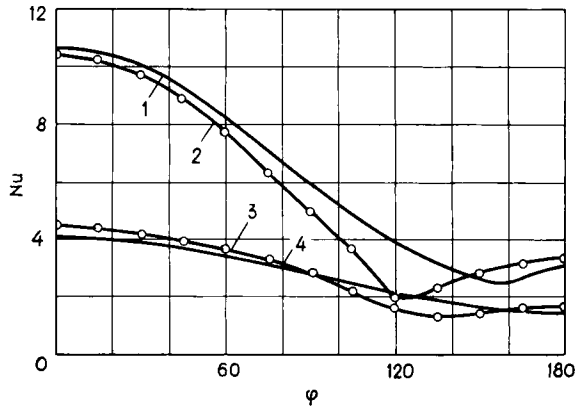

FIG. 24. Local heat transfer of a tube at low Re. Curves 1, 4—calculations [49] at Re = 100 and 20, respectively; curves 2, 3—experimental data [50] at Re = 120 and 23, respectively.

of heat transfer is greatly under the influence of the Reynolds number. At low Reynolds numbers, the heat transfer in the front portion is higher than in the rear (Fig. 25). With increasing Reynolds number, the heat transfer in

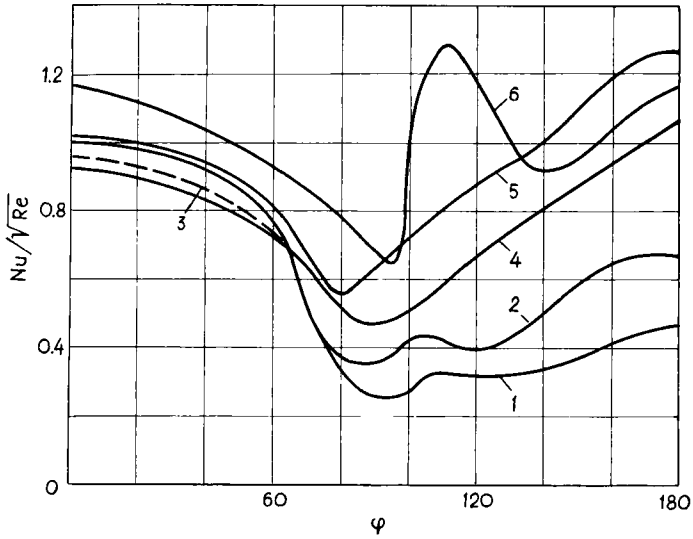

FIG. 25. Variation of heat transfer around a tube at different Re. Curve 1—Re = 5.3×10^3, and curve 2—Re = 3.2×10^4, after Meel [51]; 3—theoretical curve, after Frössling [48]; curve 4—Re = 2.1×10^4, after Kruzhilin and Shvab [14]; curve 5—Re = 9.9×10^4, and curve 6—Re = 2.1×10^5, after Giedt [52].

the rear portion increases, and for $Re > 5 \times 10^4$ it is higher than in the front portion. For $Re > 2 \times 10^5$ the variation of the heat transfer coefficient acquires a new character under the influence of the transition from laminar to turbulent flow in the boundary layer. The point of minimum heat transfer in this case is removed downstream. A vortex shed favors the access of a new cold mass of fluid to the surface, and the heat transfer increases suddenly. It is obvious that the heat transfer reaches a maximum at $\phi = 110°$, and decreases downstream.

It should be noted that heat transfer is also influenced by the turbulence of the main flow. The calculations refer to the laminar main flow. Therefore a coincidence of calculated results with experimental data obtained in the flow with low turbulence is possible. Experimental points for a highly turbulent main flow are considerably higher than the theoretical curves in Fig. 25.

Recent investigations [53–56] suggest that the local heat transfer of a circular tube increases considerably with the turbulence of the main flow. Figure 26 presents the results of heat transfer measurements around a tube [53] for different levels of turbulence of the main flow. A regular increase of heat transfer is obvious. It is interesting to note that even for Re = 39,000 with an increase of turbulence to Tu = 11.5% two minima appear in the heat transfer, the first of which is due to the transition from laminar to

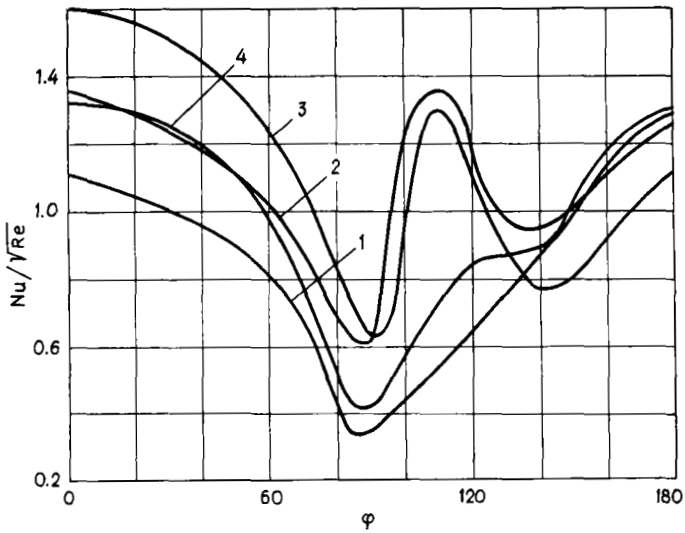

FIG. 26. Variation of heat transfer around a tube at different levels of turbulence [53]. Curve 1—Tu = 0.9%, curve 2—Tu = 3%, at $Re = 1.1 \times 10^5$, curve 3—Tu = 11.5%, at $Re = 3.9 \times 10^4$; curve 4—Tu = 3%.

turbulent flow. Thus with an increase in turbulence of the main flow, at lower Reynolds numbers the critical flow regime is established.

Experiments suggest a nonuniform influence of turbulence along the perimeter, which can be described by the following factor

$$\epsilon_\phi = \mathrm{Nu}_{\mathrm{Tu}\neq 0}/\mathrm{Nu}_{\mathrm{Tu}=0}. \tag{25}$$

As seen in Fig. 27, in the subcritical flow regime the dependence of heat transfer on turbulence at different Re has a similar character. For higher values of Re and Tu, because of the transition to turbulent flow in the

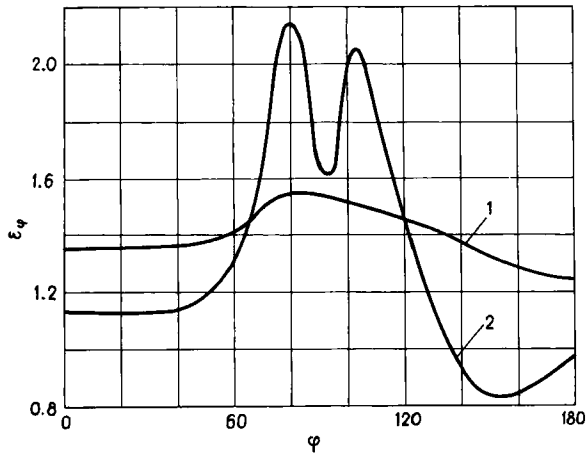

FIG. 27. Variation of ratio ϵ_ϕ around a tube. Curve 1—Re = 15,600, Tu = 12 % [56]; curve 2—Re = 67,000, Tu = 2.5 % [38].

boundary layer, the influence of turbulence is most appreciable at $\phi = 110°$. It may be concluded from the results that the critical flow regime is established at

$$\mathrm{Re\,Tu} \geqslant 1500.$$

The influence of turbulence on heat transfer is least in the rear critical point.

Dyban and Epick [56] proposed the relation

$$\epsilon_\phi = 1 + 0.01(\mathrm{Re\,Tu})^{0.5} \tag{26}$$

for the evaluation of the influence of turbulence on heat transfer from the front portion up to $\phi = 60°$, which is thought to give high results. This would mean that say, for Re = 60,000, with the turbulence level increasing from 0.2 to 4%, the heat transfer increases by 30% in the front and 25% in the rear of the tube.

3. *Heat Transfer in the Flow of Viscous Fluids*

The local heat transfer from a circular tube in air flow, transformer oil, and water at q_w = const. is thoroughly investigated in [38]. It is obvious from Fig. 28 that for approximately equal Reynolds numbers, the variations of local heat transfer coefficient have a similar character in all of the fluids examined. The ratio of the heat transfer intensities in the front and in the

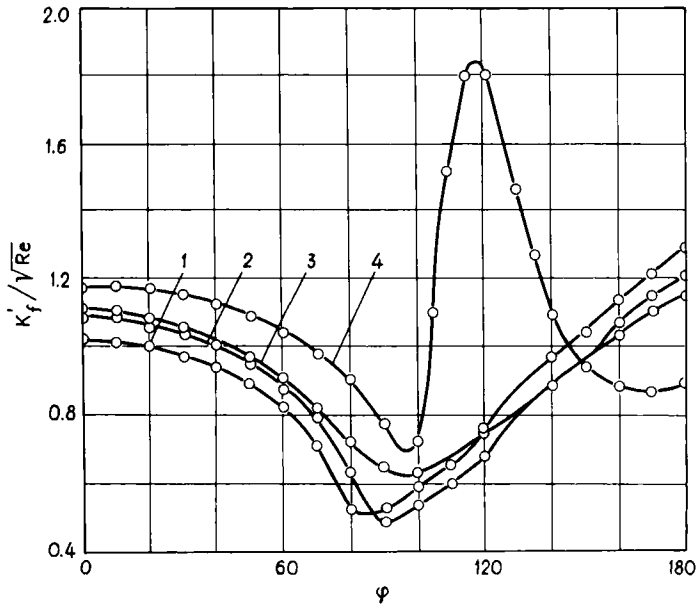

FIG. 28. Variation of heat transfer around a tube in various liquids [38]. Curve 1—Re = 20,000, transformer oil; curve 2—Re = 25,000, and curve 4—Re = 130,000, water; curve 3—Re = 39,000, air; $K_f' = Nu_f\, Pr_f^{-0.37}(Pr_f/Pr_w)^{-0.25}$.

rear is also the same for different fluids, in spite of the variation of Pr from 0.7 to 95. This implies that in the range of Re examined, the physical properties of the fluid have no effect on the character of heat transfer. The variations of the local heat transfer in different flow regimes show that with an increase in Reynolds number and turbulence level the curve of heat transfer in the rear portion of the tube undergoes similar changes in flows of viscous fluids and in air. Curve 4, representing variations of local heat transfer in water for Re = 130,000 and Tu = 2% has two minima, the first relating to the laminar–turbulent transition in the boundary layer, and the second to the separation of the boundary layer.

The variations in the flow pattern around the tube lead to changes of the power indexes in Eq. (12). According to [38], the average power index of the Reynolds number is 0.5 and 0.73, in the front and in the rear portions, respectively (Fig. 29). The power index of the Prandtl number for $Pr > 10$ is equal to approximately 0.34 and 0.39, in the front and in the rear, respectively.

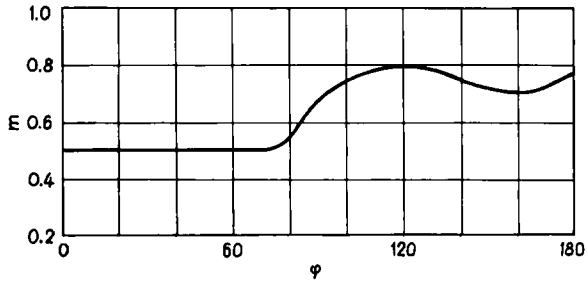

FIG. 29. Variation of m power index of Re around a tube [38].

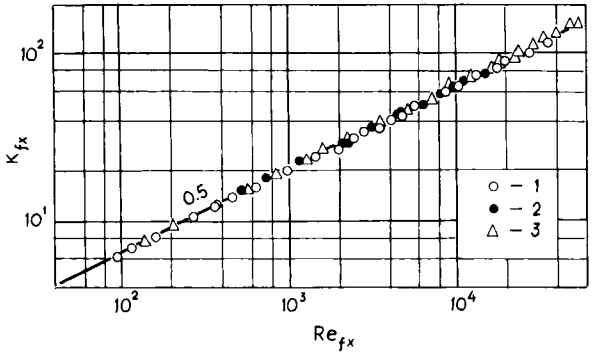

FIG. 30. Local heat transfer of the front portion of a tube [38]. 1—Transformer oil; 2—water; 3—air; $K_{fx} = Nu_{fx}\, Pr_{f,x}^{-0.34}(Pr_f/Pr_w)^{-0.25}$.

In Fig. 30, the experimental points of local heat transfer at the front portion of a circular tube are located on a single curve for flows of air, water, and transformer oil and may well be generalized by a single relation

$$Nu_{fx} = 0.65\, Re_{fx}^{0.5}\, Pr_f^{0.34}(Pr_f/Pr_w)^{0.25}. \tag{27}$$

In this case experimental data were referred to the local velocity from Eq. (4).

As we see, the local heat transfer is higher for q_w = const. than for

t_w = const. In heat transfer calculations and in the analysis of experimental results, a consideration of surface temperature variation is necessary. Different temperature distributions on the wall lead to different values of the heat transfer coefficient. Therefore, applying the relations of heat transfer for a tube with a constant surface temperature to the case of a variable surface temperature will be only approximate, and in the case of a considerable surface temperature gradient may be misleading. The influence of a temperature gradient is similar to that of a pressure gradient. The surface temperature gradient determines the temperature distribution in the thermal boundary layer and its thickness. The boundary layer thickness varies under the influence of a surface temperature gradient, causing corresponding variations of the heat transfer coefficient, which is inversely proportional to the thickness of the thermal boundary layer.

The derivation of a general relation for the local heat transfer of the rear portion of a tube is connected with the difficulties of determining the local velocity. This problem is very complicated and requires a more detailed analysis, which will be the object of our future investigations. The mean heat transfer in the rear portion of a circular tube in flows of liquids for q_w = const. is presented in Fig. 31. Calculations of the mean heat transfer from a tube are referred to the velocity in the minimum free cross section from Eq. (5a).

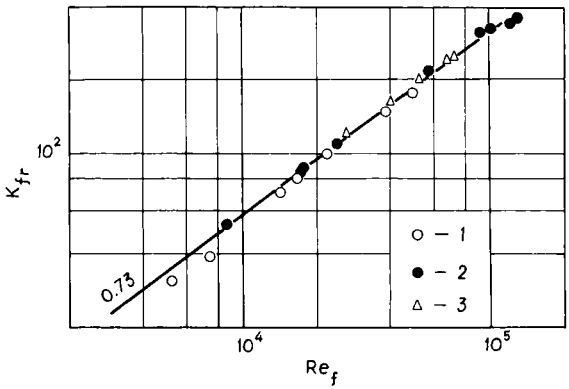

FIG. 31. Mean heat transfer of the rear portion of a tube, $K_{fr} = Nu_f\, Pr_f^{-0.4}(Pr_f/Pr_w)^{-0.25}$.

B. MEAN HEAT TRANSFER

If the coefficient of local heat transfer along the perimeter has been determined, the mean heat transfer of the tube as a whole can be derived. The choice of the method of calculation is of some importance. According to

the first of the two known methods, the mean heat transfer coefficient is determined by integrating the local heat transfer relation

$$\alpha = \frac{1}{l}\int_0^l \alpha(x)\,dx. \tag{28}$$

Dividing an integral mean heat flux by an integral mean temperature difference,

$$\alpha = \frac{(1/l)\int_0^l q_w(x)\,dx}{(1/l)\int_0^l \Delta t(x)\,dx}, \tag{29}$$

is the second calculation method of the mean heat transfer coefficient.

Calculations by these two different methods may lead to discrepancies in the results. The results are identical for isothermal surfaces, but with surface temperature variations discrepancies between the two methods do occur. For example, the mean heat transfer coefficient, determined from Eq. (28), is considerably higher for q_w = const. than for t_w = const., while the mean heat transfer determined by the second method from Eq. (29) is approximately equal for both cases.

In theoretical calculations, the first method is more convenient. In experiments, however, the mean heat transfer is usually found by the second method. In the case of heat transfer from wires at low Reynolds numbers the mean temperature is determined from their electrical resistance.

1. *Low Range of Reynolds Numbers*

At low Reynolds numbers, the heat transfer is affected by free convection, while at high values of Reynolds numbers the influence of free convection is negligible. The total heat transfer may be determined by adding up the vectors of free and forced convection, as proposed in [57], where the relation

$$(\mathrm{Nu} - 0.35)\left[1 - \left(\frac{0.24\,\mathrm{Gr}^{1/8} + 0.41\,\mathrm{Gr}^{1/4}}{\mathrm{Nu} - 0.35}\right)^2\right]^{1/2} = 0.5\,\mathrm{Re}^{0.5} \tag{30}$$

is used for calculations at low Reynolds numbers. For the case of a weak influence of free convection it simplifies to

$$\mathrm{Nu} = 0.35 + 0.5\,\mathrm{Re}^{0.5}. \tag{31}$$

For calculations of heat transfer from wires at $\mathrm{Re} < 0.5$, when they are streamlined, the following relation is proposed [58]:

$$\mathrm{Nu}\,(T_m/T_f)^{-0.17} = 1/(1.18 - 1.1 \log \mathrm{Re}), \tag{32}$$

where T_m is the arithmetical mean value of the wire temperature and T_f is the main flow temperature.

In connection with developments in thermoanemometry, a number of works have been devoted to the heat transfer of thin wires which are used as the working elements in sensors. Specific problems of heat transfer from thin wires lie outside the scope of the present study. Recent publications [59, 60] in this field can be recommended.

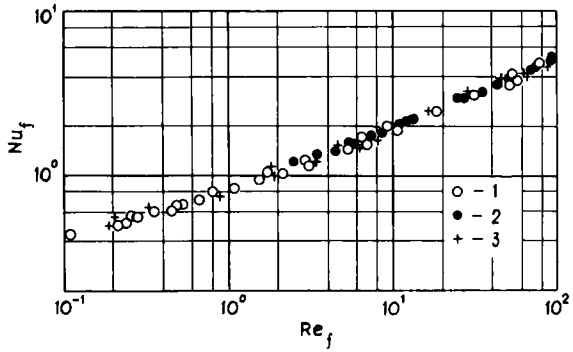

FIG. 32. Heat transfer of a tube in flow of air at $Re < 10^2$. 1—After [13]; 2—after [1] 3—after Collis and Williams [58].

Figure 32 presents the data of various authors on heat transfer in air at low Reynolds numbers. A considerable scatter of the points is obvious, but the slope of the curves corresponds to the power index of Reynolds number $m = 0.40$ at $Re < 40$ and $m = 0.50$ at $Re > 40$.

The process of heat transfer in liquids at low Reynolds numbers is similar (Fig. 33). The influence of the physical properties of the liquid in this case

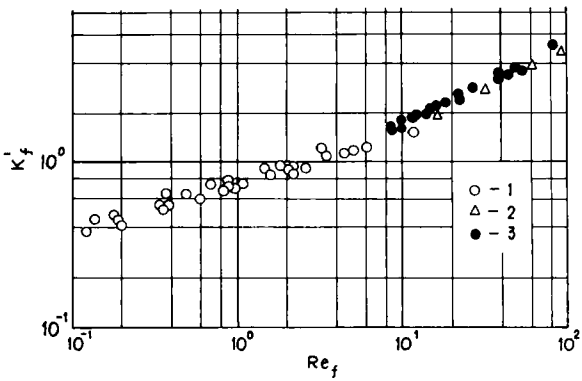

FIG. 33. Heat transfer of a tube in flow of liquids at $Re < 10^2$. 1, 2—Water flow, after Piret *et al.* [61] and Davis [16], respectively; 3—transformer oil flow, after Žukauskas [37]; $K'_f = Nu_f\, Pr^{-0.37}(Pr_f/Pr_w)^{-0.25}$.

is accounted for by the Prandtl number to the power 0.37. Some authors propose $n = 0.3$. Lower values of n may be expected, but the data available are insufficient for any conclusions.

2. *High Range of Reynolds Numbers*

The preliminary results of the correlation of our experimental data on mean heat transfer in flows of air, water, and transformer oil at various heat flux directions are presented in Fig. 34. All the experiments were performed under identical conditions (t_w = const., Tu < 1%) in the same experimental apparatus.

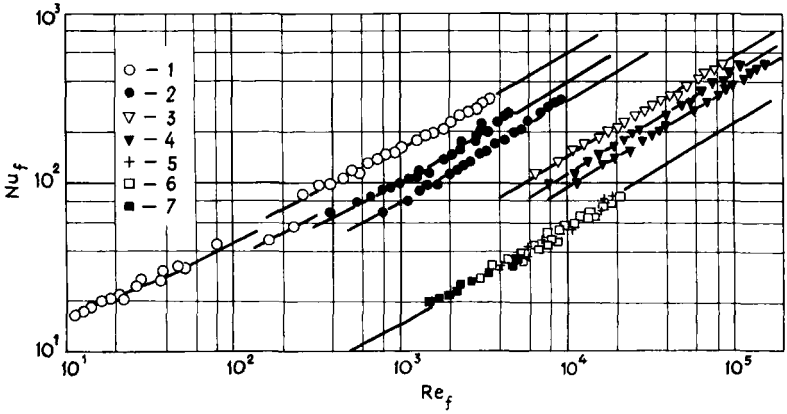

FIG. 34. Influence of the type of liquid on heat transfer of a tube [37]. 1, 3, 5—Heating of transformer oil, water, and air, respectively; 2, 4, 5—cooling of above fluids, respectively; 6, 7—experimental data in air flow of Mikhe'yev [15] and Hughes [2].

It is obvious that the experimental points for the flow of transformer oil and water are higher for heating than for cooling. Thus the relative positions of the heat transfer data are determined by fluid type, fluid temperature, and heat flux direction. Our data in air flow correlate well with the results of other authors [2, 15] presented here. Through the experimental points two straight lines of different slopes may be drawn, corresponding to different values of the power index of Reynolds number. At $Re < 10^3$, $m = 0.48$ and in the range of Reynolds numbers from 10^3 to 2×10^5, $m = 0.61$ both for liquids and air.

In Fig. 35 the final results according to Eq. (12) are presented, together with the recent results [38] of investigations of mean heat transfer from a circular tube in crossflow of air, water, and transformer oil for q_w = const.

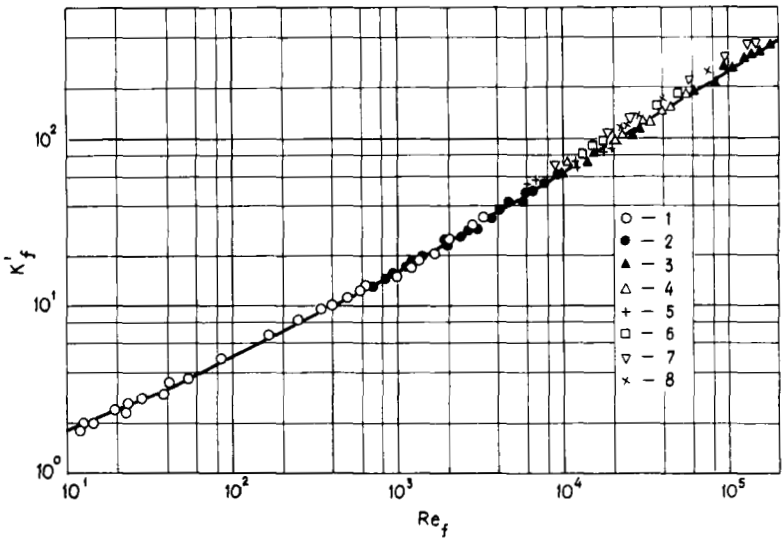

FIG. 35. Heat transfer of a tube at different boundary conditions. 1, 4, 5—Heating transformer oil, water, and air, respectively; 2, 3, 5—cooling of above fluids, respectively, at t_w = const. [37]; 6, 7, 8—heating transformer oil, water, and air, respectively, at q_w = const. [38].

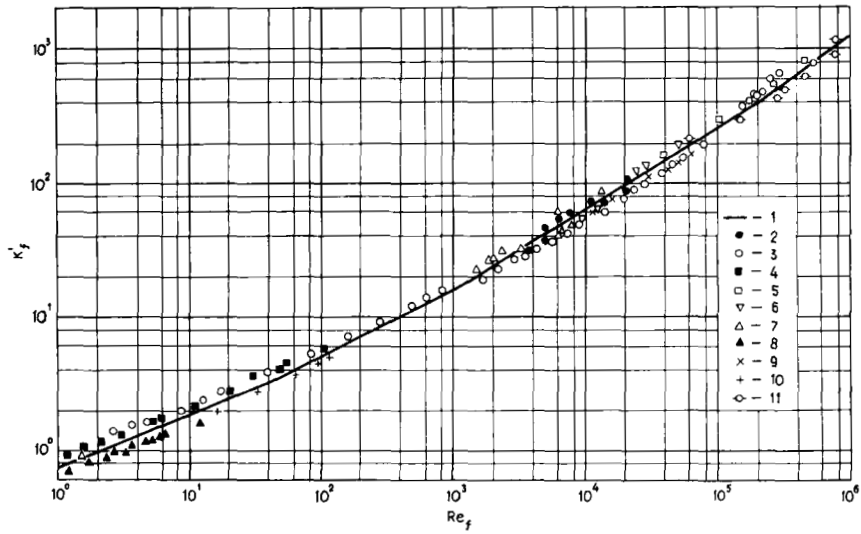

FIG. 36. Comparison of heat transfer of a tube data obtained by various authors. 1—[37]; 2—[15]; 3—[13]; 4—[58]; 5—[63]; 6—[64]; 7—[2]; 8—[61]; 9—[62]; 10—[16]; 11—[40]. Experimental data in the first row of a staggered bank.

Based on an analysis of the experimental results, the power index of the Prandtl number $n = 0.37$ is chosen. As mentioned in Section IV, in the range of $Pr > 10$ the mean value of n along the perimeter is 0.36. The experimental results in Fig. 35 exhibit a good correlation and an unambiguous determination of the law of heat transfer.

The results of mean local heat transfer calculated according to Eq. (29) for $q_w = \text{const.}$ correlate well with the results for $t_w = \text{const.}$

3. *Relations for Heat Transfer Calculations*

The continuous curve in Fig. 36 represents heat transfer data of a circular tube in crossflow with viscous fluids and gases, when the turbulence of the main flow is less than 1 %. The curve has been derived from our experimental data. Data of other authors, presented for comparison, correlate well with our relation. Thus the following equation is recommended for practical calculations:

$$Nu_f = c\, Re_f^m\, Pr_f^{0.37} (Pr_f/Pr_w)^{0.25}. \tag{33}$$

The values of c and m at various Reynolds numbers are given in Table I.

TABLE I

VALUES OF CONSTANTS IN EQ. (33)

Re	c	m
1 – 40	0.75	0.4
40 – 1×10^3	0.51	0.5
1×10^3 – 2×10^5	0.26	0.6
2×10^5 – 1×10^6	0·076	0.7

For $Pr > 10$, $n = 0.36$ should be chosen. For convenience approximate values of m are used in practical calculations. For gases the relation is simplified, e.g., for air $Pr = 0.7 = \text{const.}$ and $Pr^{0.37}(Pr_f/Pr_w)^{0.25} = 0.88$.

For $Re \leqslant 1$, the heat transfer in flows of gases may be calculated from Eqs. (30)–(32). In some works [30] relations of the type

$$Nu = c_1\, Re^{0.5} + c_2\, Re^{0.7} \tag{34}$$

are proposed for the whole range of Reynolds numbers, where the first term stands for heat transfer through the laminar boundary layer on the front portion, and the second for heat transfer in the rear. It has, however,

been shown that the power index of the Prandtl number is not constant along the perimeter. Thus for viscous liquids Eq. (34) becomes

$$\mathrm{Nu}(\mathrm{Pr_f}/\mathrm{Pr_w})^{-0.25} = c_1\,\mathrm{Re}^{0.5}\,\mathrm{Pr}^{0.35} + c_2\,\mathrm{Re}^{0.7}\,\mathrm{Pr}^{0.4}. \tag{35}$$

Solutions of this type of equation are complicated and hardly feasible in practice.

C. Heat Transfer of a Tube in a Restricted Channel

The influence of channel blockage on the flow pattern was analyzed in Section II. Heat transfer also changes under the influence of the decreased free space between the tube and the wall of the channel. According to theoretical calculations, the heat transfer on the front portion of a tube increases with an increase in blockage ratio. This is confirmed by Fig. 37, representing calculations [29] by the method of Merk [47] using the potential flow velocity distribution around a tube

Measurements of local heat transfer on a tube in a channel (Fig. 38) suggest that for $D/H > 0.6$ the distribution of heat transfer coefficient in

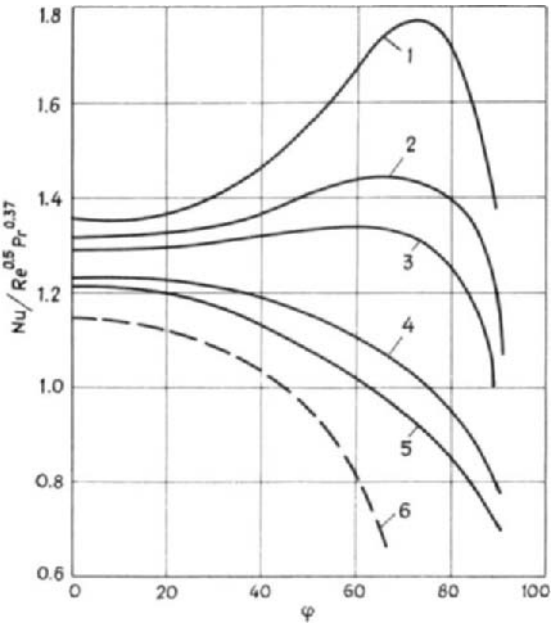

FIG. 37. Calculated heat transfer data from the front portion of a tube for different D/H [29]. Curve 1—0.83, curve 2—0.75; curve 3—0.71, curve 4—0.52; curve 5—0.39; curve 6—0.

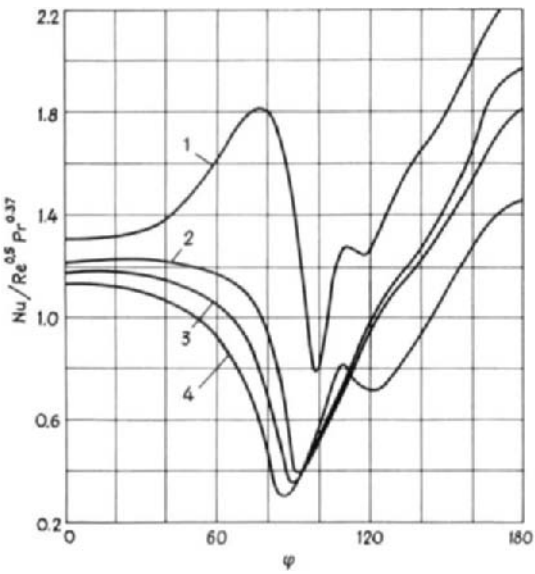

FIG. 38. Local heat transfer of a tube for different D/H [29]. Curve 1—0.83; curve 2—0.63; curve 3—0.52; curve 4—0.39.

the rear also has a different character. In the region near $\phi = 120°$, the second minimum of heat transfer appears.

The curves and the plot correspond to Re = 50,000, referred to the velocity of the main flow of air. The influence of blockage ratio on mean heat transfer is taken into account when choosing the reference velocity. In calculations of the mean velocity for the case $D/H < 0.8$, Eq. (5c) may be applied. But for higher blockage ratios its influence on the heat transfer is different in the front and in the rear. Therefore, Akilba'yev [29] suggests Eq. (35) for heat transfer calculations at $D/H > 0.8$, with separate empirical corrections for the front and the rear of a tube.

VI. Heat Transfer of a Tube in a Bank

A. Local Heat Transfer

1. *Heat Transfer in Flow of Gas*

The variation of heat transfer around a tube in a bank is determined by the flow pattern, which depends greatly on the arrangement of the tubes in the bank. Thus in banks of in-line arrangement, two impact points and

consequently two heat transfer maxima are observed. On the other hand, in banks of a staggered arrangement, the process of heat transfer is to some extent similar to that of a single tube.

As mentioned above, a tube in one of the inner rows is influenced by a highly turbulent flow, and the boundary layer near the impact point is purely laminar only at low Reynolds numbers.

Heat transfer variations in inner rows of banks of in-line and staggered arrangements are compared with that of a single tube in Fig. 39. In banks

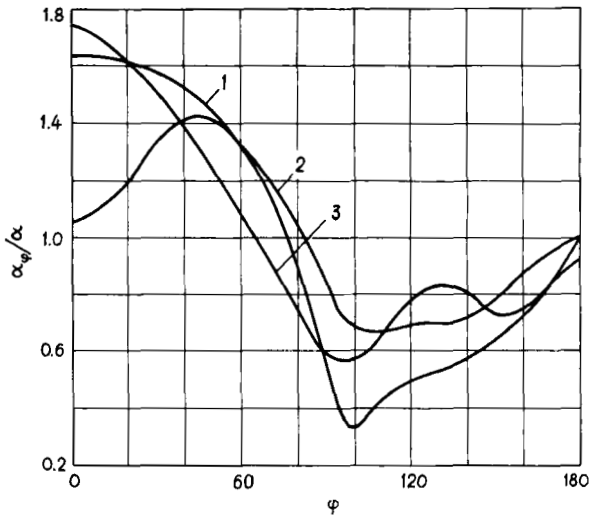

FIG. 39. Variation of local heat transfer of a single tube and a tube in a bank. Curve 1—single tube; curve 2—in an in-line bank; curve 3—in a staggered bank.

of both arrangements a higher turbulence intensity in the flow causes an increase in the heat transfer at the front as well as the rear portions of a tube. Nevertheless, the maximum value of the heat transfer in the case of an in-line bank is observed at $\phi = 50^\circ$ because the impact of the stream on the surface occurs at this point.

Let us consider the heat transfer in different rows of a staggered bank (Fig. 40). The heat transfer from a tube in the first row is similar to that of a single tube. As the fluid passes through the first row, it is disturbed. This causes an increase in heat transfer in subsequent rows. This is observed up to the third row, downstream of which the heat transfer becomes stable and equal to the value of the latter. This applies to the front and rear portions of the tube [65].

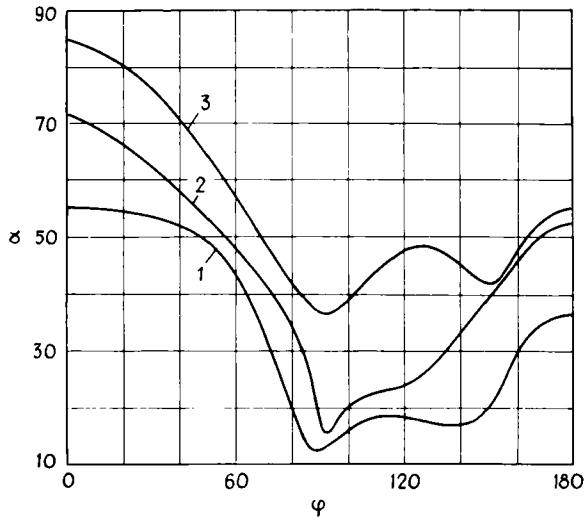

FIG. 40. Local heat transfer of a tube in a staggered bank, 2.0 × 2.0, at Re = 14,000 [65]. Curves 1, 2, 3—first, second, and inner row, respectively.

In banks with a staggered arrangement, a change of longitudinal and transverse pitches from 1.3 to 2.0 has hardly any effect on the character of heat transfer (Fig. 41). An increase in heat transfer is observed at about

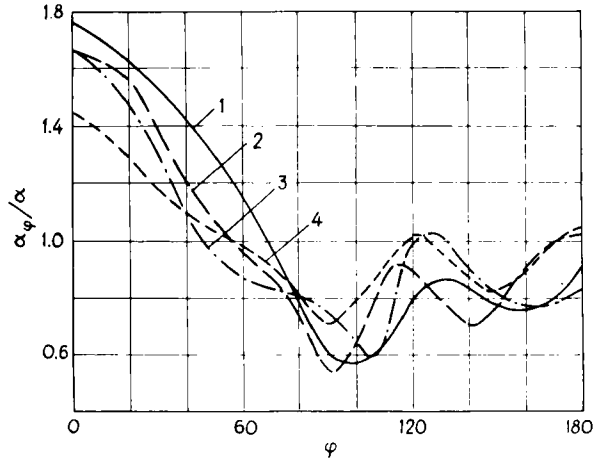

FIG. 41. Local heat transfer of a tube in various staggered banks at Re < 70,000. Curve 1—2.0 × 2.0, after Mikhaylov [65] and Kazakevich [66]; curve 2—1.5 × 1.5, after Mayinger and Schad [67]; curve 3—1.3 × 1.13, after Bortoli *et al.* [68]; curve 4—1.5 × 2.0, after Winding and Cheney [69].

$\phi = 120°$ in the banks examined, which corresponds to the laminar–turbulent transition in the boundary layer. Boundary layer separation occurs at $\phi = 150°$.

The variation of heat transfer around a tube in a staggered bank is almost independent of Reynolds number in the subcritical flow regime. In closely spaced staggered banks, the heat transfer of the inner tubes decreases in the front up to $\phi = 50°$, and later increases again. This is explained by large pressure gradients and subsequent velocity increases.

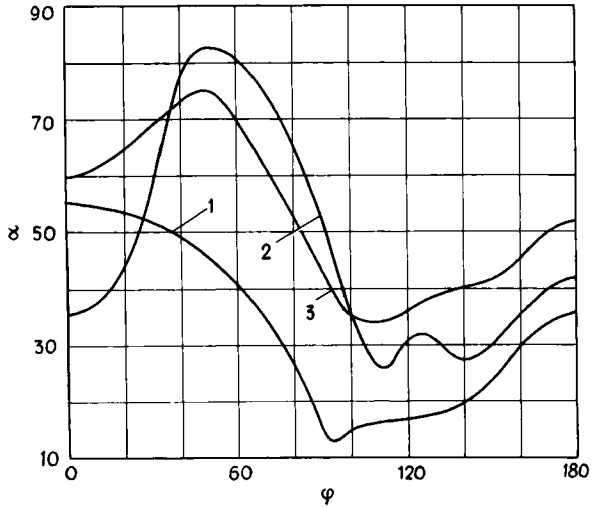

FIG. 42. Local heat transfer of a tube in an in-line bank, 2.0 × 2.0, at Re = 14,000 [65]. Curves 1, 2, 3—first, second, and inner row, respectively.

Figure 42 presents heat transfer variations in an in-line bank after [65]. The heat transfer is stable from the fourth row on. Tubes of the second and subsequent rows are "shaded" by the preceding ones with the character of heat transfer changing accordingly. Because of the two impact points, expressed by sharp maxima of heat transfer, the laminar boundary layer on an inner tube begins at $\phi = 40$–$60°$, instead of the front stagnation point. With subsequent growth of the boundary layer in both directions from the impact points, the heat transfer decreases.

It is interesting to note that the heat transfer at the front stagnation point of the inner tubes increases from row to row, and approaches the maximum heat transfer at the impact point. This is connected with the increase of flow turbulence in the bank. This also leads to more intensive heat transfer in the rear. Heat transfer in the rear constitutes a significant part of the total heat transfer, which means that flow in the rear is not stagnant.

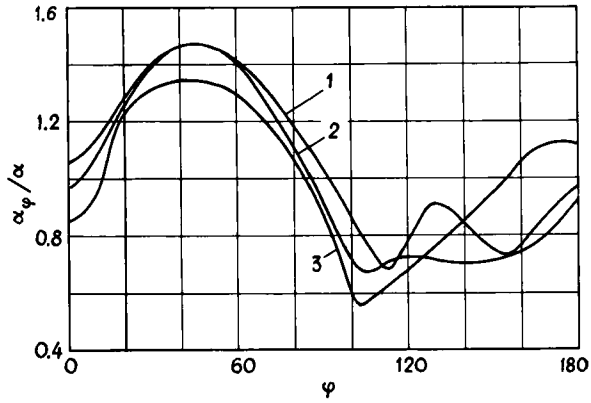

FIG. 43. Local heat transfer of a tube in various in-line banks at Re = 30,000. Curve 1—1.5 × 1.5, after Mayinger and Schad [67]; curve 2—1.6 × 2.0, after Kazakevich [66]; curve 3—1.5 × 1.1, after Mayinger and Schad [67].

With an increase of Reynolds number, the flow in the bank becomes more turbulent, and the distribution of local heat transfer coefficients on tubes in inner rows levels out. This is confirmed by Fig. 43, comparing the results of various authors, where tube arrangement has little effect on the character of heat transfer.

2. *Heat Transfer in Flow of Viscous Fluid*

The physical properties of the fluid have no effect on the character of the heat transfer, the distribution of the local heat transfer coefficient being the same in all fluids. This is seen from Fig. 44 which represents data of local

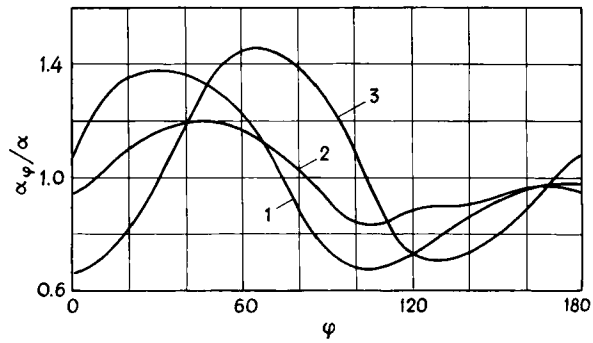

FIG. 44. Local heat transfer of tubes in an in-line bank in flow of liquids. Curve 1—2.6 × 1.3, water, Re = 6000; curve 2—2.6 × 1.3, transformer oil, Re = 360; curve 3—1.3 × 1.3, transformer oil, Re = 240.

heat transfer of inner tubes in banks of in-line arrangements in flows of water and transformer oil [20]. A certain effect of the pitch, both longitudinal and transverse, is obvious.

The determination of the power index m of the Reynolds number has been attempted from local values of heat transfer and velocity. In the region from the impact point to the separation point $m = 0.5$ was obtained. In the rest of the perimeter, m varies from 0.5 to 0.8, which implies a different flow regime at the surface. Thus one may judge the flow pattern from the local values of m.

B. Mean Heat Transfer

For practical purposes, the power index of the Prandtl number $n = 0.36$ is sufficiently accurate for all sorts of banks (see Section IV). Thus the following relation may be applied for heat transfer from banks

$$\mathrm{Nu_f} = c\,\mathrm{Re_f}^m\,\mathrm{Pr_f}^{0.36}(\mathrm{Pr_f}/\mathrm{Pr_w})^{0.25}. \tag{36}$$

The results are referred to the tube diameter and to the flow velocity in the minimum free cross section.

The final results for the mean heat transfer in the form of

$$K_\mathrm{f} = \mathrm{Nu_f}\,\mathrm{Pr_f}^{-0.36}(\mathrm{Pr_f}/\mathrm{Pr_w})^{-0.25} = f(\mathrm{Re_f}) \tag{37}$$

are presented in the following figures.

1. *Heat Transfer in Separate Rows* [20]

Experiments suggest that the heat transfer from a tube is determined by its position in the bank. In most cases, the heat transfer from tubes in the first row is considerably lower than in inner rows (Figs. 45 and 46).

In the range of low Reynolds numbers, the heat transfer from a tube in the first row is similar to that of a single tube or a tube in an inner row. The increase of flow turbulence in a bank at higher Reynolds numbers leads to an increase of heat transfer of the inner tubes, as compared to the first row. The rows of tubes in a bank in fact act as a turbulence grid. In most banks, the heat transfer becomes stable from the third or fourth row in the mixed flow regime. A comparison of heat transfer between the first row and inner rows in a fully developed flow reveals the influence of turbulence intensity on heat transfer.

The heat transfer of inner tubes generally increases as the longitudinal pitch decreases. This correlates well with known investigations of the heat transfer of a tube placed at various distances from the turbulence grid.

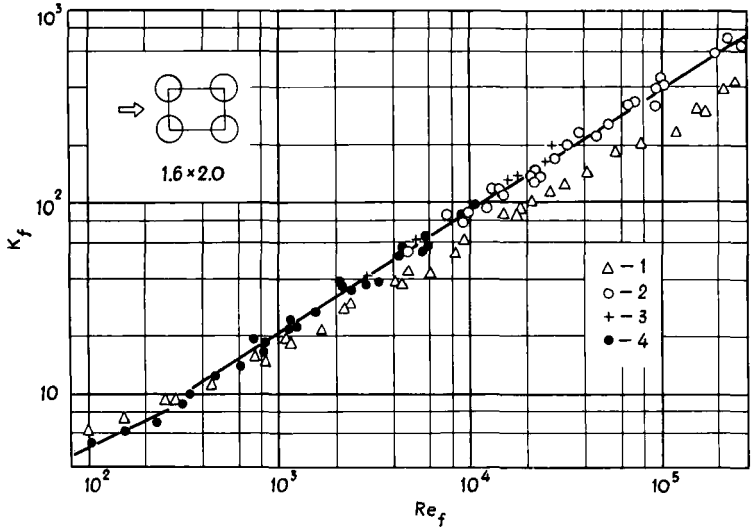

FIG. 45. Heat transfer of tubes of in-line banks, 1.6 × 2.0. 1—First row, and 2, 3, 4—inner rows in water, air, and transformer oil, respectively.

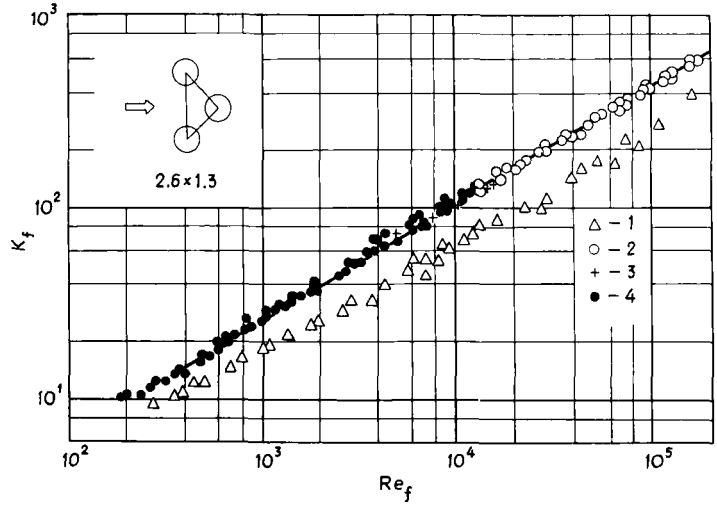

FIG. 46. Heat transfer of tubes of staggered banks, 2.6 × 1.3. 1—First row, and 2, 3, 4—inner rows in water, air, and transformer oil, respectively.

As a result of turbulence, the heat transfer in inner tubes exceeds by 30 to 70% that of the first row, the difference depending on the longitudinal pitch. Thus heat transfer in inner rows is mainly determined by turbulence intensity, which increases with a decrease in the distance from the turbulizer, i.e., from the preceding row.

The dependence of the heat transfer variation in a bank on Reynolds number may be of interest. The development of flow turbulence in a bank is different for different values of Reynolds number. As is obvious from Fig. 47, in a staggered bank the heat transfer of a tube in the second row is

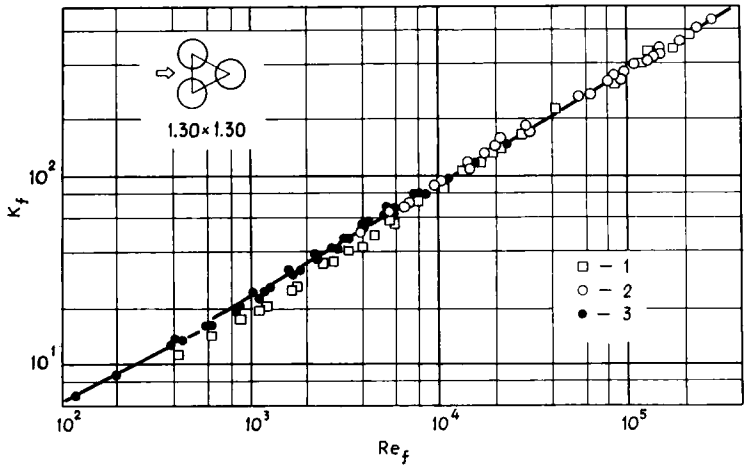

FIG. 47. Heat transfer of tubes of staggered banks, 1.3 × 1.3. 1—Second row; 2, 3—inner rows.

somewhat lower than that of an inner tube for $Re < 10^4$, and equal for $Re > 10^4$. The same applies to banks with in-line arrangements. The heat transfer of a tube in the second row is in most cases 10 to 25% lower than that of inner tubes.

The following discussion deals mainly with the heat transfer of a tube in an inner row of a bank.

2. *Heat Transfer in a Range of Low Reynolds Numbers*

As noted in Section III, at low Reynolds numbers laminar flow patterns prevail with large vortices in the circulation zones. This is also reflected in the character of the heat transfer. The influence of free convection is observed, in some cases, but is not usually taken into account in calculation formulas. Available experimental data for the heat transfer of banks of tubes for low Reynolds numbers is rather scarce [70–73].

Transition of the predominantly laminar flow to a mixed flow usually takes place at Re = 200. In some banks, however, especially in those with a large longitudinal and small transverse pitch, transition occurs at Re = 10^3. A certain influence of initial turbulence in the main flow preceding the bank is possible.

Data of different authors [72–74] on the heat transfer in banks with in-line arrangements for low Reynolds numbers (Fig. 48) suggest that in some banks, with decreasing Reynolds number the heat transfer coefficient becomes proportional to the velocity to the power 0.5 at Re < 10^3 or even 0.4 at Re < 2 × 10^2. In some banks the mixed flow pattern persists at lower Reynolds numbers, and the heat transfer coefficient is proportional to the velocity to the power 0.6 or 0.63.

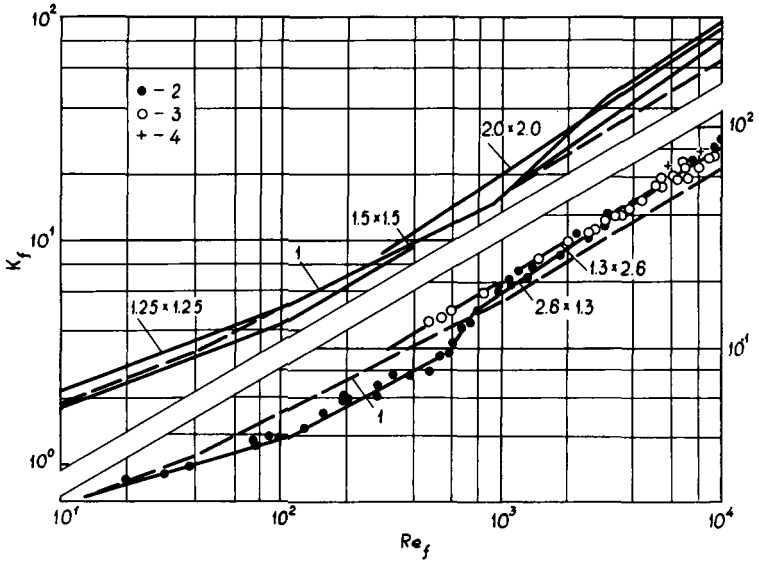

FIG. 48. Heat transfer of tubes of in-line banks: 2.6 × 1.3 and 1.3 × 2.6, after Makarevičius and Žukauskas [74]; 1.25 × 1.25 and 1.5 × 1.5, after Bergelin *et al.* [72]; 2.0 × 2.0, after Isachenko [73]. 1—Heat transfer of a single tube; 2, 3, 4—data in flow of transformer oil, water, and air, respectively.

For 10^2 < Re < 10^3 the heat transfer of inner tubes of in-line banks with large and moderate longitudinal pitch is close to that of a single tube. In banks with in-line arrangements an additional effect of "shading" is observed with a decrease of the longitudinal pitch. Thus in a predominantly laminar flow, the heat transfer of an inner tube is lower than that of a single tube.

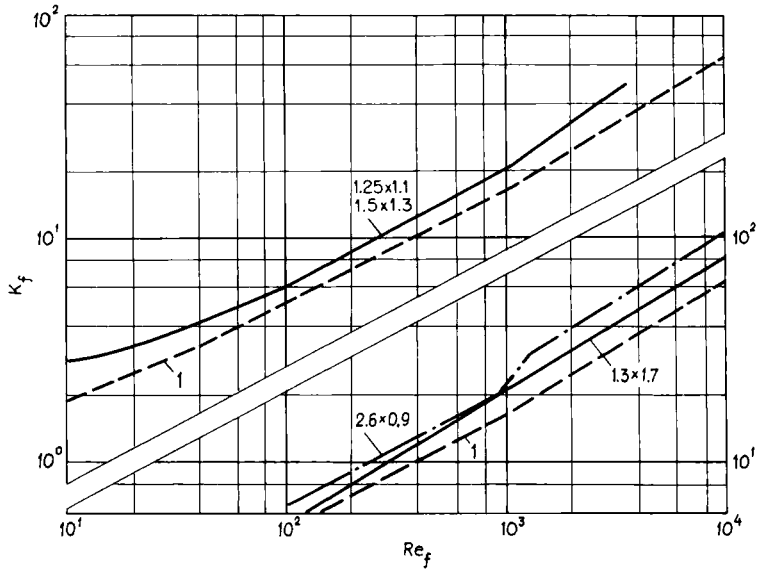

FIG. 49. Heat transfer of tubes of staggered banks: upper—after Bergelin *et al.* [72]; lower—after Žukauskas and Šlančiauskas [75]. 1—Heat transfer of a single tube.

The heat transfer of tubes in a staggered arrangement is similar at low Reynolds numbers (Fig. 49). Heat transfer curves of inner tubes of staggered banks are, however, higher than that of a single tube. In the range of Re from 10 to 100 the heat transfer from inner tubes is close to

$$Nu_f = c\, Re_f^{0.4}\, Pr_f^{0.36}(Pr_f/Pr_w)^{0.25}, \tag{38}$$

where for banks with an in-line arrangement $c = 0.8$ and for staggered banks $c = 0.9$.

3. *Heat Transfer in the Mixed (Subcritical) Flow Regime*

This regime covers Re from 10^3 to 2×10^5. Transition of the predominantly laminar to the mixed flow takes place at different Reynolds numbers, depending on the tube arrangements (Figs. 48 and 49). For $Re > 10^3$ a laminar boundary layer forms on the front of an inner tube, but the main portion of it is influenced by vortical flow. The character of the heat transfer is determined by the flow regime in the boundary layer. Thus the power index m of the Reynolds number varies from 0.55 to 0.73 for banks of different arrangements.

Figure 50 shows a comparison of the heat transfer from 15 various banks of in-line arrangements [74]. It suggests an increase of m with constant

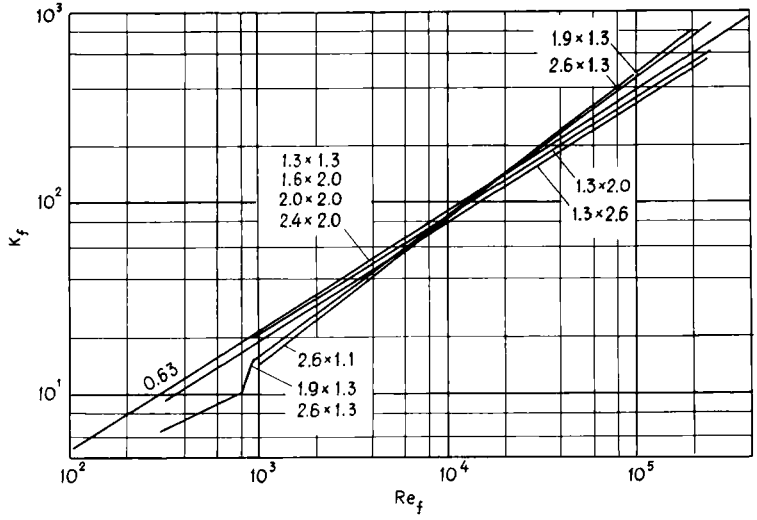

FIG. 50. Comparison of heat transfer of various in-line banks [74].

longitudinal and decreasing transverse pitch. In fact, the value of m is influenced by changes in the ratio of longitudinal and transverse pitches (Fig. 51).

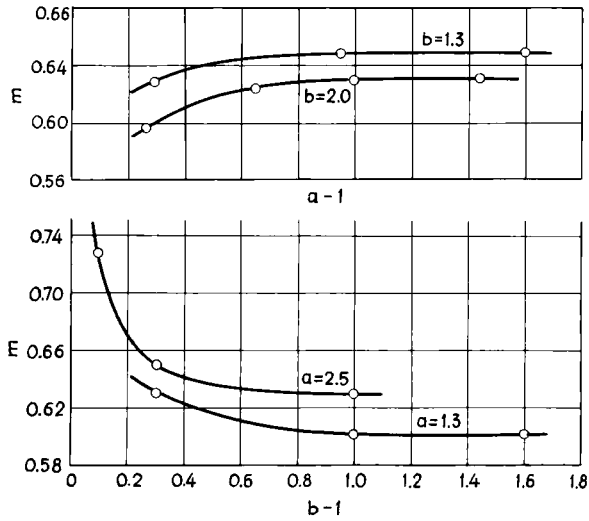

FIG. 51. The value of m, the power index of Re, in banks of in-line arrangement, as a function of the pitches.

In the mixed flow regime $m = 0.63$ is acceptable for most banks of in-line arrangement. The mean heat transfer of an inner tube is calculated from

$$Nu_f = 0.27\, Re_f^{0.63}\, Pr_f^{0.36}(Pr_f/Pr_w)^{0.25}. \tag{39}$$

In banks with $a/b < 0.7$, experimental heat transfer measurements are much lower than those calculated according to Eq. (39). Banks of this type are considered ineffective as heat exchangers.

Final experimental results of the heat transfer of different staggered banks in flows of viscous fluids [75] are presented in Fig. 52. The power index of Re is equal to 0.60 for all banks.

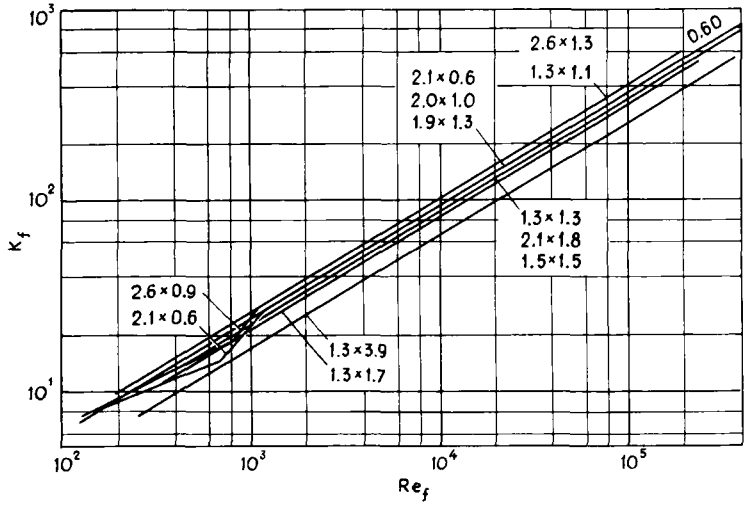

FIG. 52. Comparison of heat transfer of various staggered banks [71].

The effect of pitch is clear. Heat transfer increases with a decrease in the longitudinal pitch and, to a lesser extent, with an increase of the transverse pitch. The variation of c may be evaluated by the geometrical parameter a/b to the power 0.2 for $a/b < 2$. For $a/b > 2$, $c = 0.40$. In such banks the minimum free section is diagonal with respect to the main flow. Thus changes in c involve certain changes in the conditions of flow through a bank. The generalized formulas for heat transfer of inner tubes in various staggered banks are

for $a/b < 2$

$$Nu_f = 0.35(a/b)^{0.2}\, Re_f^{0.60}\, Pr_f^{0.36}(Pr_f/Pr_w)^{0.25}, \tag{40}$$

and for $a/b > 2$

$$Nu_f = 0.40\, Re_f^{0.60}\, Pr_f^{0.36}(Pr_f/Pr_w)^{0.25}. \tag{41}$$

4. *Heat Transfer in the Critical Flow Regime*

At $Re > 2 \times 10^5$, the critical regime in the flow past a single tube and a tube in a bank is established. Here the flow through a bank becomes increasingly turbulent, and the total heat transfer of the inner tubes increases sharply.

Investigations of heat transfer in the critical regime by Stasiulevičius *et al.* [76] are most comprehensive, so let us consider some of their results. Figures 53 and 54 present the heat transfer in inner rows of in-line and staggered banks in a crossflow of air. In the subcritical regime, the results of [76] correlate well with the results of heat transfer in banks of tubes in flows of air and liquids [74, 75] considered above.

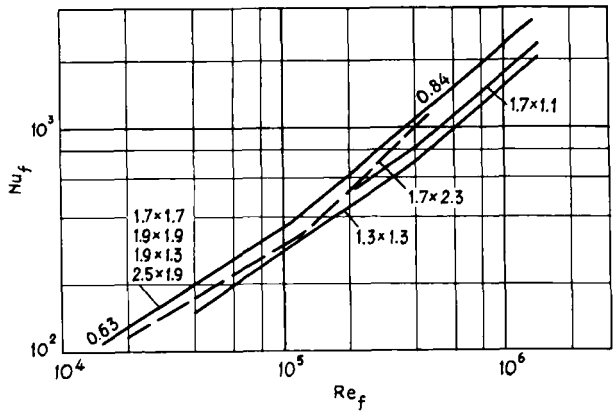

FIG. 53. Heat transfer of in-line banks at high Reynolds numbers [76].

The critical regime in the staggered and in-line banks examined is obvious at $Re > 2 \times 10^5$, expressed by the increase of the power index m from 0.6 to 0.8–0.9. The results of Hammecke *et al.* [77] are similar. The power index m of the Reynolds number in many banks exceeds 0.80, which corresponds to the power index in the relation for heat transfer in the turbulent boundary layer formed on the front portion of the tube. This means that with an increase of Reynolds number, the heat transfer increase in the rear portion of a tube is much faster than on a plate with a turbulent boundary layer. The rate of heat transfer increase in the rear is somewhat similar to that of heat transfer increase on a plate in the transition from laminar to turbulent flow. Therefore it should be supposed that in the critical regime the value of the power index m is not only influenced by the tube arrangement, but also by surface roughness, temperature difference, and the value

of Pr. From this point of view, measurements of the interaction of velocity and temperature fields in the boundary layer of a tube would be of interest, similar to measurements on a plate [78]. The mean value of $m = 0.84$ may be chosen in the critica! regime for all banks.

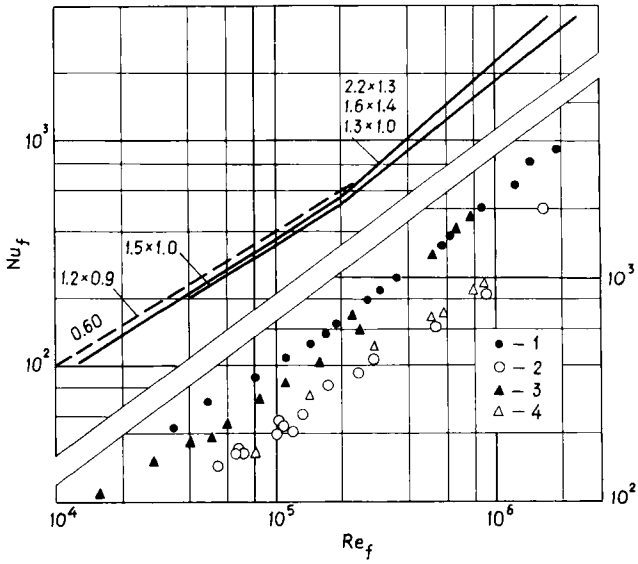

FIG. 54. Heat transfer of staggered banks at high Reynolds numbers [76]. 1—Fifth, and 2—first rows of a bank, 1.2 × 0.9; 3—fifth, and 4—first rows of a bank, 2.5 × 1.3.

As is seen from Fig. 54, with an increase of Re, the heat transfer of an inner row increases more, as compared to the first row.

The influence of pitch on heat transfer in the critical regime is similar to that in the subcritical regime. The heat transfer of all staggered banks with widely spaced tubes, i.e., with large a/b ratio is more intensive, but never differs from others by more than 25%.

Similar results are obtained for in-line banks. Heat transfer is most intensive in those banks with large transverse and small longitudinal pitch. The heat transfer intensity of most in-line banks, with the exception of some closely spaced banks, is the same. The heat transfer from tubes in inner rows of in-line banks can be calculated from

$$Nu_f = 0.021\ Re_f^{0.84}\ Pr_f^{0.36}(Pr_f/Pr_w)^{0.25}. \tag{42}$$

The following relations are recommend for calculating heat transfered from tubes in inner rows of staggered banks:

for $Pr > 1$

$$Nu_f = 0.022\, Re_f^{0.84}\, Pr_f^{0.36}(Pr_f/Pr_w)^{0.25}, \tag{43}$$

and for $Pr = 0.7$

$$Nu_f = 0.019\, Re_f^{0.84}. \tag{44}$$

5. *Heat Transfer of Closely Spaced Banks*

In the previous cases of heat transfer of banks of tubes, the results were referred to the velocity in the minimum free cross section from Eq. (7), i.e., to the maximum velocity. In fact, heat transfer is determined not by the maximum velocity, but by the average velocity, integrated over the perimeter of the tube. In wider spaced banks, the average velocity scarcely differs from the maximum and the acceptance of the latter is justified by the simpler calculation. But when the free cross section is small, the maximum velocity exerts its influence only on a small portion of the surface.

Investigations of heat transfer [79] in staggered and in-line banks, with clearance between tubes from 0.5 to 4 mm, revealed that the heat transfer curves for separate banks referred to the maximum velocity differ from each other, and their general level is lower than the actual heat transfer. Thus, for closely spaced banks, the results should be referred to the average velocity given by Eq. (8]. Such results for various closely spaced banks correlate satisfactorily (Fig. 55).

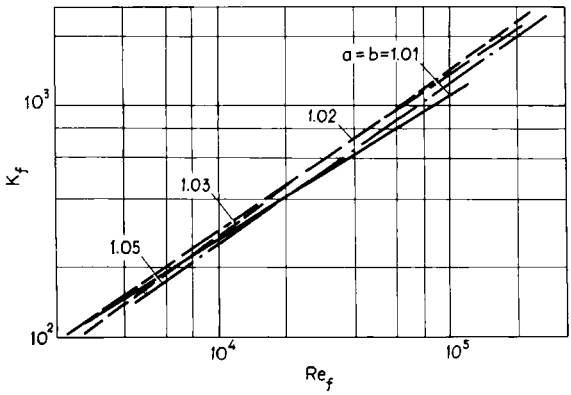

FIG. 55. Heat transfer of closely spaced in-line banks [79].

6. *Comparison of the Results*

Our equations (38)–(44) concerning the heat transfer in different banks with various fluids actually describe the results of investigations of 49 banks of different arrangements at Re from 20 to 2×10^6 and Pr from 0.7 to 500.

These investigations have been performed at the Institute of Physico-Technical Problems of Energetics, Lithuanian Academy of Sciences. Our relationship for heat transfer, denoted by the continuous line, is compared with the results of other authors for in-line and staggered banks in Figs. 56 and 57, respectively. The results correlate well in the whole range of Re examined.

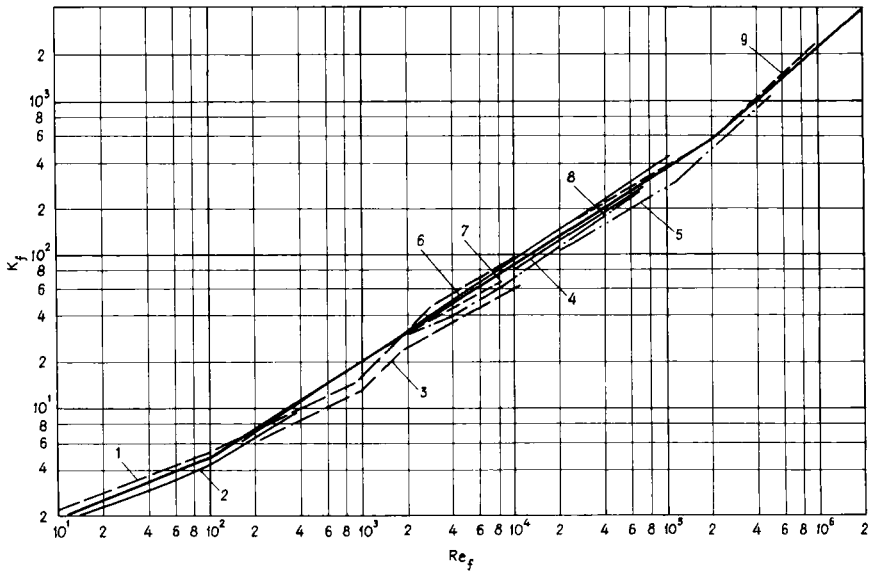

FIG. 56. Comparison of heat transfer of in-line banks. Curve 1—1.25 × 1.25, and curve 2—1.5 × 1.5, after Bergelin *et al.* [72]; curve 3—1.25 × 1.25, after Kays and London [18]; curve 4—1.45 × 1.45, after Kuznetsov and Turilin [39]; curve 5—1.3 × 1.5, after Lyapin [80]; curve 6—2.0 × 2.0, after Isachenko [73]; curve 7—1.9 × 1.9, after Grimison [9]; curve 8—2.4 × 2.4, after Kuznetson and Turilin [39]; curve 9—2.1 × 1.4, after Hammecke *et al.* [77].

The results of heat transfer in staggered banks are compared with those in in-line banks, using the experimental data of square in-line banks [20]. For the case of the staggered arrangement, this bank was turned by 45°. Figure 58 shows that at low Reynolds numbers the heat transfer of in-line banks is considerably lower than that of staggered banks. With an increase of Reynolds number, the heat transfer of in-line banks increases more rapidly and at high Re it approaches the heat transfer intensity of staggered banks. However, it should be mentioned that the efficiency of banks depends not only on heat transfer intensity but also on hydraulic resistance.

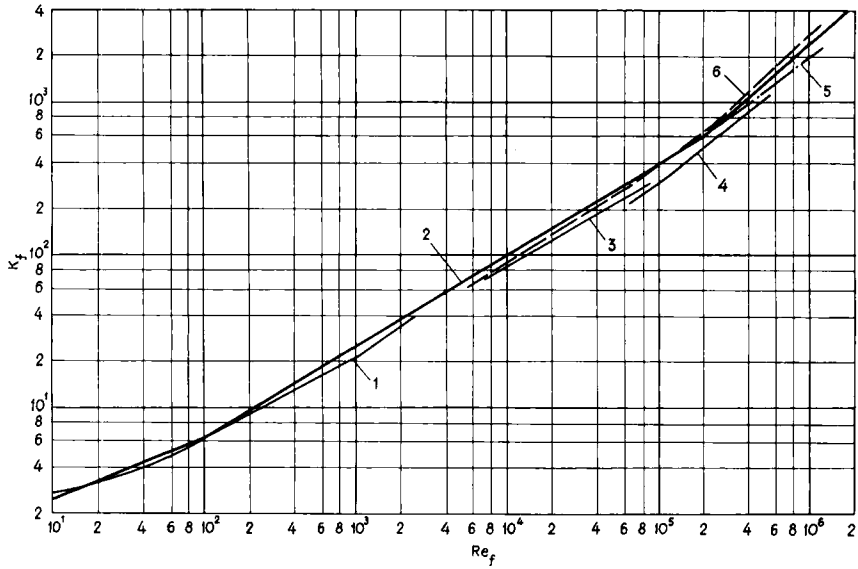

FIG. 57. Comparison of heat transfer of staggered banks. Curve 1—1.5 × 1.3, after Bergelin *et al.* [72]; curve 2—1.5 × 1.5 and 2.0 × 2.0, after Grimison [9], and Isachenko [73]; curve 3—2.0 × 2.0, after Antuf'yev and Beletsky [17], and Kuznetsov and Turilin [39], and Kazakevich [66]; curve 4—1.3 × 1.5, after Lyapin [80]; curve 5—1.6 × 1.4, after Dwyer and Sheeman [81]; curve 6—2.1 × 1.4, after Hammecke *et al.* [77].

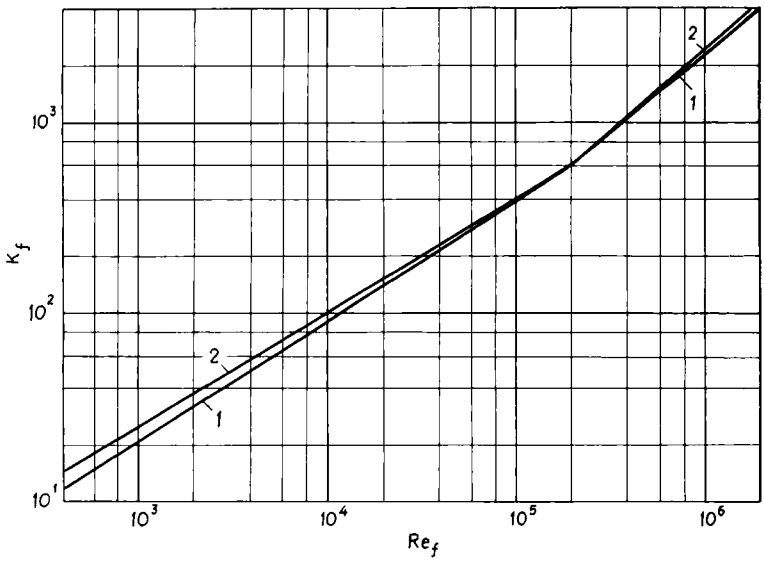

FIG. 58. Comparison of heat transfer of in-line and staggered banks. Curve 1—in-line; curve 2—staggered with $a/b > 2$.

VII. Hydraulic Resistance of Banks

A. Resistance Calculation Methods

Hydraulic resistance is one of the most important characteristics of heat exchangers and is characterized by the total pressure drop in flow across banks of tubes. As is known, the total pressure drop across a bank is a function of flow velocity, bank arrangement, and the physical properties of the fluid. The resistance of a bank with viscous fluids of constant density is expressed by the following functional relation

$$\Delta p = f(u, s_1, s_2, D, z, \mu, \rho). \tag{45}$$

The dimensionless form of this relation will be

$$\mathrm{Eu} = \phi(\mathrm{Re}, s_1/D, s_2/D, z) \tag{46}$$

or the exponential form

$$\mathrm{Eu} = k\,\mathrm{Re}^r z. \tag{47}$$

In generalizations of experimental results and in calculations according to Eq. (47) the choice of reference velocity and number of rows to which pressure drop is related is of considerable importance. The use of average velocity, calculated along the perimeter from the front stagnation point to $\phi = 90°$, as a reference is most suitable. This allows the comparison of the hydraulic resistance of various types of banks.

In banks with $a > 1.25$ the average value of the velocity is closer to the maximum, and here the latter is more convenient. In closely spaced banks with $a < 1.25$, the average value of the velocity is of the order of the main flow velocity, and here the latter may be used as reference.

For the generalization of experimental data, the maximum velocity is more acceptable as a reference, and it was used in the calculations below. It reflects the actual resistance with sufficient accuracy, except for closely spaced banks.

Experiment suggests that the pressure drop across banks is proportional to the number of rows and is determined by the tube arrangement. With a decreasing number of rows, the entrance and exit conditions in the bank contribute more to the total loss of kinetic energy. This must be taken into account in calculations for banks with a small number of rows. However, in experiments, banks with many rows are usually used. The results of hydraulic resistance are represented by the number Eu referred to one row or to a bank of ten rows.

B. MEAN RESISTANCE OF BANKS

Let us consider now the resistance of banks as dependent on the tube arrangement and Reynolds number. Our measurements of the pressure drop across 49 different banks in flows of air and liquids [20, 82] suggest that resistance is mainly determined by the transverse pitch a, and increases with a decrease of the latter. This applies both to staggered and in-line banks. With the longitudinal pitch b increasing, the larger space between two neighboring rows permits the formation of vortices which in many cases affects the resistance of the bank. The dependence of resistance on Re in a predominantly laminar flow has a different character than in a mixed flow.

1. *Predominantly Laminar Flow*

Viscous forces prevail in the resistance of in-line banks at $\mathrm{Re} < 10^3$, and the power index of Re is equal to -0.5. In this range the resistance of staggered banks is determined mainly by the value of the minimum free cross section and increases with a decrease of the latter (Fig. 59).

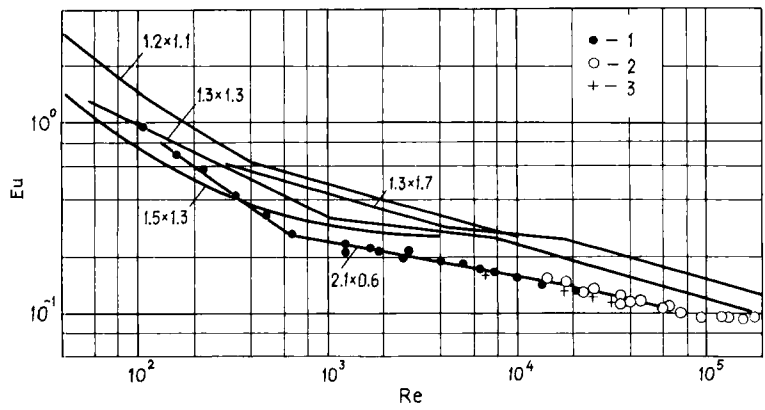

FIG. 59. Hydraulic resistance of staggered banks [20, 72]. 1—Transformer oil; 2—water; 3—air.

The figure presents generalized results of the resistance of several staggered banks, related to one row according to Eq. (47). The variation of resistance of in-line banks is similar. The relative resistance of in-line banks is, however, somewhat lower than that of staggered banks.

2. *Mixed Flow*

Data on hydraulic resistance (Fig. 59) show that the transition of the predominantly laminar to the mixed flow occurs at $\mathrm{Re} = 10^3$ in staggered banks, and at lower Re in banks in which the minimum free cross section s_2' is found along the diagonal (Fig. 10). After the transition and with a further increase of Re to 2×10^5, curves in the figure fall more gradually.

An increase of the longitudinal pitch leads to an increase of the resistance, the latter being influenced mainly by the space between the tubes in the bank. A decrease of the longitudinal pitch involves a decrease of the free cross section, and the effect of tube arrangement on resistance in such banks is reflected only in the value of the pitch along a diagonal. This applies for banks with $a < 2$.

The flow pattern in staggered banks with $a > 2$ is to some extent similar to that of in-line banks.

In most in-line banks, the transition of the predominantly laminar to the mixed flow also takes place at $\mathrm{Re} = 10^3$. In banks of large longitudinal pitch $b > 1.70$, and Eu becomes essentially independent of Reynolds number. In this case, the resistance of a bank is determined solely by the transverse pitch. In banks with $b < 1.5$, the pressure drop coefficient depends on Re, and is influenced by the longitudinal pitch.

3. *Critical Flow*

Let us first consider the results on the flow resistance in the transition to the critical regime as a function of the number of rows in a bank.

Experiments on staggered banks in air flows [82] suggest, as might be expected, that the resistance of a single row is similar to that of a single tube. It decreases at the critical Reynolds numbers and increases a little with a further increase of Re (Fig. 60). The pressure drop coefficient of a

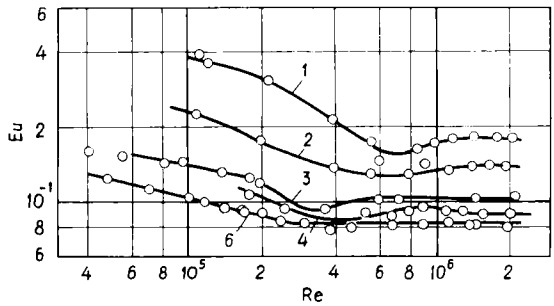

FIG. 60. Hydraulic resistance of a staggered bank, 1.5×1.04, referred to one row. Figures denote the total number of rows [82].

staggered bank with many rows also decreases with an increase of Re, and at $Re > 2 \times 10^5$ it becomes independent of Reynolds number. As can be seen, the character of the resistance of a bank differs slightly from that of a single row, the effect of the turbulence generated by preceding rows causing the difference.

In Fig. 61 the resistance characteristics of staggered banks with many rows are presented. Transition to the critical regime is noted at $Re > 2 \times 10^5$ in all the banks.

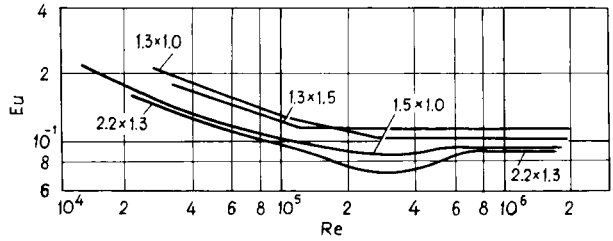

FIG. 61. Hydraulic resistance of staggered banks [82].

The resistance of banks is influenced also by the amount of free space between the tubes in a bank. Closely spaced banks with a staggered arrangement can be imagined as a number of obstacles, periodically narrowing and widening the channel, which leads to the disturbance of the flow. Thus for banks with $a/b < 1.7$, the automodel character of the pressure drop variation with Eu = const. and independent of Re begins abruptly. In wider spaced banks with $a/b > 1.7$ the flow across banks can be stable only at high Reynolds numbers.

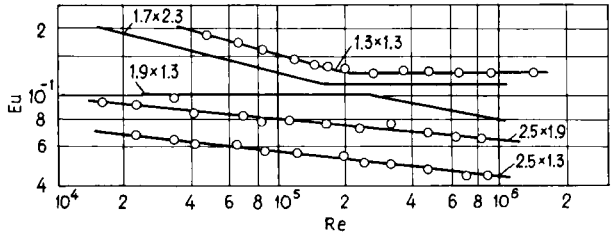

FIG. 62. Hydraulic resistance of in-line banks [76].

Figure 62 presents data on the pressure drop of in-line banks with a crossflow of air. It is obvious that in the closely spaced bank, 1.3×1.3, and banks with a large longitudinal pitch the automodel character of the pressure drop variation is established at $Re = 2 \times 10^5$. In banks of large

transverse and small longitudinal pitch, 2.5 × 1.3, the automodel character of the pressure drop variation never occurs in the range of Re examined. Apparently banks of this type are not capable of turbulizing the flow sufficiently and the automodel character of the pressure drop is established at even higher Reynolds numbers.

In predominantly turbulent flow, the pressure drop across banks of in-line arrangement with large transverse and small longitudinal pitches is less. The largest pressure drop is observed, of course, across banks with closely spaced tubes.

C. Proposals for Calculations of Hydraulic Resistance

As suggested by the analysis of experimental results, for simplicity of calculation a graphical interpretation of the data is most convenient. General graphs have been compiled from our results described previously, including the results of other authors on the pressure drop across banks in flows of gases and liquids. A satisfactory correlation has been achieved.

The general graphs of in-line banks are based on the resistance of banks of square arrangements, with the reference distance being the longitudinal pitch. Graphic corrections have been introduced for other banks to account for different pitches and Reynolds numbers.

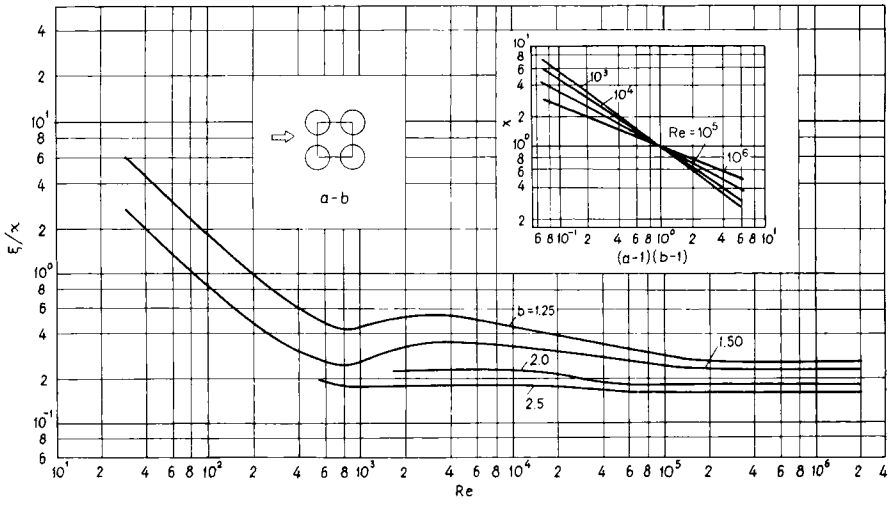

FIG. 63. Pressure drop coefficient of in-line banks as referred to the relative longitudinal pitch b.

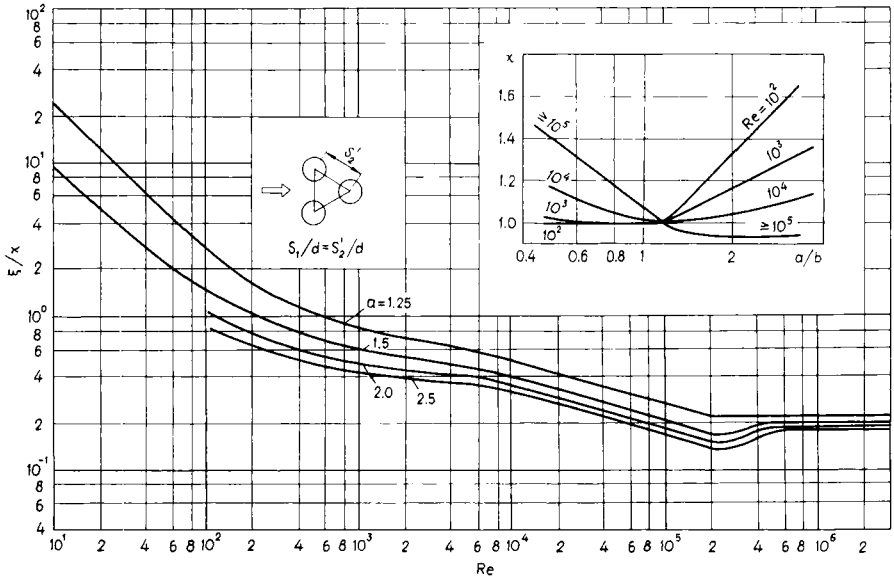

FIG. 64. Pressure drop coefficients of staggered banks as referred to the relative transverse pitch a.

The graphs of staggered banks are based on the equilateral-triangular arrangement with corrections for the evaluation of different arrangements and Re.

The graphs of the pressure drop coefficient as a function of Re for in-line and staggered banks are presented in Figs. 63 and 64, calculated for one row of a bank. Comparison of the pressure drop across staggered and in-line banks suggests that in the transition region from the predominantly laminar to the mixed flow, the banks of in-line arrangement exhibit a considerably lower pressure drop coefficient which must be ascribed to the structure of the turbulent flow in the rear portions of tubes due to different pitches.

With increasing Reynolds number, the flow in a bank becomes increasingly turbulent, and the pressure drop across in-line and staggered banks becomes equal.

VIII. Calculation of Banks of Tubes in Crossflow

The preceding sections were devoted to the heat transfer of tubes in banks and the hydraulic resistance of banks. The main factors exerting an influence on the heat transfer process were analyzed. Calculation formulas were

proposed, reflecting the general characteristics of the heat transfer of tubes in crossflow. The derivation of various equations and charts for various cases of tubes in crossflow are out of the scope of this paper. Equations and charts for all practical cases can be easily derived from the graphs presented here. Thus Fig. 55 may be used for heat transfer calculations in closely spaced banks.

For gases, the formulas are simplified; say, for air $Pr = 0.7 = \text{const.}$ and $Pr_f^{0.36}(Pr_f/Pr_w)^{0.25} = 0.88$. Multiplication of the constants in the formulas by 0.88 gives simplified formulas for banks in air at moderate temperature differences. Thus for $Re > 10^3$ the heat transfer of a tube of an in-line bank is determined by the relation

$$Nu_f = 0.27 \cdot 0.88\, Re_f^{0.63} = 0.24\, Re_f^{0.63}. \tag{48}$$

The author is not concerned with the processes of convective heat transfer at high temperatures of gases and in the presence of chemical reactions in the boundary layer, and the formulas cannot be applied for these conditions.

In Section VI formulas were proposed for the calculations of heat transfer of the inner tubes or banks of many rows. If the number of rows is small, one should take into account the lower heat transfer intensity of the first rows. In banks of less than 20 rows, the difference between the heat transfer of the first row and the inner rows is evaluated by the factor c_z, relating to the corresponding Nusselt numbers

$$Nu_z = c_z\, Nu_{z\geqslant 20}. \tag{49}$$

The values of c_z are presented in Fig. 65 as a function of number of rows.

The formulas apply only if the flow is perpendicular to the tube axis. At attack angles $\psi < 90°$, the heat transfer decreases, and is determined

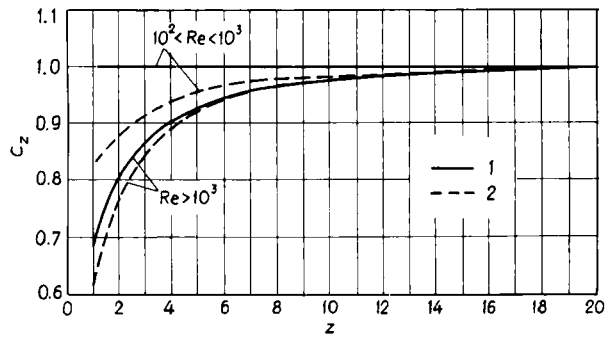

FIG. 65. Correction for the number of rows in the heat transfer calculation. 1—In-line; 2—staggered.

by the multiplication of the heat transfer coefficient by the correction factor depending on the angle

$$\epsilon_\psi = \alpha_\psi/\alpha_{\psi=0}.$$

The values of the correction factor are given in Fig. 66 for different angles of attack. At $\psi = 0$, we are dealing with the case of longitudinal flow past a bank of tubes.

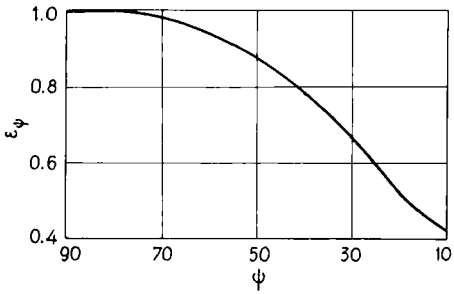

FIG. 66. Dependence of heat transfer of banks on the angle of attack.

The optimal arrangement of tubes is one of the main problems in the construction of heat exchangers. The choice in each case is connected with the amount of investment and operation cost which makes the knowledge of the power characteristics of heat exchangers so important.

The efficiency of heat exchangers from the energy point of view is characterized by the ratio of the amount of heat transferred through a definite surface to the energy consumed to overcome the hydraulic resistance. This problem can be solved using the data for heat transfer and hydraulic resistance.

An efficiency comparison of in-line and staggered banks reveals that for Re from 5×10^2 to 5×10^4 the in-line banks are more efficient. In spite of the fact that the heat transfer of in-line banks is lower in this range of Re, their efficiency is increased by the lower hydraulic resistance. At higher Reynolds number, the efficiency of banks of different types becomes comparable, being mainly determined by the pitch.

The efficiency of the process of heat transfer in a tube bank reflects its efficacy from an energy point of view. A decrease of velocity leads to higher efficiency, and from an energy point of view, heat transfer seems more effective at low velocities. But in this case the heated surface increases correspondingly, and only a complex solution of capital investment and operating costs leads to the optimal results for each specific case.

The problems of optimal arrangements and the calculations of heat exchangers have been analyzed in a number of special publications [17–19, 83].

NOMENCLATURE

a	relative transverse pitch, s_1/D
b	relative longitudinal pitch, s_2/D
C_D	drag coefficient, $D_f/(\rho u_0^2\, DL/2)$
c	constant
c_P	specific heat at constant pressure, J/kG C
D	diameter of tube, m
D_f	total drag of tube, N
F	heat transfer surface, m^2
f	frequency, Hz
g	acceleration of gravity, m/sec^2
H	height, m
K_f	complex dimensionless terms, $\mathrm{Nu_f}\,\mathrm{Pr}_f^{-0.36}\,(\mathrm{Pr_f}/\mathrm{Pr_w})^{-0.25}$
L	length, m
m	power index of Re
m_1	power index, Eq. (14)
n	power index of Pr
P	pressure coefficient, Eqs. (3) and (6)
p	pressure, N/m^2
p_0	static pressure, N/m^2
Δp	pressure drop, N/m^2
q	specific heat flux, W/m^2
R	radius of tube, m
r	power index of Re, Eq. (47)
s_1	transverse pitch of bank of tubes, m
s_2	longitudinal pitch of bank of tubes, m
s_2'	diagonal pitch of staggered bank, m
t	temperature, C
u	fluid flow velocity, m/sec
v	normal component of velocity, m/sec
x	distance measured from front stagnation point, m
y	distance measured normal to wall, m
z	number of tube rows in bank
α	heat transfer coefficient, W/m^2 °C
β	coefficient of expansion
ξ	pressure drop coefficient, $2\,\Delta p/\rho u^2 z$
λ	thermal conductivity, W/m°C
μ	dynamic viscosity, Nsec/m^2
ν	kinematic viscosity, m^2/sec
ρ	density, kg/m^3
τ	shear stress, N/m^2
ϕ, φ	angle measured from front stagnation point, deg
ψ	the angle of attack, deg
χ	coefficient, Figs. 63 and 64
Gr	Grashof number, $(gL^3/\nu^2)\beta\,\Delta t$
Nu	Nusselt number, $\alpha d/\lambda$
Nu(x)	local Nusselt number
Pr	Prandtl number, $c_P\mu/\lambda$
Re	Reynolds number, $u_0 d/\nu$
Eu	Euler number, $\Delta p/\rho u_0$
Sh	Strouhal number, fD/u_0
Tu	turbulence intensity, $\sqrt{\overline{u'^2}}/u_0$

SUBSCRIPTS

f, 0	conditions of the main flow
w	conditions on the wall
m	mean value
x, ϕ	local conditions

REFERENCES

1. L. V. King, *Phil. Trans. Roy. Soc. London, Ser. A* **214,** 374 (1914).
2. J. A. Hughes, *Phil. Mag. London* **31,** No. 181, 118 (1916).
3. H. Rietschel, *Mitt. Prüfunganstalt Heiz. Luftung. König. Tech. Hochschule, Berlin* 3, (1910).
4. W. H. Carrier and F. L. Busey, *Trans. ASME* **33,** 1055 (1911).
5. H. Thoma, "Hochleistungskessel", Springer, Berlin, 1921.
6. H. Reiher, *Forschungsarbeiten* No. 269, 1 (1925).
7. W. L. Lohrisch, *Forschungsarbeiten* No. 322, 1 (1929).
8. V. M. Antuf'yev and L. S. Kozachenko, *Sovietskove kotloturbostroyeniye* No. 5, 24 (1937).
9. E. D. Grimison, *Trans. ASME* **59,** 583 (1937).

10. O. L. Pierson, *Trans. ASME* **59**, 563 (1937).
11. E. S. Huge, *Trans. ASME* **59**, 573 (1936).
12. N. V. Kuznetsov and V. A. Lokshin, *Teplo Sila* No. 10, 19 (1937).
13. L. Hilpert, *Forsch. Gebiete Ingenieurw.* **4**, 215 (1933).
14. G. N. Kruzhilin and V. A. Shvab, *Zh. Tekhn. Fiz.* **5**, 703 (1935).
15. M. A. Mikhe'yev, *Zh. Tekhn. Fiz.* **13**, 311 (1943).
16. A. H. Davis, *Phil. Mag.* **47**, 972 (1924).
17. V. M. Antuf'yev and G. S. Beletsky, "Teploperedacha i aerodinamicheskiye soprotivleniya trubchatikh poverkhnostey v poperechnom potoke," Mashgiz, Moscow, 1948.
18. W. M. Kays and A. L. London, "Compact Heat Exchangers," McGraw-Hill, New York, 1958 (2nd ed., 1964).
19. R. Gregorig, "Wärmeaustauscher," Verlag H. R. Sauerländer u. Co, Frankfurt am Main, 1959.
20. A. Žukauskas, V. J. Makarevičius, and A. Šlančiauskas, "Heat transfer in Banks of Tubes in Crossflow of Fluid," Mintis, Vilnius, 1968 (In Russian).
21. H. Lamb, "*Hydrodynamics*," p. 617 Dover, New York, 1945.
22. E. Achenbach, *J. Fluid Mech.* **34**, 625 (1968).
23. H. Schlichting, "Encyclopedia of Physics," Vol. 8, p. 351. Springer, Berlin, 1959.
24. A. Roshko, On the Development of Turbulent Wakes from Vortex Streets. NACA Rep. No. 1191 (1954).
25. A. Roshko, *J. Fluid Mech.* **10**, 345 (1961).
26. R. Gregorig and H. K. M. Andritzky, *Chem. Ingenieur-Tech.* **15**, 894 (1967).
27. A. Fage. and V. M. Folkner, *Aero Res. Counc., Rep. and Mem.*, London, No. 1369, 1931.
28. V. Žiugžda and T. Ruseckas, *Mokslas ir Tech.* No. 3, 61 (1971).
29. Zh. S. Akilba'yev, S. I. Isata'yev, P. A. Krashtalev, and N. V. Masle'yeva, *Prob. teplo. prikl. teplofiz.* **3**, 180 (1966).
30. H. C. Perkins, Jr. and G. Leppert, *Int. J. Heat Mass Transfer* **7**, 143 (1964).
31. R. Bressler, *Kältetechnik* **11**, 365 (1958).
32. Ž. Kostić, Int. seminar, Herceg-Novi, Yugoslavia (1969).
33. E. Achenbach, *Wärme Stopfübertragung* **2**, 47 (1969).
34. Ž. Kostić and S. Oka, Int. seminar, Herceg-Novi, Yugoslavia, 1968.
35. A. A. Žukauskas and J. J. Žiugžda, "Heat Transfer in Laminar Flow of Fluid," Mintis, Vilnius, 1969 (In Russian).
36. A. A. Žukauskas and A. B. Ambraziavičius, *Int. J. Heat Mass Transfer* **3**, 305 (1961).
37. A. A. Žukauskas, *Teploenergetika* No. 4, 38 (1954).
38. V. J. Katinas, J. J. Žiugžda, and A. A. Žukauskas, *Lietuvos TSR MA Darbai, Ser B*, **4**(63), 209 (1970).
39. N. V. Kuznetsov and S. I. Turilin, *Izv. VTI* No. 11, 23 (1952).
40. J. K. Stasiulevičius and P. S. Samoška, *Inzh. Fiz. J.* **7**, No. 11, 10 (1964).
41. M. A. Mikhe'yev, "Osnovi teploperedachi," Gosenergoizdat, Moscow, 1956; "Fundamentals of Heat Transfer," Mir, Moscow, 1956; "Fundamentals of Heat Transfer." Mir, Moscow, 1968.
42. P. P. Švenčianas, V. J. Makarevičius, M. M. Tamonis, and A. A. Žukauskas, *Lietuvos TSR MA Darbai, ser. B* **4** (59), 149 (1969).
43. A. A. Šlančiauskas, R. V. Ulinskas, and A. A. Žukauskas, *Lietuvos TSR MA Darbai, ser. B* **4**(59), 163 (1969).
44. R. Gregorig, *Wärme Stoffübertragung* **3**, 26 (1970).
45. G. N. Kruzhilin, *J. Tekhn. Fiz.* **6**, 858 (1936).
46. E. R. G. Eckert, *VDI-Forschungsh.* **416** (1942).

47. H. J. Merk, *J. Fluid Mech.* **5,** 460 (1959).
48. N. Frössling, *Lunds. Univ. Arskrift. N.F.*2 **36, 1** (1940).
49. K. M. Krall and E. R. Eckert, "*Heat Transfer*, 1970" Vol. 3, FC7.5 Paris-Versailles, 1970.
50. E. R. Eckert and E. Soengen, *Trans. ASME* **74** 343 (1952).
51. D. S. Meel, *Int. J. Heat Mass Transfer* **5,** 715 (1962).
52. W. H. Giedt, *J. Aeronaut. Sci.* **18,** 725 (1951).
53. G. M. Zapp, M. S. Thesis, Oregon State College (1950).
54. J. Kestin, *Advan. Heat Transfer* **3,** 1 (1966).
55. J. Kestin and R. T. Wood, "*Heat Transfer, 1970*," Vol. 2, PC 2. 7. Paris-Versailles, 1970.
56. E. P. Dyban and E. V. Epick, "*Heat Transfer 1970*," Vol. 2, FC 5.7. Paris-Versailles, 1970.
57. B. S. Van der Hegge Zijnen, *Appl. Sci. Res., Sect. A.* **6,**
58. D. S. Collis and M. J. Williams, *J. Fluid Mech.* **6,** 359 (1959).
59. P. O. Davies and M. J. Fisher. *Proc. Roy. Soc. A.* **280,** 486 (1964).
60. P. O. Davies, Int. seminar, Herceg-Novi, Yugoslavia (1969).
61. E. L. Piret, W. James, and E. Stacy, *Ind. Eng. Chem.* **39,** 1088 (1947).
62. R. M. Fand, *Int. J. Heat Mass Transfer* **8,** 995 (1965).
63. E. Schmidt and K. Wenner, *Forsch. Gebiete Ingenieurw.* **12,** 65.
64. L. N. Ilyin, *Teplo. aerodinamika, sb. TsKTI* **18,** No. 4, 3 (1950).
65. G. A. Mikhaylov, *Sovietskoye kotloturbostroyeniye* No. 12, 434 (1939)
66 F. P. Kazakevich, *Teploenergetika* No. 8, 22 (1954).
67. F. M. Mayinger and O. Schad, *Wärme Stoffübertragung* **1,** 43 (1968).
68. R. A. Bortoli, R. E. Grimmble, and J. E. Zerbe, *Nuc. Sci. Eng.* **1, 2**39 (1956).
69. C. C. Winding and A. J. Cheney, *Ind. Eng. Chem.* **40,** 1087 (1948).
70. G. A. Omohundro, O. P. Bergelin, and A. P. Colburn, *Trans. ASME* **71,** 27 (1949).
71. O. P. Bergelin, G. A. Brown, H. L. Hell, and F. W. Sullivan, *Trans. ASME* **72,** 881 (1950).
72. O. P. Bergelin, G. A. Brown, and S. C. Doberstein, *Trans. ASME* **74,** 953 (1952).
73. V. P. Isachenko, Teploperedacha i teplovoye modelirovaniye, *Izd. Ahad. Nauk SSSR* 213 (1959).
74. V. J. Makarevičius and A. A. Žukauskas, *Lietuvos TSR MA Darbai ser. B* **3(26),** 231 (1961).
75. A. A. Žukauskas and A. A. Šlančiauskas, *Teploenergetika* No. 2, 72 (1961).
76. J. K. Stasiulevičius and P. S. Samoška, *Lietuvos TSR MA Darbai, ser. B* **4(35),** 77 (1963): **4(55),** 133 (1968).
77. K. Hammecke, E. Heinecke, and F. Scholz, *Int. J. Heat Mass Transfer* **10,** 427 (1967).
78. A. A. Šlančiauskas, A. A. Pedišius, and A. A. Žukauskas, *Lietuvos TSR MA Darbai, ser. B* **3(58),** 193 (1969).
79. P. S. Samoška, V. J. Makarevičius, A. A. Šlančiauskas, J. J. Žiugžda, and A. A. Žukauskas, *Lietuvos TSR MA Darbai, ser. B* **3** (50), 105 (1965).
80. M. B. Lyapin, *Teploenergetika* No. 9, 49 (1956).
81. O. E. Dwyer and T. V. Sheeman, *Ind. Eng. Chem.* **48,** No. 10, 1836 (1956).
82. J. K. Stasiulevičius and P. S. Samoška, *Lietuvos TSR MA Darbai, ser. B* **4(35),** 83 (1963).
83. A. F. Fritzsche, "Gestaltung und Berechnung von Ölkühlern," Leeman, Zürich, 1953.

Natural Convection in Enclosures

SIMON OSTRACH

Division of Fluid, Thermal, and Aerospace Sciences, Case Western Reserve University, Cleveland, Ohio

I. Introduction 161
A. Review of Existing Work 162
B. Outline of Problems 171
II. Rectangular Cavities 174
A. Heat Transfer in the Conduction Regime 179
B. Heat Transfer in the Boundary Layer and Transition Regimes 181
C. Boundary Layer Flow 184
III. Horizontal Circular Cylinder 196
A. Analysis 196
B. Results and Discussion 204
C. Experiments 209
D. Analysis for Heating-from-the-Side 213
E. Further Experiments 216
IV. Concluding Remarks 224
Nomenclature 225
References 226

I. Introduction

Over the past years convection phenomena induced by body forces have been the object of extensive research efforts. A rather broad classification into two types of problems can be made: the *external* problem such as the flow and heat transfer from a heated rod or plate to a fluid at rest, and the *internal* problem such as the flow and heat transfer between parallel plates or in fluid-filled cavities.

Thus far, external problems have received a great deal of attention while relatively little has been done about internal ones. The reason for this is not the greater importance of the external problem but rather that internal natural convection problems are considerably more complex. For large Rayleigh numbers (product of Prandtl and Grashof numbers) convection

effects are important and for external problems Prandtl boundary layer theory yields the same simplifications that are so helpful in other problems; the region exterior to the boundary layer can be assumed to be unaffected by the boundary layer. For confined natural convection problems, on the other hand, a boundary layer will exist near the walls but the region exterior to it will be enclosed by the boundary layer and will form a core region. Because this core is encircled by the boundary layer it cannot be considered to be independent of it. Hence, the boundary layer and core are closely coupled to each other and this coupling constitutes the main source of difficulty in obtaining analytic solutions to internal problems.

A. REVIEW OF EXISTING WORK

Most of the early work on internal flows with body forces was of an experimental or semiempirical nature and was presented by Elenbaas [1–3]. The second phase of work (not chronological but in order of complexity) on such problems consists of a number of analyses of fully-developed flows between vertical parallel plates or in tubes and started with the work of Ostrach [4]. This work is extensively reviewed by Ostrach [5] and it indicated a number of new and interesting results. For example, it showed that viscous dissipation could be important and that it would act like heat sources in the fluid; also it could lead to a second state of flow and heat transfer. Further, it was found that thermal instabilities could be encountered in such configurations when the heating was from below. These studies of fully-developed flows are applicable to configurations in which the length in the direction of the body force is large compared to the width or radius. To simulate completely enclosed regions, the condition of no net mass flow was added, but no information is obtained in this way about the flow and heat transfer near the ends. None of the aforementioned difficulties were encountered in these analyses because the resulting linear equations could be solved without recourse to a boundary layer analysis.

The next step was taken by Lighthill [6] who analyzed the natural convection in a closed-end tube with constant temperature walls by an integral method. He found that the type of flow in such a tube depends primarily on the height–radius ratio l/R_0, for fixed Prandtl and Rayleigh numbers. For very small values of l/R_0 the flow is essentially like the free convection about a vertical plate, i.e., the effect of the confining walls is negligible if the boundary layer thickness is much smaller than the tube radius. For somewhat larger l/R_0 values, however, this effect is no longer negligible. The three flow regimes to be expected if the walls influence each other are shown in Fig. 1. The first, for small values of l/R_0, is just the free convection

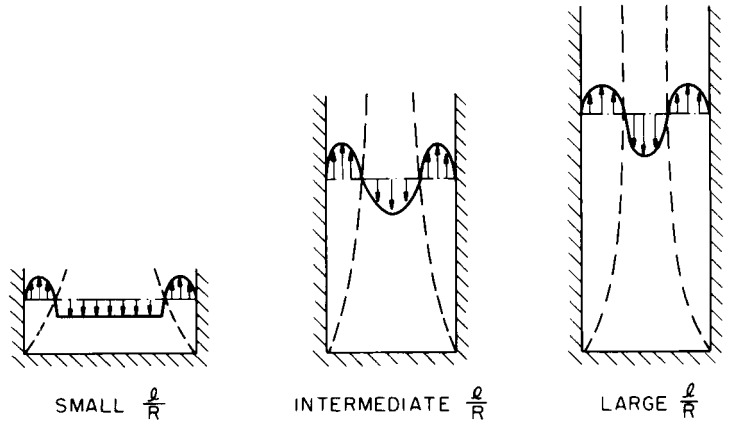

FIG. 1. The three flow regimes in a closed-end tube [52].

boundary layer flow modified to account for a downward flow outside the boundary layer, equal to the upward flow. This regime breaks down at a value of l/R_0 for which there is no longer a maximum volume flow of cool fluid at the orifice cross section. When l/R_0 exceeds this critical value the boundary layer mixes with the central flow and, when steady state is attained, the profiles fill the whole tube. This type of flow may be difficult to perceive intuitively so consider the extreme case $l/R_0 \gg 1$. In this case the tendency of the upward layer to thicken with axial distance disappears. Then the velocity and temperature distributions are similar at each cross section; only their scale increases as the orifice is approached. Therefore, in the intermediate l/R_0 range the velocity and temperature profiles fill the tube completely but vary along the tube. For the similarity regime (large l/R_0) Lighthill found that the flow fills the entire tube for only one value of l/R_0. If l/R_0 exceeds this value the motion stops near the closed end so that the effective l/R_0 becomes equal to that value. Ostrach and Thornton [7] considered the same configuration but the temperature varied linearly along the cylinder wall. For large l/R_0 they found that flow in the entire tube was possible over a range of parametric values rather than for discrete values, as in Lighthill's case. The significant effect of confining boundaries can be seen from a plot of the total Nusselt number over the tube length as a function of (R_0/l) Ra (Fig. 2). For these problems the difficulties associated with the analysis of confined regions are again avoided by use of an integral method which does not attempt to deal accurately with the flow details.

Experimental verification of the three laminar flow regimes and the predicted heat transfer results was obtained by Martin [8]. Hartnett and Welsh [9] performed experiments similar to Martin's but with uniform heat

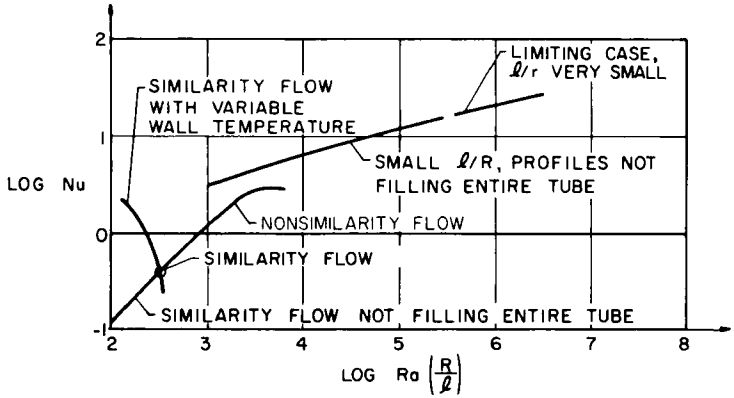

FIG. 2. Nusselt number as function of the product of the Rayleigh number and the radius–length ratio for closed-end tube flows [52].

flux at the wall rather than uniform temperature. They found that as long as $Pr > 0.1$ the average heat transfer performance in a vertical tube closed at the bottom is equivalent for the cases of uniform wall temperature and uniform wall heat flux.

The earliest investigation of natural convection in a completely confined configuration seems to have been made by Lewis [10] who studied the flow and heat transfer in the interior of a horizontal circular cylinder with a cosine wall temperature distribution; the maximum and minimum wall temperatures were on opposite ends of the horizontal diameter. Lewis considered only the case of Rayleigh number less than unity for which no boundary layer phenomena are encountered. By means of a perturbation analysis he found that convection was negligible for this case and that the principal mode of heat transfer was, therefore, conduction. A similar problem was treated by Zhukhovitskii [11]. An excellent survey of low Rayleigh number internal natural convection problems is presented by Ostroumov [12]. Low Rayleigh number convection inside a spherical cavity was investigated by Drakhlin [13].

Another completely confined natural convection problem in which the difficulties associated with coupling of the boundary layer and the core do not occur was analyzed by Ostrach and Braun [14]. Specific consideration was given to the flow and heat transfer of a fluid subject to an axial body force inside a rotating right circular cylinder of small height which is heated at its lower surface. This configuration was studied to see if the centrifugal force would generate large natural convection flows. A perturbation method was used that led to simplified equations that could be solved exactly so that no boundary layer type of analysis with the incumbent difficulties mentioned above was necessary. It was found that the Coriolis force inhibits

the motion so that no appreciable convection is obtained unless radial vanes are inserted in the cylinder to inhibit this force.

1. *Boundary Layer Aspects*

The first work dealing with the much more difficult large Rayleigh number internal natural convection problem was that of Ostrach [15] who studied the same configuration as Lewis. The case he considered corresponded to that of a large Grashof number and a Prandtl number of unit order.[1] He therefore concluded that both flow and thermal boundary layers were adjacent to the cylinder wall and he assumed that the core would be isothermal and would rotate as a solid body, i.e., the vorticity would be uniform. His boundary layer solutions could not be carried out to a high degree of accuracy because no high speed computers were available. Nevertheless, his postulate of an isothermal rotating interior core was used by all investigators until recently.

A somewhat similar configuration was studied by Pillow [16] who wanted to determine the heat transfer through a fluid in cellular convective motion between two infinite horizontal planes. When the lower plate in such a configuration is at a higher temperature than the upper one, the configuration is thermally unstable and a cellular motion occurs after a critical value of the Rayleigh number is exceeded. (See Ostrach [5] for more discussions of thermal instabilities.) The cells were assumed to be two-dimensional, with the cell axes horizontal. The boundaries of the cell were taken to be the two horizontal plates and two parallel vertical planes of symmetry. Pillow considered the large Grashof number, unit-order Prandtl number case, and showed that in the limit of infinite Grashof number, viscous and thermal diffusion could be neglected in the interior, and general solutions for the temperature and vorticity in the interior were obtained from the resulting simplified equations. These solutions, when coupled with appropriate symmetry arguments, also led Pillow to conclude that the interior of the cell was an isothermal region of uniform vorticity. The boundary layer equations, however, presented a nonlinear problem which could only be solved in a very approximate manner. Still, it was possible to ascertain that the heat transfer was proportional to the five-fourths power of the temperature difference between the horizontal plates, a result previously determined by the experiments of Mull and Reiher [17]. Experimental verification of the existence of an isothermal interior region in such a configuration appeared earlier in the work of Schmidt and Saunders [18].

[1] Since the Rayleigh number is equal to the product of the Prandtl and Grashof numbers, a large Rayleigh number could, obviously, also correspond to a large Prandtl number and a unit-order Grashof number. This possibility will be discussed subsequently.

The heat transfer through gas layers confined in rectangular cavities composed of isothermal vertical walls and either perfectly conducting or perfectly insulating horizontal surfaces was investigated by Batchelor [19] for the case of height-to-width ratios of the layers between 5 and 200. It was reasoned that several different flow regimes could occur within the cavity depending on the values of the height to width ratio (l/d) and the Rayleigh number (Ra). For small values of the Rayleigh number, Batchelor employed a perturbation scheme similar to that of Lewis [10] and, as expected, concluded that convection was unimportant compared to conduction. Conduction was also found to be the sole means of heat transfer in the asymptotic case of $l/d \to \infty$ and general Ra. In this case the temperature distribution in the gas (air) was found to vary linearly between the walls and the fluid flow was entirely vertical. Convection effects were restricted to the upper and lower ends of the cavity and as the Rayleigh number approached those values appropriate to a boundary layer analysis, these end effects propagated into the rest of the cavity. This asymptotic case of infinite height-to-width ratios had also been investigated earlier by Ostrach [4] who treated it as a special case in a general analysis of natural convection flows between parallel, vertical, isothermal plates. In the work of Ostrach, the effect of viscous dissipation was also included.

The boundary layer case corresponding to large Rayleigh numbers with general height-to-width ratios was also formulated by Batchelor and, based on the work of Pillow [16], the interior was taken to be isothermal and to have constant vorticity. It should be noted, however, that thermal boundary conditions in the problems treated by Pillow and Batchelor were distinctly different. The problem as formulated in this way was later solved numerically by Poots [20] using a method based on expansions in orthogonal polynomials. These results, as well as those obtained by Batchelor for the lower Rayleigh number situations were also compared in the respective papers to the work of Mull and Reiher [17].

The question of the nature of the interior region of a closed streamline flow in which viscous effects were restricted to the vicinity of an enclosing solid surface was investigated by Batchelor [21] in a formal way. As a theorem he was able to show that as long as the interior was not stagnant, the vorticity there was constant. The nature of the equations was such that the proof applied only to isothermal regions. The boundary of the interior region had to be a closed streamline lying completely in the region of the small viscous forces (i.e., this bounding streamline could not pass through any part of the viscous boundary layer adjacent to the solid surface). With this work, then, it appeared that the nature of the core was now well understood and described.

Martini and Churchill [22] presented experimentally determined velocity and temperature profiles for the case of natural convection of air within a horizontal cylinder. The cylinder wall was cut along a vertical plane and the two halves were maintained at different uniform temperatures. The Rayleigh number was varied between approximately 2×10^5 and 8×10^6. Obviously, although the circumferential temperature distribution was a step function instead of a cosine, this configuration was quite similar to that of Ostrach [15]. Some of the more interesting observations made by Martini and Churchill were: (1) most of the flow took place in a narrow ring adjacent to the cylinder wall, (2) the interior region was relatively stagnant, and (3) the temperature distribution in the interior was that of a stratified fluid with the isothermals being horizontal and the temperature increasing vertically upward. For the first time, these experimental results cast more than a little doubt on the intuitively plausible supposition that when a fluid is heated from the side, the interior should be isothermal and should rotate as a solid body.

A numerical integration of the differential equations with boundary conditions corresponding to the case investigated experimentally by Martini and Churchill [22] was carried out by Hellums and Churchill [23]. Reasonably good agreement was obtained between the numerical and experimental results.

These experiments of Martini and Churchill dealing with a horizontal cylinder were followed closely in the literature by those of Eckert and Carlson [24], who dealt with air layers enclosed between vertical isothermal walls, the same case investigated analytically by Batchelor [19] as already discussed. The apparatus used by Eckert and Carlson could be assembled with height-to-width ratios from 2.1 to 46.7 and the temperature difference between the vertical sides was varied between 10°F and 160°F. The selection of widths and temperature differences used enabled the Rayleigh number to be varied from approximately 200 to 2×10^5. The temperature field was determined in great detail using a Zehnder–Mach interferometer while no velocity determinations were made. As predicted by Batchelor, the experimental results showed that below a certain Rayleigh number (prior to the formation of a boundary layer regime) and above a certain height-to-width ratio, heat was transferred from the hot to the cold boundary by conduction in the central part of the layer, while convection effects were restricted to the corner regions. However, in the boundary layer regime (above a certain Rayleigh number and below a certain height-to-width ratio) the core of the layer was not found to be isothermal as predicted by Batchelor, but instead, the temperature was uniform along horizontal lines only and increased in the vertical direction. Based on their experimental observations, Eckert and Carlson concluded that it was extremely doubtful whether a core of uniform

temperature would ever exist at large Rayleigh numbers unless the height-to-width ratio was extremely small.

Using finite difference methods, Wilkes [25] numerically solved the transient and steady-state problems for natural convection in rectangular cavities having isothermal vertical walls. For a height-to-width ratio of unity and for a Rayleigh number of order 10^5, his results show the isothermals to be almost horizontal lines in the interior with a temperature gradient established in the vertical direction such that the temperature increases upward. A plot of the streamlines for this case indicated a definite decrease in velocity as one left the boundary layer region and moved toward the interior indicating a relatively stagnant core. Gershuni and his co-workers [26] obtained similar numerical results. Clearly these results tended to corroborate the findings of Eckert and Carlson [24] for the boundary layer regime.

Experiments which further support the stratified core configuration are reported by Elder [27]. These experiments were made in a rectangular slot across which a constant temperature difference was maintained and the end walls were insulated corresponding to Wilkes' configuration. The cavity was such that the motion remained two-dimensional and the ranges of parametric values were: height–width ratios from unity to 60, Prandtl number equal to 10^3, and Rayleigh numbers up to 10^8.

For Rayleigh numbers below 10^3 the temperature field was essentially the same as for conduction and there was a weak stable unicellular circulation generated. For Rayleigh numbers between 10^3 and 10^5 boundary layers formed near the wall and the interior region exhibited a uniform vertical temperature gradient. The flow resembled that along an isolated isothermal vertical wall except that the boundary layer growth on each wall is inhibited in the central part of the slot by the presence of the other wall. In the lower half of the slot the interior fluid is entrained as the boundary layer grows. In the upper part the interior temperature gradient decreases the buoyancy force which decreases the boundary layer thickness. Near Rayleigh numbers of 10^5 secondary flows also appeared in the interior.

Gill [28] recently analyzed the configuration studied experimentally by Elder [27]; his work is also meant to be an extension of Batchelor's [19] for the case of large Rayleigh number (Rayleigh number much larger than the slot height–width ratio). By an order of magnitude argument, Gill contends that there can only be horizontal motions in the core and the temperature can be a function only of the vertical coordinate. By an Oseen-like method he linearizes the boundary layer equations and obtains results that agree with Elder's experiments in regard to the entrainment of fluid by the boundary layer in the lower half of the slot and ejection by the boundary layer in the upper half, on the warmer wall.

A numerical study similar to that of Wilkes, also for a rectangular cavity, was made by de Vahl Davis [29] for steady flow only and for large Prandtl numbers and unit-order Grashof numbers. Again the horizontal isotherms and streamlines in the core were indicated with the slope of these isotherms tending to become negative for increasing Rayleigh number; in other words, outside the boundary layer on the cold wall, say, the fluid temperature is greater than that at the corresponding location outside the boundary layer on the hot wall. The vertical temperature gradient in the center of the cavity is essentially zero for small Rayleigh numbers and approaches an asymptotic positive value as the Rayleigh number becomes very large. This asymptotic value was found to be dependent on the horizontal wall conditions, namely, whether they were insulated or had a prescribed linear variation between the two vertical wall temperatures.

Polezhaev [30] numerically integrated the Navier–Stokes and energy equations for unsteady natural convection of a compressible fluid in a square cavity to show the origin and development of secondary flows in the core at large Grashof numbers.

Prior to the work of Elder and Gill, Weinbaum [31] reconsidered the horizontal cylinder configuration with a cosine wall temperature distribution that was first treated by Lewis [10] and Ostrach [15]. He generalized the configuration (see Fig. 3) by introducing an arbitrary phase angle between

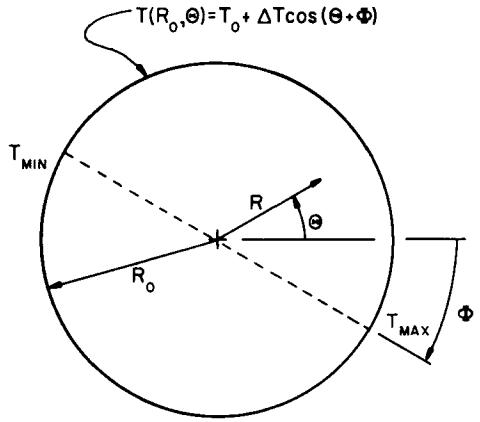

FIG. 3. The horizontal cylinder configuration.

the horizontal direction and the diameter on which the imposed wall temperature maximum and minimum occur. In this way situations ranging from heating-from-the-side (phase angle of zero), corresponding to Ostrach's case, to the thermally unstable case of heating-from-below (phase angle of 90°) could be treated. For small Rayleigh numbers he used a perturbation

method similar to that of Lewis [10]. For large Rayleigh numbers (large Grashof number and unit-order Prandtl number) Weinbaum considered that the flow field could be broken into interior and boundary layer regions as did Ostrach. After proving the interior to be isothermal, Weinbaum invoked the theorem of Batchelor [21] pertaining to a closed-streamline region of small viscosity and demonstrated that the vorticity in the interior would be uniform. Then, in order to solve the rather complicated boundary layer equations (a set of nonlinear, coupled partial differential equations) he introduced a linearization scheme known as the "modified Oseen" technique developed by Lewis and Carrier [32]. Through the application of this method it was possible to render both the vorticity transport and energy equations linear, and at the same time uncouple the energy equation from the boundary layer equations. Solutions were obtained in this way only for the case of heating-from-below, because for heating-from-the-side Weinbaum was unable to match the boundary layer solution to an interior of uniform nonzero vorticity. In order to overcome this difficulty he introduced a variation of the modified Oseen method to the full describing equations. For the heated-from-below case it was found that the interior rotated essentially as a solid body, but when the heating was directed from the side the interior tended to stagnate but was isothermal. Velocity and temperature profiles for this latter case were compared with those obtained experimentally by Martini and Churchill [22] for a similar geometry but different thermal boundary conditions and qualitative agreement was observed. No discussion of the situation for intermediate values of the phase angle was given. Also the role of the modified Oseen constant involved in the method of solution was not clarified and the means for determining it was left rather arbitrary.

Simultaneously with Weinbaum, Ostrach and Menold [33, 34] considered the same configuration except that they restricted interest to the large Prandtl number and unit-order Grashof number. The advantage of this is that the nonlinear inertia terms in the equations of motion are negligible so that considerable mathematical simplification is obtained. The essential physical aspects of the problem, however, are retained.

Ostrach and Menold, using a boundary layer analysis and modified Oseen linearization on the energy equation alone, also made the *a priori* assumption of closed-core streamlines and then were able to prove that the core was isothermal. This led to the result that the core stream function satisfies the biharmonic equation. This implies a region of slow viscous flow and is consistent with the limit of large viscosity, i.e., large Prandtl number. (This is in contradistinction to Weinbaum's result for a core of constant vorticity wherein the stream function satisfied Poisson's equation, corresponding to a frictionless flow.) By matching the boundary layer and

core solutions they found analytical expressions which included the heating phase angle, ϕ, and the modified Oseen parameter, c, and which were consistent with a rotating isothermal core. They gave an extensive discussion of methods to obtain this latter parameter and showed its dependence on the heating angle. As the heating phase angle approached zero (heating-from-the-side) the velocity distributions violated the assumption of closed-core streamlines and the temperature distribution did not permit thermal stratification in the core.

At this point it was decided that a complete experimental analogue of the mathematical model should be studied to try to clarify some of the unusual aspects of the results obtained by Weinbaum and Ostrach and Menold. The purpose of this experiment was to provide data that would indicate which of the various ways of determining the modified Oseen constant was best, to show the behavior of the core region as the heating angle approached zero, to obtain an indication of the type of motion for heating-from-the-side and heating-from-below, and to obtain detailed velocity and temperature distributions for all heating angles. The results of this study are reported by Sabzevari and Ostrach [35]. The detailed results will be presented later but it was found that the analysis of Menold and Ostrach with a rotating isothermal core closely predicted the phenomena when the heating phase angle was not close to zero. For heating-from-the-side (phase angle zero) the core was found to be relatively stagnant and stratified.

B. OUTLINE OF PROBLEMS

The work discussed this far indicates that the character of the core velocity and temperature distribution for natural convection at large Rayleigh number in a closed cavity depends on the imposed thermal conditions. The relatively few existing experiments have shown that under proper conditions different core configurations can be obtained. The numerical work also has led to different core conditions. With the exception of Gill's work [28] all the analytical work to that time considered an isothermal core with constant vorticity regardless of the thermal boundary conditions. Obviously, additional work is required to gain an understanding of the complex phenomena involved and to see how the thermal boundary conditions affect the type of core flow.

Numerical methods would seem to have one advantage over the analytical boundary layer approach. The numerical work is carried out as a one-point boundary value problem by forward integrations and, therefore, requires no *a priori* knowledge of the core configuration whereas boundary layer theory does require information at the outset on the nature of the core. The only exception to this is Weinbaum's variation of the modified

Oseen method; even though in his paper he states that this method applied for a specific core configuration this restriction actually is unnecessary.

On the other hand, machines with large capacity are required to do problems of this type. Furthermore, even for the problems solved, considerable ingenuity and trial and error were required which made the cost of the solutions very high. More importantly, in boundary layer problems very steep gradients exist. Solutions of this type are difficult to obtain numerically and the problems of numerical stability associated with such solutions can be more difficult than the actual physical problems themselves. The mathematical theory of numerical stability is generally not applicable for practical boundary conditions. Finally, numerical solutions do not easily show parametric effects or unusual physical behavior. For these reasons and the fact that the configuration shown in Fig. 3 permits a wide range of different thermal boundary conditions the present writer decided to continue with the analytical and experimental investigation of this configuration with his students.

Because of the prediction of different core conditions for different heating configurations, the failure of the modified Oseen method for the heating-from-the-side case, the limited calculations, and the ambiguity in the evaluation of the Oseen constant a more general mathematical model is necessary to account for the complex phenomena observed. Hantman [36] therefore reevaluated the linearized solutions of the full describing equations and carefully examined the implications of various linearizations. Unfortunately, these were found to be not applicable to a stratified core situation. Then, for large Prandtl number and unit-order Grashof number, he formulated a boundary layer problem which is mathematically tractable and accounts for coupling between the core and boundary layer and permits consideration of both types of core configurations.

The results of this work predict a thermally stratified core with a slow cross flow from one boundary layer to the other for thermal conditions near to and including heating-from-the-side; this is in consonance with observations. Concurrently, Brooks and Ostrach [37] carefully mapped the streamlines and temperature distributions in Sabzevari's apparatus (slightly modified) over a wide range of heating phase angles in order to demonstrate the various different flow regimes.

To summarize then, the detailed nature of the natural convection in a cavity at large Rayleigh number seems to depend on the thermal boundary conditions. Experiments applicable to the heating-from-below configuration, e.g., Schmidt and Saunders [18], indicate that the core streamlines are closed, i.e., a rotating core, and that the core is isothermal. In contrast, experiments applicable to the heating-from-the-side case, e.g., Martini and Churchill [22], Eckert and Carlson [24], Sabzevari and Ostrach [35], Elder

[27], and Brooks and Ostrach [37], indicate a thermally stratified core with relatively slow flow; in a few instances where flow details were obtained the core streamlines were found to be horizontal with beginnings and ends in the boundary layers and the streamlines coincided with the isotherms. With the exception of the work of Poots [20] all the numerical work, e.g., Wilkes [25], de Vahl Davis [29], Gershuni *et al.* [26], and Elder [27], was in essential agreement with this picture.

All the analytical work, e.g., Ostrach [15], Batchelor [19], Weinbaum [31], and Menold and Ostrach [33], except Gill's [28] and Hantman [36] assumed that the core was isothermal and rotating regardless of the thermal boundary conditions. The failure of this assumption for heating-from-the-side was brought out especially by the solutions of Weinbaum and Menold and Ostrach.

The experiments of Sabzevari and Ostrach [35] and Brooks and Ostrach [37] indicate that the transition from one type of core flow to the other as the heating phase angle decreases is gradual.

Although a rotating isothermal core has not as yet been experimentally observed for heating-from-the-side the possibility of its occurring cannot be dismissed. Its occurrence may depend on the initial conditions under which the flow is established. Brooks and Ostrach [37] made a preliminary study of this by starting the flow with the heating angle such that a steady rotating isothermal core was established. They then changed the thermal condition to that for heating-from-the-side and found that the stratified relatively stagnant core appeared after a long time. This aspect of the problem warrants further study.

One more point must be made here concerning the heating-from-below configuration (phase angle 90°). This is the thermally unstable case which is not of direct concern herein. However, one aspect of this case is relevant to the present discussion. Weinbaum [31] and Menold and Ostrach [33] obtained two-dimensional solutions for this case on the basis of their assumption that the core flow formed a single isothermal rotating cell. However, because of symmetry a double-cell core would appear to be equally possible. Which configuration will appear in reality depends on their relative stability. Sabzevari and Ostrach [35] in their experimental study of this problem were, however, unable to establish any planar flow at all for this heating configuration. Thus, the physical meaning of the two-dimensional solutions for this case is questionable. A further discussion of this point will be presented subsequently.

The review of existing work on confined natural convection presented above was meant to be comprehensive but not all-inclusive, i.e., there are some publications to which no reference was made. However, all the significant physical phenomena, observations, and methods of study have been

mentioned. In the following section the most important aspects of the problem will be described in detail and comparisons among related work will be given where possible. Because the existing work has centered around two basic configurations, viz., a rectangular cavity and a horizontal circular cylinder, the following discussion will be divided into two parts, each dealing with a given configuration.

II. Rectangular Cavities

In this section consideration is given to the two-dimensional convective motion generated by the buoyancy force on the fluid in a rectangle and to the associated heat transfer. The two long sides are vertical boundaries held at different temperatures and the short sides can be either heat conducting or insulated (see Fig. 4). Particular attention will be given to the different flow

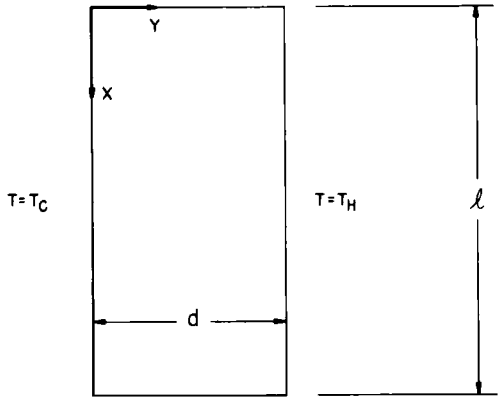

FIG. 4. The rectangular configuration.

regimes that can occur and the heat transfer across the fluid space between the two plane parallel vertical boundaries. Although heat transfer by radiation may not be negligible it is independent of the other types of heat transfer and can be fairly accurately calculated separately.

Interest in this problem arose in connection with the thermal insulating value of such a cavity. Such diverse applications of this are double-glazed windows and gas-filled cavities surrounding a nuclear reactor core.

To formulate the boundary value problem that describes this phenomena it is assumed that: (a) the motion is two-dimensional and steady, (b) the fluid is incompressible and frictional heating is negligible, (c) the difference

between the hot wall and cold wall temperatures is small relative to the absolute temperatures of the cold wall. This permits the so-called Boussinesq approximation to be invoked which permits fluid properties to be taken as constant except for the effect of the density variation in producing the buoyancy force. Thus the basic equations are:

$$\frac{\partial U}{\partial X} + \frac{\partial V}{\partial Y} = 0, \tag{1}$$

$$U\frac{\partial U}{\partial X} + V\frac{\partial U}{\partial Y} = -\frac{1}{\rho}\frac{\partial P}{\partial X} - g\left(\frac{T - T_C}{T_C}\right) + \nu\nabla^2 U, \tag{2}$$

$$U\frac{\partial V}{\partial X} + V\frac{\partial V}{\partial Y} = -\frac{1}{\rho}\frac{\partial P}{\partial Y} + \nu\nabla^2 V, \tag{3}$$

$$U\frac{\partial T}{\partial X} + V\frac{\partial T}{\partial Y} = \alpha\nabla^2 T. \tag{4}$$

The associated boundary conditions are:

$$U = V = 0, \quad T = T_C \quad \text{at} \quad Y = 0 \quad \text{for} \quad 0 \leqslant X \leqslant l, \tag{5a}$$

$$U = V = 0, \quad T = T_H \quad \text{at} \quad Y = d \quad \text{for} \quad 0 \leqslant X \leqslant l, \tag{5b}$$

$$U = V = 0 \quad \text{at} \quad X = 0,\ l \quad \text{for} \quad 0 \leqslant Y \leqslant d, \tag{5c}$$

$$T = T_C + (T_H - T_C)(Y/d),$$

or

$$\partial T/\partial X = 0 \quad \text{at } X = 0,\ l \quad \text{for } 0 \leqslant Y \leqslant d. \tag{5d}$$

To make the equations dimensionless let:

$$x = X/d, \quad y = Y/d, \quad u = (\alpha/d)(\partial\psi/\partial y),$$
$$v = -(\alpha/d)(\partial\psi/\partial x), \quad \theta = (T - T_C)/(T_H - T_C). \tag{6}$$

Substitution of Eqs. (6) and elimination of the pressure yield the following basic equations which are applicable to all types of flow in the cavity:

$$\nabla^4\psi = \mathrm{Ra}\frac{\partial\theta}{\partial y} + \frac{1}{\mathrm{Pr}}\left[\frac{\partial}{\partial x}(\nabla^2\psi)\frac{\partial\psi}{\partial y} - \frac{\partial}{\partial y}(\nabla^2\psi)\frac{\partial\psi}{\partial x}\right], \tag{7}$$

$$\nabla^2\theta = \frac{\partial\psi}{\partial y}\frac{\partial\theta}{\partial x} - \frac{\partial\psi}{\partial x}\frac{\partial\theta}{\partial y}. \tag{8}$$

The boundary conditions become:

$$\psi = \partial\psi/\partial y = 0, \quad \theta = 0 \quad \text{at} \quad y = 0,$$
$$\psi = \partial\psi/\partial y = 0, \quad \theta = 1 \quad \text{at} \quad y = 1 \quad \text{for} \quad 0 \leqslant x \leqslant a,$$
$$\psi = \partial\psi/\partial x = 0, \quad \theta = y \quad \text{or} \quad \partial\theta/\partial x = 0 \quad \text{at} \quad x = 0,\ a. \tag{9}$$

From the equations and boundary conditions it can be seen that the Rayleigh number, Ra, the Prandtl number, Pr, and the aspect ratio, a, are the dimensionless parameters associated with this problem. Because the boundary value problem posed above is very complex, appropriate solutions for limiting values of the dimensionless parameters can be sought. As mentioned earlier Batchelor [19] used this approach to investigate three cases, viz., small Rayleigh numbers, infinite aspect ratios (fully-developed flow), and large Rayleigh numbers. The last of these is the interesting boundary layer case and he was not able to obtain a solution which was consistent with his choice of a core which was isothermal and had constant vorticity. Poots [20] obtained a numerical solution which was consistent with Batchelor's model and found good agreement with Jakob's [38] correlation of Mull and Reiher's [17] experimental data. This appears surprising in view of the fact that the assumed core configuration has not been experimentally observed to date. However, the validity of Mull and Reiher's experiments and those of de Graff and van der Held [39] have been questioned by Emery [40] and Jakob [38]. The only other attempt to find an analytical solution to the problem was made by Gill [28] but since he relied heavily on experimental results, discussion of his work will be delayed until later.

The flow and temperature distributions can best be described from the works of Eckert and Carlson [24] and Elder [27]. In the former the temperature field is quantitatively obtained by evaluating the interferograms. Representative examples of these fields are presented in Fig. 5. In these figures the difference between the local temperature, T, and the cold-plate temperature, T_C, is plotted over the distance, Y, from the hot plate, in inches. The temperature scales on the ordinate are for two of the temperature profiles; the others are shifted in the vertical direction. A temperature field with a linear drop in the center portion is shown in Fig. 5(a). This situation is referred to as the "conduction regime." On the other hand, in Fig. 5(c) the appearance of thermal boundary layers can be observed near the surfaces and the profiles are horizontal in the central core. The boundary layer thickness on the hot plate increases upward and increases downward on the cold plate. The temperature profiles in the boundary layers resemble those in free convection on a single plate. This type of profile is said to be in the "boundary layer regime." Temperature profiles for conditions between the conduction and boundary layer regimes are shown in Fig. 5(b). The profiles are curved throughout the entire height of the air layer which indicates that convection contributes to the heat flow from the hot to the cold surface. These profiles have no horizontal part. In a sense this situation can be considered as one in which the boundary layers are not thin relative to the width and, therefore, they interact. This case is referred to as the

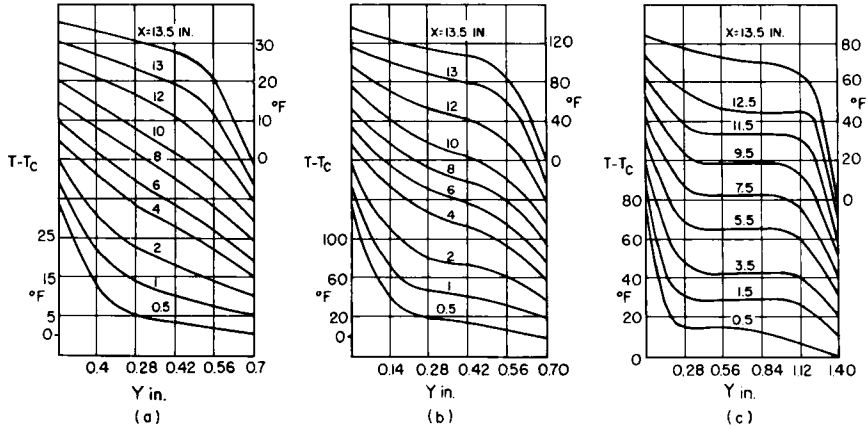

FIG. 5. Temperature field in air layer with 14 in. height [24]. (a) Conduction regime (b) transition regime; (c) boundary layer regime.

"transition regime." It should be noted that these types of flow are essentially the same as those indicated by Lighthill [6] for a closed-end tube.

The temperatures measured along a vertical line midway between the hot and cold surfaces are presented in Fig. 6. In Fig. 6(a) the centerline temperatures are presented for the conduction and transition regimes. The experimental data indicated by crosses are for the conduction regime. The region with a linear temperature drop from the hot to the cold plate coincides with the region in Fig. 6(a) in which the dimensionless temperature is 0.5. The other points are for measurements in the transition region. Measurements in the boundary layer regime are presented in Fig. 6(b) for an aspect ratio of 10 and in Fig. 6(c) for an aspect ratio of 2.5. The temperatures in the core of the air layer are by no means constant but vary approximately linearly with vertical distance. The centerline temperature variation in this regime does not appear to be significantly affected by the aspect ratio as can be seen by comparison of Figs. 6(b) and 6(c). This then is the contradiction of Batchelor's conclusion [19] that the core temperature is uniform.

For small temperature differences one would expect symmetry in the temperature field about the midpoint in the sense that the field in the lower half of the airspace is the negative image of that in the upper half if the ends were perfect thermal insulators. If this were so the centerline profiles would pass through the value 0.5 at $X/d = 0.5$. From Figs. 6(b) and 6(c) it can be seen that this is not quite so which indicates either a slight heat loss through the ends or that the air properties had some dependence on the temperature.

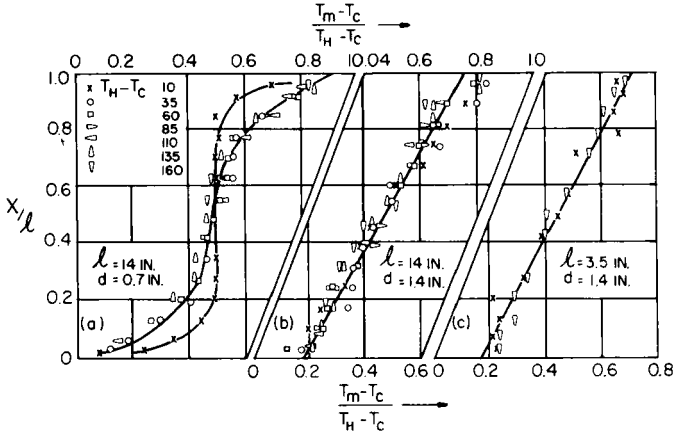

FIG. 6. Centerline temperatures [24].

Because the heat transfer will depend on the type of flow regime that occurs, Eckert and Carlson [24] then attempted to delimit the various regimes in terms of the range of values of the Grashof number and aspect ratio. To this end the interferograms were studied and those in which a linear temperature drop exists in some part of the flow field are indicated by circles in Fig. 7. The conditions for which the temperature profile has a

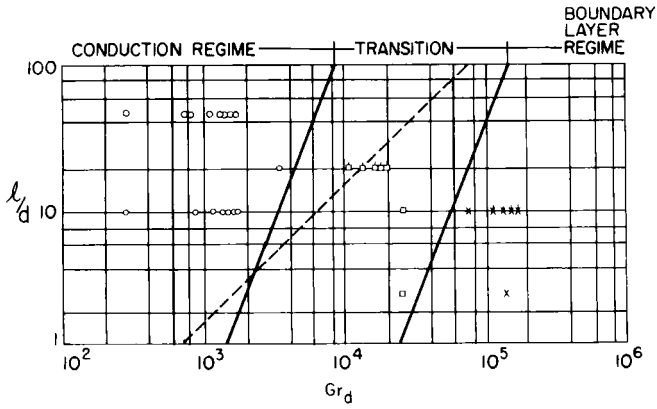

FIG. 7. Extent of various regimes [24].

horizontal part over at least a portion of the flow field are indicated by crosses. All other experimental data are indicated by squares. The number of experiments was not sufficient to establish the limits of the heat transfer regimes exactly. However, the heavy lines in the figure are expected to give

reasonable approximations. From various estimates Batchelor [19] obtained the relation $\mathrm{Ra} = 500\ (l/d)$ for the limit of the conduction regime. This relation is represented on Fig. 7 by the dashed line and its location agrees fairly well with the data. However, its slope appears to be somewhat too small.

In some of the experiments turbulent fluctuations were observed and, in most cases, these were restricted to the core region. Data points taken with such fluctuations are indicated by symbols to which are added short vertical lines. From the figure it appears that the turbulent fluctuations are not connected with the establishment of the various flow regimes. The intensity of the fluctuations increased with Grashof number for a fixed aspect ratio. The fluctuations had a comparatively low frequency and in some cases regular wave motions similar to those observed in boundary layers were obtained.

A. Heat Transfer in the Conduction Regime

In this regime heat is transferred between the two vertical surfaces by conduction alone in the central part of the air layer. From

$$q = (k/d)(T_{\mathrm{H}} - T_{\mathrm{C}}) = h_{\mathrm{c}}(T_{\mathrm{H}} - T_{\mathrm{C}}), \tag{10}$$

which defines the local heat transfer coefficient on the hot or cold surface, the local Nusselt number in that region is

$$\mathrm{Nu}_{\mathrm{d,c}} = h_{\mathrm{c}}d/k = 1. \tag{11}$$

Eq. (11) can also be interpreted as the ratio of an apparent conductivity of the air layer to the actual conductivity, k. The evaluations from the interferograms agree very closely with Eq. (11).

The local heat transfer conditions, however, are different in the corners of the air layer. From symmetry one would expect that almost the same heat transfer coefficients apply for the hot and the cold plate at diagonally opposite corners. From the interferograms it was found that in one pair of corners heat transfer coefficients were larger than in the central part. These are the lower corner on the hot and the upper corner of the cold plate and are, accordingly, called "starting corners." In the other two corners the heat transfer coefficients were lower than in the central part and those corners are referred to as "departure corners."

As long as end effects do not penetrate to the center the local heat transfer in the corners should be independent of the height, l, of the cavity. Therefore, the local Nusselt numbers in the corners should be of the form

$$\mathrm{Nu}_X = f(\mathrm{Gr}_X, X/d), \tag{12}$$

where

$$\mathrm{Nu}_X = h/Xk \quad \text{and} \quad \mathrm{Gr}_X = \beta g(T_{\mathrm{H}} - T_{\mathrm{C}})X^3/\nu^2.$$

1. *Starting Corners*

The interferograms indicated that the local Nusselt number in the starting corners is also independent of X/d. The experimental data for both the hot and cold plates can be reasonably approximated by

$$\mathrm{Nu}_{X,c} = 0.256(\mathrm{Gr}_X)^{0.24}. \tag{13}$$

The length X on which the dimensionless parameters are based is the distance from the corner measured along the hot or cold surface.

It can be seen from Eq. (12) that the heat transfer coefficient decreases as the distance X increases. The limit of applicability of Eq. (13) is reached at a point where the heat transfer coefficient determined by that equation becomes equal to that in the center part of the plate. The corresponding distance, X_p, from the corner is called the "depth of penetration." It is determined by setting the local Nusselt number, Nu_X, for the central part which is, according to Eq. (11), equal to X/d, equal to the local Nusselt number as given by Eq. (13). Accordingly,

$$X_{p,s}/d = 0.256(\mathrm{Gr}_X)^{0.24} = 0.256(\mathrm{Gr}_d)^{0.24}(X_{p,s}/d)^{0.72}.$$

The ratio of penetration depth to distance between the plates is, therefore,

$$X_{p,s}/d = 0.0075(\mathrm{Gr}_d)^{0.857}. \tag{14}$$

An average heat transfer coefficient for the corner region is defined by

$$\bar{h}_s = \frac{1}{X_p}\int_0^X h_s \, dX, \tag{15}$$

and the average Nusselt number is, thus

$$\overline{\mathrm{Nu}}_{d,s} = \bar{h}_s d/k. \tag{16}$$

Substitution of the heat transfer coefficient obtained from Eq. (13) into Eq. (15), integrating, using Eq. (14), and substituting the average heat transfer coefficient into Eq. (16) yields the average Nusselt number in the starting corners

$$\overline{\mathrm{Nu}}_{d,s} = 1.389 \tag{17}$$

2. *Departure Corners*

A study of the interferograms indicated that the local Nusselt number for departure corners was of the form given by Eq. (12). To correlate the data a second Grashof number, Gr_d, was used rather than the ratio X/d because it does not depend on the local distance, X. The data is well

approximated by

$$\mathrm{Nu}_{X,\mathrm{d}} = 2.58(\mathrm{Gr}_X)^{0.4}(\mathrm{Gr}_\mathrm{d})^{-0.55}. \tag{18}$$

This relation describes a heat transfer coefficient which is zero in the corner and increases with X. The limit of applicability is again reached at a position, X_p, where the heat transfer coefficient described by Eq. (18) becomes equal to that in the center part. In a manner similar to that for starting corners it is found to be

$$X_{\mathrm{p,d}}/d = 0.00875(\mathrm{Gr}_\mathrm{d})^{0.75} \tag{19}$$

An average Nusselt number for departure corners can also be obtained in the same way as above and is

$$\overline{\mathrm{Nu}}_{\mathrm{d,d}} = 0.835. \tag{20}$$

3. *Average Heat Transfer*

The total heat flux, Q, from the hot to the cold surface including the corner regions can be obtained from

$$Q = [h_\mathrm{c}l + (\bar{h}_\mathrm{s} - h_\mathrm{c})X_{\mathrm{p,s}} + (\bar{h}_\mathrm{d} - h_\mathrm{c})X_{\mathrm{p,d}}](T_\mathrm{H} - T_\mathrm{C}). \tag{21}$$

If the heat transfer coefficients are changed to Nusselt numbers

$$\begin{aligned}\overline{\mathrm{Nu}}_\mathrm{d} &= Qd/kl(T_\mathrm{H} - T_\mathrm{C}) \\ &= 1 + (\overline{\mathrm{Nu}}_{\mathrm{d,s}} - 1)(X_{\mathrm{p,s}}/d) + (\overline{\mathrm{Nu}}_{\mathrm{d,d}} - 1)(X_{\mathrm{p,d}}/d).\end{aligned} \tag{22}$$

Substitution of Eqs. (14), (17), (19), and (20) into Eq. (22) yields

$$\overline{\mathrm{Nu}}_\mathrm{d} = 1 + (d/l)[0.00292(\mathrm{Gr}_\mathrm{d})^{0.857} - 0.00144(\mathrm{Gr}_\mathrm{d})^{0.75}].$$

In the range of Grashof numbers considered this can be well approximated by

$$\overline{\mathrm{Nu}}_\mathrm{d} = 1 + 0.00166(d/l)(\mathrm{Gr}_\mathrm{d})^{0.9}. \tag{23}$$

This relation is in reasonable agreement with the expression derived by Batchelor [19].

B. Heat Transfer in the Boundary Layer and Transition Regimes

1. *Local Heat Transfer*

No satisfactory correlation of the data in these regimes was obtained by the use of Nu_X and Gr_X as given below Eq. (12), which are based on the temperature difference between the hot and the cold walls. Therefore, since

the temperature field in the boundary layer regime, Fig. 5(c), indicates that the boundary layers on the vertical walls are similar to those on a single vertical plate a correlation was attempted based on the difference between the wall and centerline temperatures which is characteristic of the single plate problem. Therefore, the heat transfer coefficient is defined by

$$q = h'(T_w - T_m),$$

where T_m is the centerline temperature at the height X for which the heat flux, q, and the local heat transfer coefficient, h', are defined. This distance is measured from the starting corner of the plate and it increases in the direction in which the boundary layer grows. The corresponding Nusselt and Grashof numbers are

$$\mathrm{Nu}_X' = h'X/k, \qquad \mathrm{Gr}_X' = \beta g(T_w - T_m)X^3/\nu^2. \tag{24}$$

If the properties in Eq. (24) are evaluated at wall conditions, these parameters correlate the data quite well in both the transition and boundary layer regimes and the relation

$$\mathrm{Nu}_X' = 0.231(\mathrm{Gr}'_X)^{0.30} \tag{25}$$

can be used to determine the local heat transfer in these regimes. However, to use this equation the centerline temperature must be known. The centerline temperatures presented in Fig. 6 together with others measured are shown in Fig. 8. From these two figures it can be deduced that the centerline temperature is constant for small values of Gr_d and large values of l/d throughout the entire height of the layer. As Gr_d increases or l/d decreases, temperature variations occur first near the upper and lower boundaries of the layer. The centerline temperature moves closer to the hot wall temperature near the upper boundary and closer to the cold wall temperature near the lower one. The regions of varying temperature cover a range which increases with increasing Gr_d until they meet in the center. Further on the profile straightens out until it becomes essentially linear within the boundary layer regime. In this regime the centerline temperature varies linearly with local position, X, and the layer thickness has a comparatively small influence.

The temperature field in the conduction and in the boundary layer regimes explains a peculiar behavior of the heat flow through enclosed vertical air layers, which was predicted by Batchelor [19] and observed experimentally by Schmidt [41]. It was found that for a vertical air layer enclosed by a cooled and a heated vertical plane the heat flux increased when the air layer was subdivided into smaller cells by the horizontal partitions. This is because the horizontal partitions cause heat to be transported by convection in the conduction regime and new thermal boundary layers start on the hot and cold surfaces in the boundary layer regime. The average boundary layer

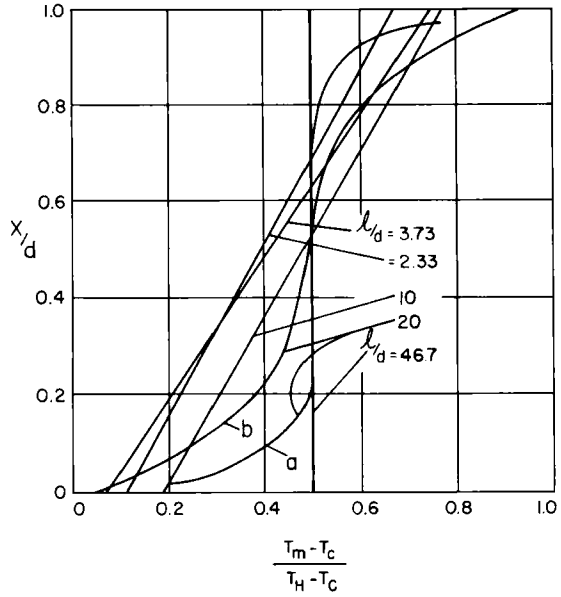

FIG. 8. Centerline temperatures, curve a, holds for $T_H - T_C = 10°F$, all other curves for $T_H - T_C$ from 35° to 160°F [24].

thickness in the space with partitions will, therefore, be smaller than when the partitions are absent.

2. *Average Heat Transfer*

An average heat transfer coefficient can be calculated from Eq. (25) for the boundary layer region. With the definitions

$$\overline{\mathrm{Nu}}_l = \frac{\bar{h}l}{k} \quad \text{and} \quad \bar{h}(T_H - T_C) = \frac{1}{l}\int_0^1 g\, dX \tag{26}$$

one obtains

$$\overline{\mathrm{Nu}}_l = \frac{1}{k(T_H - T_C)}\int_0^l q\, dX = \int_0^l \frac{\mathrm{Nu}'_X}{X}\frac{T_H - T_m}{T_H - T_C}\, dX. \tag{27}$$

The dimensionless centerline temperature in Fig. 6(b) can be approximated by

$$\frac{T_H - T_m}{T_H - T_C} = 0.83 - 0.60\frac{X}{l}. \tag{28}$$

Substitution of this equation and Eq. (25) into Eq. (27) leads to

$$\overline{\mathrm{Nu}}_l = 0.119(\mathrm{Gr}_l)^{0.3}. \tag{29}$$

Batchelor [19] estimated that the Nusselt number in the boundary layer region should be given by

$$\overline{\mathrm{Nu}}_l = C(\mathrm{Gr}_l)^{1/4},$$

where the constant C takes on values of 0.38 and 0.48. This difference between his relation and Eq. (29) is probably due to Batchelor's unrealistic assumption of a uniform core temperature.

Eq. (29) can be written as

$$\overline{\mathrm{Nu}}_d = 0.119(\mathrm{Gr}_d)^{0.3}(d/l)^{0.1}.$$

This indicates the small effect of the aspect ratio on $\overline{\mathrm{Nu}}_d$ or the equivalent ratio, k_a/k, of apparent conductivity to true conductivity of the fluid. The heat transfer coefficients calculated from this equation agree within approximately 20% with the measurements of Mull and Reiher [17]. It should be noted that Eq. (29) is valid only for the boundary layer regime because the linear relation for the centerline temperature, Eq. (28), was used in its derivation.

The exponent in Eq. (25) might suggest that the flow in the boundary layers is turbulent. However, this does not agree with the visual observations. The temperature variation in the core of the fluid is believed responsible for the relatively high value of the exponent.

Eckert and Carlson's [24] observations with air described above were confirmed by Mordchelles-Regnier and Kaplan [42] using carbon dioxide gas at high pressures.

C. BOUNDARY LAYER FLOW

Elder [27] gave further insight into the boundary layer flows through his experiments in which the fluids used were medicinal paraffin and silicone oil which have Prandtl numbers near one thousand. Velocity measurements were made by direct observation of aluminum powder suspended in the fluid, either by timing the passage of a single particle between fixed marks in the eyepiece of a traveling microscope or from time photographs in which streak length was proportional to velocity. The upper end of his cavity was open to the air so that his thermocouples for temperature measurements could be inserted. This caused his two end boundary conditions to be different and also made his configuration different from Eckert and Carlson's in this regard.

Elder points out that for $\mathrm{Ra} < 10^3$ (conduction regime) the temperature distribution is such that the fluid is not in hydrostatic equilibrium. The column of fluid near the cold wall has greater weight than a similar column

near the hot wall. Therefore, a weak, steady circulation of constant sign is generated in the cavity. This is a unicellular motion with fluid ascending over half the slot width near the hot wall and descending in the other half near the cold wall.

Since Elder's particular interest is in the flow in the case of strong convection, especially insofar as it produces secondary flows, he presents in Fig. 9 the temperature distribution in an enclosure with an aspect ratio $a = 20$ and $\mathrm{Ra} = 4.0 \times 10^5$; under these conditions the flow is approaching the situation under which secondary flow appears.

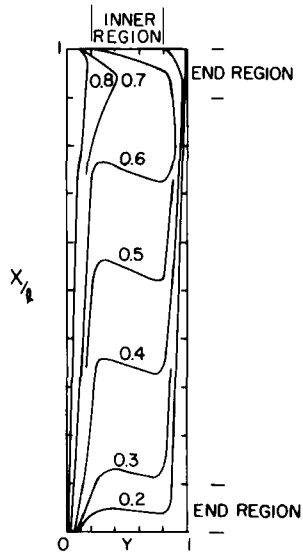

FIG. 9. Temperature distribution: $a = 20$; $\mathrm{Ra} = 4.0 \times 10^5$ ($d = 3$ cm, $\Delta T = 16.0$°C paraffin). Note: vertical scale is $\frac{1}{5}$ horizontal scale. Lines drawn at constant values of θ [27].

Three regions can be distinguished: a wall region, an interior region, and an end region. In the wall region $0 < (y,\bar{y}) < 0.2$ the isotherms are slightly inclined to the wall and the temperature gradients are largest there. The interior region $0.2 < y < 0.8$ has nearly horizontal and regularly spaced isotherms from $\theta = 0.35$ to 0.65 and is a region of nearly uniform, positive, vertical temperature gradient. Near the ends, $X < 0.1a$, $X < 0.9a$, the pattern is strongly influenced by the end boundary conditions. The end regions act as buffers between the end boundary conditions and the nearly unidirectional flow between them. The end region is not sharply defined but for small Rayleigh numbers its vertical extent is about $2d$ and at large

Rayleigh numbers about $0.1a$. Elder never found secondary flows originating in the end regions; these always appeared to be regions of strong damping.

The temperature profiles measured by Elder are quite similar to those found by Eckert and Carlson [see Fig. 5(c)]. In the inner region $0.2 < y < 0.8$ all points taken at different vertical locations lie along the same curve which indicates that $\theta = (T - T_m)/(T_H - T_C)$ is independent of X. Near the walls, however, θ is a function of both X and Y. From measurements of the centerline temperatures Elder also found the vertical gradient of this temperature to be nearly uniform over an order of magnitude variation of the Rayleigh number and more than a sixfold variation of the aspect ratio. The centerline vertical temperature gradient was found to reach an asymptotic value beyond Rayleigh numbers of 10^5 and up to at least 10^8. The product of this gradient and the aspect ratio, $\Gamma a = 1/(T_H - T_C)(dT_m/dx)a$, approaches 0.50 for paraffin, 0.55 for 100 centistoke silicone oil, and Eckert and Carlson's results for air give 0.60. Thus, Γa is a weak function of the Prandtl number. Note that Γ is approximately equivalent to the temperature gradient given by half the slot temperature drop established over the height of the slot.

Experimental velocity profiles measured at one-half the gap height for four different values of the Rayleigh number are shown in Fig. 10. The various parameters associated with these profiles are summarized in Table I.

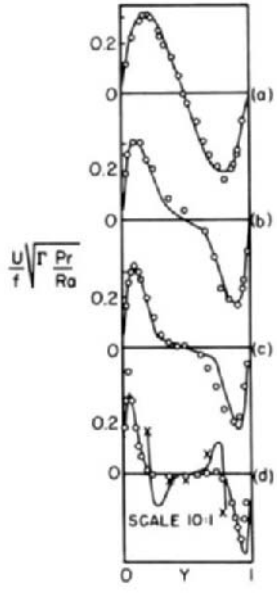

FIG. 10. Velocity profiles at $X = l/2$ at various Ra; (a) 3.08×10^4; (b) 2.95×10^5; (c) 6.56×10^6; (d) 3.61×10^4 [27].

TABLE I
VELOCITY PROFILE PARAMETERS

Profile	d (cm)	l (cm)	$T_H - T_C$ (°C)	$\sqrt{Pr}$	Ra
10(a)	2.00	38.8	5.40	50.6	3.08×10^4
10(b)	4.08	56.0	5.75	49.0	2.95×10^5
10(c)	4.08	56.5	11.6	46.7	6.56×10^5
10(d)	4.08	29.3	33.5	33.8	3.61×10^6

The profiles are all antisymmetric about $y = \frac{1}{2}$ as required by symmetry and the symmetry of the boundary conditions, except for a tendency to higher velocities and smaller wall layer thickness in the flow near the hot wall. This is a result of the variation of viscosity with temperature. Profile 10(a) has an infection point at $y = \frac{1}{2}$ and is very similar in form to that required as the Rayleigh number approaches zero. Profiles 10(b) and 10(c) have three inflection points which become more widely separated as the Rayleigh number increases and the velocity profile becomes increasingly localized near the two vertical surfaces. The velocity profiles at various values of X for fixed Ra and a are presented in Fig. 11. The velocity is greatest near $x = a/2$ but the profiles at $X = 30$, 40, and 50 cm are indistinguishable.

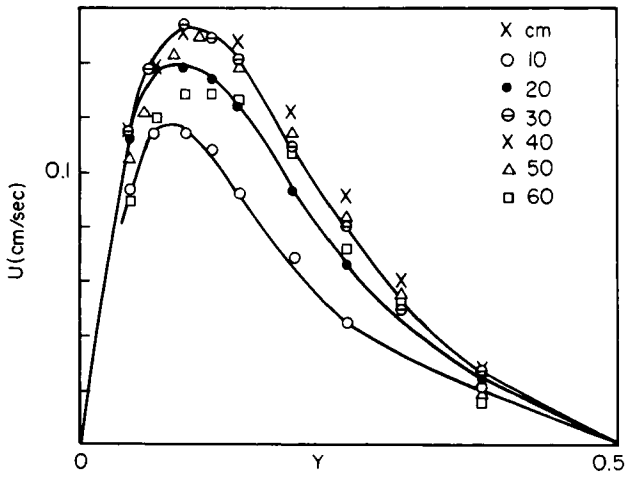

FIG. 11. Velocity profiles for $d = 4.08$ cm, $l = 75.7$ cm, Ra $= 4.0 \times 10^5$ at various values of X [27].

1. *Inner Flow as Rayleigh Number Becomes Very Large*

There is little experimental information for the inner flow at large Rayleigh numbers but existing information strongly suggests that the inner

region has zero vorticity and a finite, positive temperature gradient. This evidence is of necessity restricted to $Ra < 10^8$ because at about that Rayleigh number the motion is no longer steady. To obtain further insight into what is occurring in this region consideration is given to a nearly square cavity ($a = 0.92$) filled with silicone oil and a Rayleigh number of 9.4×10^6. In this experiment both upper and lower boundary conditions are identical; the upper free surface is replaced by one identical with the lower one. The results are sketched in Fig. 12 from a sequence of time photographs and confirmed by visual inspection. Three distinct areas can be seen: (1) a wall region with strong clockwise circulation in which the streamlines closely

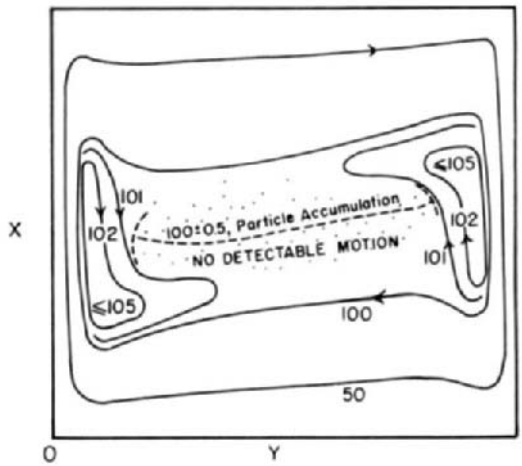

FIG. 12. Streamlines of laminar flow in a nearly square cavity. $a = 0.92$, $Ra = 9.6 \times 10^6$. The stream function has been scaled to 100 units at the cavity center [27].

follow the shape of the wall, (2) a part of the interior adjacent to the vertical wall layers also with clockwise circulation but in which the streamlines do not follow everywhere the wall shape; these weak circulations are attached to the vertical layers and produce a weak return flow in the outer portion of the vertical layers, (3) the central part, or core, of the interior where no detectable flow could be observed even though a velocity of 1% of the maximum in the boundary layer would have been easily detectable. However, the experiments did not find the motion in the core to be zero because, in the course of several runs, a characteristic distribution of the aluminum powder was found, namely, a concentration of randomly oriented particles along a line near $x = a/2$ as drawn in the figure. This suggests a zone of both very small velocity and shear. (Elder does admit that this distribution could have been established during the transient heating period.)

2. *Secondary Flow*

Representative streamlines traced from photographs for flows with increasing Rayleigh number are shown in Fig. 13. For Ra = 3.0×10^5 the flow is unicellular, Fig. 13(a), with the streamlines circulating from one end of the slot to the other. As the Rayleigh number is increased to 3.6×10^5 a second set of streamlines appeared, Fig. 13(b), one short cell and one which reaches to the upper end region. These cells are very weak and near the critical Rayleigh number are extremely difficult to detect especially when the wavelength is large. Further increases of the Rayleigh number causes the wavelength to decrease, Fig. 13(c), and more cells are fitted into the inner region, Figs. 13(d)–13(f). The critical Rayleigh number for the onset of the secondary flows was found to be Ra = $3 \times 10^5 \pm 30\%$. The large uncertainties are due to the difficulty of detecting the onset of the very weak secondary flow.

Under some conditions there appears to be a nonlinear interaction between the secondary flows and the primary flow. The dimensionless centerline temperature is shown in Fig. 14 for two values of the Rayleigh number. For Ra = 5.3×10^5 which is near critical the profile is nearly linear except for a weak barely significant periodicity of wavelength approximately eight. At Ra = 3.3×10^6 the oscillations are pronounced with

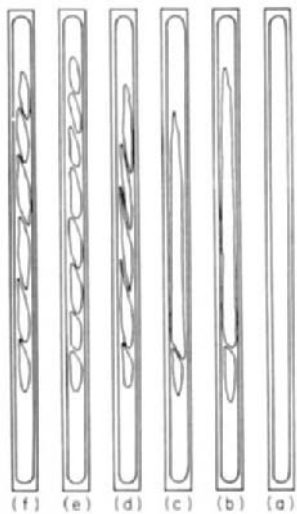

FIG. 13. Sketch of streamlines of the secondary flow at various values of Ra: (a) 3.0×10^5; (b) 3.6×10^5; (c) 4.9×10^5; (e) 5.8×10^5; (f) 6.8×10^5. $d = 2$ cm, $l = 38$ cm [27].

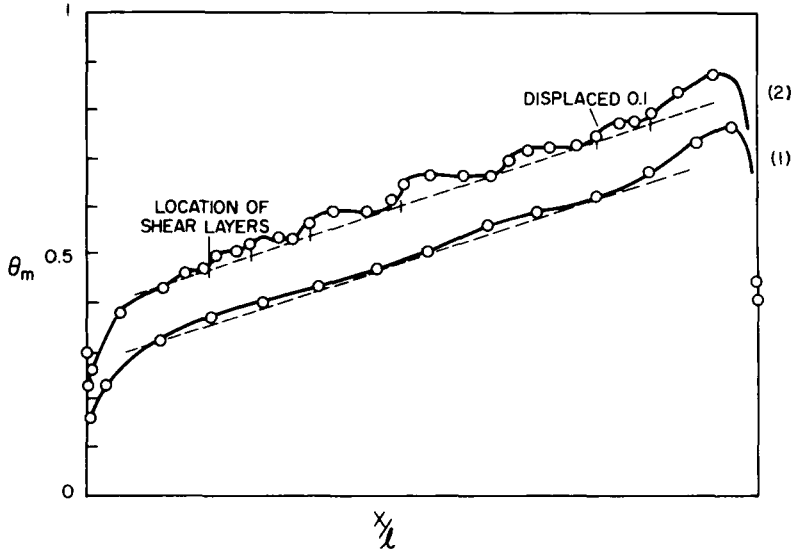

FIG. 14. Centerline temperature θ_m when the secondary flow is present, $d = 4.08$ cm; (1) Ra $= 5.3 \times 10^5$; (2) Ra $= 3.3 \times 10^6$. The position of the shear layers between cells is indicated [27].

distinct and extensive portions where the vertical gradient of the centerline temperature is zero. Visual observation of the slot shows that the shear layers between each cell coincide with regions of large vertical gradients of the centerline temperature.

The interaction with the primary flow is strikingly shown in the temperature distribution on Fig. 15 for Ra $= 3.3 \times 10^6$. While the basic variation is still dominant in the inner region the isotherms are both steepened and given a periodic variation of spacing. The local temperature variation due to the interactions is $\pm 0.015\,\Delta T$ in the figure. Colder fluid is carried from near the cold wall across the cavity and up the hot wall where it is heated and again carried across the slot to the cold wall.

3. *Tertiary Flow*

The most intriguing feature of Elder's work occurs near Ra $= 10^6$. After the occurrence of secondary flow as the Rayleigh number is increased, a pronounced and rapid change is observed in the weak shear layers between successive cells of the secondary flow. The shear layers become thicker and the patterns indicate that the aluminum particles are trapped and suggest that a new flow has appeared. Close inspection confirms this. From photo-

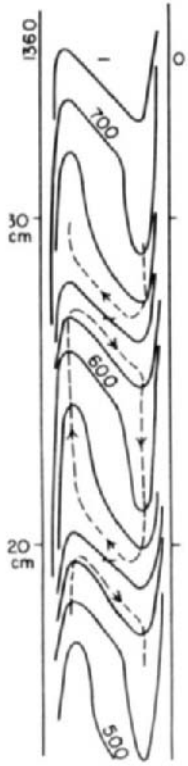

FIG. 15. Detail of the temperature distribution showing the interaction of the primary and the secondary temperature field. Isotherms are in units of 1/40°C. Ra = 3.3×10^6; $d = 4.08$ cm [27].

graphs (presented in Elder's paper [27]) and visual observations the tertiary flow is of the form of a circulation with closed streamlines. Whereas the primary and secondary flows both have a clockwise motion the tertiary flow has the opposite sense.

Detailed measurements of the tertiary flow are difficult. The velocity distribution can be determined with acceptable accuracy but the temperature variation produced by the secondary flow is only of the order of $\pm$ 0.02 $(T_H - T_C)$.

From his experiments and a study of the basic equations that describe the phenomena Elder concludes his paper with a general discussion of the flow and some of the mechanisms that produce it and, as a summary, it is instructive to present some of this information here.

The flow can be considered as an interaction between two thermal

boundary layers, one on the hot vertical surface and the other on the cold one. If the two walls are widely separated the flow near one plate can be expected to be essentially independent of the other plate. If attention is focused on the hot plate then from the results for a single vertical plate, e.g., Ostrach [43], it is seen that the velocity in the thermal boundary, which grows near the wall, is nearly vertical except for a small horizontal entrainment velocity, which is a function only of the vertical coordinate. Thus the fluid far from the plate is at a constant temperature but has a horizontal velocity which is a function of height. Similar considerations apply to the cold surface. However, the entrainment velocity required for an isolated plate cannot simultaneously satisfy the requirements of both plates.

The role of the vertical temperature gradient in this process is as follows: Near the bottom of the slot the buoyancy forces exceed the viscous forces and accelerate the fluid, but because of the vertical temperature gradient the buoyancy force diminishes until at the mid-height it is balanced by the viscous forces. Beyond this point the fluid is decelerated. Outside the wall layers there will again be a horizontal entrainment flow. Near the mid-height the entrainment velocity approaches zero as required by continuity and the symmetry of the boundary layer growth. Thus, the horizontal entrainment velocity is negative in the lower half of the slot and positive in the upper half, which corresponds to entrainment of fluid into the growing layers but out of the layers beyond their point of maximum growth. The measurements of Eckert and Carlson [24] clearly demonstrate these features.

When the centerline vertical temperature gradient is zero the two boundary layers completely fill the slot. Heat is then transferred across the slot by thermal conduction alone and the consequent motion corresponds to a balance between buoyancy and viscous forces. When the centerline vertical temperature gradient is constant there is a complete separation of the two wall layers with an interior region in which there is almost no motion and the horizontal temperature gradient is zero. In this case no heat is transferred between the two layers.

On the basis of a crude argument Elder showed that the experimentally determined result that the product of the centerline vertical temperature gradient and the aspect ratio is constant is in consonance with boundary layer growth on an isolated vertical surface. He therefore suggests that wall layers in the slot grow like on a single surface. More importantly he claims that this suggests that the vertical temperature gradient arises from the interaction of the boundary layers, i.e., by inhibiting entrainment rather than from effects in the end regions with mere conduction from the hot upper to the cold lower end producing the gradient.

Above Rayleigh numbers of approximately 10^5 a secondary flow appears in the interior region with streamlines resembling a "cats-eye" pattern.

A curious feature of the secondary flow is the strong tilting of the shear layers between the cells.

In another paper Elder [44] studies the transition in a vertical slot from laminar to unsteady and then to turbulent flow. For Rayleigh numbers above approximately $8 \times 10^8(\sqrt{\mathrm{Pr}}/a^3)$ travelling wavelike motions grow up the hot wall of the slot and down the cold wall. These waves grow most readily midway between the two ends. At higher Rayleigh numbers when the wave amplitude is finite the phase of successive wavefronts becomes increasingly random until near $\mathrm{Ra} = 1.0 \times 10^{10}/a^3$ an intense entrainment and mixing process starts between the wall region and the interior. The middle portion of the interior is then turbulent and the extent of the region grows further toward the ends as the Rayleigh number increases.

As mentioned earlier, Gill [28], guided by Elder's experiments, developed an analytical model for the convection phenomena in the limit of large Prandtl number. He first reduced the complete equations to boundary layer form by assuming that the boundary layer thickness is small compared with the slot height. In so doing he had to forgo the satisfaction of exact boundary conditions at the ends. He then used an order-of-magnitude argument relating the boundary layer and core quantities to show that the core stream function and temperature depended on the vertical coordinate only. Thus, the vertical motion is confined to the boundary layers and the transfer of heat from one vertical wall to the other is mainly by convection.

Gill obtained an approximate solution of his boundary layer equations by means of a generalization of a modified Oseen linearization which coupled the boundary layer and core solutions. The linearizing functions were functions of the vertical coordinate such that the boundary layer equations retained only derivatives in the horizontal direction. The model which he analyzed is based on the flow phenomena described by Elder [27], particularly with regard to entrainment, which is presented above. Gill's results agree quite well with Elder's experiments except near the horizontal boundaries. Gill's work is particularly significant in that it was the first of the analytical treatments which did not assume an isothermal rotating core.

It has already been pointed out that the numerical solutions to this problem essentially agree with the flow and heat transfer as presented above. No details of the numerical papers will be presented herein because they dwell on the intricacies of the particular method used and this is beyond the scope of the present paper. de Vahl Davis [29] discusses the limitations of the work preceding his and compares the results obtained numerically. For example, he mentions that Wilkes' [25] work was limited by stability difficulties to a Rayleigh number below a certain value and even then the solution is not physically acceptable because the vorticity was used as one of the dependent variables and boundary conditions for it are not known at

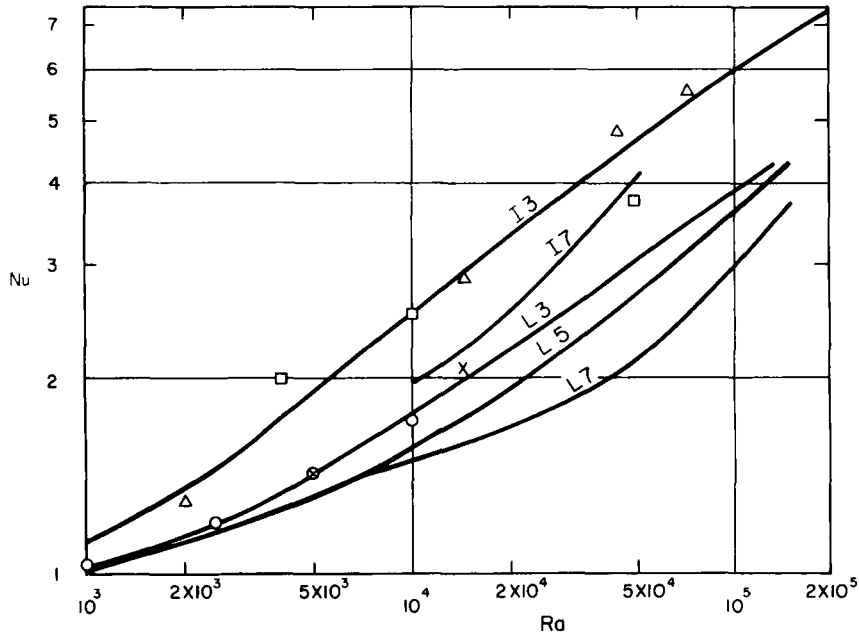

FIG. 16. Average Nusselt number for the square cavity, as a function of Rayleigh number, compared with previous solutions [29]. ○—Poots (L); ×—Wilkes (L); □—Elder (I); △—Wilkes (I).

the start. Boundary condition problems were also encountered by Elder [44]. To achieve numerical stability he required the normal gradient of vorticity to vanish on the horizontal boundaries of the cavity. This arbitrary condition (which has no physical justification) was claimed to affect only the end regions. However, since almost all the results are for a square cavity the numerical results are of limited accuracy. Some quantitative comparisons are also presented by de Vahl Davis and his results agree very well with those of Poots [20] and Wilkes [25] whereas Elder's results differ appreciably (see Fig. 16).

The curves determined by de Vahl Davis are distinguished in Fig. 16 by two symbols. The first (letter) denotes the thermal boundary condition on the horizontal ends; the I indicates that the ends are insulated and L indicates a linear temperature variation across the cavity at the ends. The second symbol (number) denotes the finite difference approximation, e.g., 3 is a three-point approximation, 5 a five-point one, etc. The most notable feature of the results is their variation with the finite difference approximation used. This variation is more apparent in the heat transfer results than in any

other. It should be noted that the three-point formula gives results that agree best with other work.

Newell and Schmidt [45] obtained numerical solutions to investigate more fully the effects of aspect ratio. Their calculations were made for a Prandtl number of 0.733. They then compared their results with those discussed above and, in addition, with those of Han [46] and MacGregor and Emery [47]. The various expressions for the average Nusselt number based on the slot width can be written as

$$\overline{\mathrm{Nu}}_d = A(\mathrm{Gr}_d)^B(l/d)^C. \tag{30}$$

A summary of the various expressions of the form of Eq. (30) determined for a square $l/d = 1$ and rectangular cavities is presented in Table II.

TABLE II
AVERAGE NUSSELT NUMBER RELATIONS

Reference	A	B	C	l/d
Newell and Schmidt [45]	0.0547	0.397	—	1
Han [46]	0.0782	0.3594	—	1
Elder [44]	0.231	0.25	—	1
Newell and Schmidt [45]	0.155	0.315	−0.265	$2 \leqslant l/d \leqslant 20$
Eckert and Carlson [24]	0.199	0.3	−0.1	$2 \leqslant l/d \leqslant 20$
Jakob [38]	0.18	0.25	−0.111	$2 \leqslant l/d \leqslant 20$
MacGregor and Emery [47]	0.25	0.25	−0.25	$2 \leqslant l/d \leqslant 20$

Some calculations for specific values of l/d are also presented in Fig. 17. It can be seen that the exponent on the Grashof number determined by Newell and Schmidt is higher than those given by all previous investigators. The exponent on l/d which they found is also higher than those obtained by

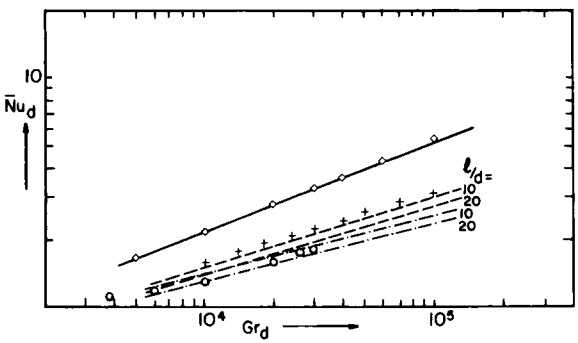

FIG. 17. Average Nusselt numbers versus Grashof number [45]. ——— Han (46); - - - Eckert and Carlson (*24*); —·— Jakob (*38*). ◇—$l/d = 1$; +—$l/d = 10$; ○—$l/d = 20$.

Jakob or Eckert and Carlson but is of the same order as that of MacGregor and Emery.

For the square a comparison of Newell and Schmidt's equation with those of Han and Elder indicates similar Grashof number trends. MacGregor and Emery have used their expression with $l/d = 1$ to compare their numerical and experimental results. However, the equation of Newell and Schmidt agrees better with the data so that the validity of MacGregor and Emery's expression for a square is questionable.

For a more graphic comparison of results, calculations made by Newell and Schmidt are shown as points on Fig. 17 and the results of Eckert and Carlson, Jakob, and Han as lines. If Newell and Schmidt's results are used as a reference the good agreement between them and Han's work for a square is readily apparent. The results of Eckert and Carlson lie below them for $l/d = 10$ and above them for $l/d = 20$. Thus, good agreement between them might be expected for l/d midway between those two values, which is the range over which Eckert and Carlson's results were intended to apply. Jakob's results lie below all the others.

From the above heat transfer rates through air enclosed in a rectangular slot can be calculated for various conditions. The agreement with experiments is tolerable.

III. Horizontal Circular Cylinder

A detailed review of the work done on the boundary layer flow in a horizontal circular cylinder will be most instructive for a number of reasons. Considerably more analytical study of this problem has been made, only two parameters are associated with this configuration because the aspect ratio does not enter, there are no corner effects (and, therefore, no mixed boundary conditions), and the inclusion of a heating phase angle permits a complete variation of the thermal boundary conditions from heating-from-the-side to heating-from-below. In the last regard recall that the rectangular cavity was restricted to heating-from-the-side. Also, from the Introduction it appears that the core configuration is strongly affected, if not determined, by the thermal boundary condition. Thus, some insight should be obtained how the core configuration varies with the thermal boundary condition.

A. ANALYSIS

Consideration is given to the large Rayleigh number flow, with the Prandtl number large and the Grashof number of unit order of magnitude.

1. *Basic Equations*

In this case of steady natural convection of a very viscous (large Prandtl number) fluid the Boussinesq approximation is made so that density variations only modify the body force term. For the cylindrical geometry depicted in Fig. 3 the natural choice of coordinates is a plane polar system with space points located by (R, θ) and the corresponding radial and azimuthal velocities are U and V, respectively.

The driving force for the flow is due to a nonuniform temperature distribution around the cylinder circumference. This distribution is given by

$$T(R_0,\theta) = T_0 + \Delta T \cos(\theta + \phi). \tag{31}$$

The basic equations in dimensionless form expressing the conservation of momentum and energy, respectively, are, in terms of a stream function which satisfies the continuity equation identically:

$$\frac{1}{r}\left(\frac{\partial\psi}{\partial\theta}\frac{\partial\nabla^2\psi}{\partial r} - \frac{\partial\psi}{\partial r}\frac{\partial\nabla^2\psi}{\partial\theta}\right) = \frac{1}{\mathrm{Gr}}\nabla^2\nabla^2\psi - \frac{1}{\mathrm{Gr}}\left(\cos\theta\frac{\partial\tau}{\partial r} - \frac{\sin\theta}{r}\frac{\partial\tau}{\partial\theta}\right), \tag{32}$$

$$u\frac{\partial\tau}{\partial r} + \frac{v}{r}\frac{\partial\tau}{\partial\theta} = \frac{1}{\mathrm{Pr\,Gr}}\nabla^2\tau + \frac{K}{\mathrm{Pr\,Gr}}\Phi. \tag{33}$$

The corresponding boundary conditions expressing the impermeability of the wall, the no-slip condition, and the imposed temperature distribution are, respectively,

$$\partial\psi/\partial r = \partial\psi/\partial\theta = 0 \quad \text{at} \quad r = 1, \tag{34a}$$

$$\tau = \cos(\theta + \phi) \quad \text{at} \quad r = 1. \tag{34b}$$

The relations between the dimensionless and dimensional (denoted by capital letters) variables are

$$R = R_0 r, \qquad \theta = \theta, \qquad \Psi = \nu\mathrm{Gr}\psi, \qquad \tau = (T - T_0)/\Delta T. \tag{35}$$

The specific nondimensionalization of the stream function as given in Eq. (35) is obtained by equating viscous and body forces which seems to be the most reasonable choice for the large Prandtl number unit-order Grashof number case under consideration herein. The frictional heating parameter, K, discussed by Ostrach [5] is much smaller than unity for the present case so that the viscous dissipation (last term in Eq. 33) can be neglected.

For this case of large Prandtl number and unit-order Grashof number the boundary layer character of the problem is evident from the energy equation, Eq. (33), because the conduction term with the highest order derivatives is multiplied by a small quantity (1/PrGr). This indicates that a

region must exist in which derivatives of temperature become so large that there will be a balance between the conduction and convection terms so that all the boundary conditions can be satisfied. This region is adjacent to the cylinder wall and will vary in depth inversely with the Prandtl number.

By the same reasoning, the conduction term should be negligible compared to the convection terms in the core region.

2. *Solutions*

a. The Core Region. If the conduction term is neglected in the interior region, as was argued above, Batchelor's method of proof [21] can be modified to show that the core must be isothermal

$$T = \tau = \tau_0 = \text{const.} \tag{36}$$

if it is not stagnant and no bounding streamlines pass through the boundary layer. (See Menold and Ostrach [33] for details.) In Menold and Ostrach [33] the other possibility (not considered by Batchelor) is also considered, viz., that the core is stagnant. It is then found that the interior temperature distribution could correspond to that for a stratified fluid. Thus, it appears that two core configurations are possible. The delineation of the conditions for the existence of each requires a separate study. For the present the rotating core configuration will be the one studied as it was in earlier works.

For this case, then, the buoyancy term will vanish identically from the equation of motion, Eq. (32), in the interior region.

b. The Thermal Boundary Layer. Because of the boundary layer character of the problem further simplification of the equations can be obtained by the usual scaling transformations of boundary layer theory. For the present problem these are

$$\rho = (1 - r)\mathrm{Pr}^{1/4}, \qquad \psi_1 = \mathrm{Pr}^{-3/4} f(\rho, \theta), \qquad \tau = \tau(\rho, \theta). \tag{37}$$

The nonlinear inertia terms in the equation of motion can also be shown to be negligible for this case of large Prandtl number. For details of these steps and others in the analysis and solution which have to be omitted because of space limitations see Menold and Ostrach [33]. The linearization of the equation of motion is one of the major simplifications obtained by the choice of a large Prandtl number fluid.

Even with the simplifications indicated above, the solution of the boundary layer equations is still a formidable task. Therefore, to facilitate the solution the modified Oseen linearization will now be applied. This permits the use of a superposition technique so that the stream function, ψ, and the temperature, τ, can each be taken as the sum of two variables, one describing core conditions and the other, boundary layer conditions. Each of these variables must satisfy the differential equation valid in the appropriate

region. The solutions for the two parts of ψ and τ, respectively, can be matched at the boundary $r = 1$ by means of the boundary conditions on the complete functions. By this superposition the difficulties associated with the interaction between the interior and boundary layer regions are avoided and the problem is reduced to a matching of two solutions at the cylinder wall.

Before applying the modified Oseen linearization recall that the inertia terms in the equation of motion and the viscous dissipation are negligible. Therefore, the basic equations are:

$$\nabla^2\nabla^2\psi - \left(\cos\theta\frac{\partial\tau}{\partial r} - \frac{\sin\theta}{r}\frac{\partial\tau}{\partial\theta}\right) = 0, \tag{38}$$

$$\frac{1}{\mathrm{Pr\,Gr}}\nabla^2\tau - \frac{1}{r}\left(\frac{\partial\psi}{\partial\theta}\frac{\partial\tau}{\partial r} - \frac{\partial\psi}{\partial r}\frac{\partial\tau}{\partial\theta}\right) = 0. \tag{39}$$

The modified Oseen approximation consists of making the substitutions

$$\partial\psi/\partial r = -c', \qquad \partial\tau/\partial\theta = 0 \tag{40}$$

in the energy equation. The constant, c', is to be evaluated *a posteriori* by some suitable means, such as an averaging process. Experiments have sometimes been used to evaluate the constant. The energy equation thus becomes

$$\frac{1}{\mathrm{Pr\,Gr}}\nabla^2\tau - \frac{c'}{r}\frac{\partial\tau}{\partial\theta} = 0. \tag{41}$$

The two basic equations, (38) and (41), are both linear and now also uncoupled.

The stream function and the temperature are next written as

$$\psi(r, \theta) = \psi_0(r, \theta) + \psi_1(r, \theta), \tag{42a}$$

$$\tau(r, \theta) = \tau_0 + \tau_1(r, \theta), \tag{42b}$$

where ψ_0 must satisfy the equation valid in the core and since the core has been shown to be isothermal τ_0 is a constant. The functions with the subscript 1 must satisfy the boundary layer equations. The boundary conditions imposed on these separate parts will be such that the total function given by their sum exhibits the proper behavior at the cylinder wall.

Use is now made of the boundary layer scaling given by Eq. (37) to write Equation (42a) as

$$\psi(r, \theta) = \psi_0(r, \theta) + \mathrm{Pr}^{-3/4}f(\rho, \theta) \tag{43}$$

In the isothermal core the buoyancy terms in Eq. (38) vanish identically so that ψ_0 must satisfy

$$\nabla^2\nabla^2\psi_0 = 0. \tag{44}$$

The equations for f and τ_1 are found from Eqs. (38) and (41) by applying Eq. (37) and then Eqs. (43) and (42b), respectively. The resulting equations for the boundary layer are

$$\frac{\partial^4 f}{\partial \rho^4} + \cos\theta \frac{\partial \tau_1}{\partial \rho} = 0, \tag{45}$$

$$\frac{\partial^2 \tau_1}{\partial \rho^2} - c\,\mathrm{Gr} \frac{\partial \tau_1}{\partial \theta} = 0, \tag{46}$$

where

$$c = \mathrm{Pr}^{1/2} c', \tag{47}$$

with c being of unit order.

When Eqs. (43) and (42b) are substituted into the boundary conditions given by Eq. (34) the following relationships result:

$$\mathrm{Pr}^{-1/2}(\partial f/\partial \rho)_{\rho=0} = (\partial \psi_0/\partial r)_{r=1}, \tag{47a}$$

$$\mathrm{Pr}^{-3/4}(\partial f/\partial \theta)_{\rho=0} = -(\partial \psi_0/\partial \theta)_{r=1}, \tag{47b}$$

$$\tau_1 = \cos(\theta + \phi) - \tau_0 \quad \text{at} \quad \rho = 0. \tag{47c}$$

In order that the interior be described solely by ψ_0 and τ_0 it is also required that the boundary layer contributions f and τ_1 both approach zero as ρ approaches infinity, i.e.,

$$f \to 0, \qquad \tau_1 \to 0 \quad \text{as} \quad \rho \to \infty. \tag{47d}$$

The problem as it now stands is considerably simpler and is also uncoupled as a result of the modified Oseen linearization.

The first solution to be determined is that for the interior stream function, ψ_0, which is described by the biharmonic Eq. (44). The general solution valid in the region $0 \leqslant r \leqslant 1$, $0 \leqslant \theta \leqslant 2\pi$ is

$$\psi_0(r, \theta) = \sum_{n=0}^{\infty} [(A_n \cos n\theta + B_n \sin n\theta) r^n + (C_n \cos n\theta + D_n \sin n\theta) r^{n+2}] \tag{48}$$

where A_n, B_n, C_n, and D_n are constants.

Since the energy equation in the boundary layer region has been uncoupled from the equation of motion the temperature can be found directly by separation of variables. Thus, upon satisfaction of the boundary conditions, Eqs. (47c) and (47d),

$$\tau_1(\rho, \theta) = e^{-\bar{\lambda}\rho}[\xi \cos(\theta - \bar{\lambda}\rho) - \gamma \sin(\theta - \bar{\lambda}\rho)], \tag{49}$$

where $\bar{\lambda} = \sqrt{c\mathrm{Gr}/2}$, $\xi = \cos\phi$, and $\gamma = \sin\phi$. In the course of satisfying the boundary conditions it is found that $\tau_0 = 0$ which means that the

interior assumes the average temperature T_0 that appears in the boundary condition, Eq. (31).

The solution for τ_1 is now used in the second term of Eq. (45). Four integrations with respect to ρ and application of the boundary condition, Eq. (47d), yield

$$f(\rho, \theta) = \frac{e^{-\bar{\lambda}\rho}}{4\bar{\lambda}^3} \cos\theta[(\xi + \gamma)\sin(\theta - \bar{\lambda}\rho) - (\xi - \gamma)\cos(\theta - \bar{\lambda}\rho)]. \quad (50)$$

The conditions, Eqs. (47a) and (47b), together with the condition that $\psi(1, \theta) = 0$ are then used to determine the constants. Thus the complete solutions are

$$\psi(r, \theta) = A_0 + (C_0 + A_2 \cos 2\theta + B_2 \sin 2\theta)r^2 + (C_2 \cos 2\theta + D_2 \sin 2\theta)r^4 + \frac{1}{4\lambda^3} e^{-\lambda(1-r)}\cos\theta \{(\xi + \gamma)\sin[\theta - \lambda(1 - r)] - (\xi - \gamma)\cos[\theta - \lambda(1 - r)]\}, \quad (51)$$

$$\tau(r, \theta) = e^{-\lambda(1-r)}\{\xi \cos[\theta - \lambda(1 - r)] - \gamma \sin[\theta - \lambda(1 - r)]\}, \quad (52)$$

where $\lambda \equiv \mathrm{Pr}^{1/4}\,\bar{\lambda}$ and

$$A_0 = \frac{1}{8\lambda^2}\left[\gamma + \frac{(\xi - \gamma)}{\lambda}\right], \qquad C_0 = -\frac{\gamma}{8\lambda^2},$$

$$A_2 = \frac{1}{8\lambda^2}\left[\gamma + \frac{2(\xi - \gamma)}{\lambda}\right] = -C_2,$$

$$B_2 = \frac{1}{8\lambda^2}\left[\xi - \frac{2(\xi + \gamma)}{\lambda}\right] = -D_2.$$

The boundary layer contributions to these total solutions are easily recognized by the exponential factor. Explicit expressions for the velocity components can, of course, be obtained by differentiating the stream function ψ. It should be noted that the modified Oseen constant still appears as a parameter in the solution through λ and is yet to be evaluated.

Since only a thermal boundary layer exists in the present problem it is not necessary to separate the stream function into two parts. The complete equation of motion was also solved directly by Menold and Ostrach [33] and they showed that the solutions differed only slightly from those given above so that the additional mathematical complexity is not warranted. However, the direct solution is of interest because it was shown to represent a first improvement on the asymptotic solution presented above, i.e., the

direct solution is valid for large but finite Prandtl numbers whereas the other is valid asymptotically as the Prandtl number becomes infinite.

c. Evaluation of the Modified Oseen Constant. Because there is practically no experimental information from which a value for the modified Oseen constant, c, could be obtained, some other method must be developed. This in turn introduces a certain degree of arbitrariness since no unique method is readily apparent.

The modified Oseen technique was introduced in order to simplify the convection term in the energy equation. Therefore, the resulting solutions satisfy the complete energy equation only approximately. An estimate of the accuracy of these solutions could be obtained by substituting them into the complete energy equation (39) with the convection term unaltered. A direct indication of the error is the magnitude of the departure of the right side of this equation from zero. This error, of course, would be a function of both r and θ and the dimensionless parameters, and, most importantly, it would also depend on c. The error will be denoted by $\epsilon(\rho, \theta, c, \mathrm{Gr}, \phi)$. Thus, if ϵ were integrated over the boundary layer and the result set equal to zero an equation should be obtained relating the modified Oseen constant, the Grashof number, and the phase angle from which the constant could be determined. However, the particular form of the θ-dependence in the solutions causes all terms in the integrand to vanish identically. Thus to obtain nontrivial results it is necessary to weight the integrand with some function of θ, here designated by $W(\theta)$. The choice of $W(\theta)$ is completely arbitrary provided that it leads to nontrivial results for the integration.

In the present work the simplest weighting function which selects both odd and even θ-dependence in the integrand is

$$W(\theta) = \cos\theta + \sin\theta \equiv W_1. \tag{53}$$

The resulting expression for the modified Oseen constant is

$$c = [(1/8\mathrm{Gr}\gamma)(1 + 2\gamma^2)]^{1/2} \equiv c_1. \tag{54}$$

Note that this expression for c becomes infinite as the phase angle, ϕ, approaches zero ($\gamma = \sin\phi \to 0$). Weinbaum's evaluation [31] also displayed the same behavior and it was at first thought that this was the reason for his difficulty in treating the heating-from-the-side case ($\phi = 0$).

Since the choice of a weighting function is completely arbitrary it is of interest to see how the constant will be affected by a different choice of a weighting function. Thus, a second weighting function with the required properties is taken to be

$$W_2(\theta) = \cos^3\theta + \sin^3\theta. \tag{55}$$

The corresponding expression for the modified Oseen constant is

$$c = [(1/24\gamma \mathrm{Gr})(9 + 6\gamma^2 + 2\xi\gamma)]^{1/2} \equiv c_2. \tag{56}$$

This also becomes infinite for a phase angle of zero. Thus, neither of these can be used to investigate the character of the solutions as ϕ approaches zero. A third approach is therefore developed to overcome the two undesirable aspects of the above, viz., the arbitrariness of the choice of the weighting function and the singular behavior of c at $\phi = 0$. This approach consists of integrating the square of the error over the boundary layer. Since the resulting integral will be positive definite the constant c can be chosen such that the integral and, hence, the error is a minimum. The result obtained in this way is

$$c = [(1/120\mathrm{Gr})\{\xi - 13\gamma + [(\xi - 13\gamma)^2 + 100\,\delta(\xi, \gamma)]^{1/2}\}]^{1/2} \equiv c_3 \tag{57}$$

where

$$\delta(\xi, \beta) \equiv 9 - 6\gamma^2 + 46\xi\gamma + 120\xi^2\gamma^2.$$

This result has no singularities over the entire range of ϕ values and requires no arbitrary weighting function.

A comparison of modified Oseen constants obtained from the three schemes can be made from Fig. 18. Their values differ appreciably, in general. The effect of the value of c on the quantities of physical interest will be discussed subsequently.

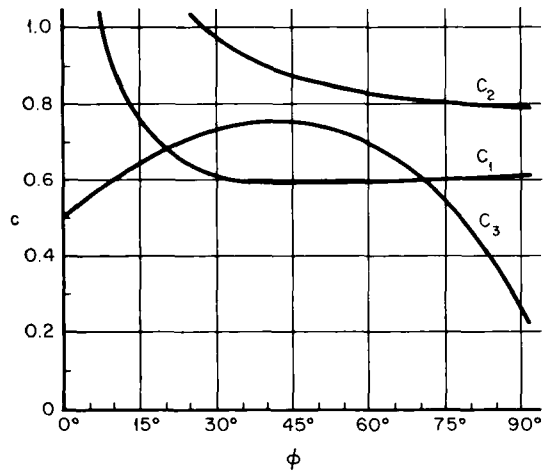

FIG. 18. The modified Oseen constant versus phase angle for various evaluation schemes (Gr = 1) [33]. c_1—$W_1(\theta) = \cos\theta + \sin\theta$; c_2—$W_2(\theta) = \cos^3\theta + \sin^3\theta$; c_3—minimization.

B. RESULTS AND DISCUSSION

1. *Temperature and Velocity Solutions*

In this section the general form of the solutions and the effect of the parameters on them will be presented. Typical temperature and tangential velocity distributions for $\phi = 45°$ are presented in Figs. 19 and 20. These were computed using c_1, from Eq. (24), because it was simplest. Note that τ is antisymmetric and v is symmetric at $\theta + 180°$.

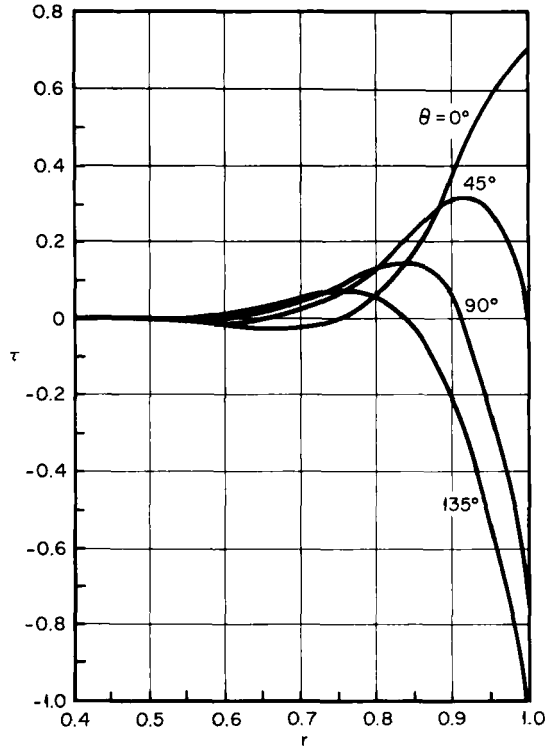

FIG. 19. Temperature profiles at various θ positions [33]. [$W(\theta) = \cos\theta + \sin\theta$, $\mathrm{Pr} = 10^5$, $\mathrm{Gr} = 1$, $\phi = 45°$.)

The boundary layer character of the temperature is clearly shown in Fig. 19 because τ is essentially zero for $r < 0.5$ for all values of θ, whereas relatively large changes appear in the region close to the wall ($r \to 1$). Thus, the isothermal core is essentially bounded by the circle $r = 0.5$.

Also indicated on that figure is the fact that the temperature changes at the edge of the boundary layer are out of phase with those near the wall.

If the edge of the boundary layer is taken to lie within $0.5 < r < 0.7$ then it can be seen that for increasing θ, the temperature at the edge of the boundary layer is increasing while that of the fluid near the wall is decreasing. This behavior is caused by a diffusion of the thermal effects of the wall through the fluid as the fluid moves through increasing values of θ. The thermal diffusion process is evidenced in a qualitative way by the fact that as θ increases from 0° to 135° the maximum temperature for each profile occurs at smaller values of the radius, r. As expected, the thermal boundary layer shrinks closer to the wall with increasing Prandtl numbers.

The action of this overall temperature distribution in driving the flow is indicated in Fig. 20 by the evolution of the velocity profiles between $\theta = 0°$

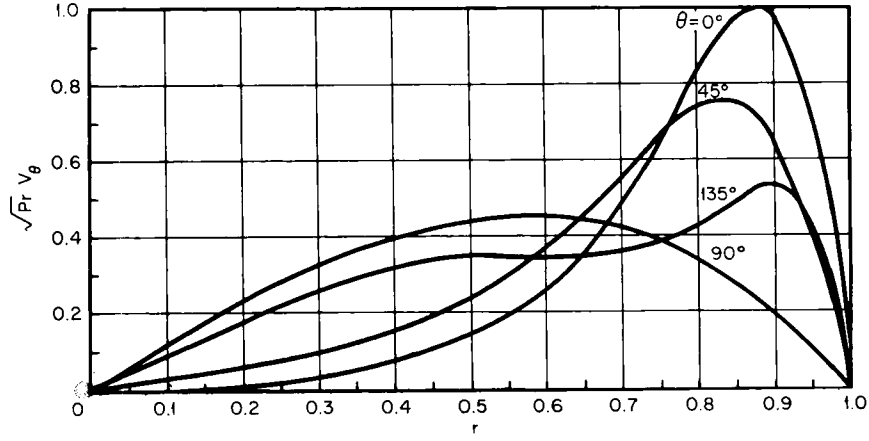

FIG. 20. Velocity profiles at various θ positions [33]. [$W(\theta) = \cos\theta + \sin\theta$, $Pr = 10^5$, $Gr = 1$, $\phi = 45°$.]

and $\theta = 135°$. The maximum fluid velocities occur in the vicinity of $\theta = 0°$ and 180°. (The velocity distributions at $\theta = 0°$ and 180° are identical because of symmetry.)

It is important to note that the velocity in the core (i.e., the region encircled by $r = 0.5$) is not zero everywhere. Thus for $\phi = 45°$ the computed temperature and velocity distributions are compatible with the assumed core configuration. The effect of Prandtl number is the same for the velocity distribution as it was for the temperature. Note that the tangential motion is of the order of $Pr^{-1/2}$ which agrees with the result obtained earlier.

2. *Streamlines*

Streamline patterns are plotted in Figs. 21 through 23 for ϕ values of 45°, 22½°, and 0°. The calculations were made using c_3 because it was not

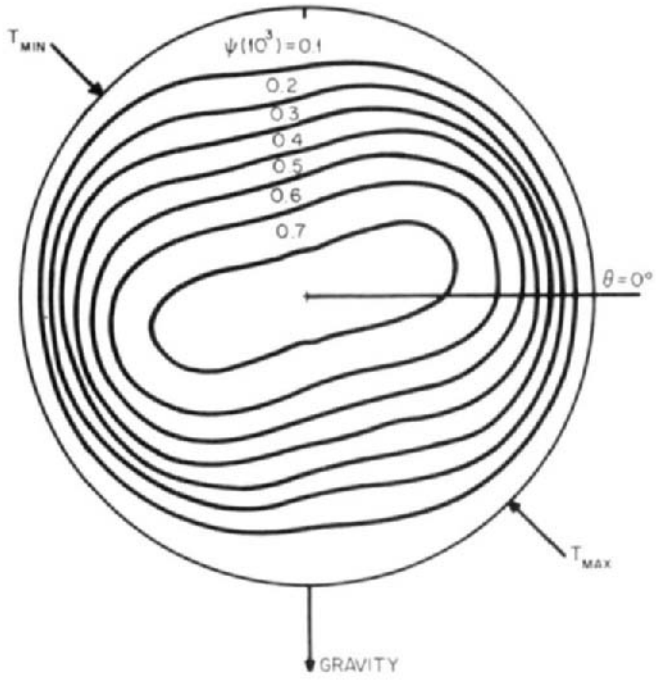

FIG. 21. Streamline pattern for $\phi = 45°$ [33]. ($Pr = 10^5$, $Gr = 1$, c from minimization.)

singular. The pattern for $\phi = 45°$ is representative of those for phase angles between 90° and about 30°. The streamlines are closed and elliptic in shape with centers about the origin. The major axis rotates in a counterclockwise direction when ϕ decreases.

For $\phi = 22\frac{1}{2}$, Fig. 22, two regions appear in which the streamlines are closed but do not enclose the origin. This result might be quite possible from a physical point of view. However, it can be seen in Fig. 22 that a definite tendency now exists for the streamlines centered about the origin to pinch in towards the origin. This in turn means that there is a danger of violating the assumption used in proving the interior to be isothermal that the boundary streamline does not pass through the boundary layer region. In other words, as the streamlines pinch closer to the origin, more boundary layer streamlines curve closer to $r = 0$ and the result is that the region in which the isothermal proof is valid becomes negligible compared to the entire flow field. In Fig. 23 the pattern for $\phi = 0°$ (heating from the side) is shown and it is rather irregular. Based on this picture and the above argument it can be concluded that the temperature and velocity solutions are not compatible with each other when $\phi = 0°$. Thus, the difficulty with

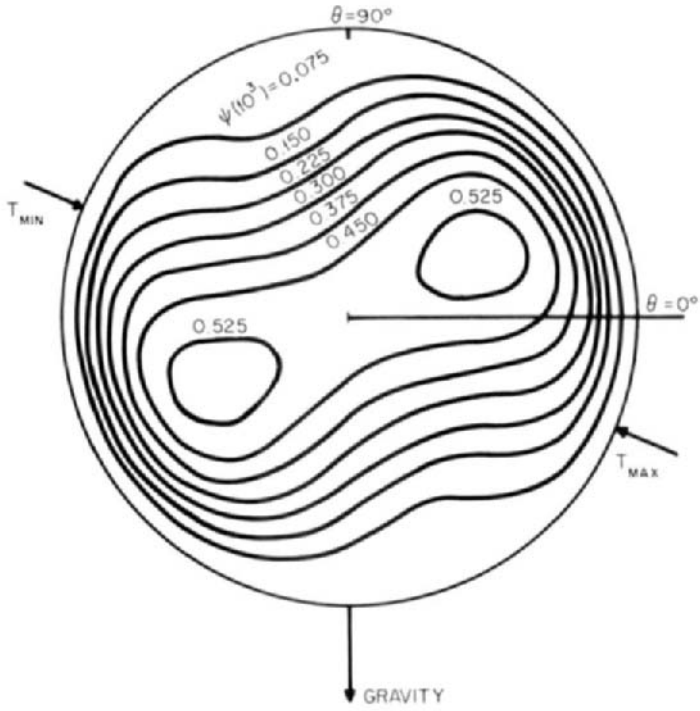

FIG. 22. Streamline pattern for $\phi = 22\frac{1}{2}°$ [33]. ($Pr = 10^5$, $Gr = 1$, c from minimization.)

this case persists even when the mathematical problems are resolved and it would seem that the physical situation is more complicated than the present theory has allowed. In view of the above it can be concluded that the problem is properly described by the solutions presented herein for phase angles greater than 20° to 30°. Although the solutions for heating from below, $\phi = 90°$, are consistent they are not presented for reasons to be given later. For configurations near the heating-from-the-side case an approach different from the present one will have to be developed.

3. *Effect of the Modified Oseen Constant*

The effect of the value of c on temperature and tangential velocity is shown in Figs. 24 and 25 for $\phi = 45°$. Since c plays the role of a parameter in the solutions their shapes will not be affected by changes in its value. This is clear from the figures. It is also obvious from the figures that the temperature is much less affected by the value of c than is the tangential velocity. This is fortunate since in natural convection problems the temperature field and heat transfer are of prime importance.

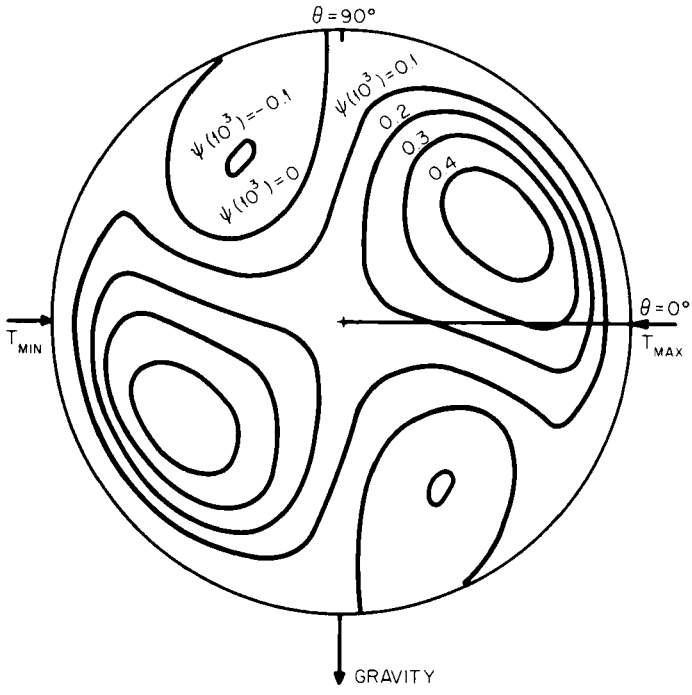

FIG. 23. Streamline pattern for $\phi = 0°$ [33]. ($\mathrm{Pr} = 10^5$, $\mathrm{Gr} = 1$, c from minimization.)

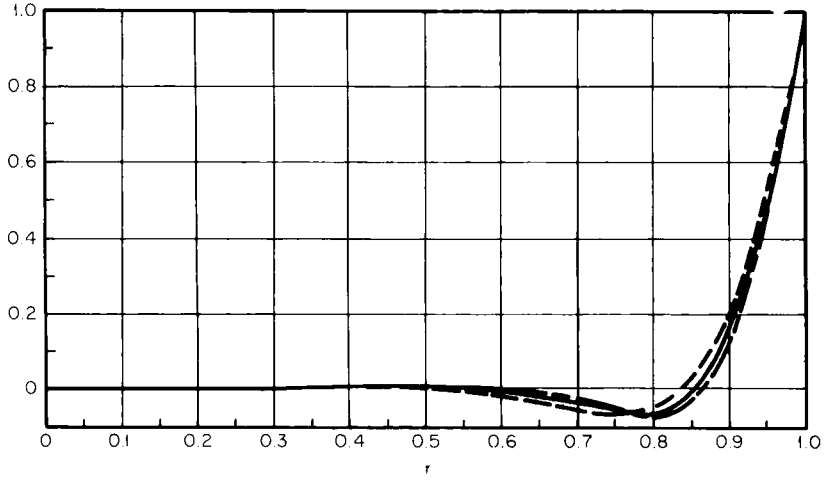

FIG. 24. Effect of the modified Oseen constant on the temperature [33]. ($\mathrm{Pr} = 10^5$, $\mathrm{Gr} = 1$, $\phi = 45°$, $\theta = -45°$.) $---$ $c = C_1 = 0.595$ $[W_1(\theta) = \cos\theta + \sin\theta]$; $c = C_2 = 0.875$ $[W_2(\theta) = \cos^3\theta + \sin^3\theta]$; $c = C_3 = 0.757$ (minimization).

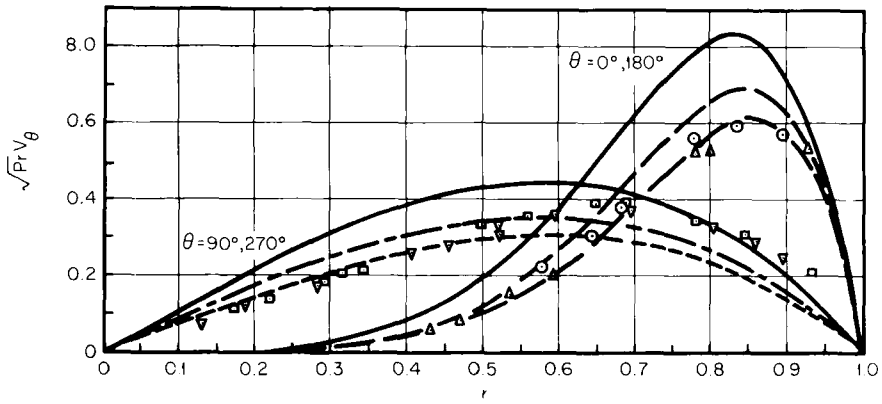

FIG. 25. Comparison of tangential velocities from solutions with experimental results for $\phi = 45°$ [33]. (Pr = 17,710, Gr = 1.012.) ———, solution using $c = C_1$; — —, solution using $c = C_2$; — - —, solution using $c = C_3$. ○—experimental point for $\theta = 0°$; △—experimental point for $\theta = 180°$; □—experimental point for $\theta = 90°$; ▽—experimental point for $\theta = 270°$.

C. EXPERIMENTS

In the above analysis considerable mathematical simplification was obtained by linearizing and uncoupling the equations that describe the physical phenomena and one might wonder whether the solutions properly describe the physical aspects. Furthermore, a number of other questions have been raised such as what is the overall nature of the flow as a function of the phase angle ϕ, and which of the methods of finding the modified Oseen constant leads to the best results. Therefore, a direct experimental analog of the mathematical model was made to try to answer these questions.

1. *The Apparatus*

As shown in Fig. 26 the test vessel consisted of an 8-in. length of copper pipe with an inside diameter of 5 in. and a $\frac{1}{4}$-in. thick wall. This particular length was the maximum possible, consistent with the photographic scheme used for visualizing the flow. The ends of the vessel were sealed with $\frac{1}{4}$-in. thick clear plexiglass plates. The entire vessel was supported beneath the aluminum end rings by two roller bearings at each end so that the vessel could be rotated to vary the phase angle.

The maximum and minimum temperatures for the cosine wall distribution were maintained by two heat exchangers that were soldered into circular slots milled axially into the wall. Distilled water was circulated through these heat exchangers with the temperatures controlled to within $\pm$ 0.01°F

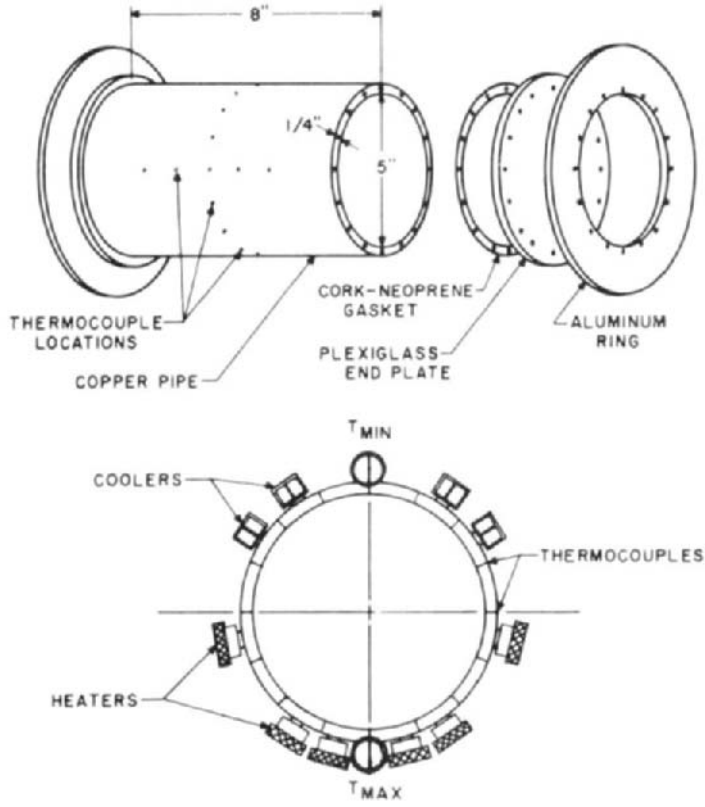

FIG. 26. The test cylinder [33].

by two Haake (Model Ne) constant temperature circulators. The wall temperature distribution between the maximum and minimum points was controlled by a series of heaters and coolers soldered to the outer wall in the locations shown on the figure. The heaters were made from copper bars on which nichrome wires, properly insulated, were attached lengthwise. Distilled water was bled from the Haake thermostats for the coolers. More details on the specific sizes and construction can be found in Menold and Ostrach [33] and Sabzevari and Ostrach [35]. In this way it was possible to maintain indefinitely a circumferential temperature distribution to within 3% of a cosine, with a difference of about 4°F between the maximum and minimum temperatures.

The entire vessel was insulated from the surroundings and the tests were in addition conducted in a special room in which the temperature and humidity could be maintained constant.

The test fluid in these experiments was a silicone oil with a kinematic viscosity of approximately 2000 centistokes. The flow visualization and measuring technique consisted of tracking with a camera the motion of particles suspended in the oil. A light source was placed at one end of the vessel and a camera at the other which was focused at the vessel midplane. The motion of the particles which were essentially neutrally buoyant was determined by making a series of three exposures on the same film. The time intervals were measured by a stopwatch. The velocity could be determined by measuring the distance traveled in the interval. The camera could move to cover different parts of the cross section at the midplane. Temperatures were measured by four manganin–constantan thermocouples inserted through probes. (See Menold and Ostrach [33] and Sabzevari and Ostrach [35] for more details.)

2. *Experimental Observations*

Experimentally determined velocity distributions for $\phi = 45°$ and values of the Prandtl and Grashof numbers respectively of 17,710 and 1.012 are presented in Fig. 25. From the photographs of the particle tracks it was evident that the flow streamlines agreed well with the picture predicted analytically, Fig. 21. Furthermore, the good agreement between experimental points 180° apart in the θ-direction indicate that the velocity profiles were quite symmetric over the entire diameter. From Fig. 25 it can be seen that there is good agreement between the experimental velocities and the calculations based on the modified Oseen constant that yields the lowest values for the velocities. The experimental temperature data are closest to the theoretical curves computed with c_3 (obtained by the minimization method) (see Sabzevari and Ostrach [35]). However, the temperature distributions are much less sensitive to the manner in which the modified Oseen constant is evaluated. Therefore, the best c for an overall picture of flow and heat transfer should be selected on the basis of the good agreement between the tangential velocity data and the lowest theoretical curve. For heat transfer results alone use of the constant determined from the minimization scheme should be satisfactory.

When the fluid was heated from the side, $\phi = 0°$, no cellular pattern like that for $\phi = 45°$ was found, but, rather, a relatively stagnant core was observed in which no recognizable flow pattern exists. Thus, even for the very viscous fluid used in this experiment the tendency to form a stagnant core is indicated when the heating is directed from the side. Investigation of the temperature field for this case indicated that this stagnant region is thermally stratified (see Fig. 27). The formation of this stagnant core appears to result from the phase difference between the fluid temperature in the boundary layer and that imposed on the walls that was noted from Fig.19.

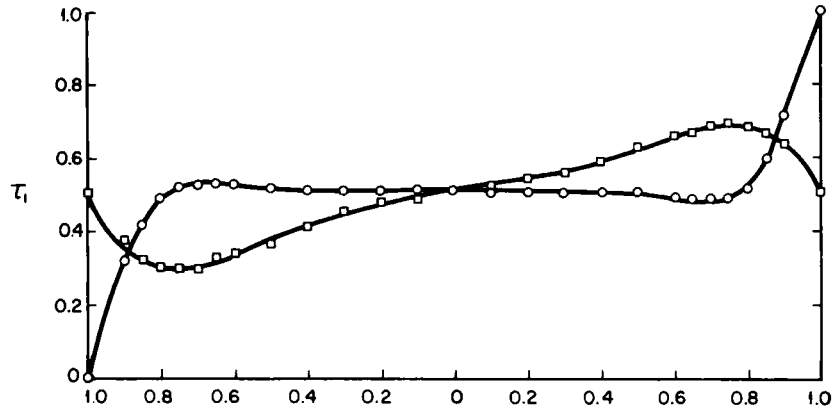

FIG. 27. Temperature distribution along horizontal and vertical diameters for phase angle $\phi = 0$ [35]. (Gr = 2.40, Pr = 18,600.) ○—horizontal, $\theta = 0°$; □—vertical, $\theta = 90°$.

When the heating is from the side, $\phi = 0°$, this phase difference is such that the outer edge of the boundary layer reaches its maximum temperature near the top of the vessel ($\theta = 90°$) and its minimum near the bottom ($\theta = 270°$). In this way hotter fluid accumulates near the top of the core and colder fluid near the bottom to form a stably stratified core. This core acts like a "weighted disk," (Martini and Churchill [22]), and resists the viscous torque of the fluid circulating around it. No comparison between theory and experiments can be made for this case because the modified Oseen solution is not meaningful. It is now clear that the difficulties for this case, $\phi = 0°$, are due to the different physical configuration and, therefore, any analytic treatment must permit the possibility of a stagnant and thermally stratified core.

The final case investigated experimentally was the one in which the heating was from below, $\phi = 90°$. This was done to see if the flow pattern was in the form of a single cell or a double cell. However, photographs taken over long periods of time (8 to 10 hr) indicated that no steady pattern established itself for this configuration. Instead, the fluid at one instant showed a tendency to form a double cell, at another instant a tendency to form a single cell, and usually had superimposed on it a net upward flow which indicated that axial cells were also present. The explanation for this behavior is associated with the fact that in this configuration the fluid is thermally unstable in that the heating from below causes heavier fluid to be above lighter fluid. This instability has been discussed by Gershuni and Zhukhovitskii [48] who have indicated that both the single and double cell patterns are almost equally probable to occur. Furthermore, Ostrach and

Pnueli [49] and Sherman and Ostrach [50] have shown that solid boundaries exert a stabilizing influence on the problem so that motion is first to be expected in the longest dimension. Since in the present experiments the length was the longest dimension the axial cells should appear before the planar ones. If the length were shortened by moving the end plates closer together (to a distance less than the diameter) to inhibit the axial cells then three-dimensional effects from the end-wall boundary layers would most likely preclude the occurrence of the pure planar cells. It is for this reason that a two-dimensional treatment of the heating-from-below case does not appear to be meaningful.

D. Analysis for Heating-from-the-Side

Although the work of Menold and Ostrach gives a good description of the phenomena when the heating phase angle is not close to zero (heating-from-the-side) the analyses discussed to this point do not predict the thermal stratification for heating-from-the-side and give no insight into the role of the heating phase angle, ϕ, on the degree of core stratification. Therefore, Hantman and Ostrach [36] reconsidered the problem in order to obtain a proper description for the observed phenomena.

Two specific aspects of the previous work on the circular geometry warrant reevaluation. Firstly, the core streamlines were always assumed to be closed. Therefore, it would seem to be advisable to formulate the problem such that no *a priori* statements need be made regarding the nature of the core flow or temperature distribution. Secondly, the modified Oseen linearization decoupled the core variables from those in the boundary layer. Since the core is driven by the boundary layer flow a stronger coupling might be anticipated. This point is examined through the redevelopment of the core and boundary layer equations.

The geometric configuration, boundary conditions, and fluid (large Prandtl number) are identical to those of Menold and Ostrach for these considerations. Thus, the one-point boundary value problem defined by Eqs. (31) to (35) is the starting point for this new analysis. The complete equations as they stand are nonlinear and coupled so approximate solutions will have to be obtained.

The reasons for studying these full equations should be quite apparent. The equations are a well-defined set with no apparent singularities. The circular geometry presents no difficulties (e.g., no corner regions) and the boundary conditions are easily treated. Thus, if an approximate analytical technique would yield solutions to this one-point boundary value problem that properly describes the physics then no boundary layer orderings or decisions about the nature of the core at the outset would be needed.

Various generalizations of the modified Oseen linearization were tried but they all led to temperature distributions which yield an isothermal core. These solutions which were made with no assumptions about the core were shown to be equivalent to Menold and Ostrach's and, hence, are valid for some range of heating angles away from $\phi = \pi/2$ but not near $\phi = 0$. These solutions give further insight into the physical mechanisms, in particular, the phase difference between the imposed wall temperature and that at the outer edge of the boundary layer (see Hantman and Ostrach [36] for more details).

Since the desired results (solutions for heating-from-the-side) could not be obtained by the approach described just above a return to a boundary layer treatment was necessary. However, now the method of matched asymptotic expansions, described by Van Dyke [51], was formally applied to derive the asymptotic equations in the limit of large Prandtl number and unit-order Grashof number. Without going into details, the boundary layer equation for vorticity transport is identical to Eq. (45) and that for energy transport is similar to Eq. (46) without the Oseen linearization, i.e., both convection terms remain. However, the dependent variables now are the first terms in the asymptotic series for the stream function and dimensionless temperature difference.

Continuation of this approach for the core leads to the result that there can be no convection of energy in the core which means that there is no diffusion of heat in the core and the streamlines and isotherms must coincide therein. Furthermore, it is found that there can be no horizontal temperature gradients perpendicular to the body-force direction. Thus, the buoyancy force cannot act in the core. These results have been obtained with no assumptions concerning the core streamlines or isotherms. It should be noted, however, that these results imply that two core configurations are possible. For an isothermal core Menold and Ostrach [33] used a condition equivalent to that expressing the coincidence of the streamlines and isotherms to show that the core stream function satisfies the biharmonic equation (with no buoyancy). Another interpretation of the fact that there are no horizontal temperature gradients which is appropriate for a stratified core is that the core temperature is a function of the vertical coordinate alone.

The results for the core follow independently of the wall temperature boundary condition; in particular, independently of the heating phase angle, ϕ. The direct ordinary procedure used here in no way makes a distinction in the core between, say, the extreme cases of heating from below and heating from the side, although experimental evidence does appear to indicate important distinctions. Therefore, since the boundary layer flow must, in some sense, affect the core flow the boundary conditions can affect

the core only implicitly through their direct influence on the boundary layer.

To obtain uniformly valid solutions the inner (boundary layer) expansion must be matched in an overlapping region to the outer (core) expansion. Here, again, two choices exist corresponding to the two different possible core configurations. For the isothermal rotating core the boundary layer and core temperatures, azimuthal, and radial velocity components are matched. For the stratified core the additional condition that the temperature is a function of the vertical coordinate alone is imposed. To match the stream functions for that case the mass flow rates in the core and boundary layer are equated.

From this matching the order of magnitude of the various flow quantities can be readily determined. For the rotating isothermal core configuration it is found that the azimuthal velocity component in both the core and boundary layer are of the same order of magnitude ($Pr^{-1/2}$). However, the radial velocity in the boundary layer is of the order of $Pr^{-3/4}$ whereas that in the core is of the order of $Pr^{-1/2}$ so that the radial velocity in the boundary layer is of lower order than in the core. In the case of a stratified core the highest order velocity is the azimuthal component in the boundary layer. All other velocity components are of lesser magnitude by the factor $Pr^{-1/4}$. Thus, for the rotating isothermal core the flows in the boundary layer and core are of the same order. In contrast, for the thermally stratified core, both velocity components in the core are of lower order than the azimuthal component in the boundary layer so that for increasingly large Prandtl number the core tends to stagnate relative to the boundary layer. This is in accord with the experimental observations of Sabzevari and Ostrach [35].

To solve the boundary layer equations so obtained for a stratified core, Hantman and Ostrach [36] linearized the energy equation in a new way. Both radial derivatives in the convection terms are retained and, rather than setting their coefficients equal to constants as in the modified Oseen method, the coefficients are now taken to be functions of the azimuthal angle which are related to the core temperature and stream function. This azimuthal dependence of the coefficients permits the boundary layer thickness to be determined explicitly as a function of the azimuthal angle. Since this linearization retains both convection terms in the energy equation the two way coupling between that equation and the vorticity equation is maintained in the linearized form. Also, because this linearization introduces core variables into the boundary layer equations the solution for the core and boundary layer variables are coupled.

The detailed determination of the solutions is rather extensive and, therefore, will be omitted. These solutions describe a flow field with a boundary layer contribution which is circumferentially oriented and which joins a horizontal crossflow in the core which is weaker than the boundary layer

flow. This core flow has opposite directions in the upper and lower halves of the cylinder. In the lower half the flow is from left to right and in the upper half from right to left. This implies that the boundary layers in the first and third quadrants eject fluid into the core and those in the second and fourth quadrants entrain fluid from the core.

The solutions obtained are not valid near the ends of the vertical diameter and also when the heating phase angle approaches $\pi/2$ (heating from below). Extensive discussion of the mathematical and physical reasons for the breakdown of the solution under those conditions is presented by Hantman and Ostrach [36]. Thus, the results obtained in this way are meaningful only for heating angles near zero (heating from the side). In this range the indicated behavior is in agreement with experimental findings. Also, for this case the solutions evaluated at the horizontal diameter agree in form with Gill's [28] evaluated at the mid-height of a rectangular cavity.

To summarize, the analysis of Hantman and Ostrach [36] is valid for heating phase angles near zero and that of Menold and Ostrach [34] is meaningful for heating angles sufficiently greater than zero. However, these two analyses and the experiments of Sabzevari and Ostrach [35] indicate two different core possibilities but how or when the transition from one type to the other takes place has not been determined. Another aspect of the problem that requires further consideration is the uniqueness of the core configuration for a given heating angle. Specifically, for heating-from-the-side only the stratified core has been observed experimentally. It remains to be shown whether an isothermal core (either rotating or relatively stagnant) can exist for this situation if the initial conditions are varied.

E. FURTHER EXPERIMENTS

In order to gain insight into these questions Brooks and Ostrach [37] modified the apparatus used by Sabzevari and Ostrach by changing the imposed thermal boundary condition. Rather than having a cosine variation around the periphery the temperature at two points 180° apart on the cylinder circumference was imposed. This resulted in a sawtooth type of distribution but it remained essentially unchanged when the heating angle was varied in contrast to the cosine variation. A method was developed to trace the streamlines directly. This was done by following both in time and space neutrally-buoyant plastic particles through an optical system (see Brooks and Ostrach [37] for details). Velocity and temperature measurements were also made in the same way as Sabzevari and Ostrach. In this way more precise information on the intricacies of the motion was obtained.

Steady-state results were obtained when the flow was started from rest for four values of the heating angle: 0°, 15°, 45°, and 60°. Temperature profiles and streamline patterns are presented for each of these cases. Velocity profiles along the vertical and horizontal diameters are presented for heating angles of 0° and 45° only.

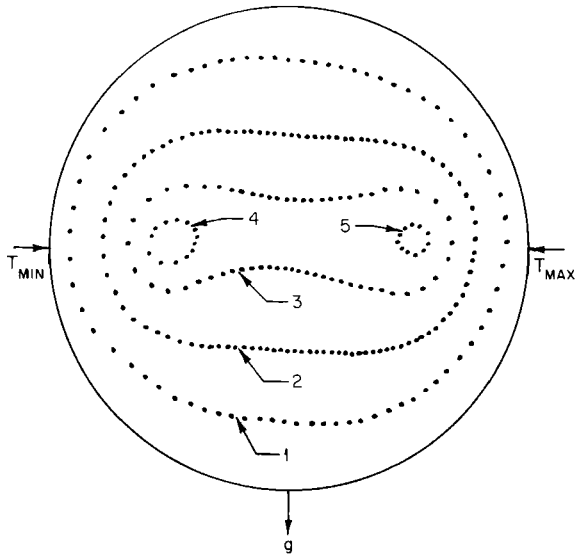

STREAMLINE	INTERVAL BETWEEN POINTS	TOTAL TIME
1	1 minute	71 minutes
2	1 minute	98½ minutes
3	4 minutes	235 minutes
4	8 minutes	100 minutes
5	8 minutes	86 minutes

FIG. 28. Streamline pattern for $\phi = 0°$ (from rest) [37].

Figures 28, 29, and 30 represent the streamline pattern, velocity profiles, and temperature profiles, respectively, when heating is directed from the side. From Fig. 28 it can be seen that the motion of the interior "core" region consists of two small cells whose centers lie along the horizontal diameter. Both cells rotate counterclockwise, as is the motion of all the streamlines presented. The time interval between points on streamlines 1 and 2 is one minute, while on streamlines 4 and 5, it is eight minutes. Since the distances between points on streamlines 4 and 5 are, at most, the same as the distances on streamlines 1 and 2, the velocities encountered on streamlines 4 and 5 are about an order of magnitude less than those encountered on streamlines 1 and 2. The shape of the streamlines should

be noted in that, at a distance from the center of the cylinder, they are elliptical in shape with the major axis being along the horizontal diameter. Streamline 2 in particular exhibits an almost horizontal shape except in the neighborhood of $\theta = 0°$ and 180°. This would tend to agree with the prediction of Hantman and Ostrach [36] of horizontal streamlines when heating is directed from the side. The figure-eight shape of streamline 3 seems to be the result of the influence of the two small cells pulling the fluid towards the center of the cylinder as the fluid approaches $\theta = 90°$ and 270°. Streamline 1 follows the geometry of the cylinder to a greater extent than the other streamlines which is expected since it is closest to the cylinder wall. The horizontal nature of streamline 2 is actually intermediate between streamlines 1 and 3 where the effect of the two cells as apparent in streamline 3 is offset by the effect of the cylinder geometry as apparent in streamline 1. The velocity changes along a streamline can be detected by the relative spacing of the dots comprising the streamline. Since the time intervals between dots are constant for a streamline, greater spacing of the dots along a streamline is equivalent to a greater velocity. With this in mind, and with reference to streamlines 1, 2, and 3, it can be seen that the flow is fastest in the areas near $\theta = 0°$ and 180°, and slows down in the areas near $\theta = 90°$ and 270°. The streamline pattern seems to be almost symmetrical about the horizontal diameter, but perfect symmetry is not present.

Note that the particles observed could not be chosen with respect to any specific values of a stream function. Therefore, the streamline spacing presented does not correspond to equal increments of the stream function.

From the velocity profile along the horizontal diameter, as shown in Fig. 29, it can be seen that for values of r less than about 0.6 when $\theta = 0°$

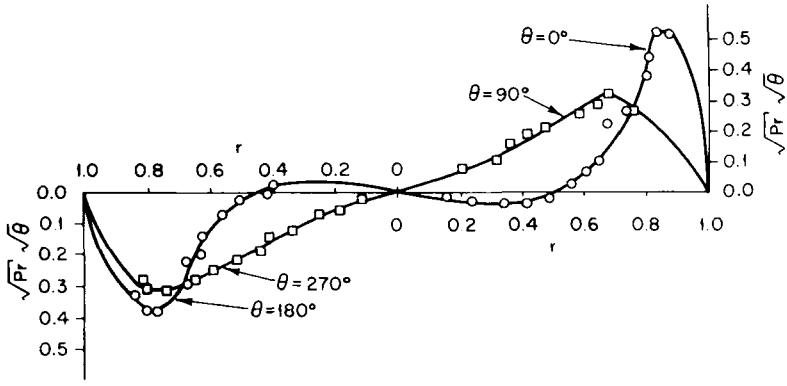

FIG. 29. Velocity profiles for $\phi = 0°$ (from rest) [37]. ○—horizontal diameter; □—vertical diameter.

or 180°, the velocity is very small, as much as an order of magnitude less than the maximum velocities encountered. This is an agreement with the velocity analysis proposed from the streamline trace. The places where this curve crosses the axis, at either side of the center of the cylinder, indicate the centers of rotation of the two small cells. This too agrees with the streamline trace. The shapes of the curves along both the horizontal and vertical diameters agree qualitatively with those found experimentally by Sabzevari and Ostrach [35] when a cosine boundary condition was used. However, they found no evidence of the two small cells. Consequently, their curve does not cross the axis but indicates the velocity to be zero in this region. In the area where these small velocities were encountered, the time intervals between exposures of the film were two minutes and one minute. When smaller time intervals were used, it did appear as if the fluid was stagnant. It must be remembered that time intervals of ten seconds and five seconds were used in other areas of the cross section. Sabzevari and Ostrach used the same velocity measurement technique as was used in this work. It is therefore quite conceivable that these two small cells might have been present in their work, but went undetected.

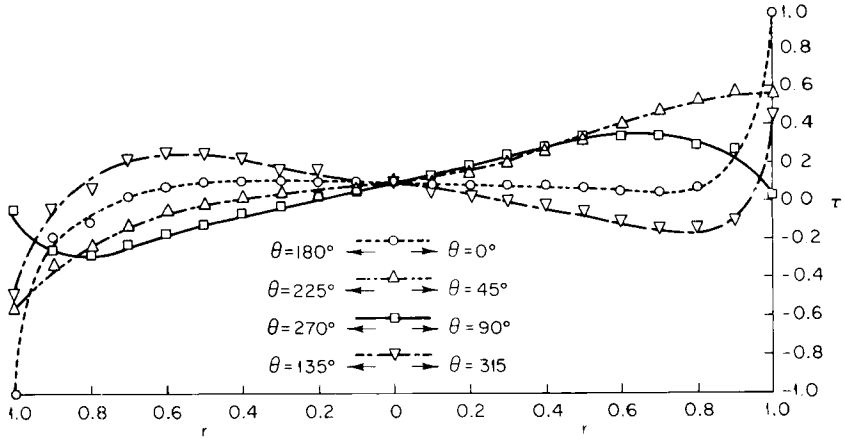

FIG. 30. Temperature profiles for $\phi = 0°$ (from rest) [37].

Figure 30 shows the temperature profiles along four diameters. It is obvious from the profile along the vertical diameter that in the central portion of the cylinder, the fluid is thermally stratified. The four curves are nearly straight lines in this region indicating constant temperature gradients, $\partial\tau/\partial r$. The gradient along the vertical diameter is largest and yields a value of $|\partial\tau/\partial r| \simeq 0.473$. These temperature profiles too are near to symmetrical in the core region. The temperature at $r = 0$ is slightly above T_0, the average of the two imposed temperatures.

The streamline pattern for a heating angle of 15° is very similar in shape to that for $\phi = 0°$. However, the velocities at the same locations are increased with the heating angle. The temperature profiles are also similar but the degree of stratification is less for $\phi = 15°$ than it was for $\phi = 0°$. The temperature gradient along the vertical diameter was found to be 0.374 as compared to 0.473 for $\phi = 0°$.

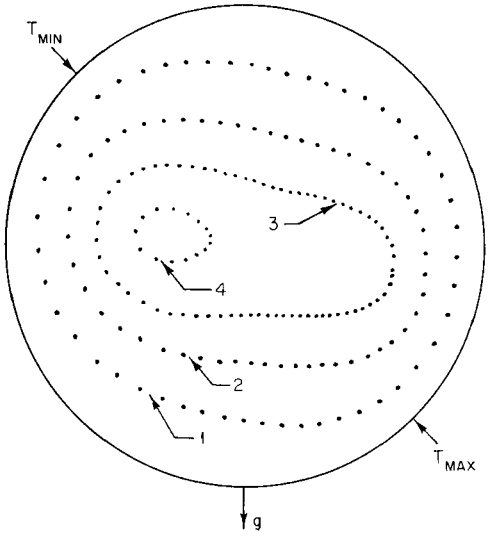

STREAMLINE	INTERVA BETWEEN POINTS	TOTAL TIME
1	1 minute	50 minutes
2	1 minute	51 minutes
3	1 minute	68½ minutes
4	4 minutes	60 minutes

FIG. 31. Streamline pattern for $\phi = 45°$ (from rest) [37].

Figure 31 represents the streamline pattern when $\phi = 45°$. This pattern is markedly different from the patterns for $\phi = 0°$ and $\phi = 15°$ in that the motion consists entirely of one cell. The pattern is unsymmetric with the cell being centered to the left of the center of the cylinder. The area to the right of streamline 4 was investigated in search of another cell, but none could be found. The movement of the particles there was such as to circumscribe streamline 4. The streamlines are elliptical in shape again, but now the major axis has a slightly negative slope. This negative slope may be explained on the basis of physical reasoning. The driving force for the fluid motion is the density differences in the fluid caused by the thermal boundary condition. The extrema in the thermal boundary condition are located at either end of a diameter of the cylinder. As the fluid passes these

extrema the driving force is most influential. The driving force, however, acts in the vertical direction. Therefore the fluid would tend towards vertical motion in the vicinity of the extrema, vertically upwards near T_{max} and vertically downwards near T_{min}. This factor, together with the physical constraint of the cylinder walls, would cause the major axis to be at an angle intermediate between the horizontal and the value of the heating angle. Menold and Ostrach [33] predicted elliptical-like streamlines when $\phi = 45°$ with the major axis having a positive slope. Note also that the fluid in the core is moving faster now than it was when $\phi = 0°$ or 15°. Figure 32 shows the velocity profiles along the vertical and horizontal

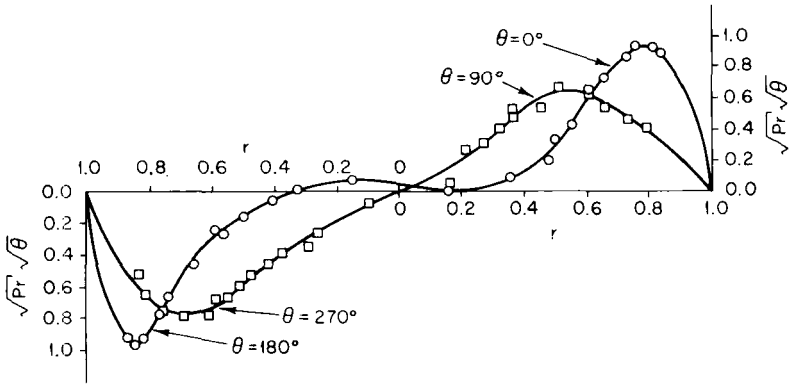

FIG. 32. Velocity profiles for $\phi = 45°$ (from rest) [37]. ○—horizontal diameter; □—vertical diameter.

diameters when $\phi = 45°$. Along the horizontal diameter, there is a large region near the center of the cylinder in which the velocities are very small. The curve only crosses the axis once indicating that the motion consists of one cell. The fact that the point at which the curve crosses the axis is to the left of the center of the cylinder agrees with the streamline trace in Fig. 31, showing the center of the cell to be left of the center of the cylinder. Both curves agree qualitatively with those of Sabzevari and Ostrach [35]. Again, Sabzevari and Ostrach show the velocity to be zero near the center of the horizontal diameter where small velocities were found in this study. Figure 33 shows the temperature profiles when $\phi = 45°$. There is a temperature gradient present but it is much smaller than when $\phi = 0°$ or 15°. The maximum gradient, along the vertical diameter, is only 0.225 now as compared to 0.374 for $\phi = 15°$ and 0.473 for $\phi = 0°$.

The streamline pattern for $\phi = 60°$ is quite similar to that for $\phi = 45°$ except that the fluid moves slightly faster. The slope of the major axis of the streamlines is also more pronounced. The temperature profiles for

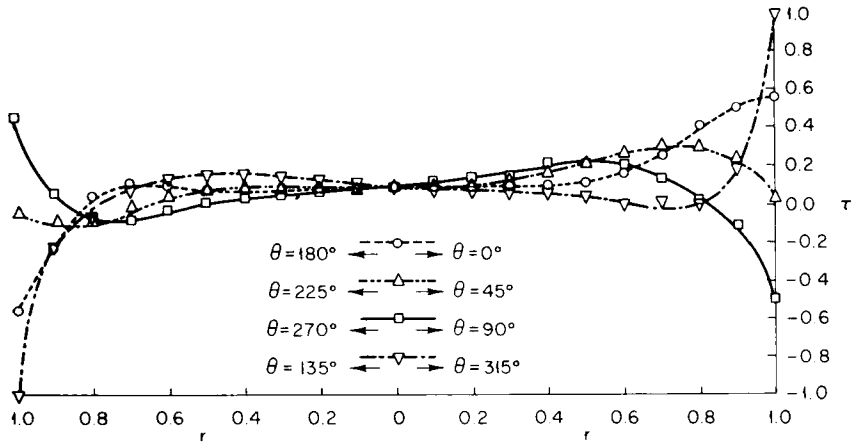

FIG. 33. Temperature profiles for $\phi = 45^\circ$ (from rest) [37].

$\phi = 60^\circ$ indicate even less stratification than for $\phi = 45^\circ$. The indicated vertical temperature gradient now is 0.146.

Several trends can be observed from the preceding results. When the heating angle is zero the motion of the core region consists of two small slowly rotating cells situated along the horizontal diameter. The motion of the remainder of the fluid is such as to circumscribe both of these small cells. This causes the velocity to be nearly horizontal above and below the cells, with a motion towards the left above the cells and towards the right below them. The velocity of the fluid in these cells is about an order of magnitude less than the velocities encountered further from the center of the cylinder. This is in accord with the analytical results of Hantman and Ostrach [36]. Also, the fluid in the central region is thermally stratified, with a relatively large temperature gradient, and with the temperature increasing vertically upward. As ϕ is increased from zero, this behavior continues but the velocities increase as the temperature gradients decrease. At some value of ϕ, intermediate between $\phi = 15^\circ$ and $\phi = 45^\circ$, the two-cell behavior ceases, and one cell, centered to the left of the center of the cylinder, appears. The streamline pattern is much less symmetric than before. The fluid in the core is still thermally stratified, but the temperature gradient is a fraction of what it was for the smaller values of ϕ. As ϕ is increased further, the one-cell behavior persists with the velocities continuing to increase and the temperature gradient continuing to decrease.

Tests were run at values of ϕ greater than 60°, but if ϕ became too large, axial motion was observed. For $\phi = 67\frac{1}{2}^\circ$, the two-dimensional model started to break down. For $\phi = 75^\circ$, there was too much axial motion to make any meaningful measurements. Ostrach and Pnueli [49] showed that

when heating is directed from below, $\phi = 90°$, a thermal instability exists and the flow always starts in the direction of the longest dimension. Axial motion will dominate as long as the length of the cylinder is greater than its diameter. Since this is the case here, a two-dimensional flow is not possible when heating is directed from below. It appears that as the heating angle increases beyond 60° this effect becomes important.

In all the cases studied, some unsymmetric behavior was encountered, more at large values of the heating angle than at smaller values. This behavior is principally attributed to two factors. First, the thermal boundary condition, which is the driving force for the fluid motion, is slightly unsymmetric. Second, the viscosity temperature relation for the working fluid, as provided by the General Electric Company, shows that the viscosity change will be about 10% over the temperature range indicative of this experiment. In every case, the temperature at the center of the cylinder was slightly greater than the average of the two imposed temperatures.

It was now desired to see if the initial condition would have an effect on the steady-state solution. Two different steady-state types of flow were previously encountered: the two-cell, highly stratified, slower flow indicative of small heating angles; and the one-cell, slightly stratified, faster moving flow indicative of greater heating angles. The plan now was to set up the cylinder at $\phi = 45°$ and let the flow reach steady state. Then the cylinder would be rotated so $\phi = 0°$ and again allowed to reach steady state. In this way the steady-state results for $\phi = 45°$, as depicted in Figs. 31 and 33, would become the initial conditions for $\phi = 0°$. The new steady-state results indicated that the two-cell mode again appeared and that the velocities slowed down and that the degree of thermal stratification increased. The gradient along the vertical diameter is now 0.467 as compared to 0.473 for $\phi = 0°$ starting from rest and 0.225 for the initial condition. It is concluded that the resulting flow is the same as that depicted in Figs. 28 and 30. In other words, the steady-state results for heating from the side are the same whether the flow was started from rest or from the state depicted in Figs. 31 and 33. Certainly, the initial condition did not persist at $\phi = 0°$.

In much of the previous work, the core is referred to as either stagnant and thermally stratified or as isothermal and rotating. In the work of Brooks and Ostrach some motion in the core was always observed and some degree of thermal stratification was always detected. If the results for $\phi = 45°$ were to be interpreted as a nearly isothermal rotating core, it is seen that this situation does not remain at $\phi = 0°$. It is still possible that other initial conditions will cause other steady-state results, but that is a task for future investigations. In this work, only these two initial conditions were investigated.

The results presented here agree qualitatively with other experimental

work. Other works do not present experimentally found streamlines, but velocity and temperature profiles are presented. Martini and Churchill [22], using the step function boundary condition, conclude that there is a narrow ring of circulating fluid when heating is directed from the side. This ring is narrowest near $\theta = 0°$ and 180° and increases in thickness near $\theta = 90°$ and 270°. Also the velocities are largest near $\theta = 0°$ and 180° and decrease as the fluid approaches $\theta = 90°$ and 270°. This behavior is indicative of the streamlines presented in this study. Martini and Churchill conclude that the core region is thermally stratified and essentially stagnant but has slow-moving eddies. Again, the results here bear this out.

The results of Sabzevar and Ostrach [35] agree to a certain extent with the present results although they used a cosine boundary condition. For heating from the side, their velocity profiles agree qualitatively with the ones presented here, thus indicating a core region of the same general shape as was found here. However, they found no evidence of two cells. They do agree that the fluid is thermally stratified. At $\phi = 15°$, Sabzevari and Ostach find evidence of the two cells, but do not find them to be situated along the horizontal diameter. For $\phi = 45°$ and 60°, they conclude that the core region is isothermal and rotating. The present work also found the core to be rotating but did detect a small temperature gradient. The two works agree in that the types of flow are different for large values of ϕ as opposed to small values of ϕ.

IV. Concluding Remarks

The work presented above indicates the extremely complex nature of natural convection phenomena in enclosures. The difficulties arise from the coupling of the flow and thermal aspects, the coupling of the boundary layer and the core, and the sensitivity of the flow configuration to the imposed thermal boundary condition. These effects lead to core configurations in which the velocities can vary from values equal to those in the boundary layer to ones which are an order of magnitude or less, to secondary and tertiary flows, and to different types within a given geometric configuration, e.g., in the wall, interior, and end regions. All of these make both theoretical and experimental investigation extremely difficult.

Nevertheless, analytical, numerical, and experimental studies have been made which describe parts of the entire process well so that at least a qualitative understanding of the associated phenomena now exists. Considerably more research is required to obtain greater insight into the entire flow regime and how one situation changes to another so that accurate quantitative predictions can be made.

ACKNOWLEDGEMENT

All the author's research on this problem was supported by the U.S. Air Force Office of Scientific Research under Grant No. AFOSR-68-1485.

NOMENCLATURE

a aspect ratio, l/d
c, c' modified Oseen parameter, Eqs. (47), (40)
c_P specific heat
d width
f constant in Fig. 10, Ref. [27]
g acceleration of gravity
Gr Grashof number, $\beta g(T_H - T_C)d^3/\nu^2$
h heat transfer coefficient, Eq. (10)
h' heat transfer coefficient based on $(T_w - T_m)$
K frictional heating parameter, PrGr $(\beta g R_0/c_P)$
k thermal conductivity
k_a apparent thermal conductivity
l height
Nu Nusselt number
P pressure
Pr Prandtl number, $c_P\mu/k$
Q total heat flux, Eq. (21)
q heat flow per unit area and time, Eq. (10)
R radial coordinate
r dimensionless radial coordinate, R/R_0
R_0 radius
Ra Rayleigh number, PrGr
T temperature
T_0 average temperature
ΔT amplitude of wall temperature distribution
U vertical or radial velocity component
u dimensionless vertical or radial velocity component
V horizontal or azimuthal velocity component
v dimensionless horizontal or azimuthal velocity component
X vertical coordinate
X_P depth of penetration
x dimensionless vertical coordinate
Y horizontal coordinate
y dimensionless horizontal coordinate
$\bar{y}$ transformed coordinate, $1 - y$
α thermal diffusivity, $k/\rho c_P$
β volumetric expansion coefficient
Γ dimensionless centerline vertical temperature gradient $(T_H - T_C)^{-1}(dT_m/dx)$
γ sin ϕ, Eq. (54)
Θ dimensionless centerline temperature difference, $(T - T_m)/(T_H - T_C)$
θ dimensionless temperature difference, Eq. (6) or azimuthal coordinate
λ $\mathrm{Pr}^{1/4}\bar{\lambda}$
$\bar{\lambda}$ $\sqrt{c\,\mathrm{Gr}/2}$
μ absolute viscosity
ν kinematic viscosity
ξ cos ϕ, Eq. (57)
ρ fluid density
τ dimensionless temperature difference, Eq. (35)
ϕ heating phase angle, Eq. (31)
Ψ stream function
ψ dimensionless stream function, Eqs. (6) and (35)

SUBSCRIPTS

C cooler wall
c conduction regime
d departure corner
H hotter wall
m centerline
s starting corner

REFERENCES

1. W. Elenbaas, *Physica* **9,** 1–28 (1942).
2. W. Elenbaas, *Physica* **9,** 865–874 (1942).
3. W. Elenbaas, *Philips Res. Rep.* **3,** 338–360, 450–465 (1948).
4. S. Ostrach, NACA TN 2863 (1952).
5. S. Ostrach, *in* "High Speed Aerodynamics and Jet Propulsion" (F. K. Moore, ed.), Vol. 4, Chapter F, Princeton Univ. Press, Princeton, New Jersey, 1964.
6. M. J. Lighthill, *J. Mech. Appl. Math.* **6,** (1953).
7. S. Ostrach and P. R. Thornton, *Trans. ASME* **80** (1958).
8. B. W. Martin, *Proc. Roy. Soc. London* **A230,** 502–531 (1955).
9. J. P. Hartnett and W. E. Welsh, *Trans. ASME* **79,** 1551–1557 (1957).
10. J. A. Lewis, Free Convection in Commercial Insulating Materials, Ph.D. Thesis, Brown Univ., Providence, Rhode Island, 1950.
11. E. M. Zhukovitskii, *Zh. Tekh. Fiz.* **22,** 832 (1952).
12. G. A. Ostroumov, "Svobodnaya convectzia v ousloviakh vnoutrennei zadachi." State Publ. House, Technio-Theoretical Literature, Moscow Leningrad, 1952 (Also available as NACA TM 1407, 1958).
13. E. Drakhlin, *Zh. Tekh. Fiz.* **22,** 829 (1952).
14. S. Ostrach and W. H. Braun, NACA TN 4323 (1958).
15. S. Ostrach, A Boundary Layer Problem in the Theory of Free Convection, Ph.D. Thesis, Brown Univ., Providence, Rhode Island, 1950.
16. A. F. Pillow, Aero Res. Lab. Rep. A79 (1952).
17. W. Mull and H. Reiher, *Gesundh.-Ing.* **1,** No. 28 (1930).
18. R. J. Schmidt and O. A. Saunders, *Proc. Roy. Soc. London* **A165,** 216 (1938).
19. G. W. Batchelor, *Quart. Appl. Math.* **12,** 209 (1954).
20. G. Poots, *Quart. J. Mech. Appl. Math.* **11,** 257 (1958).
21. G. W. Batchelor, *J. Fluid Mech.* **1,** 177 (1956).
22. W. D. Martini and S. W. Churchill, *AIChE J.* **6,** 251 (1960).
23. J. D. Hellums and S. W. Churchill, *AIChE J.* **8,** 692 (1962).
24. E. R. G. Eckert and W. O. Carlson, *Int. J. Heat Mass Transfer* **2,** 106 (1961).
25. J. O. Wilkes, The Finite Difference Computation of Natural Convection in an Enclosed Rectangular Cavity, Ph.D. Thesis, Univ. of Michigan, Ann Arbor, Michigan, 1963.
26. G. Z. Gershuni, E. M. Zhukhovitskii, and E. L. Tarunin, *Mech. Liquids Gases, Akad. Sci. USSR* No. 5, 56–62 (1966).
27. J. W. Elder, *J. Fluid Mech.* **23,** Part 1, 77 (1965).
28. A. E. Gill, *J. Fluid Mech.* **26,** Part 3, 515 (1966).
29. G. de Vahl Davis, Laminar Natural Convection in a Rectangular Cavity, New York Univ., Dept. of Mech. Eng. Rep. No. F-67-2, 1967. Also *Int. J. Heat Mass Transfer* **11,** 1675–1693 (1968).
30. V. I. Polezhaev, *Mech. Liquids Gases, Akad. Sci. USSR* No. 2, 103–111 (1967).
31. S. Weinbaum, *J. Fluid Mech.* **18,** 409 (1964).
32. J. A. Lewis and G. F. Carrier, *Quart. Appl. Math.* **7,** 228 (1949).
33. E. R. Menold and S. Ostrach, Natural Convection in a Horizontal Cylinder at Large Prandtl Numbers, Case Inst. of Technol., Cleveland, Ohio, FTAS/TR-65-4, AFOSR Tech. Rep. No. AFOSR 65-2239, 1965.
34. S. Ostrach and E. R. Menold, in "Teplo-y Massoperenos" (A. V. Luikov and B. M. Smol'kova, eds.), Vol. 1 *Proc. All Union Conf. Heat Mass Transfer*, 3*rd* Minsk, BSSR, pp. 640–660 (1968).

35. A. Sabzevari and S. Ostrach, Experimental Studies of Natural Convection in a Horizontal Cylinder, Case Inst. of Tech., Cleveland, Ohio, FTAS/TR-66-8, AFOSR Sci. Rep. No. AFOSR 66-1401 (1966).
36. R. Hantman and S. Ostrach, Natural Convection Inside a Horizontal Circular Cylinder, Case Western Reserve Univ., Cleveland, Ohio, FTAS/TR-69-36 (1969).
37. I. Brooks and S. Ostrach, *J. Fluid Mech.* **44,** Part 3, 545–561 (1970).
38. M. Jakob, "Heat Transfer," Vol. 1, p. 538. Wiley, New York, 1959.
39. J. G. A. de Graff and E. F. M. van der Held, *Appl. Sci. Res. Sec. A* **3,** No. 6 (1953).
40. A. F. Emery, *J. Heat Transfer Ser. C* **85,** No. 2 (1963).
41. E. Schmidt, *Chem. Ing.-Tech.* **28,** 175 (1956).
42. G. Mordchelles-Regnier and C. Kaplan, *Proc. Int. Heat Mass Transfer Conf.* 94, 1963.
43. S. Ostrach, NACA Rep. 1111 (1953).
44. J. W. Elder, *J. Fluid Mech.* **23,** Part 1, 99 (1965).
45. M. E. Newell and F. W. Schmidt, ASME Paper 69-HT-42, 1969.
46. J. T. Han, MASc Thesis, Dept. of Mech. Eng., Univ. of Toronto (1967).
47. R. K. MacGregor and A. F. Emery, ASME Paper No. 68-WA/HT-4 (1968).
48. G. Z. Gershuni and E. M. Zhukovitskii, *PMM* **25,** 1035 (1961).
49. S. Ostrach and D. Pnueli, *Trans. ASME. Ser. C* **85,** (1963).
50. M. Sherman and S. Ostrach, *J. Appl. Mech. Ser. E* **34,** No. 2 (1967).
51. M. Van Dyke, "Perturbation Methods in Fluid Mechanics." Academic Press, New York, 1964.
52. S. Ostrach, "Internal Viscous Flows with Body Forces, Boundary Layer Research" (H. Görtler, ed.), pp. 185–209. Springer-Verlag, Berlin, 1958.

This Page Intentionally Left Blank

Infrared Radiative Energy Transfer in Gases*

R. D. CESS AND S. N. TIWARI†

College of Engineering, State University of New York, Stony Brook, New York

I. Introduction 229
II. Band Absorptance Models 230
A. Band Absorption 230
B. Band Absorptance 235
C. Elsasser Model 237
D. Rigid-Rotor, Harmonic-Oscillator Model 240
E. Band Absorptance Correlations 244
III. Basic Equations 246
A. Rate Equations and Relaxation Time 247
B. Equation of Transfer 248
C. Radiative Flux Equation 250
D. Optically Thin Limit 252
E. Large Path Length Limit 253
IV. Radiative Transfer Analyses 254
A. Radiative Transfer 255
B. Radiation–Conduction Interaction 264
C. Vibrational Nonequilibrium 273
D. Radiative Equilibrium 277
V. Concluding Remarks 280
Nomenclature 281
References 282

I. Introduction

The object of this article is to illustrate the incorporation of spectroscopic information into the radiative transfer equations, and to present a reasonable means of treating radiative energy transfer within gases. Specific restriction

* Supported by The National Science Foundation, Grant Number GK-16755.

† Present address: Department of Thermal Engineering, College of Engineering, Old Dominion University, Norfolk, Virginia 23508.

is made to infrared gaseous radiation, which results from molecular transitions involving both vibrational and rotational energies, and emphasis will be placed upon the application of molecular band models to radiative transfer analyses. In a sense, the present chapter may be regarded as a continuation of the chapter by C. L. Tien, appearing in Volume 5 of *Advances in Heat Transfer*, within which detailed information regarding vibration-rotation bands is included. Consequently, the present chapter will only briefly review vibration-rotation spectra, while the main objective will be to apply band information to the formulation of radiative energy transfer within gases, i.e., to the application of local conservation of energy within a gas.

The chapter is divided into several sections, and the following section, Section II, briefly reviews infrared band spectra, introduces very simple band models, and proceeds to discuss the formulation of total band absorptance information with the aid of these models. The basic equations describing radiative transfer within an infrared absorbing-emitting gas are formulated in Section III, and these allow for radiatively induced departures from local thermodynamic equilibrium. The final section, Section IV, presents some illustrative radiative transfer analyses, with emphasis upon physical interpretations and the relative importance of thermal radiation versus molecular conduction as energy transport mechanisms.

II. Band Absorptance Models

The purpose of this section is to formulate and discuss spectroscopic models describing the total band absorptance for infrared radiating gases. As will be seen in Section III, the total band absorptance plays an essential role in describing the equations for the radiative energy flux. First, however, it will be necessary to review briefly several aspects of the basic structure of vibration-rotation bands. As previously discussed, no attempt at completeness will be made, since a description of infrared band structure has been given in the article by Tien [1].

A. BAND ABSORPTION

Infrared absorption and emission of thermal radiation is a consequence of coupled vibrational and rotational energy transitions. Quite obviously, a diatomic molecule is the simplest molecule which will undergo such transitions. However, symmetric diatomic molecules, such as O_2 and N_2, have no permanent dipole moment, and thus they are transparent to infrared

radiation.[1] For unsymmetric diatomic molecules, such as CO, the infrared spectrum will consist of a fundamental vibration-rotation band occurring at the fundamental vibrational frequency of the molecule, i.e., the band arises due to an energy transition between two adjacent vibrational energy levels. Vibrational transitions spanning three vibrational levels produce the first overtone band located at twice the fundamental frequency of the molecule, and subsequent overtone bands occur at higher multiples of the fundamental frequency. In general, the overtone bands are quite insignificant relative to the fundamental band.

The picture is much the same for polyatomic molecules, except that these have more vibrational degrees of freedom. For example, carbon dioxide is a linear triatomic molecule and thus possesses four vibrational degrees of freedom. The two bending frequencies, however, are identical, while one of the stretching modes is symmetric and thus has no permanent dipole moment. Consequently, carbon dioxide has two fundamental bands. In addition to fundamental and overtone bands, the infrared spectrum of polyatomic molecules also includes combination and difference bands which occur at linear combinations or differences of the fundamental frequencies. Again choosing carbon dioxide as an example, the important infrared bands are the 15 μ and 4.3 μ fundamental bands and the 2.7 μ combination band.

While the location of a vibration-rotation band is described by the associated vibrational transition, the band structure is governed by simultaneous rotational transitions which accompany a vibrational transition. As a consequence of the unequal spacing of rotational energy levels, the coupled vibration-rotation transitions occur at discrete frequencies located about the vibrational frequency. The resulting band structure in turn consists of an array of discrete rotational lines.

Before proceeding, it should be mentioned that while a vibrational transition is always coupled with a rotational transition, rotational transitions do occur by themselves. Since the transition energies are very small, the resulting spectrum is normally in the microwave region and has no influence on infrared radiation. There are exceptions, such as water vapor which possesses a pure rotation band in the far infrared. Often, however, this pure rotation band is treated in a manner similar to a vibration-rotation band.

In order to describe the absorption characteristics of a vibration-rotation band, it is first necessary to consider the variation of the spectral absorption coefficient for a single line. For infrared radiation, the most important line-broadening mechanism is pressure broadening [1], and the variation of

[1] Symmetric diatomic molecules may have pressure-induced bands which can play a significant role in atmospheric radiation. For example, infrared transmission by hydrogen is important in the atmospheres of the Jovian planets [2, 3].

the spectral absorption coefficient with wave number is given by the Lorentz line profile as

$$\frac{\kappa_{\omega j}}{P} = \frac{S_j}{\pi} \frac{\gamma_j}{\gamma_j^2 + (\omega - \omega_j)^2}. \tag{1}$$

Here κ_ω denotes the volumetric absorption coefficient, and ω is the wave number ($\omega = \nu/c$ where c is the speed of light and ν the frequency). The rotational quantum number is denoted by j, such that the subscript j refers to a specific line within the band. Thus the wave number location of the line is ω_j, and γ_j and S_j refer to the half-width and intensity of the line, respectively. For the time being, no distinction will be made between total and partial pressures. The line intensity is defined as

$$S_j = \int_{-\infty}^{\infty} (\kappa_{\omega j}/P)\, d(\omega - \omega_j), \tag{2}$$

and this is consistent with Eq. (1). The line intensity may be described in terms of the molecular number density and Einstein coefficients, and for a perfect gas it follows that S_j is a function solely of temperature.

From kinetic theory, the line half-width may be shown to vary with pressure and temperature as

$$\gamma_j \sim P/\sqrt{T}. \tag{3}$$

More detailed quantum-mechanical calculations again show the linear dependency upon pressure, but indicate that the inverse square-root variation with temperature is often true only for the band wings (large values of j). Again considering CO_2 as an example, Yamamoto *et al.* [4] have shown that the temperature dependency of the line half-width may be described by $\gamma_j \sim T^{-n_j}$, and that n_j approaches 0.75 for small j, decreases with increasing j to approximately 0.3, and then increases with a further increase in j to the kinetic theory value of 0.5.

The Lorentz line profile, as described by Eq. (1), is illustrated in Fig. 1. There are two points worth noting. The first is that increasing pressure broadens the line, and, with respect to a complete band consisting of many lines, this will at sufficiently high pressures lead to a smearing out of the discrete line structure. The second point is that the maximum absorption coefficient, which occurs at $\omega = \omega_j$, is invariant with pressure, since

$$(\kappa_{\omega j})_{\omega = \omega_j} = PS_j/\pi\gamma_j \tag{4}$$

from Eq. (1), while $\gamma_j \sim P$.

It remains to describe the variation of line intensity with rotational quantum number, and for present purposes the simple model of a harmonic oscillator

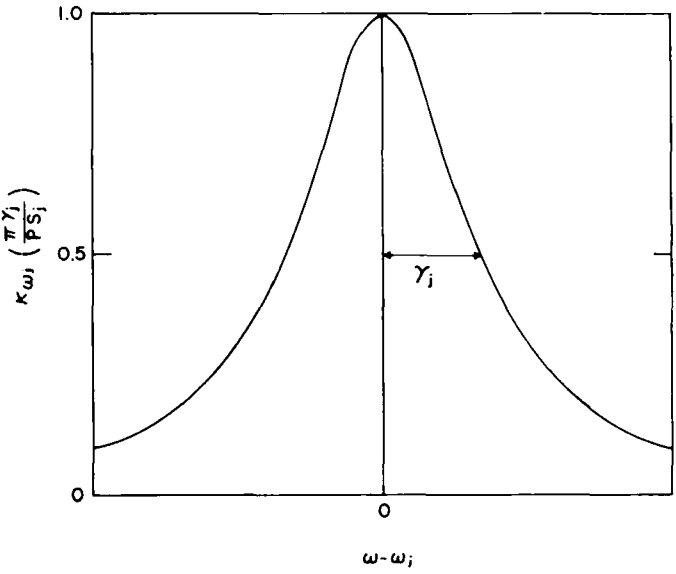

FIG. 1. Lorentz line profile.

and rigid rotor will be assumed. Following Penner [5], and assuming a large number of lines (large j), the variation of S_j with j is

$$S_j = (ShcBj/kT) \exp(-hcBj^2/kT), \tag{5}$$

where h is Planck's constant, k Boltzmann's constant, and B the rotational constant of the molecule. Furthermore, S denotes the intensity of the total band, such that

$$S = \int_{-\infty}^{\infty} (\kappa_\omega/P)\, d(\omega - \omega_0), \tag{6}$$

where ω_0 is the wave number at the band center. It should be realized, of course, that the integration limits in Eq. (6) imply integration over the entire band, as opposed to Eq. (2), where the limits indicate integration over a single line.

A further consequence of the rigid rotor approximation is that the lines are equally spaced, with the spacing $d = 2B$. Consequently, the line locations may be expressed in terms of wave number by

$$\omega - \omega_0 = \pm 2jB. \tag{7}$$

Combination of Eqs. (6) and (7) allows a continuous representation of S_j with wave number, and this is illustrated in Fig. 2. In actuality, for a real

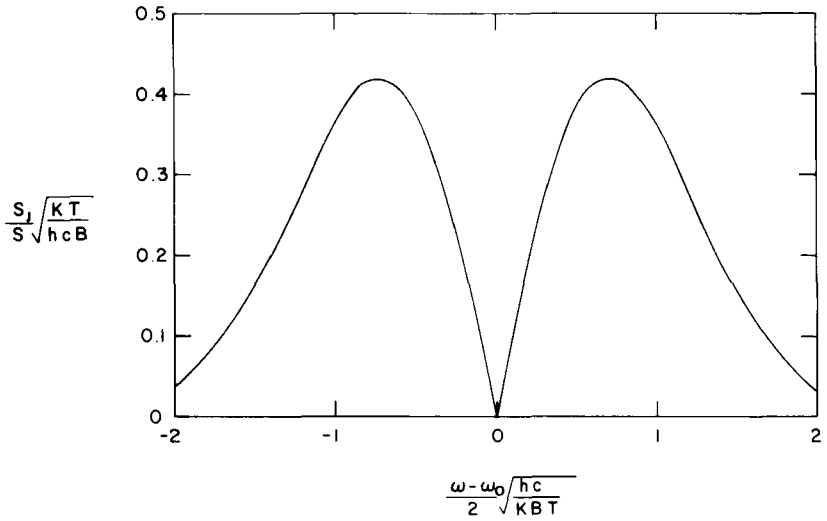

FIG. 2. Variation of S_j for a harmonic oscillator and rigid rotor.

band the two branches (P and R branches) are not symmetric, while vibrational modes involving bending exhibit a third central branch (Q branch). Nevertheless, the present simplified model will serve the purpose for which it is intended, i.e., to illustrate the basic features of the total band absorptance.

With regard to the variation of κ_ω over the entire band, this will consist of the superposition of the contributions from the individual lines, such that

$$\kappa_\omega = \sum_j \kappa_{\omega j} = \frac{P}{\pi} \sum_j \frac{S_j \gamma_j}{\gamma_j^2 + (\omega - \omega_j)^2}. \tag{8}$$

It is further apparent that

$$S = 2 \sum_{j=0}^{\infty} S_j,$$

where the factor of two is included to account for both branches. Again assuming a large number of lines, the summation may be replaced by integration, and employing Eq. (5)

$$S = 2 \int_0^\infty S_j \, dj = S,$$

which illustrates that the separate applications of the assumption of a large number of lines are mutually compatible. Since S_j is a function solely of temperature, the above equation additionally illustrates that the band intensity is a function only of temperature.[2]

[2] While the conclusion is correct, the situation is really not this simple, since summation over vibrational quantum number has been ignored.

B. BAND ABSORPTANCE

The spectral band absorptance is defined as

$$\alpha_\omega = 1 - e^{-\kappa_\omega y}. \tag{9}$$

The physical interpretation of α_ω is that it is the fraction of energy which is absorbed when a beam of radiant energy passes through an isothermal slab of gas of thickness y. The total band absorptance is in turn

$$A = \int_{-\infty}^{\infty} \alpha_\omega \, d(\omega - \omega_0), \tag{10}$$

where the integration over the single band is again implied. The physical interpretation of the total band absorptance is not as simple as for its spectral counterpart α_ω. For present purposes, it will be sufficient to state that the total band absorptance will be needed later to generate the kernel function in the radiative flux equations.

A convenient form of Eq. (10) follows to be

$$A = \int_{-\infty}^{\infty} \{1 - \exp[-(\kappa_\omega/P)Py]\} \, d(\omega - \omega_0). \tag{11}$$

From Eq. (8) it is evident that κ_ω/P depends both upon pressure and temperature, such that

$$A = A(Py, P, T). \tag{12}$$

It is important to note the dual role that pressure plays. Its appearance in the pressure path length, Py, is due simply to the fact that absorption is dependent upon the number of molecules which are present along a line of sight. The second dependency upon pressure is a result of the line structure of the band being a function of pressure. For sufficiently high pressures the line structure is smeared out, and in this limit pressure enters solely through the pressure path length Py. This will be illustrated in quantitative terms later.

In the following two subsections, simple band models will be employed to illustrate certain basic features of the total band absorptance. There is, however, one important limiting form of A which is completely independent of the band model, and this applies when $\kappa_\omega y \ll 1$, i.e., for the conventional optically thin limit in radiative transfer. Upon expanding the exponential in Eq. (11), then

$$A = Py \int_{-\infty}^{\infty} (\kappa_\omega/P) \, d(\omega - \omega_0) = PyS. \tag{13}$$

This is the so-called linear limit, and the important feature of this limit is

the fact that the total band absorptance is independent of rotational line structure.

A second limiting form for the total band absorptance is that of strong nonoverlapping lines. Although the actual limiting result for A depends upon the band model employed, the conditions for achieving this limit may be discussed in general terms. The limit requires that two separate conditions be satisfied. The first is the requirement of strong lines, for which total absorption occurs in the vicinity of the line centers. From Eq. (9), this is equivalent to requiring that $\kappa_{\omega j} y \gg 1$ for $\omega = \omega_j$, and upon combining this with Eq. (4), the strong line condition becomes

$$S_j P y / \pi \gamma_j \gg 1. \tag{14}$$

The second condition pertains to nonoverlapping lines, and the motivation for this limit is to be able to employ the expression

$$A = \sum_j A_j, \tag{15}$$

where A_j is the total absorptance of a single line

$$A_j = \int_{-\infty}^{\infty} (1 - e^{-\kappa_{\omega j} y})\, d(\omega - \omega_j), \tag{16}$$

with the integration being performed over the individual lines. Equation (15) is, of course, applicable only if the integrands in Eq. (16) do not overlap, since Eq. (15) constitutes simply a summation of individual line absorptances. What is required, then, is that the integrand in Eq. (16) approach zero for $\omega - \omega_j = O(d)$, where d is the line spacing. With reference to Eq. (1), the nonoverlapping line limit will be satisfied providing

$$(S_j P y / \pi)[\gamma_j / (\gamma_j^2 + d^2)] \ll 1. \tag{17}$$

At this point, it should be noted that if we were to allow $\gamma_j \geq O(d)$, then Eq. (17) would yield

$$S_j P y / \pi \gamma_j \ll 1,$$

and this is a direct contradiction to the strong line condition of Eq. (14). Hence, to avoid this contradiction it is necessary to require that $\gamma_j \ll d$. The conditions which must be satisfied in order to achieve nonoverlapping lines are thus

$$\gamma_j / d \ll 1, \qquad S_j P y \gamma_j / \pi d^2 \ll 1, \tag{18}$$

where the second condition follows from Eq. (17). The above conditions, together with Eq. (14), describe the strong nonoverlapping line limit. The application of these three conditions in deriving this limit will be illustrated in the following subsection.

C. ELSASSER MODEL

The simplest band model that accounts for line structure is the Elsasser model, for which equally spaced lines of equal intensity and equal half-width are assumed. A portion of such a band is illustrated in Fig. 3, where the

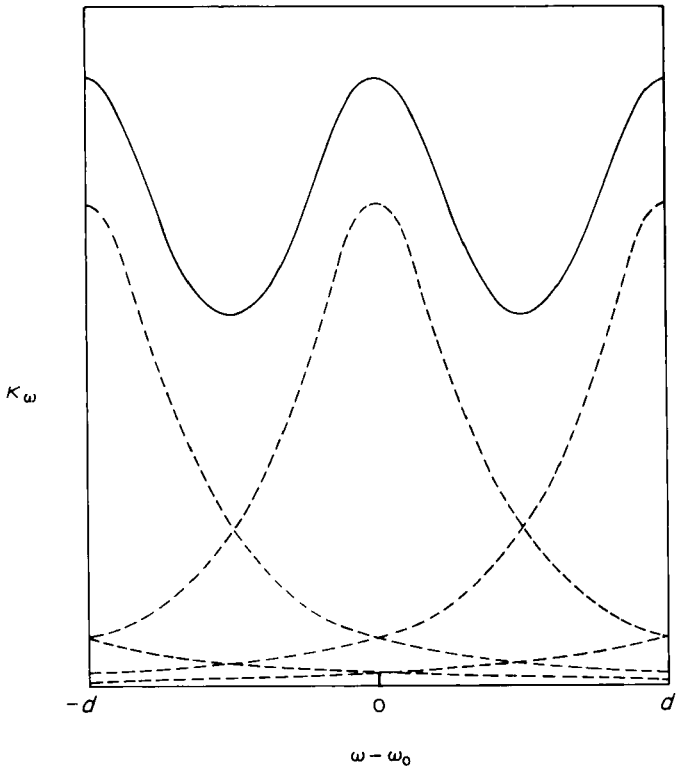

FIG. 3. Elsasser band model.

broken curves represent the absorption coefficient of the individual lines, while the solid curve is the absorption coefficient as given by Eq. (8), and this may be rephrased as

$$\frac{\kappa_\omega}{P} = \frac{S_j \gamma}{\pi} \sum_{j=0}^{\infty} \frac{1}{\gamma^2 + (\omega - \omega_0 \pm jd)^2} . \tag{19}$$

The subscript j has been dropped from γ_j in accord with the previous assumption, but it is retained in S_j, even though S_j is independent of j, in order to denote that this is a line intensity. Carrying the summation to infinity does

not preclude restriction to a finite band width (finite number of lines), but is merely consistent with the earlier assumption of a large number of lines. The above series may be expressed in closed form as [6]

$$\frac{\kappa_\omega}{P} = \frac{S_j}{d}\left[\frac{\sinh(\pi\beta/2)}{\cosh(\pi\beta/2) - \cos(\pi z/2)}\right], \tag{20}$$

where

$$\beta = 4\gamma/d, \qquad z = 4(\omega - \omega_0)/d.$$

The quantity β is a particularly significant parameter, since it represents the role of line structure. Recalling that $\gamma \sim P$, the limit of large pressure correspond to $\beta \to \infty$. This is the limit for which line structure is smeared out, and Eq. (20) reduces to

$$\kappa_\omega/P = S_j/d. \tag{21}$$

The ratio S_j/d also has an alternate interpretation. If an average absorption coefficient is defined over a line spacing as

$$\bar{\kappa}_\omega/P = (1/d)\int_{-d/2}^{d/2} (\kappa_\omega/P)\, d(\omega - \omega_j),$$

it follows from Eq. (20) that $\bar{\kappa}_\omega/P = S_j/d$.

The wave number width of the total band will be denoted by A_0, and letting n be the number of lines in the band, then $A_0 = nd$. Furthermore

$$S = \sum_j S_j = nS_j,$$

and the total absorptance of the Elsasser band follows from Eqs. (11) and (20) to be

$$A = \frac{A_0}{2}\int_0^2 \left\{1 - \exp\left[-\frac{u\sinh(\pi\beta/2)}{\cosh(\pi\beta/2) - \cos(\pi z/2)}\right]\right\} dz, \tag{22}$$

where u is a dimensionless pressure path length defined by

$$u = SPy/A_0.$$

Equation (22) has a form that is characteristic of all band models, namely, that the total absorptance may be expressed as

$$A = A_0\bar{A}(u, \beta), \tag{23}$$

where $A(u, \beta)$ is a dimensionless function. Recall from the previous discussion that pressure enters into the band absorptance in two ways, both through the pressure path length and a line structure effect. This dual role is clearly illustrated by Eq. (23), since u is a dimensionless pressure path length, while β is a line structure parameter.

Consider now limiting forms of the total band absorptance. The linear limit, applicable for $u \ll 1$, readily follows from Eq. (22) to be

$$\bar{A} = u, \qquad u \ll 1, \tag{24}$$

and this is consistent with Eq. (13). Note once again that line structure plays no role in the limit of small path lengths. In the large path length limit, $u \gg 1$, and Eq. (22) yields

$$\bar{A} = 1, \qquad u \gg 1. \tag{25}$$

Physically, of course, this represents total absorption within the finite-width band. It should be emphasized, however, that more realistic band models yield considerably different results, as will be illustrated in the next subsection.

A third limit corresponds to strong nonoverlapping lines, and following Penner [5] or Goody [6], Eq. (22) may be reduced to

$$\bar{A} = \operatorname{erf}(\tfrac{1}{2}\sqrt{\pi u \beta}/2), \tag{26}$$

subject to certain constraints. As discussed by Penner [5], these consist of $\beta \ll 1$ and $u/\beta \gg 1$. With reference to Eqs. (14) and (18), the remaining requirement for the strong nonoverlapping line limit is $\beta u \ll 1$, for which Eq. (26) yields

$$\bar{A} = \sqrt{\beta u}, \qquad \beta \ll 1, \quad u/\beta \gg 1, \quad \beta u \ll 1. \tag{27}$$

This is also referred to as the square-root limit.

A final limiting form of Eq. (22) is that for which line structure is smeared out, and letting $\beta \to \infty$, then

$$\bar{A} = 1 - e^{-u}, \qquad \beta \gg 1. \tag{28}$$

As should be expected, this is simply Beer's law.

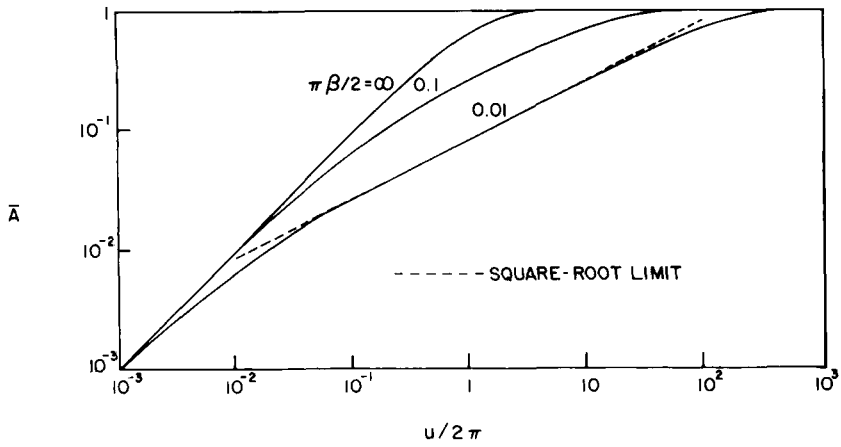

FIG. 4. Total band absorptance for Elsasser model.

The Elsasser band absorptance is illustrated in Fig. 4, and the various limiting forms are clearly evident. For $u \ll 1$, the linear limit, $\bar{A} = u$, is obtained, with the band absorptance being independent of line structure. The three constraints on the square-root limit are also apparent. This limit requires $\beta \ll 1$, but it still departs from the complete solution for either large or small u. The departure for small u denotes a violation of the requirement that $u/\beta \gg 1$, such that the strong line condition is no longer satisfied. For large u, the condition $\beta u \ll 1$ is not fulfilled, and Eq. (15) is no longer applicable. The present large path length limit, $\bar{A} = 1$, simply denotes total absorption within the band, and this is a consequence of the Elsasser model having a prescribed finite width. For a more realistic band model, as described in the following subsection, the total band absorptance will asymptotically approach a function of u rather than unity.

D. RIGID-ROTOR, HARMONIC-OSCILLATOR MODEL

Assuming the molecular model of a rigid rotor and harmonic oscillator, the distribution of line intensities is given by Eq. (5), while the line spacing corresponds to Eq. (7). Lorentz line shapes will again be assumed. In contrast to the Elsasser model, there is no defined bandwidth, since the line intensities approach zero asymptotically in the band wings. Thus, the bandwidth parameter A_0 will not correspond to a simple specified width, but instead will arise as an effective width resulting from the line intensity distribution of Eq. (5). No attempt at a complete formulation of the total band absorptance will be made; however, the limiting expressions will be presented. Since the linear limit is completely general, then Eq. (24) is applicable to the present band model.

Considering the large path length limit ($u \gg 1$), it will be convenient to initially assume a high pressure such that line structure is smeared out, which corresponds to the limit $\beta \to \infty$. Thus, in accord with Eq. (21), and upon combining Eqs. (5), (7), and (9), the spectral band absorptance is described by

$$\alpha_\omega = 1 - \exp(-u\xi e^{-\xi^2}) \tag{29}$$

where again $u = SPy/A_0$, while

$$\xi = (\omega - \omega_0)/A_0, \tag{30}$$

$$A_0 = \sqrt{4kBT/hc}.$$

Furthermore, since the band is symmetric, and with $\bar{A} = A/A_0$, then

$$\bar{A} = 2\int_0^\infty \alpha_\omega(\xi)\, d\xi. \tag{31}$$

Combination of Eqs. (29) and (31) thus describes the total band absorptance in the limit as $\beta \to \infty$, and numerical results are given by Penner [5]. Concerning an asymptotic expression for large u, one procedure is to combine Eqs. (29) and (31) and perform an asymptotic expansion. A physically more useful method, however, with reference to the inclusion of line structure, follows that employed by Edwards and Menard [7]. Upon defining

$$\xi_1 = \sqrt{\ln u},$$

Eq. (31) may be written as

$$\bar{A} = 2\Gamma_1 + 2\Gamma_2, \tag{32}$$

where

$$\Gamma_1 = \int_0^{\xi_1} [1 - \exp(-u\xi e^{-\xi^2})]\, d\xi,$$

$$\Gamma_2 = \int_{\xi_1}^{\infty} [1 - \exp(-u\xi e^{-\xi^2})]\, d\xi.$$

It may readily be shown that for $u \gg 1$

$$\Gamma_1 \to \sqrt{\ln u}, \tag{33a}$$

$$\Gamma_2 < \tfrac{1}{2}. \tag{33b}$$

Thus, the large path length limit follows to be

$$\bar{A} = 2\sqrt{\ln u}, \qquad u \gg 1. \tag{34}$$

While Eq. (34) has been derived subject to the condition $\beta \to \infty$, it is easily shown that this restriction may be removed. With reference to Fig. 5,

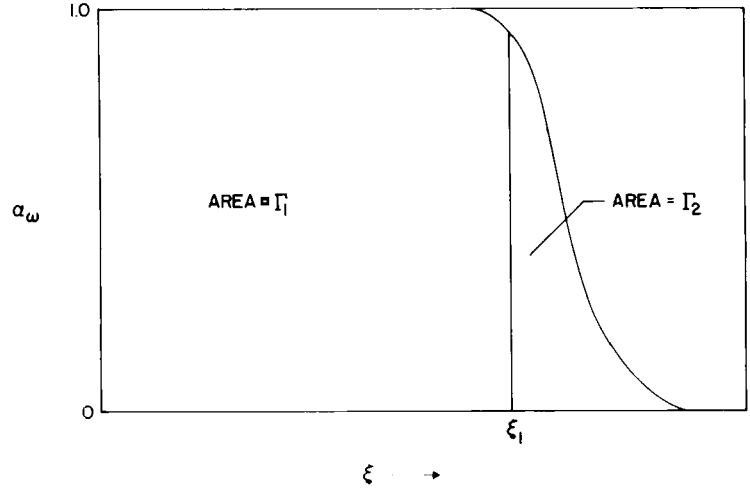

FIG. 5. Spectral band absorptance for large path lengths.

Γ_1 denotes the area of the saturated portion of the band, and the inclusion of line structure will not alter Eq. (33a) as a proper asymptotic limit. Thus, only Γ_2 will be affected. Again with reference to Fig. 5, if the region $\xi > \xi_1$ is considered to consist of a series of Elsasser bands, it follows that the inclusion of line structure will result in a decrease in Γ_2, and Eq. (33b) is again valid. Equation (34) therefore constitutes the asymptotic limit for the total band absorptance regardless of the value the line structure parameter β.

The third limit is the square-root limit, and recall that this corresponds to strong nonoverlapping lines. For strong lines, the Lorentz line profile, Eq. (1), may be expressed by [6]

$$\kappa_{\omega j}/P = S_j\gamma_j/(\omega - \omega_j)^2,$$

and upon substituting this into Eq. (16), we have

$$A_j = 2(S_j\gamma_j Py)^{1/2}.$$

In turn, from Eq. (15),

$$A = 2\sum_{j=0}^{\infty} A_j = 4\sum_{j=0}^{\infty}(S_j\gamma_j Py)^{1/2} = 4\sqrt{\gamma Py}\sum_{j=0}^{\infty}\sqrt{S_j},$$

where γ is a rotationally averaged mean line width defined by

$$\sqrt{\gamma} = \sum_{j=0}^{\infty}\sqrt{\gamma_j S_j}\Big/\sum_{j=0}^{\infty}\sqrt{S_j}. \tag{35}$$

Again employing the assumption of a large number of lines, then

$$A = 4\sqrt{\gamma Py}\int_0^{\infty}\sqrt{S_j}\,dj,$$

and upon combining this with Eq. (5), and noting from Eq. (7) that $d = 2B$, it follows that

$$A = 2^{3/4}\Gamma(3/4)[SPyA_0(4\gamma/d)]^{1/2}. \tag{36}$$

At this point it should again be emphasized that summation over vibrational quantum number has not been taken into account. While this has no direct bearing on the linear and large path length limits, since the band intensity S already denotes a summation over vibrational quantum number, it does affect the interpretation of the mean line width. Equation (36) is true only when all transitions have the same lower vibrational state. Upon letting v be the quantum number of the lower vibrational state, then Eq. (36) should be recast as

$$A_v = 2^{3/4}\Gamma(3/4)[S_vPyA_0(4\gamma/d)]^{1/2}, \tag{37}$$

where S_v represents the distribution of intensity with vibrational quantum

number, such that $S = \sum_{v=0}^{\infty} S_v$. It has been assumed in Eq. (37) that the rotationally averaged line width γ is independent of vibrational quantum number v, and this has been confirmed by Yamamato *et al.* [4] for CO_2.

Following Edwards and Menard [8], and Edwards [9], it will further be assumed that rotational lines resulting from different vibrational levels do not overlap, and the total band absorptance may thus be written as

$$A = \sum_{v=0}^{\infty} A_v. \tag{38}$$

From Eq. (37), it follows that a vibrationally averaged mean line width may be defined as [8, 9]

$$\bar{\gamma} = \gamma \left(\sum_{v=0}^{\infty} \sqrt{S_v/S} \right)^2. \tag{39}$$

Thus, upon letting $\beta = 4\bar{\gamma}/d$, the square-root limit follows from Eqs. (37) and (38) to be

$$A = 2.06\sqrt{\beta u}, \qquad \beta \ll 1, \quad u/\beta \gg 1, \quad \beta u \ll 1. \tag{40}$$

At sufficiently low temperatures, for which only the vibrational ground state is populated, Eq. (39) will reduce to $\bar{\gamma} = \gamma$. As temperature increases, however, the summation in Eq. (39) will become a significant function of temperature, and the temperature dependence of $\bar{\gamma}$ may differ substantially from that of γ. To give an illustration, consider the 4.3 μ fundamental band of CO_2. Employing the $\gamma_J(T)$ results of Yamamoto *et al.* [4] in Eq. (35), the temperature variation of $\gamma(T)$ may be expressed by

$$\gamma(T) = \gamma(T_0)(T/T_0)^{-2/3}, \tag{41}$$

and for temperatures of roughly 300°K and lower, this should adequately describe $\bar{\gamma}(T)$. Edwards and Menard [8], on the other hand, have found an average temperature dependence for the range 300°K to 1390°K of

$$\bar{\gamma} = \bar{\gamma}(T_0)(T/T_0)^{1/2}. \tag{42}$$

The discrepancy between Eqs. (41) and (42) implies a rapid change in the temperature dependence of $\bar{\gamma}$ as temperature is increased.

The primary utility of the present molecular model of a rigid rotor and harmonic oscillator has been to illustrate limiting solutions of the total band absorptance for a semirealistic molecular model. One important conclusion is that line structure appears only in the square-root limit, and thus this limit has been employed to describe the mean line width as defined by Eqs. (35) and (39).

E. BAND ABSORPTANCE CORRELATIONS

While the preceding subsection dealt with limiting forms of the total band absorptance, it is necessary to have at hand an expression for $\bar{A}(u, \beta)$ which is applicable for all values of u and β. Several such expressions are available, and they are all based upon constructing an expression for $\bar{A}(u, \beta)$ which satisfies certain limiting conditions. For present purposes, the same limits are employed by Edwards and Menard [7] will be used, and these are

$$\bar{A} = u, \qquad u \ll 1, \tag{43a}$$

$$\bar{A} = 2\sqrt{\beta u}, \qquad \beta \ll 1, \quad u/\beta \gg 1, \quad \beta u \ll 1, \tag{43b}$$

$$\bar{A} = 1 + \ln u, \qquad u \gg 1. \tag{43c}$$

While Edwards and Menard interpreted the above in terms of a reordered exponential distribution of line intensities, a slightly different explanation will be given here. The first limit, Eq. (43a), is simply the general linear limit, while Eq. (43b) is essentially Eq. (40) for the rigid rotor and harmonic oscillator. The third limit is of a different form than that of Eq. (34) for the rigid rotor and harmonic oscillator. For moderately large values of u the two expressions are in reasonable numerical agreement, but for increasingly large u they begin to diverge. The rational for using Eq. (43c) is twofold. First, Edwards and Menard have shown that a logarithmic limit is attained for nonrigid rather than rigid rotation, and second, existing empirical correlations are of the same form as Eq. (43c).

The first band absorptance correlation to satisfy all three limits is that proposed by Edwards and Menard [7], and this consists of an analytic interpolation of the form

$$\begin{aligned}
\beta \le 1: \quad & \bar{A} = u, && \bar{A} < \beta, \\
& \bar{A} = 2\sqrt{u\beta} - \beta, && \beta < \bar{A} < (2 - \beta), \\
& \bar{A} = \ln(\beta u) + (2 - \beta), && \bar{A} > (2 - \beta). \\
\beta > 1: \quad & \bar{A} = u, && \bar{A} < 1, \\
& \bar{A} = 1 + \ln u, && \bar{A} > 1.
\end{aligned}$$

By comparing the above correlation with experimental data over a large range of pressure and temperature, Edwards and co-workers have empirically determined the necessary correlation quantities $S(T)$, $A_0(T)$, and $\beta(T, P_e)$, where P_e is the effective broadening pressure, for the important bands of CO, CO_2, H_2O, and CH_4. In determining $\beta(T, P_e)$, both self-broadening and nitrogen broadening were considered. These results are summarized by

Edwards *et al.* [10].[3] In particular, for the CO fundamental and the 6.3 μ fundamental of H_2O, it was found that

$$A_0 = 1.91(kBT/hc)^{1/2}, \tag{44}$$

and this is in excellent agreement with Eq. (30).

A continuous band absorptance correlation has been proposed by Tien and Lowder [11], and this is of the form

$$\bar{A} = \ln\left\{uf(\beta)\left[\frac{u+2}{u+2f(\beta)}\right] + 1\right\}, \tag{45}$$

where

$$f(\beta) = 2.94[1 - \exp(-2.60\beta)].$$

The choice of Eq. (45) was based on the specification of five conditions, and the form of $f(\beta)$ was chosen so as to give agreement with the correlation of Edwards and Menard. The square-root limit, Eq. (43b), was not, however, one of the specified conditions, and Eq. (45) does not satisfy this requirement.

A continuous correlation for $\bar{A}(u, \beta)$ has also been proposed by Goody and Belton [12], and in terms of the present nomenclature this may be written as

$$\bar{A} = 2\ln\{1 + [\sqrt{\beta}u/(u + 4\beta)^{1/2}]\}. \tag{46}$$

Although this correlation satisfies the three limits as specified by Eqs. (43), there appears to be one shortcoming. Upon letting $\beta \to \infty$, which corresponds to smeared out line structure, Eq. (46) reduces to

$$\bar{A} = 2\ln(1 + u/2),$$

and for large u this yields $2 \ln u$. The linear and logarithmic limits are, however, independent of line structure, such that Eqs. (43a) and (43c) should be achieved irrespective of whether one does or does not let $\beta \to \infty$. Thus, it would appear that the use of Eq. (46) should be restricted to relatively small values of β.

A fairly simple correlation, which does satisfy the above constraint, in addition to all of Eqs. (43), is of the form

$$\bar{A} = 2\ln\{1 + u/[2 + u^{1/2}(1 + 1/\beta)^{1/2}]\} \tag{47}$$

Preliminary comparisons indicate that Eq. (47) does an excellent job of correlating band absorptance data for CO_2.

[3] The correlation quantities C_1 and C_3 of Edwards *et al.* [10] correspond to the present nomenclature through $A_0 = C_3$ and $S = C_1/RT$, where R is the gas constant.

III. Basic Equations

In this section the basic equations will be developed which describe the radiative flux vector within an infrared absorbing-emitting gas. Knowledge of the radiative flux vector, $\mathbf{q}_R$, is of course necessary in any conservation of energy analysis, since the energy equation for a radiatively participating gas is of the form

$$\rho c_P \frac{DT}{Dt} = \text{div}\,(\lambda\,\text{grad}\,T) + \frac{DP}{Dt} - \text{div}\,\mathbf{q}_R \tag{48}$$

where ρ, c_P, and λ denote density, specific heat at constant pressure, and thermal conductivity, respectively. With reference to Eq. (48), it is necessary to have a description of $\mathbf{q}_R$ in terms of temperature within the gas, and this is precisely the purpose of the present section.

Strictly speaking, Eq. (48) applies only to a molecular continuum under the condition of local thermodynamic equilibrium (LTE). The energy equation may, however, be extended to radiatively induced departures from LTE, and such an extension is particularly appropriate to infrared transfer. This simply requires replacing $\mathbf{q}_R$ in Eq. (48) by its non-LTE counterpart. At the same time, however, it must be assumed that any departure from equilibrium population distributions will not significantly change the internal energy and transport properties from their equilibrium values. As discussed by Zel'dovich and Raizer [13], this assumption is justified providing the characteristic vibrational temperature $h\nu/k$ (where ν is a band frequency) is greater than the vibrational temperature. Thus, the temperature appearing in Eq. (48) will be regarded as the kinetic temperature.

Radiatively induced departures from LTE occur when the gas molecules either emit or absorb radiative energy at such a high rate that collisional equilibration cannot maintain a state of equilibrium between translational, vibrational, and rotational energies. Rotational energies, however, require only a few collisions to attain equilibrium, and significant departures from LTE will first involve solely vibrational energies. It may further be assumed that even for non-LTE, vibrational energy levels are populated according to the Boltzmann distribution. However, this distribution does not correspond to the local kinetic temperature, but instead is governed by a separate vibrational temperature.

In summary, the purpose of the present section is to develop an expression for the infrared radiative flux vector, and to allow in this development radiatively induced departures from vibrational equilibrium. In describing the radiative flux, the kernel function will be expressed in terms of the total band absorptance. This approach is analogous to the LTE formulations of

Goody [6], Gille and Goody [14], and Wang [15, 16], for which the kernel function is expressed in terms of a modified gas emissivity. For present purposes, the physical model and coordinate system is that illustrated in Fig. 6. This consists of a gas bounded by two plates whose surfaces are assumed to be gray and to emit and reflect in a diffuse manner.

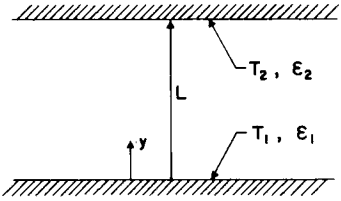

FIG. 6. Physical model and coordinate system.

A. RATE EQUATIONS AND RELAXATION TIME

In considering radiatively induced vibrational nonequilibrium (non-LTE), it will be necessary to have information pertaining to vibrational rate equations and the vibrational relaxation time. The rate of change of vibrational energy of a system of oscillators may be expressed as

$$dE_v/dt = (dE_v/dt)_{coll} + (dE_v/dt)_{rad}, \tag{49}$$

where the terms on the right represent contributions due to collisional and radiative processes, respectively, and E_v denotes the vibrational energy per unit volume. Furthermore,

$$-\operatorname{div} \mathbf{q}_R = (dE_v/dt)_{rad}, \tag{50}$$

where, due to the small separation of rotational levels, the contribution of rotational energy has been neglected.

The divergence of the radiative flux is also related to the specific intensity I_ω, and for the present one-dimensional problem this is given by the expression

$$\operatorname{div} \mathbf{q}_R = \int_0^\infty (dq_{R\omega}/dy)\, d\omega = \int_0^\infty \int_0^{4\pi} (dI_\omega/ds)\, d\Omega\, d\omega, \tag{51}$$

where Ω is the solid angle and s a coordinate measured along the pencil of rays. Combination of Eqs. (49) through (51) thus yields

$$dE_v/dt = (dE_v/dt)_{coll} - \int_0^\infty \int_0^{4\pi} (dI_\omega/ds)\, d\Omega\, d\omega. \tag{52}$$

This relation clearly illustrates the influence of radiation, through the second term on the right side, upon vibrational energy.

The vibrational relaxation of a system of oscillators undergoing collisional relaxation may be described in terms of the Bethe-Teller relation

$$dE_v/dt = (E_v^* - E_v)/\eta \tag{53}$$

where E_v^* represents the equilibrium value of vibrational energy, and η is the vibrational relaxation time. A simple derivation of Eq. (53) is given by Zel'dovich and Raizer [13], and by Vincenti and Kruger [17], while anharmonic effects have been investigated by Bazley and Montroll [18], and Northup and Hsu [19] have discussed the extension to multiple quantum transitions. Goody [6], however, suggests accepting Eq. (53) simply as an experimental rather than a theoretical expression.

Information on collisional relaxation times is available only for a limited number of gases [20–26]. For diatomic gases, an empirical relation is given by Millikan and White [22] as

$$P\eta = \exp[A(T^{-1/3} - 0.015\mu^{1/4}) - 18.42]. \tag{54}$$

Values of A and μ for carbon monoxide are $A = 1.75$ and $\mu = 14$. Note that η decreases rapidly with increasing temperature.

B. EQUATION OF TRANSFER

The formulation of the equation of transfer for vibrational nonequilibrium is treated in detail by Goody [6], Gilles [27], Gilles and Vincenti [28], and Tiwari [29], and the complete derivation will not be repeated here. The formulation is based upon the assumption of a harmonic oscillator as well as two-level transitions between vibrational states which restricts the analysis to fundamental bands. However, under conditions for which the assumption of LTE is not justified, combination and overtone bands do not contribute significantly to the radiative transfer process [29]. When the assumption of LTE is valid, the equation of transfer reduces directly to the conventional macroscopic equation, and the restrictions to harmonic oscillation and two-level transitions no longer apply.

Following Goody [6], the equation of transfer may be written as

$$dI_\omega/ds = \kappa_\omega(J_\omega - I_\omega), \tag{55}$$

where the source function, J_ω, is expressed by

$$J_\omega = B_\omega E_v/E_v^* \tag{56}$$

and B_ω denotes blackbody intensity. For $E_v = E_v^*$, this of course reduces to the equation of transfer for LTE.

The important point concerning Eq. (55) is that κ_ω is the *equilibrium* absorption coefficient, i.e., it corresponds to the local kinetic temperature. An explanation of this is given by Goody [6]. More recently, Gilles [27] and Gilles and Vincenti [28] have pointed out that this is strictly a low temperature approximation. At elevated temperatures, however, collisional relaxation is very rapid, and it is doubtful that physical situations exist at elevated temperatures for which non-LTE effects would be important.

For illustrative purposes, it will be convenient to temporarily restrict attention to diatomic gases, such that only a single fundamental band is considered. Under steady-state conditions, combination of Eqs. (52), (53), and (55) yields

$$\left(\frac{E_\nu}{E_\nu{}^*}\right)\left(\frac{E_\nu{}^*}{\eta} + \int_0^{4\pi} d\Omega \int_0^\infty \kappa_\omega B_\omega \, d\omega\right) = \frac{E_\nu{}^*}{\eta} + \int_0^{4\pi} d\Omega \int_0^\infty \kappa_\omega I_\omega \, d\omega.$$

Further, upon defining a time constant

$$\eta_r = E_\nu{}^* \Big/ \int_0^{4\pi} d\Omega \int_0^\infty \kappa_\omega B_\omega \, d\omega, \tag{57}$$

the source function, J_ω, may now be written as

$$J_\omega = B_\omega[(\eta_r + \eta X)/(\eta_r + \eta)], \tag{58}$$

where

$$X = \int_0^{4\pi} d\Omega \int_0^\infty \kappa_\omega I_\omega \, d\omega \Big/ \int_0^{4\pi} d\Omega \int_0^\infty \kappa_\omega B_\omega \, d\omega. \tag{59}$$

The time constant η_r is the radiative lifetime for vibrational states, and by assuming that, within the narrow band, B_ω may be taken as independent of wave number, then it may be shown that [6]

$$1/\eta_r = 8\pi c \omega_0{}^2 (P/n) S(T), \tag{60}$$

where n is the molecular number density, ω_0 is the wave number at the band center, and $S(T)$ is the band intensity. Employing the perfect gas law $P = nkT$, and since $S(T) \sim T$ for a fundamental band, it readily follows that the radiative lifetime is independent of both temperature and pressure.

Now, since B_ω and J_ω are isotropic and slowly varying functions of wave number within the band, then upon combining Eqs. (51), (55), and (58), the nonequilibrium source function may be expressed as

$$J_{\omega_0} = B_{\omega_0} + \tfrac{1}{2}(\eta/\eta_r)H, \tag{61}$$

where

$$H = -\int_0^\infty (dq_{R\omega}/dy) \, d\omega \Big/ 2\pi \int_0^\infty \kappa_\omega \, d\omega \tag{62}$$

and J_{ω_0} and B_{ω_0} denote quantities evaluated at the band center.

Since $J_{\omega_0} = B_{\omega_0}$ for LTE, Eq. (61) clearly illustrates that the degree of nonequilibrium is characterized by the parameter η/η_r. When η/η_r is small, the source function J_{ω_0} reduces to the blackbody intensity B_{ω_0}, and the assumption of LTE is justified. On the other hand, in the limit of large η/η_r the divergence of the radiative flux becomes zero [6]. This physically corresponds to the situation for which vibrational transitions are radiatively controlled, such that all photons absorbed by the gas will in turn be reemitted. There will thus be no net addition (or loss) of radiative energy to any gas element. For intermediate values of η/η_r, the divergence of the radiative flux will have a lower value than that corresponding to the condition of LTE. Consequently, the internal transfer of radiative energy within the gas will be reduced as the result of vibrational nonequilibrium. It is important to note from Eqs. (61) and (62) that, regardless of the magnitude of η/η_r, the assumption of LTE is always justified for the case of radiative equilibrium (i.e., $dq_R/dy = 0$). This conclusion, of course, applies only for the present restriction of a gas having a single band. The preceding analysis may, however, easily be extended to multiple band spectra.

C. RADIATIVE FLUX EQUATION

The equation of transfer, Eq. (55), may be integrated in the conventional manner so as to yield the expression for the spectral radiative flux, $q_{R\omega}$, with the result [30]

$$q_{R\omega} = 2B_{1\omega}E_3(\kappa_\omega y) - 2B_{2\omega}E_3[\kappa_\omega(L - y)] + 2\pi\left\{\int_0^y J_\omega(z)\kappa_\omega E_2[\kappa_\omega(y - z)]\,dz - \int_y^L J_\omega(z)\kappa_\omega E_2[\kappa_\omega(z - y)]\,dz\right\}, \tag{63}$$

where $B_{1\omega}$ and $B_{2\omega}$ are the surface radiosities, while $E_n(x)$ is the exponential integral

$$E_n(x) = \int_0^1 \mu^{n-2} e^{-x/\mu}\,d\mu.$$

The expressions for the surface radiosities are further given as [30]

$$B_{1\omega} = \epsilon_{1\omega}e_{1\omega} + 2(1 - \epsilon_{1\omega})\left[B_{2\omega}E_3(\kappa_\omega L) + \pi\int_0^L J_\omega(z)\kappa_\omega E_2(\kappa_\omega z)\,dz\right], \tag{64a}$$

$$B_{2\omega} = \epsilon_{2\omega}e_{2\omega} + 2(1 - \epsilon_{2\omega})\left[B_{1\omega}E_3(\kappa_\omega L) + \pi\int_0^L J_\omega(z)\kappa_\omega E_2(\kappa_\omega L - \kappa_\omega z)\,dz\right] \tag{64b}$$

The spectral absorption coefficient, κ_ω, has been taken to be independent

of temperature in Eqs. (63) and (64), and this effectively constitutes a linearization for small temperature differences. Note that for black surfaces $B_{1\omega} = e_{1\omega}$ and $B_{2\omega} = e_2$, whereas for LTE $J_\omega(y) = B_\omega(y) = e_\omega(y)/\pi$, with e_ω denoting Planck's function.

An often employed approximation in radiative transfer involves approximating the exponential integral $E_2(x)$ by an exponential function, such that $E_2(x) \simeq a \exp(-bx)$. Several combinations of a and b have been utilized, and for present purposes the approximation will be chosen as

$$E_2(x) \simeq \tfrac{3}{4} \exp(-3x/2), \tag{65a}$$

$$E_3(x) = -\int E_2(x)\, dx \simeq \tfrac{1}{2} \exp(-3x/2). \tag{65b}$$

The total radiative flux is further given by

$$q_R = \int_0^\infty q_{R\omega}\, d\omega. \tag{66}$$

In the subsequent discussion, attention will be directed solely to black bounding surfaces, although surface emittance effects will be discussed in Section IV. Thus, upon combining Eqs. (63), (65), and (66), the total radiative flux is given by

$$q_R = e_1 - e_2 + \tfrac{3}{2}\int_0^y [\pi J_{\omega_0}(z) - e_{1\omega_0}] \int_{\Delta\omega} \kappa_\omega \exp[-\tfrac{3}{2}\kappa_\omega(y - z)]\, d\omega\, dz$$
$$- \tfrac{3}{2}\int_y^L [\pi J_{\omega_0}(z) - e_{2\omega_0}] \int_{\Delta\omega} \kappa_\omega \exp[-\tfrac{3}{2}\kappa_\omega(z - y)]\, d\omega\, dz, \tag{67}$$

where $e = \sigma T^4$, with σ denoting the Stefan-Boltzmann constant, while $\Delta\omega$ indicates integration over the single band, again recalling that J_ω and e_ω are slowly varying functions of wave number over the single band.

The primary motivation for employing the exponential kernel approximation in the present formulation is that it allows the kernel function in Eq. (67) to be expressed in terms of the total band absorptance, since, from Eq. (11),

$$dA/dy = A'(y) = \int_{\Delta\omega} \kappa_\omega e^{-\kappa_\omega y}\, d\omega,$$

and this is the form of the kernel function in Eq. (67). Thus, letting

$$\xi = y/L, \qquad u_0 = SPL/A_0,$$

and employing the dimensionless band absorptance, $\bar{A}(u, \beta)$, as defined by

Eq. (23), the final form of the radiative flux equation is obtained by combining Eqs. (61), (62), and (67), as

$$q_R(\xi) = e_1 - e_2 + \tfrac{3}{2}A_0u_0\left\{\int_0^{\xi}[e_{\omega_0}(\xi') - e_{1\omega_0}]\bar{A}'[\tfrac{3}{2}u_0(\xi - \xi')]\,d\xi' - \int_{\xi}^{1}[e_{\omega_0}(\xi') - e_{2\omega_0}]\bar{A}'[\tfrac{3}{2}u_0(\xi' - \xi)\,d\xi'\right\} - \tfrac{3}{8}(\eta/\eta_r)\left\{\int_0^{\xi}(dq_R/d\xi')\bar{A}'[\tfrac{3}{2}u_0(\xi - \xi')]\,d\xi' - \int_{\xi}^{1}(dq_R/d\xi')\bar{A}'[\tfrac{3}{2}u_0(\xi' - \xi)]\,d\xi'\right\}, \tag{68}$$

where $\bar{A}'(u)$ denotes the derivative of $\bar{A}(u)$ with respect to u. Note that rotational line structure is included in Eq. (68) through the band absorptance. Furthermore, Eq. (68) describes the radiative flux for non-LTE in terms of the band absorptance for a gas in LTE. As previously discussed, following Eq. (56), this is appropriate since κ_ω is an equilibrium absorption coefficient even under non-LTE conditions.

The non-LTE influence in Eq. (68) is through the latter terms which are proportional to η/η_r, and which vanish in the limit of LTE (i.e., $\eta/\eta_r \to 0$). Although Eq. (68) applies only to a single band spectrum, for LTE the extension to multiple bands requires simply a summation of the important bands. This will be illustrated in Section IV.

Equation (68) possesses two convenient limiting forms. One is the conventional optically thin limit, while the other, the large path length limit, corresponds to $u_0 \gg 1$, and for infrared radiation this limit differs considerably from the optically thick or Rosseland limit. These two limiting forms of Eq. (68) will be treated in the following subsections.

D. Optically Thin Limit

As discussed by Sampson [31], the influence of non-LTE is most pronounced in the optically thin limit. Following Cess and Tiwari [32], this limit may be obtained by employing the linear limit for the band absorptance, Eq. (43a), since the optically thin limit corresponds to $u_0 \ll 1$. In the optically thin limit one is generally concerned with the divergence of the radiative flux [30], and upon differentiating Eq. (68) and employing the linear limit $\bar{A}'(u) = 1$, then the appropriate expression for $u_0 \ll 1$ becomes

$$(dq_R/d\xi)(1 + \tfrac{3}{4}\eta/\eta_r) = 3A_0u_0[e_{\omega_0}(\xi) - e_{1\omega_0}]. \tag{69}$$

An alternate approach to the optically thin limit is given in Cess *et al.* [33],

which does not make use of the exponential kernel approximation as given by Eq. (65), and it is shown that the factor of 3 appearing on the right side of Eq. (69) is replaced by 4 in the exact formulation. Further comments on the application of the exponential kernel approximation to infrared radiative transfer are given by Grief and Habib [34].

It should be observed that Eq. (69) is independent of rotational line structure, and this is consistent with the previous discussion on the invariance of $\bar{A}(u, \beta)$ with the line structure parameter β in the linear limit. The obvious simplification of the non-LTE influence in Eq. (69) should also be noted. As such, all optically thin analyses based on the assumption of LTE may be modified to include the effect of non-LTE simply by multiplying the divergence of the radiative flux by a constant involving the nonequilibrium parameter η/η_r.

E. LARGE PATH LENGTH LIMIT

Even though the optically thick (Rosseland) limit does not apply to vibration-rotation bands, since optically nonthick radiation will always occur in the band wings [33, 35], a large path length limit does exist and is achieved for $u_0 \gg 1$. Employing the method of steepest descent, it may be shown that the asymptotic form of the integrals appearing in Eq. (68) corresponds to the use of the logarithmic limit for the band absorptance, Eq. (43c). For illustrative purposes it will again be convenient to treat the divergence of the radiative flux vector. Thus, upon differentiating Eq. (68), performing a subsequent integration by parts, and utilizing the asymptotic formulation $\bar{A}(u) = \ln u$, one obtains

$$\frac{dq_R}{d\xi} = A_0 \int_0^1 \frac{de_{\omega_0}}{d\xi'} \frac{d\xi'}{\xi - \xi'} + \frac{1}{4u_0}\left(\frac{\eta}{\eta_r}\right) \int_0^1 \frac{dq_R}{d\xi'} \frac{d\xi'}{(\xi - \xi')^2} . \tag{70}$$

In arriving at Eq. (70), continuity of temperature has been assumed between the gas and the bounding surfaces. This is physically realistic, since $u_0 \gg 1$ implies that the central portion of the band is optically thick, which would insure temperature continuity. A more quantitative treatment of this point will be given in Section IV.

Since the large path length limit is an asymptotic limit for large u_0, it readily follows that the second term in Eq. (70) may be deleted, with the result that

$$\frac{dq_R}{d\xi} = A_0 \int_0^1 \frac{de_{\omega_0}}{d\xi'} \frac{d\xi'}{\xi - \xi'} , \tag{71}$$

and this is precisely the result for LTE. The vanishing of the non-LTE influence in this limit can further be illustrated by consideration of the

source function. As previously discussed, non-LTE effects enter solely through the source function, and from Eq. (61) this may be expressed as

$$J_{\omega_0}(\xi) = \frac{e_{\omega_0}(\xi)}{\pi} - \frac{1}{4\pi u_0 A_0}\left(\frac{\eta}{\eta_r}\right)\frac{dq_R}{d\xi} . \tag{72}$$

Employing Eq. (70) and taking the limit for large u_0 yields the result that $J_{\omega_0}(\xi) = e_{\omega_0}(\xi)/\pi$, which is the source function for LTE. In the large path length limit, optically thick radiation occurs in the central portion of the band, whereas the wing regions constitute a continuous transition from optically thick to optically thin radiation. Vibrational energy levels are evidently dominated by the optically thick portion of the spectrum, which suppresses non-LTE effects [31], such that this is the reason for the existence of LTE in the large path length limit.

A second significant simplification associated with Eq. (71) is that, as for the optically thin limit, the radiative transfer process is independent of line structure, since the line structure parameter does not appear in the equation. The reason for this is that the band absorptance becomes invariant with line structure for large u_0, and it is this asymptotic result for the band absorptance which yields Eq. (71). Note also that Eq. (71) is independent of both pressure and band intensity, and this will be discussed in more detail in Section IV.

IV. Radiative Transfer Analyses

This section presents several analyses illustrating the application of conservation of energy to the determination of the temperature profile within an infrared radiating gas, with primary emphasis upon the basic features of the radiative transfer process. For this purpose, simple illustrative physical models will be considered. Referring to the coordinate system of Fig. 6, Sections IV, A, IV, B, and IV, C consider the symmetric case for which $T_2 = T_1$ and there is a uniform heat source per unit volume, Q, within the gas. In Section IV, A, radiative transfer is assumed to be the sole mechanism of energy transfer through the gas, such that the energy equation constitutes a balance between the divergence of the radiative flux and the source Q. The same situation is considered in Section IV, B, except that molecular conduction is included as an energy transfer mechanism in order to illustrate the relative importance of conduction versus radiation within the gas. In both these sections restriction is made to LTE, while the influence of vibrational nonequilibrium is treated in Section IV, C. A brief discussion of radiative equilibrium is included in Section IV, D for purposes of illustrating a physical system which is not symmetric.

A. RADIATIVE TRANSFER

The first illustrative solution is that for which radiative transfer is the sole mechanism of energy transfer within the gas. The local temperature distribution is thus a consequence of the uniform heat source, Q, adding energy to the gas, which in turn is transferred through the gas to the bounding surfaces by radiative transfer. The two bounding surfaces are assumed to be at the same temperature, $T_2 = T_1$, LTE is assumed to prevail, and for the time being the bounding surfaces are taken to be black.

The energy equation for this situation is

$$dq_R/dy = Q,$$

and since the problem is symmetric, then

$$q_R = \tfrac{1}{2}QL(2\xi - 1), \tag{73}$$

where again $\xi = y/L$. For a single-band spectrum, the radiative flux is described by Eq. (68). As previously discussed, however, when LTE prevails Eq. (68) may be extended to multiple-band spectra by summing Eq. (68) over the individual bands. Furthermore, since small temperature differences have been assumed in arriving at Eq. (68), one may additionally employ the linearization

$$e_{\omega_i} - e_{1\omega_i} \simeq (de_{\omega_i}/dT)_{T_1}(T - T_1), \tag{74}$$

where the subscript i refers to the ith band, such that ω_i is the wave number location of the band. The subsequent extension of Eq. (68) thus yields

$$q_R = \tfrac{3}{2}\sum_{i=1}^{n}[A_{0i}u_{0i}(de_{\omega_i}/dT)_{T_1}]\left\{\int_0^{\xi}[T(\xi') - T_1]\bar{A}'[\tfrac{3}{2}u_{0i}(\xi - \xi')]\,d\xi' - \int_{\xi}^{1}[T(\xi') - T_1]\bar{A}'[\tfrac{3}{2}u_{0i}(\xi' - \xi)]\,d\xi'\right\}, \tag{75}$$

where n represents the number of vibration-rotation bands in the spectrum.

Upon combining Eqs. (73) and (75), conservation of energy is described by the integral equation

$$\xi - \tfrac{1}{2} = \tfrac{3}{2}\sum_{i=1}^{n}(H_i u_{0i}/H)\left\{\int_0^{\xi}\phi(\xi')\bar{A}'[\tfrac{3}{2}u_{0i}(\xi - \xi')]\,d\xi' - \int_{\xi}^{1}\phi(\xi')\bar{A}'[\tfrac{3}{2}u_{0i}(\xi' - \xi)]\,d\xi'\right\} \tag{76}$$

where

$$H_i = A_{0i}(de_{\omega_i}/dT)_{T_1}, \tag{77a}$$

$$H = \sum_{i=1}^{n} H_i, \tag{77b}$$

$$\phi = (T - T_1)/(QL/H). \tag{77c}$$

Employing the band absorptance correlation of Tien and Lowder [11], as expressed by Eq. (45), together with the empirical correlations for $S_i(T)$, $A_{oi}(T)$, and $\beta_i(T, P_e)$ given by Edwards *et al.* [10], Eq. (76) was solved numerically for CO_2, H_2O, and CH_4 [35]. These solutions were obtained by the method of undetermined parameters, in which a polynomial solution for $\phi(\xi)$ is assumed and the constants evaluated by satisfying the integral equation at equally spaced locations. Both quadratic and quartic solutions were utilized, with the two solutions yielding virtually identical results. Before discussing these results, however, it will be convenient to first investigate the optically thin and large path length solutions.

1. *Optically Thin Solution*

Following Section III, D, the optically thin solution to Eq. (76) is achieved by letting $\bar{A}'(u) = 1$, and it readily follows from Eq. (76) that

$$\phi = H \Big/ 3 \sum_{i=1}^{n} H_i u_{0i}$$

or

$$T - T_1 = Q \Big/ 3P \sum_{i=1}^{n} S_i(T_1)(de_{\omega_i}/dT)_{T_1}. \tag{78}$$

The fact that Eq. (78) predicts the gas temperature to be independent of location is consistent with the result that in optically thin limits each gas element exchanges radiation directly with the bounding surfaces, and this exchange is thus independent of position [30].

As discussed in Section III, D, Eq. (78) is independent of the line structure parameter β_i. One may further note that the optically thin limit is also independent of the bandwidth parameter A_{0i}. An indication of the relative ability of gases to transfer radiative energy is clearly given by Eq. (78), since a lower gas temperature implies a greater capability to transmit energy. Thus, the appropriate gas property that serves to measure the ability of a gas to radiative energy transfer is the quantity[4]

$$K = \sum_{i=1}^{n} S_i(T)(de_{\omega_i}/dT). \tag{79}$$

[4] The quantity K may be related to the linearized Planck mean coefficient, as defined by Goody [6], and Cogley *et al.* [36].

For example, CO_2 has a larger value of K than does H_2O, and thus CO_2 will have the greatest ability of transferring radiative energy in the optically thin limit.

2. *Large Path Length Limit*

As discussed in Section III, E, the large path length limit is achieved when $u_{0i} \gg 1$ for each band of importance, and this limit corresponds to employing $\bar{A}'(u) = 1/u$ in Eq. (76), with the result that

$$\xi - \tfrac{1}{2} = \int_0^1 \phi(\xi')\, d\xi'/(\xi - \xi'). \tag{80}$$

Aside from the obvious simplification in form in going from Eq. (76) to (80), there are other more striking consequences associated with Eq. (80). For example, of the three correlation quantities A_{0i}, β_i, and S_i, only A_{0i} appears in Eq. (80) through the definition of $\phi(\xi)$. The dependence upon this single correlation quantity in the large path length limit has also been illustrated by Edwards *et al.* [10] in dealing with laminar flow between parallel plates. The absence of the line structure parameter β_i has been discussed in Section III, E, while the invariance of the band absorptance S_i is physically logical, since the central portion of the band is saturated in the large path length limit, and consequently the radiative transfer process should not depend upon the total band area.

A further simplification associated with Eq. (80) is that the temperature profile within the gas is independent of pressure. This is not the case with respect to the general formulation, Eq. (76), for which pressure appears both in the dimensionless path length u_{0i} and in the line structure parameter β_i. This invariance of temperature profile with pressure can also be found from the results of Edwards *et al.* [10], and experimental confirmation has recently been presented by Schimmel *et al.* [37].

Equation (80) constitutes a singular integral equation with a Cauchy type kernel, for which the solution is [38]

$$\phi(\xi) = (1/\pi)[\xi(1 - \xi)]^{1/2} + C[\xi(1 - \xi)]^{-1/2},$$

where C is an arbitrary constant which arises since the solution of Eq. (80) is not unique. However, to satisfy the physical requirement of finite temperature everywhere within the gas, $C = 0$, and

$$\phi(\xi) = (1/\pi)[\xi(1 - \xi)]^{1/2}. \tag{81}$$

Note that this temperature profile yields the result that the gas temperature at a surface is equal to the surface temperature, and this absence of a temperature slip is characteristic of optically thick radiation [30]. As discussed

in Section III, E, this is a consequence of the fact that optically thick radiation is occurring in certain spectral regions. Optically nonthick radiation exists, however, in other spectral regions [33], with the result that Eq. (81) differs substantially from the temperature profile which would be predicted using a Rosseland type (or diffusion) equation.

Upon recasting Eq. (81) as

$$T - T_1 = (QL/\pi H)[\xi(1 - \xi)]^{1/2},$$

it is apparent that the gas property which measures the ability of a gas to transfer radiative energy in the large path length limit is

$$H = \sum_{i=1}^{n} A_{0i}(de_{\omega_i}/dT), \tag{82}$$

as opposed to the optically thin transport property K, defined by Eq. (79).

3. *Results*

For the sake of brevity, numerical solutions to Eq. (76) will be presented solely in terms of the centerline temperature, i.e., $T_c = T(\xi = 1/2)$. In the case of a single-band gas, the summation sign is removed in Eq. (76) and results may be expressed in terms of the single pair of parameters u_0 and β. This is illustrated by the solid curves in Fig. 7, and the results apply to any situation for which radiative transfer within the gas is the result of a single band. For small u_0 the results approach the optically thin limit as described

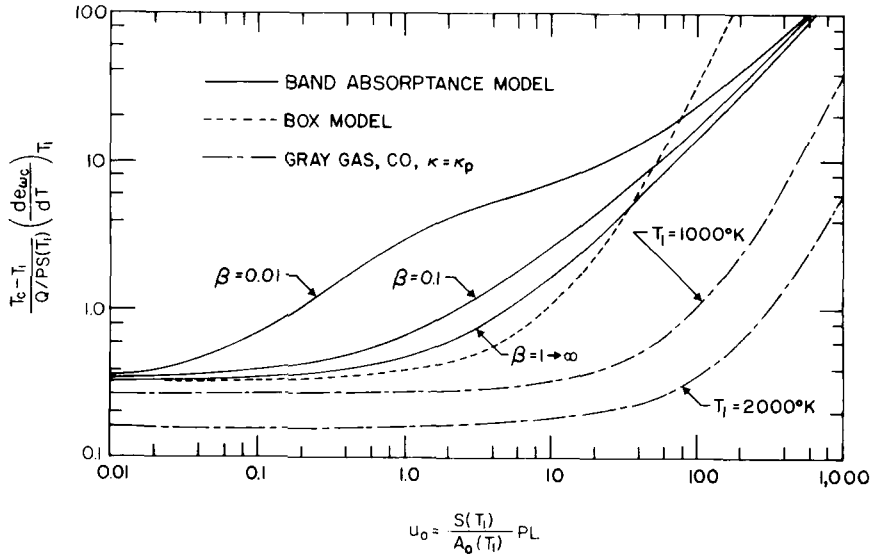

FIG. 7. Comparison of results for a single-band gas.

by Eq. (78). The maximum influence of the line structure parameter exists for intermediate values of u_0, while in the large path length limit the solution again becomes independent of β.

Also illustrated in Fig. 7 is a solution employing the box model, for which a constant absorption coefficient $\bar{\kappa}$ is assumed within a finite bandwidth $\Delta\omega$. The relation between this width and the bandwidth parameter A_0 was taken to be $\Delta\omega = (214/38)A_0$, which is appropriate for CO [33], and the value of the mean coefficient is in turn $\bar{\kappa} = SP/\Delta\omega$. Clearly, such a model does not account for line structure. Since the box model preserves the band intensity, it reduces to the correct optically thin limit, but a significant departure between the two solutions takes place for increasing u_0. This is easily explained on physical grounds. In the central portion of the band the box model underpredicts the value of the spectral absorption coefficient, and it thus will yield optically thin results for greater values of u_0 than will the solution employing the band absorptance. At large values of u_0 the box model overpredicts the centerline temperature due to the neglect of the band wings. For large path lengths the wing regions contribute primarily to radiative transfer. Since the box model neglects the wings, it underestimates the ability of the gas to transfer radiant energy for large u_0 values, and consequently it overpredicts the centerline temperature.

The inapplicability of the optically thick (or Rosseland) limit should again be emphasized. From the box model, it readily follows that $(T_c - T_1) \sim L^2$ for large u_0 [33], and this corresponds to optically thick radiation occurring throughout the finite width band. From the large path length solution of Eq. (81), however, $(T_c - T_1) \sim L$, such that the occurrence of nonthick radiation within the band wings significantly influences the nature of the radiative transfer process for large u_0.

Also shown in Fig. 7 are gray gas results [33], where, for lack of a more rational choice, the mean absorption coefficient has been chosen as the Planck mean coefficient, which is defined as

$$\kappa_P = (1/\sigma T^4)\int_0^\infty \kappa_\omega e_\omega(T)\, d\omega.$$

Specific comparisons are made for CO. It is quite obvious that the gray solution constitutes a rather large departure from reality.

With respect to multiple band spectra, dimensionless centerline temperatures for CO_2, H_2O, and CH_4, as obtained from Eq. (76), are illustrated in Figs 8 through 11. Since the abscissa variable is the pressure path length, the separate influence of pressure upon the centerline temperature is due solely to the alternation of the line structure of the bands due to pressure broadening. As the pressure is increased, the discrete line structure is eliminated, and, as illustrated in Figs. 8 through 11, pressure ceases to be a

separate parameter in the high pressure limit. This of course is analogous to the large β limit of Fig. 7.

In the large path length limit, the dimensionless centerline temperature follows from Eq. (81) to be

$$(T_c - T_1)/(QL/H) = 1/2\pi = 0.159. \tag{83}$$

Figures 8 through 11 consequently serve to illustrate the conditions under which the large path length limit constitutes a useful means of describing the radiative transfer process. Although these figures correspond to a specific physical problem, the limits of applicability of the large path length limit should be qualitatively indicative of other physical situations. Additional numerical results are given by Cess and Tiwari [35].

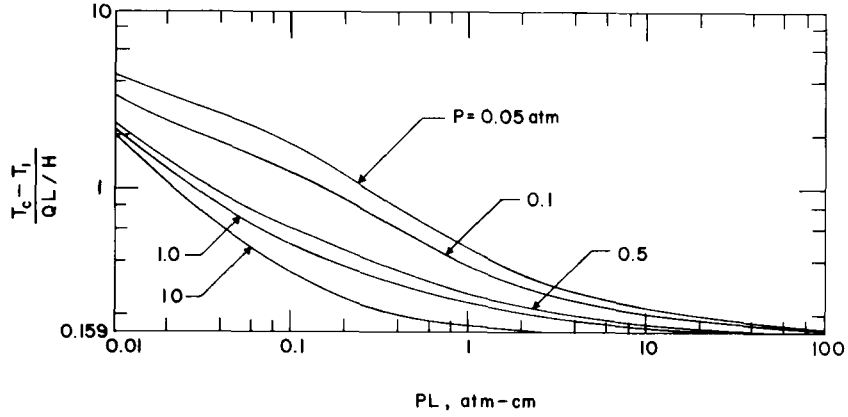

FIG. 8. Centerline temperature results for CO_2 with $T_1 = 300°K$.

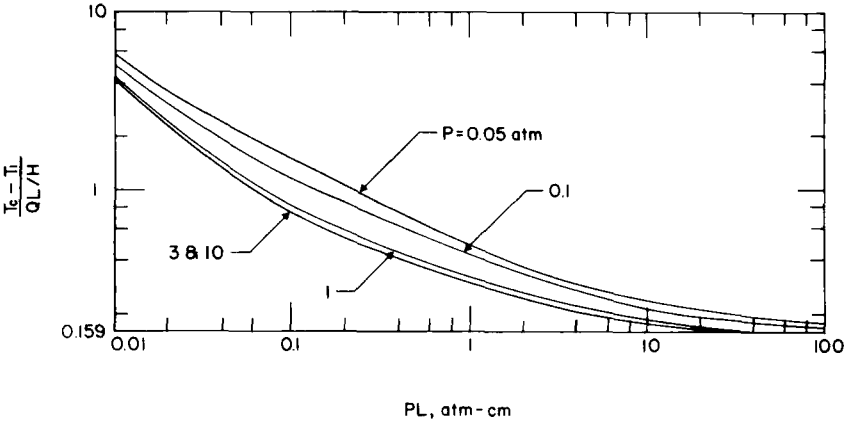

FIG. 9. Centerline temperature results for CO_2 with $T_1 = 1000°K$.

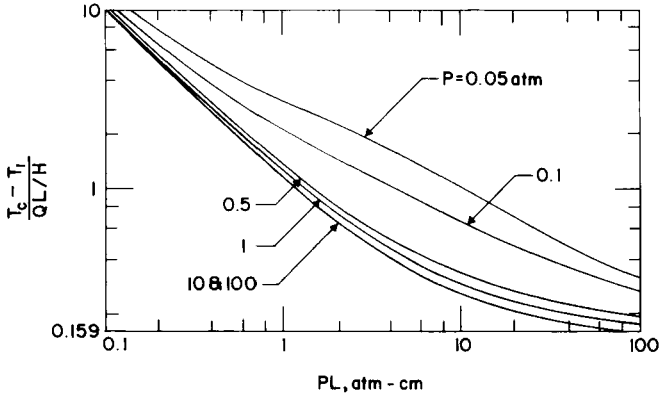

FIG. 10. Centerline temperature results for H_2O with $T_1 = 1000°K$.

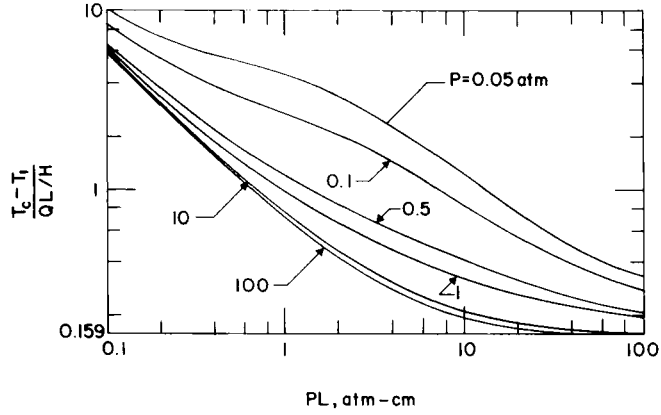

FIG. 11. Centerline temperature results for CH_4 with $T_1 = 1000°K$.

A comparison of the relative ability of various gases to transmit radiative energy may be obtained by comparing the dimensional quantity $(T_c - T_1)/QL$. This is shown in Fig. 12 for a temperature of 500°K and a pressure of 1 atm. Recall that a lower centerline temperature implies a greater ability of the gas to transmit radiative energy, and that in the optically thin limit the radiative transfer capability of a given gas is dependent upon the magnitude of K given by Eq. (79). For the four gases considered, CO_2 has the largest value of K, followed respectively by H_2O, CH_4, and CO. This is consistent

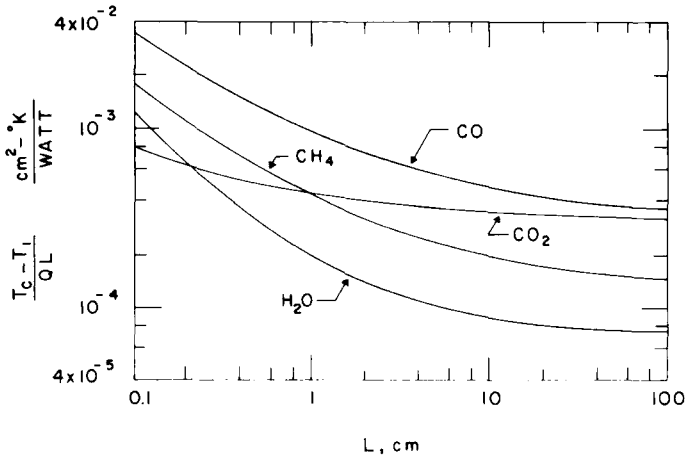

FIG. 12. Comparative results for $P = 1$ atm and $T_1 = 500°K$.

with the results shown in Fig. 12 for small path lengths, i.e., CO_2 has the lowest centerline temperature, etc. As the path length is increased, however, CO_2 undergoes a transition from the most capable to nearly the least capable transmitter of radiative energy, since CO_2 has a small relative value for H, as defined by Eq. (82), indicating that it is a poor radiator for large path lengths.

With respect to gases other than those considered here, the large path length property H may be evaluated solely from knowledge of the appropriate band locations and rotational constants by employing Eqs. (30) and (82). It should be emphasized that the large path length limit, as treated here, is not an exact asymptotic limit, since it makes use of the logarithmic asymptote for the band absorptance, which in itself is an approximate limiting expression.

4. *Effect of Surface Emittance*

The effect of nonblack surfaces upon infrared radiative transfer will now be investigated, utilizing the same physical model as previously considered. Restriction will, however, be made to single-band gases, so that this constitutes an extension of the results of Fig. 7. Both surfaces are assumed to have the same emittance, ϵ, and it is not necessary to postulate gray surfaces, since ϵ may be regarded as the spectral emittance at the wave number of the single band.

Following Tiwari and Cess [39], the combination of Eqs. (63) and (64), under the condition of LTE, yields

$$(\xi - \tfrac{1}{2})(2/3u_0) = \int_0^{\xi} \phi(\xi')\bar{A}'[(3u_0/2)(\xi - \xi')]\, d\xi' - \int_{\xi}^{1} \phi(\xi')\bar{A}'[(3u_0/2)(\xi' - \xi)]\, d\xi' + \int_0^1 \phi(\xi') \sum_{m=0}^{\infty} (1 - \epsilon)^{m+1}\{\bar{A}'[(3u_0/2)(\xi' + \xi + m)] - \bar{A}'[(3u_0/2)(\xi' - \xi + 1 + m)]\}\, d\xi' \tag{84}$$

as the appropriate energy equation. This of course reduces to the single band form of Eq. (76) for $\epsilon = 1$.

Numerical solutions of Eq. (84) are available [39], and the dimensionless centerline temperature is illustrated in Fig. 13 for $\beta = \infty$. As should be

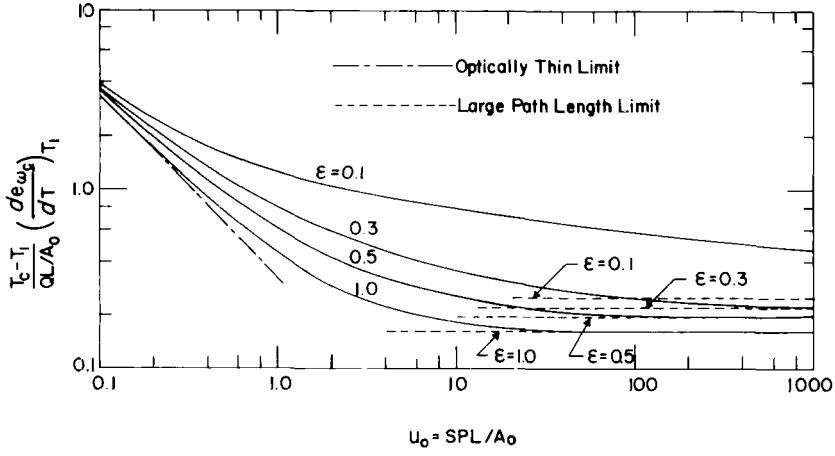

FIG. 13. Effect of surface emittance for a single band gas with $\beta = \infty$.

expected, a reduction in surface emittance gives rise to a higher centerline temperature, since a lower surface emittance corresponds to a reduction in the energy transfer capability between the gas and the surfaces.

The optically thin limit readily follows from Eq. (84) to be

$$\phi(\xi) = 1/3u_0,$$

and this coincides with the single-band form of Eq. (78) for black surfaces. The invariance of surface emittance upon gas temperature is also observed for a gray gas under optically thin conditions [40]. To explain this, recall

that under optically thin conditions the surface radiosity is evaluated as if the gas were completely transparent [30], and since this corresponds to an isothermal enclosure for the present problem, the surface radiosity is equal to blackbody radiation irrespective of the value of the surface emittance.

In the large path length limit, Eq. (84) reduces to

$$\xi - \tfrac{1}{2} = \int_0^1 \phi(\xi') \frac{d\xi'}{\xi - \xi'} + \int_0^1 \phi(\xi') \sum_{m=0}^{\infty} (1 - \epsilon)^{m+1} \left[\frac{1}{(\xi' + \xi + m)} - \frac{1}{(\xi' - \xi + 1 + m)} \right] d\xi'.$$

The solution to this equation is also illustrated in Fig. 13, and note that this limit does depend upon the surface emittance. On the other hand, for a gray gas or any gas with a nonvanishing absorption coefficient over the entire spectrum, the radiation in the optically thick (Rosseland) limit is independent of surface emittance [30, 41]. With reference to the present large path length solution, it is radiation occurring in the band wings which is neither optically thin nor optically thick that produces the influence of ϵ upon the temperature profile within the gas.

It may further be noted from Fig. 13 that as ϵ is decreased, the range of applicability of the limiting solutions is appreciably reduced. In particular, for $\epsilon = 0.1$ an extremely large value of u_0 would be required in order to approach the large u_0 limit.

B. RADIATION–CONDUCTION INTERACTION

With the exception of atmospheric applications, molecular conduction within a gas must be regarded as a possible energy transport mechanism, and, in fact, for small physical dimensions it will dominate radiative transfer. The purpose of this subsection is to investigate the relative importance of radiation versus conduction as energy transport mechanisms, and the physical model of Section IV, A is again employed for illustrative purposes.

From conservation of energy, the temperature profile within the gas is described by

$$\lambda \frac{d^2T}{dy^2} - \frac{dq_R}{dy} + Q = 0,$$

where λ is the thermal conductivity of the gas. Upon integrating this equation once, and noting that $dT/dy = 0$ and $q_R = 0$ for $y = L/2$, then

$$q_R = \lambda(dT/dy) + Q(y - L/2). \tag{85}$$

For a gas containing n vibration-rotation bands, the radiative flux is again described by Eq. (75), such that Eq. (85) yields the integrodifferential equation

$$\frac{d\theta}{d\xi} + \xi - \frac{1}{2} = \frac{3L}{2\lambda} \sum_{i=1}^{n} H_i u_{0i} \left\{ \int_0^{\xi} \theta(\xi') \bar{A}' \left[\frac{3u_{0i}}{2} (\xi - \xi') \right] d\xi' - \int_{\xi}^{1} \theta(\xi') \bar{A}' \left[\frac{3u_{0i}}{2} (\xi' - \xi) \right] d\xi' \right\}, \tag{86}$$

where

$$\theta = (T - T_1)/(QL^2/\lambda)$$

and the quantity H_i is defined by Eq. (77a). Since the presence of conduction implies continuity of temperature at the boundaries, the boundary condition for this equation is $\theta(0) = 0$. When radiative transfer within the gas is negligible, the solution of Eq. (86) follows to be

$$\theta = \tfrac{1}{2}(\xi - \xi^2). \tag{87}$$

In the optically thin limit ($u_{0i} \ll 1$), Eq. (86) may be expressed as

$$\frac{d^2\theta}{d\xi^2} - 3N\theta = -1 \tag{88}$$

subject to the boundary conditions

$$\theta(0) = 0, \quad \theta'(1/2) = 0,$$

and for which

$$N = (PL^2/\lambda) \sum_{i=1}^{n} S_i(T_1)(de_{\omega_i}/dT)_{T_1}. \tag{89}$$

Equation (88) possesses an elementary solution, from which the centerline temperature is found to be

$$\frac{T_c - T_1}{QL^2/\lambda} = \frac{1}{3N} \left\{ 1 - 2 \left[\frac{\exp(-\frac{1}{2}\sqrt{3N})}{1 + \exp(-\sqrt{3N})} \right] \right\}.$$

It readily follows that the dimensionless gas property N characterizes the relative importance of radiation versus conduction within the gas under optically thin conditions. For particular values of P and L, it is actually the dimensional quantity

$$N/PL^2 = (1/\lambda) \sum_{i=1}^{n} S_i (de_{\omega_i}/dT) \tag{90}$$

which characterizes this relative importance, and values of N/PL^2 are illustrated in Fig. 14. For CO, CO_2, H_2O, and CH_4, Eq. (90) was evaluated

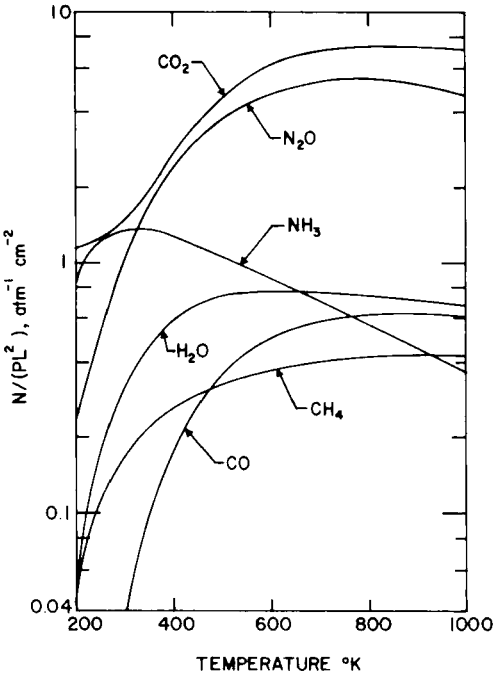

FIG. 14. Conduction–radiation interaction parameter for optically thin radiation.

employing the band intensities of Edwards *et al.* [10], while for N_2O and NH_3 the intensities where taken from Tien [1]. The appropriate thermal conductivity values are from Tsederberg [42]. It should again be emphasized that $N'PL^2$ characterizes radiation–conduction interaction only in the optically thin limit.

For the large path length limit ($u_{0i} \gg 1$), Eq. (86) reduces to

$$\frac{d\theta}{d\xi} + \xi - \frac{1}{2} = M\int_0^1 \theta(\xi')\frac{d\xi'}{\xi - \xi'}, \tag{91}$$

where $\theta(0) = 0$ is again the appropriate boundary condition, and

$$M = HL/\lambda = (L/\lambda)\sum_{i=1}^{n} A_{0i}(de_{\omega,i}/dT)_{T_1}. \tag{92}$$

The dimensionless parameter M constitutes the radiation–conduction interaction parameter for the large path length limit, and the dimensional quantity ML is illustrated in Fig. 15. For CO, CO_2, H_2O, and CH_4, this quantity was evaluated by using the A_0 values of Edwards *et al.* [10], while for N_2O and NH_3 the A_0 values were calculated from Eq. (44).

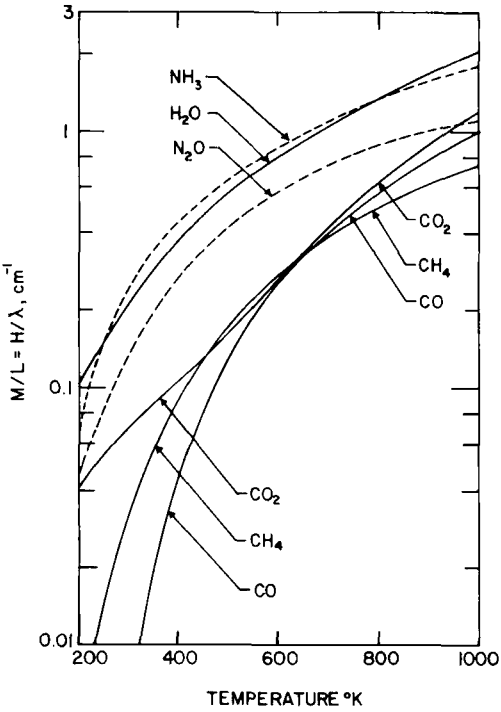

FIG. 15. Conduction–radiation interaction parameter for the large path length limit.

A comparison of Figs. 14 and 15 shows a considerable difference in the radiation–conduction interaction for the optically thin limit as opposed to the large path length limit. For example, in the optically thin limit CO_2 possesses a large radiation interaction relative to the other gases, while the reverse is true in the large path length limit. On the other hand, just the opposite trend is observed for H_2O. Since the thermal conductivities of the various gases do not differ appreciably, this behavior is due to differences in radiative transfer in the optically thin and large path length limits, and a discussion to this effect has been given in Section IV, A.

Equation (91) does not appear to possess a closed form solution. A numerical solution has thus been obtained, and the dimensionless centerline temperature is illustrated in Fig. 16.

Numerical solutions of Eq. (86), which is applicable for all u_{0i} values, have been obtained for several gases [32], and certain of these results are illustrated in Figs. 17 through 19 for CO_2 and H_2O. The large path length limit, as given by Fig. 16, is also shown. From Eq. (87), the centerline temperature for pure conduction follows to be

$$(T_c - T_1)/(QL^2/\lambda) = 0.125,$$

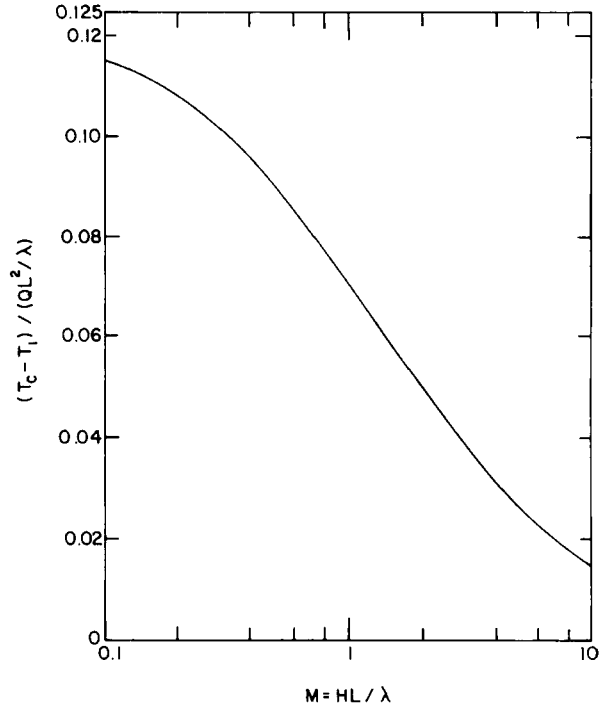

FIG. 16. Conduction–radiation results for the large path length limit.

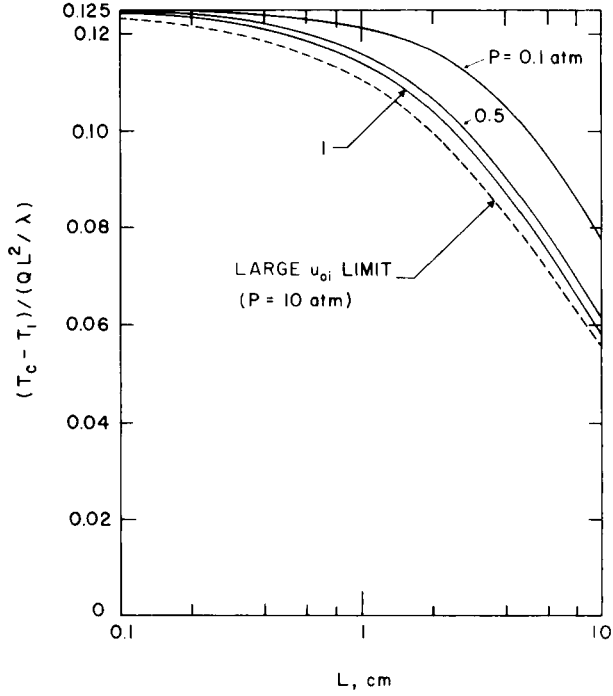

FIG. 17. Conduction–radiation results for CO_2 with $T_1 = 500°K$.

and thus Figs. 17 through 19 serve to illustrate the influence of radiative transfer upon the temperature profile within the gas. As would be expected, the importance of radiation becomes more pronounced as the plate spacing is increased.

For the sake of brevity, comparisons involving the optically thin limit will be made only for CO_2 at a pressure of one atmosphere. These are illustrated in Figs. 20 and 21 for wall temperatures of 500°K and 1000°K, respectively. In Fig. 20 it is evident that, when radiation is of importance, the radiative transfer process very nearly corresponds to the large path length limit. Conversely, this indicates that when the radiation is optically thin, it is in turn negligible relative to conduction, such that the optically thin limit does not constitute a useful limiting solution for the conditions illustrated in Fig. 20. This is not the case at higher temperatures, for which a greater departure from the large path length limit exists. This is evident from Fig. 21, where the optically thin limit is seen to be the appropriate limiting form for small values of L.

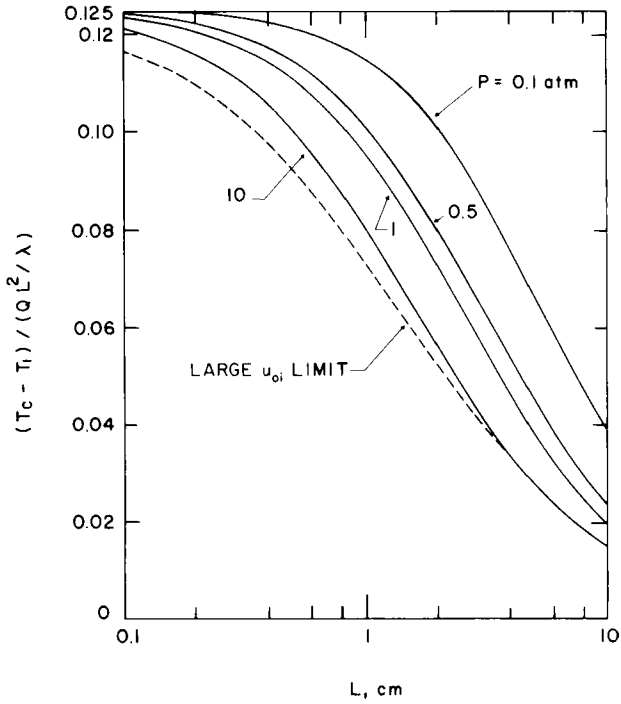

FIG. 18. Conduction–radiation results for CO_2 with $T_i = 1000$ K.

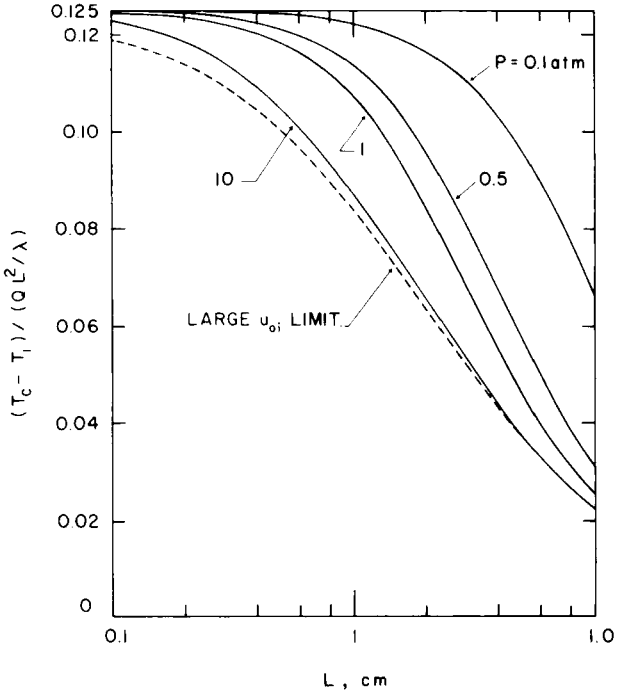

FIG. 19. Conduction–radiation results for H_2O with $T_1 = 500$ K.

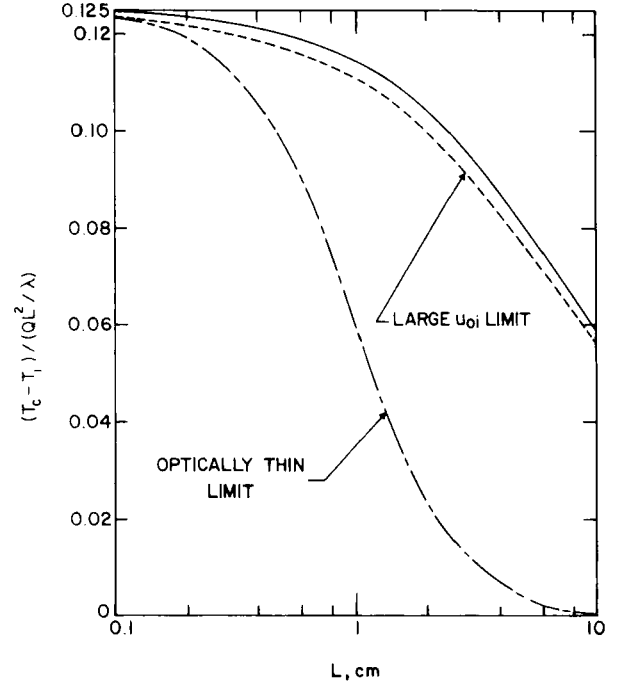

FIG. 20. Comparison of conduction–radiation solutions for CO_2 with $P = 1$ atm and $T_1 = 500$ K.

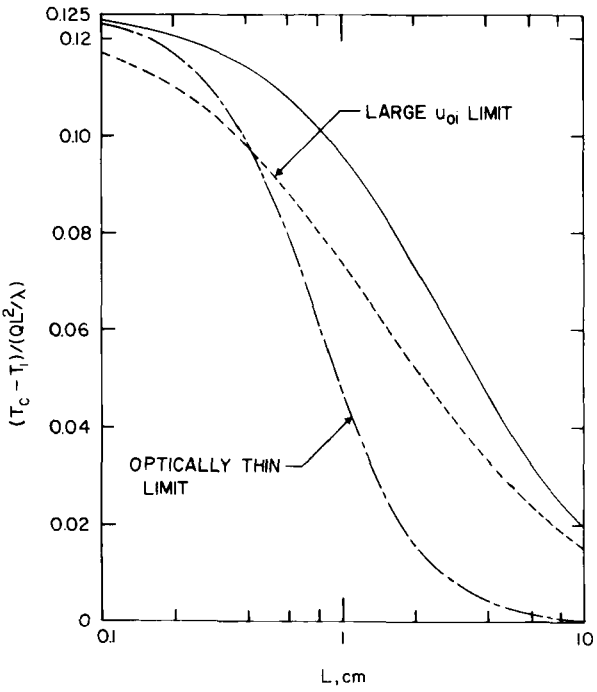

FIG. 21. Comparison of conduction–radiation solutions for CO_2 with $P = 1$ atm and $T_1 = 1000°K$.

Comparative results for CO, CO_2, H_2O, and CH_4 are shown in Figs. 22 and 23 for a pressure of one atmosphere and wall temperatures of 500°K and 1000°K, respectively. In Fig. 22, with the exception of CO_2, the results do not correspond closely to the large path length limit, although the relative positions of the curves coincide very nearly with that indicated by the interaction parameter for large path lengths (see Fig. 15). The only exceptions are the CO and CH_4 curves showing less of a radiative interaction effect, relative to CO_2, than is indicated by Fig. 15. This is evidently a consequence of departures from the large path length limit for these two gases.

In Fig. 23 the relative order of the four curves, for small values of L, is characteristic of the interaction parameter for optically thin radiation (see Fig. 14). As the value of L is increased, the relative positions of the two curves turn into those discussed for Fig. 22.

From Figs. 17 through 19, it is evident that the large path length limit constitutes an upper bound upon the influence of radiative transfer on the temperature profile within the gas. The same conclusion applies to the optically thin limit, since self-absorption is neglected. This fact that both

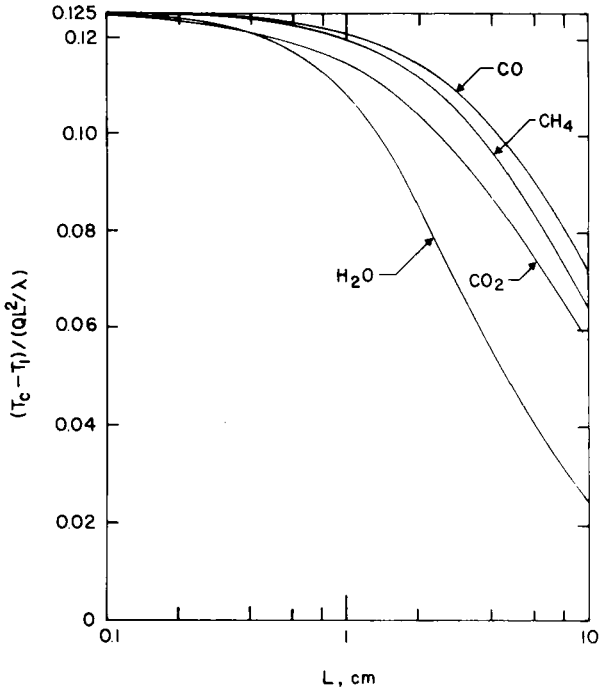

FIG. 22. Comparison of conduction–radiation results for $P = 1$ atm and $T_1 = 500°K$.

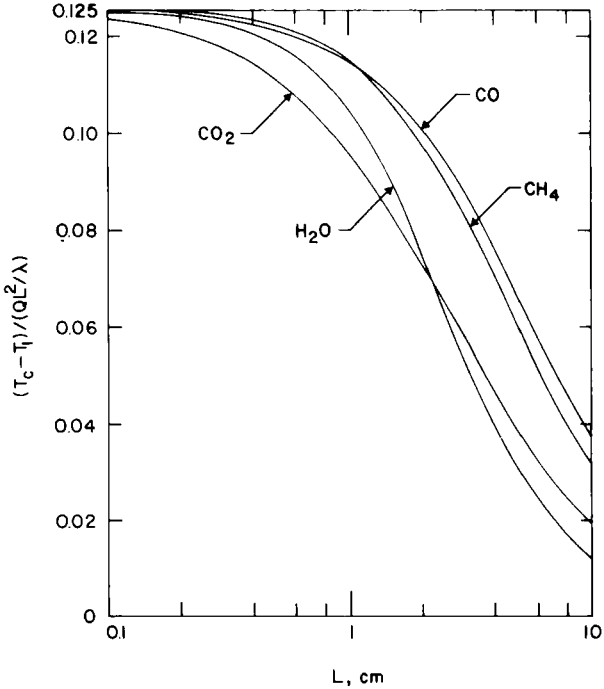

FIG. 23. Comparison of conduction–radiation results for $P = 1$ atm and $T_1 = 1000°K$.

limiting solutions constitute upper bounds on the radiative interaction can be employed to estimate whether or not, for a given gas, the interaction of radiation may be of importance.

A final comment pertaining to radiation–conduction interaction involves the experimental measurements of Schimmel *et al.* [37]. The apparatus consisted of two parallel plates spaced 2.55 cm apart and maintained at different temperatures, such that there was net energy transfer from one surface to the other. Temperature profiles were obtained with a Mach-Zehnder interferometer for pure CO_2 and N_2O, and for mixtures of CO_2–CH_4 and CO_2–N_2O. The data were compared with analytical results based upon the method of solution as employed in the present section. Agreement between the experimental and analytical results was excellent. In particular, the invariance of the temperature profile upon gas pressure in the large path length limit was clearly illustrated.

C. VIBRATIONAL NONEQUILIBRIUM

In most radiative transfer analyses the assumption of local thermodynamic equilibrium is employed. There are, however, physical situations for which such an assumption is not justified. The purpose of this subsection is to investigate the possible influence of vibrational nonequilibrium upon infrared gaseous radiation. The illustrative physical models are the same as previously considered in Sections IV, A and IV, B.

Only a limited number of nonequilibrium analyses are available in the literature pertaining to infrared radiative transfer. Goody [6] utilized the nonequilibrium transfer equation, Eq. (55), to derive an expression for the heating rate due to a vibration-rotation band in a plane atmosphere. The specific application involved the 15 μ carbon dioxide band. The linearized form of the nonequilibrium transfer equation was employed by Gilles [27] and Gilles and Vincenti [28] to obtain an expression for the radiative flux, with application to acoustics and flow through shock waves. Since an average absorption coefficient was used, their analysis is analogous to a modified gray gas analysis and does not account for the actual band structure. A formulation for energy transfer by radiation and conduction, in the presence of vibrational nonequilibrium, has been presented by Wang [43]. It was indicated that the source function, in general, satisfies a time-dependent equation involving Planck's function, the mean intensity of radiation, and a parameter representing the relative importance of collisional and radiative relaxations. Other nonequilibrium studies pertaining to atmospheric applications are given by Thomas [44] and Oxenius [45, 46], and an application involving radiation gas dynamics is presented by Mermangen [47].

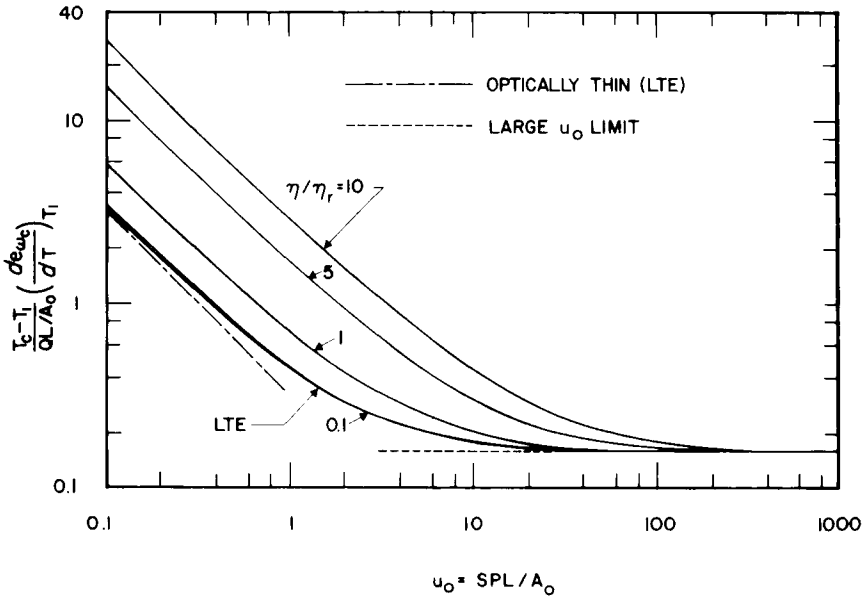

FIG. 24. Non-LTE results for a single-band gas with $\beta = \infty$.

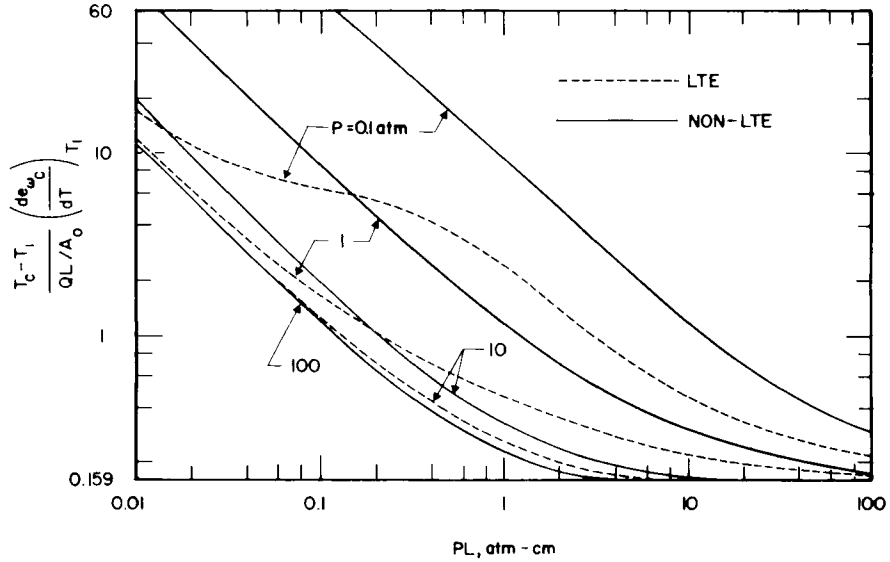

FIG. 25. LTE and non-LTE results for CO with $T_1 = 500°K$.

In the present investigation, the radiative flux equation, Eq. (68), formulated in terms of the total band absorptance and the nonequilibrium parameter η/η_r, is employed. Results are presented for diatomic gases in general and carbon monoxide in particular. The method of analysis may, however, be extended to multiple band gases. This extension to include vibrational nonequilibrium will be illustrated for the physical systems described in Sections IV, A and IV, B.

For the case in which radiation is the only mode of energy transfer, a combination of Eqs. (68), (73), and (74) yields

$$\xi - \frac{1}{2} = \frac{3u_0}{2}\int_0^{\xi}\left[\phi^*(\xi') - \frac{1}{4u_0}\left(\frac{\eta}{\eta_r}\right)\right]\bar{A}'\left[\frac{3u_0}{2}(\xi - \xi')\right]d\xi' - \frac{3u_0}{2}\int_{\xi}^{1}\left[\phi^*(\xi') - \frac{1}{4u_0}\left(\frac{\eta}{\eta_r}\right)\right]\bar{A}'\left[\frac{3u_0}{2}(\xi' - \xi)\right]d\xi', \tag{93}$$

where

$$\phi^* = \frac{T - T_1}{QL/H} = \frac{T - T_1}{QL/A_0}\left(\frac{de_{\omega_0}}{dT}\right)_{T_1}. \tag{94}$$

For a single-band gas, the definition of ϕ^* is identical to that of ϕ given by Eq. (77c). Thus, ϕ^* simply denotes a dimensionless temperature profile for non-LTE. As would be expected, Eq. (93) reduces to the single-band form of Eq. (76) for LTE (i.e., $\eta/\eta_r = 0$), and a comparison of the two equations shows that

$$\phi^*(\xi) = \phi(\xi) + (1/4u_0)(\eta/\eta_r). \tag{95}$$

Employing the LTE results for ϕ as given in Fig. 7, the centerline temperature is illustrated in Fig. 24 for $\beta = \infty$. Since β is the line structure parameter and is proportional to the ratio of mean line width to mean line spacing, then $\beta = \infty$ denotes the limit of overlapping lines. Results for other values of β, corresponding to situations for which line structure is important, are qualitatively the same. Figure 24 clearly illustrates the maximum influence of non-LTE under optically thin conditions, with the subsequent diminishing of the non-LTE influence as u_0 increases. Note that the non-LTE results yield higher centerline temperatures than the corresponding LTE curve. As discussed in Section III, C, this is a consequence of non-LTE reducing the capability of the gas to transmit radiative energy.

Specific results are illustrated in Fig. 25 for $T_1 = 500°K$. It is evident that non-LTE can exert a considerable influence upon the radiative transfer process for low pressures. The reason for this, of course, is that η/η_r varies inversely with pressure. Similar results are illustrated in Fig. 26 for $T_1 = 1000°K$, from which it is seen that the non-LTE influence is very small. This is a consequence of the strong temperature dependence of η/η_r,

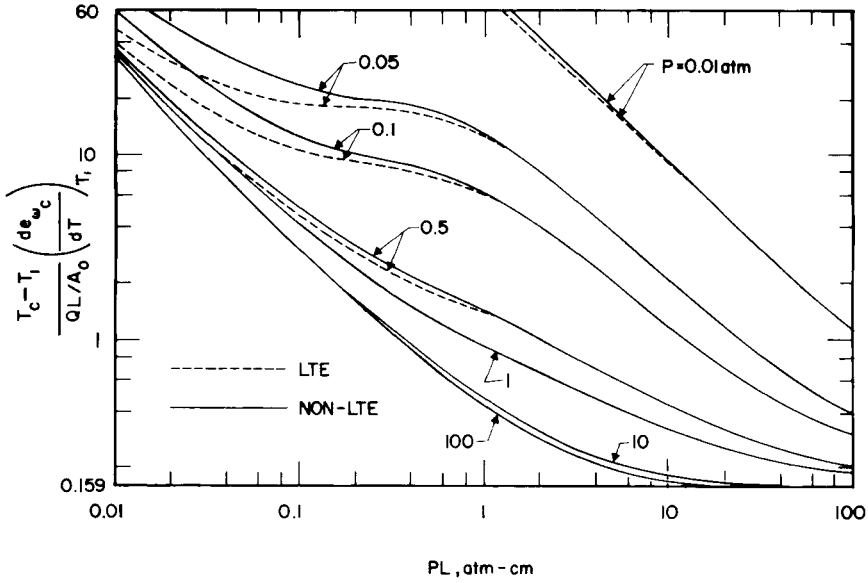

FIG. 26. LTE and non-LTE results for CO with $T_1 = 1000°K$.

such that the value of η/η_r at 1000°K is approximately two orders of magnitude less than the value for 500°K.

Considering now the inclusion of molecular conduction, a combination of Eqs. (68), (74), and (85) yields the appropriate energy equation as

$$\frac{d\theta}{d\xi} + \xi - \frac{1}{2}$$
$$= \frac{3Mu_0}{2}\left\{\int_0^{\xi}\theta(\xi')\bar{A}'\left[\frac{3u_0}{2}(\xi - \xi')\right]d\xi' - \int_{\xi}^{1}\theta(\xi')\bar{A}'\left[\frac{3u_0}{2}(\xi' - \xi)\right]d\xi'\right\}$$
$$- \frac{3}{8}\left(\frac{\eta}{\eta_r}\right)\left\{\int_0^{\xi}\left(1 + \frac{d^2\theta}{d\xi'^2}\right)\bar{A}'\left[\frac{3u_0}{2}(\xi - \xi')\right]d\xi'\right.$$
$$\left. - \int_{\xi}^{1}\left(1 + \frac{d^2\theta}{d\xi'^2}\right)\bar{A}'\left[\frac{3u_0}{2}(\xi' - \xi)\right]d\xi'\right\}, \tag{96}$$

where M is defined by Eq. (92), while

$$\theta = (T - T_1)/(QL^2/\lambda).$$

Equation (96) constitutes the non-LTE counterpart to the single-band form of Eq. (86).

Numerical solutions of Eq. (96) have been obtained by the same method previously employed for LTE [48], and centerline temperatures are shown

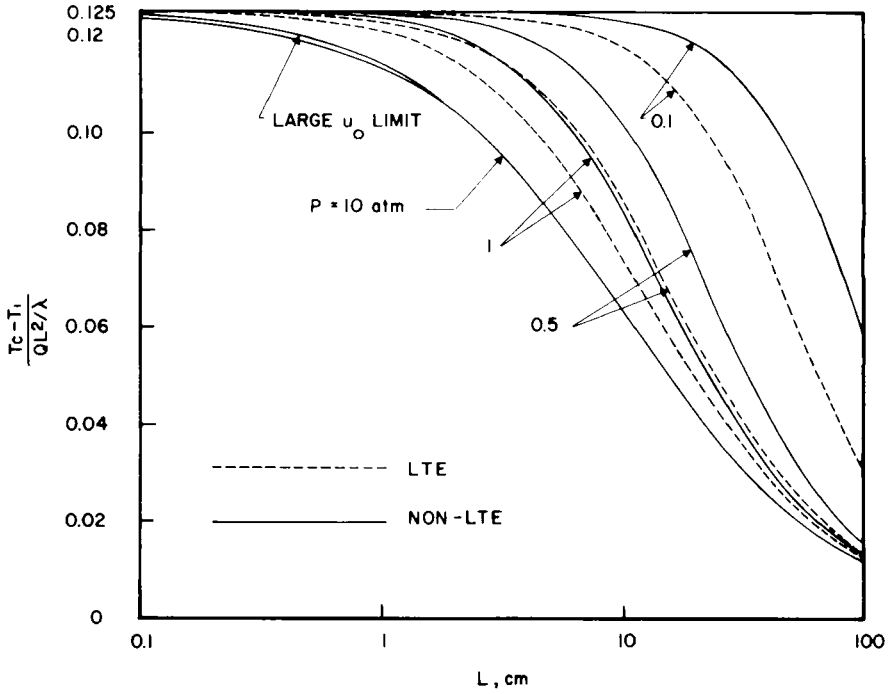

FIG. 27. Results for combined conduction and radiation with $T_1 = 500°K$.

in Figs. 27 and 28 for carbon monoxide with $T_1 = 500°K$ and $1000°K$, respectively. Recall that non-LTE effects are most pronounced for small path lengths. With reference to Fig. 27, however, this corresponds to the situation for which conduction is the predominant mode of energy transfer. Thus, for a given pressure, the non-LTE influence upon total energy transfer within the gas will vanish for either small or large values of L. The former corresponds to negligible radiative transfer, while the latter denotes the large path length limit. In other words, if nonequilibrium radiation is to have a significant influence upon the energy equation, then the physical dimension of the gas system must be sufficiently large for radiation to play a dominant role, but it cannot be so large that the large path length limit is approached. In addition, of course, both pressure and temperature must be relatively low.

D. RADIATIVE EQUILIBRIUM

The preceding analyses have dealt solely with the situation for which net energy transfer is between the gas and the bounding surfaces, i.e., there is

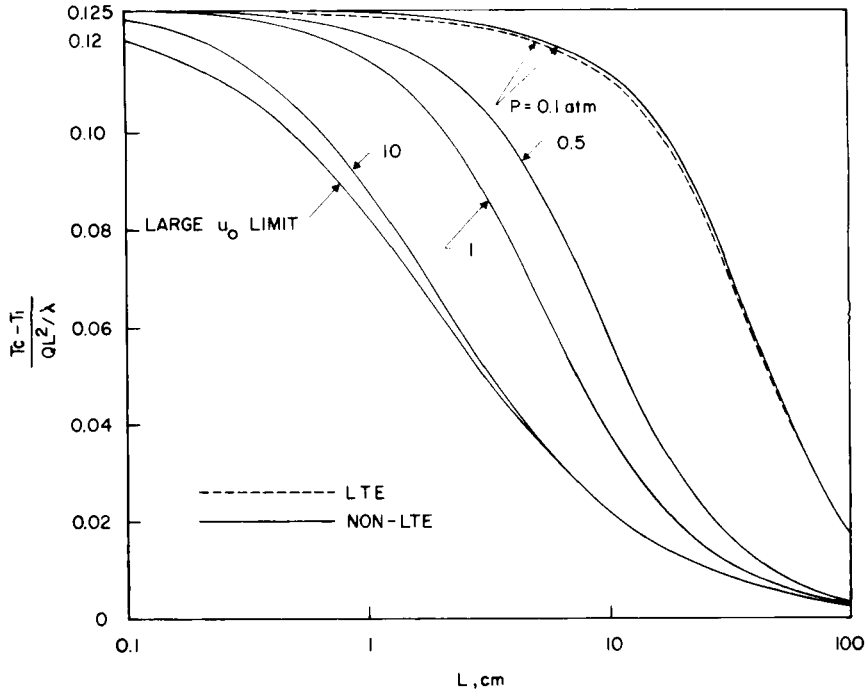

FIG. 28. Results for combined conduction and radiation with $T_1 = 1000°K$.

no net radiative transfer from one surface to the other. It will thus be of interest to consider briefly the opposite extreme for which the net radiative transfer is strictly between the surfaces. This is the case of radiative equilibrium, for which, with reference to Fig. 6, the surface temperatures T_1 and T_2 are not equal, and there is no other mechanism of energy addition or transfer within the gas. The energy equation is thus

$$dq_R/dy = 0.$$

For the sake of brevity, consideration will be given only to the large path length limit, and upon summing Eq. (68) over all bands, linearizing the resulting equation through the use of Eq. (74), and taking the large path length limit for which $\bar{A}'(u) = 1/u$, the integral equation describing the temperature profile for radiative equilibrium follows to be [49]

$$\int_0^1 \frac{d\theta}{d\xi'} \frac{d\xi'}{\xi - \xi'} = 0, \tag{97}$$

where again $\xi = y/L$, while

$$\theta = (T - T_2)/(T_1 - T_2).$$

As with Eq. (80), the summation over individual bands vanishes in the large path length limit. The solution to Eq. (97) yields [38]

$$\theta(\xi) = \tfrac{1}{2} + (1/\pi)\sin^{-1}(1 - 2\xi). \tag{98}$$

This temperature profile is illustrated in Fig. 29 together with the result for the diffusion (Rosseland) limit.

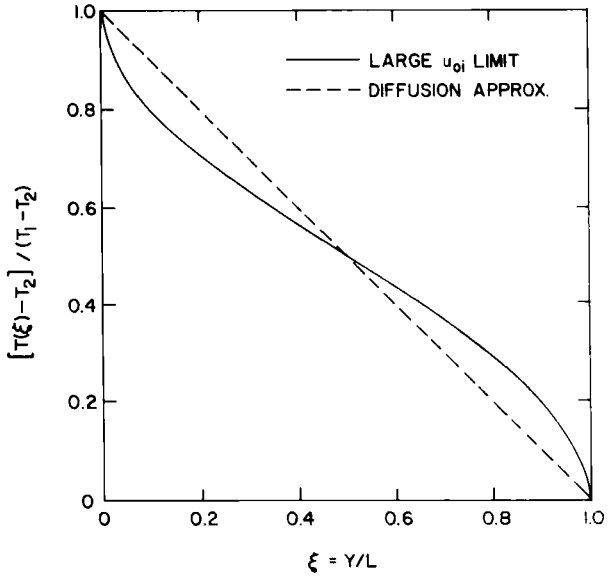

FIG. 29. Temperature distribution for radiative equilibrium in the large path length limit.

The net radiative heat flux between the plates may in turn be determined by employing Eq. (98) in the expression for the radiative flux q_R, with the result that [49]

$$\frac{q_R}{4\sigma T_1^3(T_1 - T_2)} = 1 - \frac{1}{4\sigma T_1^3}\sum_{i=1}^{n} A_{0i}\left(\frac{de_{\omega i}}{dT}\right)_{T_1} \ln\left(\frac{3S_iPL}{8A_{0i}}\right). \tag{99}$$

This has been evaluated for several gases and is illustrated in Fig. 30. Since the ordinate value of unity corresponds to the transparent limit, the effectiveness of each of these gases in reducing the net radiative flux is clearly illustrated. Furthermore, for conditions under which the large path length limit does not apply, it may readily be shown that Eq. (99) constitutes a lower limit on radiative transfer.

It is interesting to note the difference between the present results and those of Section III, A, which dealt with a uniform heat source within a

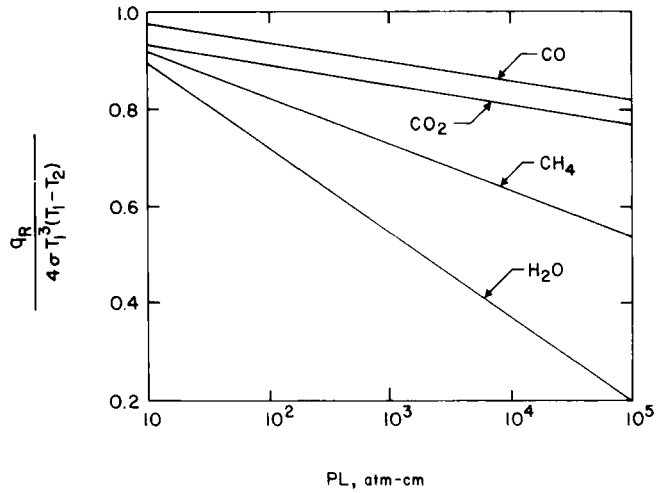

FIG. 30. Radiative flux results for radiative equilibrium and $T_1 = 500$ K.

gas bounded by symmetrically heated plates. Again these constitute two opposite extremes in that the net radiative transfer is solely between surfaces in the present situation, whereas it is between the gas and the bounding surfaces in the former case, and recall from Section III, A that the band intensities S_i do not appear in the large path length limit. This absence can be traced to the fact that the central portion of a band, since it is saturated in the large path length limit, has no effect upon the net radiative transfer between the gas and the bounding surfaces. In other words, net radiative transfer takes place only in the wing regions of the bands, and the extent of the wings depends only on A_{0i}. This is not the case in the present situation, however, since the reduction in the net radiative transfer between surfaces will depend upon the extend of the saturated central portion of the bands, and hence Eq. (99) contains both of the band parameters A_{0i} and S_i.

V. Concluding Remarks

The intent of the present chapter has been to investigate the basic features of infrared gaseous radiation through the use of extremely simple and illustrative physical models, and no attempt has been made to describe specific applications. There does exist, however, a body of literature pertaining to the inclusion of spectroscopic information into radiative transfer analyses involving the structure and dynamics of planetary atmospheres.

In such investigations infrared gaseous radiation constitutes an important mechanism of energy transfer, and for the most part, as in the present chapter, the kernel function for the radiative flux is formulated in terms of the band absorptance (or transmission function). Normally, however, attention is directed towards numerical solutions for specific planetary conditions, and little emphasis is placed upon the basic features of the radiative transfer process.

A partial summary of atmospheric radiation analyses includes the investigations of Manabe and co-workers [50–53] for Earth; studies of the structure of the Martian atmosphere by Prabhakara and Hogan [54], Ohring and Mariano [55, 56], and Gierasch and Goody [57, 58]; and the analysis of the atmosphere of Venus above the cloud tops by Bartko and Hanel [59]. A wealth of information may further be found in the book by Goody [6].

ACKNOWLEDGMENTS

The authors wish to express their gratitude to their colleagues, Professors P. Varanasi and L. S. Wang, for numerous discussions and advice. Much of the work reported herein was supported by the National Science Foundation.

NOMENCLATURE

A	total band absorptance, cm^{-1}
A_J	total absorptance of a single line
A_0	band width parameter (correlation quantity), cm^{-1}
$\bar{A}(u, \beta)$	dimensionless band absorptance, $\bar{A} = A/A_0$
B	rotational constant, cm^{-1}
B_ω	blackbody intensity at local temperature
$B_{1\omega}, B_{2\omega}$	spectral surface radiosities, (watts-cm^{-2})/cm^{-1}
c	speed of light
e_ω	Planck's function, (watts-cm^{-2})/cm^{-1}
$e_{\omega_0}, e_{\omega_c}$	Planck's function evaluated at band center
$e_{1\omega_0}, e_{1\omega_c}$	Planck's function evaluated at temperature T_1
E_v	vibrational energy
E_v^*	equilibrium vibrational energy
h	Planck's constant
H	gas property for the large path length limit, Eq. (82)
I_ω	specific intensity
$J_\omega, J_{\omega 0}$	source function
k	Boltzmann constant
K	gas property for the optically thin limit, Eq. (79)
L	distance between plates, cm
M	radiation–conduction interaction parameter, Eq. (92)
N	radiation–conduction interaction parameter, Eq. (89)
P	gas pressure, atm
P_e	equivalent (effective) broadening pressure
q_R	total radiative heat flux, watts/cm^2
$q_{R\omega}$	spectral radiative flux, (watts-cm^{-2})/cm^{-1}
s	distance along direction of radiative propagation
$S, S(T)$	total band intensity, $atm^{-1} - cm^{-2}$
S_J	line intensity
T	temperature, kinetic temperature °K

T_0	reference temperature (equilibrium)	Θ	dimensionless temperature, Eq. (97)
T_1, T_2	surface temperature	κ_ω	equilibrium spectral absorption coefficient, cm^{-1}
u	dimensionless coordinate, $u = SPy/A_0$	κ_p	Planck mean coefficient, cm^{-1}
u_0	dimensionless path length, $u_0 = SPL/A_0$	$\bar{\kappa}$	mean absorption coefficient, $\bar{\kappa} = SP/\Delta\omega$
y	physical coordinate	λ	thermal conductivity, (watts-cm^{-2})/°K
α_ω	spectral band coefficient	ν	frequency
β	line structure parameter	ρ	density
γ	rotationally averaged line half-width, Eq. (35)	σ	Stefan-Boltzmann constant
$\tilde{\gamma}$	vibrationally averaged line half-width, Eq. (39)	ϕ	dimensionless function, Eq. (77c)
γ_j	line half-width, cm^{-1}	ϕ^*	dimensionless function, Eq. (94)
ϵ	surface emittance	Ω	solid angle
η	vibrational relaxation time, sec	ω	wave number, cm^{-1}
η_r	radiative life time of vibrational state, sec	ω_0, ω_c	wave number at the band center, cm^{-1}
θ	dimensionless temperature, Eq. (86)		

REFERENCES

1. C. L. Tien, *Advan. Heat Transfer* **5,** 253 (1968).
2. L. M. Trafton, *Astrophys. J.* **147,** 765 (1967).
3. J. S. Hogan, S. I. Rasool, and T. Encrenaz, *J. Atmos. Sci.* **26,** 898 (1969).
4. G. Yamamoto, M. Tanaka, and T. Aoki, *J. Quant. Spectrosc. Radiat. Transfer* **9,** 371 (1969).
5. S. S. Penner, "Quantitative Molecular Spectroscopy and Gas Emissivities." Addison-Wesley, Reading, Massachusetts, 1959.
6. R. M. Goody, "Atmospheric Radiation." Oxford Univ. Press, London and New York, 1964.
7. D. K. Edwards and W. A. Menard, *Appl. Opt.* **3,** 621 (1964).
8. D. K. Edwards and W. A. Menard, *Appl. Opt.* **3,** 874 (1964).
9. D. K. Edwards, *Appl. Opt.* **4,** 1352 (1965).
10. D. K. Edwards, L. K. Glassen, W. C. Hauser, and J. S. Tuchscher, *J. Heat Transfer* **86,** 219 (1967).
11. C. L. Tien and J. E. Lowder, *Int. J. Heat Mass Transfer* **9,** 698 (1966).
12. R. M. Goody and M. J. S. Belton, *Planet. Space Sci.* **15,** 247 (1967).
13. Ya. B. Zel'dovich and Yu. P. Raizer, "Physics of Shock Waves and High-Temperature Hydrodynamic Phenomena," Vols. I and II. Academic Press, New York, 1967.
14. J. Gille and R. Goody, *J. Fluid Mechs.* **22,** 47 (1964).
15. L. S. Wang, *J. Quant. Spectrosc. Radiat. Transfer* **8,** 851 (1968).
16. L. S. Wang, *J. Quant. Spectrosc. Radiat. Transfer* **8,** 1233 (1968).
17. W. G. Vincenti and C. H. Kruger, Jr., "Introduction to Physical Gas Dynamics." Wiley, New York, 1965.
18. N. W. Bazley and E. W. Montroll, *J. Chem. Phys.* **28,** 700 (1958).
19. L. L. Northup and C. T. Hsu, *Phys. of Fluids* **11,** 1375 (1968).
20. J. P. Hodgson and R. J. Hine, *J. Fluid Mechs.* **35,** 171 (1969).

21. W. J. Hooker and R. C. Millikan, *J. Chem. Phys.* **38,** 214 (1963).
22. R. C. Millikan and D. R. White, *J. Chem. Phys.* **39.** 3209 (1963).
23. C. J. C. M. Simpson, K. D. Bridgeman, and T. R. D. Chandler, *J. Chem. Phys.* **49,** 509 (1968).
24. R. C. Millikan, *Phys. Rev. Lett.* **8,** 253 (1962).
25. M. G. Ferguson and R. W. Read, *Trans. Faraday Soc.* **61,** 1559 (1965).
26. R. C. Millikan, "Molecular Relaxation Processes." Academic Press, New York and Chem. Soc. of London, 1966.
27. S. E. Gilles, Flow with Coupled Radiative and Vibrational Non-equilibrium in a Diatomic Gas. Ph.D. Dissertation, Stanford Univ. (1968).
28. S. E. Gilles and W. G. Vincenti, *J. Quant. Spectrosc. Radiat. Transfer* **10,** 71 (1970).
29. S. N. Tiwari, Infrared Radiative Energy Transfer in Nongray Gases. Ph.D. Dissertation, State Univ. of New York at Stony Brook (1969).
30. E. M. Sparrow and R. D. Cess, "Radiation Heat Transfer. Brooks/Cole, Belmont, California (1966).
31. D. H. Sampson, "Radiative Contributions to Energy and Momentum Transfer." Wiley (Interscience), New York, 1965.
32. R. D. Cess and S. N. Tiwari, *Appl. Sci. Res.* **20,** 25 (1969).
33. R. D. Cess, P. Mighdoll, and S. N. Tiwari, *Int. J. Heat Mass Transfer* **10,** 1521 (1967).
34. R. Grief and I. S. Habib, *J. Heat Transfer* **91,** 282 (1969).
35. R. D. Cess and S. N. Tiwari, *Appl. Sci. Res.* **19,** 439 (1968).
36. A. C. Cogley, W. G. Vincenti, and S. E. Gilles, *AIAA J.* **6,** 551 (1968).
37. W. P. Schimmel, J. L. Novotny, and F. A. Olsofka, *Proc. Int. Heat Transfer Conf., 4th, Paris-Versailles* Vol. III (1970).
38. S. G. Mikhlin, "Integral Equations," p. 126. Pergamon Press, Oxford (1967).
39. S. N. Tiwari and R. D. Cess, *Int. J. Heat Mass Transfer* **11,** 1731 (1968).
40. M. A. Heaselet and R. F. Warming, *Int. J. Heat Mass Transfer* **8,** 979 (1965).
41. D. A. Mandell, *J. Quant. Spectrosc. Radiat. Transfer* **10,** 459 (1970).
42. N. V. Tsederberg, "Thermal Conductivity of Gases and Liquids." M.I.T. Press, Cambridge, Massachusetts, (1965).
43. L. S. Wang, The Cooling of a Gas not in Local Thermodynamic Equilibrium by Conduction and Radiation, AIAA Paper No. 69-638 (1969).
44. R. N. Thomas, "Some Aspects of Non-Equilibrium Thermodynamics in the Presence of a Radiation Field." Univ. of Colorado Press, Denver, Colorado, 1965.
45. J. Oxenius, *J. Quant. Spectrosc. Radiat. Transfer* **5,** 771 (1965).
46. J. Oxenius, *J. Quant. Spectrosc. Radiat. Transfer* **6,** 65 (1966).
47. W. H. Mermagen, *Phys. Fluids* **10,** 1801 (1967).
48. S. N. Tiwari and R. D. Cess, *J. Quant. Spectrosc. Radiat. Transfer* **11,** 237 (1971).
49. P. Mighdoll and R. D. Cess, *AIAA J.* **6,** 1778 (1968).
50. S. Manabe and F. Möller, *Mon. Weather Rev.* **89,** 503 (1961).
51. S. Manabe and R. F. Strickler, *J. Atmos. Sci.* **21,** 361 (1964).
52. S. Manabe and R. T. Wetherald, *J. Atmos. Sci.* **24,** 241 (1967).
53. S. Manabe and B. G. Hunt, *Mon. Weather Rev.* **96,** 477 (1968).
54. C. Prabhakara and J. S. Hogan, Jr., *J. Atmos. Sci.* **22,** 97 (1965).
55. G. Ohring and J. Mariano, *J. Atmos. Sci.* **23,** 251 (1966).
56. G. Ohring and J. Mariano, *J. Atmos. Sci.* **25,** 673 (1968).
57. P. Gierasch and R. Goody, *Planet. Space Sci.* **15,** 1465 (1967).
58. P. Gierasch and R. Goody, *Planet. Space Sci.* **16,** 615 (1968).
59. F. Bartko and R. A. Hanel, *Astrophys. J.* **151,** 365 (1968).

This Page Intentionally Left Blank

Wall Turbulence Studies

Z. ZARIĆ

Boris Kidrič Institute, University of Beograd, Beograd, Yugoslavia

I. Introduction 285
II. Turbulence Problem 287
A. Predictions and Mathematical Models 287
B. Statistical Models 290
C. Role of the Experiment 291
III. Current Experimental Methods 292
A. Measurements in Turbulent Flows 292
B. Hot-Wire Anemometry 293
C. Other Velocity Measurement Techniques 297
D. Temperature Measurement 299
IV. Survey of Illustrative Experimental Results 299
A. Flows without Pressure Gradient along Smooth Walls . . . 299
B. Variable Pressure Gradient Flow 305
V. Hot Wire–Cold Wire Experimental Method 309
A. Choice of the Method 309
B. Description of the Method 310
C. Calibration 312
D. Wall Effect 314
VI. Experimental Results 318
A. Experimental Procedure 318
B. Mean Flow Results 319
C. Experimentally Determined Statistical Characteristics . . . 325
VII. Statistical Analysis 335
A. Scope of the Analysis 335
B. Statistical Analysis of the Hot-Wire Signal 336
C. Results of Analysis 342
D. Probable Future Developments 344
VIII. Concluding Remarks 345
Symbols 348
References 348

I. Introduction

In the engineering profession, it is most desirable to be able to make accurate predictions on the performance of equipment and installations. The required accuracy is established on the basis of economic and safety

factors. The possible accuracy of the predictions, however, depends on the complexity of the phenomena involved and on the knowledge of the physics of these phenomena.

At present, installations costing tens of millions of dollars are being built. Both capital and running costs depend on the accuracy of predicted performance, and with such sums involved, in modern technology one obviously can not afford to be inaccurate. Fortunately, designers at present have at their disposal digital computers—powerful tools in the field of design.

In a great variety of the present-day equipment and installations turbulent flows are encountered. In a substantial number of them turbulence effects are among the most important design parameters. It is most unfortunate, then, that the present knowledge on the physics of turbulence is quite inadequate. In fact, turbulence is one of the few unsolved problems of modern mechanics.

Important turbulence studies started at the beginning of the century. They were initiated by attempts to solve the problem of heat and mass transfer from the earth's surface [1]. At present, we are aware of the fact that the solution of the problem lies in the hydrodynamics of flow. However, turbulence studies involving heat and mass transfer are rare and mostly concerned with the global, time-averaged effects of turbulence.

As a result of an impressive number of theoretical and experimental studies conducted over the last fifty years, our knowledge of the time-averaged effects of turbulence is substantial. Procedures exist which allow us to make predictions with fair accuracy in a great variety of flows, involving the effects of compressibility, heat and mass transfer, chemical reactions, etc.; but our knowledge, being phenomenological, is not general enough. Whenever a new complex flow configuration is encountered, because of the demands of technology, we have to turn again to experiment and form new phenomenological models. There is, therefore, an urgent need for a better understanding of the physics of turbulence.

Turbulence is a complex statistical phenomenon. Wall turbulence is even more complex as the randomness of the phenomenon is influenced by a certain organization in the structure. It is therefore necessary that the turbulence be treated statistically. It is only recently that statistical models have been introduced in the theoretical analysis of wall turbulence. Experimental wall turbulence studies are as a rule nonstatistical, with very rare exceptions. It is believed by the author that a statistical approach in the experimental investigation of wall turbulence could have an important role in the solution of the problem.

The main purpose of the present article is, therefore, to draw attention to to the importance of the statistical approach in wall turbulence experimental studies. Existing experimental techniques are reviewed from this standpoint.

A wall turbulence experimental study, made by the author, is presented and possible statistical approach to the analysis of the data is given. Results of the analysis are discussed from the standpoint of probable future developments.

II. Turbulence Problem

A. PREDICTIONS AND MATHEMATICAL MODELS

An engineer is usually concerned with the time-averaged effects of turbulence on equipment—usually, but not always. Fluctuations of the wall pressure and the wall heat flux, provoked by turbulence, have been experimentally detected. For some equipment these fluctuations might have undesirable consequences, and have to be taken into consideration. However, even the time-averaged effects, of prime interest, are still not well established in many cases, and are in need of reliable prediction procedures.

Reynolds was the first to introduce time-averaging in the Navier–Stokes equations. In the resulting equations, unknown quantities appear in the form of second-order correlations of the turbulence components, $\overline{u_i u_j}$. A theory for the determination of these quantities does not exist and phenomenological relations have to be introduced in order to handle the problem. A great number of prediction methods, based on various phenomenological models, have been proposed, and some of them used. In fact, the number and variety of these proposals create acute problems of choice for the users. A conference was held at Stanford in 1968 with the aim of providing a comparative evaluation of the various prediction procedures for boundary layer flows [2].

Prediction procedures proposed so far fall into two large groups. So-called "integral methods" are based on the integration of the coupled ordinary differential and algebraic equations. Potentially more powerful, and general, are "differential" methods which have appeared recently with the accessability of digital computers and advances in numerical analysis. These methods require numerical integration of coupled partial differential and algebraic equations.

The conclusions of the Evaluation Committee of the Stanford Conference illustrate well the state of the art [3]. It was found that a dozen or so prediction methods give essentially equally good predictions insofar as discrepancies in the experimental data on smooth-wall, two-dimensional, incompressible flows are taken into consideration. It is not surprising, then, that better integral methods predict as well as better differential procedures. This also results from the fact that the underlying physical evidence is the same. One

of the conclusions of the Evaluation Committee was therefore that there is an important need for new and more accurate experimental data.

To illustrate the kind of experimental data currently being used a simplified differential procedure for the steady, smooth-wall incompressible boundary layer flow is examined. The corresponding momentum equation is

$$\rho U_1 \frac{\partial U_1}{\partial x_1} = \frac{\partial}{\partial x_2}\left(\mu \frac{\partial U_1}{\partial x_2} - \overline{\rho u_1 u_2}\right) - \frac{\partial p}{\partial x_1}. \tag{2.1}$$

Different procedures vary in correlating the unknown Reynolds stress, $-\overline{\rho u_1 u_2}$, with other parameters to make the system of equations determinate [4]. The simplest employ the turbulent viscosity concept in which, following Bousinesq (1877), it is assumed that

$$\tau = -\overline{\rho u_1 u_2} = \mu_T \, \partial U_1/\partial x_2, \tag{2.2}$$

where μ_T is the "turbulent viscosity," which has to be somehow related to the other properties of the flow. In 1925 Prandtl proposed the following:

$$\mu_T = \rho \cdot L_M \cdot v_{\text{turb}},$$

in which the length, L_M, is the "mixing length," and v_{turb} is a representative random velocity for which Prandtl proposed that

$$v_{\text{turb}} = L_M \, |\partial U_1/\partial x_2|,$$

so that

$$\mu_T = \rho L_M^2 \, |\partial U_1/\partial x_2| \, (\partial U_1/\partial x_2). \tag{2.3}$$

An algebraic relation for L_M has to be prescribed, on the basis of the existing experimental evidence, and the problem is solved elegantly and efficiently. The experimental evidence needed is in the form of data on the mean velocity distributions for various flows. The procedure predicts with sufficient accuracy a whole class of simple flows. Only the algebraic relation for L_M has to be changed from flow to flow.

Turbulent viscosity, μ_T, is essentially a property of the fluctuating motion. With the aim of improving the universality of the model Kolmogorov (1942) and Prandlt (1945) proposed to relate μ_T to the kinetic energy of turbulence. Following Prandtl,

$$v_{\text{turb}} = C_\mu \sqrt{e_k},$$

where

$$e_k = 0.5(\overline{u_1^2} + \overline{u_2^2} + \overline{u_3^2}),$$

so that

$$\mu_T = \rho C_\mu \cdot L_M \sqrt{e_k}. \tag{2.4}$$

The kinetic energy of turbulence is determined from an additional differential equation:

$$\rho\, De_k/D\tau = -\overline{\rho u_1 u_2}(\partial U_1/\partial x_2) - \partial(\overline{\rho u_2 e'} + \overline{u_2 p'})/\partial x_2 - \mu\sum(\partial u_i/\partial x_j)^2. \quad (2.5)$$

The terms on the right represent turbulence energy generation, diffusion, and dissipation, respectively. Introduction of the additional differential equation does not make the system more determinate. On the contrary, it leads to the appearance of new unknowns, among them triple correlations like $\overline{u_2 e'}$. New hypotheses have therefore to be made. For instance, diffusion and dissipation terms could be approximated by [4]

$$-(\overline{\rho u_2 e'} + \overline{u_2 p'}) = C_D \mu_T (\partial e_k/\partial x_2),$$

$$\mu \sum \overline{(\partial u_i/\partial x_j)^2} = C_\epsilon \rho e_k^{3/2}/L_\epsilon,$$

where C_D and C_ϵ are new constants, and L_ϵ a new length scale. These have to be prescribed by turning to available experimental data. Experimental data on turbulence kinetic energy and shear stress distributions are needed, in addition to the data on mean velocities.

In pursuit of the methods which would be general for a wider class of flows some authors determine L_M from another differential equation, with the corresponding introduction of a new set of constants to be determined. Another approach is to abandon the concept of turbulent viscosity—a formally introduced parameter—and to solve a differential equation for the turbulent shear stress, along with the differential equation for the kinetic energy or an equivalent quantity. A particular method of this kind, proposed by Hanjalić [5], requires the determination of seven empirical constants and a prescription for a relation for the length scale.

Mathematical models even more elaborate have been proposed. For instance, the proposal by Davidov requires the integration of twenty-three coupled differential equations [6]. The consequences are always the same. The introduction of a differential equation for the nth-order correlation always leads to the appearance of new unknowns in the form of $(n + 1)$th-order correlations. The introduction of new differential equations is appropriate only when it leads to higher generality, and only when a plausible hypothesis and reliable experimental evidence allow the determination of the higher order correlations.

Theoretically all these mathematical models are comprised in the general analytical treatment of the turbulence problem formulated in 1924 by Keller and Friedman [6]. This consists of the derivation of the differential equations for the correlations of the nth order, with the determination of all of these correlations being equivalent to the determination of the probability distributions of the hydrodynamic quantities in space. However, any finite subsystem of this infinite system of equations is undetermined.

So far we have spoken only of the hydrodynamics of flow. Turbulence effects on the heat transfer rates, or in general on the rates of transport of any scalar quantity, are of great importance. If we are interested in the time-averaged effects of turbulence on heat transfer we have to perform time-averaging of the enthalpy transport equation. As in the case of the momentum equation (2.1), unknown second-order correlations of the type $\overline{u_i t}$ appear in the resulting equation. The further procedure is analogous to the hydrodynamic case. It is assumed that the turbulent heat flux is related to the gradient of the mean temperature by

$$q = -\lambda_T \operatorname{grad} T, \tag{2.6}$$

where

$$\lambda_T = \rho C_p L_T v_{turb},$$

and L_T is a mixing length equivalent. The ratio

$$Pr_t = \mu_T C_p/\lambda_T = L_M/L_T$$

is called the turbulent Prandtl number. The random velocity v_{turb} may again be taken as

$$v_{turb} = L_M \, |\partial U_1/\partial x_2|,$$

in which case we have

$$\lambda_T = \rho C_p L_M \cdot L_T \, |\partial U_1/\partial x_2|. \tag{2.7}$$

In this case the problem is solved if an adequate relation for the L_T, or the Pr_t, could be prescribed.

Alternatively we may take

$$v_{turb} = C_\mu \sqrt{e_k},$$

in which case we have to solve an additional differential equation for e_k, and determine additional constants.

It is of course possible to follow even further the hydrodynamic procedures. Reliable data on the higher order correlations involving temperatures have to be found for that. However, the prediction methods in current use are most often based on Eq. (2.7).

B. Statistical Models

Turbulence is essentially a statistical phenomenon. All the quantities involved are therefore random variables characterized by corresponding probability distributions. The complete solution of the turbulence problem would consist of the determination of the time evolution of the probability distribution of the hydrodynamic, enthalpy, and other fields, starting from a

known set of distribution functions at the initial moment and employing the relevant physical laws [6]. The task is unfortunately too difficult at present.

The statistical theory of free turbulence is in an advanced stage of development. An excellent account of this theory is given in the book by Monin and Iaglom [6]. Recently, true statistical measurements in grid turbulence have been made by Frenkiel and Klebanoff [7] and van Atta, Yeh, and Chen [8, 9]. However, as pointed out by Townsend [10], wall turbulence is of a less random and more organized nature. This organization in the wall turbulence structure has been experimentally determined and various eddy-structure models have been proposed. So far very little of the existing information from the structure studies has been included in the current prediction procedures.

Recently, attempts have been made to introduce statistical methods into wall turbulence analysis, as well as to include available data on wall turbulence structure. One possible approach is based on the use of the Cameron–Martin–Wiener method for the investigation of nonlinear random processes by expanding them in infinite series. The first term of the series is an exact Gaussian process and the higher order terms contribute successive corrections [11, 12]. Another approach, more under the influence of the structure studies approach, consists of representing wall turbulence as a random superposition of appropriate characteristic waves [13]. The development of both approaches is strongly dependent on the experimental statistical studies in the wall layers.

C. ROLE OF THE EXPERIMENT

Both physical and mathematical models of the wall turbulence rely on experimental evidence. Integral prediction methods and simple differential procedures, such as the mixing length concept, are based on experimental data on the characteristics of the mean motion, such as wall shear stress and mean velocity distributions. More elaborate models require experimental evidence of second, or higher order statistical moments of the relevant quantities. The more general the model, the higher is the order of the statistical moments for which information is needed. Statistical models require information on the repartition of the complete probability distributions, as well as the correlation functions.

At the Stanford Conference it was found that there is sufficient reliable experimental data only for the smooth-wall, two-dimensional, incompressible flows. Even for these simple flows the best data on the mean flow parameters have larger uncertainties than desired; in fact, larger than necessary to evaluate thoroughly various prediction procedures.

We might conclude that experiment plays a very important role in wall turbulence research. However, it must be stressed that the experimental

results are useful only when certain requirements on the quality of the experiment are met. Regarding mean flow parameters the accuracy is of prime concern. However, a move towards the solution of the wall turbulence problem on a more general basis depends essentially on the experimental data on the fluctuating motion parameters. Experimental evidence of the second- and third-order moments and correlations is needed at present, for the prediction procedures in current use. Such data, more or less reliable, do exist. It is felt, however, that real progress depends on the true statistical experimental studies in wall turbulence, which are at present very rare.

III. Current Experimental Methods

A. Measurements in Turbulent Flows

A description and critical review of all the measurement methods employed in turbulent flows would easily constitute a book. Therefore, only measurement methods of the quantities which are relevant to the general scope of the paper are mentioned. As turbulence is a dynamic phenomenon we will not include the methods which are insensitive to the fluctuations of the relevant quantities.

The importance of the fluid dynamics of flow has already been stressed. Of the two relevant quantities in an incompressible, isothermal flow, velocity and pressure, methods only have been developed for the measurement of the instantaneous velocities. Of all of these methods employed in wall turbulence studies, hot-wire anemometry is the one used most often, as it is the easiest to perform and very suitable for dynamic measurements up to high frequencies. Some of the other existing velocity measurement methods have certain advantages over the hot-wire method. These will also be reviewed shortly.

It would be desirable to have more information on the instream pressure fluctuations. Unfortunately methods involving pressure fluctuation measurements in the wall layers have not been developed. Quite recently such a method was developed and used in the study of a two-stream mixing layer [14]. It is based on a hot-film, bleed-type pressure transducer installed in a 1 mm diameter tube. Because of the dimensions of the tube, the method is not suitable for measurements in the vicinity of the wall, but can be used in the regions away from the wall.

As we are basically concerned with heat transfer, instream temperature measurement methods are also reviewed.

Turbulence is a random phenomenon and all the parameters of a turbulent flow have to be random. This applies to the parameters at the wall as well, a

fact which was recognized only recently. Fluctuations of the wall pressure, wall shear stress, and wall heat flux have been detected experimentally. Suitable methods for measuring wall temperature fluctuations have not been developed up to now. Wall pressure fluctuations have been measured by a number of investigators, the best results having been obtained with sensitive piezoelectric transducers mounted flush with the wall [15, 16]. Because of the dimensions of the sensors, wall pressure measurements have, in general, inadequate space resolution. Measurements of the wall shear stress fluctuations have been made by indirect methods based on analogies with heat and mass transfer. Heat transfer methods for the skin friction measurement are analogous to the hot-element anemometry in velocity measurements. Sensors consist of a micron thick resistor element having a response time of about 0.04 μsec [17]. Methods based on analogy with mass transfer are, in general, applicable in liquid flows only. They are based on an electrochemical reaction carried out at the surface of an electrode mounted flush with a wall [18, 19]. The accuracy of both methods depends on the accuracy of the calibration. Space resolution is also not wholly adequate. Fluctuations in the rate of heat transfer from a solid surface have also been measured using hot-film sensors [20].

The phenomena at the wall are the consequence of the turbulence characteristics of the in-stream quantities—velocity, pressure, and temperature. Fluctuations of the wall shear stress can be deduced from the instantaneous velocity profile gradients at the wall [21] or from the probability distributions of the velocities in the viscous sublayer [22]. Direct measurement of the wall parameter is of most value in cases where there is a lack of information on the corresponding in-stream quantities.

B. HOT-WIRE ANEMOMETRY

The hot-wire, or hot-film method for the velocity measurement is an indirect method. It is based on the relationship which exists between the rate of cooling of an electrically heated sensing element and the velocity of the fluid flowing around it. Heating can be achieved either by maintaining a constant current through the wire or by keeping its resistance quasi-constant by suitable electronic means. The latter, constant temperature mode of operation has definite advantages and has been almost universally used, since developments of solid state electronics have produced cheap and reliable amplifiers. Although the sensing element could have various forms, a 2 to 10 μm wire is most often used in moderate velocity gas flows.

An overall cooling rate of the wire

$$Q = Q_{cv} + Q_{cd} + Q_{rd}$$

consists of heat loss by convection (Q_{cv}), conduction to the supports (Q_{cd}), and radiation (Q_{rd}). For most applications, heat loss by radiation could be neglected. However, conduction to the supports for finite wire lengths is always present. For this reason the signal from the wire depends not only on the conditions pertinent to the convection from the wire, but on the overall configuration of the probe as a whole, including such influences as the inclination of the supports, the means by which the wire is attached to the supports, etc. [23]. To lessen these undesirable effects, often difficult to control, copperplating the ends of the wire has been carried out lately [23].

Although by copperplating the influence of the supports is not eliminated, it is diminished and, what is also important, it is better defined, especially concerning the contact between the wire and the supports. Since the conduction to the supports can not be neglected, the various cooling laws proposed in the literature, such as King's law or Collis law, are pertinent only to very long wires and are not directly applicable for wires of finite length. Careful calibration of the probes is thus a necessity. With copperplated wires of approximately the same length-to-diameter ratio, the form of the relationship between the signal and the velocity does not change from one probe to another. This greatly facilitates the tedious job of calibration and necessary recalibration of the probe after some hours of use.

The probes are usually calibrated in very weak turbulent flows. In these conditions one can speak of the steady state thermal equilibrium of the wire. For a linear relationship between the wire resistance and its temperature the thermal equilibrium is expressed by

$$E^2/R_w = H(R_w - R_a)/\beta R_0, \tag{3.1}$$

where R_w and R_a are wire resistances at the wire and the fluid temperature, and H is an overall heat loss coefficient.

The behavior of copperplated wires has been studied extensively by Davies and his group [23]. They found that the calibration of the wires is best described by a relation of the type

$$E^2 - E_0^2 = k \cdot U^n \cos^m \gamma, \tag{3.2}$$

where U is the velocity, γ the angle between the velocity direction and the normal to the wire, E_0 the potential difference at zero velocity, and k, n, m are empirical parameters. k and n are, in fact, not constant but both depend on the fluid velocity and the length-to-diameter ratio, l/d. The variation of these parameters with velocity is very large at low velocities. It was found that the difference $(n - m)$ is constant for a given probe but depends on the l/d ratio, the probe configuration, etc. [24].

In nonisothermal flows the influence of the flow temperature has to be taken into consideration. For moderate temperature changes it can be

assumed that the signal is proportional to the difference between the temperature of the wire and the flow temperature, so that the potential difference E_T at a temperature T is related to the potential difference E_a at a standard temperature T_a by

$$E_T^2 = E_a^2(R_w - R_T)/(R_w - R_a), \tag{3.3}$$

R_T and R_a being unheated wire resistances at temperature T and T_a, respectively. The influence of the flow temperature can be compensated for, in the case of slow temperature changes, by using another temperature sensing element. The influence of temperature fluctuations has to be taken into consideration in the determination of the velocity fluctuations.

From the form of the relation Eq. (3.2) it is seen that the wire response is strongly nonlinear to a velocity change, especially at low velocities. Electronic linearizers are now commercially available. With these, one may chose parameters k and n, for an operation in the given velocity range, and obtain a linearized output necessary for the precise determination of the intensity of fluctuations. However, under conditions of low velocity and higher turbulence intensity, which is usually the case in wall turbulence studies, no single k and n value can be selected for the whole range of instantaneous velocities. Under these conditions, other means of linearization have to be employed, such as the use of a digital computer.

In turbulence studies the fluctuating flow field is of greatest importance. The question then is: are the results of the calibration under conditions of very low turbulence level applicable to the determination of the fluctuating flow characteristics? The usual analysis is based on the assumption that the thermal inertia of the wire could be neglected so that the relation Eq. (3.2) is still applicable with E and U representing the instantaneous values. In fact, the wire is sensitive to velocity vector fluctuations so that, even if we assume that the component of the velocity parallel to the wire has negligible effect, the wire responds to both normal components. This makes the right side of Eq. (3.2) a very complicated function of the instantaneous velocities in the two normal directions (u_1, u_2). It is usually assumed that the u_1 component is much more effective than the u_2 component, so that the wire is essentially measuring the u_1 fluctuations. In the case of high turbulence intensity this is not true, and thus corrections have to be made. This is normally done by binomial expansion of the right-hand side of Eq. (3.2), with subsequent averaging and more-or-less severe assumptions about the relative orders of various terms [25]. With turbulence intensities of 20% or thereabouts this is a tedious and very inaccurate job. Some improvements on this procedure for higher turbulence intensities have been proposed by Siddall and Davis [26], who make certain assumptions about the nature of the fluctuating

voltage. They assume that the fluctuating component of the wire voltage has a square wave form—a crude enough assumption, but the approach being statistical it is basically much better than the usual procedure.

In fact, fluctuating velocity components are characterized by probability density distributions, which might depart more or less from the Gaussian distribution. The fluctuating voltage, being a function of the two normal velocity components, is then characterized by the form and the parameters of these probability density distributions, as well as by the correlation coefficient between the velocity components, the averaging being performed statistically over the perimeter of the wire. We shall return to this later in Section VII.

In addition, the time constant of the hot wire operated in a constant temperature anemometer circuit has a small but nonzero value, and the thermal inertia of the wire has to be taken into account. As shown in an analysis by Comte-Bellot [27], the neglect of thermal inertia could account for a large error in the determination of the odd moments of the probability density distribution and the evaluation of the power spectra under conditions of higher intensity turbulence. The error is strongly dependent on the nature of the fluctuations, i.e., on the probability density distribution of the velocity, and can be evaluated only by use of an analog computer.

A serious shortcoming of the hot-wire method follows from the fact that the wire is not sensitive to the direction of the velocity vector. For the determination of the instantaneous velocity components several wires, differently orientated to the flow, have to be employed. Cross-wire-probes are commonly used, with three-wire probes being already available commercially. Even neglecting the mutual interference of the wires, these probes are, however, not applicable to most turbulence studies near walls, due to their dimensions as compared to the thickness of the near-wall layers. Even away from walls the use of slanted wires is questionable when the turbulence intensity is high. With a slanted wire all three components of the fluctuations influence the signal, with the effectiveness in function of the yaw angle being difficult to evaluate.

Another serious shortcoming of the method, as employed in wall turbulence studies, is the so-called "wall effect." In fact, very near the wall the rate of cooling of the wire, and of the supports as well, is modified by the presence of the wall, increasing the apparent voltage difference. The most serious study of the problem has been done by Wills [28]. By careful measurements, he has established the corrections to wire readings as a function of the distance from a wall in a well-defined laminar flow. When employed in a turbulent flow, with the same probe and in the same channel, these corrections have produced overcorrected results for no apparent reason. To correlate the results for turbulent flow in the wall vicinity, Wills was obliged to

introduce an empirical constant $B = 0.5$ in the determination of the effective velocity U_e:

$$U_e = U - B(U - U_l),$$

where U is the uncorrected velocity and U_l the velocity corrected by the use of laminar corrections. Wills' corrections have been used successfully by many investigators. Coantic [29] proposed an improvement of the procedure which takes into account the influence of the probe configuration, wire l/d ratio, etc. The voltage difference as a function of the distance from the wall in zero velocity is first established for a given probe, and then the corrections given by Wills are applied.

Some studies of wall turbulence have indicated that the velocity is not uniform in the direction normal to the flow and parallel to the wall [30]. The space resolution of the wire is inadequate in the direction parallel to the wire. Information regarding the turbulence structure in this direction, therefore, could not be detected by a hot wire. This then represents another shortcoming of the method.

C. OTHER VELOCITY MEASUREMENT TECHNIQUES

Numerous other methods for velocity measurement are used which reflects the fact that one cannot be wholly satisfied with the hot-wire technique. We shall briefly review only those techniques which have potential advantages over the hot-wire method in any respect.

It is often useful to have an insight into the instantaneous phenomena in a whole region of the flow. The hot wire, being a single probe instrument, cannot provide information simultaneously over an extended region. Visual techniques, based on the photographic registration of the instantaneous velocities or even whole velocity profiles, have this possibility. In addition, these are direct measuring techniques since the velocity is determined from measurements of length and time. In the important advantages of the visual methods we can also include the possibility of the determination of velocity components, even in the wall vicinity, as well as a good space resolution in all three directions.

Visual techniques have to employ some kind of tracers. Valuable results have been obtained in steady flow with solid particules a few microns in diameter [31, 32]. In unsteady flows, and the instantaneous phenomena in turbulence are unsteady, the paths of the particles do not provide all the necessary information as the times associated with given particle locations are not known. This deficiency is overcome in the combined time-streak-marker hydrogen bubble technique developed at Stanford [30, 33]. Hydrogen bubbles, few microns in diameter, are generated at a fine wire acting as an

electrode. The bubbles are made visible by intense lighting at an oblique angle to the viewing direction. The wire has short sections coated with insulation at regular intervals, which provide marking in space, and is pulsed at regular time intervals. Motion picture photography of the combined time-streak markers thus produced allows the determination of the instantaneous velocities over a whole range of the flow. Wires can be placed parallel or normal to the wall for the corresponding velocity profile determination. Very good quantitative results have been obtained with this technique in low-speed water flows, revealing very interesting features of the wall turbulence structure.

Another interesting visual technique was developed in Toronto [34, 35]. This technique was based on flash photolysis—an ability of certain essentially colorless solutions to become colored under exposure to high intensity light or laser beams. Whole lateral velocity profiles are made visible by intense illumination of the trace at regular time intervals and employment of a high speed camera. As no extraneous tracers are introduced in the flow, the technique has the great advantage of being completely nondisturbing. However, as only time-marking and no streak-marking is employed, the technique is in other respects inferior to the combined time-streak-marker methods.

Apart from being, in general, restricted to liquid flows, visual techniques have in common two other more serious disadvantages. The time involved in reducing film data to velocity is considerable, even if a film reader is employed. In addition, high frequency fluctuations, over 20 Hz or so, are in general undetectable by visual techniques. These shortcomings make visual techniques basically unsuitable for statistical analysis.

Optical methods have recently begun to be employed for the velocity measurement [36]. Of these, the technique based on the Doppler shift of coherent laser light scattered from particles introduced in the flow has been successfully employed in liquid flows [37]. Durst and Whitelaw [38] have developed a new optical geometry and obtained preliminary results in applying the laser–Doppler method to gaseous flow. The method has the combined advantages of the hot-wire and the visual techniques. It is essentially direct, probeless, sensitive to flow direction and the high frequency fluctuations, and wholly suitable for statistical analysis. The main disadvantage of the laser–Doppler anemometer is that it is still in the development stage. The problem of the space resolution of the method has also to be solved.

With the exception of flash photolysis technique, visual and optical methods share with the hot-wire method a common deficiency. This is the wall effect which is important in close-to-the-wall investigations. Not much is known of this problem in visual and optical techniques except that it is present.

D. TEMPERATURE MEASUREMENT

Experimental investigations of the wall turbulence structure in non-isothermal flows are rare. For the determination of the temperature fluctuations and the velocity–temperature correlations they all employ sensors in the form of thin wires a few microns in diameter. The wires, acting as resistance thermometers, are preferred over microthermocouples because of the lower thermal inertia and smaller dimensions. More sophisticated temperature measurement methods, such as the pyroelectrical effect, have not been used in these studies.

For temperature measurements only, single wires are used [39–42]. Platinum or tungsten wires, 2 to 5 μm in diameter, are supplied with a constant current of 0.5 to 5 mA. With these small currents, wire heating is negligible so that the velocity influence is eliminated. Instead of metal wires, Blom [43] employed 5 μm quartz wires covered with a 0.1 μm thick layer of platinum. The response time of the sensors is from 0.1 to 1 msec, which makes them suitable for measuring temperature fluctuations. However, an amplification of the order of 10^3 is necessary. For high resistance sensors, the signal-to-noise ratio can be kept within the permissible range.

In turbulence studies simultaneous velocity and temperature measurements are of prime interest. Theoretically, this could be achieved by a single sensor as the wire could be made sensitive to both velocity and temperature fluctuations. However, theoretical models allowing the separation of the two influences on the signal have not been developed. In practice two sensors separated in space are employed, with the corresponding sacrifice in space resolution which might become critical in measurements close to the wall. The circuits of the two sensors can be independent [41–44] or a combined electronic circuit can be designed so that a velocity signal independent of ambient temperature fluctuations can be obtained [45].

In general, the supports of the temperature sensors are not at the same temperature as the wires. An appreciable amount of heat may be conducted along the supports in high temperature gradients near walls. Corrections for this effect can be applied in the case of mean temperature measurements. The influence of this effect on fluctation measurements is not well established.

IV. Survey of Illustrative Experimental Results

A. FLOWS WITHOUT PRESSURE GRADIENT ALONG SMOOTH WALLS

1. *Isothermal Flows*

It is quite natural that the most complete set of experimental evidence exists for the simplest flows—isothermal, incompressible, zero-pressure

gradient flows along smooth walls. In fact experimental turbulence studies of such flows are quite numerous, but it is out of the scope of this article to review them all. Somewhat arbitrarily we shall restrict ourself to those studies which have produced turbulence data in the region $0 < y^+ < 40$. The easiest turbulence characteristic to measure is the rms values of the streamwise velocity component, $k_1 = \sqrt{\overline{u_1^2}}$. Again, mention will be made only of the experimental investigations which have in addition provided information of some of the other characteristics.

With no intention of being exhaustive a list of such studies is given in Table I. As would be expected, most of the studies employed the hot-wire technique in air flows. However, also included are some studies in liquids,

TABLE I

WALL-TURBULENCE EXPERIMENTAL STUDIES

Author	Ref.	Year	Flow	Fluid	Technique	Re	y^+_{min}
Laufer	46	1951	Channel	Air	Hot-wire	3×10^4	2
Laufer	47	1954	Pipe	Air	Hot-wire	5×10^4	2
Klebanoff	48	1955	Plate	Air	Hot-wire	4×10^6	5
Marcillat	49	1964	Plate	Air	Hot-wire	—	1.5
Comte-Bellot	50	1965	Channel	Air	Hot-wire	6×10^4	4
Coantic	29	1966	Pipe	Air	Hot-wire	5×10^4	0.5
Bakewell	51	1966	Pipe	Glyc.	Hot-film	9×10^3	2
Kim *et al.*	52	1968	Plate	Water	H_2 bubble	3×10^6	4
Clark	53	1968	Channel	Air	Hot-wire	3×10^4	2
Iribarne *et al.*	54	1969	Pipe	Alcoh.	Pyrolysis	2×10^4	3
van Thinh	55	1969	Channel	Air	Hot-wire	4×10^4	2

employing other measurement techniques. The Reynolds numbers indicated in Table I correspond mostly to the maximum velocity. In two-dimensional channel flows they are based on the half width of the channel, in pipe flows on the diameter, and in boundary layer flows on the distance from the leading edge.

Turbulence characteristics, experimentally determined in the studies listed in Table I, are enumerated in Table II, excluding k_1 which was measured in all of them. An examination of Table II is not very encouraging. As it concerns the second statistical moments of the other two fluctuation components, only two out of eleven studies have measured k_3, and only three k_2, in the wall layers. Regarding correlation coefficients only three studies have determined $r_{12} = \overline{u_1 u_2}$, and none the other two, r_{13} and r_{23}. Comte-Bellot [50] noted that a few measurements have been made of the r_{13} coefficient, which was found negligible. In the wall layers, higher order moments of the streamwise component have been measured only by Marcillat

TABLE II

MEASURED TURBULENCE CHARACTERISTICS

Ref.	$\overline{u_2^2}$	$\overline{u_3^2}$	$\overline{u_1u_2}$	$\overline{u_1^3}$	$\overline{u_1^4}$	$\overline{u_1^5}$	G_{11}	G_{22}	G_{33}	R_{11}	$R_{11}x$	P^+	W^+
46							+						
47	+	+	+				+					+	+
48					+		+					+	+
49				+	+	+							
50				+	+		+						
29							+			+	+		
51							+			+	+		
52	+		+				+			+		+	
53	+	+					+	+	+				
54			+									+	+
55										+			

[49] and Comte-Bellot [50], with some data being provided by Klebanoff [48] on $\overline{u_1^4}$. No data exist for these moments of the other components. Some measurements of the triple and quadruple correlations have been provided only by Laufer [47].

Turbulence energy balance terms have been determined in a few studies. Data on the statistical moments of the streamwise component derivatives in the x_1 direction have been supplied only by Comte-Bellot [50]. It is interesting to note that next to k_1 the characteristic most often measured in these studies is the energy spectrum of the streamwise component. Only Clark [53] has provided data on the spectra of the other components in the wall layers. The autocorrelation function of the streamwise component $R_{11}(\tau)$ has received attention lately. Coantic [29] also determined the cross-correlation coefficients $R_{11}(x_3, \tau)$, while Bakewell [51] made measurements of the $R_{11}(x_1, x_3, \tau)$.

Figure 1 gives a summary of the k_1 distributions in the wall layers determined in the studies listed in Table I. Distributions are presented in the usual dimensional form, taking the friction velocity u_* as the velocity scale in an attempt to make them universal for various flows. As may be seen from Fig. 1 the nonuniversality of the distributions is striking. It is true that these data have been obtained in studies over a period from 1951 to 1969, for various Reynolds numbers, and with various fluids. Nevertheless, all these distributions correspond to flows without pressure gradient, along smooth, straight walls. And even if we take into consideration only the flows in two-dimensional channels, like those corresponding to refs. [46, 50, 53, 55] of Table I, discrepancies of up to 40% are found. In Fig. 2 existing data on the k_2 and the the k_3 distributions are plotted, and in Fig. 3 and 4 the data on the $\overline{u_1u_2}$ distributions and the turbulence production, respectively.

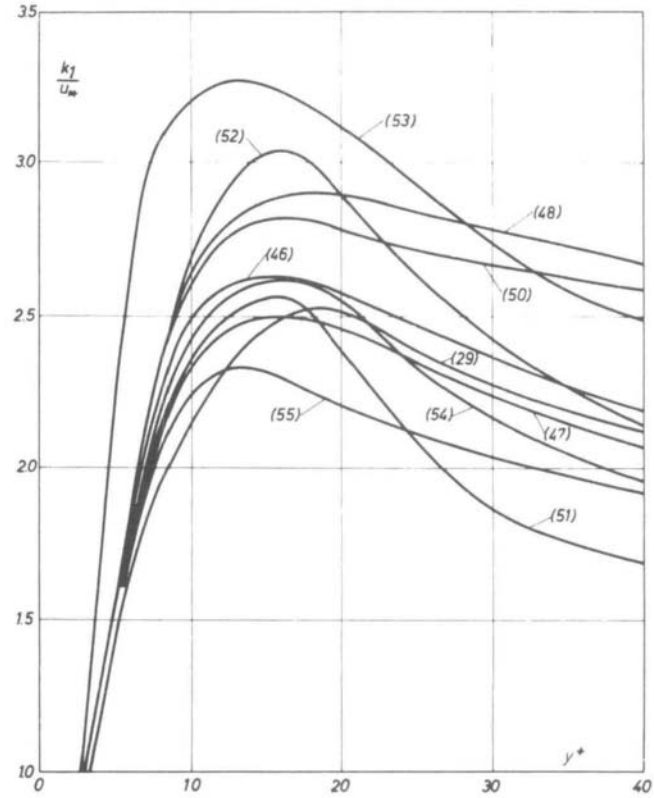

FIG. 1. Nondimensional turbulence intensity distributions of the streamwise component in the wall layers. Numbers correspond to the reference list.

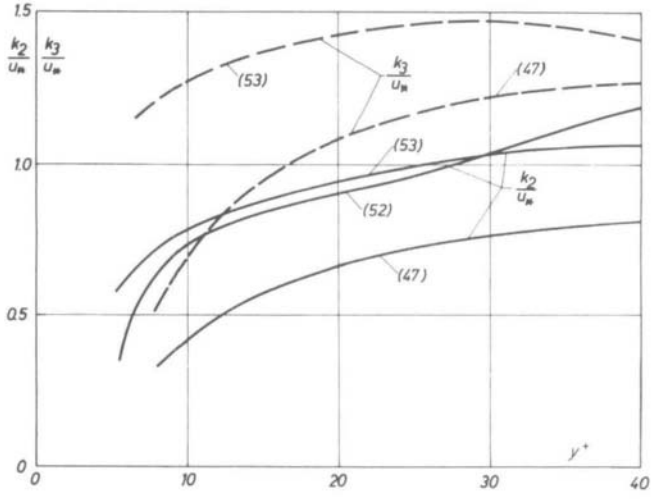

FIG. 2. Nondimensional turbulence intensity distributions of the other components in the wall layers.

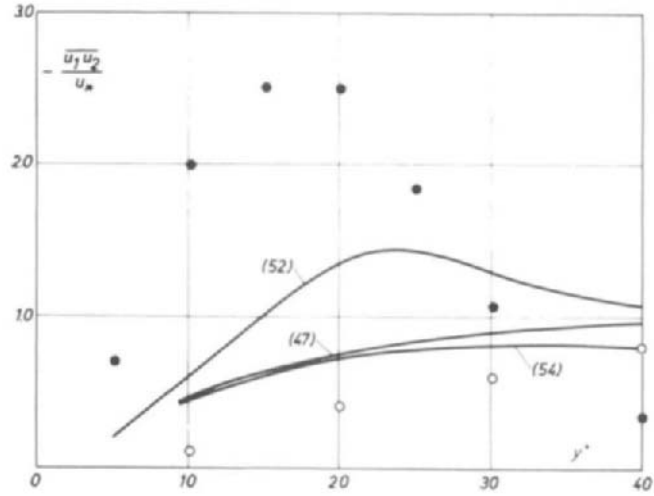

IG. 3. Shear stress distribution in the wall layers. ●, Shear stress during bursting time; during quiescent period [52].

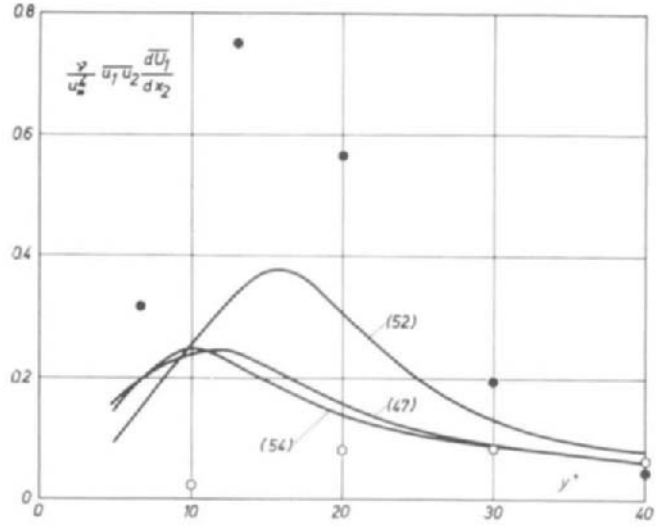

FIG. 4. Turbulence energy production distribution in the wall layers. ●, Turbulence production during bursting time; ○, during quiescent period [52].

Interesting evidence on the wall turbulence structure has been provided lately by visual studies. Popovich and Hummel [21], using the flash photolysis method, have obtained instantaneous velocity profiles in the viscous sublayer of a pipe flow. They have found that only in a layer $y^+ = 1.6$ thick are the profiles always linear, but with variable slope. In the region from

$y^+ = 1.6$ to $y^+ = 35$ very disturbed flow conditions prevail, with the nonzero probability of occurrence of either linear or turbulent profiles.

In the long range studies at Stanford, using the combined time-streak-marker technique, it was shown that a streaky structure dominates the wall layers for $y^+ < 40$ [30]. This structure consists of an alternating array of high and low speed streaks, transverse to the flow, with the streak spacing being correlated by the friction velocity [52]. This structure "bursts" intermittently with a characteristic frequency depending on the pressure gradient. It was shown quantitatively that essentially all the turbulence production in the wall layers does occur during bursting times [52]. This is illustrated in Figs. 3 and 4 where the average turbulent shear stress and turbulence production during a bursting time are compared with the corresponding values during a quiescent period [52].

In conclusion, we might say that at present we possess only scattered bits of informations on the complex structure of the wall turbulence, even in the simplest flows. The hot-wire technique has provided a considerable body of data, but only on a number of statistical moments out of an infinite array of moments that describe the turbulence structure. In addition, the data obtained in the wall layers are not reliable enough. For the reasons laid down in Section III, the hot-wire signal in the vicinity of the wall and in high intensity turbulence is not free from various influences, and the corrections are mostly inadequate.

Visual techniques are not suitable for a real statistical analysis. Kline *et al.* [56] claim that there is an extreme loss of information arising from the time-averaging done by the hot-wire technique. This is true as long as only isolated moments are concerned. A complete statistical description, consisting of the probability distributions and the autocorrelation functions, determined in a statistical way, and with an adequate accuracy contains all the relevant information. The hot-wire technique is essentially capable of providing such descriptions. However, it is necessary beforehand to perform a statistical analysis of the hot-wire signal, and determine precisely all the extraneous influences. It is probable that this could not be done with the hot-wire method alone, and that the help of more elaborate techniques, optical or visual, would be needed. However, it is felt that this is the only way to cope with the complexity of the turbulence problem.

2. *Nonisothermal Flows*

The situation being what it is for simple, isothermal flows one can hardly expect much from the studies of flows of higher complexity introduced by heat transfer at the walls. These studies are, however, necessary as a guide for the theoretical models, as well as for the preparation of more advanced studies.

Experimental turbulence studies in the wall layers of nonisothermal flows are not numerous. Johnson [44] has done a very throughout investigation in the boundary layer of a flat plate downstream of a stepwise discontinuity in wall temperature. In addition to the turbulence characteristics of the velocity fluctuations he measured temperature fluctuation rms values, as well as double and triple correlations of temperature and velocity components. His results are very descriptive but of inadequate precision. In addition, data in the vicinity of the wall are not numerous. Tanimoto and Hanratty [40] have reported measurements of temperature fluctuations well inside the region $0 < y^+ < 40$. Temperature spectra in this region have also been measured. Blom [43] measured temperature fluctuations down to $y^+ = 3$, as well as $\overline{u_2\theta}$ correlations, and the temperature spectra. All these studies have been done in air flows, with maximum in-stream temperature differences up to 15°C.

As shown by Bremhorst and Bullock [41], on the basis of spectral and cross-spectral measurements, a strong relationship exists between the temperature fluctuation and the longitudinal velocity fluctuation fields. This is supported by the high $\overline{u_1\theta}$ correlation coefficients found by Johnson [44]. These findings indicate that the temperature field could not be investigated without a thorough knowledge of the velocity field. As pointed out by Nicholl [45], who has investigated some dynamic effects of the heat addition, correlations of the type $\overline{u_i\theta}$ represent a flux of mass, not a flux of heat. Consequently, a quantitative analysis of the temperature fluctuations, as measured by a wire thermometer, requires that a statistical analysis of the signal be made. For such an analysis statistical information on the velocity components is needed.

B. VARIABLE PRESSURE GRADIENT FLOW

In practice predictions are urgently needed for much more complex flows. In particular, actual technology demands increased heat transfer rates from the surface. It is generally known that an increase in the heat transfer rates could be achieved by the turbulization of the layers in the immediate vicinity of the heated wall. Successful prediction procedures in such flows have to rely on the knowledge of turbulence parameters. As an example of what could be expected from experiments in similar situations some results are presented of a study made by the author.

Some experimental investigations of the adverse pressure gradient flows have indicated that the wall layers are turbulized under the influence of the pressure gradient [57, 58]. We have arrived at the idea of utilizing this effect for the promotion of heat transfer in channel flows. Preliminary results

obtained in a divergent–convergent channel show a substantial increase of the local Stanton number in the zone of the highest adverse pressure gradient [59].

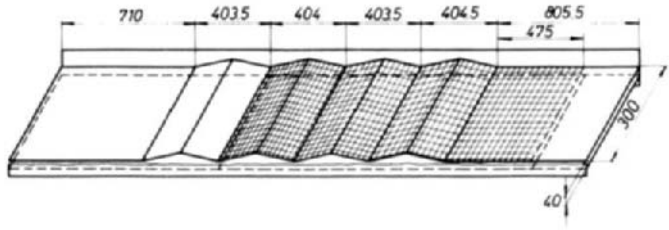

FIG. 5. Divergent–convergent test channel.

The possibility of obtaining high turbulence rates in the vicinity of a smooth wall, easy to approach with a probe, led to the construction of the test channel shown schematically in Fig. 5. A succession of four divergent–convergent sections is obtained by profiling one of the channel walls. The divergence angle is 16° and the inlet–outlet flow area ratio 2.5:1. At the exit of the channel a parallel wall section is provided. Two of the channel walls can be heated electrically, and are equipped with numerous embedded

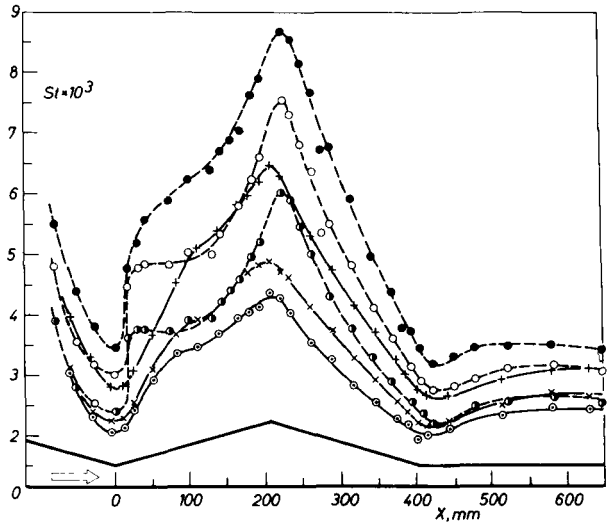

FIG. 6. Local Stanton number distribution along the test channel.

Re	Profiled wall	Straight wall
7.5×10^4	●	+
12.4×10^4	○	×
18.2×10^4	◑	⊙

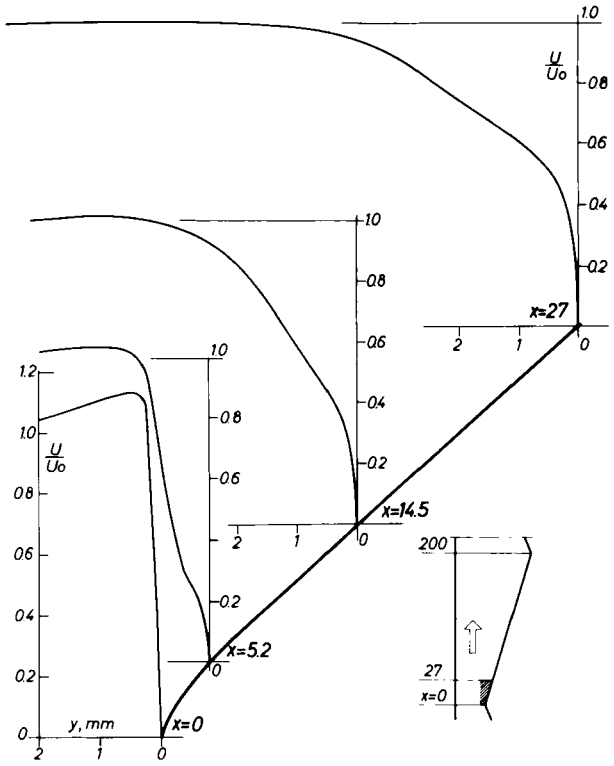

FIG. 7. Mean velocity distributions along the profiled wall at the diffusor entrance.

thermocouples. Any cross section of the last divergent–convergent section, and the portion of the straight wall section, could be investigated by a probe traversing mechanism. Other details are given elsewhere [60].

Measurements of the local Stanton number, obtained on the basis of the local wall temperature and the fluid bulk temperature measurements, are given in Fig. 6 for three flow Reynolds numbers. The interesting features are a sharp increase of the Stanton number value immediately after the entrance and the exit of the divergent section, and the difference in Stanton number values corresponding to the profiled and the straight wall in the same cross section.

The results of the mean velocity and temperature profile measurements have been reported [22, 42, 60, 61]. In Fig. 7 mean velocity profiles in the wall layers adjacent to the profiled wall, in four cross sections immediately after the entrance in the diffuser, are presented. Distributions of the corresponding longitudinal turbulence intensities are plotted in Fig. 8. The mean velocity profile at the inlet ($x = 0$) has a pronounced maximum and

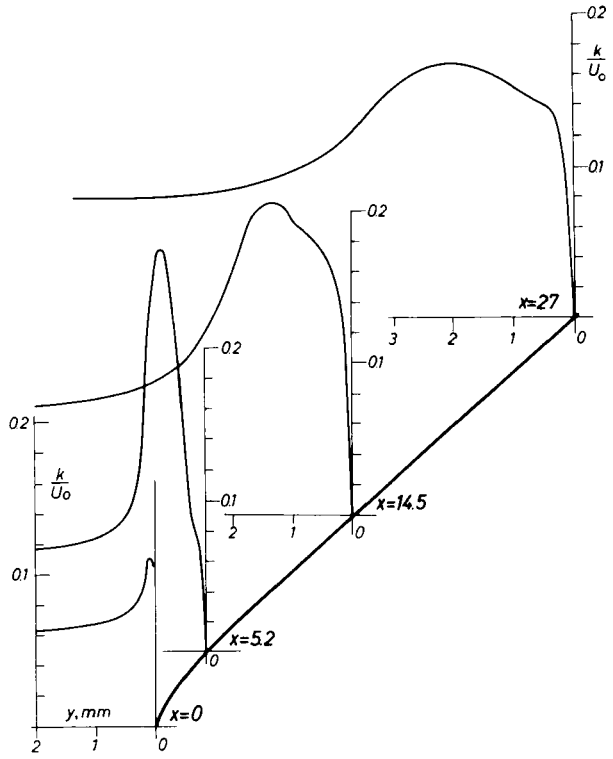

FIG. 8. Turbulence intensity distributions along the profiled wall at the diffusor entrance.

a steep gradient at the wall and indicates a laminarization of the wall layers due to the flow acceleration in the preceding convergent section. The maximum turbulence intensity is around 10% of the velocity at the center of the channel (U_0). Only 5 mm downstream the profile changes completely, exhibiting an inflection point separating a wall layer from the bulk of the flow. At the wall, the velocity gradient is still steep. The turbulence intensity increases to 27% of the U_0 and a narrow zone of high turbulence production can be detected, while in the wall layers the turbulence intensities are much lower. Further downstream the velocity profiles tend to an equilibrium with pronounced characteristics of adverse pressure gradient flows. The zone of high intensity turbulence is gradually spreading, penetrating slowly into the wall layers. Velocity profiles have been measured between $x = 0$ and $x = 5.2$ [22]. There is no apparent indication of the flow separation, although the profile at $x = 2$ has a characteristic appearance of a reattachment profile. Nondimensional turbulence intensity (k/u_*) distributions in

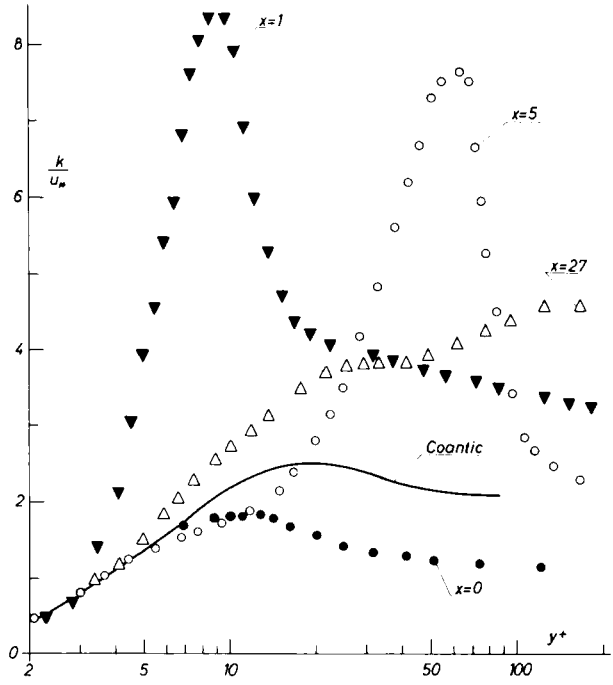

FIG. 9. Nondimensional turbulence intensity distributions along the profiled wall at the diffusor entrance.

the corresponding cross sections are given in Fig. 9. Only qualitative conclusions could be drawn from Fig. 9.

The example presented is obviously of great complexity. The flow structure changes abruptly from one cross section to another separated by a few millimeters. Turbulence intensities are of the order of 30% of the mean velocity, and incipient or steady flow separation is not excluded. However, such flows are encountered in reality and we have to study them. The measurement techniques at our disposal are inadequate for this They have to be improved to be able to produce quantitative results in all real flows.

V. Hot Wire–Cold Wire Experimental Method

A. CHOICE OF THE METHOD

What would be most desirable for experimental investigations in non-isothermal turbulent flows is a method by which velocity *and* temperature

could be measured *simultaneously* and by the *same* sensing element, having negligible dimensions, high sensitivity, and low inertia for both velocity and temperature. Only such a method would be capable of producing true velocity–temperature correlation measurements.

Theoretically, such a method exists. As suggested by Corrsin, a hot wire is sensitive to both velocity and temperature, so that when operated by two different current intensities it gives information on velocity and temperature fluctuations, as well as on the correlation coefficient between them. But when operated under the best conditions for velocity measurements, the sensitivity to temperature is an order of magnitude lower. This is why the method has been employed only by few investigators and without satisfactory results. However, it is felt that this method has not been fully investigated as yet and that it still is potentially promising.

As mentioned previously, experimental investigations of the velocity–temperature correlations usually employ two different sensors for the temperature and the velocity measurements. As a rule, a hot wire is used as a velocity sensor, and either a wire resistance thermometer or a microthermocouple is used as a temperature sensor. An obvious disadvantage of this method is the necessary space separation of the two sensors, which makes it unsuitable for measurements close to a wall under conditions of high velocity and temperature gradient. On the other hand a reduced space separation leads to mutual interference of the probes.

Another method, based on the use of the same sensor for both velocity and temperature measurements, the so-called hot wire–cold wire method, is used less frequently. The obvious disadvantage is that the measurements of the velocity and of the temperature are not performed simultaneously so that correlation measurements are not possible. It is felt, however, that the measurement of the velocity and the temperature, in the same space element, even if not carried out simultaneously, could provide valuable information on the physics of turbulent shear flows near walls.

The hot wire–cold wire method has been employed in our experimental investigations of nonisothermal turbulent shear flows and is described below in some detail. Care is given to the calibration of the sensor and the possible sources of errors. The statistical analysis of the signal is attempted in Section VII.

B. Description of the Method

A 5 μm diameter tungsten wire, approximately 1.5 mm long, was used as the sensing element. As noted previously, the velocity calibration and recalibration of the probe is made much easier by copperplating the ends of the wire. For temperature measurements by the same wire, an additional

gain is obtained by copperplating with respect to the necessary corrections for temperature readings under conditions of high temperature gradients. The probe, consisting of a tungsten wire with copperplated ends, spot-welded to stainless steel supports, is shown schematically in Fig. 10. Stainless steel was used for the supports because of its low thermal conductivity. The ends of the supports were copperplated after the welding. Much care was given to keeping the wire straight when heated in operation. To achieve this, the wires were subjected to some tension while welded to the supports.

The general electronic arrangement is shown in Fig. 10. For temperature measurements the wire acts as a resistance thermometer and is connected by four leads to a temperature bridge via a micro-ohm switch. Four leads are used to eliminate the resistance of the connecting cables. The bridge

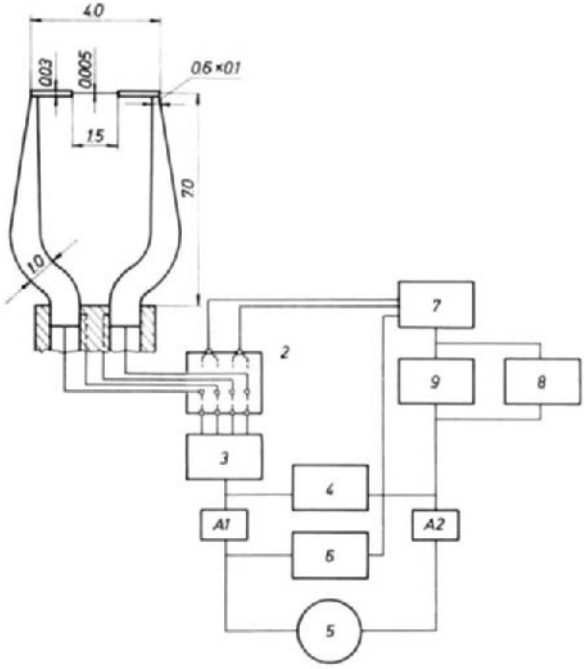

FIG. 10. Schema of the probe and the electronic circuit. 2, Micro-ohm switch; 3, Mueller bridge; 4, plotter; 5, tape recorder; 6, rms meter; 7, hot-wire anemometer; 8, digital voltmeter; 9, comparator; A1, A2, amplifiers.

used was a Leeds & Northrup Mueller Bridge, Type G2, precise to 0.0001 Ω. The bridge current was 2 mA. For mean value determinations a Sandborn plotter was used. For instantaneous temperature determinations the out-of-balance signal from the bridge was amplified by a factor varying from 1000

to 3500 in a Hewlett Packard, type 2470A, low noise dc amplifier. The amplified signal was registered on a magnetic tape with a speed of 152.4 cm/sec. The tape recorder used was an AMPEX Model FR-1300, operated in an FM mode. With 152.4 cm/sec tape speed the frequency response is up to 20 kHz. For a quick determination of the rms value, a DISA RMS Meter was used. The noise level was rather high because of the high amplification, amounting to approximately 3 mV, so that the signal-to-noise ratio based on the rms values was rather low (from 10 to 50).

For velocity measurements the probe was switched to a DISA Type 5501 Constant Temperature Anemometer operated at an overheat ratio of about 1.8. For approximate mean value determinations, the Sandborn plotter was used and the rms value of the fluctuations was read from the RMS Meter. For the determination of instantaneous velocities an appropriate dc value, measured by a digital voltmeter, was subtracted from the signal by the use of a comparator. The signal was then amplified in a dc amplifier by a factor varying from 1 to 3, and then registered on the magnetic tape operated with a speed of 152.4 cm/sec.

The registered signals of the velocity or temperature fluctuations were fed into a CDC-3600 digital computer for statistical analysis by replaying the magnetic tape with a speed of 4.76 cm/sec, via an analog-to-digital converting system. The system used was relatively slow so that the data were fed into the computer with a frequency of only 250 cps which, with the 1:32 reduction of the tape speed, amounts to an upper frequency limit of 8000 cps. Fifteen second long signals, sampled at 1/8000 sec, gave 120.000 digital values.

C. CALIBRATION

New probes, prior to the calibration, were subjected to a 24 hr aging process consisting of operating the wire at a 10% higher overheat ratio and at the highest flow velocity and temperature conditions encountered in the experiments.

Resistance–temperature, as well as the zero velocity potential difference–temperature relationship, were determined in a thermostat using a standard resistance thermometer. In the temperature range from 20 to 70°C the relationships are essentially linear:

$$R = R_0(1 + \beta T), \tag{5.1}$$

$$E_0 = C - D \cdot R, \tag{5.2}$$

with β having a value of approximately 0.004 1/°C.

The velocity calibration was performed by two methods. For higher

velocities, the calibration was performed in a modified DISA Calibration Unit, with modifications consisting of an air heater at the entrance to the unit. By this means, the flow temperature could be raised up to 70°C. A Fortier Micromanometer enabled reading pressure differences of 5×10^{-7} bars so that the precision of the calibration is adequate for velocities greater than 1 m/sec. In the statistical analysis of wall turbulence, instantaneous velocities lower than 1 m/sec are encountered. Moreover, the nonlinearity of the signal is highest in this velocity range so that a precise calibration for velocities lower than 1 m/sec is essential. For velocities from 0.1 to 2 m/sec the calibration was performed by placing probes in the centers of calibrated glass tubes in which stable laminar flow was maintained. The flow rate was determined by the use of miniature Laval nozzles.

The calibration results are well represented by a relation of the type:

$$E^2 - E_0^2 = K \cdot U^n, \tag{5.3}$$

K and n for different velocity ranges being given in Table III for the flow temperature $T_a = 25.8°C$. Very high nonlinearity of the signal at low velocities is evident. The potential difference E_T at a temperature T is adequately related to the potential difference E_a at a standard temperature T_a by

$$E_T^2 = E_a^2\left(\frac{R_w - R_T}{R_w - R_a}\right), \tag{5.4}$$

the subscripts w, T, and a being pertinent to the temperature of the wire, and the temperatures T and T_a, respectively.

Probes slowly change their characteristics in use. However, as long as the wires remained straight it was found that the relations Eqs. (5.1) and

TABLE III

HOT-WIRE CALIBRATION

Velocity range (m/sec)	K	n
0–0.4	23.79	1.60
0.4–0.7	11.31	1.02
0.7–1.0	10.02	0.88
1.0–1.4	9.15	0.725
1.4–2.0	9.08	0.645
2.0–4.0	9.61	0.555
4.0–7.0	10.07	0.515
7.0–13.0	10.71	0.49
13.0–27.0	11.29	0.47
27.0–40.0	11.93	0.45
>40.0	12.72	0.435

(5.2) are still valid with the same values of the parameters with the exception of R_0, which is easily determined in each experiment. A tedious and time-consuming recalibration of the probes is therefore eliminated.

D. WALL EFFECT

1. *Velocity*

As already mentioned, the rate of cooling of the hot wire and its supports is modified in the vicinity of the wall by the presence of the solid surface. This "wall effect" presents serious problems in wall turbulence studies in which it is important to approach the wall as closely as possible.

The problem has not been solved theoretically; thus, an empirical approach must be employed. For the determination of mean velocities we have used the method introduced by Wills [28], with the improvements proposed by Coantic [29]. For each probe to be used in the experiments, modifications to the wire response as a function of the distance from a solid surface under zero velocity conditions have been established. This was done by allowing the probe to approach a wall made of the same material used in the experiments, the exact distance of the wire from the wall being determined by precise optical means. A typical relationship

$$E_w^2 - E_0^2 = f(y), \tag{5.5}$$

where E_w is the apparent, and E_0 the corrected wire potential difference for zero velocity, and y is the distance from the wall, is shown as curve A in Fig. 11. To obtain the corrected wire potential difference for nonzero velocity (E_a), use was made of the measurements of Wills [28], from which the quantity

$$\Delta E^2 = (E_0^2 - E_a^2)/\pi\lambda l R(T_w - T_a) \tag{5.6}$$

was taken, where λ is the air thermal conductivity, l the active length of the wire, R the operating resistance, T_w the operating temperature of the wire, and T_a the air temperature. Finally, the relationship

$$E_w^2 - E_a^2 = E_w^2 - E_0^2 - \pi l\lambda R(T_w - T_a)\,\Delta E^2 \tag{5.7}$$

is obtained and presented as curve B in Fig. 11.

The relation Eq. (5.5), which is easily reproducible for a given probe, is used as a precise means of determination of the actual distance of the wire from the wall in the experimental channel. After the wire had approached the wall as near as possible, the air flow was stopped and the position of the wire determined, using the relation Eq. (5.5).

As also found by Wills [28], the corrected velocity $U(E_a)$, obtained on the

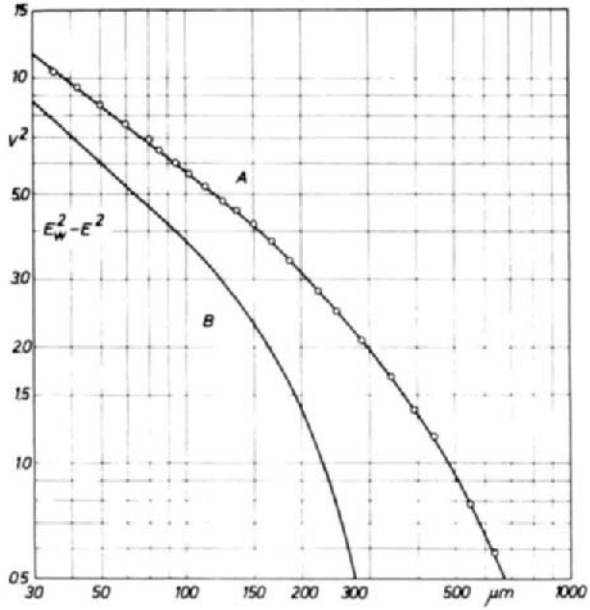

FIG. 11. Wall effect corrections. A, zero velocity; B, nonzero velocity. ○, Measured points.

basis of the corrected wire potential difference E_a, is a good match for the real velocity in the case of laminar flow but gives an overcorrected velocity in the case of turbulent flow. Wills, as well as the other investigators who employed his method, obtained fair results by introducing a second correction so that the velocity in turbulent flow is obtained from

$$U = U(E_w) - C_w[U(E_w) - U(E_a)], \tag{5.8}$$

where $C_w = 0.5$, an empirical correction factor found by Wills. We have also obtained fair results by using the same procedure, as seen from Fig. 12, in which the measured velocity distribution close to the wall is presented.

Apart from the wholly empirical character of the procedure (there is still much that is empirical in the hot-wire method), one cannot be satisfied with it for two reasons. First, as seen from Fig. 11, the corrections for zero velocity are obtained by using curve A, and for a velocity, however small but nonzero, by using curve B. There is an obvious discontinuity in the procedure. This is also illustrated by Fig. 12, in which unsatisfactory corrections are obtained for the distances closest to the wall. Second, there is no explanation for the need to use the empirical correction factor C_w in the case of turbulent flow, and why it has to be equal 0.5.

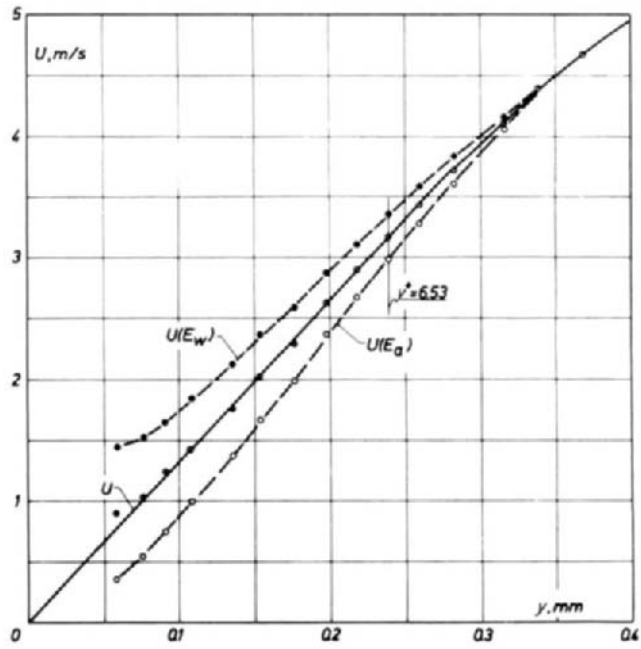

FIG. 12. Velocity distribution in the wall vicinity, cross section D, Re = 36,000. ●, Uncorrected values; ○, laminar corrections applied ($C_w = 1$); ⊙, turbulent corrections applied ($C_w = 0.5$).

2. *Temperature*

The probe prongs are inclined at an angle α to the wall so that in a non-isothermal flow there exists a temperature field in the probe prongs which leads to the heat conduction from the wire to the prongs. In the high temperature gradients found in the vicinity of the wall this conduction can not be neglected, so that the apparent mean wire temperature T_R is lower than the local flow temperature T_C.

The correction could be determined by solving the differential equations for heat conduction in the wire, in the copperplated ends of the wire, and in the prongs. These differential equations are of the type

$$\frac{d^2T_i}{dx_i^2} - \omega_i^2(T_i - T_f) = 0, \tag{5.9}$$

where x_i is the running coordinate, T_i the local temperature, T_f the flow temperature, and

$$\omega_i^2 = 4h_i/\lambda_i d_i$$

h_i being the corresponding convection heat transfer coefficient, λ_i the thermal conductivity of the material in question, and d_i the diameter. For the wire and copperplated ends $T_f = T_C$, but T_f varies along the prongs. We have used an approximation of the form

$$T_f - T_0 = (T_w - T_0) \cdot e^{-a \cdot x_3},$$

where x_3 is the running coordinate along the prongs, T_0 the air temperature at the cold end of the prongs, T_w the temperature of the wall, and

$$a = (q_w \cdot \sin \alpha)/\lambda_{fw}(T_w - T_0),$$

q_w being the wall heat flux, and λ_{fw} the thermal conductivity of the air for T_w.

The following relation for the temperature correction is obtained by solving the differential equations (5.9) with appropriate boundary conditions and assuming that the heat fluxes at the junctions, wire–copperplated ends and copperplated ends–prongs, must be equal.

$$\frac{T_C - T_R}{T_C - T_0} = \frac{\operatorname{th} \xi_1 \cdot \operatorname{th}^2 \xi_2 \cdot \operatorname{sh} \xi_2}{\xi_1 \operatorname{sh} \xi_3 [1 - (a/\omega_3)^2]} \times \frac{\operatorname{sh} \xi_3 [(a/\omega_3)^2 + (a/\omega_3) \operatorname{th} \xi_3 - 2] + \operatorname{th} \xi_3 \cdot e^{-al_2}}{[(\Omega_2/\Omega_3) \operatorname{th} \xi_3 + \operatorname{th} \xi_2][(\Omega_1/\Omega_2) \operatorname{th} \xi_1 \cdot \operatorname{th} \xi_2 - 1] \operatorname{sh}^2 \xi_2 + (\Omega_2/\Omega_3) \operatorname{th} \xi_3 \cdot \operatorname{th}^2 \xi_2}, \tag{5.10}$$

where

$$\Omega_i = \lambda_i \cdot \omega_i \cdot F_i \qquad \text{and} \qquad \xi_i = \omega_i l_i$$

and F_i are the corresponding cross section areas, with $i = 1$ for the wire, $i = 2$ for the copperplated ends, and $i = 3$ for the prongs.

By analyzing the above expression it can be shown that the increase in the length of copperplated ends l_3 diminishes the correction $(T_C - T_R)$.

In order to use the above expression to determine the correction $(T_C - T_R)$, the wall temperature and the wall heat flux must be known. These can be measured independently but Eq. (5.10) could be used also when they are only known approximately. In this case, a certain number of iterations are necessary. Certain assumptions are needed for the heat transfer coefficient h_3 which is variable along the prongs. We have evaluated h_3 on the basis of the flow velocity at $x_3 = l_3/3$. The resulting corrections are illustrated in Fig. 13, where the temperature profile in the vicinity of a smooth wall is plotted. It is seen that the values of the necessary corrections are substantial.

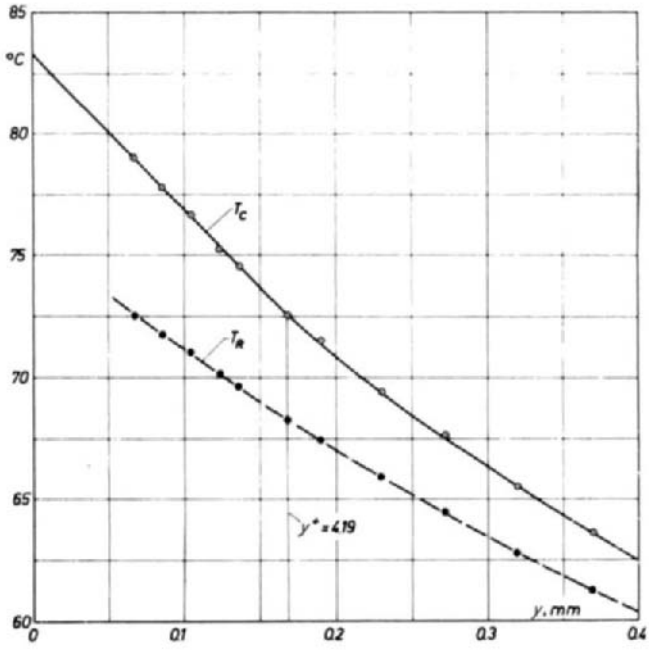

FIG. 13. Temperature distribution in the wall vicinity. ●, Uncorrected; ⊙, corrected temperatures.

VI. Experimental Results

A. Experimental Procedure

The experimental results presented in this section were obtained in the divergent–convergent channel installation described in Section IV. Measurements were made only in the wall layers adjacent to the straight plate of the channel where the flow is less disturbed and thus more suitable for statistical analysis.

Four cross sections of the channel, indicated in Fig. 14, were chosen for detailed investigation. Cross section A, located at the end of the divergent section, is characterized by the most severe adverse longitudinal pressure gradient occurring in the channel. On the other hand, the value of the favorable pressure gradient is highest in cross section C. Cross section B is situated midway in the convergent section where the degree of turbulence created in the divergent section is still high. Cross section D is located in the exit parallel-wall section of the channel where the pressure gradient is close to zero.

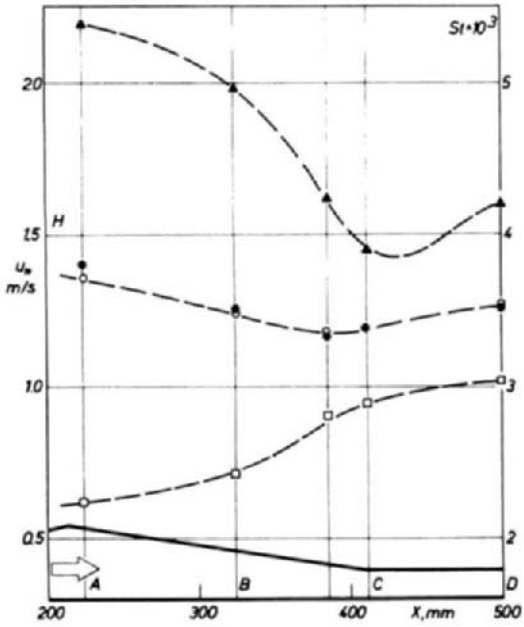

FIG. 14. Distributions of the friction velocity, form parameters, and local Stanton number along the channel. □, u^*; ○, H; ●, H_1; ▲, St.

The mass flow rate of the air in the channel was kept approximately constant in all experiments, corresponding to a Reynolds number, based on the hydraulic diameter, of about Re = 90,000. Only in cross section D were the investigations also made with Re = 36,000.

With the traversing mechanism fixed in a given cross section, velocity traverses were first made in isothermal flow without the wall heating. Subsequently, velocity and temperature traverses were made with the walls heated electrically. The wall heat flux was kept approximately constant in all the experiments at about $q_w = 2000$ W/m^2. With this heating rate and Re = 90,000, the maximum fluid temperature difference in a cross section was 30°C.

In all cross sections, at different distances from the wall, velocity and temperature signals, 30 sec long, were registered on the analog tape. Those signals were later analyzed statistically on the CDC-3600 digital computer.

B. MEAN FLOW RESULTS

1. *Isothermal Flow*

Local mean velocities at different distances from the wall were measured by the hot-wire method described in Section V on the basis of the mean

potential difference E. In the vicinity of the wall, "wall effect" corrections were applied using the modified Wills method. In all four cross sections at least three mean velocity values were determined inside the viscous sublayer ($y^+ < 6$). From the slopes of the mean velocity profiles in the viscous sublayer, which have been found linear (Fig. 12), wall shear stresses τ_w and corresponding friction velocities u_* have been determined. The distribution of the friction velocity u_* along the part of the channel under investigation is shown in Fig. 14 along with the distribution of the form parameter H calculated from the velocity profiles.

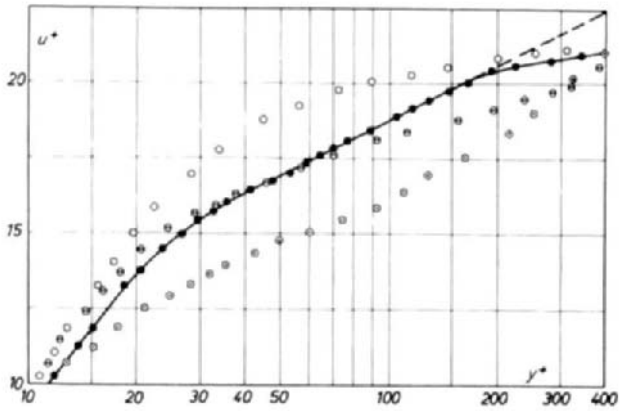

FIG. 15. Nondimensional mean velocity distributions in different cross sections. Isothermal flow, Re = 90,000. Cross section: A, ⊙; B, ⊖; C, ○; D, ●.

Mean velocity profiles in the usual nondimensional representation for all four cross sections are shown in Fig. 15. For the profile in cross section D, where the flow approaches a developed channel flow, the logarithmic law

$$u^+ = A \log y^+ + B \tag{6.1}$$

is confirmed with $A = 6.1$ and $B = 6.5$, in fair agreement with the results of Comte-Bellot [50]. However, in all three other cross sections the logarithmic portions of the profiles are hard to detect. The profile in cross section A, at the end of the divergent section, lies substantially lower and the profile in cross section C, at the end of the convergent section, substantially higher than the profile in D. The profile at cross section B approaches the profile at C in the wall layers and the profile at A away from the wall. For $y^+ < 14$ profiles B and C in the convergent section coincide and are higher than the profiles at A and D, which indicates an approach to the laminarization of the wall layers.

The distributions of the turbulence intensity k, made nondimensional

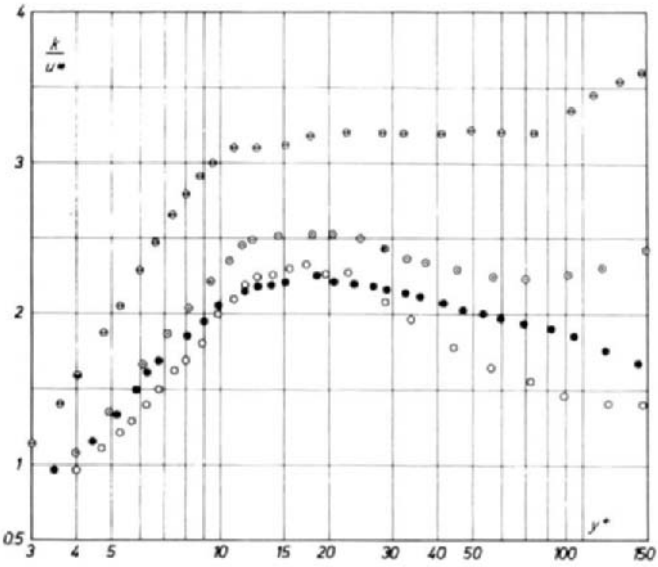

FIG. 16. Nondimensional turbulence intensity profiles. Isothermal flow, Re = 60,000. Cross section: A, ⊖; B, ⊙; C, ○; D, ●.

with the friction velocity u_*, are plotted against y^+ in Fig. 16. Turbulence intensities were obtained in the usual way on the basis of the rms values of the hot-wire signals, determined by rms meter. As the signal was not electronically linearized, for the reasons laid down in Section IV, a sort of linearization was performed in the computer by calculating k from

$$k = 0.5[U(E + e) - U(E - e)],$$

e being the rms value of the signal having a mean potential difference E, with the velocity U being determined directly from Eq. (5.3). Corrections to the wall effect have been applied. No correction for the high intensity of turbulence has been applied at this stage.

Turbulence intensity results obtained this way are presented in this section because although being not characteristic of the mean flow they are neither true characteristics of the turbulence in the statistical sense. With the turbulence intensity being equal to 40% of the local velocity, as it is at $y^+ = 5$ in cross section A, k could not represent longitudinal velocity fluctuations only. On the other hand, analog averaging at high intensity turbulence of a highly nonlinear signal is very doubtful. The results presented in Fig. 16 cannot be used for a quantitative analysis. Qualitatively, however, they do indicate a certain damping of the turbulence in the wall layers at cross section A. Once more they show nonuniversality of the turbulence intensity profiles in the wall layers at different cross sections.

2. *Nonisothermal Flow*

In nonisothermal flow at a given distance from the wall both velocity and temperature readings were taken. Velocity and temperature values were determined from these readings in the computer taking into account the mutual influence of these quantities upon each other. "Wall-effect" corrections described in Section V have been applied to both quantities in the vicinity of the wall (Eqs. 5.7, 5.8, and 5.10).

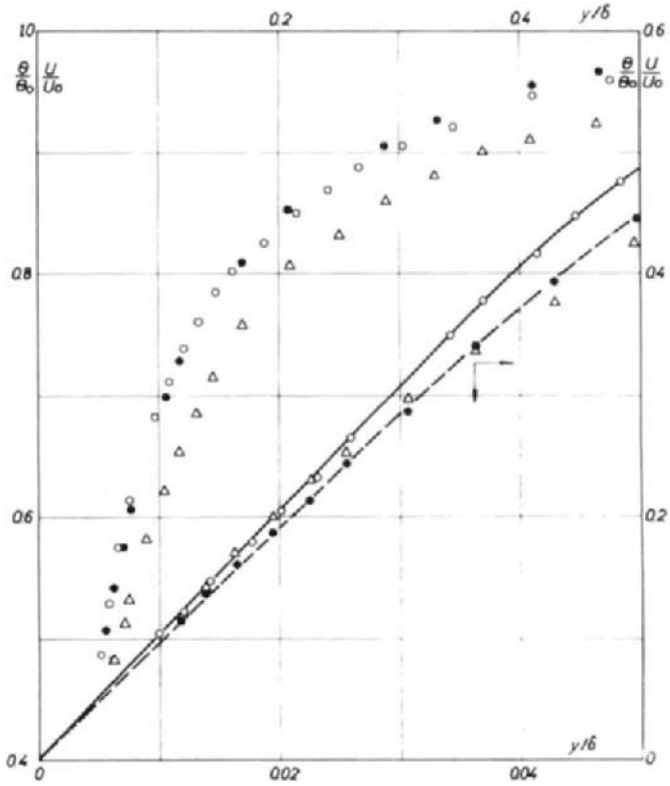

FIG. 17. Velocity and temperature difference profiles in the wall layers. Cross section D, Re = 36,000. △, Temperature difference θ/θ_0; ○, velocity, U/U_0—isothermal flow; ●, nonisothermal flow.

Velocity distributions in cross section D, corresponding to a flow with Re = 36,000, with and without wall heating, are presented in Fig. 17 along with the temperature difference distribution. Velocity and temperature values have been made nondimensional by the velocity (U_0) and the temperature difference ($T_w - T_0$) at the center of the channel ($y = \delta$) where

both profiles are fairly flat. As already noted by other investigators [45], velocity ratios U/U_0 corresponding to nonisothermal flow are lower than those for isothermal flow in the wall region, and become higher away from the wall at approximately $y/\delta = 0.15$. The friction velocity was calculated on the basis of the velocity gradient at the wall and the viscosity at the wall temperature (μ_w), with $y^+ = \rho_w \cdot y u_*/\mu_w$. Nondimensional velocity profiles in the usual semilogarithmic presentation are shown in Fig. 18. It is seen that the profiles for isothermal and nonisothermal flow fail to coincide, having, however, the same slope in the logarithmic region.

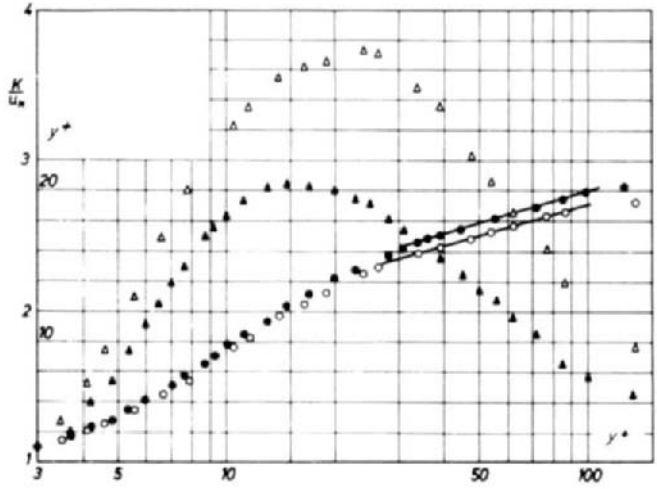

FIG. 18. Nondimensional velocity and turbulence intensity profiles in isothermal and nonisothermal flow. Cross section D, Re = 36,000. ●, Velocity—isothermal flow; ○, nonisothermal flow. ▲, Turbulence intensity—isothermal flow; △, nonisothermal flow.

In Fig. 18, the nondimensional turbulence intensity, k/u_*, profiles for isothermal and nonisothermal flow are also shown. The profiles are considerably different, k/u_* values corresponding to the nonisothermal flow being substantially higher, especially in the buffer region. We shall return to this later. Comparing Fig. 18 with Fig. 16 it is seen that the k/u_* values corresponding to the flow with Re = 36,000 are higher than those corresponding to Re = 90,000. A similar effect was reported by Coantic [29], indicating again the nonuniversality of the turbulence intensity profiles in the wall regions.

Form parameters H_1 given by

$$H_1 = \frac{1}{\delta^{**}} \int_0^{\delta} \left(1 - \frac{U}{U_0}\right) \frac{\rho}{\rho_0} \, dy \tag{6.2}$$

for nonisothermal flow and the cross sections under investigation, plotted in Fig. 14, are in a good agreement with the form parameters H for isothermal flow.

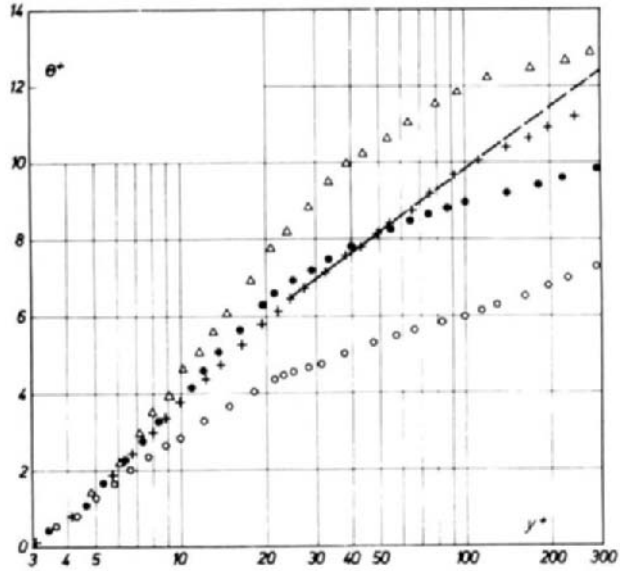

FIG. 19. Nondimensional temperature profiles in different cross sections. Re = 90,000.

Nondimensional temperature differences

$$\theta^+ = \frac{\rho_w C_p u_* (T_w - T)}{q_w}$$

for the four cross sections are plotted in Fig. 19 against y^+. The wall heat flux q_w determined from the temperature gradients at the wall was within 4% agreement with the flux determined from the dissipated heat. In cross section D, a logarithmic region corresponding to

$$\theta^+ = A_T \log y^+ + B_T \tag{6.3}$$

could be detected, with $A_T = 5.3$ and $B_T = 1.1$. A comparison with the velocity profiles gives a ratio $A_T/A = 0.87$, which is in fair agreement with the results of other authors [43]. The B_T value found is low, indicating a developing temperature profile [43]. Profiles corresponding to other cross

sections differ from the profile at D, as in the case of velocity profiles. Again, the profile at C indicates a certain laminarization, and the profile at A a turbulization of the wall layers. Local Stanton number values calculated from the temperature and velocity profiles are presented in Fig. 14. In agreement with the temperature profiles, the local Stanton number at cross section A is 39% higher than the Stanton number at C.

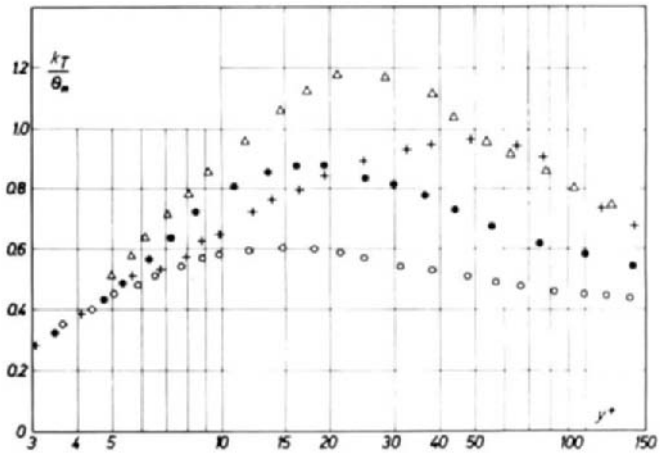

FIG. 20. Nondimensional temperature fluctuation rms value profiles in different cross sections. Re = 90,000. Symbols correspond to Fig. 19.

The rms values of the temperature fluctuations k_T, made nondimensional in the same way as the temperature differences, are presented in Fig. 20 for the four cross sections. Comparing temperature fluctuations with the velocity fluctuations at the cross section D one notes that the maximum is displayed away from the wall and that the absolute value of the nondimensional temperature fluctuations is considerably lower than the corresponding value of the velocity fluctuations. An interesting feature can be seen from Fig. 20. The temperature fluctuations are substantially higher in cross section C than those in cross section A, in contrast to the velocity fluctuations (Fig. 16).

C. EXPERIMENTALLY DETERMINED STATISTICAL CHARACTERISTICS

The first task was to determine the probability density distributions of the instantaneous velocities and temperatures at various distances from the wall. Concerning the velocities, one must be aware of the fact that the hot wire is sensitive to the intensity of the velocity vector, so that the probability density distributions measured by a hot-wire sensor correspond to this intensity and not to a single component of the velocity fluctuations. In the

case of nonisothermal flows an additional complication follows from the fact that the hot wire is also sensitive to the flow temperature, so that the influence of the temperature fluctuations has to be determined.

In all the cross sections, at various distances from the wall, 30 sec long hot-wire signals in isothermal flow have been registered on the analog tape running at maximum speed. Later the tape was replayed at a speed reduction of 1:32 and sampled with an analog-to-digital converter at a rate of 250 samples/sec so that the real-time sampling was 8000 samples/sec. The real-time sampling interval was 15 sec, giving 120,000 digital values. The digital data were processed by a CDC-3600 computer and registered on a digital tape in six records of 20,000 data each. In the process of registering the analog signal an appropriate subtraction of the dc value and a suitable amplification (not exceeding 3:1) was applied so that the voltage fluctuations were registered in the limits between 0 and 2.5 V.

For the amplitude analysis the 2.5 V range was divided into 1000 sections so that the sensitivity of digitalization was $s = 2.5/p$ mV, p being the

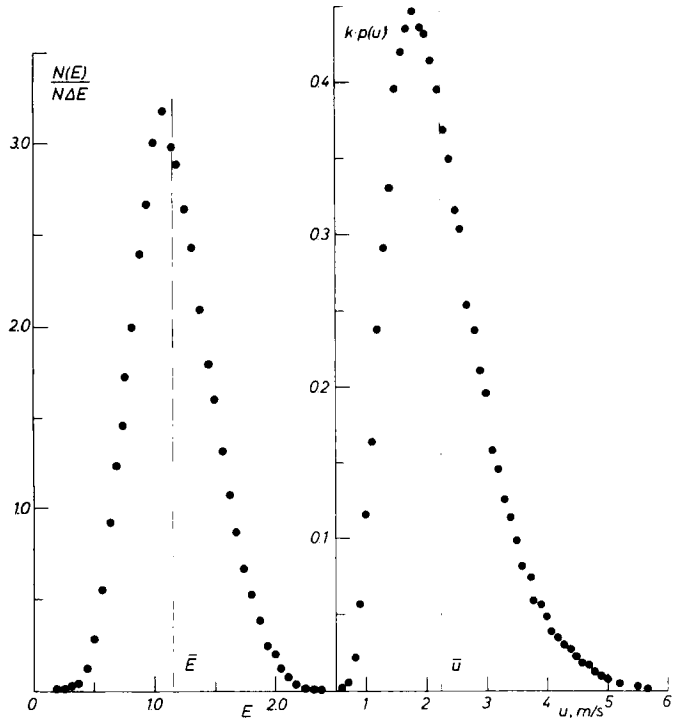

FIG. 21. Typical probability distributions of the signal (left) and of the velocity (right) in the vicinity of the wall.

amplification factor. A typical probability distribution of a hot-wire signal inside the viscous sublayer is shown in Fig. 21. Only one out of 25 points is shown. In obtaining the probability distribution of the velocity, care must be taken of the nonlinearity of the signal. The linearization was done in the computer. For each voltage fluctuation value a corresponding velocity value was obtained using expression Eq. (5.3). This is not enough since the sensitivity of the wire ($\Delta U/\Delta E$) changes in the range of the velocity fluctuations. Therefore, the velocity range ($U_{max} - U_{min}$) was divided into a suitable number of velocity intervals Δu (from 500 to 1000), and for each $U_n = U_{min} + N \cdot \Delta u$ ($N = 0, 1, 2, \ldots$) the frequency of occurrence is obtained by an interpolation of the probability distribution of the electric signal. Velocity probability density distributions corresponding to the probability distribution of the signal given on the left side of Fig. 21, calculated by this procedure, are shown on the right side of Fig. 21. Wall effect corrections were applied to each velocity value in the vicinity of the wall using the modified Wills method. For each signal analyzed, probability distributions were determined for two values of the empirical correction factor C_w appearing in expression Eq. (5.8), namely, for $C_w = 1$ and

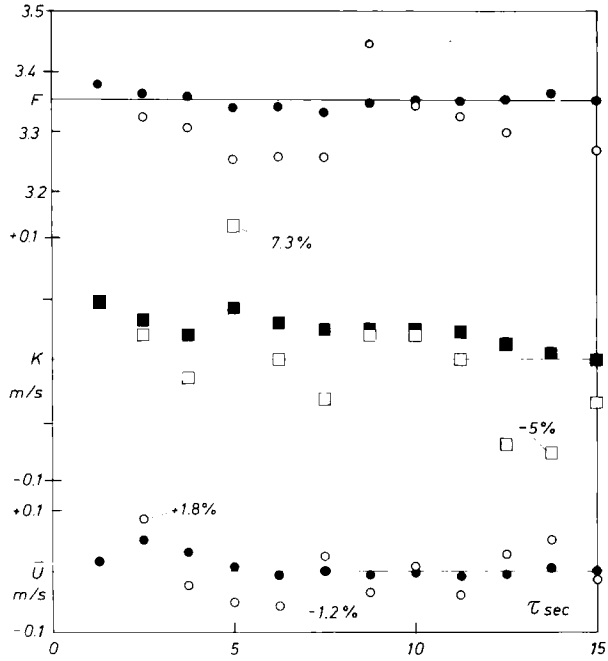

FIG. 22. Mean values of velocity, U, square root of the dispersion, k, and flatness factor, F, averaged over successive time intervals, $\tau_1 = 1.25$ sec (open symbols) and over time intervals $\tau = n \cdot \tau_1$ (solid symbols).

$C_w = 0.5$. $C_w = 1$ correspond to the laminar and $C_w = 0.5$ to the turbulent flow corrections proposed by Wills.

From the probability distributions determined, the statistical mean values as well as the central moments of order 2 to 6 were calculated. The adequacy of the chosen sampling time $\tau = 15$ sec was tested on a number of the signals. In Fig. 22, the variations in the mean velocity $\bar{U}$, dispersion k, and flatness factor F, averaged over successive time intervals $\tau_1 = 1.25$ sec, are plotted for a signal inside the viscous sublayer. Also shown are the values averaged over time intervals of $n \cdot \tau_1$, for $n = 1$ to $n = 12$. It is seen that the chosen sampling time $\tau = 12\tau_1$ seems to be just about adequate as it concerns dispersions.

The distribution of the statistically determined mean velocities in the vicinity of the wall for cross section D, with Re = 36,000, is compared in Fig. 23 with the distribution of the mean velocities determined from the

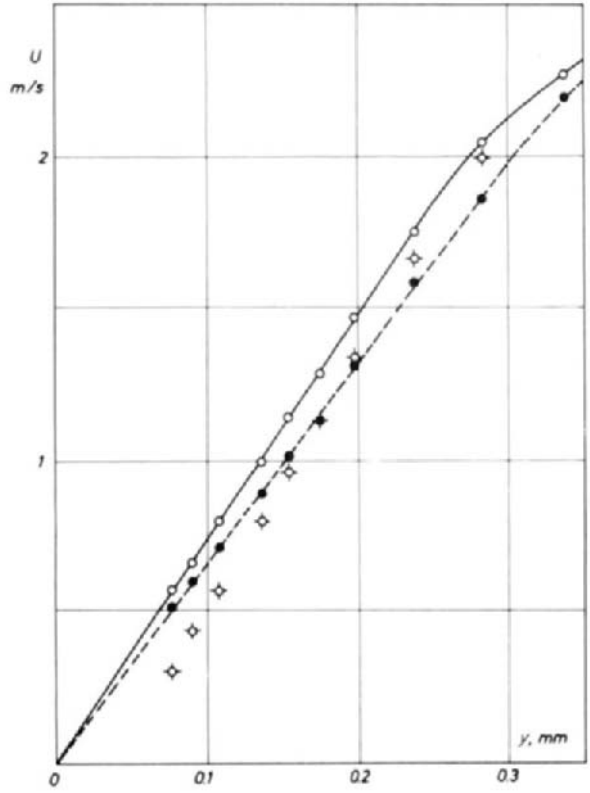

FIG. 23. Distributions of the statistically determined mean velocity, ○, and the mean velocity from the analog signal, ●.-◇-, Velocity determined with laminar corrections ($C_w = 1$).

analog nonlinearized signal. The difference between the two values is substantial in the region $y < 0.33$ mm where the wall effect corrections are applied. Also shown is the distribution of the statistically determined mean velocities calculated with the laminar wall effect correction factor $C_w = 1$. The latter does not have a linear trend in the viscous sublayer. However, it is felt that the question of the wall effect is still open. The difference in dispersion determined from the probability distributions and from the analog signals are of the same order in absolute values.

Distributions of the skewness factor

$$S = \frac{1}{k^3} \int_0^\infty (u - \bar{u})^2 p(u)\, du, \tag{6.4}$$

the flatness factor

$$F = \frac{1}{k^4} \int_0^\infty (u - \bar{u})^4 p(u)\, du, \tag{6.5}$$

the superskewness factor

$$SS = \frac{1}{k^5} \int_0^\infty (u - \bar{u})^5 p(u)\, du, \tag{6.6}$$

and the superflatness factor

$$SF = \frac{1}{k^6} \int_0^\infty (u - \bar{u})^6 p(u)\, du, \tag{6.7}$$

in the wall layers of the cross section D at Re = 36,000 are presented in Fig. 24. Wall effect corrections with $C_w = 1$ give somewhat higher values of all the above factors, as indicated in the case of the skewness factor in Fig. 24. All the factors have values substantially different from the values corresponding to the Gaussian distribution ($S = SS = 0$, $F = 3$, $SF = 15$). Inside the viscous sublayer these values became very high. It is interesting to note that both skewness factors became negative at approximately $y^+ = 15$ where both flatness factors are minimal.

The variations of the skewness and the flatness factors, plotted against y^+ for the four cross sections under investigation, with Re = 90,000, are shown in Figs. 25 and 26, respectively. Solid lines represent the measurements of Marcillat [49]. In the region outside the viscous sublayer, the highest S and F values are those corresponding to the cross section A, with those corresponding to the cross sections C and D having the lowest values. Inside the viscous sublayer a steep rise in both S and F values is observed for all four cross sections.

The temperature probability distributions were determined in a similar way. However, in the case of temperature, the signal is linear so that the

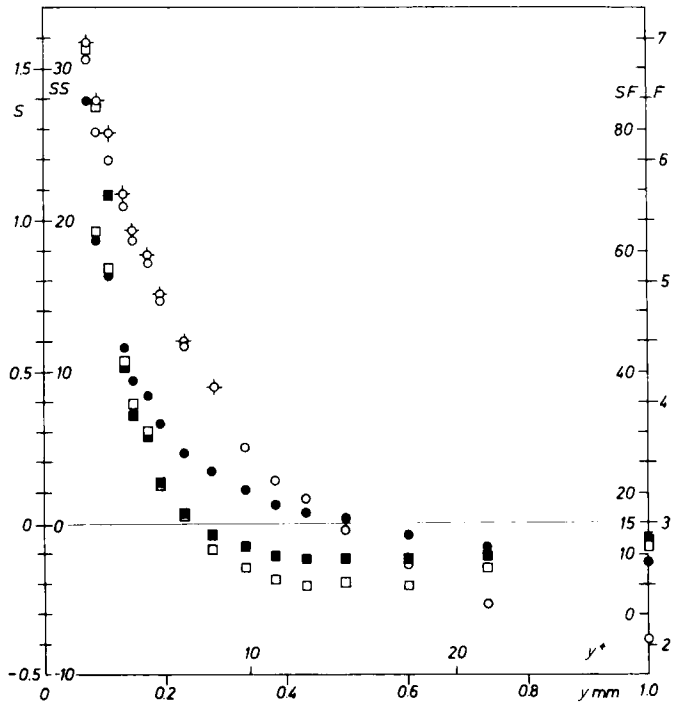

FIG. 24. Distributions of the higher order statistical moments. Cross section D, Re = 36,000. ○, skewness factor; ●, flatness factor; □, superskewness factor; ■, superflatness factor; ⊹, skewness factor for laminar corrections ($C_w = 1$).

probability distribution of the signal corresponds to the temperature probability distribution. Wall effect corrections were applied to the mean value only.

The sensitivity of digitalization was $10^2/p_T$ degrees, while the amplification factor p_T was from 2000 to 3500. The probability distribution of the noise signal was also determined and its statistical moments calculated. Central moments of the temperature distributions were corrected by corresponding moments of the noise signal. For instance, in the case of dispersion,

$$k^2_{T,\text{corr}} = k^2_{T,\text{meas}} - k^2_{\text{noise}}.$$

The corrected rms values were never less than 97% of the measured values. For other moments corrections were negligible.

The variations in the skewness, flatness, superskewness, and superflatness factors in the vicinity of the wall for cross section D is presented in Fig. 27 for the flow with Re = 90,000. The temperature difference ($\theta = T_w - T$) probability density distribution for $y^+ = 6.6$ in the same cross section

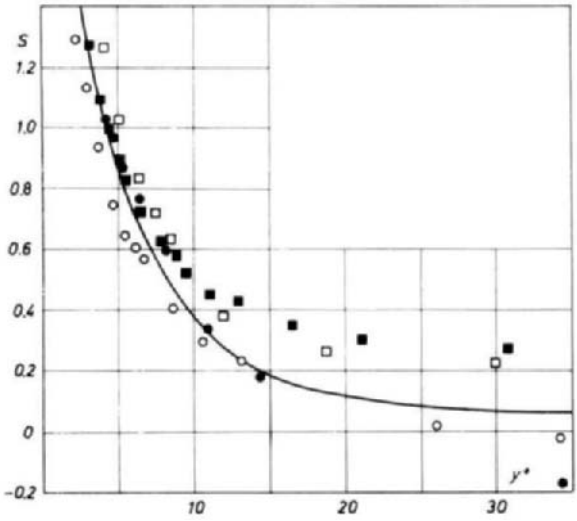

FIG. 25. Distributions of the skewness factor in different cross sections. Re = 90,000. Cross section: A, ■; B, □; C, ●; D, ○.

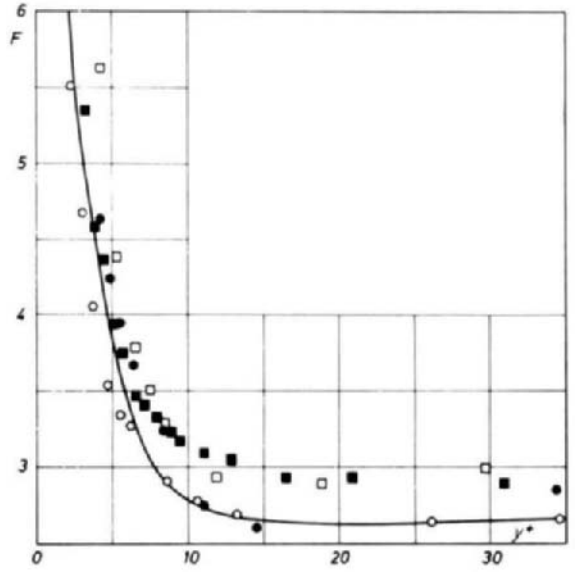

FIG. 26. Distributions of the flatness factor in different cross sections. Re = 90,000. Symbols correspond to Fig. 25.

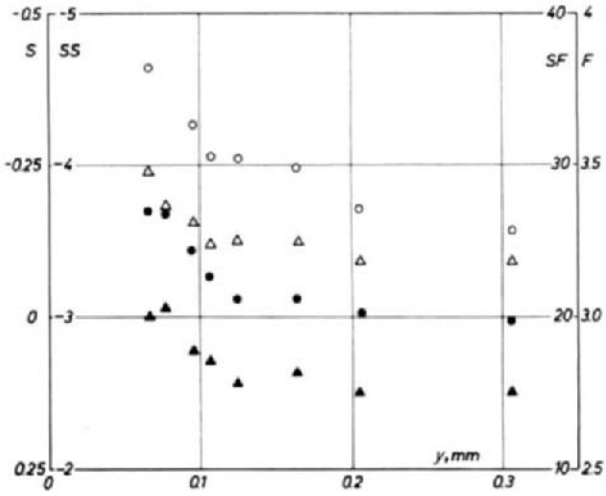

FIG. 27. Distributions of higher order statistical moments for temperature signals. Cross section D, Re = 90,000. ○, skewness factor; ●, flatness factor; △, superskewness factor; ▲, superflatness factor.

is given in Fig. 28, together with the corresponding velocity probability density distribution. There is a similarity between the two distributions, with the temperature distribution being closer to a Gaussian distribution. For all four cross sections under investigation skewness and flatness factor distributions are plotted against y^+ in Figs. 29 and 30. Comparison with Figs. 25 and 26 reveals the same general trend for the skewness and the flatness factor variations and for the velocities and the temperatures, thus indicating similarities of the probability distributions. Note that the skewness factors for the temperatures are negative as a consequence of the probability distributions being skewed in the sense of lower temperatures, while the corresponding velocity distributions are skewed in the sense of higher velocities. On the other hand, the variation of all the factors corresponding to temperatures is much less than in the case of velocities, especially inside the viscous sublayer.

Velocity and temperature rms values, determined from the probability distributions in cross section D in nonisothermal flow with Re = 90,000, are plotted in Fig. 31. On the same figure statistically determined velocity rms values corresponding to isothermal flow, as well as the rms values of the analog signal for the isothermal and the nonisothermal flows, are plotted. As already noted discrepancies between the statistically determined rms values and those determined from the nonlinearized analog signal are substantial, being, however, less in nonisothermal flow. Discrepancies

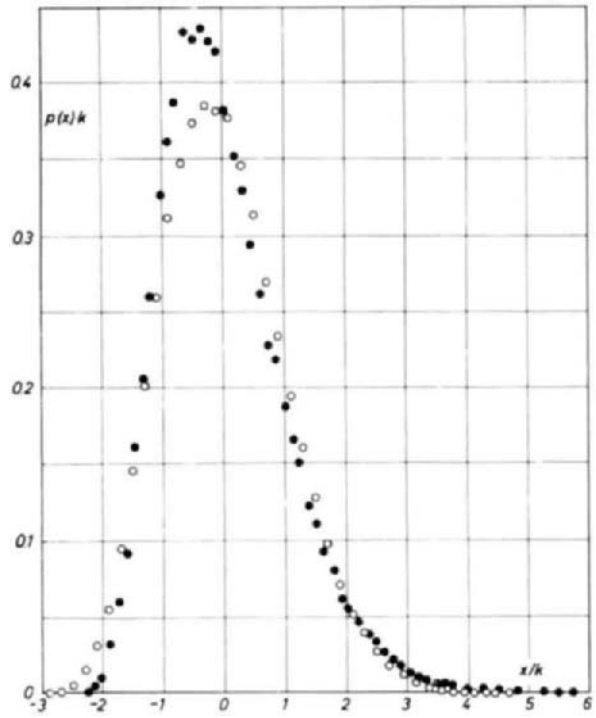

FIG. 28. Probability density distributions of the velocity, $x = u$, ●, and the temperature difference, $x = \theta$, ○. Cross section D, Re = 90,000, $y^+ = 6.6$.

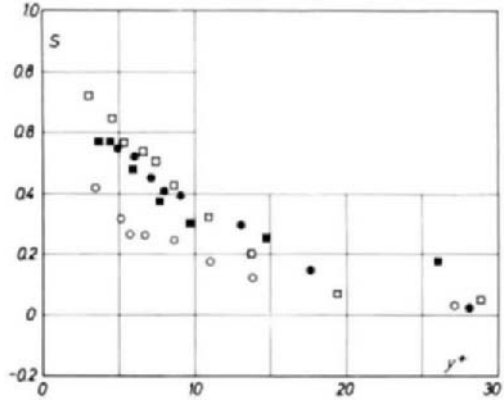

FIG. 29. Temperature skewness factor distributions in different cross sections. Re = 90,000. Cross section: A, ■; B, □; C, ●; D, ○.

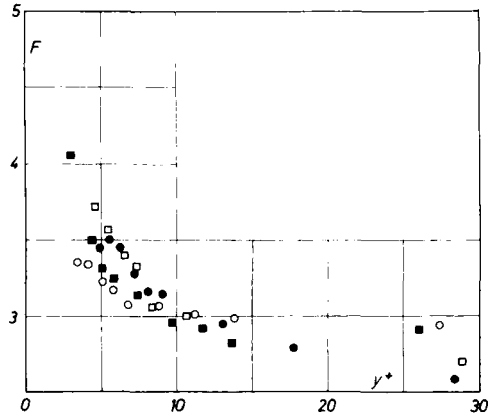

FIG. 30. Temperature flatness factor distributions in different cross sections. Re = 90,000. Symbols correspond to Fig. 29.

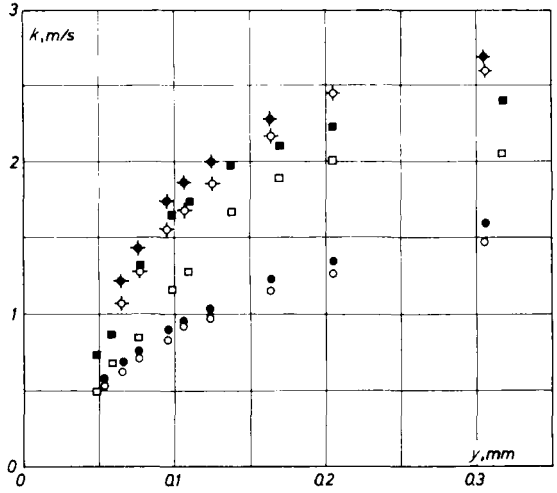

FIG. 31. Velocity and temperature rms value distributions. Cross section D, Re = 90,000. ○, temperature; ⊕, velocity—isothermal flow; ⊢, nonisothermal flow. Open symbol values determined from analog signal. Solid symbols, statistically determined values.

between the corresponding values for isothermal and nonisothermal flow are much less for the statistically determined rms values. Root-mean-square values in this particular flow were found to be approximately 10% higher for nonisothermal flow. Somewhat smaller discrepancies were found in the case of higher order moments. On the basis of the known sensitivity of the hot wire to changes in fluid temperature, Eq. (5.4), and the experimentally

determined temperature probability distributions, probability distributions of the temperature-provoked velocity signals were determined. Root-mean-square values of these temperature-noise signals, k_{ut}, were found to be at most equal to 10% of the velocity rms values. Taking into account that the correlation coefficient r_{ut} is not zero the true velocity dispersions k^2 could be obtained from

$$k_s^2 = k^2 + k_{ut}^2 + 2r_{ut}k \cdot k_{ut}, \tag{6.8}$$

where k_s^2 is the velocity dispersion in nonisothermal flow.

VII. Statistical Analysis

A. Scope of the Analysis

From the experimental results presented in Section VI one can get an impression of the importance of the true statistical analysis for serious wall turbulence studies. The intensity of the velocity fluctuations in the wall regions and the fact that the nonlinearity of the hot-wire signal is highest in this region of low velocities rule out the use of the electronic linearizers for precise measurements near walls. Digital analysis of the signal, with the linearization performed on the computer, and statistical averaging are the only alternatives. Statistical analysis is almost indispensable in non-isothermal flows.

Amplitude statistical analysis is of great importance in the understanding of the processes in the wall layers. Higher order moments determined from the probability distributions presented in Section VI are substantially different from the corresponding Gaussian values. It follows that the dispersions, or even the kinetic energy of turbulence, could not by themselves determine the process.

Probability distribution analysis of wall layers, apart from some rare measurements of the higher order statistical moments, was however not attempted. This is because the data in the form we have presented them in Section VI have very limited and only qualitative value. *A priori*, without further analysis, we could not even draw from them an answer to a simple question: are the probability distributions of the velocity components Gaussian or not?

That the probability density of the velocity measured by a hot wire is not Gaussian is evident from the data. But it could not be Gaussian even if the components had Gaussian distributions because what we are measuring is the probability distribution of the module of the velocity vector which could not be Gaussian. The wire is equally sensitive to both velocity

components normal to the wire and its signal contains information on both of them.

Before a quantitative use could be made out of the probability distribution measurements in the wall layers the respective influence of both components has to be determined. An attempt to do this is made in the following section.

B. STATISTICAL ANALYSIS OF THE HOT-WIRE SIGNAL

As already stated the instantaneous signal from a hot wire contains information on the intensity of the velocity vector. Because the heat transfer from the wire is much less effective for the velocity component parallel to the wire than for the component normal to the wire, it could be assumed that the signal is related to the normal component of the instantaneous velocity vector (u_N, Fig. 32). It is evident then that a wire placed normal to the main stream and parallel to a wall could not possibly measure a single component of the fluctuation (u_1), being necessarily influenced by the component normal to the wall (u_2).

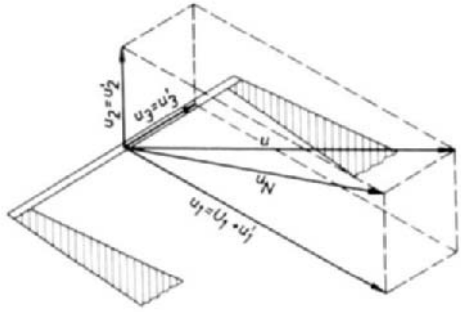

FIG. 32. Instantaneous velocity vector.

In measurements of high intensity turbulence it is the usual practice to take care of the influence of the u_2 component by introducing corrections to u_1 readings based on a binomial expansion of u_N. The procedure is wrong in principle because of the statistical nature of velocity fluctuations. The signal is influenced not only by the rms value of u_2 but by the nature of its statistical distribution, and by the correlation coefficient between u_1 and u_2.

The probability density distributions of the velocity components in wall turbulence are not known. As already noted, measured values of higher order statistical moments in wall layers could only represent statistical characteristics of the signals from the wire, not of the components. That they indicate non-Gaussian distributions is quite normal since probability

density distributions of the vector quantities are always non-Gaussian, even when the components have a Gaussian distribution, as in the case of the well known Maxwell–Boltzmann distribution.

A new approach was introduced by the author [62, 63], based on certain assumptions regarding probability distributions of the components normal to the wire. Quite naturally, the starting assumption was that the components normal to the wire have Gaussian distributions

$$p(u_i) = (1/\sigma_i\sqrt{2\pi}) \exp [-(u_i - u_1)^2/2\sigma_i], \tag{7.1}$$

but that there exists a nonzero correlation coefficient (r) between them, and that their rms values (σ_i) are not equal. In that case a two-dimensional joint probability density distribution is given by

$$p(u_1, u_2) = \frac{1}{2\pi\sigma_1\sigma_2\sqrt{1 - r^2}} \times \exp\left\{\frac{-1}{2(1 - r^2)}\left[\left(\frac{U_1 - u_1}{\sigma_1}\right)^2 - \frac{2r}{\sigma_1\sigma_2}(U_1 - u_1)u_2 + \left(\frac{u_2^2}{\sigma_2}\right)\right]\right\}. \tag{7.2}$$

If we assume that a signal from a hot wire is perfectly linearized, then, in the absence of thermal inertia, to each value of the signal corresponds a value of the velocity vector intensity u_N. The probability density distribution of the signal then corresponds directly to the probability density distribution of the velocity vector intensity. The latter is obtained by integration of the joint probability density distribution $p(u_1, u_2)$ over the perimeter of the wire:

$$p(\rho) = \rho\sigma^2 \int_0^{2\pi} p(u_1, u_2)\, d\phi, \tag{7.3}$$

where

$$\rho = u_N/\sigma \qquad \text{and} \qquad \sigma = \sqrt{\sigma_1^2 + \sigma_2^2}.$$

By a transformation of coordinates

$$v_1 = \sigma[\rho \cos \phi - \mu \cos \alpha] = (U_1 - u_1) \cos \alpha + u_2 \sin \alpha,$$
$$v_2 = \sigma[\rho \sin \phi + \mu \sin \alpha] = -(U_1 - u_1) \sin \alpha + u_2 \cos \alpha,$$

with

$$\mu = U_1/\sigma,$$
$$\Omega = \sigma_1/\sigma_2,$$
$$\epsilon = \sigma^2/2\sigma_1\sigma_2\sqrt{1 - r^2},$$
$$\eta = [1 - (1/\epsilon)^2]^{1/2},$$
$$\alpha = \tfrac{1}{2} \operatorname{arctg} [2r\Omega/(\Omega^2 - 1)],$$

the following relation is obtained:

$$p(\rho) = (\rho\epsilon/\pi)\exp\{-\epsilon^2[\rho^2 + \mu^2(1 - \eta\cos 2\alpha)]\} \times \int_0^{2\pi} \exp\{\epsilon^2\Big[\rho^2\eta\cos 2\phi + 2\rho\mu[(1-\eta)\cos\phi\cos\alpha - (1+\eta)\sin\phi\sin\alpha]\Big]\}\, d\phi. \quad (7.4)$$

The relation Eq. (7.4) represents the probability density distribution of the instantaneous velocity signal in integral form. It depends on three free parameters of the local turbulence:

$$\mu = U_1/\sigma, \qquad \Omega = \sigma_1/\sigma_2, \qquad r = \overline{u_1 u_2}/\sigma_1\sigma_2,$$

and is always non-Gaussian except in the case when $r = 0$ and $\sigma_1 = \sigma_2$.

It is very important to note that the mean value of the signal

$$\bar{\rho} = \int_0^{\infty} \rho p(\rho)\, d\rho$$

is not equal to μ, and consequently the mean value of the velocity normal to the wire $\bar{u}_N$ is not equal to the mean velocity U_1, and that the rms value of the signal

$$k = \sigma[\overline{(\rho - \bar{\rho})^2}]^{1/2},$$

which is in fact measured by the hot wire, is not equal either to σ_1 or to $\sigma = \sqrt{\sigma_1^2 + \sigma_2^2}$.

However, if the basic assumption about the statistical distributions of the components is correct, then from a measured probability density of the signal, by comparing it with the theoretical distribution Eq. (7.4), one can determine all of the local paramaters of turbulence: μ, Ω, and r, and from

$$U_1 = \bar{u}_N \cdot \mu/\bar{\rho},$$
$$\sigma_1 = k\Omega/\sigma\sqrt{1 + \Omega^2},$$
$$\sigma_2 = k/\sigma\sqrt{1 + \Omega^2},$$

calculate the true mean velocity and the rms values of the components. This would be of great importance since all the local characteristics of turbulence are obtained from a signal of a single hot wire which could easily be located in the actual vicinity of the wall.

The probability density distribution has been calculated for various values of the parameters μ, Ω, and r by numerical integration on a digital computer. Probability density distributions for some combination of the free parameters are shown in Fig. 33, and the variation of the corresponding

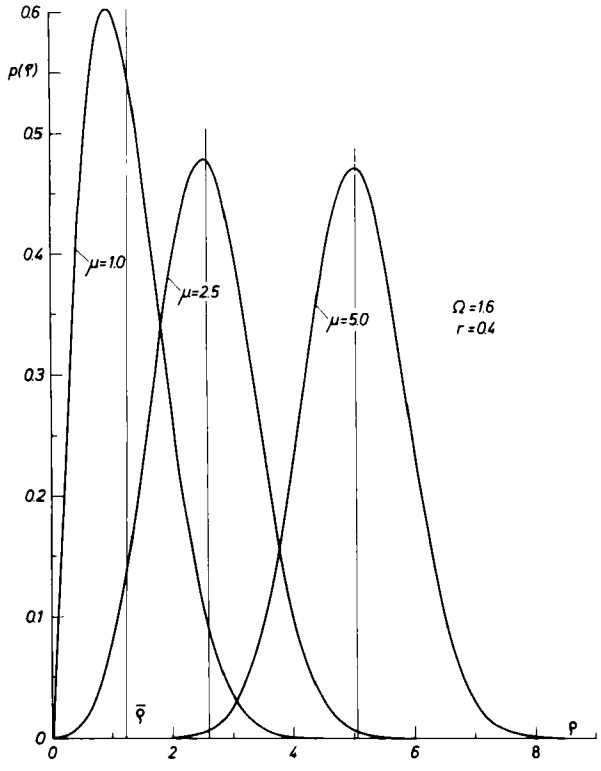

FIG. 33. Theoretical probability distributions of the velocity vector module.

skewness (S) and flatness (F) factors in the function of the free parameters is shown in Figs. 34 and 35. It is seen that both factors could have very high values for high turbulence intensity.

Some characteristics of the distribution Eq. (7.4) have to be mentioned:

—The distribution is still insensitive to the direction of the main flow, i.e., the direction of the mean velocity U_1 has to be known in advance.

—For higher μ values, i.e., lower turbulence intensities, the distribution is very close to a Gaussian distribution, so that the turbulence characteristics determination method based on the comparison of the theoretical and the experimental distributions is not sensitive enough in conditions of low turbulence intensity.

—Skewness factors corresponding to Eq. (7.4) never became negative and flatness factor values are never below $F = 2.7$.

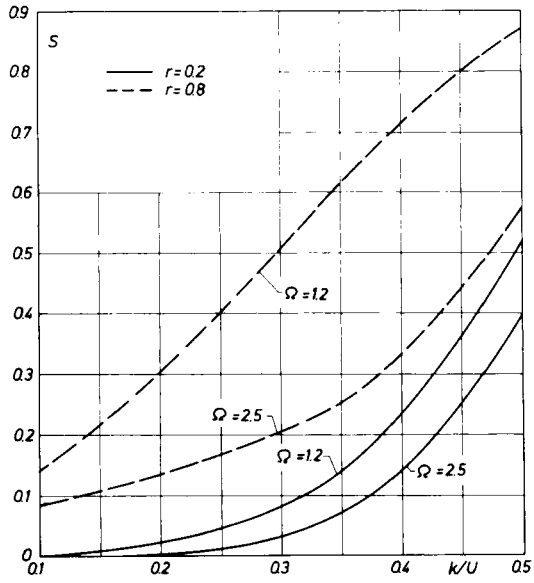

FIG. 34. Skewness factors determined from the theoretical distribution for different combinations of the free parameters.

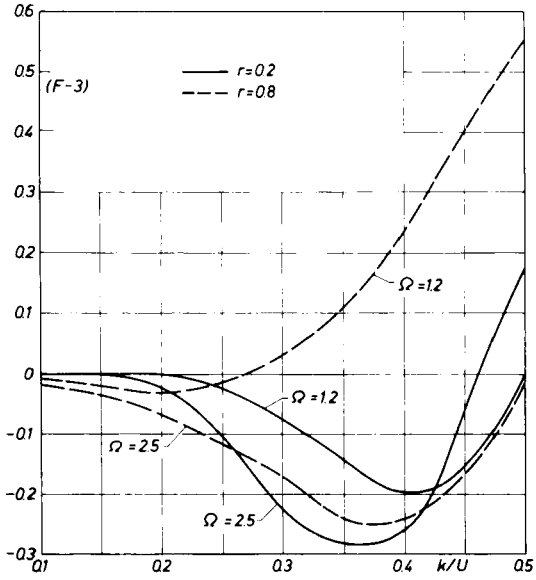

FIG. 35. Theoretical flatness factors for different combinations of the free parameters.

The above analysis could be extended to the three-dimensional case when the joint probability density is given by

$$p(u_1, u_2, u_3) = \frac{1}{(2\pi)^{3/2}\sigma_1\sigma_2\sigma_3(1 - r_{12}^2 - r_{13}^2 - r_{23}^2 + 2r_{12}r_{13}r_{23})^{1/2}} \times \exp\left\{\frac{1}{2[1 - r_{12}^2 - r_{13}^2 - r_{23}^2 + 2r_{12}r_{13}r_{23}]} \times \left[(1 - r_{23})^2\left(\frac{u_1 - U_1}{\sigma_1}\right)^2 + (1 - r_{13}^2)\left(\frac{u_2}{\sigma_2}\right)^2 + (1 - r_{12}^2)\left(\frac{u_3}{\sigma_3}\right)^2 + 2\left((r_{13}r_{23} - r_{12})\frac{u_2(u_1 - U_1)}{\sigma_1\sigma_2} + (r_{12}r_{23} - r_{13})\frac{u_3(u_1 - U_1)}{\sigma_1\sigma_3} + (r_{12}r_{13} - r_{23})\frac{u_2u_3}{\sigma_2\sigma_3}\right)\right]\right\} \tag{7.5}$$

and depends on six parameters: (U_1/σ), (σ_1/σ_2), (σ_2/σ_3), and the correlation coefficients r_{12}, r_{13}, and r_{23}.

However, the component parallel to the wire has not the same effectiveness to heat transfer from the wire as the normal component. If we suppose that this is the component u_3 then the signal is influenced by an effective value $u_{3_e} = \xi \cdot u_3$. The factor ξ is not well known. It has a value from 0.1 to 0.2, which has to be determined more accurately before a three-dimensional analysis is attempted.

We have examined the influence of the neglect of the component parallel to the wire on the two-dimensional analysis. The velocity vector could be divided into

$$u_N = u \sin \psi,$$

$$u_3 = u \cos \psi,$$

ψ being the angle between the parallel and the normal components. Then, taking into account the effectiveness of u_3,

$$\rho = (1/\sigma)[(\sigma_N\rho_N)^2 + (\xi u_3)^2]^{1/2},$$

where

$$\sigma = [\sigma_N{}^2 + (\xi \cdot \sigma_3)^2]^{1/2} \quad \text{and} \quad \sigma_N = (\sigma_1{}^2 + \sigma_2{}^2)^{1/2}.$$

For the already known two-dimensional probability density distribution, Eq. (7.4), the three-dimensional distribution of the velocity vector intensity $p(\rho)$ could be obtained by a second integration:

$$p(\rho) = \frac{\sigma\rho}{\sigma_3\sqrt{2\pi}} \int_0^\pi p_N\left(\frac{\sigma\rho \sin \psi}{\sigma_N}\right) \exp\left[-\frac{\sigma\rho \cos \psi}{2\sigma_3}\right] d\psi \tag{7.6}$$

if we assume that the u_3 component is not correlated with the normal components, i.e., if $r_{13} = r_{23} = 0$ or is negligible, which is close to the real situation according to some rare measurements. Calculations have been performed for various values of ξ from 0.1 to 0.2, and the results show that neglect of the u_3 component in the analysis is justified.

As it concerns the other basic assumption, i.e., that the components have a Gaussian distribution, the justification has to be provided by experiment. This assumption is discussed in the next section on the basis of the measurements presented in Section VI.

C. Results of Analysis

It is not too plausible to suppose that the probability distributions of the velocity components in shear flow should be Gaussian. The existing evidence suggests that wall turbulence is a nonlinear random process. Theoretically Gaussian distributions would result in all third-order moments and their derivatives $\overline{u_i^3}$ and $\overline{(\partial u_i^3/\partial x_i)}$ being zero, which is not in accordance with the existing evidence, at least in most regions of the boundary layer. Direct experimental evidence on the nature of the probability distributions of the fluctuation components could not be produced by the hot-wire method. The laser–Doppler method is well suited for measurements of the probability distributions of single components. Initial measurements with this method in Imperial College gave nonnormal distributions of single components although not in the vicinity of the wall [64].

The results of our preliminary measurements have indicated that the distributions could be Gaussian in the layers close to the wall [61]. However, these results have been obtained on a small digital computer and with a poor analog-to-digital conversion system having a low upper frequency limit. These results have also shown that the skewness factor becomes negative away from the wall so that in this region the assumption on the normality of the distributions could not hold, as also noted by Durst and Whitelaw [64].

The results presented in Section VI rule out the assumption that the velocity components could possibly have Gaussian distributions even in the wall regions. In the layers closest to the wall, higher order moments are much higher than those permissible by the theoretical distribution Eq. (7.4) for any combination of the free parameters. On the other hand in the logarithmic region and the outer layers skewness factors became negative. Comte-Bellot [27] has noted that a substantial error in the measurements of the odd-order moments in high intensity turbulence could come from the neglect of the thermal inertia of the wire. Therefore we have compared our experimental distributions with the theoretical one, Eq. (7.4), on the basis

of the moments of order 4 and 6 (flatness and superflatness factors). However, in the region where the skewness factor becomes negative, flatness and superflatness factor values are usually lower than those permissible by Eq. (7.4) for any combination of the free parameters.

In a certain flow region in each of the cross sections investigated both flatness factors for the given turbulence intensity k fall within the range permissible by Eq. (7.4) so that the free parameters μ, Ω, and r could be determined. For the cross section A the results are shown in Fig. 36. The resulting correlation coefficients r are much too high and the ratios $\Omega = \sigma_1/\sigma_2$ much too low by comparison with the existing data. The comparison of the experimental and the theoretical distributions was done on the basis of the two flatness factors (F and SF). The skewness factors calculated from the distribution Eq. (7.4), corresponding to the μ, Ω, and r values found, do not agree with the measured ones, having somewhat lower values. This could indicate that the probability distributions depend on more than three free parameters.

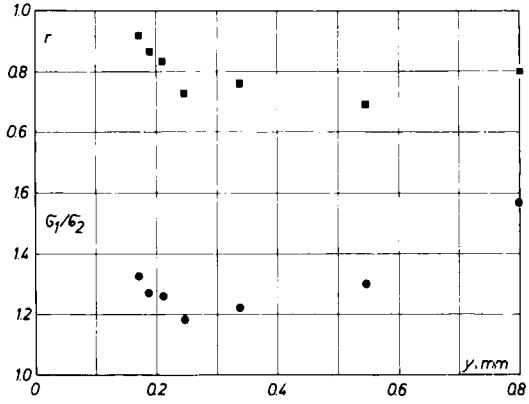

FIG. 36. Correlation coefficients, r, and rms value ratio, σ_1/σ_2 of the components determined by the analysis. ■, r; ●, σ_1/σ_2.

All these findings confirm that the result of the amplitude probability analysis presented is in fact negative. The initial assumption does not hold—the probability distributions of the velocity components in the wall layers are not Gaussian.

However, the procedure introduced by the analysis presented is sound. It is only the first assumption on the probability distributions of the velocity components which does not hold. This assumption had to be investigated before more sophisticated assumptions are introduced.

D. PROBABLE FUTURE DEVELOPMENTS

It is extremely worthwhile proceeding with the analysis by introducing new assumptions. In the case of hot-wire studies of high intensity turbulence it is even indispensable as otherwise the results of the measurements are worthless. The most interesting feature of the analysis is however the possibility of obtaining information on the probability distributions of the velocity components. This information would be of greatest interest for further studies of the structure of wall turbulence.

Two possible lines of attack for a further analysis have already been suggested by other investigators. The first would be based on the Cameron–Martin–Weiner method of investigating a nonlinear random process by expanding it in an infinite series, in which the first term is an exact Gaussian process and the higher order terms contribute successive corrections [11, 12]. This method would then provide guidance for the more sophisticated assumptions regarding the probability distributions of the velocity components. The other approach was initiated by the results of the studies in Stanford [65], and consists of representing shear flow turbulence as a random superposition of appropriate characteristic waves. This approach, introduced by Lumley, was tested experimentally by Bakewell [51] and by Hussain and Reynolds [13], using two different procedures.

In order to establish a physical basis for the choice of a possible approach to further analysis, preliminary calculations of the autocorrelation functions of some of the registered signals have been made. The maximum lag number chosen was $v = 400$, corresponding to the maximum displacement of $\tau_{max} = 50$ msec. The autocorrelation function for a signal corresponding to $y^+ = 2.2$ in cross section D for flow with Re = 36,000 is presented in Fig. 37. Note that the autocorrelation function is fairly smooth up to the time lag of approximately $\tau = 7$ msec, corresponding to $\tau^+ = \tau u_*^2/\nu = 110$, in agreement with the findings of other researchers, as for instance Van Thinh [55] who has not in fact exceeded the time lag of $\tau^+ = 80$. It is for time lags exceeding $\tau^+ = 110$ that the autocorrelation function begins to show wavy behavior. For time lags $\tau > 5$ msec the autocorrelation function is presented in the upper part of Fig. 37 in a larger scale. The wavy behavior persist up to $\tau_{max} = 50$ msec, although the region for $\tau > 25$ msec is not shown in Fig. 37. These findings are in accordance with the results of Bakewell [51] and Kim *et al.* [52] who have used glycerine and water, respectively, as working fluids.

The velocity spectra obtained by a Fourier cosine transform of the autocorrelation function presented in Fig. 37 are shown in Fig. 38, along with the spectra corresponding to $y^+ = 5.2$ and $y^+ = 14.7$, in the same cross

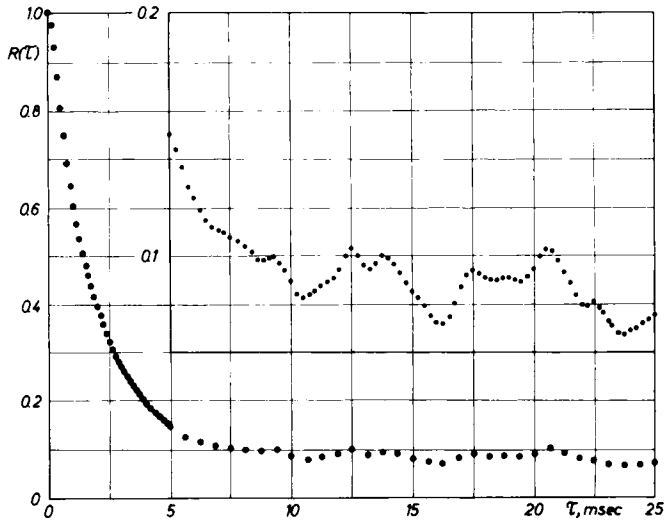

FIG. 37. Autocorrelation function. Cross section D, Re = 36,000, $y^+ = 2.2$.

section. The equivalent bandwidth, corresponding to the maximum displacement $\tau_{max} = 50$ msec, was $B_e = 1/\tau_{max} = 20$ Hz. Peaks in the spectra correspond to the waves of the autocorrelation function. Similar peaks in the spectra were found by Bakewell [51].

A harmonic analysis of the autocorrelation functions looks very promising We are proceeding with this analysis using larger lag numbers. The analysis however required much computer time. An attempt is being made to interpret the probability distributions of the velocity vector module, as measured by a hot wire, by a superposition of the Gaussian distributions and the probability distribution of the waves, using both amplitude probability density and autocorrelation function measurements.

VIII. Concluding Remarks

The brief review of the existing prediction procedures indicates that no real progress can be made without a better understanding of the physics of turbulence phenomena. At present there are more investigators who make predictions than those who supply experimental evidence to support those predictions. It is much easier to perform computer experiments then to do experimental work in wall turbulence. However, it is always dangerous to construct beautiful theoretical structures on the basis of thin and not very

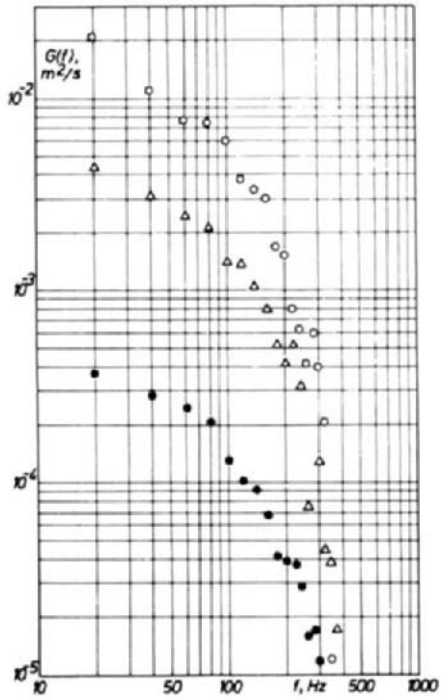

FIG. 38. One-dimensional spectra. Cross section D, Re = 36,000. ●, $y^+ = 2.2$; △, $y^+ = 5.2$; ○, $y^+ = 14.7$.

reliable experimental evidence. And the experimental evidence in wall turbulence is thin and unreliable.

Wall turbulence is a complex, random phenomenon. Therefore, the best chances for success have physical models based on statistical theory. Consequently, experimental evidence on which these models have to be built has to be obtained by statistical methods. Experimental techniques presently in use in wall turbulence studies are not well suited for this. Either these techniques are essentially inadequate for the statistical analysis, as in the case of visual methods, or the statistical analysis has not been applied in the process of data acquisition, as in case of the hot-wire technique. Quantitative visual techniques have already revealed unknown features of wall-turbulence structure. Their role in this respect is unquestionable. It is also probable that visual techniques could greatly help hot-wire or optical methods in becoming reliable tools of a real statistical analysis of the wall turbulence.

A wall turbulence experimental study, in isothermal and nonisothermal

conditions, has been presented. The aim of the study was to obtain as much statistical information in the wall layers as possible with the available technique. It is found that without a statistical analysis the data obtained are of only qualitative value. Even the determination of mean flow parameters in the wall layers from nonstatistical measurements is of a questionable reliability. This is especially true in the case of nonisothermal flows.

A statistical analysis of the velocity signal in isothermal flow was attempted on the basis of simplified assumptions. It revealed that a single-wire probe signal statistically analysed contains more information then what is usually supposed. By this analysis, it was proved that the probability distributions of the velocity components are non-Gaussian. This result could be expected but it does not follow directly from the measured values of the higher order statistical moments. Another conclusion of the analysis is far more important: it follows that by applying a similar analysis, based on more realistic assumptions, probability distributions of the components could be determined, along with the corresponding correlation coefficients.

A complete statistical description consists of the probability distribution and the autocorrelation function determination. Preliminary results of the autocorrelation function measurements were presented. It turns out that if a sufficient time lag is allowed the waves detected in visual studies make their appearance in the autocorrelation functions. The "bursts," then, are responsible for the skewness of the probability distributions. It follows that no information is lost by lengthy time-averaging, only this time-averaging has to be done properly, and statistically. A coupled time and amplitude statistical analysis thus provides a powerful tool in wall turbulence studies.

The analysis could be extended to the three-dimensional case. It could also be extended to nonisothermal flows. In fact, a nonstatistical treatment of the temperature fluctuations is purely formal and without real meaning. The probability that this could be done by the hot-wire technique alone is slight. A combination of techniques seems necessary.

ACKNOWLEDGMENTS

The author wishes to acknowledge the assistance of Mr. I. Illić and Mr. R. Rajković of the Boris Kidrić Institute, Department of Thermal Physics, in preparing the experiments and performing the measurements.

The author also wishes to express his gratitude to the staff of the Computer Center of the Boris Kidrič Institute, and especially to Dr. S. Bingulac, for help in preparing the programs, and to Mr. A. Tošić who enabled the statistical analysis to be made on the computer.

SYMBOLS

C_p	specific heat
d	diameter
e	voltage fluctuation
e_k	kinetic energy of turbulence
E	signal voltage
f	frequency
F	flatness factor, defined by Eq. (6.5)
$G(f)$	velocity spectrum
$G_{ii}(f)$	spectrum of the ith component
H	form parameter
H_1	form parameter for nonisothermal flow
k	velocity rms value, as indicated by the wire
k_i	rms value of the ith fluctuating component
k_T	temperature rms value
l	wire length
N_i	frequency of occurrence of E_i
p	pressure
$p(x)$	probability density of x
P^+	turbulence energy production
q_w	wall heat flux
r	correlation coefficient $= -\overline{u_1 u_2}$
r_{ij}	correlation coefficient between the ith and the jth fluctuating component
R	wire resistance
$R(\tau)$	autocorrelation function
$R_{11}(\tau)$	autocorrelation function of the u_1
$R_{11}(x, \tau)$	cross-correlation function
S	skewness factor, defined by Eq. (6.4)
SS	superskewness factor, defined by Eq. (6.6)
SF	superflatness factor defined by Eq. (6.7)
t	temperature fluctuations
T	temperature
u	instantaneous velocity
u_i	ith fluctuating component
u_N	instantaneous velocity normal to the wire
u_*	friction velocity
u^+	nondimensional velocity $= U/u_*$
$U, \bar{U}$	mean velocity
U_0	mean velocity at the channel axis
W^+	turbulence energy dissipation
x_i	coordinate in the ith direction
X	distance along the channel from the diffuser inlet
y	distance from the wall
y^+	nondimensional distance from the wall $= yu_*/\nu$
δ	half-width of the channel
δ^{**}	momentum thickness
θ	temperature difference
θ_0	maximum temperature difference
θ^+	nondimensional temperature difference
λ	thermal conductivity
μ	dynamic viscosity
ν	kinematic viscosity
ρ	density
σ	rms value of the velocity vector module
σ_i	rms value of the ith fluctuating component
τ	time
τ^+	nondimensional time $= \tau u_*^2/\nu$
Re	Reynolds number
St	Stanton number

REFERENCES

1. G. I. Taylor, *J. Fluid Mech.* **41**, 3–11 (1970).
2. *Proc. AFOSR-IFP Conf. Turbulent Boundary Layer Prediction* Stanford Univ. (1968).
3. S. J. Kline, Dept. Mech. Eng., Stanford Univ., Rep. MD-23 (1969).
4. B. E. Launder and D. B. Spalding, Dept. Mech. Eng., Imperial College, Rep. TM/TN/A/1-7 (1971).
5. K. Hanjalić, Ph.D. thesis, Mech. Eng. Dept., Imperial College (1970).

6. A. S. Monin and A. M. Iaglom, "Statistical Hydromechanics," Vol. I, II. Izd. Nauka, Moscow, 1965, 1967.
7. F. N. Frenkiel and P. S. Klebanoff, *Phys. Fluids* **10,** 1737–1747 (1967).
8. C. W. van Atta and W. Y. Chen, *J. Fluid Mech.* **34,** 497–515 (1968).
9. C. W. van Atta and T. T. Yeh, *J. Fluid Mech.* **41,** 169–178 (1970).
10. A. A. Townsend, "The Structure of Turbulent Shear Flow," Cambridge Univ. Press, London and New York, 1956.
11. W.-H. Kahny and A. Siegel, *J. Fluid Mech.* **41,** 593–618 (1970).
12. S. C. Crow and G. H. Canavan, *J. Fluid Mech.* **41,** 387–403 (1970).
13. A. K. M. F. Hussain and W. C. Reynolds, *J. Fluid Mech.* **41,** 241–258 (1970).
14. B. W. Spencer, Ph.D. Thesis, Univ. of Illinois, Urbana, Illinois (1970).
15. M. K. Bull, *J. Fluid Mech.* **28,** 719–754 (1967).
16. W. W. Willmarth and S. S. Yang, *J. Fluid Mech.* **41,** 47–80 (1970).
17. B. J. Bellhouse and D. L. Schultz, *J. Fluid Mech.* **24,** 379–400 (1966).
18. J. E. Mitchell and T. J. Hanratty, *J. Fluid Mech.* **26,** 199–221 (1966).
19. T. J. Hanratty, Int. Seminar, Heat and Mass Transfer in Separated Flows. Herceg Novi (1969).
20. R. A. Armistead, Jr. and J. J. Keyes, Jr., *J. Heat Transfer* **C90,** 13–21 (1968).
21. A. T. Popovich and R. L. Hummel, *AIChE J.* **13,** 854–860 (1967).
22. Z. Zarić, *in* "Heat and Mass Transfer in Turbulent Boundary Layers," Vol. II, pp. 555–571. Boris Kidrič Inst., Beograd, 1970.
23. P. O. A. L. Davies, Int. Seminar, Heat and Mass Transfer in Separated Flows. Herceg Novi (1969).
24. H. H. Bruun, Univ. of Southampton, I.S.V.R. Tech. Rep. No 21 (1969).
25. J. D. Vagt, Int. Seminar, Heat and Mass Transfer in Separated Flows. Herceg Novi (1969).
26. R. G. Sidall and T. W. Davies, Int. Seminar, Heat and Mass Transfer in Separated Flows, Herceg Novi (1969).
27. G. Comte-Bellot, *Int. J. Heat Mass Transfer* **12,** 1661–1677 (1969).
28. J. A. B. Wills, *J. Fluid Mech.* **12,** 388–398 (1962).
29. M. Coantic, Thesis, Univ. Aix-Marseille (1966).
30. F. A. Schraub and S. J. Kline, Dept. Mech. Eng., Stanford Univ., Rep. MD-12 (1965).
31. E. M. Khabakhpasheva, in "Heat and Mass Transfer in Turbulent Boundary Layers," Vol. II, 573–583. Boris Kidrič Inst., Beograd, 1970.
32. R. M. Nedderman, *Chem. Eng. Sci.* **16,** 120–126 (1961).
33. F. A. Schraub, S. J. Kline, J. Henry, P. W. Runstadler, Jr., and A. Littel, *J. Basic Eng.* **D87,** 429–444 (1965).
34. A. T. Popovich and R. L. Hummel, *Chem. Eng. Sci.* **22,** 21–25 (1967).
35. F. Frantisak, A. P. de Iribarne, J. W. Smith, and R. L. Hummel, *I&EC Fundamentals* **8,** 160–167 (1969).
36. N. F. Derevianko and A. M. Trohan, *Zh. Prikl. Mekhan. Tekhn. Fiz.* No. 4, 105–116 (1968).
37. R. J. Goldstein and D. K. Kreid, Univ. of Minnesota, Rep. HTL TR No. 85 (1968).
38. F. Durst and J. H. Whitelaw, Mech. Eng. Dept., Imperial College, Rep. EF/TN/C/23 (1969).
39. D. B. Thomas and A. A. Townsend, *J. Fluid Mech.* **2,** 473–492 (1957).
40. S. Tanimoto and T. J. Hanratty, *Chem. Eng. Sci.* **18,** 307–311 (1963).
41. K. Bremhorst and K. J. Bullock, *Int. J. Heat Mass Transfer* **13,** 1313–1329 (1970).
42. Z. Zarić, *in* "Teplo- i Massoperenos," Vol. IX, pp. 36–56. Minsk, 1968.
43. J. Blom, Ph.D. Thesis, Technological Univ., Eindhoven (1970).
44. D. S. Johnson, *J. Appl. Mech.* **26,** 325–336 (1959).

45. C. I. H. Nicholl, *J. Fluid Mech.* **40,** 361–384 (1970).
46. J. Laufer, Nat. Advisory Comm. Aeron. Rep. 1053 (1951).
47. J. Laufer, Nat. Advisory Comm. Aeron. Rep. 1174 (1954).
48. P. S. Klebanoff, Nat. Advisory Comm. Aeron. Rep. 1247 (1955).
49. J. Marcillat, Thesis, Univ. Aix-Marseille (1964).
50. G. Comte-Bellot, Pub. Sci. Tech. Min. de l'Air, No 419 (1965).
51. H. P. Bakewell, Thesis, Dept. Aerospace Eng., Pennsylvania State Univ. (1966).
52. H. T. Kim, S. J. Kline, and W. C. Reynolds, AFOSR Rep. 68-0383 (1968).
53. J. A. Clark, *J. Basic Eng.* **D90,** 455–468 (1968).
54. A. P. de Iribarne, R. L. Hummel, J. W. Smith, and F. Frantisak, *Chem. Eng. Progr. Symp. Ser.* **65,** 60–70 (1969).
55. N. van Thinh, Int. Seminar, Heat and Mass Transfer in Separated Flows. Herceg Novi (1969).
56. S. J. Kline, H. T. Kim, and R. Lahey, *Proc. AFOSR-IFP Conf.* Stanford Univ. (1968).
57. J. M. Robertson and G. L. Calehuff, *Proc. ASCE J. Hydraulics Div.* **83,** 1393 (1957).
58. S. J. Kline and P. W. Runstadler, *J. Appl. Mech.* **81,** 166–170 (1959).
59. Z. Zarić, *Proc. UN Conf. Peaceful Uses Nucl. Energy*, 3*rd* P/698, Geneva (1968).
60. Z. Zarić, *Proc. ISME Semi-Int. Symp.* pp. 161–170. Tokyo (1967).
61. Z. Zarić, *Proc. Int. Heat Transfer Conf.*, 4*th* Vol. 2, FC3.10. VDI, Düsseldorf (1970).
62. Z. Zarić, *C. R. Acad. Sci. Paris* **A269,** 986–989 (1969).
63. Z. Zarić, Int. Seminar, Heat and Mass Transfer in Separated Flows. Herceg Novi (1969).
64. F. Durst and J. H. Whitelaw, Mech. Eng. Dept., Imperial College, Rep. ET/TN/A/3 (1970).
65. S. J. Kline, W. C. Reynolds, F. A. Schraub, and R. W. Runstadler, *J. Fluid Mech.* **30,** 741–773 (1967).

Author Index

Numbers in parentheses are reference numbers and indicate that an author's work is referred to although his name is not cited in the text. Numbers in italics show the page on which the complete reference is listed.

A

Achari, P. J., 57, 61, *90*
Achenbach, E., 97 (22), 100, 101, 110 (33), 111 (33), *159*
Acrivos, A., 36 (198, 202), *89*
Agrawal, H. C., 24, 26, 32, *86*, *87*
Ahuja, K. L., 6, 24, *84*, *87*
Ainola, L. Y., 33, *88*
Akheizer, I., 22 (107), *86*
Akilba'yev, Zh. S., 103 (29), 104 (29), 105 (29), 132 (29), 133 (29), *159*
Aldoshin, G. T., 36 (206), *89*
Ambraziavičius, A. B., 112 (36), *159*
Andritzky, H. K. M., 99 (26), *159*
Antuf'yev, V. M., 94, 149, 157 (17), *158*, *159*
Aoki, T., 232 (4), 243 (4), *282*
Armistead, R. A., Jr., 293 (20), *349*

B

Bakewell, H. P., 300, 301 (51), 344 (51), 345, *350*
Balcerzok, M. J., 49, *89*
Bankoff, S. G., 33, *88*
Baron, J. R., 56, *90*
Bartko, F., 281, *283*
Bartman, A. B., 40 (211), *89*
Batchelor, G. W., 166, 167, 168, 170, 173, 176, 177, 179, 182, 184, 198, *226*
Bazley, N. W., 248, *282*
Bazzin, A. P., 13, *85*
Beckwith, I. E., 12, *85*
Beletsky, G. S., 94, 149, 157 (17), *159*
Bellhouse, B. J., 293 (17), *349*
Belton, M. J. S., 245, *282*
Bergelin, O. P., 140 (70, 71, 72, 73), 141 (72), 142 (72), 144 (71), 148 (72), 149 (72), 151 (72), *160*
Biot, M. A., 23 (108, 109), 24, 25 (125), 26, 31 (111), 32 (109, 111), *86*, *87*
Blom, J., 299 (43), 305, 324 (43), *349*
Boley, B. A., 34, *88*
Bortoli, R. A., 135, *160*
Bourne, D. E., 36, *88*
Bowlus, D. A., 19 (88), *86*
Braun, W. H., 164, *226*
Bremhorst, K., 299 (41), 305, *349*
Bressler, R., 107 (31), 108, *159*
Bridgeman, K. D., 248 (23), *283*
Brindley, J., 19, *86*
Brooks, I., 172, 173, 216, 217, 218, 219, 220, 221, 222, *227*
Brown, G. A., 140 (71, 72), 141 (72), 142 (72), 144 (72), 148 (72), 149 (72), 151 (72), *160*
Bruun, H. H., 294 (24), *349*
Bukhvotsov, A. P., 24, *86*
Bull, M. K., 293 (15), *349*
Bullock, K. J., 299 (41), 305, *349*
Burgraff, O. R., 11, *85*
Busbridge, L. W., 34, *88*
Busey, F. L., 94 (4), *158*
Bush, W. B., 19, *86*
Butler, H. W., 29, *87*
Byrd, P. F., 47 (225), *89*

C

Calehuff, G. L., 305 (57), *350*
Canavan, G. H., 291 (12), 344 (12), *349*
Carlson, W. O., 167, 168, 172, 176, 177 (24), 178 (24), 183 (24), 184, 192, 195, *226*
Carrier, G. F., 34, *88*, 170, *226*
Carrier, W. H., 94 (4), *158*
Carslaw, H. S., 3, 53 (10), 75 (10), 78 (10), *84*

Case, K. M., 70, *90*
Cess, R. D., 11, 22, 71, 73, 74, *85*, *86*, *91*, 250 (30), 252 (30), 253 (33, 35), 256 (30, 35), 258 (33), 259 (33), 260, 263 (39), 264 (30), 267 (32), 276 (48), 278 (49), 279 (49), *283*
Chambre, P. L., 36 (198, 201, 202), 38 (203), *89*
Chandler, T. R. D., 248 (23), *283*
Chandrashekhar, S., 34, *88*
Chao, B. T., 19, *86*
Chapman, D. R., 22, *86*
Charpakov, P. V., 67, *90*
Chen, W. Y., 291, *349*
Cheney, A. J., 135, *160*
Cheng, P., 14, *86*
Chi, M., 49, *89*
Chu, H. N., 24, 26, *87*
Chung, P. M., 36 (207), 42 (207), *89*
Churchill, S. W., 167, 170, 172, 212, 224, *226*
Clark, J. A., 300, 301 (53), *350*
Coantic, M., 297, 300, 301 (29), 314, 323, *349*
Cochran, J., 12, *85*
Cogley, A. C., 256, *283*
Cohen, N. B., 12, *85*
Colburn, A. P., 140 (70), *160*
Coles, D. E., 12, *85*
Cole, J. D., 7, 13, *84*, *85*
Collis, D. S., 127 (58), 128, 130 (58), *160*
Comte-Bellot, G., 296, 300, 301 (50), 320, 342, *349*, *350*
Conti, R. J., 14, *85*
Cooper, L. Y., 19, *86*
Courant, R., 34 (174), 54 (238), 67 (174), *88*, *90*
Crow, S. C., 291 (12), 344 (12), *349*
Curd, H. N., 29, *87*
Curle, N., 36 (197), *89*

D

Dacosta, M., 53 (236), *90*
Daughaday, H., 24, 31 (111), 32 (111), *86*
Davies, D. R., 36, *88*
Davies, P. O. A. L., 128 (59, 60), *160*, 294 (23), *349*
Davies, T. W., 295 (26), *349*
Davis, A. H., 94 (15), 128, 130 (16), *159*
de Graff, J. G. A., 176, *227*
deGroot, S. R., 26 (134), 29 (134), *87*
de Iribarne, A. P., 298 (35), 300, 301 (54), *349*, *350*
Dennis, S. C. R., 70, *90*
Derevianko, N. F., 298 (36), *349*
de Vahl Davis, G., 169, 173, 193, 194 (29), *226*
Dewey, C. F., 12, *85*
Doberstein, S. C., 140 (72), 141 (72), 142 (72), 148 (72), 149 (72), *160*
Doetsch, G., 3 (13), *84*
Donnelly, R. J., 26 (135), *87*
Dorfman, A., 74 (275), 75, *91*
Drake, D. G., 12, *85*
Drakhlin, E., 164, *226*
Duffin, R. J., 33 (156), *87*
Durst, F., 298, 342 (64), *349*, *350*
Dwyer, O. E., 149, 151 (72), *160*
Dyban, E. P., 122 (56), 123, *160*

E

Eckert, E. R. G., 35 (182, 183), *88*, 117 (46), 119 (49, 50), 120 (49, 50), 121 (49, 50), *159*, *160*, 167, 168, 172, 176, 177 (24), 178 (24), 183 (24), 184, 192, 195, *226*
Edwards, D. K., 241, 243 (8, 9), 244, 245, 256, 257, 266, *282*
Elder, J. W., 168, 173 (27), 176, 184, 185 (27), 186 (27), 187 (27), 188 (27), 189 (27), 190 (27), 191 (27), 193, 195, *226*, *227*
Elenbaas, W., 161, *226*
Ellinwood, J. W. E., 11, *85*
Emery, A. F., 176, 195, *227*
Encranez, T., 231 (3), *282*
Epick, E. V., 122 (56), 123, *160*
Erdelyi, A., 7 (30), 13, 19 (96), 20, *84*, *85*, *86*
Evgrafov, M. A., 41 (213), *89*

F

Fage, A., 100, 101, *159*
Fand, R. M., 130 (62), *160*
Feddosev, D. V., 49 (228), *89*
Fendell, F. E., 12, *85*
Ferguson, M. G., 248 (25), *283*
Fernandez, F. L., 12 (46), *85*
Fersiger, J. H., 70, *90*
Feshbach, H., 14 (77), 33 (77), 45 (77), *86*
Fife, P. C., 13, *85*

Finlayson, B. A., 2, 24 (8), 25 (126), 32 (8, 126, 155), *84*, *87*
Fisher, M. J., 128 (59), *160*
Folkner, V. M., 100, 101, *159*
Fowkes, N. D., 13, *85*
Fox, H., 67, 68, *90*
Frank, B., 36 (205), *89*
Frankel, L. E., 12, *85*
Frankel, W. V., 24, *86*
Frank-Kamenetskii, D.A., 36, *89*
Frantisak, F., 298 (35), 300 (54), 301 (54), *349*, *350*
Frenkiel, F. N., 291, *349*
Friedman, A., 13, *85*
Friedman, M. D., 47 (225), *89*
Friedrichs, K. O., 53 (238), *90*
Fritzsche, A. F., 157 (83), *160*
Frössling, N., 119, 120, 121, *160*
Froman, N., 19 (95), *86*
Froman, P. O., 19 (95), *86*

G

Gal-Or, B., 29, *87*
Gamayunov, N. I., 66, *90*
Gantmacher, F. R., 64 (249), *90*
Gernier, E. M., 49 (228), *89*
Gershuni, G. Z., 168, 173, 212, *226*, *227*
Giedt, W. H., 121, *160*
Gierasch, P., 281, *283*
Gill, A. E., 168, 171, 173, 176, 193, 216, *226*
Gille, J., 247, *282*
Gilles, S. E., 248, 249, 256 (36), 273, *283*
Gladkov, A. A., 13, *85*
Glansdorff, P., 26, 27 (139), 29 (142), 87 (137, 139), *87*
Glassen, L. K., 245 (10), 256 (10), 257 (10), 266 (10), *282*
Goldstein, R. J., 298 (37), *349*
Golosov, A. C., 36 (206), *89*
Goodman, T. R., 2 (9), 4, 24 (9), *84*
Goody, R. M., 238 (6), 242 (6), 245, 247, 248, 249 (6), 250 (6), 256, 273, 281, *282*
Gregorig, R., 94, 99 (26), 115 (44), 157 (19), *159*
Grief, R., 253, *283*
Grimison, E. D., 94, 148, 149, *158*
Grimmble, R. E., 135 (68), *160*
Grinchenkov, V. T., 35, *88*
Grosh, R. J., 34 (167), *88*
Gross, J. F., 12, *85*
Gunn, G. C., 19, *86*
Gupta, S. C., 26 (132), 30 (150), 31 (150), 32, *87*
Gurtin, M. E., 33, *88*

H

Habib, I. S., 253, *283*
Hammecke, K., 146, 148, 149, *160*
Han, B. S., 70, *90*
Han, J. T., 195, *227*
Hanel, R. A., 281, *283*
Hanjalić, K., 289, *348*
Hanratty, T. J., 293 (18, 19), 299 (40), 305, *349*
Hantman, R., 172, 213, 214, 215, 216, 218, 222, *227*
Hartnett, J. P., 2 (1–7), 34, *88*, 163, *226*
Hartree, D. R., 21, *86*
Hauser, W. C., 244 (10), 256 (10), 257 (10), 266 (10), *282*
Hayday, A. A., 19 (88), 35 (182, 183), *86*, *88*
Hays, D. F., 29, *87*
Heaselet, M. A., 264 (40), *283*
Heinecke, E., 145 (77), 148, 149, *160*
Hell, H. L., 140 (71), 144 (71), *160*
Hellums, J. D., 167, *226*
Henry, J., 297 (33), *349*
Herman, R., 26 (135), *87*
Hilbert, D., 34 (174), 67 (174), *88*
Hildebrand, F. B., 54 (243), *90*
Hilpert, L., 94 (13), 128 (13), 130 (13), *159*
Hine, R. J., 248 (20), *282*
Hodgson, J. P., 248 (20), *282*
Hogan, J. S., 231 (3), 281, *282*, *283*
Hooker, W. J., 248 (21), *283*
Horvay, G., 53 (236), *90*
Howell, J. R., 34, *88*
Hsia, H. M., 66, *90*
Hsu, C. C., 19 (90), *86*
Hsu, C. J., 56, *90*
Hsu, C. T., 248, *282*
Huge, E. S., 94 (11), *159*
Hughes, J. A., 94 (2), 129 (2), 130 (2), *158*
Hummel, R. L., 293 (21), 298 (34, 35), 300 (54), 301 (54), 303 (21), *349*, *350*
Hunt, B. G., 281 (50), *283*
Hussain, A. K. M. F., 291 (13), 344 (13), *349*

I

Iaglom, A. M., 289 (6), 291 (6), *349*
Illingworth, C. R., 36, *88*
Ilyin, L. N., 130 (64), *160*
Imai, I., 21, 22 (97), *86*
Inger, G. R., 7, *84*
Irvine, T. F., Jr., 2 (1–7), *84*
Isachenko, V. P., 140 (73), 141 (73), 148, 149, *160*
Isata'yev, S. I., 103 (29), 104 (29), 105 (29), 132 (29), 133 (29), *159*

J

Jaeger, J. C., 3, 53 (10), 75 (10), 78 (10), *84*
Jakob, M., 176, 195, *227*
James, W., 128 (61), 130 (61), *160*
Jarmai, L., 66, *90*
Jaworski, W., 76 (279), 77 (279), *91*
Jefferys, B. S., 19 (94), *86*
Jeng, D. R., 19, *86*
Jischke, M. C., 56, *90*
Johnson, D. S., 299 (44), 305, *349*
Jones, J. R., 36 (205), *89*

K

Kahny, W.-H., 291 (11), 344 (11), *349*
Kantorovich, L. V., 22 (106), 28 (106), 57 (106), *86*
Kao, H. C., 13 (69), 14 (69), *85*
Kaplan, C., 184, *227*
Kaplun, S., 7, 13, *84*, *85*
Kasnov, M. L., 34 (178), *88*
Katinas, V. J., 113 (38), 123 (38), 124 (38), 125 (38), 129 (38), 130 (38), *159*
Kays, W. M., 94, 148, 157 (18), *159*
Kazakevich, F. P., 135, 137, 149, *160*
Keller, J. R., 13, *85*
Kestin, J., 122 (54, 55), *160*
Kevorkian, J., 13, *85*
Keyes, J. J., Jr., 293 (20), *349*
Khabakhpasheva, E. M., 297 (31), *349*
Kim, H. T., 300, 301 (52), 303 (52), 304 (52, 56), 344 (52), *350*
King, L. V., 94 (1), 128 (1), *158*
Kirk, P. S., 19, *86*
Kiselev, A. I., 34 (178), *88*
Klein, J. S., 22 (102), *86*
Klebanoff, P. S., 291, 300, 301 (48), *349*, *350*
Kline, S. J., 287 (2), 297 (30, 33), 300 (52), 301 (52), 303 (52), 304 (30, 52), 304 (30, 52), 305 (58), 344 (52, 65), *348*, *349*, *350*
Knopp, K., 14 (78), 17 (78), *86*
Kober, H., 49 (232), *89*
Koh, J. C., 34, *88*
Kostič, Ž, 108 (32), 109 (32), 110 (34), *159*
Kotorynski, W. P., 15 (79), 19, 68, 69 (267), 70 (267), *86*, *90*
Kourganoff, V., 34, *88*
Kozachenko, L. S., 94, *158*
Krall, K. M., 119, 120 (49), 121 (49), *160*
Krashtalev, P. A., 103 (29), 104 (29), 105 (29), 132 (29), 133 (29), *159*
Kreid, D. K., 298 (37), *349*
Kruger, C. H., Jr., 248, *282*
Kruskal, M., 28, *87*
Kruzhilin, G. N., 94 (14), 116, 120, 121, *159*
Krylov, V. I., 22 (106), 28 (106), 57 (106), *86*
Krylovich, V. I., 75, 76, 77 (278), *91*
Kubota, T., 12 (46), *85*
Kuiken, H. K., 12, *85*
Kumar, I. J., 6, 29, 30 (150), 31 (150), 40, 42 (213), 45, 46, 48, 56, 57, 61, 78 (281–283), *84*, *87*, *89*
Kuo, Y. H., 4, *84*
Kuznetsov, N. V., 94, 114 (39), 148, 149, *159*

L

Lagerstrom, P. A., 7, 12, *84*, *85*
Lahey, R., 304 (56), *350*
Lam, S. H., 11, *84*
Lamb, H., 96 (21), 100 (21), 103 (21), *159*
Landau, H. G., 31, 32, *87*
Lardner, T. J., 124 (110), *86*
Laufer, J., 300, 301 (46, 47), *350*
Launder, B. E., 288 (4), *348*
Laura, P. A., 49, *89*
Legras, J., 4, *84*
Leppert, G., 104, 105 (30), *159*
Levy, S., 22, *86*
Lewis, J. A., 164, 166, 169, 170, *226*
Li, T. Y., 19, *86*
Libby, P. A., 67, 68, *90*
Liepmann, H. W., 36, *88*

Lieu, S. W., 36 (207), 42 (207), *89*
Lighthill, M. J., 4, 22, 35, 36, 40, 42, *84*, *86*, 162 (6), *226*
Lilley, G. M., 36, *88*
Lindauer, G. C., 56, *90*
Liu, C. Y., 33 (157), *87*
Lock, G. S. H., 19, *86*
Lohrisch, W. L., 94 (7), *158*
Lokshin, V. A., 94 (12), *159*
London, A. L., 94, 148, 157 (18), *159*
Lorass-Nagy, V., 66, *90*
Love, T. J., 66, *90*
Lowder, J. E., 245, 256, *282*
Luikov, A. V., 3, *84*
Lyapin, M. B., 148, 149, *160*
Lyusternik, L. A., 13, *85*

M

MacGregor, R. K., 195, *227*
Mackie, J. W., 13, *85*
Mahony, J. J., 12, *85*
Makarenko, G. I., 34 (178), *88*
Makarevičius, M. M., 114 (42), 115 (42), *159*
Makarevičius, V. J., 95 (20), 109 (20), 113 (20), 116 (20), 138 (20), 141 (74), 142 (74), 143 (74), 145 (74), 146 (79), 151 (20), *159*, *160*
Malmuth, N. D., 11, 12 (35), *85*
Manabe, S., 281, *283*
Mandell, D., 264 (41), *283*
Mann, W. R., 36, *89*
Marcillat, J., 300, 301 (49), 329, *350*
Mariano, J., 281, *283*
Martin, B. W., 163, *226*
Martini, W. D., 167, 170, 172, 212, 224, *226*
Masle'yeva, N. V., 103 (29), 104 (29), 105 (29), 132 (29), 133 (29), *159*
Matsumoto, M., 78 (285), *91*
Mayinger, F. M., 135, 137, *160*
Mazur, P., 26 (134), 29 (134), *87*
Meel, D. S., 121, *160*
Meksyn, D., 14, 15 (76), *86*
Menard, W. A., 241, 243 (8, 9), 244, *282*
Menold, E. R., 170 (33, 34), 173, 198, 201, 203, 204, 205, 206, 207, 208, 209, 210, 211 (33), 216, 221, *226*
Mercer, A. McD., 70 (268), *90*
Merk, H. J., 19, *86*, 118, 120, 132, *160*
Mermangen, W. H., 273, *283*
Mighdoll, P., 252 (33), 253 (33), 258 (33), 259 (33), 278 (49), 279 (49), *283*
Mikhaylov, G. A., 134 (65), 135 (65), 136 (65), *160*
Mikhaylov, Y. A., 3, *84*
Mikhe'yev, M. A., 94 (15), 114 (15), 129 (15), 130 (15), *159*
Mikhlin, S. G., 34 (175), 57 (175), *88*, 258 (38), 279 (38), *283*
Millikan, R. C., 248 (21, 22, 24, 26), *283*
Milne-Thomson, L. M., 49 (231), *89*
Minkowycz, W. J., 35 (182, 183), *88*
Mirels, H., 36 (207), 42 (207), *89*
Mitchell, J. E., 293 (18), *349*
Möller, F., 281 (50), *283*
Monin, A. S., 289 (6), 291 (6), *349*
Montroll, E. W., 248, *282*
Mordchelles-Regnier, G., 184, 214, *227*
Morris, W. D., 6, *84*
Morse, P. M., 14 (77), 33 (77), 45 (77), *86*
Muchnik, G. F., 24, *87*
Mueller, H. F., 11, 12 (35), *85*
Mull, W., 165, 166, 176, 184, *226*
Murgai, M. P., 11, 13, *85*
Murray, J. D., 13, *85*
Muskhelishvili, N. I., 34 (176), 42, 53 (176), *88*, *89*

N

Nayfeh, A. H., 22 (105), *86*
Nazarov, N. I., 25, *87*
Nedderman, R. M., 297 (32), *349*
Negi, J. G., 65, *90*
Newell, M. E., 195 (45), *227*
Nicholl, C. I. H., 299 (45), 305, *350*
Nichols, R. A., 33, *88*
Nigam, S. D., 26, *87*
Noble, B., 49 (233), 50 (233), 52, *90*
Northup, L. L., 248, *282*
Novotny, J. L., 12, *85*, 257 (37), 273 (37), *283*

O

Ölcer, N. Y., 67, *90*
Ohring, G., 281, *283*
Oka, S., 110 (34), *159*

Olsofka, F. A., 257 (37), 273 (37), *283*
Olstad, W. G., 6, *84*
O'Melley, R., 13, *85*
Omohundro, G. A., 140 (70), *160*
Ostrach, S., 162 (4, 5), 163 (7, 52), 164 (52), 165, 166, 167, 169, 170 (33, 34), 171, 172 (36), 173, 192, 197, 201, 203–210, 211 (33), 212 (35), 213 (49), 214–222, 224, *226*, *227*
Ostroumov, G. A., 164, *226*
Oxenius, J., 273, *283*

P

Patankar, S. V., 35, *88*
Pedišius, A. A., 146 (78), *160*
Penner, S. S., 233, 241, *282*
Perelman, T. L., 36, 37, 38, 40, 42, *89*
Perkins, H. C., Jr., 104, 105 (30), *159*
Perlmutter, M., 54 (240, 241), 90
Pierson, O. L., 94 (10), *159*
Pillow, A. F., 165, 166, *226*
Piret, E. L., 128 (61), 130 (61), *160*
Pnueli, D., 33, *88*, 213 (49), 222, *227*
Poincaré, H., 4, *84*
Polezhaev, V. I., 169, *226*
Polykov, Yu. A., 24, *87*
Poots, G., 70 (268), *90*, 166, 173, 176, 194, *226*
Popovich, A. T., 293 (21), 298 (34), 303 (21), *349*
Prabhakara, C., 281, *283*
Prigogine, I., 26 (133, 135), 27 (138, 140), 32 (137, 138), *87*

R

Rackley, R. L., 29, *87*
Rafalski, P., 24, 33, *86*, *88*
Raizer, Yu. P., 246, 248, *282*
Rasool, S. I.. 231 (3) *282*
Rayner, S., 49, *89*
Read, R. W., 248 (25), *283*
Reiher, H., 94 (6), 158, 165, 166, 176, 184, *226*
Reynolds, W. C., 291 (13), 300(52), 301(52), 303 (52), 304 (52), 344 (13, 52, 65), *349*, *350*
Rhodes, P. C., 12, *85*
Richardson, P. D., 24, *87*
Rietschel, H., 94 (3), *158*
Robertson, J. M., 305 (57), *350*
Rosenweig, M. L., 70, 72, *91*
Roshko, A., 98, 99, 100, *159*
Rosner, D. E., 36 (199), *89*
Rubesin, M. W., 22, *86*
Runstadler, P. W., Jr., 297 (33), 305 (58), 344 (65), *349*, *350*
Ruseckas, T., 101, *159*
Rutner, Ya. F., 50, *90*

S

Sabzevari, A., 170, 172, 173, 210, 211, 212 (35), 215, 216, 219, 221, 224, *227*
Samoška, P. S., 114 (40), 130 (40), 145 (76), 146 (76), 147 (79), 151 (82), 152 (82), 153 (76, 82), *159*, *160*
Sampson, D. H., 252, 254 (31), *283*
Saunders, O. A., 165, 172, *226*
Savino, J. M., 35, *88*
Schad, O., 135, 137, *160*
Schechter, R. S., 32, *87*
Schenk, J., 70, *90*
Schimmel, W. P., 257, 273, *283*
Schlichting, H., 97 (23), *159*
Schmidt, E., 130 (63), *160*, 182, *227*
Schmidt, F. W., 195 (45), *227*
Schmidt, R. J., 165, 172, *226*
Scholz, F., 145 (77), 148, 149, *160*
Schraub, F. A., 297 (30, 33), 304 (30), 344 (65), *349*
Schultz, D. L., 293 (17), *349*
Scriven, L. E., 2, 24 (8), 25 (126), 32 (8, 126), *84*, *87*
Seader, J. D., 26, *87*
Sellars, J. R., 22 (102), *86*
Shastry, U. A., 44, *89*
Shea, J. J., 4, *84*
Sheeman, T. V., 149, *160*
Sherman, M., 213, *227*
Sholokhov, A. A., 49, *89*
Shreshta, G. M., 11 (33), *85*
Shvab, V. A., 94 (14), 121, *159*
Sidall, R. G., 295 (26), *349*
Siegel, A., 291 (11), 344 (11), *349*
Siegel, R., 33, 34, 35, 49, 53, 54 (240, 241, 242, 244), 55, *88*, *89*, *90*
Sih, G. C., 53, *90*
Simmons, G. M., 70, *90*
Simpson, C. J. C. M., 248 (23), *283*
Singh, R. N., 65, *90*
Skryabina, L. P., 50, *90*

Šlančiauskas, A. A., 95 (20), 109 (20), 110 (20), 115 (43), 116 (20), 138 (20), 142, 144 (75), 145 (75), 146 (78), 147 (79), 151 (20), *159*, *160*
Sleicher, C. A., 22 (103), *86*
Smith, J. W., 298 (35), 300 (54), 301 (54), *349*, *350*
Sneddon, I. N., 78 (280), *91*
Soengen, E., 120 (50), 121 (50), *160*
Sovershenny, V. D., 19, *86*
Spalding, D. B., 35, 36, *88*, 288 (4), *348*
Sparrow, E. M., 22, 33, 34, 74, *86*, *88*, 250 (30), 252 (30), 256 (30), 264 (30), *283*
Spencer, B. W., 292 (14), *349*
Stacy, E., 128 (61), 130 (61), *160*
Stallybrass, M. P., 33, *88*
Stasiulevičius, J. K., 114 (40), 130 (40), 145 (76), 146 (76), 151 (82), 152 (82), 153 (76, 82), *159*, *160*
Stein, R. P., 70, *90*
Sterling, C. W., 22 (103), *86*
Strickler, R. F., 281 (51), *283*
Sullivan, F. W., 140 (71), 144 (71), *160*
Surkov, G. A., 75, 76, 77 (277, 278), *91*
Švenčianas, P. P., 114 (42), 115 (42), *159*
Swigart, R. J., 13, *85*

T

Tamonis, M. M., 114 (42), 115 (42), *159*
Tanaka, M., 232 (4), 243 (4), *282*
Tanimoto, S., 299 (40), 305, *349*
Tao, L. N., 42, 43, 44 (216, 217, 218), *89*
Tarunin, E. L., 168, 173, *226*
Taylor, G. I., 286 (1), *348*
Terrill, R. M., 11 (33), *85*
Thiruvenkatachar, V. R., 78 (283), *91*
Thoma, H., 94 (5), *158*
Thomas, D. B., 299 (39), *349*
Thomas, R. N., 273 (44), *283*
Thornton, P. R., 163, *226*
Tien, C. L., 230, 231 (1), 245, 256, *282*
Tifford, A. N., 36, *88*
Tirski, G. A., 19, *86*
Tiwari, S. N., 248 (29), 252 (33), 253 (33, 35), 256 (35), 258 (33), 259 (33), 260, 263 (39), 267 (32), 276 (48), *283*
Tolubinski, E. V., 35, *88*
Townsend, A. A., 291, 299 (39), *349*
Trafton, L. M., 231 (2), *282*
Tribus, M., 22 (102), *86*
Tricomi, F. G., 34 (177), *88*
Trivedi, V. K., 42, *89*
Trohan, A. M., 298 (36), *349*
Tsederberg, N. V., 266, *283*
Tsien, H. S., 4, *84*
Tsoi, P. V., 33, 62, *88*, *90*
Tuchscher, J. S., 254 (10), 256 (10), 257 (10), 266 (10), *282*
Turilin, S. I., 114 (39), 148, 149, *159*
Tyagi, V. P., 44 (220, 222, 223), *89*

U

Ulinskas, R. V., 115 (43), *159*
Ulitko, A. F., 35, *88*

V

Vagt, J. D., 295 (25), *349*
van Atta, C. W., 291, *349*
Van der Hegge Zijnen, B. S., 127 (57), *160*
Van der Held, E. F. M., 176, *227*
Van Dyke, M., 4, 7, 12, 14, *84*, *85*, 214, *227*
Vanko, V. I., 65, *90*
van Thinh, N., 300, 301 (55), 344 (55), *350*
Varma, R. K., 11, 13, *85*
Varshavski, G. A., 49, *89*
Vasileva, A. B., 13, *85*
Vasilevski, K. K., 35, *88*
Vincenti, W. G., 14, *86*, 248, 249, 256 (36), 273, *282*, *283*
Visik, M. I., 13, *85*
Viskanta, R., 34 (167, 168), *88*
Vodicka, V., 65, *90*

W

Wang, L. S., 247, 273, *282*
Warming, R. F., 263 (40), *283*
Weihs, D., 29, *87*
Weinbaum, S., 169, 173, 202 (31), *226*
Weiss, R. O., 24, *87*
Welch, W. E., 163, *226*
Wenner, K., 130 (63), *160*
Wetherald, R. T., 281 (52), *283*
White, D. R., 248 (22), *283*
Whitelaw, J. H., 298, 342 (64), *349*, *350*
Wilkes, J. O., 168, 173, 193, 194, *226*
Wilkins, J E., 33 (158), *88*
Williams, M. J., 127 (58), 128, 130 (58), *160*
Willmarth, W. W., 293 (16), *349*

Wills, J. A. B., 296, 314, *349*
Winding, C. C., 135, *160*
Wolf, F., 36, *89*
Wood, R. T., 122 (55), *160*

Y

Yamamoto, G., 232, 243, *282*
Yang, K. T., 12, *85*
Yang, S. S., 293 (16), *349*
Yeh, T. T., 291, *349*
Yih, C. S., 19 (80), *86*

Z

Zapp, G. M., 122 (53), *160*
Zarič, Z., 293 (22), 299 (42), 306 (59), 307 (22, 42, 60, 61), 308 (22), 337 (62, 63), *349*
Zel'dovich, Ya. B., 246, 248, *282*
Zerbe, J. E., 135 (68), *160*
Zhuk, V. I., 36 (206), *89*
Zhukhovitskii, E. M., 164, 168, 173 (26), 212, *226*, *227*
Žiugžda, V., 101, 112 (35), 113 (38), 115 (35), 123 (38), 124 (38), 125 (38), 130 (38), 147 (79), *159*, *160*
Žukauskas, A.A., 95, 109 (20), 112 (35, 36), 113 (20, 37, 38), 114 (37, 42), 115 (35, 42), 116 (20), 123 (38), 124 (38), 125 (38), 128, 129 (37, 38), 130 (37, 38), 138 (20), 141 (74), 142 (74), 143 (74), 144 (75), 145 (74, 75), 146 (78), 147 (79), 151 (20), *159*, *160*
Zyszkowski, W., 24, 33, *87*, *88*

Subject Index

A

Ablation, 32
Absorption coefficient, 232
  in Elsasser band model, 237
Analytic iteration, 56
Aspect ratio, influence of, on free convection inside rectangular cavities, 184
Asymptotic expansion, 13
Asymptotic methods, 14, 37
Autocorrelation function, 344, 345

B

Band absorptance correlation, 256
Band absorptance models, 230
Beer's law, 239
Bethe–Teller relation, 248
Biharmonic equation, 42
Binary boundary layers, 19
Biot's variational principle, 23
Blasius solution, 67
Blockage ratio, 103
Blunt bodies, 13
Body forces, 164
Boltzmann distribution, 246
Boundary layers, 9–12, 14, 29
  for convection inside rectangular cavities, 181, 184
  in compressible flow, 35
  in dissociating gases, 36
  in laminar flow, 35
  in turbulent flow, 35
  with chemical reactions, 36, 40
  with dissociation, 42
  with heat transfer, 35
  with injection, 11, 12, 40
  with pressure gradient, 12, 35
  with radiation, 19
  with variable wall temperatures, 35
Boundary layer equations, 15, 117
Boundary layer separation, 100, 101
Boundary layer theory, 162
Boussinesq approximation, 175
Box model, 259

C

Calculus of variations, 22
Calibration, of hot wire probes, 312, 313
Carbon dioxide, gaseous radiation in, 273
  radiative transfer in, 256, 259, 260
  radiation–conduction interaction in, 266–273
  thermodynamic nonequilibrium in, 273
  variation with temperature of line half widths in, 232
Carbon monoxide
  collisional relaxation times in, 248
  comparison of thermodynamic equilibrium and nonequilibrium radiation results for, 274, 275, 276
  conduction–radiation interaction for thermodynamic nonequilibrium in, 277, 278
  infrared bands in, 231
  radiation–conduction interaction in, 266, 267, 272
  radiative transfer in, 259
Catalytic wall, 8
Cellular convection, 165
Centrifugal forces, 164
Change of phase, 75

Channel flow, 11, 32
  developed laminar flow in, 43
  forced convection in, 42
  in elliptic ducts, 70
  in rectangular ducts, 70
  with MHD, 56
  with slug flow, 54
Chemically frozen flow, 8
Chemically reacting boundary layers, 40
Collisional relaxation times
  in carbon monoxide, 248
  in diatomic gases, 248
Complex variables, 42
Composite media, 62
Conduction, 19, 33, 36, 166
  nonlinear problems in, 40
Conduction–radiation interaction
  comparisons for large path length limit, 268
  comparison of CO, CO_2, H_2O, and CH_4 results, 271, 272
  experimental measurements of, 273
  for carbon dioxide, 268, 269
  for carbon monoxide, 270, 277, 278
  for water vapor, 270
  thermodynamic nonequilibrium effects on, 276–278
Conduction regime, limits of, 179
Conjugate problems, 37, 40
Conservation equations, 27, 43
Constant heat flux, 119, 124
Constant surface temperature, 119
Convergence, 59, 60
Coriolis forces, 164
Couette flow, 29
Critical flow regime, 145
Critical point, 19
Critical Rayleigh number, 189
Crossflow, 93, 94, 99

D

d'Alembert paradox, 96
Degrees of freedom, 231
Depth of penetration, 180
Diatomic gases
  collisional relaxation times in, 248
  local thermodynamic nonequilibrium, 249
  radiation results for thermodynamic nonequilibrium, 275
Diatomic molecules, 230
Diffusion equation, 27
Dipole moment, 231
Dispersion, 327, 328
Dissociated boundary layers, 8, 9, 14, 19, 42
Dorfman's method, 74
Double correlations, of temperature and velocity components, 305
Drag, 99
  effect of roughness on, 112
  influence of free stream turbulence on, 103
  influence of heating on, 101
  influence of Reynolds number on, 102, 103
  influence of surface roughness on, 103
  in tube banks, 106, 111
  single tubes, 100
  convective heat transfer in, 33
Duhamel's principle, 78

E

Eigenfunction expansions, 66
Einstein coefficients, 232
Electric analogy, 111
Elliptical channel, 44
Elliptical equations, 13
Elsasser model, 237
Energy equation, 8, 21, 27, 43, 67, 71
  for radiatively participating gas, 246
  for transient conditions, 25
Entrance lengths, 32, 33
Entropy, 23
  minimum production of, 23
  production of, 27
Equations of transfer, for local thermodynamic nonequilibrium, 248
Equilibrium flow, 8
Euler–Lagrange equation, 27
Euler number, 150
Euler's transformation, 15
Exponential integral, 250

Exponential Kernel approximations, 251, 252
External problems, 161

F

Fins, 32
Flash photolysis, use of, in velocity measurements, 298
Flatness factor, 237–332, 340
Flat plate
  flow of transformer oil over a, 115
  glycerine flow over a, 115
  heat transfer in laminar flow, 115
  influence of heating or cooling on heat transfer, 115
  influence of Prandtl number on heat transfer, 115
  velocity and temperature measurements for turbulent flow over, 305
Flow regimes, in tube banks, 107
Fluid properties
  influence of, on heat transfer, 112
  influence of, in heat transfer to liquids, 128
Forced convection, 22
Form parameters, 319, 324
Fourier transform, 50
Fredholm integral equation, 35
Free convection, 11, 19, 53
Free convection effects, 127
Free stream turbulence level, influence of, on heat transfer, 122, 123
Free stream turbulence, influence of, on heat transfer in tube banks, 134
Free turbulence, 291
Freezing, 49
Friction velocity, 319
Fundamental band, 231

G

Gas flows, 94
Gaussian distribution, 335
Geophysical applications, 66
Graetz problem, 22
Gray gas, 259
Green's function, 53

H

Harmonic equation, 42
Harmonic oscillator, 232
  vibrational nonequilibrium in, 248
Hartree flow, 21
Heat conduction, 23, 29, 45, 48, 66, 67, 77
  in prismatic bar, 49
  solution by Wiener–Hopf method, 49, 50
  unsteady, 57
Heat conductivity, of rocks and soils, 45
Heat exchangers, 144, 150, 157
Heat shields, 11
Heat transfer
  in noncircular ducts, 44
  in separated regions, 120
  measurement of, in turbulent flows, 293
  natural convection in rectangular cavities, 179
Horizontal circular cylinders
  flow patterns for natural convection inside, 212
  governing equations for natural convection inside, 197
  influence of initial conditions on natural convection inside, 223
  influence of thermal boundary conditions on natural convection inside, 216, 217
  natural convection experiments using silicone oil, 211
  natural convection inside, 196
  streamline patterns for natural convection inside, 206–208, 216–219, 220, 221
  temperature profile for natural convection inside, 204, 205, 211, 212, 217, 219, 220, 222
  velocity profiles for natural convection inside, 204, 205, 209, 211, 217–219, 221, 222

Horizontal cylinders, natural convection in, 164, 165, 167, 169, 172
Hot-film sensors, 293
Hot-wire anemometers, 292, 293
  calibration procedures in, 294
  influence of nonisothermal flow on, 294
  influence of turbulence intensity on, 295
  influence of wire length on, 294
  statistical analysis of signals from, 336
Hot wire–cold wire method, 310
Hot wire probes
  aging of, 312
  calibration of, 312, 313
  construction of, 311
  cross-wire probes, 296
  electronic circuit of, 311
  sensitivity of, to flow direction, 296
  time constant of, 296
  wall effects on, 296
Hydraulic resistance, 150
  calculation of, in tube banks, 154
  influence of Reynolds number on, 151
  influence of tube pitch on, 152
  in in-line tube banks, 153
  in staggered tube banks, 152, 153
  in tube banks, 151
Hydrogen bubble technique, 297
Hyperbolic equations, 53
Hypersonic nozzles, 11

I

Ideal fluids, 95
Infinite horizontal plates, natural convection between, 165
Infrared emission, 230
Infrared radiating gas, temperature profiles in, 254
Infrared radiation, 229
Infrared spectrum, 231
Injection, 12, 40
In-line tube banks, 136, 137, 139–141, 143, 145, 146
  hydraulic resistance in, 151, 153
  pressure drop coefficients, 154
Inner expansion, 7
Integral equations, 34
Integral methods, 116, 163, 287
Interferometry, 176, 178, 179
Internal flows, 162
  effect of viscous dissipation in, 162
  influence of body forces on, 162
  thermal instabilities in, 162
Internal problems, 161
Inviscid flows, 13
Iteration, 28, 35

J

Jacobi-elliptic integral, 47
Joint probability density distribution, 337, 341

K

King's law, 294

L

Lagrangian thermodynamics, 23
Laguerre polynomials, 69
Laminar flow, in a circular tube, 22
Laminarization, 320
Langer's transformation, 21
Laplace transform, 38, 50
Large path length limit, 253, 257, 264
Laser–Doppler method, 298, 342
Line broadening, 231
Line intensity, 232
  variation of, with wavenumber, 233
Liouville's differential equation, 20
Liquid metals, 70
Liquids
  flow of, over single tubes, 128
  heat transfer in, 128
Local heat transfer
  forward stagnation point, 118
  influence of wall temperature distribution on, 126
  to flat plates, 116
  to single tubes, 116
  to wedge-shaped bodies, 117

Lorentz line profile, 232
for strong overlapping lines, 242
influence of pressure on, 232

M

Mach–Zehnder interferometer, 167, 273
Matched asymptotic expansions, 7, 214
Matching, 10
Mathematical methods, 1
Matrix algebra, 62
Mean heat transfer, 126, 138
in tube banks, 138
Mean heat transfer coefficients, calculation of, 127
Mean line width, 243
temperature effect on, 243
Meksyn's method, 14
Mellin transformation, 37–40
Melting, 30, 31, 34, 75
Melting cylindrical tube, 6
Melting slab, 4
Methane
radiation–conduction interaction in, 266, 267, 272
radiative transfer in, 259, 261
Method of steepest descent, 253
Method of characteristics, 53, 54
Method of intermediate limits, 13
Method of multiple scales, 12
Method of strained coordinates, 4
MHD channel flow, 56
Mixing length, 288
Modified Oseen linearization, 193
Momentum equation, 8, 27, 43, 67
for turbulent boundary layers, 288

N

Natural convection, 11, 12, 15, 161
between vertical isothermal plates, 167
between infinite parallel horizontal plates, 165
in a closed-end tube, 162, 163
in confined channels, 162
in interior of a horizontal cylinder, 164
inside horizontal cylinders, 167, 169, 196
in rectangular cavities, 166, 168, 169, 175
in rotating cylinders, 164
in spherical cavities, 164
Noncircular ducts
elliptical channels, 44
triangular channels, 44
Nonequilibrium, 250
Nonequilibrium source function, 249
Nonisothermal flows, 304
Nonlinear problems, 40
Nonoverlapping line limit, 236
Numerical stability, 172
Nusselt numbers
for natural convection in closed-end tubes, 164
for natural convection in rectangular cavities, 179–183, 195, 196
for natural convection inside square cavities, 194–196
influence of aspect ratio on, 184

O

Onsager's reciprocity relations, 25
Optically thick limit, 252, 253, 264
Optically thick radiation, 257, 258
Optically thin limit, 235, 252, 254, 256, 263, 265
influence of thermodynamic nonequilibrium on, 252, 258
Optical thickness, 12
Oscillators, rate of change of vibration energy in system of, 247
Oseen constants
for natural convection inside horizontal circular cylinders, 203
influence of, on temperature profiles, 208
Oseen method, 170, 172, 199, 214
Outer expansions, 7
Overtone bands, 231

P

Parabolic equations, 13, 57
Paraffin, natural convection to, inside rectangular cavities, 184

Penetration depth, 24
Perelman's method, 37
Perturbation methods, 3
  coordinate perturbation, 3
  parameter perturbation, 3
  regular perturbation, 3
  singular perturbation, 3
Perturbation solutions, 67
Phase change, 24, 29, 75
Planck mean coefficient, 259
PLK method, 3
Poiseuille flow, 29
Polyatomic molecules, 231
Porous media, 29
Power series, 13
Prandtl number, influence of, on heat transfer to tubes and tube banks, 112
Pressure broadening, 231
Pressure coefficient, 107
Pressure drop coefficients, in tube banks, 154
Pressure gradient flows, 305
Pressure path length, 235
Prismatic bars, conduction in, 49
Probability density distribution, 296, 337, 338
  of temperature, 325, 326, 329
  of velocity, 325, 326, 339, 342
Probability distribution, comparison of, for temperature and velocity measurements, 332, 333

R

Radiation, 11, 12, 34, 66
  application of Duhamel's principle to, 78
Radiation–conduction interaction, 264
  comparison between optically thin limit and large path length limit, 267
  in carbon dioxide, 266, 267
  in carbon monoxide, 266, 267
  in methane, 266, 267
  in water vapor, 266, 267
Radiatively participating gas, energy equation for, 246
Radiative equilibrium, 250, 277
Radiative flux equations, 250, 252
Radiative flux vector, 246
Radiative heat flux, 279
  comparison of, for several gases, 280
Radiative lifetime, 249
Radiative transfer, 255
  in carbon dioxide, 256, 259, 260
  in methane, 256, 259, 261
  in water vapor, 256, 259, 261
Radiative transfer equations, 70
Rayleigh number, 161, 166
  critical value of, 165
Rectangular cavities, 166, 174
  boundary layer regime in, 177
  centerline temperatures for free convection in, 178
  conduction regime in, 177
  dimensionless parameters for free convection in, 176
  flow oscillations for natural convection in, 189
  influence of horizontal partitions on free convection in, 182
  Nusselt numbers for natural convection in, 195, 196
  secondary flows for natural convection in, 189
  streamline patterns for natural convection in, 189
  temperature profile for natural convection in, 176
  tertiary flows for natural convection in, 190, 191
  transition regime in, 177
  velocity profiles for natural convection in, 176
Rectangular ducts, 70
Rectangular slot, natural convection in, 168, 169
Reference temperature, 95, 113
  use of, for heat transfer to single tubes and tube banks, 113
Regular perturbation, 3
Regular regime, 67
Resistance thermometers, 299
Reynolds number, influence of, on flow around cylinders, 97
Reynolds number effects, 121
Reynolds stress, 288
Rigid-rotor approximations, 233

Rigid-rotor, harmonic-oscillator model, 240
Ritz method, 28
Rosenzweig's matching technique, 70
Rosseland approximation, 264
Rosseland limit, 252, 253
Rotating disk, 22
Rotating cylinder, 164
Rotational quantum number, 232
Rotational transitions, 231
Roughness, 103
Round disks, 24

S

Schwartz–Christoffel transformation, 45, 46
  for natural convection inside rectangular cavities, 189
  for natural convection inside rectangular channels, 193
Semi-infinite solid, 24
Separation, 96
  heat transfer at, 120
  influence of Reynolds number on, 98
  in tube banks, 110
Separation point, 97
Series inversion, 14
Series truncation, 13
Shear stress distribution, 303
Shock wave–boundary layer interaction, 11
Silicone oil
  experiments with, in horizontal circular cylinders, 211
  natural convection to, in rectangular cavities, 184
Similarity regime, 163
Similarity theory, 94
Simultaneous heat and mass transfer, 62
Single band gas, 258
Single tubes, 94
  boundary layer on, 96
  combined free and forced convections, 127
  constant surface temperature, 119
  cross flow of air in, 113
  cross flow of oil in, 113
  cross flow of water in, 113
  distribution of skin friction around, 102
  drag coefficient for flow around, 102
  experimental velocity distribution around, 99
  flow pattern around, 95
  gas flows around, 94
  heat transfer to, 94, 112, 116
  heat transfer to air flow over, 124, 127, 129
  heat transfer to oil flow over, 124, 129
  influence of blockage ratio on heat transfer to, 132
  influence of blockage ratio in flow around, 103
  influence of heating or cooling on heat transfer to, 129
  local heat transfer on, 116, 119
  local Nusselt numbers on, 116
  mean heat transfer to, 126
  pressure distribution around, 96
  separation point on, 97, 100, 101
  turbulent boundary layer on, 97
  wake regime, 98
Singularities, 3
Singular perturbation, 3
Skewness factor, 329–332, 340
Slip, 95
Slug flow, 54
Solidification, 35
Sources, 15
Species equation, 8, 27
Spectral absorption coefficient, 231
Spectral band absorptance, 235, 240, 241
Spectral lines, 231
  half-width of, 232
  spacing of, 233
  strong overlapping lines, 236
  variation of intensity with rotational quantum number, 232
  variation with pressure and temperature, 232
Spectral radiative flux, 250
Spheres, 12
Square cavities
  natural convection inside, 188
  Nusselt numbers for natural convection in, 194, 195

Staggered tube banks, 135, 136, 139, 140, 142, 144, 146
  heat transfer in, 116
  hydraulic resistance in, 151–153
  influence of Reynolds number in, 110
  pressure drop coefficients, 155
  separation points in, 110
Stagnation point, 7, 19
Stanton number, 306
  increase in, due to turbulization, 306
  measured values of, in pressure gradient flows, 306, 307, 319
Statistical analysis, 335
  of hot wire signals, 336
Statistical models, 290
Steepest descent, 14
Streamlines
  for natural convection inside horizontal circular cylinders, 206–208, 211, 216–222
  for natural convection inside rectangular cavities, 189
Streamwise velocity component, RMS values of, in turbulent flows, 302
Stretched coordinates, 12
Strong nonoverlapping line limit, 239, 242
Strouhal number, 98, 99
  dependence of, on Reynolds number, 99
Sturm–Liouville equation, 68
Subcritical flow regime, 136, 142
Supercritical flow regime, 97
Sublimation, 19
Substitute kernel method, 34
Superflatness factor, 329, 330, 332
Superskewness factor, 329, 330, 332
Supersonic flow, 53
Surface emittance, 262
  influence on radiative transfer in gases, 262, 263
Surface radiosity, 250, 264
Surface roughness, 145

T

Taylor series, 34
Temperature
  measurements of, in turbulent flows, 316, 318
  measurement of, simultaneous with velocity, 309, 310
Temperature continuity, 253
Temperature distribution, for free convection in rectangular cavities, 166
Temperature flatness factor, 334
Temperature fluctuation
  for turbulent flows with pressure gradient, 325
  in turbulent boundary layer on a flat plate, 305
Temperature measurements
  correlation to, due to conduction, 317
  in turbulent flows, 299
Temperature profiles
  comparison of various methods for determining values of, in turbulent flow, 334
  comparison of, with velocity profiles, 334
  for free convection between vertical isothermal plates, 167
  for free convection in rectangular slot, 168
  for free convection inside horizontal cylinders, 167
  for natural convection in enclosed cavities, 171
  for natural convection inside horizontal circular cylinders, 170, 204, 205, 211, 212, 217, 219–222
  for natural convection in rectangular cavities, 176, 182–185, 191, 192
  for radiative equilibrium in gases, 279
  for turbulent flows with pressure gradient, 322, 324
  within an infrared radiating gas, 254
Temperature skewness factor, 333
Temperature slip, 257
Temperature spectra, 305
Tertiary flows, 190
  for natural convection inside rectangular cavities, 190, 191
Thermal boundary conditions, influence of, on natural convection inside cavities, 172
Thermal boundary layers, 14
  influence of Prandtl number on, 35
Thermal instabilities, 162, 165, 169, 212

for natural convection inside horizontal circular cylinders, 223
Thermal potential, 23
Thermodynamics, 23
Thermodynamic equilibrium, departures from, due to radiation, 246
Thermodynamic nonequilibrium
effects of, on conduction–radiation interaction, 277
for radiation in carbon monoxide, 274–276
for radiation in diatomic gases, 275
for radiation in single band gases, 274, 275
in gaseous radiation, 273
Total band absorptance, 234, 235, 241, 243
general correlations for, 244, 245
limiting forms of, 239
limiting solution of, by rigid-rotor, harmonic-oscillator band model, 242, 243
limiting values of, 235, 236
square root limit of, 239
Total band absorption, for Elsasser band model, 238, 239, 240
Total band intensity, 233
Trailing function, 25
Transducers, 292, 293
Transition, 97, 141
Transition regime, for natural convection inside rectangular cavities, 181
Transpiration, 32
Triangular channels, 44
Triple correlations, 289
of temperature and velocity components, 305
Tube banks
calculation of hydraulic resistance in, 154
closely spaced geometries, 147
combined free and forced convection, 140
comparison of available heat transfer results in, 148
comparison of heat transfer to staggered and in-line tube banks, 142, 148
comparison with single tubes, 134
critical flow in, 152
drag in, 106, 111
effect of roughness of heat transfer in, 145
efficiency of, 148
flow of gases in, 95
flow of viscous liquids in, 95
flow pattern in, 105
flow regimes in, 107
heat transfer in 94, 112, 141
heat transfer to, at high Reynolds numbers, 145
heat transfer to, at low Reynolds numbers, 140
heat transfer to, at subcritical or mixed flow conditions, 142
hydraulic resistance in, 94, 150
heat transfer to viscous liquids in, 144
hydraulic resistance of, 150, 151
influence of number of rows on heat transfer, 156
influence of pitch on heat transfer in, 111, 135, 142, 144, 146
influence of Reynolds number in, 106
influence of tube pitch, 108
influence of turbulence intensity on heat transfer in, 134
in-line arrangement, 105
local heat transfer in, 133, 135, 137, 138
mean heat transfer in, 138
Nusselt number calculations for gas flow through, 156
optimal arrangement of, 157
physical properties, influence of, 95
potential flow through, 111
pressure coefficient in, 107, 108
relative efficiency of in-line and staggered tube banks, 157
staggered arrangement, 105
transition in, 141, 152
velocity distribution in, 107
Tube flow, 22, 29
Tubes, natural convection in, 163
Turbulence, 285
as a statistical phenomenon, 286
energy diffusion in, 289
energy dissipation in, 289
energy generation in, 289
experimental methods in, 292
influence of, on heat transfer, 290

in grids, 291
kinetic energy of, 288, 289
length scales in, 289
near walls, 291
statistical model of, 290
wave approach to study of, 344
Turbulence energy production, 303
Turbulence intensities, comparison of, for isothermal and nonisothermal turbulent flows, 323
Turbulence intensities, 122, 138
Turbulence intensity
influence of, on heat transfer, 138, 140
measurements of, for turbulent channnel flow, 321
measurement of, in pressure gradient flow, 308, 309
influence of, in hot-wire anemometry, 295
Turbulence intensity distributions, experimental measurements of, 302
Turbulence level, influence of, on flow pattern, 103
Turbulent boundary layers, 35
Turbulent flows
comparison of nonisothermal and isothermal conditions, 323
for isothermal, incompressible, zero-pressure, gradient conditions, 299
for nonisothermal conditions, 305
momentum equations for, 288
prediction methods for, 287
simultaneous measurement of velocity and temperature in, 310
statistical analysis of, 335
velocity and temperature profiles in, 334
Turbulent fluctuations, 287
Turbulent heat flux, 290
Turbulent Prandtl number, 290
Turbulent viscosity, 288
Turbulization, 305

U

Unicellular motion, 185
Uniform heat sources, in radiating gases, 254, 255
Unstretched coordinates, 12

V

Variable surface temperature, 126
Variable wall temperature, 35, 163, 164
Variational calculus, 32
Variational methods, 22
based on local potentials, 26
Velocity
comparison of various methods for determining values of, 328, 329
measurement of, by laser–Doppler method, 298
measurement of, by visual techniques, 297
measurement of, in turbulent flows, 292
measurements of, in turbulent pressure gradient flows, 320
measurement of, near a wall in turbulent flows, 314, 316
measurement of, simultaneous with measurement of temperature, 309, 310
Velocity profiles
comparison of, for isothermal and nonisothermal turbulent flows, 323
comparison of various methods for determining values of, in turbulent flows, 334
experimental measurements of, in pressure gradient flows, 307
for free convection inside horizontal cylinders, 167
for natural convection in enclosed cavities, 171
for natural convection inside circular cylinders, 170, 204, 205
for natural convection inside horizontal circular cylinders, 209, 211, 217–219, 221, 222
for natural convection in rectangular cavities, 176, 184–186, 191, 192
for nonisothermal turbulent flows with pressure gradient, 322
measurement of, in turbulent pipe flow, 303
Velocity spectra, 346

Vertical parallel plates, 162
  natural convection between, 165, 166
Vibrational nonequilibrium, 248, 250
Vibrational relaxation time, 247, 248
Vibrational transitions, 231
Vibration–rotation bands, 230, 231
Vibrations, 99
Volumetric absorption coefficient, 232
  variation of, over entire band, 234
Viscosity, influence of, on heat transfer to tubes and tube banks, 114
Viscous dissipation, 162
Visual techniques, 297
  hydrogen bubble technique, 297
  use of, in velocity measurements, 297
  use of, for velocity profile measurements, 303
Volterra integral equation, 38
Volume dissipation function, 23
Von-Misses transformation, 74
Vorticity, 165, 166, 170
Vortex shedding, 98
Vortices, 96, 97
  shedding of, 99
  vibrations due to, 99

W

Wakes, 98
  influence of Reynolds number on, 98
  symmetrical regime in, 98
  velocity fluctuations in, 98
Wall effects, 314
  in turbulence measurements, 296, 297
  measurements of, 315
  on probability density distributions, 326
Wall shear stress, fluctuations in, 293
Wall turbulence, 304
  experimental measurements of, 300, 301
Water vapor
  radiation–conduction interaction in, 266, 267, 270, 272
  radiative transfer in, 256, 259, 260
  rotation bands in, 231
Wavenumber, 232
Wedge flows, 35
Wedge-shaped bodies, 117
Weighted residuals, 32
Wiener–Hopf method, 49
Wires, 127
WKBJ method, 19

This Page Intentionally Left Blank